Universidade de Aveiro Departamento de Engenharia Cerâmica e do Vidro
2009

Olena Okhay

Filmes à base de $SrTiO_3$ para aplicações em dispositivos sintonizáveis

Strontium titanate based films for tunable device applications

Universidade de Aveiro Departamento de Engenharia Cerâmica e do Vidro
2009

Olena Okhay

Filmes à base de $SrTiO_3$ para aplicações em dispositivos sintonizáveis

Strontium titanate based films for tunable device applications

dissertação apresentada à Universidade de Aveiro para cumprimento dos requisitos necessários à obtenção do grau de Doutor em Engenharia e Ciência de Materiais, realizada sob a orientação científica da Dr. Paula M. L. S. Vilarinho, Professora Associada do Departamento de Engenharia Cerâmica e do Vidro da Universidade de Aveiro e do Dr. Aiying Wu, Investigador auxiliar do Departamento de Engenharia Cerâmica e do Vidro da Universidade de Aveiro

Dissertation presented to the University of Aveiro to obtain the Doctor degree in Materials Science and Engineering, under the scientific guidance of Dr. Paula M. L. S. Vilarinho, Associate Professor of the Department of Ceramics and Glass Engineering of the University of Aveiro, and Dr. Aiying Wu, Researcher of the Department of Ceramics and Glass Engineering of the University of Aveiro

o júri

presidente

Dr. Henrique Manuel Morais Diz

Professor Catedrático do Departamento Economia, Gestão e Engenharia Industrialda Universidade de Aveiro

Dr. Joaquim Manuel Viera

Professor Catedrático do Departamento de Engenharia Cerâmica e do Vidro da Universidade de Aveiro

Dr. Abílio de Jesus Monteiro Almeida

Professor Associado com Agregação do Departamento de Física, Faculdade de Ciências da Universidade do Porto

Dr. Maria Clara Henriques Baptista Gonçalves

Professora Auxiliar do Departamento de Engenharia de Materias, Instituto Superior Técnico da Universidade Técnica de Lisboa

Dr. Paula Maria Lousada Silveirinha Vilarinho

Professora Associada do Departamento de Engenharia Cerâmica e do Vidro da Universidade de Aveiro (orientadora)

Dr. Aiying Wu

Equiparada a Investigadora Auxiliar do Centro de Investigação em Materias Cerâmicos e Compósitos (CICECO) da Universidade de Aveiro (co-orientadora)

acknowledgments

This work is a result of a wide collaboration with many people who helped me on different stages of this work. I want to express my thanks to all of them.

First of all, I am very grateful to my supervisor Paula Vilarinho for invitation to the PhD study in Aveiro and constant support. Her extended answers on all my questions and our discussions helped not only to interpret the results reported herein but also to understand many related phenomena.

Many thanks to my co-supervisor Aiying Wu for her guidance and support.

I have enjoyed working with the members of my group, who have supported me from the beginning. This concerns not only scientific work but also friendly and cheerful atmosphere in the department. In order not to miss some of their names, I want to thank all of them.

I have benefited greatly from the collaboration and discussions with Prof. Ian Reaney and Dr. Jan Petzelt, to whom I express my gratitude.

I am very grateful to my husband Oleksandr Tkach, who has assisted me greatly with this research and preparation of the Thesis, and to my very little son Ostap for their support, patience and love, which helped me to surmount all obstacles during this work.

I would also like to thank my family for their patience over the years. Most importantly, I thank my parents, Ivan and Lubov, and my brother, Oleksandr, to whom I owe everything. They have been my most valuable source of encouragement, and I thank them for all their love and support.

I acknowledge the Portuguese Foundation for Science and Technology for financial support.

palavras-chave

titanato de estrôncio, filmes, caracterização estrutural, tensões da rede, tensões térmicas, efeito de dopantes, propriedades dieléctricas, sintonabilidade

resumo

O $SrTiO_3$ (ST) cristaliza com a estrutura da perovesquite e apresenta propriedades de um paraeléctrico quântico; isto é, exibe um aumento continuo da permitividade dieléctrica com o decréscimo da temperatura até 4K, seguido de um patamar de valor constante até cerca de 0K. A presença de imperfeições na rede, tais como defeitos pontuais, impurezas e tensões podem modificar apreciavelmente as propriedades do ST puro e mesmo induzir ferroelectricidade.

Neste trabalho foi conduzido um estudo sistemático da estrutura, microestrutura e comportamento dieléctrico de filmes finos não dopados e dopados de ST policristalino preparados por sol gel e depositados sobre diferentes substratos. As propriedades dieléctricas foram estudadas numa gama alargada de temperatura e frequência do campo eléctrico. A caracterização dieléctrica dos filmes foi efectuada em função da temperatura e frequência desde o regime das frequências rádio (rf), terahertz (THz-TDS) e infra vermelho (IR). As características cristalográficas e microestuturais dos filmes de ST foram analisadas por difracção de raios X (DRX), espectroscopia de Raman, microscopia electrónica de varrimento (SEM) e de transmissão (TEM), espectroscopia de Rutherford Backscattering (RBS). Foi feito um estudo detalhado da dinâmica de rede destes materiais.

É mostrado neste trabalho que filmes finos de ST não dopados e crescidos em diferentes substratos (Al_2O_3/Pt, Si/SiO_2/TiO_2/Pt, $(LaAlO_3)_{0.3}$-$(Sr_2AlTaO_6)_{0.7}$/Pt, $SrTiO_3$/Pt and MgO/Pt) apresentam diferentes características estruturais e propriedades eléctricas, directamente dependentes das tensões criadas nos filmes. Nos grãos dos filmes de ST depositados sobre substratos de MgO/Pt devido às elevadas tensões compressivas originadas pelo substrato observam-se deslocações do tipo “slip band dislocations”, Enquanto que o modo TO1 de filmes de ST depositados sobre Al_2O_3 se comporta de maneira muito semelhante aos cristais de ST na gama de temperatura entre 300K e 150K, o modo TO1 dos filmes de ST depositados sobre substratos de MgO apresenta-se endurecido, o que se pode explicar pela influência das tensões geradas nos filmes pelo substrato. Filmes de ST com as tensões compressivas mais elevadas, depositados sobre substratos de MgO/Pt exibem os valores mais elevados da parte real da permitividade dieléctrica (ε'), a maior resposta histerética da polarização em função do campo eléctrico aplicado e os maiores valores da sintonabilidade dieléctrica (n_r), em oposição aos filmes de ST, depositados sobre substratos de Al_2O_3/Pt com as tensões tractoras mais elevadas.

Neste trabalho é também salientada a importância dos aspectos tecnológicos da preparação por sol gel, na qualidade dos filmes finos de ST, que se reflecte nos valores elevados de ε' and n_r, que são obtidos por pela introdução de camadas intermédias tampão (buffer layers) e pelo aumento da temperatura de

queima de 750°C para 900°C.

Com base em previsões teóricas, de que o deslocamento de iões de pequenas dimensões ("off centre") como o Mg, nos locais dos iões Sr da rede induzem uma anomalia na resposta dieléctrica do ST, foi estudada a incorporação de Mg na rede dos filmes de ST. Foi observado que o limite de solubilidade sólida de Mg na rede de ST é dependente do local da rede no qual ocorre a incorporação do dopante e da temperatura do tratamento térmico. Aumentando a temperatura do tratamento térmico decresce a solubilidade do magnésio nos filmes de $Sr_{1-x}Mg_xTiO_3$ de $x > 0.30$ a 750°C para $x < 0.15$ a 900°C. De acordo com este estudo, o Mg não induz um estado ferroeléctrico nem um comportamento do tipo relaxor em filmes finos de titanato de estrôncio preparados por sol gel, quer quando a substituição ocorre nos locais A ou B da rede do ST.

A estrutura, dinâmica de rede e propriedades dieléctricas de filmes finos de ST dopados com Bi são também apresentados neste trabalho e discutidos pela primeira vez. Nos filmes de $Sr_{1-1.5x}Bi_xTiO_3$ o modo TO1 torna-se mais duro e independente da temperatura e uma relaxação a baixas frequências aparece com o aumento do conteúdo de Bi. A posição do máximo de ε' dos filmes estudados desloca-se para temperaturas mais altas com o aumento da concentração de Bi e com o aumento da frequência. A presença de "clusters" de dimensões nanométricas e dos iões de Bi em posição "off centre" causa uma relaxação dieléctrica complexa. A relaxação dieléctrica induzida segue, a lei de Arrhenius para as amostras com baixo teor de Bi ($x < 0.04$), e a relação de Vogel-Fulcher para as amostras com as concentrações de dopante mais elevadas ($0.04 \leq x \leq 0.167$). A dispersão da frequência de ε' em filmes finos de $Sr_{1-1.5x}Bi_xTiO_3$ com pequenos teores de Bi é ligeiramente suprimida, quando em comparação com os cerâmicos correspondentes, o que pode ser explicado pela influência do substrato no caso dos filmes finos. Este estudo ilustra que a incorporação de Bi na rede de ST origina um comportamento do tipo relaxor, aumentando a tunabilidade dieléctrica. Filmes finos de $Sr_{1-1.5x}Bi_xTiO_3$ com elevados factores de qualidade (> 2000 numa gama de temperatura alargada) são candidatos apropriados para utilização em sintonizadores.

keywords

Strontium titanate, films, structural characterisation, lattice strain, thermal stress, dielectric properties, doping effect, tunability

abstract

$SrTiO_3$ (ST), crystallizing in the perovskite type structure, is a quantum paraelectric, i.e., it exhibits a continuous increase of the dielectric permittivity with decreasing temperature down to 4K, followed by the levelling off of the permittivity to near 0K. The presence of lattice imperfections such as strain, point defects, grain boundaries, and impurity atoms can appreciably modify the properties of pure ST and even induce ferroelectricity.

In this work, systematic research on the structure, microstructure and dielectric behaviour of polycrystalline $SrTiO_3$ - based thin films prepared by sol-gel is performed. The dielectric properties are studied in a wide temperature, frequency and electric field ranges. For some films the dielectric characterisation is assessed at radio-frequency (rf), time-domain terahertz (THz-TDS), and infrared (IR) spectroscopy. The crystallographic and micro structures of the undoped and doped ST films are analysed by X-ray diffraction (XRD), Raman spectroscopy, scanning and transmission electron microscopy (SEM and TEM) and Rutherford Backscattering Spectrometry (RBS) techniques. Detailed investigations of the lattice dynamics in a wide frequency range is undertaken as well.

It was observed, that undoped ST films grown on different substrates (Al_2O_3/Pt, Si/SiO_2/TiO_2/Pt, $(LaAlO_3)_{0.3}$-$(Sr_2AlTaO_6)_{0.7}$/Pt, $SrTiO_3$/Pt and MgO/Pt) have different structural and dielectric properties dependent on the strain/stress effect induced by the substrate. For the case of ST films on MgO substrates the appearance of some “slip band dislocations” within the film grains was detected due to the high compressive stresses from the substrate. Whereas TO1 mode of ST films deposited on Al_2O_3 behaves similarly to that of ST single crystals in the temperature range from 300K to 150K. TO1 mode of ST films deposited on MgO substrate is stiffened, what can also be explained by influence of the stresses. ST films, with the highest compressive stress, deposited on MgO/Pt substrate shows the highest value of the real part of the dielectric permittivity (ε'), the largest hysteresis loop, and the highest value of the dielectric tunability (n_r) in opposition to ST films, with the highest tensile stress, deposited on Al_2O_3/Pt substrates.

The role of the technological aspects associated with the preparation of high-quality sol-gel ST films is reflected in the elevated ε' and n_r of ST films, obtained by introducing buffer layers, intermediately annealed at 600°C, and by increasing films annealing temperature from 750°C to 900°C. As a consequence ε' and n_r of ~700 and ~50% are attained, being among the highest values reported for ST sol gel based films.

Based on the theoretical prediction, that the off-centre displacements of small Mg ions at the large Sr sites can induce dielectric anomalies in ST, the incorporation of Mg in ST films was addressed in this work. Solid solubility limit

of Mg was found to depend on the lattice site of incorporation and annealing temperature. Increasing annealing temperature decreases the solubility in $Sr_{1-x}Mg_xTiO_3$ thin films from $x > 0.30$ for 750°C to $x < 0.15$ at 900°C. Moreover Mg does not induce ferroelectricity or relaxor-like behaviour in strontium titanate, either located in A- or B-site of the $SrTiO_3$ lattice.

Within this work, the structure, low temperature lattice dynamics and dielectric properties of Bi doped ST films are described and discussed for the first time. In $Sr_{1-1.5x}Bi_xTiO_3$ films TO1 mode becomes harder and, concomitantly a temperature independent and low-frequency relaxation appears with increasing of Bi content. The position of the maximum of ε' of the investigated films shifts to high temperatures with increasing Bi content and frequency. The presence of nanoclusters and off-centred Bi ions causes a complex relaxation dynamics in these films. The induced dielectric relaxation follows the Arrhenius law for the samples with low Bi content ($x < 0.04$) and the Vogel-Fulcher law for the samples with a higher doping concentration ($0.04 \leq x \leq 0.167$). The frequency dispersion of ε' in $Sr_{1-1.5x}Bi_xTiO_3$ thin films with small amount of the Bi is slightly suppressed, compared to the corresponding ceramics, what can be explained by the influence of substrate. Bi incorporation in ST lattice leads to a relaxor-type dielectric response, increasing the dielectric tunability. $Sr_{1-1.5x}Bi_xTiO_3$ thin films with high value of the quality factor (> 2000 in wide temperature range) are appropriate candidates for using in tunable applications.

Table of Contents

List of Symbols xv
List of Figures xix
List of Tables xxxiii

Chapter 1. Introduction and objectives 1
1.1. Why sol-gel derived $SrTiO_3$ films? 1
1.2. Why $SrTiO_3$ films doped by Mg? 4
1.3. Why $SrTiO_3$ films doped by Bi? 5

Chapter 2. Background and literature review 7
Introduction 7
2.1. Bulk $SrTiO_3$: an incipient ferroelectric 8
2.1.1. Crystal structure and phase transitions 8
2.1.2. Lattice dynamics of $SrTiO_3$ 10
2.1.3. Dielectric behaviour of undoped $SrTiO_3$ bulk 13
2.2. Undoped $SrTiO_3$ films 19
2.2.1. Lattice dynamics and dielectric response 19
2.2.2. Temperature dependence of the dielectric response 20
2.2.3. Field effect on dielectric response and tunability in $SrTiO_3$ films 26
2.2.4. Strain influence 32
2.3. Dielectric behaviour in doped $SrTiO_3$ 44
2.3.1. Ba doped $SrTiO_3$ bulk and films 44
2.3.2. Pb doped $SrTiO_3$ bulk and films 50
2.3.3. Ca doped $SrTiO_3$ bulk and films 53
2.3.4. Mg doped $SrTiO_3$ bulk 57
2.3.5. Bi doped $SrTiO_3$ bulk 61
2.4. Methods for deposition of ferroelectric thin films 69
2.4.1. Pulsed laser deposition 72
2.4.2. *rf*-sputtering deposition 74
2.4.3. Molecular beam epitaxy 75
2.4.4. Metallo-organic chemical vapour deposition 76
2.4.5. Sol-gel fabrication of films 77
2.4.5.1. Preparation of chemical solutions 78
2.4.5.2. Deposition process 79
2.4.5.3. Heat treatment process 81

2.5. Application of $SrTiO_3$ films 83
2.5.1. Memory applications 83
2.5.2. Tunable application 87
Summary 94

Chapter 3. Experimental procedure: preparation and characterization of thin films 95
3.1. Sol-gel fabrication of thin films 95
3.1.1. Preparation of solutions 95
3.1.2. Deposition of films 97
3.2. Crystallographic and microstructure characterization 99
3.2.1. X-Ray diffraction analysis 99
3.2.1.1. Standard X-Ray diffraction measurements 99
3.2.1.2. Grazing incidence measurements 100
3.2.1.3. Residual strain measurements and stress calculations 103
3.2.2. Microstructure analyses 106
3.2.2.1. Scanning electron microscopy 106
3.2.2.2. Transmission electron microscopy 108
3.2.2.3. Atomic force microscopy 110
3.2.3. Raman spectroscopy 112
3.2.4. Rutherford backscattering spectrometry 113
3.3. Dielectric measurements 114
3.3.1. Dielectric response measurements in *rf* range 115
3.3.2. Dielectric measurements at applied field in *rf* range 116
3.3.2.1. Permittivity under bias field 116
3.3.2.2. Polarization versus electric field 117
3.3.3. Infrared spectroscopy 118
3.3.4. Terahertz time-domain spectroscopy 119

Chapter 4. Polycrystalline $SrTiO_3$ thin films: influence of processing on the microstructure, structure and low temperature dielectric properties 121
Introduction 121
4.1. Preparation and characterisation 123
4.2. Microstructural properties 124
4.2.1. SEM analysis 124
4.3.2. AFM analysis 126
4.3. Crystal structure and stress calculation 128
4.4. Low temperature dielectric properties 134

4.4.1. Dielectric response as function of temperature and frequency 134
4.4.2. *dc* field effect and dielectric tunability 141
4.4.3. *P(E)* hysteresis response 146
Summary 149

Chapter 5. Polycrystalline $SrTiO_3$ thin films: influence of substrate on the microstructure, structure and low temperature dielectric properties 151
Introduction 151
5.1. Preparation and characterisation 152
5.2. Structural characterization 153
5.2.1. Crystal structure and lattice parameter 153
5.2.2. Strain measurements and stress calculations 158
5.2.3. Raman analysis 162
5.3. Microstructure analysis 164
5.3.1. SEM analysis 164
5.3.2. AFM analysis 166
5.3.3. TEM analysis 168
5.4. Low temperature dielectric properties 171
5.4.1. Dielectric response as function of temperature 171
5.4.2. IR measurements 178
5.4.3. *dc* field effect and dielectric tunability 181
5.4.4. *P(E)* hysteresis response 187
Summary 191

Chapter 6. Mg-doped $SrTiO_3$ thin films: microstructure, structure and low temperature dielectric properties 193
Introduction 193
6.1. Preparation and characterisation 194
6.2. Microstructure properties 195
6.2.1. SEM analysis 195
6.2.2. AFM analysis 199
6.2.3. TEM analysis 202
6.3. Rutherford backscattering spectrometry analysis 205
6.4. Crystal structure and lattice parameters 207
6.5. Lattice dynamics study 212
6.5.1. Raman spectroscopy analysis 212
6.5.2. IR and THz-TDS analysis 214

6.6. Low temperature dielectric properties 218
6.6.1. Dielectric response as function of temperature 218
6.6.2. *dc* field effect and dielectric tunability 216
6.6.3. *P(E)* hysteresis response 233
Summary 237

Chapter 7. Bi doped $SrTiO_3$ thin films: microstructure, structure and low temperature dielectric properties 239
Introduction 239
7.1. Preparation and characterisation 240
7.2. Microstructural properties 241
8.3.1. SEM analysis 241
8.3.2. AFM analysis 242
8.3.3. TEM analysis 244
7.3. Crystal structure and lattice parameter 245
7.4. Lattice dynamics study 247
7.4.1. Raman spectroscopy analysis 247
7.4.2. IR spectroscopy analysis 248
7.5. Low temperature dielectric properties 251
7.5.1. Dielectric response as function of temperature and Bi content 251
7.5.2. Frequency dependence and relaxation dynamics 260
7.5.3. *dc* field effect and dielectric tunability 267
7.5.4. *P(E)* hysteresis response 272
Summary 277

Chapter 8. Conclusions 279
8.1. Polycrystalline thin films of undoped $SrTiO_3$: influence of the deposition procedure and substrate 279
8.2. Effect of Mg incorporation in $SrTiO_3$ thin films 283
8.3. Effect of Bi incorporation in $SrTiO_3$ thin films 284
8.4. Suggestions for further work 286
Bibliography 287
List of publications 301

List of Symbols

A - fitting parameter
a - cubic unit cell parameter
a, b, c - unit cell parameters (*a - in-plane lattice parameter*, *c – out-of-plane lattice parameter*)
a_0 –lattice parameter of a mechanical free unit cell
$a_{\parallel}$ - in-plane lattice spacing
a_{film} –lattice parameter of film
$a_{substrate}$ –lattice parameter of substrate
C - Curie constant
Cp – capacitance of parallel plate capacitor
d - space between the planes (lattice spacing)
d_{ψ} – lattice spacing for each ψ
E – Young's modulus
E_{dc} - *dc* bias electric field
E_{max} - maximum applied bias electric field
f - frequency
ħ - reduced Plank constant (1.05458×10^{-34} Js)
$\hbar\omega_{in}$ – simultaneously annihilating the incident phonon
$\hbar\omega_{sc}$ – creating the scattering phonon
$\hbar\Omega$ – energy associated with the phonon created or annihilating in the scattering process
i - imaginary operator
K - quality factor of a tunable component
k – short range force coefficient between ions (5.5×10^4dyn/cm)
k_B - Boltzmann constant (1.38066×10^{-23}J/K)
m - mass
N_c - coordination number
n - tunability
n_r - relative tunability
n_{max} - relative tunability at maximum applied bias electric field
OR – reactive alkoxy group
OR' – less reactive methoxyethoxy group
P - polarization
P_r -remnant polarization
P_s - spontaneous polarization
P_{satur} - saturation polarization
Q - quality factor
Q_{11}, Q_{12} – electrostrictive constants
q - wave-vector
r - ionic radius
S - area of electrodes
S_1^{hkl}, S_2^{hkl} – X-Ray elastic constants for the *hkl* planes
s_{11}, s_{12} – elastic compliance

T - temperature
T_0 - Curie temperature
T_1 - temperature of crossover between classical and quantum behaviour
T_a - temperature of antiferrodistortive phase transition
$T_{ann.}$ – annealing temperature
T_c - temperature of ferroelectric phase transition
T_f - freezing temperature
T_{free} – transition temperature for a mechanically free film
$T_{in\text{-}plane}$ – transition temperature for the film under tensile stress resulting in polarization being oriented "in-plane"
$T_{out\text{-}of\text{-}plane}$ – transition temperature for the film under compressive stress resulting in polarization being oriented "out-of-plane"
$T_{\varepsilon'max}$ - temperature of the maximum of the real part of dielectric permittivity
$T_{\varepsilon''max}$ - temperature of the maximum of the imaginary part of dielectric permittivity
t – film thickness
$\tan\delta$ - dielectric loss or dissipation factor
$\tan\delta(0)$ - zero-field dissipation factor
$\tan\delta(E_{max})$ - dissipation factor under maximum applied bias electric field
U - activation energy
V – voltage
V_o – vacancy of oxygen
V_{Sr} – vacancy of strontium
x - A-site dopant concentration
x_c - critical concentration
y - B-site dopant concentration
α – thermal expansion coefficient
α_f - thermal expansion coefficient of film
$\alpha_f(T)$ – temperature dependence of thermal expansion coefficient of film
α_s - thermal expansion coefficient of substrate
$\alpha_s(T)$ – temperature dependence of thermal expansion coefficient of substrate
γ – Poisson ratio
γ_i - inverse dielectric susceptibilities
ΔE - energy uncertainty
Δq - uncertainty in the structural coordinate
Δp - impulse uncertainty
$\Delta\omega$ - Raman shift
Δz – ferroelectric displacement
$\overline{\Delta z}$ - quantum mechanical displacement
δx - deviation of concentration
ε_0 - dielectric permittivity of vacuum (8.854×10^{-12} F/m)
ε^* - complex dielectric permittivity
ε' - real part of dielectric permittivity
ε'' - imaginary part of dielectric permittivity
ε_{dc} - static dielectric permittivity

ε_∞ - dielectric permittivity at high frequency
$\varepsilon'(0)$ - zero-field real part of dielectric permittivity
$\varepsilon'(E_{dc})$ - real part of dielectric permittivity under bias electric field
ε'_{max} - maximum real part of dielectric permittivity
μ_B - Bohr magneton (9.274×10^{-24} J/T)
θ - diffraction angle
λ - wavelength
π – constant (3.1416)
σ - uniaxial stress
$\sigma_\parallel$ -in-plane stress
σ_{c1}, σ_{c2} - critical values of uniaxial stress
σ_{th} – thermal stress
τ - relaxation time
τ_0- relaxation time pre-exponential factor
τ_ε - temperature coefficient of dielectric σ - uniaxial stress
Φ - thermodynamic potential
Φ_0 - thermodynamic potential for the case of zero spontaneous polarisation
χ' - real part of dielectric susceptibility
χ'' - imaginary part
ψ - angle 90°-δ
ω - angular frequency
ω_{LO} - long-wave longitudinal optical phonon frequency
ω_{TO} - long-wave transverse optical phonon frequency
ω_{in} - incident phonon frequency
ω_{sc} - scattering phonon frequency
ω_s - soft mode frequency
Ω - created phonon or annihilated phonon frequency

Abbreviations

ac - alternating current
AFM – atomic force microscope
a.u. - arbitrary units
BST - barium strontium titanate
CRO – $CaRuO_3$
CSD – chemical solution deposition
CV – capacitance – voltage
CVD – chemical vapour deposition
dc - direct current
DPT - diffused phase transition
DRAM – dynamic access memory
EBE – electron beam evaporation
ED - electron diffraction
EDS - energy dispersive spectroscopy

FeRAM – ferroelectric random access memory
HRTEM – high resolution transmission electron microscopy
IR – infrared
LAO – $LaAlO_3$
LO - longitudinal optical phonons
LSAT – $(LaAlO_3)_{0.3}$-$(Sr_2AlTaO_6)_{0.7}$
LST – Lyddane Sachs-Teller relation
MBE – molecular beam epitaxy
MOCVD - Metallo-organic chemical vapour deposition
NV- FeRAM – non-volatile ferroelectric random access memory
QFTC - quality factor of a tunable component
PLD – pulsed laser deposition
PZT – lead zirconium titanate
RBS – Rutherford backscattering spectrometry
rf - radio-frequency
RHEED - Reflection-High Energy Electron Diffraction
SBiT – $Sr_{1-1.5x}Bi_xTiO_3$
SEM - scanning electron microscopy
SMT – $Sr_{1-x}Mg_xTiO_3$
SPT - strontium lead titanate
SRO – $SrRuO_3$
ST - strontium titanate
ST 2l 750°C - strontium titanate films prepared according to the "*two-steps*" procedure, i.e. after the deposition of the two first layers, a first heat treatment at 600°C during 30min. was conducted and, after cooling the films to room temperature 8 layers more were deposited and a final annealing step took place at 750°C for 60min. in air.
ST 2l 900°C - strontium titanate films prepared according to the "*two-steps*" procedure, i.e. after the deposition of the two first layers, a first heat treatment at 600°C during 30min. was conducted and, after cooling the films to room temperature 8 layers more were deposited and a final annealing step took place at 900°C for 60min. in air.
ST 750°C - strontium titanate films prepared according to the *"one-step"* procedure in which no intermediate heat treatment was done between the deposited layers and the samples were submitted only to one final annealing step at different temperatures 750°C during 60min. in air.
ST 900°C - strontium titanate films prepared according to the *"one-step"* procedure in which no intermediate heat treatment was done between the deposited layers and the samples were submitted only to one final annealing step at different temperatures 900°C during 60min. in air.
STM – $SrTi_{1-y}Mg_yO_{3-\delta}$
TDTTS - time-domain terahertz transition spectroscopy
TEC – thermal expansion coefficient
TO - transversal optical phonons
TEM - transmission electron microscopy
XRD - X-ray diffractometry
XEC – x- ray elastic constant

List of Figures

FIGURE 1.1. Temperature dependence of the real part of dielectric permittivity ε' of: [1] $SrTiO_3$ crystal, *parallel-plate capacitor* [Müller and Burkard, 1979]; [2] $SrTiO_3$ ceramics obtained by conventional mixed oxide method, *parallel-plate capacitor* [Tkach et *al.*, 2004a]; [3] $SrTiO_3$ ceramics obtained from solutions prepared by sol-gel, *parallel-plate capacitor* [Tkach et *al.*, 2008]; [4] $SrTiO_3$ film deposited by *rf*-sputtering, thickness 300nm, *parallel-plate capacitor* $YBa_2Cu_3O_7/SrTiO_3/YBa_2Cu_3O_7/SrTiO_3$, [Fuchs et *al.*, 1999]; [5] $SrTiO_3$ film deposited by MBE, thickness 500Å, *planar capacitor* $Ag/SrTiO_3/DyScO_3$ [Haeni et. *al.*, 2004]; [6] $SrTiO_3$ film deposited by PLD, thickness 1μm, *parallel-plate capacitor* $Au/SrTiO_3/SrRuO_3/SrTiO_3$ [Ang et *al.*, 2001a]; [7] $SrTiO_3$ film deposited by PLD, thickness 1μm, *parallel-plate capacitor* $YBa_2Cu_3O_7/SrTiO_3/YBa_2Cu_3O_7/SrTiO_3$ [Takashima et *al.*, 2003]; [8] $SrTiO_3$ film deposited by PLD, thickness 320nm, *parallel-plate capacitor* $Pt/SrTiO_3/Ni/Cr/Au/ST+Nb$ [Lippmaa et *al.*, 1999]; [9] $SrTiO_3$ film deposited by PLD, thickness 1.2μm, *parallel-plate capacitor* $Au/SrTiO_3/SrRuO_3/LaAlO_3$ [Li et *al.*, 1998a]; [10] $SrTiO_3$ film deposited by PLD, thickness 350nm, *parallel-plate capacitor* $Au/SrTiO_3/SrRuO_3/LaAlO_3$ [James et *al.*, 2002]; [11] $SrTiO_3$ film deposited by PLD, thickness 800nm, *parallel-plate capacitor* $YBa_2Cu_3O_7/SrTiO_3/YBa_2Cu_3O_7/LaAlO_3$ [Findikoglu et *al.*, 1993]; [12] $SrTiO_3$ film deposited by sol-gel, thickness 1.1μm, *parallel-plate capacitor* $Al/SrTiO_3/Pt/Si$ [Thomas et *al.,* 1997].

FIGURE 2.1. Perovskite structure of $SrTiO_3$ [Last, 1957].
FIGURE 2.2. Lattice parameters of $SrTiO_3$ crystal *versus* temperature [Landolt-Börnstein, 1981].
FIGURE 2.3. Oxygen octahedra tilting at antiferrodistortive phase transition of $SrTiO_3$ from cubic to tetragonal phase at 105-110 K (a) [Unoki and Sakudo, 1967] and tetragonal rotation angle φ of oxygen octahedra in $SrTiO_3$ as a function of temperature below T_a (b) [Müller et *al.*, 1968].
FIGURE 2.4. Temperature dependence of ε' for a ferroelectric with a first order phase transition displaying Curie-Weiss behaviour.
FIGURE 2.5. Temperature dependence of the soft-mode frequency for various values of applied electric field [Worlock and Fleury, 1967].
FIGURE 2.6. Temperature dependence of the $\varepsilon'(T)/\varepsilon'(RT)$ in bulk $SrTiO_3$, $KTaO_3$, $CaTiO_3$ and TiO_2. ε' (RT) is the ε' at room temperature [Lemanov et *al.*, 1999].
FIGURE 2.7. Temperature dependence of ε' of $SrTiO_3$ crystal along [110] direction. Inset shows $10^3/\varepsilon'$ *versus* temperature T [Müller and Burkard, 1979].
FIGURE 2.8. Temperature dependence of ε' (*top panel*) and ε'' (*bottom panel*) as measured for several frequencies along the [110] direction of $SrTiO_3$ single crystal. Inset depicts the temperature dependence of the tanδ at a frequency of 5.5kHz (after [Viana et *al.*, 1994]).
FIGURE 2.9. ε' of $SrTiO_3$ single crystals at 1kHz as a function of temperature under different *dc* fields [Saifi and Cross, 1970].
FIGURE 2.10. Phase diagram (a) and tanδ of Modes I, II, II and Peak A at 10kHz (b) of $SrTiO_3$ single crystal for different electric fields [Ang et *al.*, 2000].

FIGURE 2.11. Tunability of $SrTiO_3$ single crystal at 10kHz as a function of temperature under 20kV/cm (a) and as a function of *dc* field at 12K (b) [Ang et *al.*, 2000c].
FIGURE 2.12. The square of the soft-mode TO1 phonon frequency *versus* temperature (a) and the inverse ε' *versus* temperature for 2μm-thick $SrTiO_3$ film, grown by PLD between $SrRuO_3$ electrodes on $LaAlO_3$ substrate, and of $SrTiO_3$ single crystal (b) [Sirenko et *al.*, 2000a].
FIGURE 2.13. Temperature dependence of the real part of dielectric permittivity ε' of: [1] $SrTiO_3$ crystal [Müller and Burkard, 1979]; [2] $SrTiO_3$ ceramics, obtained by conventional mixed oxide method [Tkach et *al.*, 2004a]; [3] 800-nm-thick $SrTiO_3$ film, epitaxially deposited by PLD between $YBa_2Cu_3O_7$ electrodes on $LaAlO_3$ substrate [Findikoglu et *al.*, 1993], measured as *parallel-plate capacitors*.
FIGURE 2.14. Loss factor, tanδ, of $SrTiO_3$ as a function of temperature for single crystal and thin film samples at 10GHz [Vendik, 1999b].
FIGURE 2.15. Temperature dependence of the out-of-plane ε' of 600-nm-thick $SrTiO_3$ films, epitaxially fabricated by PLD between $YBa_2Cu_3O_{7-\delta}$ electrodes on $SrTiO_3$ substrate, for various frequencies. Inset shows the $1/\varepsilon'$ (100kHz) *versus* temperature [Takashima et *al.*, 2003].
FIGURE 2.16. Out-of-plane ε' (a) and tanδ (b) of $SrTiO_3$ films with different thickness, epitaxially grown by PLD between $SrRuO_3$ electrodes on $LaAlO_3$ substrates, as a function of temperature at 1kHz. Inset shows the low temperature part of the same curves plotted in the linear scale [Li et *al.*, 1998b].
FIGURE 2.17. Temperature dependence of ε' (a) and tanδ (b) of $SrTiO_3$ films, epitaxially deposited by PLD on $LaAlO_3$ substrates with $SrRuO_3$ electrode layers of 150, 200, 350 and 500nm thickness and measured as parallel-plate Au/$SrTiO_3$/$SrRuO_3$/$LaAlO_3$ capacitors at 1kHz [James and Xi, 2002].
FIGURE 2.18. ε' and loss tangent, tanδ, of 1.1-μm-thick sol-gel derived $SrTiO_3$ film on stainless steel with Al top electrode as a function of temperature at various frequencies [Thomas et *al.*, 1997].
FIGURE 2.19. Temperature dependence of ε' of ~1.1-μm-thick $SrTiO_3$ films, epitaxially deposited by PLD on $SrTiO_3$ (a) and $LaAlO_3$ (b) substrates and measured as parallel-plate Au/$SrTiO_3$/$SrRuO_3$/substrate capacitor at 10kHz under different *dc* electric fields. Inset shows ε' peak temperature T_m *versus dc* electric field for $SrTiO_3$ film on $SrTiO_3$ substrate [Yu et *al.*, 2002].
FIGURE 2.20. Temperature dependence of out-of-plain ε' of 300-nm-thick $SrTiO_3$ film, epitaxially deposited by magnetron sputtering between $YBa_2Cu_3O_{7-\delta}$ electrodes on $SrTiO_3$ substrate for various applied *dc* electric field strengths [Fuchs et *al.*, 1999].
FIGURE 2.21. Out-of-plain ε' of 300-nm-thick $SrTiO_3$ film, epitaxially deposited by magnetron sputtering on $SrTiO_3$ substrate with $YBa_2Cu_3O_{7-x}$ as ground electrode and Au top electrode, *versus* bias voltage at different temperatures; the dotted lines are fits to the data. The measurements were carried out at a frequency of f=120Hz [Fuchs et *al.*, 1999].
FIGURE 2.22. Out-of-plain ε' and tanδ of 2.5-μm-thick $SrTiO_3$ film, epitaxially deposited by PLD between $SrRuO_3$ electrodes on $LaAlO_3$, as a function of *dc* electric field at 4.2K (a) (tunability ~72%, tanδ_{max}=0.0036) and 190K (b) (tunability ~46%, tanδ_{max}=0.00094) [Li et *al.*, 1998b].

FIGURE 2.23. Relative tunability of 2.5-μm-thick $SrTiO_3$ film, epitaxially deposited by PLD between $SrRuO_3$ electrodes on $LaAlO_3$ substrate, under 40-50 V/μm and of $SrTiO_3$ single crystal under 0.4V/μm as a function of temperature [Li et *al.*, 1998b].
FIGURE 2.24. Frequency of *A* and *E* components of TO1 phonon of $SrTiO_3$ thin film as a function of temperature for different values of external electric field, given in 10^4V/cm. Temperature dependence of the soft modes in bulk $SrTiO_3$ (stars and crosses) is shown for comparison [Akimov et *al.*, 2000].
FIGURE 2.25. Temperature dependence of tanδ of ~1.1-μm-thick $SrTiO_3$ film, epitaxially deposited by PLD on $SrTiO_3$ substrate, measured at 10kHz under *dc* electric fields of 0, 10, 30, 50, 80, 120, 160, 200, 280, 350kV/cm, labelled from 1 to 10, respectively [Yu et *al.*, 2002].
FIGURE 2.26. Temperature dependence of tanδ of ~1.1-μm-thick $SrTiO_3$ films, epitaxially deposited by PLD on $LaAlO_3$ substrates, measured at 10kHz under *dc* electric field of 0, 10, 20, 30, 40, 50, 60, 80, 100, 120, 140, 160, 180, 200, 250kV/cm (from top to bottom) [Yu et *al.*, 2002].
FIGURE 2.27. Phase diagram of (001) oriented single-domain $SrTiO_3$ thin film, epitaxially grown on (001)-oriented cubic substrates, (a) and its enlarged section near zero misfit strain (b), theoretically predicted by Pertsev et *al.* [Pertsev et *al.*, 2000]. HT - high temperature tetragonal phase, ST - "structural" tetragonal states SO - "structural" orthorhombic states, FTI - ferroelectric tetragonal phases, FOI - ferroelectric orthorhombic phases, FTII, FOII, and FOIII - "mixed" states where both *P* and *q* differ from zero (see Table 1.1 for details) [Pertsev et *al.*, 2000].
FIGURE 2.28. In-plane ε' of strained epitaxial $SrTiO_3$ films, epitaxially grown by MBE on $DyScO_3$ and on $(LaAlO_3)_{0.29}\times(SrAl_{0.5}Ta_{0.5}O_3)_{0.71}$ (LSAT) substrates, as a function of temperature at 10GHz. The inset shows a Curie-Weiss fit to $1/\varepsilon'$ [Haeni et *al.*, 2004].
FIGURE 2.29. In-plane ε' of 250-nm-thick $SrTiO_3$ thin film, epitaxially deposited by PLD on MgO (a) and $LaAlO_3$ (b) substrates, as a function of temperature, measured at 1MHz [Astafiev et *al.*, 2003].
FIGURE 2.30. Polarisation *P* versus *ac* electric field *E* hysteresis loops measured at room (a) and liquid nitrogen (b) temperatures on planar capacitors based on $SrTiO_3$ thin film, epitaxially deposited by PLD on $LaAlO_3$ substrate [Astafiev et *al.*, 2003].
FIGURE 2.31. Temperature dependence of in-plane ε' of 250-nm-thick $SrTiO_3$ films with various first layers (FLs) thickness, deposited by PLD two-step growth technique on $LaAlO_3$ substrates. The hatched areas show theoretical predictions of $SrTiO_3$ in paraelectric phase with/without a 10-nm-thick FL [Yamada et *al.*, 2005a].
FIGURE 2.32. *dc* electric field dependence of in-plane ε' of normally grown 250-nm-thick $SrTiO_3$ film (a) and two-step-grown 250-nm-thick $SrTiO_3$ film with 10-nm-thick first layer (b), deposited by PLD on $LaAlO_3$ substrates, measured at a frequency of 8GHz and temperature of 78K [Yamada et *al.*, 2005b].
FIGURE 2.33. Temperature dependence of in-plane ε' (a) and inverse ε' (b) of 400-nm-thick $SrTiO_3$ films, deposited by PLD on CeO_2-coated Al_2O_3 substrates at different temperatures. Additionally the data obtained from measurements of a *planar* capacitor on a single crystalline $SrTiO_3$ substrate are presented. All data are recorded at 1MHz [Wördenweber et *al.*, 2007].

FIGURE 2.34. Out-of-plane ε' *versus* electric field, measured at 77K and 100kHz on $Au/SrTiO_3/CaRuO_3/SrTiO_3$ (a), $Au/SrTiO_3/SrRuO_3/SrTiO_3$ (b), $Au/SrTiO_3/CaRuO_3/LaAlO_3$ (c) and $Au/SrTiO_3/SrRuO_3/LaAlO_3$ (d) parallel plate capacitors, prepared by PLD [Hyun and Char, 2001].
FIGURE 2.35. Tunability *versus* tetragonality (*c/a* ratio), measured at 10V/μm, 77K and 100kHz on $Au/SrTiO_3/CaRuO_3/SrTiO_3$ (STO/CRO/STO), $Au/SrTiO_3/SrRuO_3/SrTiO_3$ (STO/SRO/STO), $Au/SrTiO_3/CaRuO_3/LaAlO_3$ (STO/CRO/LAO) and $Au/SrTiO_3/SrRuO_3/LaAlO_3$ (STO/SRO/LAO) parallel plate capacitors, prepared by PLD [Hyun and Char, 2001].
FIGURE 2.36. Phase diagram of $Ba_xSr_{1-x}TiO_3$ solid solution [Lemanov et *al.*, 1996].
FIGURE 2.37. Temperature dependences of the ε' of $Ba_xSr_{1-x}TiO_3$ ceramics (a) [Tagantsev *et al.*, 2003] and $Ba_xSr_{1-x}TiO_3$ crystals (b) [Lemanov *et al.*, 1996] (numbers near the curves refer to $BaTiO_3$ concentration *x*).
FIGURE 2.38. Temperature dependences of the capacitance (*left axis*) and ε' (*right axis*) of $Sr_{0.9}Ba_{0.1}TiO_3$ ceramics under bias field of 0, 3.125, 6.25, 12.5 and 25kV/cm at 100kHz (a) [Wu et *al.*, 1994] and tanδ of $Ba_xSr_{1-x}TiO_3$ system scaled to 10GHz (b) [Vendik et *al.*, 1999].
FIGURE 2.39. Variation of the ε' of $Ba_{0.7}Sr_{0.3}TiO_3$ bulk ceramic and 100-nm-thick $Ba_{0.7}Sr_{0.3}TiO_3$ film, prepared by chemical vapour deposition method between Pt electrodes on Si substrate, as a function of temperature [Shaw et *al.*, 1999].
FIGURE 2.40. Temperature dependence of out-of-plane ε' of $Ba_{0.7}Sr_{0.3}TiO_3$ films, prepared by chemical vapour deposition method between Pt electrodes on Si substrate, with different thicknesses [Parker et *al.*, 2002].
FIGURE 2.41. Room-temperature in-plane capacitance *C* (*left scale*), real part of dielectric permittivity ε' (*right scale*) (a) and tunability as $\Delta C/C(0V)$ (b) of 300-nm-thick $Ba_{1-x}Sr_xTiO_3$ films, prepared by PLD on $LaAlO_3$ substrates, as a function of Sr content *x* [Gim et *al.*, 2000].
FIGURE 2.42. Phase diagram of $Sr_{1-x}Pb_xTiO_3$ solid solution [Lemanov et *al.*, 1997a].
FIGURE 2.43. Dielectric responses of $Sr_{1-x}Pb_xTiO_3$ ceramics with x=0.20 (a), 0.25 (b) and 0.30 (c) at 10kHz as a function of temperature under -20, -15, -10, -5 and 0kV/cm [Somiya et *al.*, 2001].
FIGURE 2.44. Temperature dependence of ε' and tanδ of 380-nm-thick $Sr_{0.7}Pb_{0.3}TiO_3$ films, synthesized by chemical solution deposition on Pt/Si and $LaAlO_3$ substrates [Jain et *al.*, 2004].
FIGURE 2.45. Temperature dependence of ε' of $Sr_{1-x}Ca_xTiO_3$ crystals (x=0.00-0.12) at ~1.6kHz (a) [Bednorz and Müller, 1984] and of $Sr_{1-x}Ca_xTiO_3$ (SCT) ceramics (x=0.18-0.40) at 10kHz (b). Inset shows Curie-Weiss fit for x=0.30 [Ranjan et *al.*, 2000].
FIGURE 2.46. Capacitance (*left axis*) and tanδ (*right axis*) of 500-nm-thick undoped $SrTiO_3$ film (a) and $SrTiO_3$ film with a 5% of Ca substitution (b), grown by PLD on $LaAlO_3$ substrate. The measurements were made at 1MHz under 0-40V *dc* bias with increment of 5V across a 5 μm gap (a) and 7.5 μm gap (b) [Knauss et *al.*, 1997].
FIGURE 2.47. Local adiabatic potential for Ca (1), Ba (2), Pb (3), Cd (4), Mg (5) and Zn (6) doping atoms on Sr site of $SrTiO_3$ [Kvyatkovskii, 2002].
FIGURE 2.48. ε' of $Ca_{0.01}Sr_{0.99}TiO_3$ (1), $Ba_{0.01}Sr_{0.99}TiO_3$ (2), $SrTiO_3$ (3) and $Mg_{0.01}Sr_{0.99}TiO_3$ (4) ceramics at 10, 100 and 500kHz *versus* temperature [Wang et *al.*, 2000a].
FIGURE 2.49. Temperature dependence of ε' of $SrTiO_3$, $Sr_{0.99}Mg_{0.01}TiO_3$ and $SrTi_{0.98}Mg_{0.02}O_{3-\delta}$ ceramics at 10^2, 10^4 and 10^6Hz [Tkach et *al.,* 2004a].

FIGURE 2.50. Temperature dependence of tanδ of $SrTiO_3$, $Sr_{0.99}Mg_{0.01}TiO_3$ and $SrTi_{0.98}Mg_{0.02}O_{3-\delta}$ ceramics at 10^2, 10^4 and 10^6Hz [Tkach et *al.,* 2004a].
FIGURE 2.51. Field dependence of the tunability of $SrTiO_3$, $Sr_{0.99}Mg_{0.01}TiO_3$ (a), $SrTi_{0.99}Mg_{0.01}O_{3-\delta}$ and $SrTi_{0.95}Mg_{0.05}O_{3-\delta}$ (b) ceramics, measured at 10kHz and temperatures of 10, 15, 25, 50, 100 and 295K [Tkach et *al.,* 2005c].
FIGURE 2.52. Temperature dependence of ε' (*left axis*) and ε'' (*right axis*) of $Sr_{0.92}Bi_{0.0533}TiO_3$ ceramics annealed in O_2 at 0.1, 1 and 10kHz (a), as-sintered $Sr_{0.92}Bi_{0.0533}TiO_3$ at 0.1, 1 and 10kHz (b) and of $Sr_{0.96}Bi_{0.0133}TiO_3$ annealed at different conditions at 1kHz (c) [Ang et *al*., 2000c].
FIGURE 2.53. Temperature dependences: of ε' and ε'' of $Sr_{1-1.5x}Bi_xTiO_3$ ceramics with x=0.2, 0.1, 0.053 and 0.04 at 0.1, 1, 10 and 100kHz (a); of ε' of $Sr_{1-1.5x}Bi_xTiO_3$ ceramics with x=0.0133, 0.0067, 0.0053 and 0.0033 at 0.1, 1, 10, 100 and 1000kHz (b); and of ε'' of $Sr_{1-1.5x}Bi_xTiO_3$ ceramics with x=0.0133, 0.0067, 0.0053 and 0.0033 at 0.1kHz (c). Frequency increases from top to bottom for ε' and from left to right for ε'' [Ang and Yu, 2002].
FIGURE 2.54. Arrhenius plots (inverse relaxation time τ^{-1} *versus* inverse temperature of maximum ε' $1000/T_m$) for $Sr_{1-1.5x}Bi_xTiO_3$ ceramics with x=0.2, 0.1, 0.04, 0.0533, 0.0267 [Ang and Yu, 2002].
FIGURE 2.55. *P(E)* hysteresis loops of $Sr_{0.92}Bi_{0.0533}TiO_3$ ceramics at different temperatures [Ang et *al.*, 2000d].
FIGURE 2.56. Temperature dependence of the ε' for $Sr_{1-1.5x}Bi_xTiO_3$ with x=0.002, 0.001 (a) and x=0.0005 and 0 (b) at 0.1, 1, 10, 100 and 1000kHz (*from top to bottom*). Insets show the temperature dependence of ε'' at 0.1kHz [Ang and Yu, 2002].
FIGURE 2.57. Variation of ε' at 10, 50 and 100kHz (*from top to bottom*) (variation of ε'' at 1kHz is shown in inset) under 0 (1), 5 (2), 10 (3), 15 (4), 20 (5), 25 (6), 30 (7) and 35kV/cm (8) (a); and of the polarisation under zero field cooling/field heating (ZFC/FH) and field cooling/field heating (FC/FH) at 1kV/cm (b) of $Sr_{0.997}Bi_{0.002}TiO_3$ with temperature T [Ang and Yu, 2000; Ang and Yu, 2002].
FIGURE 2.58. Schematic projection on the (100) plane for $Sr_{1-1.5x}Bi_xTiO_3$, showing two types of local environment of Bi ions [Ang and Yu, 2002].
FIGURE 2.59. Schematic of pulsed laser deposition process: steps of deposition process (*text*) in different time (t) [Eason, 2006].
FIGURE 2.60. Schematic of an *rf*-sputtering system [Reed et *al*., 2004].
FIGURE 2.61. Schematic view of molecular beam epitaxy apparatus [Ledentsov, 1999].
FIGURE 2.62. Typical metalorganic chemical vapour deposition equipment for $(Ba,Sr)TiO_3$ films deposition [York et *al.*, 2000].
FIGURE 2.63. Flow diagram of the films preparation [Waser, 2003].
FIGURE 2.64. Schematic of the spin coating process: drop of solution (a), acceleration (b), final spinning (c) [Franssila, 2004].
FIGURE 2.65. Classification of semiconductor memory [adapted from FUJITSU 2005].
FIGURE 2.66. Cross-sectional schematic representation of the 1Gbit dynamic random access memory capacitor structure [Lesaicherre et *al.*, 1994].
FIGURE 2.67. TEM image of a stacked-capacitor structure with a $(Ba,Sr)TiO_3$, Pt electrodes, and a TaSiN barrier layer (a) and expected area of a dynamic random access memory cell and the area available for the capacitor as a function of the minimum feature size (b) [Kotecki et *al.*, 1999].

FIGURE 2.68. Layout (a) and schematic view (b) of the power amplifier module integrated on a silicon substrate with thin-film passives [Suzuki et *al.*, 2005].
FIGURE 2.69. Planar (a) and trilayer (b) planar capacitors based on ferroelectric film [Vendik et *al.*, 1999b; Vendik et *al.*, 1993].
FIGURE 2.70. Cross section of the ST-based tunable capacitor [Petrov et *al.*, 2000].
FIGURE 2.71. Photograph of a portion of a monolithic tunable resonator, in which $SrTiO_3$ and $YBa_2Cu_3O_{7-x}$ are deposited on the same substrate [Moeckly et *al.*, 2003].
FIGURE 2.72. Ferroelectric planar capacitor (a) and the microstrip resonator (b) based on $SrTiO_3$ films for intermodulation distortion measurements [Kozyrev et *al*., 1998].
Figure 2.73. Cross-sectional schematic of tunable and adaptive bandpass coplanar waveguide (CPW) filter. LPF and HPF stand for Low-Pass Filter and High-Pass Filter, respectively [Findikoglu et *al.*, 1996].
Figure 2.74. Simplified equivalent circuit diagram of tunable and adaptive bandpass CPW filter [Findikoglu et *al.*, 1996].
FIGURE 2.75. Corporate fed phased array [Microwave encyclopedia].
FIGURE 2.76. Ferroelectric microwave phase shifters: coplanar line analog phase shifter (a) [Kozyrev et *al*., 2000], periodically loaded line phase shifter (b) [Kozyrev et *al.*, 1999], reflection type digital phase shifter (c) [Sherman et *al*., 2001].

FIGURE 3.1. Scheme of grazing incidence XRD experiment.
FIGURE 3.2. Schematic representation of the diffraction system configuration used in (a) texture and stress determination and (b) low incident beam angle (LIBAD) experiments. ψ is the angle between the surface normal and the diffraction vector *k*, ϕ is the rotation angle, σ_{11} and σ_{22} are the in-plane stress, σ_{33} is the perpendicular stress, α_{LI} is the angle between the incident beam and the film surface, and 2θ is the Bragg angle [Noyan and Cohen, 1987].
FIGURE 3.3. Schematic drawing of SEM [Iowa State University SEM Homepage].
FIGURE 3.4. Schematic drawing of TEM [Encyclopaedia Britannica, Inc.].
FIGURE 3.5. Schematic diagram showing the operating principles of the atomic force microscope in the contact mode [Blanchard, 1996].
FIGURE 3.6. Equivalent circuit diagrams of capacitive cell (a) of charging and loss current (b) and of loss tangent for a typical dielectric (c) [Buchanan, 1991].
FIGURE 3.7. A typical *P(E)* hysteresis loop of ferroelectric materials [Xu, 1991].

FIGURE 4.1. SEM cross-section (a) and plan view (b) micrographs of $STiO_3$ thin films prepared by "one-step" procedure and annealed at 750°C (ST 750°C).
FIGURE 4.2. SEM cross-section (a) and plan view (b) micrographs of $STiO_3$ thin films prepared by "one-step" procedure and annealed at 900°C (ST 900°C).
FIGURE 4.3. SEM cross-section micrographs of $STiO_3$ thin films prepared by "two-steps" procedure and annealed at 750°C (ST 2l 750°C) (a) and 900°C (ST 2l 900°C) (b).
FIGURE 4.4. Surface morphology and 3D view of $STiO_3$ thin films prepared by "one-step" procedure and annealed at 750°C (ST 750°C) (a,b) and 900°C (ST 900°C) (c,d).

FIGURE 4.5. Surface morphology and 3D view of $STiO_3$ thin films prepared by "two-steps" procedure and annealed at 750°C (ST 2l 750°C) (a,b) and 900°C (ST 2l 900°C) (c,d).
FIGURE 4.6. Average grain size (*left axis*) and roughness (*right axis*) of $SrTiO_3$ films prepared under different processing conditions: by "one-step" procedure and annealed at 750°C (ST 750°C) and at 900°C (ST 900°C), and by "two-steps" procedure and annealed at 750°C (ST 2l 750°C) and 900°C (ST 2l 900°C).
FIGURE 4.7. XRD spectra of $SrTiO_3$ films prepared under different conditions: by "one-step" procedure and annealed at 750°C (ST 750°C) and 900°C (ST 900°C), and by "two-steps" procedure and annealed at 750°C (ST 2l 750°C) and 900°C (ST 2l 900°C).
FIGURE 4.8. In-plane lattice parameters *a* and out-of-plane lattice parameters *c* of $SrTiO_3$ films prepared under different conditions: by "one-step" procedure and annealed at 750°C (ST 750°C) and 900°C (ST 900°C), and by "two-steps" procedure and annealed at 750°C (ST 2l 750°C) and 900°C (ST 2l 900°C).
FIGURE 4.9. Theoretically calculated (*open square*) and obtained after XRD measurements (*closed triangle*) in-plane lattice mismatch for $SrTiO_3$ films prepared under different conditions: by "one-step" procedure and annealed at 750°C (ST 750°C) and 900°C (ST 900°C), and by "two-steps" procedure and annealed at 750°C (ST 2l 750°C) and 900°C (ST 2l 900°C).
FIGURE 4.10. Average values for the total stress of $SrTiO_3$ films prepared under different conditions: by "one-step" procedure and annealed at 750°C (ST 750°C) and 900°C (ST 900°C), and by "two-steps" procedure and annealed at 750°C (ST 2l 750°C) and 900°C (ST 2l 900°C).
FIGURE 4.11. Temperature dependence of the real part of the dielectric permittivity ε' of $SrTiO_3$ films prepared under different conditions: "one-step" procedure and annealed at 750°C (ST 750°C) and 900°C (ST 900°C), and "two-steps" procedure and annealed at 750°C (ST 2l 750°C) and 900°C (ST 2l 900°C) at 100Hz, 1kHz, 10kHz, 100kHz and 1MHz.
FIGURE 4.12. Temperature dependence of tanδ of $SrTiO_3$ films prepared under different conditions: by "one-step" procedure and annealed at 750°C (ST 750°C) (a) and 900°C (ST 900°C) (b), and by "two-steps" procedure and annealed at 750°C (ST 2l 750°C) (c) and 900°C (ST 2l 900°C) (d) at 10kHz.
FIGURE 4.13. Arrhenius plots of ln(τ) versus $1000/T_{\varepsilon''\max}$ ($T_{\varepsilon''\max}$ is the temperature at which maximum of ε'' occurs at the angular frequency $w = 2\pi f$; $\tau = w^{-1}$) for the loss peaks *A*, *B* and *C* of $SrTiO_3$ films prepared under different conditions: by "one-steps" procedure and annealed at 750°C (ST 750°C) and 900°C (ST 900°C), and by "two-steps" procedure and annealed at 750°C (ST 2l 750°C) and 900°C (ST 2l 900°C). The correlation coefficients R^2 for the obtained fits are presented inside in Figure.
FIGURE 4.14. Temperature dependence of real part of the dielectric permittivity ε' of $SrTiO_3$ thin films prepared under different conditions: "one-step" procedure and annealed at 750°C (ST 750°C) (a) and 900°C (ST 900°C) (b), and "two-steps" procedure and annealed at 750°C (ST 2l 750°C) (c) and 900°C (ST 2l 900°C) (d) under different bias fields at 10kHz.
FIGURE 4.15. Field dependence at selected temperatures of real part of dielectric permittivity ε' (*top panel*), tanδ (*middle panel*) and relative tunability n_r (*bottom panel*) of $STiO_3$ films prepared under different conditions: "one-step" procedure and annealed at 750°C (ST 750°C) (a) and 900°C

(ST 900°C) (b), and "two-steps" procedure and annealed at 750°C (ST 2l 750°C) (c) and 900°C (ST 2l 900°C) (d) at 10kHz.
FIGURE 4.16. Temperature dependence of the relative dielectric tunability n_r of $SrTiO_3$ films prepared under different conditions: "one-step" procedure and annealed at 750°C (ST 750°C) and 900°C (ST 900°C), and "two-steps" procedure and annealed at 750°C (ST 2l 750°C) and 900°C (ST 2l 900°C) at 10kHz and 100kV/cm.
FIGURE 4.17. Hysteresis loops *P(E)* of $SrTiO_3$ films prepared by "one-step" procedure and annealed at 750°C (ST 750°C) at 15K (a) and 100K (b) at 100Hz.
FIGURE 4.18. Hysteresis loops *P(E)* of $SrTiO_3$ films prepared by "one-step" procedure and annealed at 900°C (ST 900°C) at 15K (a) and 100K (b) at 100Hz.
FIGURE 4.19. Hysteresis loops *P(E)* of $SrTiO_3$ films prepared by "two-steps" procedure and annealed at 750°C (ST 2l 750°C) at 15K (a) and 100K (b) at 100Hz.
FIGURE 4.20. Hysteresis loops *P(E)* of $SrTiO_3$ films prepared by "two-steps" procedure and annealed at 900°C (ST 2l 900°C) at 15K (a) and 100K (b) at 100Hz.
FIGURE 4.21. Hysteresis loops *P(E)* of $SrTiO_3$ thin films prepared $SrTiO_3$ films prepared under different conditions: by "one-step" procedure and annealed at 750°C (ST 750°C) and 900°C (ST 900°C), and by "two-steps" procedure and annealed at 750°C (ST 2l 750°C) at 750°C (ST 2l 750°C) and 900°C (ST 2l 900°C) at 15K at 100Hz.

FIGURE 5.1. XRD spectra of $SrTiO_3$ films prepared on different substrates: Al_2O_3/Pt, Si/SiO_2/TiO_2/Pt (Si/…/Pt), $SrTiO_3$/Pt (ST/Pt), $(LaAlO_3)_{0.3}$-$(Sr_2AlTaO_6)_{0.7}$/Pt (LSAT/Pt) and MgO/Pt obtained from low incident beam angle experiments.
FIGURE 5.2. Lattice parameters *a* and *c* of $SrTiO_3$ films *vs* different substrates: Al_2O_3/Pt, Si/SiO_2/TiO_2/Pt (Si/…/Pt), $(LaAlO_3)_{0.3}$-$(Sr_2AlTaO_6)_{0.7}$/Pt (LSAT/Pt), $SrTiO_3$/Pt (ST/Pt), MgO/Pt (a) and lattice parameters *a* and *c* of $SrTiO_3$ films (*left axis*) *vs* different platinized substrates (*bottom axis*) together with the lattice parameters of bare substrate (*right axis*) Al_2O_3, Si, $SrTiO_3$ (ST), $(LaAlO_3)_{0.3}$-$(Sr_2AlTaO_6)_{0.7}$ (LSAT) and MgO (*top axis*) (b).
FIGURE 5.3.Theoretical in-plane lattice mismatch for $SrTiO_3$ films deposited on bare Al_2O_3, Si, $(LaAlO_3)_{0.3}$-$(Sr_2AlTaO_6)_{0.7}$ (LSAT), $SrTiO_3$ and MgO substrates without Pt.
FIGURE 5.4. Theoretical in-plane lattice mismatch (*open circle*) and in-plane lattice mismatch obtained from XRD spectra (*solid square*) of $SrTiO_3$ films deposited on Al_2O_3/Pt, Si/SiO_2/TiO_2/Pt (Si/…/Pt), $SrTiO_3$/Pt (ST/Pt), $(LaAlO_3)_{0.3}$-$(Sr_2AlTaO_6)_{0.7}$/Pt (LSAT/Pt) and MgO/Pt substrates.
FIGURE 5.5. Strain $(d_\psi-d_0)/d_0$ of $SrTiO_3$ films deposited on different substrates: Al_2O_3/Pt, Si/SiO_2/TiO_2/Pt (Si/…/Pt), $SrTiO_3$/Pt (ST/Pt), $(LaAlO_3)_{0.3}$-$(Sr_2AlTaO_6)_{0.7}$/Pt (LSAT/Pt) and MgO/Pt.
FIGURE 5.6. Values of the average total stress of $SrTiO_3$ films deposited on different substrates: Al_2O_3/Pt, Si/SiO_2/TiO_2/Pt (Si/…/Pt), $SrTiO_3$/Pt (ST/Pt), $(LaAlO_3)_{0.3}$-$(Sr_2AlTaO_6)_{0.7}$/Pt (LSAT/Pt) and MgO/Pt.
FIGURE 5.7. Calculated values of the theoretical thermal stress (*closed symbol*) for $SrTiO_3$ films deposited on: Al_2O_3, Si, $(LaAlO_3)_{0.3}$-$(Sr_2AlTaO_6)_{0.7}$ (LSAT), $SrTiO_3$ (ST), and MgO substrates without Pt layer. (*left axis*) And TEC's of substrates according to supplier data (*half-closed symbol*) and measured under the current work (*open symbol*) for $T_{ann.}$=900°C (*right axis*).

FIGURE 5.8. Raman spectra of $SrTiO_3$ films prepared on different substrates: Al_2O_3/Pt, Si/SiO_2/TiO_2/Pt (Si/…/Pt), $SrTiO_3$/Pt (ST/Pt), $(LaAlO_3)_{0.3}$-$(Sr_2AlTaO_6)_{0.7}$/Pt (LSAT/Pt) and MgO/Pt.
FIGURE 5.9. Raman spectra of $SrTiO_3$ films deposited on Al_2O_3 substrate (*left picture*) and on MgO substrate (*right picture*) measured from 300K to 10K.
FIGURE 5.10. SEM cross-section micrographs of $STiO_3$ thin films deposited on different substrates: Si/SiO_2/TiO_2/Pt (a), Al_2O_3/Pt (b), $SrTiO_3$/Pt (ST/Pt) (c), $(LaAlO_3)_{0.3}$-$(Sr_2AlTaO_6)_{0.7}$/Pt (LSAT/Pt) (d) and MgO/Pt (e).
FIGURE 5.11. Atomic force micrographs of $SrTiO_3$ thin films deposited on different substrates: Al_2O_3/Pt (a), Si/SiO_2/TiO_2/Pt (b), $(LaAlO_3)_{0.3}$-$(Sr_2AlTaO_6)_{0.7}$/Pt (c), $SrTiO_3$/Pt (d), and MgO/Pt (e) substrates.
FIGURE 5.12. In-plane average grain size (*left axis*) and roughness (*right axis*) of $SrTiO_3$ films deposited on different substrates: Al_2O_3/Pt, Si/SiO_2/TiO_2/Pt (Si/…/Pt), $(LaAlO_3)_{0.3}$-$(Sr_2AlTaO_6)_{0.7}$/Pt (LSAT/Pt), $SrTiO_3$/Pt (ST/Pt) and MgO/Pt.
FIGURE 5.13. Cross-section TEM micrographs of film/substrate (a) and area of film near film/Pt interface (b) of $SrTiO_3$ film deposited on Si/SiO_2/TiO_2/Pt substrate.
FIGURE 5.14. Cross-section TEM micrographs of film/Pt interface (a) and film/Pt interface more detail (b) of $SrTiO_3$ films deposited on $(LaAlO_3)_{0.3}$-$(Sr_2AlTaO_6)_{0.7}$/Pt substrate.
FIGURE 5.15. Cross-section TEM micrographs of $SrTiO_3$ (ST) films on Al_2O_3/Pt (a) and on $SrTiO_3$/Pt (b) substrates.
FIGURE 5.16. Cross-section TEM micrographs of full cross-section (a) and smaller areas (b,c) of $SrTiO_3$ films deposited on MgO/Pt substrates. Slip band type dislocations are clearly seen in some $SrTiO_3$ grains (b,c).
FIGURE 5.17. Temperature dependence of real part of the dielectric permittivity of ε' of $SrTiO_3$ thin films deposited on Al_2O_3/Pt (a), Si/SiO_2/TiO_2/Pt (Si/…/Pt) (b), $SrTiO_3$/Pt (ST/Pt) (c), $(LaAlO_3)_{0.3}$-$(Sr_2AlTaO_6)_{0.7}$/Pt (LSAT/Pt) (d) and MgO/Pt (e) substrates at 100Hz, 1kHz, 10kHz and 100kHz.
FIGURE 5.18. Temperature dependence of the real part of the dielectric permittivity ε' of $SrTiO_3$ thin films deposited on different substrates: Al_2O_3/Pt, Si/SiO_2/TiO_2/Pt (Si/…/Pt), $SrTiO_3$/Pt (ST/Pt), $(LaAlO_3)_{0.3}$-$(Sr_2AlTaO_6)_{0.7}$/Pt (LSAT/Pt) and MgO/Pt at 10kHz.
FIGURE 5.19. Temperature dependence of the tanδ of $SrTiO_3$ thin films deposited on different substrates: Al_2O_3/Pt, Si/SiO_2/TiO_2/Pt (Si/…/Pt), $SrTiO_3$/Pt (ST/Pt), $(LaAlO_3)_{0.3}$-$(Sr_2AlTaO_6)_{0.7}$/Pt (LSAT/Pt) and MgO/Pt at 10kHz.
FIGURE 5.20. Arrhenius plots of ln(τ) versus $1000/T_{\varepsilon''max}$ ($T_{\varepsilon''max}$ is the temperature at which maximum of ε'' occurs at the angular frequency $w = 2\pi f$; $\tau = w^{-1}$) for the loss peaks *A* and *C* of $SrTiO_3$ films deposited on different substrates: Al_2O_3/Pt, Si/SiO_2/TiO_2/Pt (Si/…/Pt), $SrTiO_3$/Pt (ST/Pt), $(LaAlO_3)_{0.3}$-$(Sr_2AlTaO_6)_{0.7}$/Pt (LSAT/Pt) and MgO/Pt. Correlation coefficients for the obtained fits are the following: for peak *A:* R^2=0.91361 on Al_2O_3/Pt and R^2=0.9615 on ST/Pt, for peak *C*: R^2=0.9353 on Al_2O_3/Pt, R^2=0.97277 on Si/.../Pt, R^2=0.91936 on ST/Pt, R^2=0.89549 on LSAT/Pt and R^2=0.94794 on MgO/Pt substrate.
FIGURE 5.21. IR transmittance spectra of $SrTiO_3$ films deposited on Al_2O_3 (a) and on MgO (b) substrates at different temperatures.

FIGURE 5.22. Spectra of the real (ε') and imaginary (ε'') part of the dielectric permittivity in the IR range, of $SrTiO_3$ thin films deposited on Al_2O_3 (a) and on MgO (b) substrates, obtained from the transmittance fits at different temperatures.
FIGURE 5.23. Temperature dependence of the fitted parameters of the TO1 (a) and TO2 (b) modes in $SrTiO_3$ (ST) films deposited on Al_2O_3 and MgO substrates and comparison with a single crystal [Ostapchuk et *al.*, 2002] and ceramics [Petzelt et. *al.*, 2004].
FIGURE 5.24. Temperature dependence of the real part of the dielectric permittivity ε' of $SrTiO_3$ (ST) films deposited on different substrates: Al_2O_3/Pt, Si/SiO_2/TiO_2/Pt (Si/…/Pt), $SrTiO_3$/Pt (ST/Pt), $(LaAlO_3)_{0.3}$-$(Sr_2AlTaO_6)_{0.7}$/Pt (LSAT/Pt) and MgO/Pt under different bias fields at 10kHz.
FIGURE 5.25. Field dependence of the real part of the dielectric permittivity ε' (*top panel*), tanδ (*middle panel*) and relative tunability n_r (*bottom* panel) of $SrTiO_3$ (ST) films on Al_2O_3/Pt (a), Si/SiO_2/TiO_2/Pt (Si/…/Pt) (b), $SrTiO_3$/Pt (ST/Pt) (c), $(LaAlO_3)_{0.3}$-$(Sr_2AlTaO_6)_{0.7}$/Pt (LSAT/Pt) (c) and MgO/Pt (d) substrates at 10kHz and at selected temperatures.
FIGURE 5.26. Field dependence of the real part of the dielectric permittivity ε' of $SrTiO_3$ films deposited on different substrates: Al_2O_3/Pt, Si/SiO_2/TiO_2/Pt (Si/…/Pt), $SrTiO_3$/Pt (ST/Pt), $(LaAlO_3)_{0.3}$-$(Sr_2AlTaO_6)_{0.7}$/Pt (LSAT/Pt) and MgO/Pt at 10kHz and at 10K.
FIGURE 5.27. Temperature dependence of the relative dielectric tunability n_r of $SrTiO_3$ (ST) films deposited on different substrates: Al_2O_3/Pt, Si/SiO_2/TiO_2/Pt (Si/…/Pt), $SrTiO_3$/Pt (ST/Pt), $(LaAlO_3)_{0.3}$-$(Sr_2AlTaO_6)_{0.7}$/Pt (LSAT/Pt) and MgO/Pt at 10kHz and 100kV/cm.
FIGURE 5.28. Hysteresis loops *P(E)* of $SrTiO_3$ (ST) thin films on Al_2O_3/Pt substrate at 10K (a) and 100K (b) at 100Hz.
FIGURE 5.29. Hysteresis loops *P(E)* at 100Hz of $SrTiO_3$ (ST) thin films on Si/SiO_2/TiO_2/Pt (Si/…/Pt) substrate at 10K (a) and 100K (b).
FIGURE 5.30. Hysteresis loops *P(E)* of $SrTiO_3$ (ST) thin films on $SrTiO_3$/Pt (ST/Pt) substrate at 10K (a) and 100K (b) at 100Hz.
FIGURE 5.31. Hysteresis loops *P(E)* of $SrTiO_3$ (ST) thin films on $(LaAlO_3)_{0.3}$-$(Sr_2AlTaO_6)_{0.7}$/Pt (LSAT/Pt) substrate at 10K (a) and 100K (b) at 100Hz.
FIGURE 5.32. Hysteresis loops *P(E)* of $SrTiO_3$ (ST) thin films on MgO/Pt substrate at 10K (a) and 100K (b) at 100Hz.
FIGURE 5.33. Hysteresis loops *P(E)* of $SrTiO_3$ thin films deposited on different platinized substrates Al_2O_3/Pt, Si/SiO_2/TiO_2/Pt (Si/…/Pt), $SrTiO_3$/Pt (ST/Pt), $(LaAlO_3)_{0.3}$-$(Sr_2AlTaO_6)_{0.7}$/Pt (LSAT/Pt) and MgO/Pt at 10K and 100Hz.

FIGURE 6.1. SEM cross-section and plan view micrographs of $Sr_{1-x}Mg_xTiO_3$ thin films with x=0.01 (a, b), x=0.05 (c,d), x=0.10 (e,f), x=0.30 (g,h) annealed at 750°C.
FIGURE 6.2. SEM cross-section and plan view micrographs of $SrTi_{1-y}Mg_yO_{3-\delta}$ thin films with y=0.01 (a, b), y=0.05 (c), y=0.10 (d,e), y=0.15 (f) annealed at 750°C.
FIGURE 6.3. SEM cross-section and plan view micrographs of $Sr_{1-x}Mg_xTiO_3$ thin films with x=0.01 (a, b), x=0.10 (c,d), x=0.30 (e,f) annealed at 900°C.
FIGURE 6.4. Atomic force micrographs of in-plane surface (*left pictures*) and 3D view (*right pictures*) of $Sr_{1-x}Mg_xTiO_3$ thin films with x=0.01 (a), x=0.10 (b) and x=0.20 (c) annealed at 750°C.

FIGURE 6.5. Atomic force micrographs of in-plane surface (*left pictures*) and 3D view (*right pictures*) of $SrTi_{1-y}Mg_yO_{3-\delta}$ thin films with y=0.01 (a), y=0.05 (b) and y=0.10 (c) annealed at 750°C.
FIGURE 6.6. Atomic force micrographs of in-plane surface (*left pictures*) and 3D view (*right pictures*) of $Sr_{1-x}Mg_xTiO_3$ thin films with x=0.10 (a), x=0.20 (b) and x=0.30 (c) annealed at 900°C.
FIGURE 6.7. Average grain size (*left axis*) and roughness (*right axis*) *vs* Mg concentration of $Sr_{1-x}Mg_xTiO_3$ films annealed at 750°C and 900°C and $SrTi_{1-y}Mg_yO_{3-\delta}$ films annealed at 750°C. Values of grain size and roughness for undoped $SrTiO_3$ films are from Chapter 4.
FIGURE 6.8. TEM plan view micrographs of $Sr_{1-x}Mg_xTiO_3$ (a) and $SrTi_{1-y}Mg_yO_{3-\delta}$ (b) thin films with x,y=0.01annealed at 750°C.
FIGURE 6.9. Cross-section TEM micrographs (a) and EDS spectra (b) of $Sr_{0.90}Mg_{0.10}TiO_3$ films annealed at 750°C (a) and cross- section TEM micrographs of $Sr_{0.80}Mg_{0.20}TiO_3$ films annealed at 900°C (c).
FIGURE 6.10. Plan section images of $Sr_{0.30}Mg_{0.30}TiO_3$ films annealed at 750°C (a) and at 900°C (b). EDS spectra (c) and ED pattern (d) from ilmenite grain in $SrTiO_3$ matrix annealed at 900°C.
FIGURE 6.11. RBS analysis of $Sr_{0.70}Mg_{0.30}TiO_3$ thin films annealed at 750°C: RBS data (—) and simulation (Δ).
FIGURE 6.12. Distribution of the elements of $Sr_{0.70}Mg_{0.30}TiO_3$ thin films annealed at 750°C (a) and 900°C (b).
FIGURE 6.13. XRD patterns of $Sr_{1-x}Mg_xTiO_3$ (a) and $SrTi_{1-y}Mg_yO_{3-\delta}$ (b) films.
FIGURE 6.14. XRD patterns of $Sr_{1-x}Mg_xTiO_3$ thin film annealed at 800°C (a), 850°C (b) and 900°C (c) (* denotes $MgTiO_3$ phase).
FIGURE 6.15. Out-of-plane lattice parameter c of $Sr_{1-x}Mg_xTiO_3$ and $SrTi_{1-y}Mg_yO_{3-\delta}$ thin films annealed at 750°C as a function of Mg concentration in analyzed films.
FIGURE 6.16. Out-of-plane lattice parameter c of $Sr_{1-x}Mg_xTiO_3$ films annealed at different temperatures (750°C, 800°C, 850°C and 900°C) as a function of Mg concentration.
FIGURE 6.17. Ionic radii of several ions *versus* coordination number following Shannon [Shannon, 1976].
FIGURE 6.18. Room temperature Raman spectra of $Sr_{1-x}Mg_xTiO_3$ films annealed at 750°C and 900°C (▪ denotes $MgTiO_3$ phase) and $SrTi_{1-y}Mg_yO_{3-\delta}$ films annealed at 750°C.
FIGURE 6.19. IR transmittance spectra of $Sr_{1-x}Mg_xTiO_3$ films annealed at 750°C.
FIGURE 6.20. IR transmittance spectra of $Sr_{1-x}Mg_xTiO_3$ films annealed at 900°C.
FIGURE 6.21. Spectra of real ε' and imaginary ε'' parts of the dielectric permittivity in the IR range, obtained from the room temperature transmittance spectra of $Sr_{1-x}Mg_xTiO_3$ thin films with x=0.10, 0.15 and 0.30 annealed at 750°C (open symbols – fit to IR spectra, fill symbol – THz-TDS data).
FIGURE 6.22. Spectra of real ε' and imaginary ε'' parts of the dielectric permittivity in the IR range, obtained from the room temperature transmittance spectra of $Sr_{1-x}Mg_xTiO_3$ thin films with x=0.10, 0.15 and 0.30 annealed at 900°C (open symbols – fit to IR spectra, fill symbol – THz-TDS data).
FIGURE 6.23. IR transmittance spectra of $SrTi_{1-y}Mg_yO_{3-\delta}$ films annealed at 750°C.

FIGURE 6.24. Spectra of real ε' and imaginary ε'' part of the dielectric permittivity in IR range, obtained from the room temperature transmittance spectra of $SrTi_{1-y}Mg_yO_{3-\delta}$ films annealed at 750°C.
FIGURE 6.25. Temperature dependence of real part of dielectric permittivity of ε' of $Sr_{1-x}Mg_xTiO_3$ (a) and $SrTi_{1-y}Mg_yO_{3-\delta}$ (b) thin films annealed at 750°C at 1kHz, 10kHz and 100kHz.
FIGURE 6.26. Temperature dependence of tanδ of $Sr_{1-x}Mg_xTiO_3$ and $SrTi_{1-y}Mg_yO_{3-\delta}$ thin films annealed at 750°C at 10kHz.
FIGURE 6.27. Temperature dependence of real part of the dielectric permittivity of ε' at 1kHz, 10kHz and 100kHz (a) and tanδ at 10kHz (b) of $Sr_{1-x}Mg_xTiO_3$ thin films with x=0, 0.01 and 0.05 annealed at 900°C.
FIGURE 6.28. Temperature dependence of real part of the dielectric permittivity ε' of undoped and Mg-doped $SrTiO_3$ films annealed at 750°C under different *dc* bias fields at 10kHz.
FIGURE 6.29. Temperature dependence of real part of dielectric permittivity ε' of undoped and Mg-doped $SrTiO_3$ films at $T_{ann.}$=900°C under different *dc* bias fields at 10kHz.
FIGURE 6.30. Field dependence of the real part of the dielectric permittivity ε' (*top panel*), tanδ (*middle panel*) and relative tunability n_r (*bottom panel*) of $Sr_{1-x}Mg_xTiO_3$ films with x=0.01 (a), x=0.10 (b) and $SrTi_{1-y}Mg_yO_{3-\delta}$ films with y=0.01 (c), y=0.05 (d) annealed at 750°C at 10kHz at selected temperatures.
FIGURE 6.31. Field dependence of real part of dielectric permittivity ε' (*top panel*), tanδ (*middle panel*) and relative tunability n_r (*bottom panel*) of $Sr_{1-x}Mg_xTiO_3$ films with x=0.05 (a), x=0.10 (b) films annealed at 900°C at 10kHz at selected temperatures.
FIGURE 6.32. *dc*-field dependence of the real part of the dielectric permittivity ε' of undoped and Mg-doped $SrTiO_3$ films annealed at 750°C (a) and 900°C (b) at 10kHz at 20K and 110K.
FIGURE 6.33. Temperature dependence of the relative dielectric tunability n_r of undoped and Mg-doped $SrTiO_3$ films annealed at different temperatures at 10kHz and 100kV/cm.
FIGURE 6.34. Hysteresis loops *P(E)* of $Sr_{0.99}Mg_{0.01}TiO_3$ thin film annealed at 750°C at 10K (a) and 100K (b) at 100Hz.
FIGURE 6.35. Hysteresis loops *P(E)* of $Sr_{0.95}Mg_{0.05}TiO_3$ thin film annealed at 750°C at 10K (a) and 100K (b) at 100Hz.
FIGURE 6.36. Hysteresis loops *P(E)* of $Sr_{0.95}Mg_{0.05}TiO_3$ thin film annealed at 900°C at 10K (a) and 100K (b) at 100Hz.
FIGURE 6.37. Hysteresis loops *P(E)* of $SrTi_{0.99}Mg_{0.01}O_{3-\delta}$ thin film annealed at 750°C measured at 10K (a) and 100K (b) at 100Hz.
FIGURE 6.38. Hysteresis loops *P(E)* of $SrTi_{0.95}Mg_{0.05}O_{3-\delta}$ thin film annealed at 750°C at 10K (a) and 100K (b) at 100Hz.
FIGURE 6.39. Hysteresis loops *P(E)* of undoped and Mg-doped $SrTiO_3$ thin films annealed at different temperatures at 10K at 100Hz.

FIGURE 7.1. SEM cross-section micrographs of $Sr_{1-1.5x}Bi_xTiO_3$ thin films with x=0.002 (a), 0.0053 (b), 0.0067 (c), 0.04 (d) and 0.167 (e).
FIGURE 7.2. AFM micrographs of $Sr_{1-1.5x}Bi_xTiO_3$ films with x=0.0053 (a), 0.04 (b) and 0.167 (c).

FIGURE 7.3. Average grain size distribution (*left axis*) and roughness (*right axis*) *versus* Bi concentration of $Sr_{1-1.5x}Bi_xTiO_3$ films.
FIGURE 7.4. Plan view TEM micrographs (a,c) and EDS spectra (b,d) of $Sr_{1-1.5x}Bi_xTiO_3$ (SBiT) films with x=0.0267 (a,b) and 0.10 (c,d).
FIGURE 7.5. X-ray diffraction patterns of $Sr_{1-1.5x}Bi_xTiO_3$ thin films (* denotes $Bi_4Ti_3O_{12}$ as a second phase).
FIGURE 7.6. Lattice parameter c of $Sr_{1-1.5x}Bi_xTiO_3$ thin films as a function of Bi concentration.
FIGURE 7.7. Ionic radii of several ions *versus* coordination number following Shannon [Shannon, 1976].
FIGURE 7.8. Raman spectra of $Sr_{1-1.5x}Bi_xTiO_3$ thin films with x=0.0053 (a) and 0.167 (b) at selected temperatures.
FIGURE 7.9. IR transmittance spectra of $Sr_{1-1.5x}Bi_xTiO_3$ thin films with x=0.0053 (a) and 0.167 (b) at selected temperatures.
FIGURE 7.10. Spectra of real ε' and imaginary ε'' part of dielectric permittivity in IR range, obtained from the transmittance fits of $Sr_{1-1.5x}Bi_xTiO_3$ thin films with x=0.0053 (a) and 0.167 (b) at selected temperatures.
FIGURE 7.11. Temperature dependence of the real part of dielectric permittivity ε' of $Sr_{1-1.5x}Bi_xTiO_3$ films with x=0, 0.002, 0.0053, 0.0067, 0.0133 (*top panel*) and x=0.04, 0.10, 0.133, 0.167 (*bottom panel*) at 10kHz.
FIGURE 7.12. Temperature dependence of the imaginary part of dielectric permittivity ε'' of $Sr_{1-1.5x}Bi_xTiO_3$ films with x=0, 0.002, 0.0053, 0.0067, 0.0133 (*top panel*) and x=0.04, 0.10, 0.133, 0.167 (*bottom panel*) at 10kHz.
FIGURE 7.13. Temperature dependence of the tanδ of $Sr_{1-1.5x}Bi_xTiO_3$ films with x=0, 0.002, 0.0053, 0.0067, 0.0133 (*top panel*) and x=0.04, 0.10, 0.133, 0.167 (*bottom panel*) at 10kHz.
FIGURE 7.14. Variation of the maximum of the real part of the dielectric permittivity ε'_{max} (*left scale*) and of the temperature of the maximum of the real part of the dielectric permittivity $T_{\varepsilon'max}$ (*right scale*) of $Sr_{1-1.5x}Bi_xTiO_3$ thin films with Bi content at 10kHz.
FIGURE 7.15. Diagram of temperature positions of peaks 1, 2 and 3 detected in $Sr_{1-1.5x}Bi_xTiO_3$ thin films in comparison to peaks *A, B* and *C* of undoped $SrTiO_3$ obtained from $\varepsilon''(T)$ at 10kHz.
FIGURE 7.16. Plots of $1/\varepsilon'-1/\varepsilon'_{max}$ at 10kHz *vs* $T-T_{\varepsilon'max}$ in logarithmic scale (*solid squares*) and fits to the Eq.7.3 (*solid lines*) for $Sr_{1-1.5x}Bi_xTiO_3$ films with x=0.002 (a), 0.0053 (b), 0.0067 (c), 0.0133 (d), 0.04 (e), 0.10 (f), 0.133 (g) and 0.167 (h).
FIGURE 7.17. Temperature dependence of real part of dielectric permittivity ε' at 100Hz, 1kHz, 10kHz, 100kHz, 1MHz (*left picture*) and imaginary part of dielectric permittivity ε'' at 1kHz, 10kHz, 100kHz (*right picture*) of $Sr_{1-1.5x}Bi_xTiO_3$ films with x=0.002, 0.0053, 0.0067, 0.0133, 0.04, 0.10, 0.133 and 0.167.
FIGURE 7.18. ln(τ) versus $1000/T_{\varepsilon''max}$ ($T_{\varepsilon''max}$ is the temperature at which maximum of ε'' occurs at the angular frequency $\omega=2\pi f$; $\tau=\omega^{-1}$) for the peak 1 in $\varepsilon''(T)$ of $Sr_{1-1.5x}Bi_xTiO_3$ films with $x \leq 0.10$ (symbols correspond to the experimental data, the solid line to the fitting to the Arrhenius law). Correlation coefficients R^2 for obtained fits of $Sr_{1-1.5x}Bi_xTiO_3$ films presented inside the Figure.
FIGURE 7.19. Plots ln(τ) versus $1000/T_{\varepsilon''max}$ ($T_{\varepsilon''max}$ is the temperature at which maximum of ε'' occurs at the angular frequency $\omega=2\pi f$; $\tau=\omega^{-1}$) for the peak 2 in $\varepsilon''(T)$ of $Sr_{1-1.5x}Bi_xTiO_3$ films with

$x \geq 0.04$ (symbols: the experimental data, the solid line: the fitting to the Vögel-Fulcher relation). Correlation coefficients R^2 for obtained fits of $Sr_{1-1.5x}Bi_xTiO_3$ films presented inside the Figure.
FIGURE 7.20. Variation of real part of the dielectric permittivity ε' of $Sr_{1-1.5x}Bi_xTiO_3$ thin films as a function of temperature under selected *dc* bias fields at 10kHz.
FIGURE 7.21. Variation of real part of the dielectric permittivity ε' (*top panel*), tanδ (*middle panel*) and relative tunability n_r (*bottom panel*) of $Sr_{1-1.5x}Bi_xTiO_3$ thin films with x=0.002 (a), 0.0133 (b), 0.04 (c) and 0.167 (d) as a function of *dc* electric field at 10kHz .
FIGURE 7.22. Temperature variation of the relative tunability n_r of $Sr_{1-1.5x}Bi_xTiO_3$ thin films.
FIGURE 7.23. Temperature variation of communication quality factor K of $Sr_{1-1.5x}Bi_xTiO_3$ films.
FIGURE 7.24. Hysteresis loops *P(E)* of $Sr_{1-1.5x}Bi_xTiO_3$ thin films with x=0.002 at 15K (a), 30K (b), 50K (c), 70K (d), 100K (e) and 295K (f) at 100Hz.
FIGURE 7.25. Hysteresis loops *P(E)* of $Sr_{1-1.5x}Bi_xTiO_3$ thin films with x=0.04 at 15K (a), 30K (b), 52K (c), 70K (d), 100K (e) and 295K (f) at 100Hz.
FIGURE 7.26. Hysteresis loops *P(E)* of $Sr_{1-1.5x}Bi_xTiO_3$ thin films with x=0.10 at 15K (a), 30K (b), 50K (c), 70K (d), 100K (e) and 295K (f) at 100Hz.
FIGURE 7.27. Remnant polarisation P_r (a) and coercive field E_c (b) of $Sr_{1-1.5x}Bi_xTiO_3$ films with x=0, 0.002, 0.04 and 0.10 as a function of temperature.

FIGURE 8.1. Temperature dependence of the real part of dielectric permittivity ε' of: [1] $SrTiO_3$ crystal, *parallel-plate capacitor* [Müller and Burkard, 1979]; [2] $SrTiO_3$ ceramics obtained by conventional mixed oxide method, *parallel-plate capacitor* [Tkach et *al.*, 2004a]; [3] $SrTiO_3$ ceramics obtained from solutions prepared by sol-gel, *parallel-plate capacitor* [Tkach et *al.*, 2008] [4] $SrTiO_3$ film deposited by *rf*-sputtering, thickness 300nm, *parallel-plate capacitor* $YBa_2Cu_3O_7/SrTiO_3/YBa_2Cu_3O_7/SrTiO_3$, [Fuchs et *al.*, 1999]; [5] $SrTiO_3$ film deposited by MBE, thickness 500Å, *planar capacitor* $Ag/SrTiO_3/DyScO_3$ [Haeni et. *al.*, 2004]; [6] $SrTiO_3$ film deposited by PLD, thickness 1μm, *parallel-plate capacitor* $Au/SrTiO_3/SrRuO_3/SrTiO_3$ [Ang et *al.*, 2001a]; [7] $SrTiO_3$ film deposited by PLD, thickness 1μm, *parallel-plate capacitor* $YBa_2Cu_3O_7/SrTiO_3/YBa_2Cu_3O_7/SrTiO_3$ [Takashima et *al.*, 2003]; [8] $SrTiO_3$ film deposited by PLD, thickness 320nm, *parallel-plate capacitor* $Pt/SrTiO_3/Ni/Cr/Au/ST+Nb$ [Lippmaa et *al.*, 1999]; [9] $SrTiO_3$ film deposited by PLD, thickness 1.2μm, *parallel-plate capacitor* $Au/SrTiO_3/SrRuO_3/LaAlO_3$ [Li et *al.*, 1998a]; [10] $SrTiO_3$ film deposited by PLD, thickness 350nm, *parallel-plate capacitor* $Au/SrTiO_3/SrRuO_3/LaAlO_3$ [James et *al.*, 2002]; [11] $SrTiO_3$ film deposited by PLD, thickness 800nm, *parallel-plate capacitor* $YBa_2Cu_3O_7/SrTiO_3/YBa_2Cu_3O_7/LaAlO_3$ [Findikoglu et *al.*, 1993]; [12] $SrTiO_3$ film deposited by sol-gel, thickness 1.1μm, *parallel-plate capacitor* $Al/SrTiO_3/Pt/Si$ [Thomas et *al.,* 1997] and $SrTiO_3$ thin films prepared by "two-steps" procedure annealed at 900°C (ST 2l 900°C), deposited by sol-gel, thickness 350nm, *parallel-plate capacitor* $Au/SrTiO_3/Pt/TiO_2/SiO_2/Si$ [analyzed in current Thesis].

List of Tables

TABLE 1.1. Examples of basic research carried out in Japan and of commercialized sol-gel products (adapted from [Sakka, 2006]).

TABLE 2.1. Nonzero components of the polarization *P* and the structural parameter *q* in different stable phases forming in (001) ST single-domain film, epitaxially grown on a cubic (001)-oriented substrate (according to [Pertsev et *al.*, 2000]).
TABLE 2.2. Thin and thick films deposition methods.
TABLE 2.3. The main advantages and disadvantages between physical vapour deposition, chemical vapour deposition, and chemical solution deposition techniques.

TABLE 3.1. List of the compositions of the fabricated films for which corresponding precursor solutions were prepared.
TABLE 3.2. List of the samples analysed in the "Chapter 4. Polycrystalline $SrTiO_3$ thin films: influence of processing on the microstructure, structure and low temperature dielectric properties".
TABLE 3.3. The lattice parameters and thermal expansion coefficients (TEC) of the used substrates in the "Chapter 5. Polycrystalline $SrTiO_3$ thin films: influence of substrate on the microstructure, structure and low temperature dielectric properties".
TABLE 3.4. Summary of various measurement techniques and their attributes: values of resolution, penetration and accuracy of technique (adopted from [Withers and Bhadeshia, 2001]).

TABLE 4.1. List of the samples analysed in the current Chapter.
TABLE 4.2. Temperature of position of the loss peaks *A*, *B*, *C* and parameters of the Arrhenius law describing the dynamics of the relaxation of loss peaks of $SrTiO_3$ thin films prepared under different conditions: by "one-step" procedure and annealed at 750°C (ST 750°C) and 900°C (ST 900°C), and by "two-steps" procedure and annealed at 750°C (ST 2l 750°C) at 750°C (ST 2l 750°C) and 900°C (ST 2l 900°C).
TABLE 4.3. Relaxation mechanisms observed for undoped $SrTiO_3$ crystals, ceramics and films and their Arrhenius-law parameters.
TABLE 4.4. Remnant polarization P_r and coercive field E_c obtained from hysteresis loop measurements at 15K and 100K for $SrTiO_3$ thin films prepared under different conditions: by "one-step" procedure and annealed at 750°C (ST 750°C) and 900°C (ST 900°C), and by "two-steps" procedure and annealed at 750°C (ST 2l 750°C) at 750°C (ST 2l 750°C) and 900°C (ST 2l 900°C).

TABLE 5.1. The lattice parameters and Thermal Expansion Coefficients (TEC's) of the substrates used in the current Chapter.

TABLE 5.2. The in-plane *a* and out-of-plane *c* lattice parameters of $SrTiO_3$ films prepared on different substrates.

TABLE 5.3. In-plane lattice mismatch from XRD, average total stress and theoretical thermal stress obtained for $SrTiO_3$ films on different substrates Al_2O_3/Pt, Si/SiO_2/TiO_2/Pt (Si/…/Pt), $SrTiO_3$/Pt (ST/Pt), $(LaAlO_3)_{0.3}$-$(Sr_2AlTaO_6)_{0.7}$/Pt (LSAT/Pt) and MgO/Pt.

TABLE 5.4. Total stress values, maximum of ε', $T_{\varepsilon'max}$ and positions of peaks *A*, *B* and *C* in tanδ *(T)* of $SrTiO_3$ films deposited on different platinized substrates.

TABLE 5.5. Arrhenius law parameters used to describe the relaxational dynamics of the loss peaks *A* and *C* in $SrTiO_3$ thin films deposited on Al_2O_3/Pt, Si/SiO_2/TiO_2/Pt (Si/…/Pt), $SrTiO_3$/Pt (ST/Pt), $(LaAlO_3)_{0.3}$-$(Sr_2AlTaO_6)_{0.7}$/Pt (LSAT/Pt) and MgO/Pt.

TABLE 5.6. The average value of the remnant polarization P_r and coercive field E_c of $SrTiO_3$ films deposited on different platinized substrates.

TABLE 6.1. Values of ε' in the maximum and positions of $T_{\varepsilon'max}$ and of the peaks *A*, *B* and *C* in tanδ*(T)* spectra of $Sr_{1-x}Mg_xTiO_3$ and $SrTi_{1-y}Mg_yO_{3-\delta}$ films annealed at 750°C at 10kHz.

TABLE 6.2. The average value of remnant polarization P_r and coercive field E_c of undoped ST films, $Sr_{1-x}Mg_xTiO_3$ and $SrTi_{1-y}Mg_yO_{3-\delta}$ films annealed at $T_{ann.}$=750°C and 900°C at selected 10K and 100K.

TABLE 7.1. Effective exponent γ, maximum real part of the dielectric permittivity ε'_{max}, its temperature $T_{\varepsilon'max}$ deduced from $\varepsilon'(T)$ of $Sr_{1-1.5x}Bi_xTiO_3$ films at 10kHz.

TABLE 7.2. Positions of peak 1 and peak 2 detected in the $\varepsilon''(T)$ of $Sr_{1-1.5x}Bi_xTiO_3$ films at 10kHz and their relaxation dynamics parameters, obtained for peak 1 from the fitting to Arrhenius law and for peak 2 from the fitting to Vögel-Fulcher relation.

Chapter 1. Introduction and objectives

The current trend of miniaturization of the electronic devices and the ability to increase the packing of different materials are challenges of the electronic industry [Rohrer, 1996]. As a consequence, it is expected that in future years the miniaturization process becomes a crucial aspect of research in the area of materials engineering [Murarka, 1997; Rohrer, 1996]. After semiconductors, functional insulators have been gradually included in the miniaturization process, including ferroelectric materials [Yu and Ang, 2003; Morita, 2003].

Due to their peculiar properties, ferroelectrics are attractive for a wide range of applications. Their high dielectric response is being used in capacitor applications, their piezoelectric properties utilized in transducers, pyroelectricity in sensors, non linear effects in electrooptic devices, and more recently their ferroelectric behaviour (polarization switching) is being utilized in memories circuits. In the field of ferroelectric materials miniaturization, quantum paraelectric strontium titanate ($SrTiO_3$, ST) and ST-based materials in a thin layer form has been investigated and utilized, due to the extensive use of microwaves in radar and communication applications, including military, airport and police radars, satellite communication systems, mobile phones and wireless computer networks [Scott, 1993]. And due to the approaching of the computer clock frequency to the GHz range, the most important applications for ST-based materials are related to microwave microelectronic elements. Currently, the use of ST-based films in tunable microwave devices is under consideration for industrial applications due to the substantial cost reduction, comparing with single crystals [Tagantsev et *al.*, 2003].

1.1. Why sol-gel derived $SrTiO_3$ films?

The sol-gel approach is a low-cost and low-synthesis temperature technique. It also allows the fine control of the product's chemical composition, even of small quantities of dopants, such as organic dyes and rare earth metals that can be introduced in the sol and end up in the final product finely dispersed. This process has been used to produce a wide range of compositions in various forms, including powders, fibbers, coatings and thin films, monoliths and composites, and porous membranes. Organic hybrids, where a gel is impregnated with polymers or organic dyes to provide specific properties, can also be

made. One of the most attractive features of the sol-gel process is that it can produce compositions that cannot be created with conventional methods. Another benefit is that the mixing level of the solution is retained in the final product, often on the molecular scale. One more advantage of the sol-gel deposition process is that it does not require a vacuum ambience to operate. In addition it has a low energetic budget since a template of the metal oxide lattice is already formed in the precursor solution and only a small amount of energy is needed for crystallization [Gaucher et *al.*, 1995]. The sol-gel method is interesting not only for a study but also for developmental work. A good presentation that sol-gel research activities are very prosperous can be observed in Table 1.1, showing many successful commercial products obtained by sol-gel Japan universities works and industry [Sakka, 2006].

TABLE 1.1. Examples of basic research carried out in Japan and of commercialized sol-gel products (adapted from [Sakka, 2006]).

Examples of basic research carried out in Japan	
Subject	**Research group**
Low temperature processing of refractory oxide coatings	Nippon Sheet Glass; Osaka Prefecture University; Keio University
Processing of coating films: cracks, striation	Kansai University
Semiconductor and metal particles in silica matrix	Nagoya Institute of Technology; Mie University; Kyoto University
Processing of functional ceramic nanoparticle-polymer hybrid	Nagoya University
Coating films with controlled microstructure	Kyoto University; Waseda University
X-ray structure of sol-gel derived silica gel	Mie University
Bioactive organic-inorganic hybrid	Okayama University; Nara Advanced Institute for Science and Technology; Kyushu University
Examples of commercialized sol-gel products	
Product	**Company**
Photocatalyst	University of Tokyo
Anti-fogging coating for mirrors	Central Glass
Porous silica column for liquid chromatography	Merck
Hydrophilic silica aerogel	Matsushita Electric Works
Coatings on automobile windows	Asahi Glass; Central Glass; Nippon Sheet Glass
Coatings for television glass panel	Toshiba

However, it is well known and depicted in Figure 1.1 that the dielectric properties of functional materials, such as ST are highly dependent on the preparation condition.

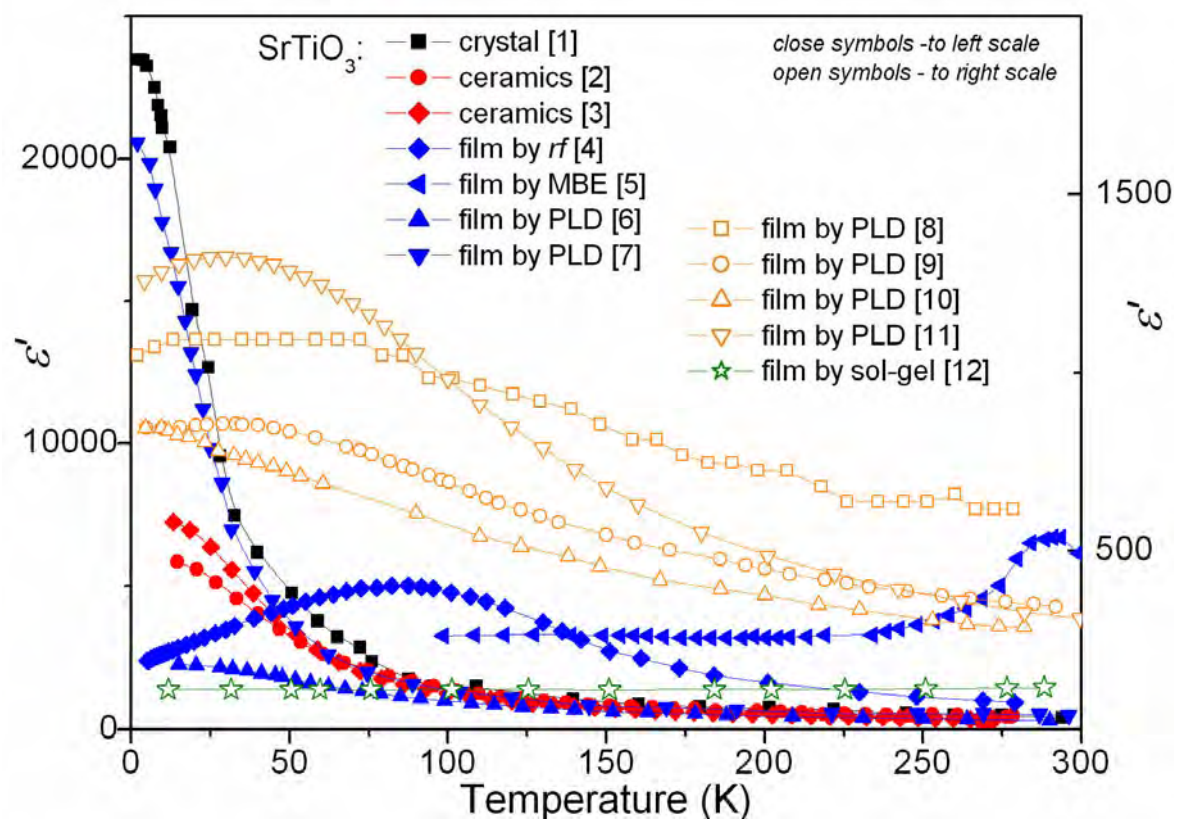

FIGURE 1.1. Temperature dependence of the real part of dielectric permittivity ε' of: [1] $SrTiO_3$ crystal, *parallel-plate capacitor* [Müller and Burkard, 1979]; [2] $SrTiO_3$ ceramics obtained by conventional mixed oxide method, *parallel-plate capacitor* [Tkach et *al.*, 2004a]; [3] $SrTiO_3$ ceramics obtained from solutions prepared by sol-gel, *parallel-plate capacitor* [Tkach et *al.*, 2008] [4] $SrTiO_3$ film deposited by *rf*-sputtering, thickness 300nm, *parallel-plate capacitor* $YBa_2Cu_3O_7/SrTiO_3/YBa_2Cu_3O_7/SrTiO_3$, [Fuchs et *al.*, 1999]; [5] $SrTiO_3$ film deposited by MBE, thickness 500Å, *planar capacitor* $Ag/SrTiO_3/DyScO_3$ [Haeni et. *al.*, 2004]; [6] $SrTiO_3$ film deposited by PLD, thickness 1µm, *parallel-plate capacitor* $Au/SrTiO_3/SrRuO_3/SrTiO_3$ [Ang et *al.*, 2001a]; [7] $SrTiO_3$ film deposited by PLD, thickness 1µm, *parallel-plate capacitor* $YBa_2Cu_3O_7/SrTiO_3/YBa_2Cu_3O_7/SrTiO_3$ [Takashima et *al.*, 2003]; [8] $SrTiO_3$ film deposited by PLD, thickness 320nm, *parallel-plate capacitor* $Pt/SrTiO_3/Ni/Cr/Au/ST+Nb$ [Lippmaa et *al.*, 1999]; [9] $SrTiO_3$ film deposited by PLD, thickness 1.2µm, *parallel-plate capacitor* Au/ $SrTiO_3/SrRuO_3/LaAlO_3$ [Li et *al.*, 1998a]; [10] $SrTiO_3$ film deposited by PLD, thickness 350nm, *parallel-plate capacitor* Au/ $SrTiO_3$/ $SrRuO_3/LaAlO_3$ [James et *al.*, 2002]; [11] $SrTiO_3$ film deposited by PLD, thickness 800nm, *parallel-plate capacitor* $YBa_2Cu_3O_7/SrTiO_3/YBa_2Cu_3O_7/LaAlO_3$ [Findikoglu et *al.*, 1993]; [12] $SrTiO_3$ film deposited by sol-gel, thickness 1.1µm, *parallel-plate capacitor* $Al/SrTiO_3/Pt/Si$ [Thomas et *al.,* 1997].

Although the data represent in the Figure 1.1 corresponds to *i)* samples prepared under different technological process (different temperatures, substrates, electrodes, *etc*.) and *ii)* measurements conducted under dissimilar conditions, including different frequencies and directions of measurements (parallel-plate or planar capacitor), the real part of the dielectric permittivity ε' of undoped ST films prepared by sol-gel is indeed considerably lower than that of ST films deposited by Molecular Beam Epitaxy, radio-frequency sputtering or by Pulsed Laser Deposition. However, it is known that the physical deposition methods are expensive, not appropriated for large areas deposition and not convenient for stoichiometry control.

In this way, study of the polycrystalline, prepared by sol-gel**,** undoped $SrTiO_3$ films, comparable to the works done on single crystals and bulk materials, is still poor and need to be continued.

1.2. Why $SrTiO_3$ films doped by Mg?

For many of the proposed device applications, ST-based thin films need to present optimised dielectric properties not only at low temperatures, at which strontium titanate shows the highest dielectric response [Müller and Burkard, 1979], but also at room temperature. For this reason, a main effort has been concentrated on modifying ST dielectric properties by doping with different elements. It is well know from the studies reported in the literature that one can expect the appearance of a polar phase in ST induced by the presence of small divalent atoms, occupying off-centre positions on Sr sites. Though these effects were thoroughly studied in single crystals and ceramics, the dopant effect in ST thin films has been barely address and in particular in sol gel derived films. The electric instability created by dopants on the lattice of ST was forseen by theoretical calculations, which predicted a dielectric relaxation mechanism, based on the displacement of ions smaller than Sr^{2+} (such as Mg^{2+}) in a multi-well local potential [Kvyatkovskii, 2002]. According to Kvyatkovskii, the incorporation of Mg into structure is expected to induce a ferroelectric instability in $SrTiO_3$ as Li in $K_{1-x}Li_xTaO_3$ [Kvyatkovskii, 2002].

As shown above, no systematic studies on the crystallographic structure, microstructure and dielectric behaviour of Mg doped ST films have been reported so far.

1.3. Why $SrTiO_3$ films doped by Bi?

The influence Bi doping on the dielectric properties of ST solid solutions was explained by Scanavi's simple "ionic hopping" model [Scanavi et *al.*, 1958]. However, later studies [Smolenskii et *al.*, 1961; Cross, 1994] pointed to ferroelectric behaviour with a diffuse phase transition for this system. Indeed a more recent systematic study of $Sr_{1-1.5x}Bi_xTiO_3$ ceramics clearly demonstrated the dependency of the dielectric response on the Bi concentration with a crossover from the ferroelectric (for very small concentration of Bi $0.0005 \leq x \leq 0.002$) to a relaxor type behaviour (for concentration of Bi $x \geq 0.133$) [Yu, 1997; Ang et *al.*, 1998; Ang et *al.*, 1999a; Ang et *al.*, 1999b; Ang et *al.*, 2000c; Ang et *al.*, 2002]. However, the influence of Bi on the structural, microstructural and dielectric properties of ST films is not investigated enough.

Accordingly ***the first objective*** of the present work is to fabricate undoped $SrTiO_3$ films by sol-gel method, to establish the relations between the processing and the dielectric properties and to exploit the substrate effect (Al_2O_3/Pt, Si/SiO_2/TiO_2/Pt, $(LaAlO_3)_{0.3}$-$(Sr_2AlTaO_6)_{0.7}$/Pt, $SrTiO_3$/Pt and MgO/Pt substrates) on the dielectric response. The strain / stress effects on the microstructure development and the relation with the dielectric properties envisaging practical applications are discussed.

And ***the second objective*** of the present work is the systematic study of the effect of selected dopants, such as Mg and Bi on the structure, microstructure and dielectric response of sol-gel derived ST films and to establish the processing-structure-dielectric property relationships for $Sr_{1-x}Mg_xTiO_3$, $SrTi_{1-y}Mg_yO_{3-\delta}$, and $Sr_{1-1.5x}Bi_xTiO_3$ thin films on Si/SiO_2/TiO_2/Pt substrates. The influence of doping site occupation on the dielectric relaxation and relation with the existence of polar anomalies will be discussed to elucidate the nature of the polar state induced by Bi in sol-gel derived ST thin films.

In agreement and to fulfil the work objectives "*Chapter 2"* of the Thesis revises with detail the background knowledge on the incipient ferroelectricity of $SrTiO_3$ giving a special emphasis to the lattice dynamics and dielectric characterization of the system. The influence of the applied field, doping process by different elements, and stress effect on the low temperature dielectric properties of ST is also discussed. The different methods of the

deposition of films are described detail and compared from the application point of view. *"Chapter 2"* ends with the presentation of the several possible applications for ferroelectric thin films and particular ST based films applications are illustrated.

"Chapter 3" is dedicated to the methodologies used within this work for the fabrication and characterization of the ST based thin films.

"Chapter 4" is devoted to the analysis of the role of some processing parameters, such as the temperature of the heat treatment process and influence of buffer layers on the structural and dielectric properties of ST films on $Si/SiO_2/TiO_2/Pt$ substrates.

In the *"Chapter 5"* study of the strain/stress effect on the structural and dielectric properties ST films grown on 5 different substrates (Al_2O_3/Pt, $Si/SiO_2/TiO_2/Pt$, $(LaAlO_3)_{0.3}$-$(Sr_2AlTaO_6)_{0.7}/Pt$, $SrTiO_3/Pt$ and MgO/Pt) is described.

The next two chapters cover the doping studies. The structural, microstructural and dielectric properties are described and discussed in detail. The dependence of the dopants solid solubility limit on lattice site occupancy and annealing temperature is discussed. The relations between composition / processing / properties are established. The role of the dopants on the dielectric response of ST is described in detail and for some cases compared with doped ceramics. *"Chapter 6"* is devoted to the study of polycrystalline $Sr_{1-x}Mg_xTiO_3$ and $SrTi_{1-y}Mg_yO_{3-\delta}$ films on $Si/SiO_2/TiO_2/Pt$ substrates. And the subject of *"Chapter 7"* is $Sr_{1-1.5x}Bi_xTiO_3$ films on $Si/SiO_2/TiO_2/Pt$ substrates: structural and dielectric properties are described and discussed in first for Bi doped ST films.

By the end of the Thesis the results are summarised, conclusions made and future work suggested.

Chapter 2. Background and literature review

This chapter will review the current knowledge on strontium titanate ($SrTiO_3$, ST) with particular emphasis on the structural and dielectric properties of undoped ST bulk and films. The influence of the applied electric field, stress, and different doping elements on the dielectric properties of ST will be presented in detail as well. Finally the methods for the preparation and examples of possible application of ST films will close the present Chapter.

Introduction

Ferroelectricity is a phenomenon, which was discovered by Valasek in 1921, and it is characterized by the presence of a spontaneous polarization at zero external electric field that can be switched under an alternated electric field [Valasek, 1920; Valasek, 1921].

Spontaneous polarization is related to the collective displacement of the ions in the lattice. Therefore, for the 32 points groups found in the nature, ferroelectricity can be observed only in the non-centrosymmetric groups of materials. All ferroelectric materials are piezoelectrics, i.e. they are able to develop an electrical charge proportional to an applied mechanical stress [Cady, 1946; Jaffe et *al.*, 1971].

In most cases ferroelectrics have a transition temperature to a higher symmetry group. As the temperature is increased, a ferroelectric undergoes a phase transition, which is accompanied by the disappearance of spontaneous polarization and by a change in the symmetry of the crystal lattice. This temperature is called a Curie temperature T_c, where the real part of dielectric permittivity ε', tends to the infinite, $\varepsilon' \rightarrow \infty$. This temperature defines the state of the material: below T_c the material is in the ferroelectric state and above T_c the material is in non-ferroelectric or in the paraelectric state. When T_c is close to 0K, the ferroelectric order is suppressed by quantum fluctuations and such materials are called quantum paraelectrics or called incipient ferroelectrics [Müller and Burkard, 1979; Hemberger et *al.*, 1996; Kiat and Roisnel, 1996; Vacher et *al.*, 1992; Nes et *al.*, 1992; Hünnefield et *al.*, 1998]. However, ferroelectric-like behaviour may be induced by stress [Uwe and Sakudo, 1976], applied electric field [Hemberger et *al.*, 1996], and doping [Lemanov et *al.*, 1999].

A ferroelectric is termed “displacive” when the elementary dipoles strictly vanish in the paraelectric phase and “order–disorder” when they are non-vanishing but thermally average out to zero in the paraelectric phase [Lines and Glass]. A similar distinction may also be made in terms of the dynamics of the phase transition.

2.1. Bulk $SrTiO_3$: an incipient ferroelectric

2.1.1. Crystal structure and phase transitions

At room temperature, ST single crystals have a simple cubic perovskite type structure of space group *Pm3m* typical for ABO_3 oxides consisting of 1-, 2-, or 3-valent A-site and 5-, 4-, or 3-valent B-site cations, respectively, and 2-valent anions. As indicated by the space group, the perovskite structure is formed from a primitive lattice, which in the case of ST consists of small titanium (Ti) atoms at the cube centre, oxygen (O) atoms in each of the six cube faces forming a cage around Ti atoms, and strontium (Sr) atoms at the cube corners (Fig.2.1).

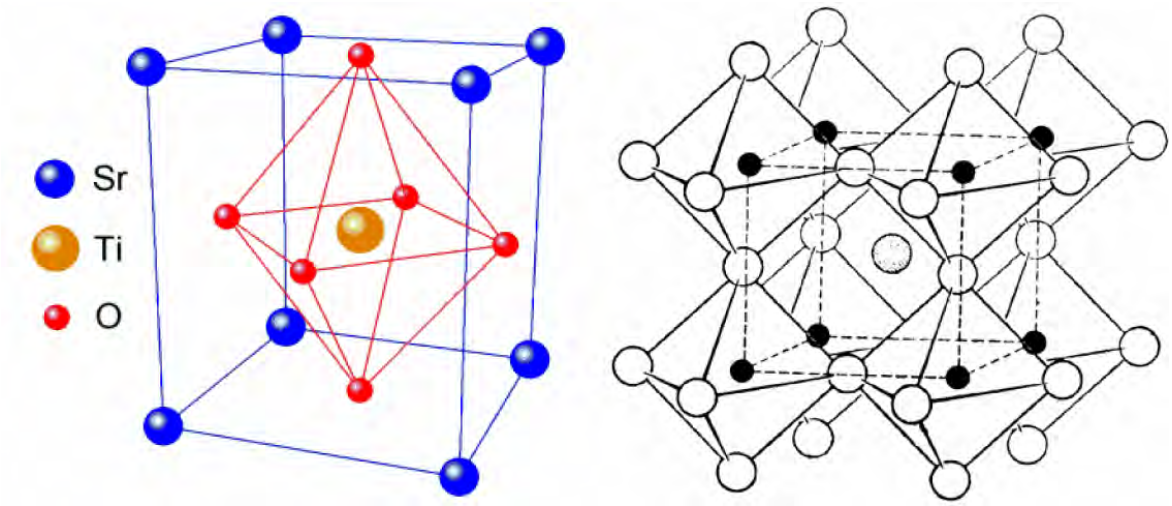

FIGURE 2.1. Perovskite structure of $SrTiO_3$ [Last, 1957].

The room-temperature lattice parameter of bulk ST is a=3.905Å [Mitsui and Westphal, 1961]. With decreasing temperature, ST undergoes a structural phase transition at T_a~105K, from cubic to tetragonal phase [Müller, 1959]. The variation of the lattice parameters (a,c) of ST as a function of temperature is shown in Figure 2.2.

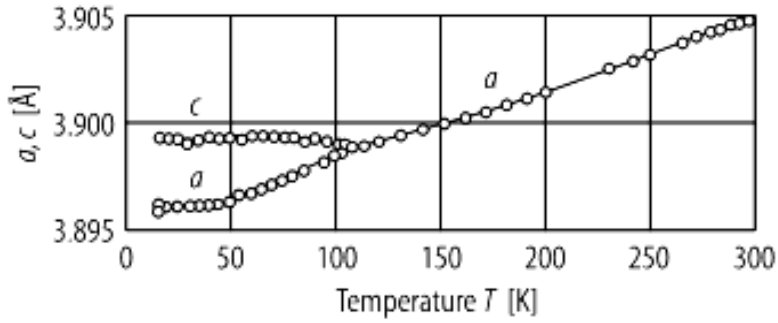

FIGURE 2.2. Lattice parameters of $SrTiO_3$ crystal *versus* temperature [Landolt-Börnstein, 1981].

Since the phase transition is connected to an anti-phase tilting of the oxygen octahedra around one of the [100] axes, as presented in Figure 2.3a [Unoki and Sakudo, 1967], ST goes from a high-temperature cubic to low-temperature tetragonal but centrosymmetric phase [Müller, 1959; Rimai and deMars, 1962; Lytle, 1967] with a doubling of the unit cell [Fleury et. *al.*, 1968b; Shirane and Yamada, 1969]. Hence no polarisation is induced in ST below T_a and the transition is a non-ferroelectric structural phase transition with almost no influence on the dielectric response. The order parameter of such transition is a rotation angle φ. The electron paramagnetic resonance (EPR) analysis of Fe-doped ST allowed Müller and Berlinger to measure the local symmetry and, consequently, φ, as shown in Figure 2.3b [Müller and Berlinger, 1971].

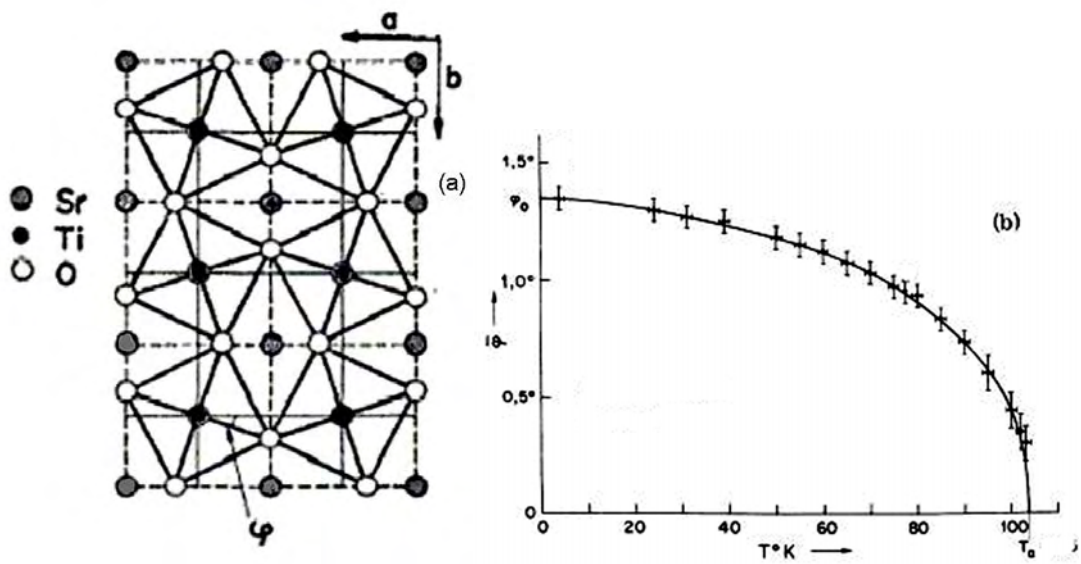

FIGURE 2.3. Oxygen octahedra tilting at antiferrodistortive phase transition of $SrTiO_3$ from cubic to tetragonal phase at 105-110 K (a) [Unoki and Sakudo, 1967] and tetragonal rotation angle φ of oxygen octahedra in $SrTiO_3$ as a function of temperature below T_a (b) [Müller et *al.*, 1968].

2.1.2. Lattice dynamics of $SrTiO_3$

From the lattice dynamics point of view, the cubic-to-tetragonal (antiferrodistortive) phase transition, observed in ST single crystals at ~105K, is due to the instability of the zone-corner soft mode [Shirane and Yamada, 1969]. The mode at the Brillouin zone boundary (R point) softens as the temperature approaches T_a, [Fleury et *al.*, 1968b]. The doubling of the lattice unit cell at the phase transition leads to a folding of Brillouin zone, so that the R point is in the zone centre, and hence 6 new zone-centre phonons appear, whose progenitor were the zone-boundary phonons [Petzelt et *al.*, 2001]. Thus, lattice dynamics is of central importance for the understanding of the structural properties of materials, including mechanism of ferroelectricity [Lines and Glass, 1977].

In general, the transition to the ferroelectric state is accompanied by the lowering of the symmetry associated with the lowering of the free energy during the ferroelectric displacement of the ions [Burns, 1985].

The hallmark of ferroelectrics, i.e. the spontaneous polarization, arises from a displacement of the centre of positive charge with respect to the centre of negative charge in the ferroelectric crystal. Such displacement as that of the Ti ion with respect to the oxygen octahedra in $SrTiO_3$, involves the same small ionic movement as the zone-centre transverse optical (TO) mode of the lattice vibration (phonon), the so-called “soft mode”. The soft mode is defined as the TO phonon of the lowest frequency which decreases on cooling as:

$$\omega_{TO_1}(T) = const \times \left|T - T_c\right|^{1/2} \tag{2.1}$$

until the point where frequency of transverse optical phonon mode ω_{TO} becomes too small for the crystal to maintain such a motion. When the temperature approaches the Curie temperature T_c, the soft-mode frequency tends to zero [Servoin et *al.*, 1980; Shirane and Yamada, 1969] and the soft mode is frozen in the crystal, which transforms to a ferroelectric phase [Cochran, 1960].

The soft-mode behaviour can also explain the high dielectric permittivity ε in the paraelectric phase of ferroelectrics [Frölich, 1949]. For a crystal with N optical modes, the Lyddane-Sachs-Teller (LST) relation [Lyddane et *al.*, 1941] relates the macroscopic dielectric permittivity to the microscopic parameter, the optical phonon frequencies:

$$\frac{\varepsilon_{st}}{\varepsilon_{\infty}} = \prod_{j}^{N} \frac{\omega_{LOj}^{2}}{\omega_{TOj}^{2}} \tag{2.2}$$

where ε_{st} and ε_{∞} stand for the static and the high frequency dielectric permittivities, and ω_{LOj} and ω_{TOj} for the frequencies of the longitudinal and transverse optical phonon modes, respectively. It is generally found that the frequencies of the higher optical modes exhibit no sizeable variation with temperature.

As ferroelectric material is cooled from high temperatures in their paraelectric phase, the real part of the dielectric permittivity ε' of the material increases non-linearly as a phase-transition is approached, as shown in Figure 2.4 for a first-order transition. Such behaviour is governed by the Curie-Weiss law

$$\varepsilon' \approx \frac{C}{T - T_c} \tag{2.3}$$

where C stands for the Curie constant.

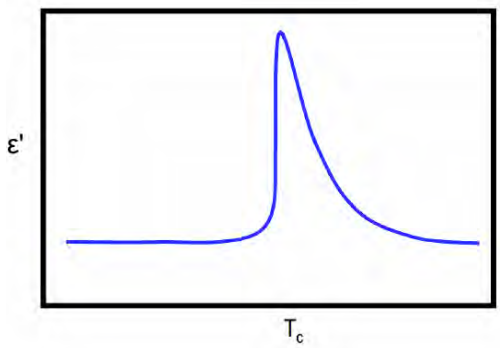

FIGURE 2.4. Temperature dependence of ε' for a ferroelectric with a first order phase transition displaying Curie-Weiss behaviour.

In general, the dielectric permittivity is a complex function

$$\varepsilon^* = \varepsilon' - i\varepsilon''. \tag{2.4}$$

Ratio between the imaginary part of the dielectric permittivity ε'' and the real part of the dielectric permittivity ε' gives another important parameter for the applications of ferroelectric materials, the dielectric loss ($\tan\delta$):

$$\tan\delta = \frac{\varepsilon''}{\varepsilon'} \tag{2.5}$$

tanδ is considerably higher in ferroelectric phase compared to that in paraelectric phase.

Indeed, Equations (2.1), (2.2), and (2.3) are related and the connection between the lattice dynamics and the ferroelectric behaviour was first realized by Cochran [Cochran, 1960], who noted that LST relation [Burns, 1985] connects the dielectric permittivity to the lattice vibration frequencies, in particular to the soft-mode phonon. From this point of view ST is of historical importance since it was in this material that the soft-mode phonon was observed for the first time and confirmed the LST relation [Riste et *al.*, 1971; Lyons and Fleury, 1977]. However, the zone-centre soft mode approach but not reach 0 and the ferroelectric phase transition does not occur in ST under normal conditions due to the quantum fluctuations, or the zero-point motion of the Ti ions [Müller and Burkard, 1979; Tosatti and Martoňák, 1994]. Therefore, ST is an incipient ferroelectric (or quantum paraelectric).

Worlock and Fleury have shown that the soft-mode behaviour is also the basis for the dielectric nonlinearity in ST. They reported that the zone-centre soft mode phonon increases with increasing of applied electric field (Fig.2.5) [Worlock and Fleury, 1967].

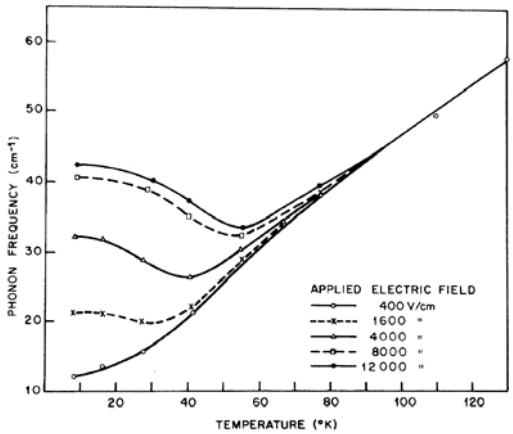

FIGURE 2.5. Temperature dependence of the soft-mode frequency for various values of applied electric field [Worlock and Fleury, 1967].

This indicates that the mechanism for the reduction of the ε' under applied field is due to the hardening of the soft mode [Worlock and Fleury, 1967], which arises from the anharmonic restoring forces on Ti ions when displaced from their equilibrium positions [Rupprecht et *al.*, 1961].

2.1.3. Dielectric behaviour of undoped $SrTiO_3$ bulk

As mentioned previously $SrTiO_3$ falls into the unique category of ferroelectrics known as incipient ferroelectrics (or quantum paraelectric), along with $KTaO_3$, $CaTiO_3$ and TiO_2 [Müller and Burkard, 1979; Lemanov et *al.*, 1999].

ST has a high ε' that follows the Curie-Weiss law (Eq.2.3) in the paraelectric regime but saturates at cryogenic temperatures rather than exhibiting the expected ferroelectric discontinuity (Fig.2.6) [Müller and Burkard, 1979; Lemanov et *al.*, 1999].

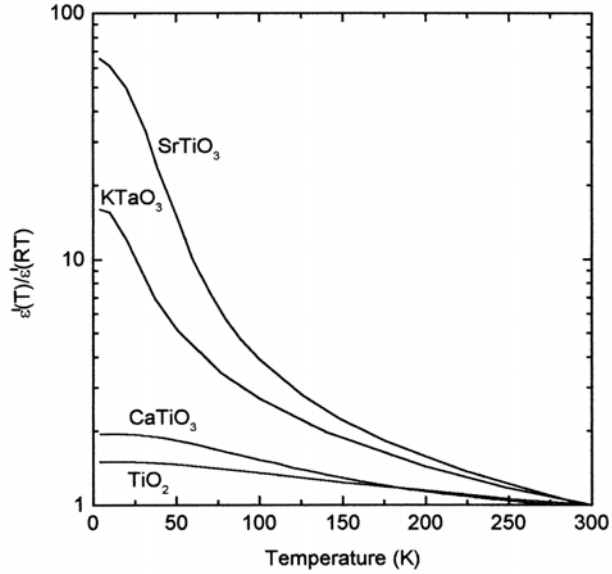

FIGURE 2.6. Temperature dependence of the $\varepsilon'(T)/\varepsilon'(RT)$ in bulk $SrTiO_3$, $KTaO_3$, $CaTiO_3$ and TiO_2. ε' (RT) is the ε' at room temperature [Lemanov et *al.*, 1999].

Plotting the temperature dependence of the real part of the dielectric permittivity as *1/ε′ versus T* (Fig.2.7) [Müller and Burkard, 1979], the Curie temperature T_c of ST has been extrapolated to 35±5K for ST single crystals [Müller and Burkard, 1979; Neville, 1972 et *al.*; Vendik and Zubko, 2000]. So ST is reported as a paraelectric above T=35K and a quantum paraelectric below (Fig.2.7) [Müller and Burkard, 1979].

The steep increase of the ε' and its levelling-off at high values, as temperature approaches 0K, was described by the Barrett relation [Barrett, 1952]:

$$\varepsilon' = C/[(T_1/2)\coth(T_1/2T) - T_0], \qquad (2.6)$$

where, T_1 stands for the temperature of the crossover between classical and quantum behaviour, and T_0 for the transition temperature at which the lattice instability would occur

in the absence of quantum fluctuations. At $T >> T_1$ values $(T_1/2)\coth(T_1/2T)$ approximates to T and the equation transforms into Curie-Weiss law.

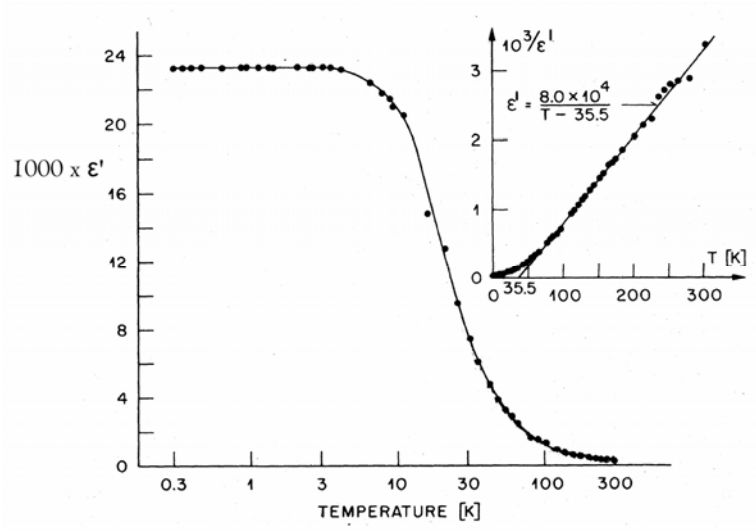

FIGURE 2.7. Temperature dependence of ε' of $SrTiO_3$ crystal along [110] direction. Inset shows $10^3/\varepsilon'$ *versus* temperature T [Müller and Burkard, 1979].

Barrett theory is a quantum version of the classical microscopic theory proposed by Slater to explain the dielectric behaviour of ferroelectric $BaTiO_3$ [Slater, 1950]. Ti ions were supposed to be rather loosely bound in the too large oxygen octahedron in $BaTiO_3$ and to act as an independent harmonic oscillator with small additional anharmonic terms and the only interaction between these oscillators is through the electric field. Hence, the ferroelectric phase transition was supposed to be created by the displacement of anharmonicaly vibrating ions from the equilibrium, i.e., the displacement of Ti ions with respect to oxygen ones. In such a way, the transition to the ferroelectric state is accompanied by a lowering of the symmetry associated with the lowering of the free energy. The Slater theory became the main theory of displacive-type phase transitions.

According to Barrett, deviation from the Curie-Weiss law at low temperatures comes from the quantum effect on the displacement of Ti ions [Barrett, 1952]. The displacive ferroelectric transition in $SrTiO_3$ would be created by the shift of the titanium ions with respect to oxygen ions with a displacement value of 0.045Å, evaluated by Müller and Burkhard [Müller and Burkhard, 1979].

$\varepsilon'(T)$ of ST is almost frequency independent at all temperatures (Fig.2.8, *top panel*) [Viana et *al.*, 1994]. However, comparing Figures 2.7 and 2.8, it is seen that maximum value of ε' depends on the sample and measurement conditions. If conditions are such that

elastic domains below 110K are not eliminated, their walls have effect in crystals is similar to grain boundary effect in ceramics that leads to the decrease of ε' [Viana et *al.*, 1994, Müller and Burkard, 1979; Petzelt et *al.*, 2001].

The ε'' of ST is much smaller, typically by a factor of 10^3, when compared to ε' (Fig.2.8, *bottom panel*) [Viana et *al.*, 1994].

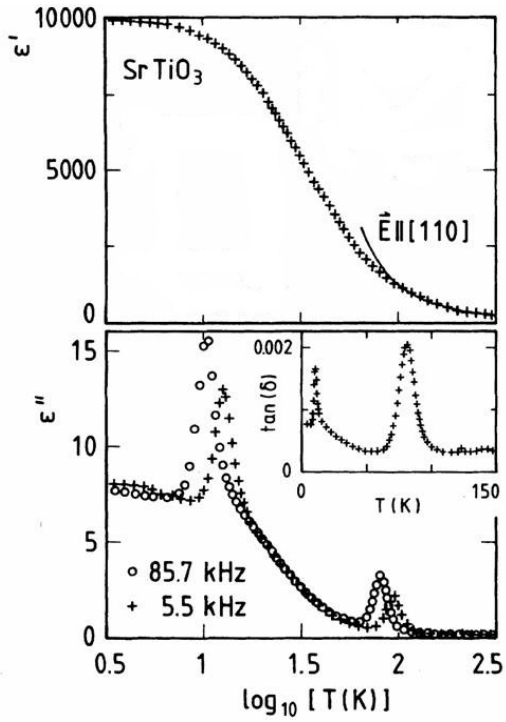

FIGURE 2.8. Temperature dependence of ε' (*top panel*) and ε'' (*bottom panel*) as measured for several frequencies along the [110] direction of $SrTiO_3$ single crystal. Inset depicts the temperature dependence of the tanδ at a frequency of 5.5kHz (after [Viana et *al.*, 1994]).

With decreasing temperature the imaginary part of the dielectric permittivity ε'' increases steadily, however, with two characteristic loss peaks in the vicinity of 10K and 80K. At these temperatures ε'' reveals dispersion effects characteristic of the dielectric relaxation phenomena. The former peak was attributed to an unknown impurity or defect [Dec et *al.*, 1999; Venturini et *al.*, 2004]. The later one was explained in terms of the dynamics of the elastic domain walls [Mizaras and Loidl, 1997] and was not observed for ST single crystals in single-domain state [Dec et *al.*, 1999].

In addition to the high value of the ε', important for a wide range of applications for ST, ferroelectric materials exhibit electric field dependent dielectric properties, making them attractive candidates for microwave applications [Tagantsev et *al.*, 2003]. The high ε' (~24000 [Müller and Burkard, 1979]) and low tanδ (~10^{-4} [Linz, 1953]) observed in ST

single crystals at room temperature are important in microwave devices. Saifi and Cross reported for the first time that ε' of ST single crystals at low temperatures can be reduced by an order of magnitude under applied electric field as small as 5kV/cm (Fig.2.9) [Saifi and Cross, 1970].

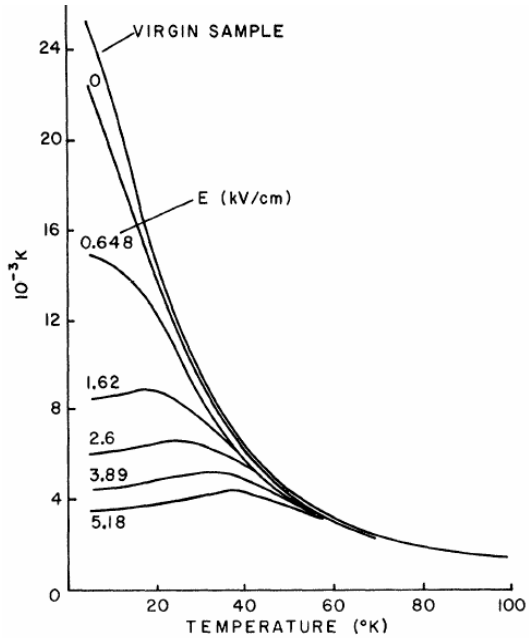

FIGURE 2.9. ε' of $SrTiO_3$ single crystals at 1kHz as a function of temperature under different *dc* fields [Saifi and Cross, 1970].

Meanwhile, besides the decreasing of the value of ε', a peak is induced in $\varepsilon'(T)$ of ST by the application of an external electric field [Saifi and Cross, 1970; Frenzel and Hegenbarth, 1974; Unoki and Sakudo, 1967; Fleury and Worlock; 1968a; Hemberger et *al.*, 1995; Hemberger et *al.*, 1996]. No peak but a reduction of the low-temperature ε' was observed in the $\varepsilon'(T)$ under *dc* bias increasing from 0 to 0.648kV/cm (Fig.2.9). However, at further increase of the electric field, a broad peak in the $\varepsilon'(T)$ appears with the peak temperature increasing with increase of fields [Saifi and Cross, 1970]. As was shown by Müller and Burkhard, there are off-centre local potential minima in ST as a typical example of incipient ferroelectrics, but they are not deep enough to fix the titanium ions due to the quantum fluctuations [Müller and Burkhard, 1979]. The application of a bias electric field stabilises the local potential of a dipolar entity, making one of its potential minima deeper and other shallower. Thus, at certain bias value, the zero-point energy is not enough to overcome the deeper barrier and thermal energy is necessary, corresponding to the appearance of the peak in the $\varepsilon'(T)$. As higher bias electric field, as bigger thermal

energy is necessary to overcome the deeper barrier, leading to higher peak temperature. Additionally, the field aligns and clamps the polarisation of the sample, suppressing ε'.

The maxima occurred in *ε'(T)* of ST were reported to be accompanied with a double hysteresis loop [Saifi and Cross, 1970; Eriksson et *al*., 2003], and to look as normal ferroelectric hysteresis with non-zero remnant polarisation [Hemberger et *al*., 1995; Itoh et *al*., 1999]. The former was attributed to the *dc* field-induced processes associated with impurities [Gevorgian et *al*., 2002], while the latter indicates the onset of induced displacive-type ferroelectric state [Hemberger et *al*., 1995; Itoh et *al*., 1997]. In addition, the field induced ferroelectric instability in ST was shown to be easily suppressed by applying moderate hydrostatic pressure [Venturini et *al*., 2003].

An additional evidence of the onset of ferroelectricity by a *dc* bias field is a field-dependent peak in tan*δ(T)* (designated as Peak *A* in Fig.2.10), accompanying the peak in the temperature dependence of the *ε'* of ST single crystal [Ang et *al*., 2000a]. Moreover, several small temperature independent peaks were detected in tan*δ(T)* and designated as Mode I (at ~30K), Mode II (at ~50K) and Mode III (at ~75K) (Fig.2.10) [Ang et *al*., 2000a]. However, these additional peaks disappear with increasing field from 25 to 50kV/cm and only one Peak *A* remains, whose temperature corresponds exactly to that of the maximum of *ε'*. According to Ang et *al*., Modes I, II and III are "defects modes" and could be attributed to the reorientation of the dipoles (formed by the impurities and defects) [Ang et *al*., 2000a].

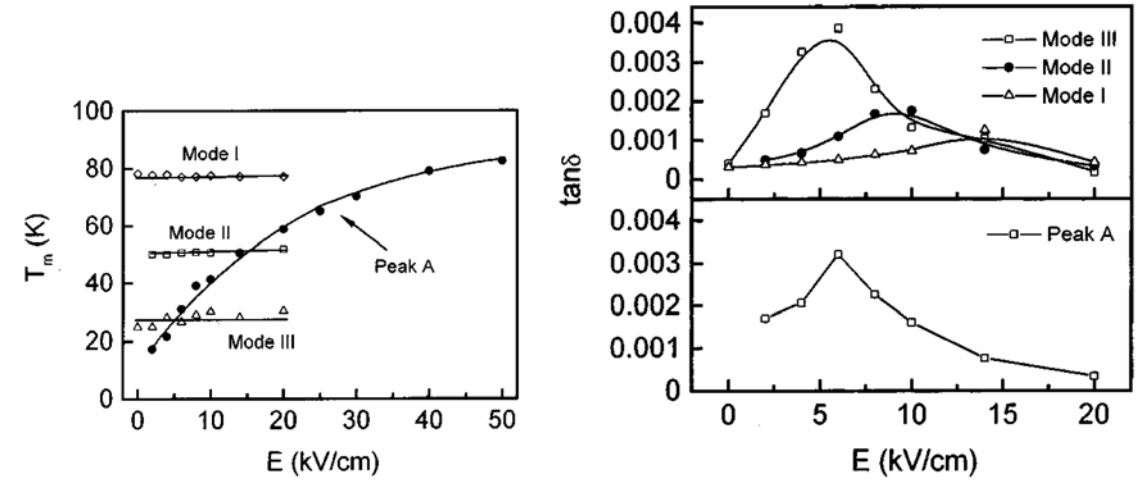

(a) (b)

FIGURE 2.10. Phase diagram (a) and tan*δ* (b) of Modes I, II, II and Peak *A* at 10kHz of $SrTiO_3$ single crystal for different electric fields [Ang et *al*., 2000].

The magnitude of loss peaks measured at 10kHz increases with the bias field until certain field value and decreases for higher *dc* bias (Fig.2.10b) [Ang et *al.*, 2000a]. At the same time, a significant increase of the loss factor of ST with increasing *dc* field was observed at 1GHz near liquid nitrogen temperature [Gevorgian et *al.*, 1996], and further at 52K and 40K [Gevorgian et *al.*, 2002; Eriksson et *al.*, 2003].

For the characterisation of the dependence of the real part of dielectric permittivity ε' on the applied *dc* bias electric field two parameters were introduced:

1) tunability n, defined as the ratio of ε' of the material at zero electric field to ε' at some non-zero electric field;

2) relative tunability n_r, defined as

$$n_r(E) = [\varepsilon'(0) - \varepsilon'(E)]/\varepsilon'(0) = (n - 1)/n, \quad (1.7)$$

where $\varepsilon'(0)$ stands for the real part of the dielectric permittivity at zero field and $\varepsilon'(E)$ for the real part of the dielectric permittivity under the applied field E.

dc electric field dependence of the dielectric properties of ST single crystals has also been studied in several other works [Vendik and Zubko, 1997; Wooldridge et *al.*, 1999; Dec et *al.*, 1999, Ang et *al.*, 2000c]. For example Ang and co-workers [Ang et *al.*, 2000c] reported that a relative tunability up to 88% can be reached under 20kV/cm near 12K for ST single crystals, as shown in Figure 2.11.

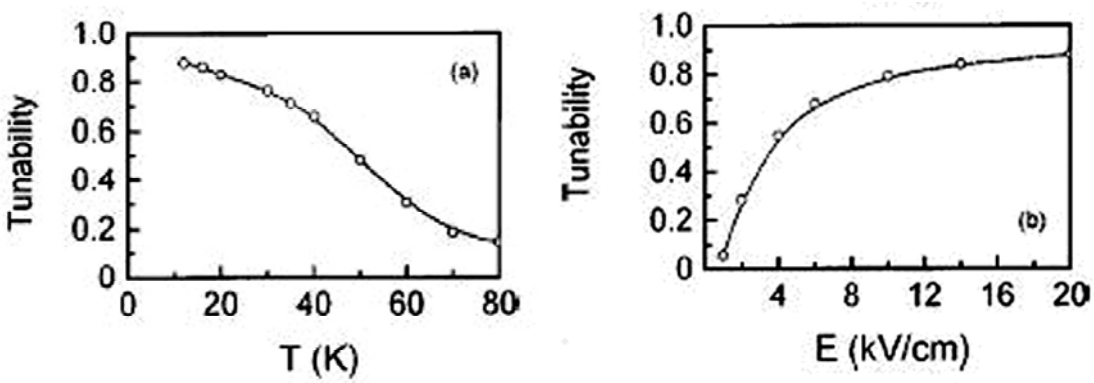

FIGURE 2.11. Tunability of $SrTiO_3$ single crystal at 10kHz as a function of temperature under 20kV/cm (a) and as a function of *dc* field at 12K (b) [Ang et *al.*, 2000c].

2.2. Undoped $SrTiO_3$ films

It is well known from literature reports, that films (with nanometers or micrometers of thickness) of strontium titanate possess very different properties in comparison to bulk materials. Usually, the main reasons to that are the presence of the substrate, that generally has a lattice mismatch with the film and induces strain in the film [Pertzev et *al.*, 2000a]; effect of dead layers between the film and metal electrode [Bascieri et *al.*, 1997; Li et *al.*, 1998a]; thickness dependencies [Li et *al.*, 1998b; Nagarajian et *al.*, 1999]; and defects that arises from film processing (microcraks and microporosity), among others. In this view, the published results of the lattice dynamics and dielectric properties of ST films are reviewed and presented.

2.2.1. Lattice dynamics and dielectric response

There is a number of investigations of the phonon behaviour in ST bulk that were carried out during many decades, using far infrared (IR) spectroscopy [Servoin et *al.*, 1980], neutron scattering [Axe et *al.*, 1970], Raman scattering [Worlock and Fleury, 1967], and hyper-Raman scattering [Vogt, 1995]. However, there are only several reports on the lattice dynamics of ST films [Sirenko et *al.*, 1999; Sirenko et *al.*, 2000a; Sirenko et *al.*, 2000b; Gupta and Katiyar, 2001; Ostapchuk et *al.*, 2002; Nuzhnyy et *al.*, 2009]. According to them, the soft mode of the films is usually much harder than that in the bulk materials at low temperature (Fig.2.12a). Correspondingly, the phonon contribution to the low-temperature dielectric permittivity is strongly suppressed in ST films compared to bulk ST (Fig.2.12b). For epitaxial films deposited by pulsed laser deposition (PLD), it was explained by influence of some specific local polar regions occurred in ST thin films during the deposition process [Sirenko et *al.*, 2000a]. For polycrystalline films, porosity and acentricity of the grain boundaries are suggested as the main reasons for such behaviour [Ostapchuk et *al.*, 2002].

Sirenko et *al.* reported also that at high temperatures the soft-mode frequency in the film and the bulk are close at zero field, indicating that either the density of the local polar regions is low or the polarization of these regions is weak or small [Sirenko et *al.*, 2000a]. However, whereas the electric-field hardening of the soft mode vanishes in ST crystals above T~80K [Fleury and Worlock, 1968a], it persists in ST thin films until high

temperatures. Such fact was attributed to the polarization by the electric field of the easily polarizable local regions around oxygen vacancies which are expected to increase the dielectric loss in thin films [Sirenko et *al.*, 2000a].

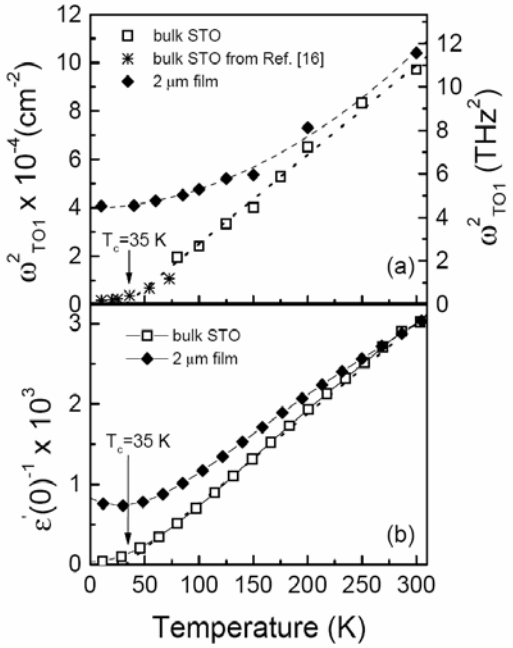

FIGURE 2.12. The square of the soft-mode TO1 phonon frequency *versus* temperature (a) and the inverse ε' *versus* temperature for 2μm-thick $SrTiO_3$ film, grown by PLD between $SrRuO_3$ electrodes on $LaAlO_3$ substrate, and of $SrTiO_3$ single crystal (b) [Sirenko et *al.*, 2000a].

Meanwhile, Ostapchuk et *al.* reported that in contrast to polycrystalline ST films a 300-nm-thick ST film, quasiepitaxially grown on a (0001) sapphire substrate with a perfect (111) orientation, displays a ferroelectric transition near 125K induced in the film plane by a tensile residual stress [Ostapchuk et *al.*, 2002].

2.2.2. Temperature dependence of the dielectric response

It was mentioned before, that the dielectric response of thin films reflects the effects of substrates (strain/stress influence), presence of grain boundaries (for polycrystalline films), defects (cracks, porosity, *etc.*), interfacial "dead layer" between film and electrode [Abe and Komatsu, 1993; Zhou and Newns, 1997; Basceri et *al.*, 1997; Li et *al.*, 1998b; Dietz et *al.*, 1995; Dietz and Waser, 1997].

As a consequence, the magnitude and behaviour of the dielectric properties of ST films strongly depend on the film's fabrication method (the type of deposition, parameters

of the process), thickness of the film, type of substrates, electrode materials, configuration of capacitors (planar or parallel-plate geometry), *etc*. In general, the dielectric response of ST films is lower than that reported for their bulk counterpart (either single crystals or ceramics). An illustration of this behaviour is presented in Figure 2.13, in which the typical temperature dependence of the real part of dielectric permittivity ε' of ST is plotted for single crystals, ceramics and films.

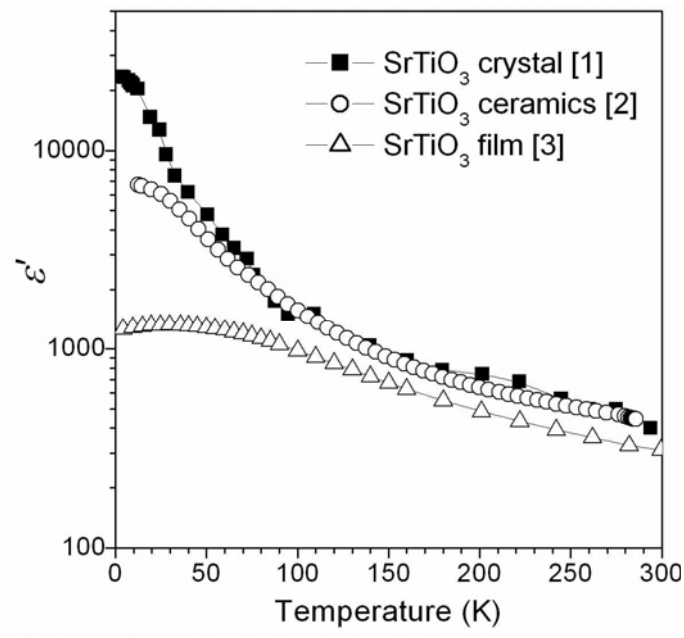

FIGURE 2.13. Temperature dependence of the real part of dielectric permittivity ε' of: [1] $SrTiO_3$ crystal [Müller and Burkard, 1979]; [2] $SrTiO_3$ ceramics, obtained by conventional mixed oxide method [Tkach et *al.*, 2004a]; [3] 800-nm-thick $SrTiO_3$ film, epitaxially deposited by PLD between $YBa_2Cu_3O_7$ electrodes on $LaAlO_3$ substrate [Findikoglu et *al.*, 1993], measured as *parallel-plate capacitors*.

It is important to stress from Figure 2.13 that in contrast to ST single crystals (and ceramics), in which ε' saturates below 10K, a broad peak was detected in ST thin films at about 30K [Findikoglu et *al.*, 1993]. Such a broad peak in ε' was observed in many ST films deposited by different methods and on different substrates and is usually attributed to the appearance of the ferroelectricity [Astafiev et *al.*, 2003; Yamada et *al.,* 2005a; Li et *al.*, 1998a; Kaene et *al.*, 2006]. In contrast to the ε', which maximum value is usually at least one order of magnitude smaller for ST films compared to ST crystals, tanδ of ST thin films ($\sim 1\times10^{-2}$) is usually about 10 times higher than that of single crystals ($\sim 1\times10^{-3}$) in all

temperature range, as shown in Figure 2.14 [Vendik, 1999].

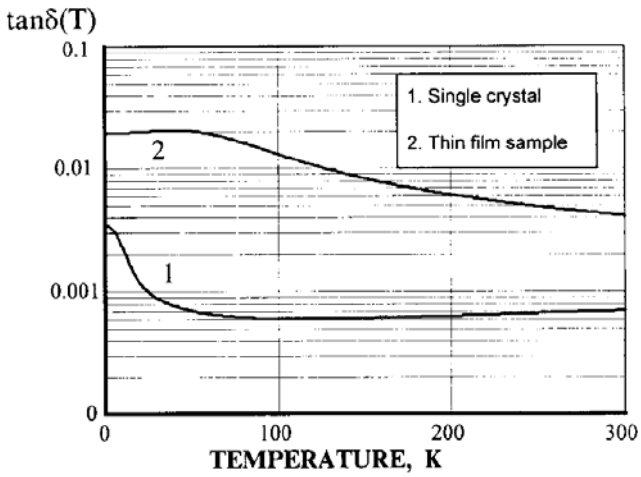

FIGURE 2.14. Loss factor, tanδ, of $SrTiO_3$ as a function of temperature for single crystal and thin film samples at 10GHz [Vendik, 1999].

However, it is possible to prepare films with dielectric response close to the one of single crystals. For example, Takashima et *al*., adapting the film fabrication process and measuring the obtained ST films at 100kHz, presented their ε' at 300K and 2K as high as 330 and 20000, respectively (Fig.2.15) [Takashima et *al.*, 2003], which is comparable to that of single crystals [Sakudo and Unoki, 1971; Müller and Burkard, 1979].

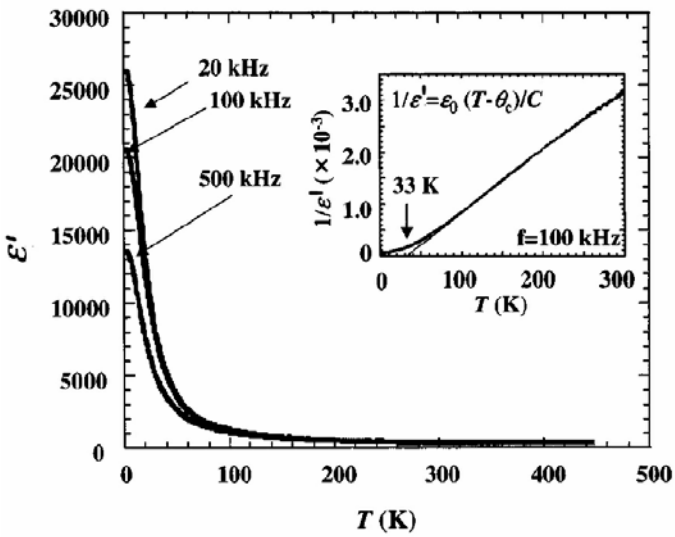

FIGURE 2.15. Temperature dependence of the out-of-plane ε' of 600-nm-thick $SrTiO_3$ films, epitaxially fabricated by PLD between $YBa_2Cu_3O_{7-\delta}$ electrodes on $SrTiO_3$ substrate, for various frequencies. Inset shows the $1/\varepsilon'$ (100kHz) *versus* temperature [Takashima et *al.*, 2003].

Analyzed ST films were epitaxially grown by PLD with introduction of special chemical-mechanical planarization process during capacitor fabrication (described detail in [Takashima et *al.,* 2002]). However, ε' of these films is frequency dependent and decreases with increasing frequency [Takashima et *al.*, 2003]. Concomitantly, the variation of $1/\varepsilon'$ versus temperature at 100kHz was found to obey the Curie-Weiss law above 150K, and T_c was calculated to be 33K [Takashima et *al.*, 2003], i.e. similar to that of ST single crystals.

The importance of the processing is further highlighted by the fact that for ST films, deposited by similar PLD method but without the special chemical-mechanical planarization step, ε' is smaller than 1000, as seen from Figure 2.16a [Li et *al.*, 1998a]. Moreover, as the film thickness decreases down to 100nm, ε' falls down to ~250 (Fig.2.16a) [Li et *al.*, 1998a]. However, an advantage of these ST films is magnitude and temperature dependence of the tanδ similar to that of single crystals (Fig.2.16b) [Li et *al.*, 1998a; Li et *al.*, 1998b]. In addition, the existence of the two peaks at low temperatures (<100K) in tan$\delta(T)$, resembles ST single crystals as well [Viana et *al.,* 1994]. tanδ of ST thin films shows also a strong dependency on thickness of the film, material of the bottom electrode and type of the substrate. An example of the influence of thickness of the film on the behaviour and values of tanδ of ST films is presented in Figure 2.16b [Li et *al.*, 1998a].

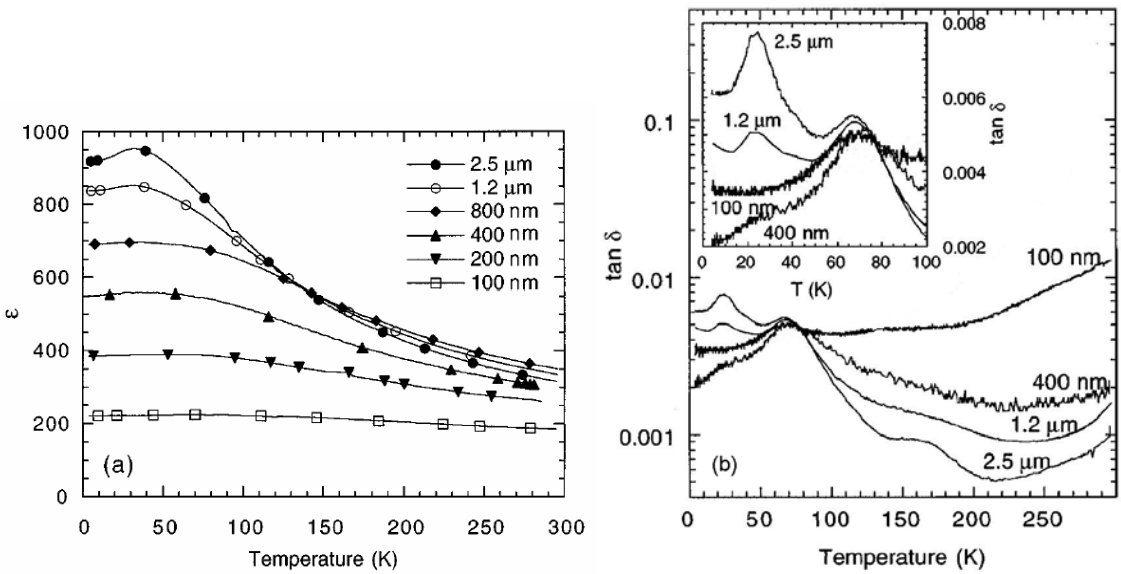

FIGURE 2.16. Out-of-plane ε' (a) and tanδ (b) of $SrTiO_3$ films with different thickness, epitaxially grown by PLD between $SrRuO_3$ electrodes on $LaAlO_3$ substrates, as a function of temperature at 1kHz. Inset shows the low temperature part of the same curves plotted in the linear scale [Li et *al.*, 1998b].

The electrode layer (sometime called in publications as buffer layer) between the film and substrate can also impact on dielectric response of ST films. However, ε' of $SrTiO_3$ films was reported to change very slightly and non-monotonously with increasing thickness of the bottom $SrRuO_3$ electrode from 150nm to 500nm, as shown in Figure 2.17a [James and Xi, 2002]. Moreover, a small broad peak in $\varepsilon'(T)$ of ST film was found around T=50K only for $SrRuO_3$ layer of 200nm but not for others (Fig.2.17a). On the other hand, several peaks with positions and intensity dependent on the thickness of $SrRuO_3$ layer were detected in tan$\delta(T)$ of these films, presented in Figure 2.17b [James and Xi, 2002]. The low-temperature peak in tan$\delta(T)$ (observed <50K) was attributed to the possible onset of ferroelectricity in the films [James and Xi, 2002]. An appearance of the high-temperature peak in tan$\delta(T)$ (observed at 130-150K) was related by to the strain induced in the film as a consequence of lattice mismatch between the $LaAlO_3$ substrate and the $SrRuO_3$ layer and between the $SrRuO_3$ layer and the $SrTiO_3$ film. However, as was mentioned by James and Xi, it was hard to separate the in-plane lattice parameter of the ST films and the $SrRuO_3$ layers and hence to determine the magnitude of the strain [James and Xi, 2002].

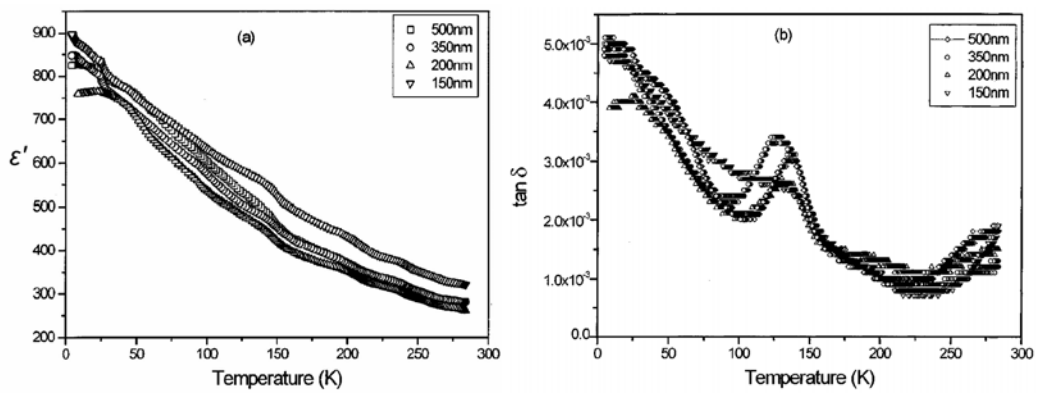

FIGURE 2.17. Temperature dependence of ε' (a) and tanδ (b) of $SrTiO_3$ films, epitaxially deposited by PLD on $LaAlO_3$ substrates with $SrRuO_3$ electrode layers of 150, 200, 350 and 500nm thickness and measured as parallel-plate Au/$SrTiO_3$/$SrRuO_3$/$LaAlO_3$ capacitors at 1kHz [James and Xi, 2002].

Properties of ST films are dependent on the film preparation method as well. Among them the sol-gel based chemical methods are particularly important. This methodology is chosen for the fabrication of the ST films in the present work. However, there are only few reports in the literature on some structural analysis, lattice dynamics and room-temperature dielectric properties of ST films deposited by sol-gel [Tsuzuki and Torhi, 1997;

Kamalasanan et *al.*, 1993; Hofman et *al.*, 1997; Gupta and Katiyar, 2001; Ostapchuk et *al.*, 2002] and only one report is about the low-temperature dielectric properties of sol-gel derived ST film, depicted in Figure 2.18 [Thomas et *al.*, 1997].

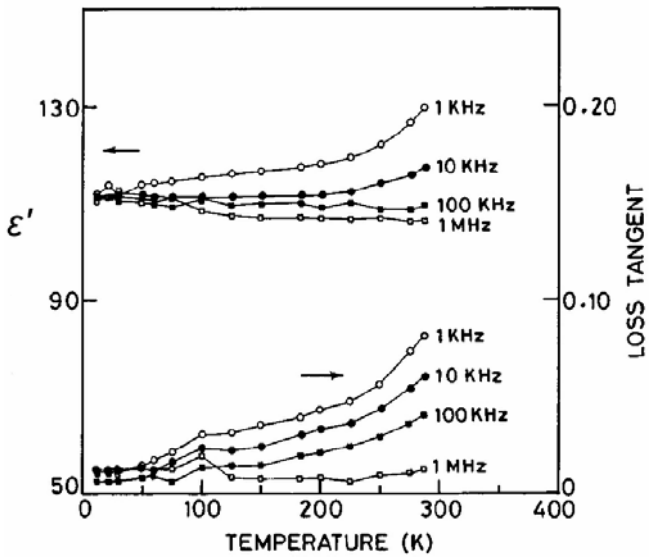

FIGURE 2.18. ε' and loss tangent, tanδ, of 1.1-μm-thick sol-gel derived $SrTiO_3$ film on stainless steel with Al top electrode as a function of temperature at various frequencies [Thomas et *al.*, 1997].

ε' of sol-gel derived ST film deposited on stainless steel and annealed at 650ºC for 0.5h is much smaller than that of all ST films prepared by others methods and on different substrates described above. Moreover, at low frequencies ε' of this film decreases as the sample is cooled from room temperature down to 10K (Fig.2.18), in contrast to incipient ferroelectric behaviour of ST. Only at 1MHz ε' is ~107 from room temperature down to ~150K and slowly rises to 112 at 10K (Fig.2.18). According to Thomas and co-authors, the major factors likely to cause the low ε' of this sol-gel derived ST film include the strain in the film, induced by the substrate and by the "clamping" effect between the neighbouring grains, as well as the grain-size effect [Thomas et *al.*, 1997].

Concerning the tanδ, the value of loss is high at room temperature and decreases at low temperature (Fig.2.18, *right axis*). Moreover, there are indications of a weak dispersion around 100K at 1MHz, which was intended to attribute to ferroelectricity in $SrTiO_3$ below 110K. However, attempts to record ferroelectric hysteresis loops in this sol-gel derived ST film failed [Thomas et *al.*, 1997].

Due to the importance of the sol-gel technique, the lack of information and necessity

in reproducible results, there is a need of systematic studies on the sol-gel preparation of ST films. Indeed one of the goals of this work is to methodically report on the sol-gel fabrication and characterization of ST films.

2.2.3. Field effect on dielectric response and tunability in $SrTiO_3$ films

In relation to the *dc* electric field effect, the behaviour of the real part of dielectric permittivity ε' of ST films is somehow similar to that of single crystals (described in subchapter 1.1.3), i.e. ε' decreases under applied field, as presented in Figure 2.19a [Yu et *al.*, 2002]. The broad peak that appears in $\varepsilon'(T)$ with increasing *dc* electric field shifts to high temperature, as shown in inset of Figure 2.19a [Yu et *al.*, 2002]. However, the broad peak, induced by *dc* bias, usually exist in $\varepsilon'(T)$ of ST films already at zero field, as reported in a number of publications [Findikoglu et *al.*, 1993; Li et *al.*, 1998a; Li et *al.*, 1998b; James and Xi, 2002; Astafiev et *al.*, 2003; Yamada et *al.,* 2005a; Kaene et *al.*, 2006] and presented in Figures 2.19b [Yu et *al.*, 2002] and 2.20 [Fuchs et *al.*, 1999].

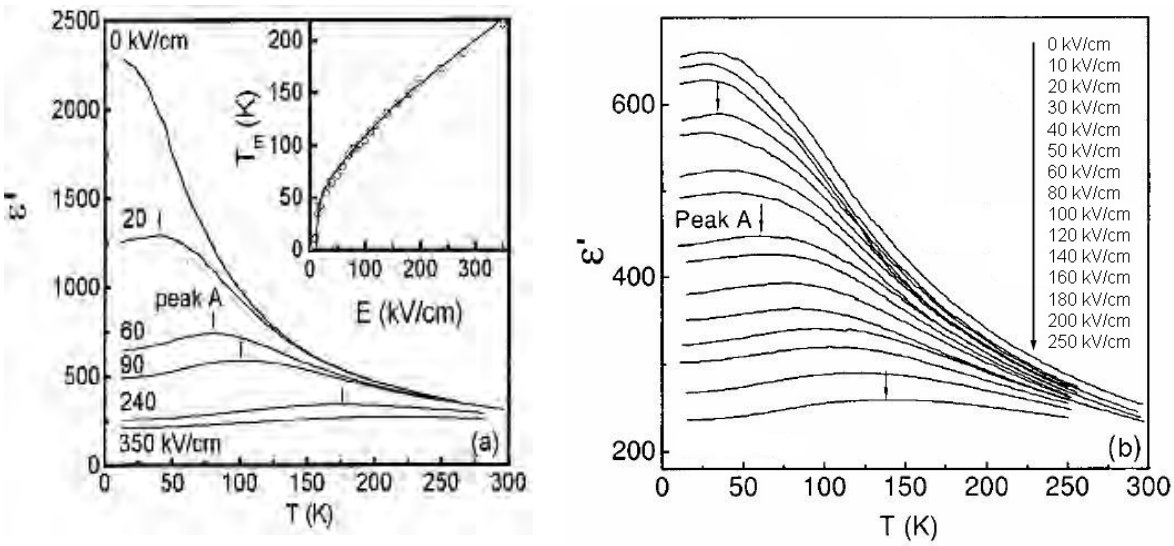

FIGURE 2.19. Temperature dependence of ε' of ~1.1-µm-thick $SrTiO_3$ films, epitaxially deposited by PLD on $SrTiO_3$ (a) and $LaAlO_3$ (b) substrates and measured as parallel-plate Au/$SrTiO_3$/$SrRuO_3$/substrate capacitor at 10kHz under different *dc* electric fields. Inset shows ε' peak temperature T_m *versus dc* electric field for $SrTiO_3$ film on $SrTiO_3$ substrate [Yu et *al.*, 2002].

Difference between ε' and as a consequence its dependence on the applied *dc* electric field (tunability) of ST films, presented in Figure 2.19a and 1.19b, is due the type of the

used substrates [Yu et *al.*, 2002]. For ST film deposited by PLD on $SrTiO_3$ substrate, ε' at zero field continuously increase with decreasing temperature up to ~2300 and its strong decrease with increasing *dc* electric field is obvious, as shown in Figure 2.19a. At the same time, zero field ε' of ST film deposited on $LaAlO_3$ substrate is only ~650 at peak temperature ~30K and does not show such a strong decrease of ε' under equivalent field (Fig.2.20b) [Yu et *al.*, 2002]. Although the nature of the difference between tuning of ε' of $SrTiO_3$ films deposited on $SrTiO_3$ and $LaAlO_3$ substrates was not explained by Yu and co-workers [Yu et *al.*, 2002], one possible reason can be different thermal stress/strain induced in the films by substrates ($SrTiO_3$ and $LaAlO_3$) and affecting the dielectric properties of ST thin films. The substrate influence will be analyzed in detail in the following subchapter.

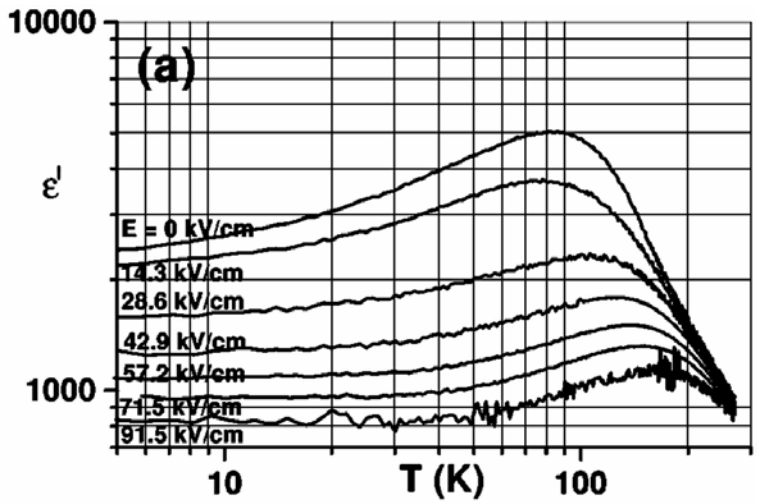

FIGURE 2.20. Temperature dependence of out-of-plain ε' of 300-nm-thick $SrTiO_3$ film, epitaxially deposited by magnetron sputtering between $YBa_2Cu_3O_{7-\delta}$ electrodes on $SrTiO_3$ substrate for various applied *dc* electric field strengths [Fuchs et *al.*, 1999].

On the other hand, $\varepsilon'(T)$ curves under several *dc* electric fields of ST films deposited on $SrTiO_3$ substrates with $YBa_2Cu_3O_{7-\delta}$ electrodes by magnetron sputtering (Fig.2.20) [Fuchs et *al.*, 1999] are also very different from those deposited on $SrTiO_3$ substrates with $SrRuO_3$ electrodes by PLD (Fig.2.19a) [Yu et *al.*, 2002]. So, change of the electrodes from $SrRuO_3$ to $YBa_2Cu_3O_{7-\delta}$ (with corresponding change of the mismatch strain) leads to induction of the peak in zero field $\varepsilon'(T)$ at ~89K with magnitude as high as ~5000, as

shown in Figure 2.20 [Fuchs et *al.*, 1999]. The deposition method and conditions can play a role as well, although both films were epitaxial.

On the contrary to the bottom electrode, the top electrode was reported by Fuchs et *al.* to have no significant influence on the dielectric response of ST film, at least when $YBa_2Cu_3O_{7-\delta}$ top electrode was substituted by Au [Fuchs et *al.*, 1999]. So, results for Au/$SrTiO_3$/$YBa_2Cu_3O_{7-\delta}$ capacitor, shown in typical ε' *versus* bias voltage representation in Figure 2.21, are well compatible with $\varepsilon'(T)$ dependence under different fields of $YBa_2Cu_3O_{7-\delta}$/$SrTiO_3$/$YBa_2Cu_3O_{7-\delta}$ capacitor from Figure 2.20. Below the peak temperature $T_{\varepsilon'max}$ at zero bias field of 90K, the bell-shape $\varepsilon'(V)$ characteristics show an increasing hysteretic behaviour with decreasing temperature, implying a ferroelectric phase transition. The highest effect of *dc* electric field on ε' is observed near $T_{\varepsilon'max}$, where ε' can be decreased to 20% of the maximum value by applying a bias voltage of 3V, corresponding to bias field E_{dc}~10^5V/cm.

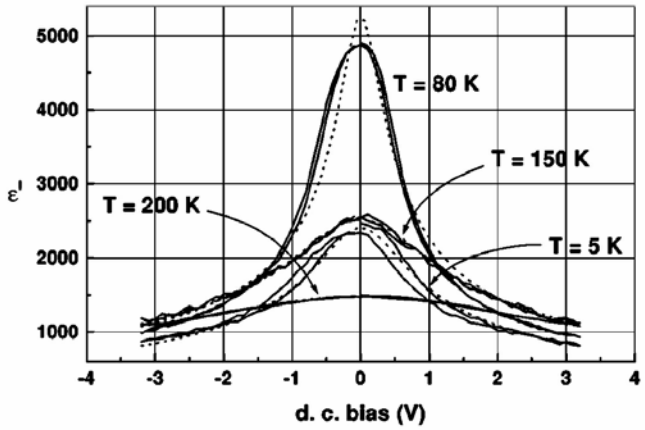

FIGURE 2.21. Out-of-plain ε' of 300-nm-thick $SrTiO_3$ film, epitaxially deposited by magnetron sputtering on $SrTiO_3$ substrate with $YBa_2Cu_3O_{7-x}$ as ground electrode and Au top electrode, *versus* bias voltage at different temperatures; the dotted lines are fits to the data. The measurements were carried out at a frequency of f=120Hz [Fuchs et *al.*, 1999].

Similar results of tuning were obtained by different research groups, as shown in Figure 2.22.

For the characterisation of the dependence of ε' of ST films on applied *dc* bias electric field, the tunability n and relative tunability n_r can be used as for bulk ST (described in subchapter 1.1.3). However, since the ε' of thin films is smaller than that of bulk materials, the tunability of films is expected to be smaller as well. The relative tunability of 2.5-μm-

thick ST film, prepared by PLD between $SrRuO_3$ electrodes on $LaAlO_3$ substrate, is plotted *versus* temperature in Figure 2.23 along with the results for ST single crystals [Li et *al.*, 1998b]. The relative tunability of this ST film under *dc* field of 40-50V/µm at low temperatures is about 70%, which persists up to about 100K and slowly decreases but remains nonzero upon further heating. For the single crystal, the large tunability up to 85% could be obtained at low temperatures even under two orders smaller *dc* field of 0.4V/µm, but it drops to near zero at about 70K (Fig.2.23) [Li et *al.*, 1998b].

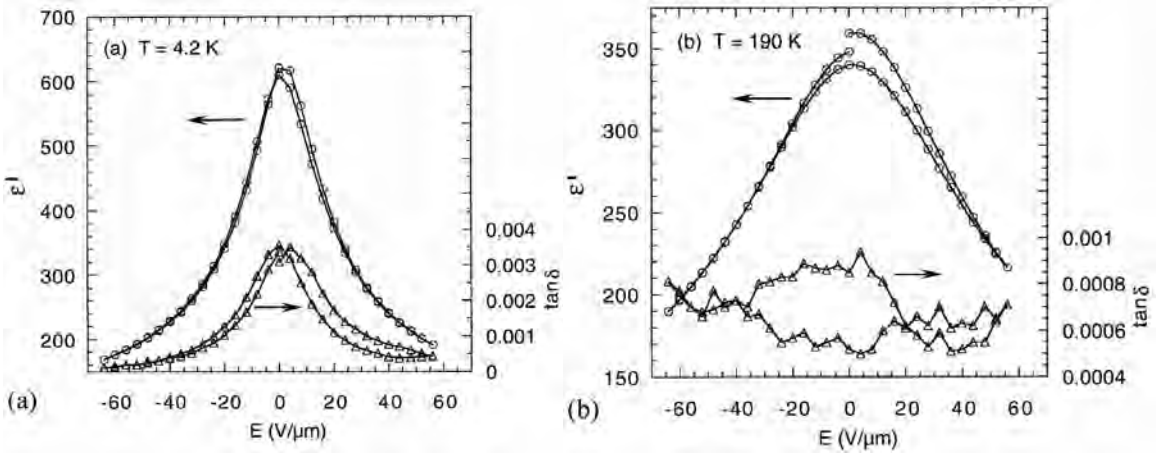

FIGURE 2.22. Out-of-plain ε' and tanδ of 2.5-µm-thick $SrTiO_3$ film, epitaxially deposited by PLD between $SrRuO_3$ electrodes on $LaAlO_3$, as a function of *dc* electric field at 4.2K (a) (tunability ~72%, tanδ_{max}=0.0036) and 190K (b) (tunability ~46%, tanδ_{max}=0.00094) [Li et *al.*, 1998b].

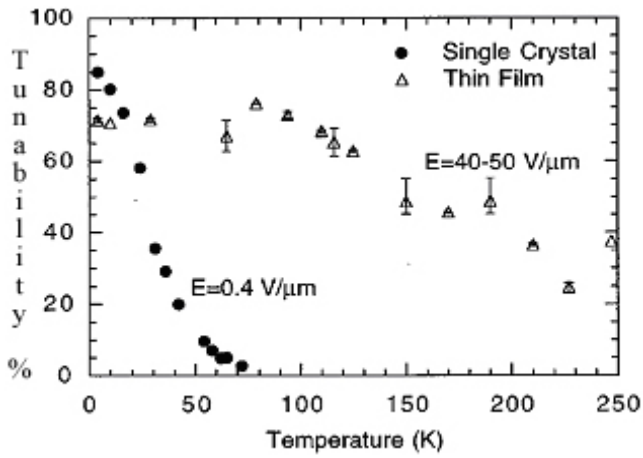

FIGURE 2.23. Relative tunability of 2.5-µm-thick $SrTiO_3$ film, epitaxially deposited by PLD between $SrRuO_3$ electrodes on $LaAlO_3$ substrate, under 40-50V/µm and of $SrTiO_3$ single crystal under 0.4V/µm as a function of temperature [Li et *al.*, 1998b].

While the single crystal results can be explained by the electric-field hardening of the soft mode [Fleury and Worlock, 1968a], which diminishes above ~70K, in the case of thin films the result suggests either a much modified soft mode or a persistent nanoscale ferroelectric type ordering as in the relaxor ferroelectrics or in dipole glasses [Li et *al.*, 1998b]. Akimov et *al*. measured the TO1 phonon frequency of ST films as a function of external electric fields and showed that the soft mode frequency increases when an electric field is applied in the entire temperature range of the measurement, as shown in Figure 2.24 [Akimov et *al.,* 2000]. Hence the mechanism of electric-field tunability of ε' in ST films is, as in the crystals, the field induced hardening of the soft mode. However, since the soft-mode properties and their responses to the external electric field are different in thin film and bulk ST, the difference in the dielectric nonlinearity is observed [Akimov et *al.,* 2000].

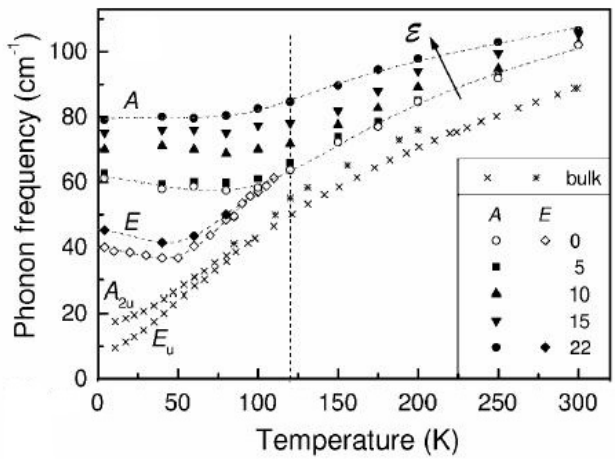

FIGURE 2.24. Frequency of *A* and *E* components of TO1 phonon of $SrTiO_3$ thin film as a function of temperature for different values of external electric field, given in 10^4V/cm. Temperature dependence of the soft modes in bulk $SrTiO_3$ (stars and crosses) is shown for comparison [Akimov et *al*., 2000].

As shown in Figure 2.22, the dielectric loss of ST thin films are also affected by *dc* electric field, revealing a bell-shape curves at low temperatures [Li et *al.*, 1998b].

Meanwhile, it was also reported about different behaviour and value of tanδ under *dc* electric field for ST films deposited on different substrates [Yu et *al.*, 2002]. As shown in Figures 2.25 and 2.26, there are differences between tanδ of ST films deposited on $SrTiO_3$ substrate on $LaAlO_3$ substrate. The peak A, which corresponds to the field induced peak in $\varepsilon'(T)$ of ST single crystal and whose temperature of the maximum increased with *dc*

electric field, was detected in tan*δ(T)* of both ST films under different *dc* field (Figs.2.25 and 1.26) [Yu et *al.*, 2002]. Moreover, a peak around 70K ~at 10kHz (denoted as mode II) was detected also in both analyzed samples (Figs.2.25 and 2.26) [Yu et *al.*, 2002]. However, a peak around 165K at 10kHz (denoted as mode I) was found only in ST film on $SrTiO_3$ substrate (Fig.2.25) [Yu et *al.*, 2002]. Intensity of the modes I and II continuously decreased with *dc* electric field, whereas temperatures of their maximum were field independent. Yu et *al.* [Yu et *al.*, 2002] noted that such behaviour is different from any "ordered phase" or "induced ferroelectric peak", whose temperature increases with increasing electric field [Ang et *al.*, 2000a; Frenzel and Hegenbarth, 1974; Fleury and Worlock, 1968a; Hemberger et *al.*, 1995], but is similar to the so-called defect/impurity mode observed in ST doped with Bi [Ang et *al.*, 1999b, Ang and Yu, 2000e].

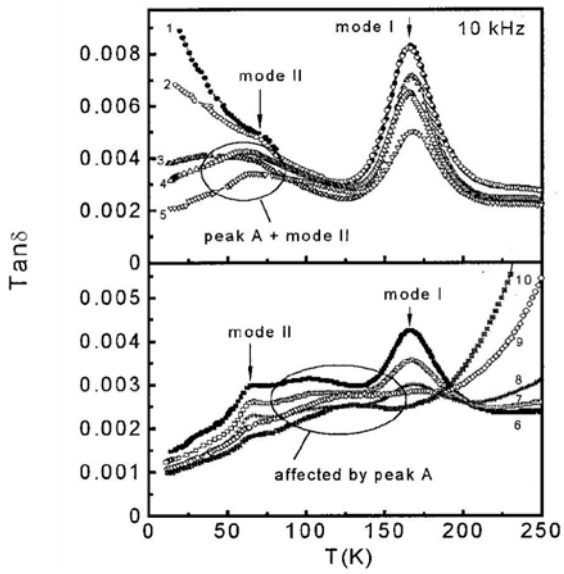

FIGURE 2.25. Temperature dependence of tan*δ* of ~1.1-µm-thick $SrTiO_3$ film, epitaxially deposited by PLD on $SrTiO_3$ substrate, measured at 10kHz under *dc* electric fields of 0, 10, 30, 50, 80, 120, 160, 200, 280, 350kV/cm, labelled from 1 to 10, respectively [Yu et *al.*, 2002].

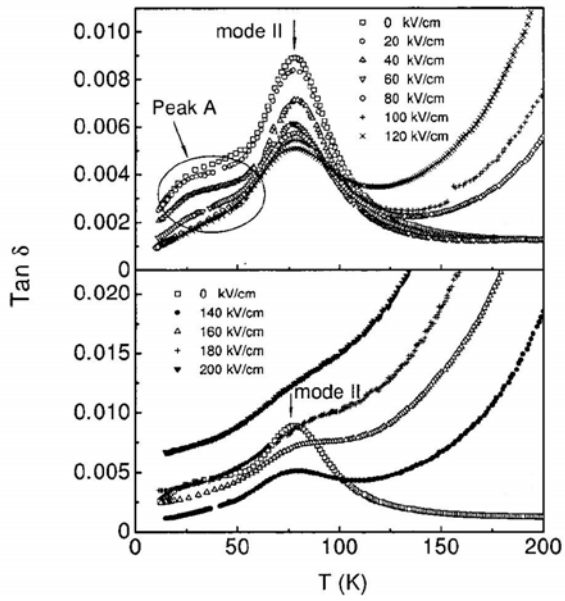

FIGURE 2.26. Temperature dependence of tan*δ* of ~1.1-µm-thick $SrTiO_3$ films, epitaxially deposited by PLD on $LaAlO_3$ substrates, measured at 10kHz under *dc* electric field of 0, 10, 20, 30, 40, 50, 60, 80, 100, 120, 140, 160, 180, 200, 250kV/cm (from top to bottom) [Yu et *al.*, 2002].

However, Yu and co-workers [Yu et *al.*, 2002] did not explain why ST films deposited on different substrates with the same procedure show different behaviour and different value of tanδ under applied field, leaving these questions still open.

2.2.4. Strain influence

It is known that mechanical stresses have a marked impact on the modification of the phase transitions, lattice structure and electrical response of bulk materials. For example, the application of a uniaxial clamping stress is known to increase T_c in bulk perovskite ferroelectrics [Forsbergh, 1953; Schimizu, 1997; Pertsev et *al.*, 1998] and induce ferroelectric phase transitions in incipient ferroelectrics [Burke and Pressley, 1971; Uwe et *al.*, 1973; Schimizu, 1997; Pertsev et *al.*, 2000b; Pertsev et *al.*, 2002], while a hydrostatic pressure is known to decrease T_c in perovskite ferroelectrics with displacive phase transitions [Forsbergh, 1953; Samara, 1966; Samara et *al.*, 1975; Ishidate et *al.*, 1997; Schimizu, 1997]. These facts prognosticate rather interesting effects in thin films clamped to the substrate.

As mentioned above, ferroelectric phase transitions can generally be analysed by phenomenological theory employing a thermodynamical free energy approach, though the situation is rather complicated in the case of ST at low temperatures due to the coexistence of two kinds of order parameters, one represented by the polarisation and another one by the rotation of the oxygen octahedra. Interaction between them and also with the lattice strain or stress must then be taken into account. In such a way, the ε' and the frequencies of the ferroelectric and structural soft modes for ST crystals were derived theoretically as a function of the stress by Uwe and Sakudo [Uwe and Sakudo, 1976]. These authors experimentally observed by using dielectric measurements and Raman scattering experiments that ferroelectricity in ST was induced at liquid helium temperature under stress [Uwe and Sakudo, 1976, and references therein]. The inverse dielectric susceptibilities γ_i (susceptibility $\chi'=\varepsilon'-1$) were found to change linearly with stress up to some critical values [Uwe and Sakudo, 1976]. By means of Raman scattering measurements, the ferroelectric soft modes were observed above the critical stresses [Uwe and Sakudo, 1976].

Regarding the films, they are always under stress due to presence of the substrate, heat treatments during deposition, *etc*. However, stresses in epitaxial films are easier to be

predicted and calculated than in the case of polycrystalline films due to the presence of grain boundaries in these last. For this reason the studies of the stress effects on the dielectric response of ST films tend to be done in epitaxialy grown films rather than in polycrystalline films such as sol-gel derived ones, as is the case of the films analysed within this Thesis.

One cause of stresses in thin films is the lattice mismatch between the film and the substrate and it was observed to play a critical role in the dielectric response of ferroelectric thin films [Pertzev et *al.*, 2000b]. Interfacial defects due to lattice-mismatch induced strains have been demonstrated to exist in ferroelectric thin films [Speck et *al.*, 1995; Wu et *al.*, 2001]. So it has been suggested that a combination of strain and interface effects are responsible for the differences in the dielectric properties of thin films and single crystals [Streiffer et *al.*, 1999].

The lattice mismatch [Van Der Merwe et *al.*, 1986; Haeni et *al.*, 2004], also called as *in-plane elastic strain* or *misfit strain* [Speck and Pompe, 1994; Pertsev et *al.*, 2000b], between film and substrate can be defined as Eq.2.8

$$Lattice\ Mismatch = \frac{a_{substrate} - a_{film}}{a_{substrate}} \tag{2.8}$$

where $a_{substrate}$ stands for the substrate lattice parameter and a_{film} stands for the free-standing film lattice parameter. It is of considerable importance in thin epitaxial films where film growth takes the orientation of the underlying single crystal or textured substrate. Concomitantly, the compatibility / coexistence of the substrate underneath the film may result in strains in the films of two different types: tensile ($a_{film} < a_{substrate}$) and compressive ($a_{film} > a_{substrate}$).

By definition, strain is the change of length per unit length and its dimensionless value can be measured in films as will be described in details in Chapter 3. At the same time the *stress* value (that is force per unit of area, measured in kN/m^2 or Pa) can be calculated as:

$$stress \sim E \times strain \tag{2.9}$$

where E is the elastic Young's modulus of the material. So stress can be calculated from the strain values either in compressive or tensile state as will be described in details in Chapter 3.

Another cause of stress in thin films can be connected with annealing process after or during their deposition. Since high temperatures are usually necessary for the crystallization of the required film phase (perovskite phase for the case of ST), stress between the substrates and films develops upon cooling to room temperature due to the difference in the thermal expansion coefficients (TEC, α) of the film (α_{film}) and substrate ($\alpha_{substrate}$). This thermal stress σ_{th} can be expressed as:

$$\sigma_{th} = \int_{RT}^{T_{ann.}} \frac{E_f}{1-\gamma_f} \times (\alpha_{film}(T) - \alpha_{substrate}(T))dT \tag{2.10}$$

where E_f stands for the Young´s modulus of the film and γ_f stands for the Poisson ratio of the film. σ_{th} may induce stress driven preferred orientation and structural changes of the films that results in the change of their dielectric response as well as cracking of the films, leading to short circuiting between their top and bottom electrodes.

In the case of ferroelectrics, Landau-Ginzburg-Devonshire formalism provides a framework for understanding of the effect of stress on the dielectric properties. Within this framework it was predicted that for strained $BaTiO_3$ and $PbTiO_3$ thin films *1)* the temperature of the phase transition should be higher than in the corresponding bulk material and *2)* the phase transition would be changed from a first order transition as in bulk materials to a second order one in films [Pertsev et *al.*, 1998]. These theoretical predictions were later experimentally verified on epitaxial (001) oriented $PbTiO_3$ and $BaTiO_3$ films on cubic substrates [Pertsev et *al.*, 1999]. Obtained results were explained as influence of the compressive stress (that resulting in polarization being oriented "out-of-plane") or tensile stress (that leads to the polarization oriented "in-plane") according to theory of Pertsev and co-authors [Pertsev et *al.*, 1999].

For incipient ST films, Pertsev et *al.* have also developed a strain temperature phase diagram taking into account that ST crystals have two coupled instabilities – antiferrodistortive, characterized by the structural order parameter *q*, and ferroelectric, characterized by the spontaneous polarization *P* (Fig.2.27) [Pertsev et *al.*, 1999; Pertsev et *al.*, 2000b]. The authors showed that ST films remain paraelectric down to 0K only in a narrow range of small negative misfit strains between -2×10^{-3} and -2.2×10^{-4} [Pertsev et *al.*, 2000b]. Outside this "paraelectric gap" the two-dimensional (2D) clamping and straining

of the film by the substrate lead to the appearance of ferroelectricity in ST films [Pertsev et *al.*, 2000b]. Even though the stress-induced ferroelectric phase transition was observed in ST single crystals [Okai and Yoshimoto, 1975; Uwe and Sakudo, 1976], the predicted thin-film phase diagram is much richer than the single crystal one due to the mechanical stress film/substrate interaction [Pertsev et *al.*, 2000b].

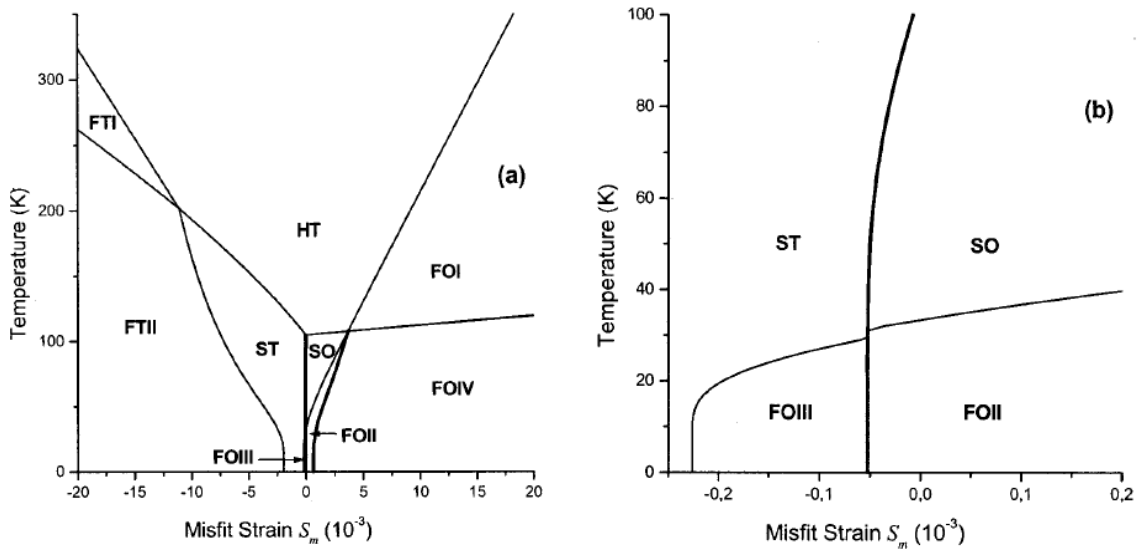

FIGURE 2.27. Phase diagram of (001) oriented single-domain $SrTiO_3$ thin film, epitaxially grown on (001)-oriented cubic substrates, (a) and its enlarged section near zero misfit strain (b), theoretically predicted by Pertsev et *al.* [Pertsev et *al.*, 2000b].
HT - high temperature tetragonal phase, ST - "structural" tetragonal states SO - "structural" orthorhombic states, FTI - ferroelectric tetragonal phases, FOI - ferroelectric orthorhombic phases, FTII, FOII, and FOIII - "mixed" states where both *P* and *q* differ from zero (see Table 2.1 for details) [Pertsev et *al.*, 2000b].

TABLE 2.1. Nonzero components of the polarization *P* and the structural parameter *q* in different stable phases forming in (001) ST single-domain film, epitaxially grown on a cubic (001)-oriented substrate (according to [Pertsev et *al.*, 2000b]).

Phase	HT	ST	SO	FTI	FTII	FOI	FOII	FOIII	FOIV
P				P_3	P_3	$\|P_1\|=\|P_2\|$	P_1 (or P_2)	$\|P_1\|=\|P_2\|$	$\|P_1\|=\|P_2\|$
q		q_3	q_1 (or q_2)		q_3		q_2 (or q_1)	q_3	$\|q_1\|=\|q_2\|$

One of the problems of the confirmation/application of theoretical predictions is that (and in this particular case) it describes perfect epitaxially grown single-crystalline films. And these films are very difficult to be fabricated. Although technologies developed during the last decade enables growing films highly oriented, usually the thickness of such films is less than ~100nm, causesing limitations in experimental terms. The other difficulty is associated with the fact that polycrystalline films are randomly oriented and three-dimensional (3D) clamping stress acting on each grain from the neighbour grains, leading to grain-boundary interfaces effects. Such properties do not satisfy the developed thermodynamic theory any more and require different theoretical approach.

Only recently the experimental confirmation of the theoretical prediction developed by Pertzev et *al*. concerning strained ST films [Pertsev et *al.*, 2000b] has been published [Haeni et *al.*, 2004]. Haeni and co-authors showed that strain from a particular $DyScO_3$ substrate can be harnessed to increase T_c by hundreds of degrees and produce near-room-temperature ferroelectricity in 50-nm-thick ST thin films prepared by molecular beam epitaxy (MBE) technology (Fig.2.28) [Haeni et *al.*, 2004].

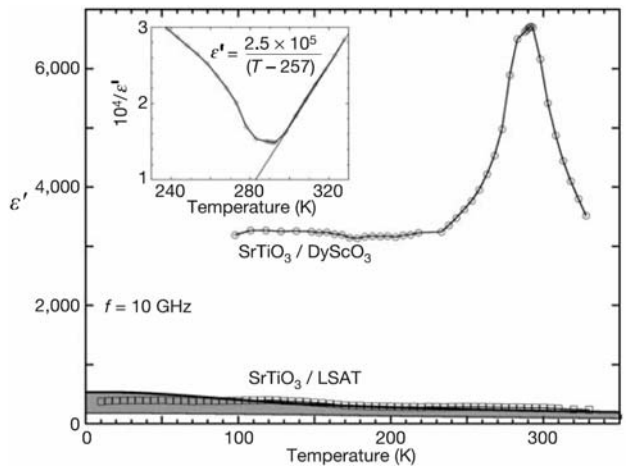

FIGURE 2.28. In-plane ε' of strained epitaxial $SrTiO_3$ films, epitaxially grown by MBE on $DyScO_3$ and on $(LaAlO_3)_{0.29}\times(SrAl_{0.5}Ta_{0.5}O_3)_{0.71}$ (LSAT) substrates, as a function of temperature at 10GHz. The inset shows a Curie-Weiss fit to $1/\varepsilon'$ [Haeni et *al.*, 2004].

In that work, Haeni et *al.* reported about a tensile lattice mismatch (+1.0% at room temperature) between the (110) $DyScO_3$ substrate and (100) ST film [Haeni et *al.*, 2004]. For comparison, compressive lattice mismatch (-0.9% at room temperature) was calculated for epitaxial (100) ST films on $(LaAlO_3)_{0.29}\times(SrAl_{0.5}Ta_{0.5}O_3)_{0.71}$ (LSAT) substrates [Haeni

et *al.*, 2004]. A dielectric anomaly at almost room temperature was observed for ST films on $DyScO_3$ substrates but no anomaly was observed of LSAT substrate. So, the appearance of a dielectric anomaly in epitaxial ST film on $DyScO_3$ substrate is a confirmation of Pertsev et *al.* theory for epitaxial thin films [Pertsev et *al.*, 2000]. Meanwhile, this strain-induced enhancement in T_c of ST films on $DyScO_3$ substrates is the largest ever reported. Thus, the high ε' of these films at room temperature (nearly 7000 at 10GHz) (Fig.2.28) and its sharp dependence ε' on electric field are highly promising for device applications at least at presented frequency 10GHz, although no information about frequency dependence of dielectric response was shown [Haeni et *al.*, 2004].

The strain effect on the ST film properties depends not only on the type of substrates but also on the film deposition method and its conditions. Differences in the dielectric properties of ST thin films, fabricated under different conditions by pulsed laser deposition method onto MgO and $LaAlO_3$ substrates, are clearly seen from Figure 2.29 [Astafiev et *al.*, 2003]. In the case of $LaAlO_3$ substrates, an evident maximum in the temperature dependence of ε' appeared, which suggests the appearance of ferroelectricity in ST thin films, whereas, in the case of MgO substrates, the films exhibit a monotonic temperature dependence of ε' [Astafiev et *al.*, 2003].

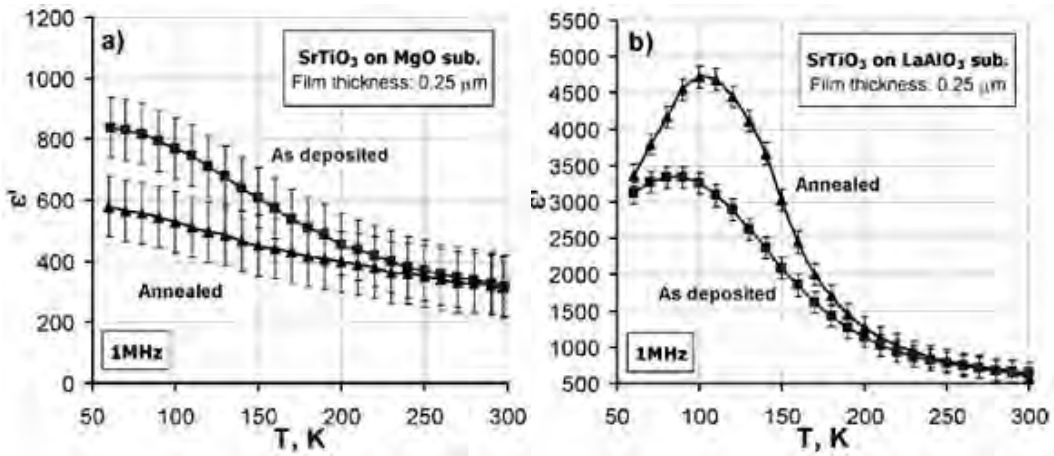

FIGURE 2.29. In-plane ε' of 250-nm-thick $SrTiO_3$ thin film, epitaxially deposited by PLD on MgO (a) and $LaAlO_3$ (b) substrates, as a function of temperature, measured at 1MHz [Astafiev et *al.*, 2003].

Moreover, a post-deposition annealing at 1100°C in the oxygen atmosphere during 4 hours resulted in a shift of the peak in $\varepsilon'(T)$ to a higher temperature in the case of $LaAlO_3$ substrates and in a decrease of ε' in the case of MgO substrate [Astafiev et *al.*, 2003].

Furthermore, below the temperature of the peak in *ε'(T)* of these ST films on $LaAlO_3$ substrates of about 100K clear ferroelectric-type polarisation *P* versus *ac* electric field *E* hysteresis loops were observed (Fig.2.30) [Astafiev et *al.*, 2003].

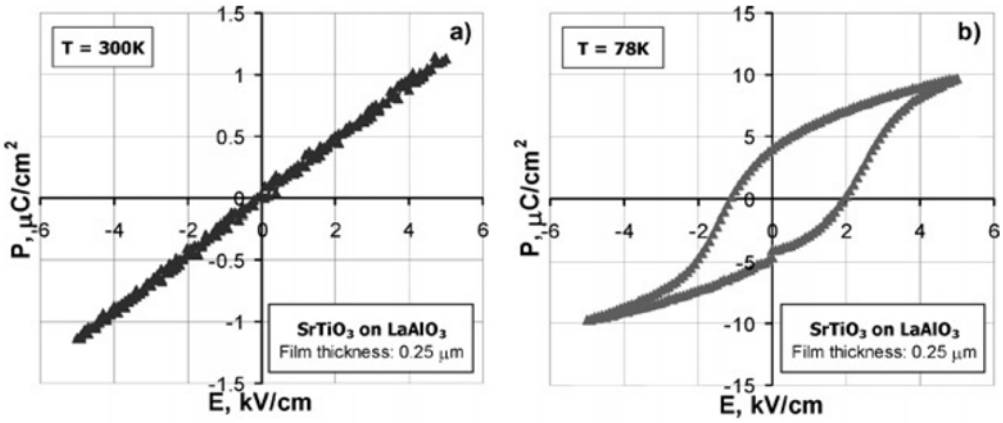

FIGURE 2.30. Polarisation *P versus ac* electric field *E* hysteresis loops measured at room (a) and liquid nitrogen (b) temperatures on planar capacitors based on $SrTiO_3$ thin film, epitaxially deposited by PLD on $LaAlO_3$ substrate [Astafiev et *al.*, 2003].

To understand the nature of the dielectric anomaly in *ε'* and its dependence on annealing process, a deep analysis of the obtained results, including the data of thermal expansion coefficients of the substrates and ST single crystal, lattice parameters of strained ST films and ST single crystal and elastic constants of bulk ST, was performed [Astafiev et *al.*, 2003]. XRD measurements have shown that the annealing procedure results in an increase of the in-plane lattice parameter of ST film on MgO substrate and in its decrease on $LaAlO_3$ substrate. According to the thermodynamic theory for the influence of misfit strain in the film on its dielectric properties and phase transition temperature, the increase of the in-plane lattice parameter should lead to an increase of the in-plane Curie-Weiss temperature and vice versa. However, it is just opposite to the obtained results from Figure 2.29. Therefore, Astafiev et *al.* suggested that in this case the misfit strain does not play the principal role in the shift of the Curie-Weiss temperature of the films and the temperature dependence of dielectric response of analyzed ST films cannot be interpreted in terms only of the mechanical coupling between the film and the substrates. A possible explanation for the impact of annealing and the substrate material on the dielectric properties of these films is non-stoichiometry of the film composition caused by the chemical contact of the film with the substrate during deposition and by annealing in oxygen atmosphere [Astafiev et *al.*, 2003]. However, there is no confirmation of this hypothesis.

Another example of the effect of processing conditions on the dielectric response of ST films is reported by Yamada et *al*. [Yamada et *al.*, 2005a]. In that work, ST films were deposited on $LaAlO_3$ substrates by PLD two-step growth technique that consisted of the deposition of a first 10-nm-thick layer at 100°C, its annealing at 750°C for 30min and deposition of a second 250-nm-thick layer at 750°C. Such sequence provides an effective strain relaxation between ST film and LAO substrate. The dielectric permittivity of ST films without and with first layer (of different thickness) is depicted in Figures 2.31 and 2.32 as a function of temperature and *dc* electric field, respectively.

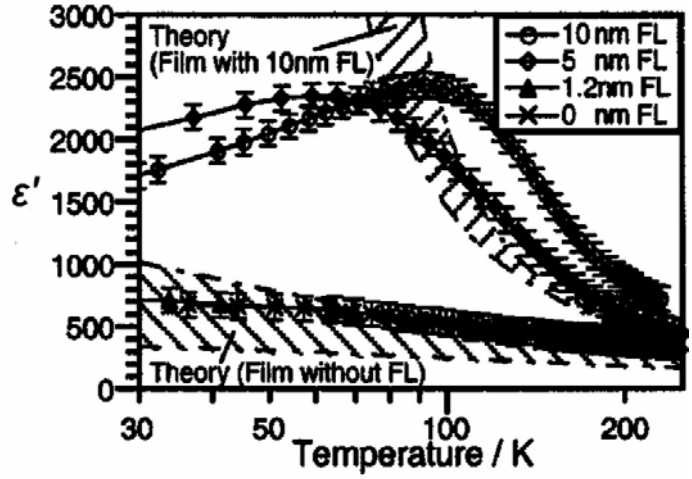

FIGURE 2.31. Temperature dependence of in-plane ε' of 250-nm-thick $SrTiO_3$ films with various first layers (FLs) thickness, deposited by PLD two-step growth technique on $LaAlO_3$ substrates. The hatched areas show theoretical predictions of $SrTiO_3$ in paraelectric phase with/without a 10-nm-thick FL [Yamada et *al.*, 2005a].

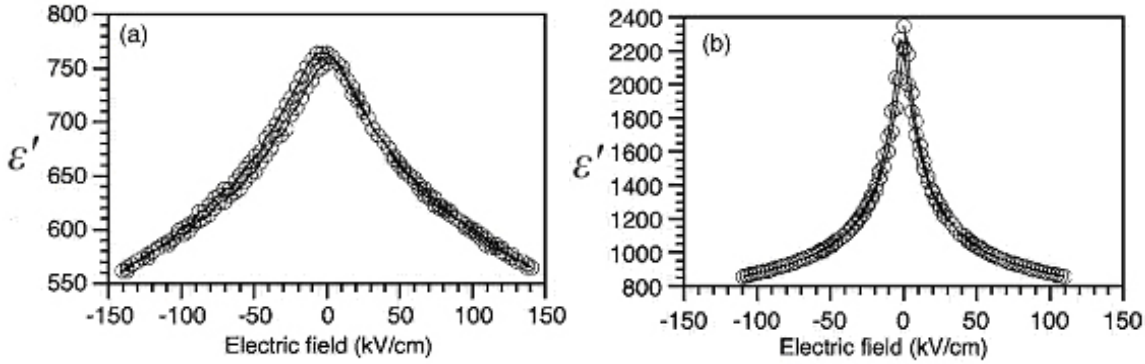

FIGURE 2.32. *dc* electric field dependence of in-plane ε' of normally grown 250-nm-thick $SrTiO_3$ film (a) and two-step-grown 250-nm-thick $SrTiO_3$ film with 10-nm-thick first layer (b), deposited by PLD on $LaAlO_3$ substrates, measured at a frequency of 8GHz and temperature of 78K [Yamada et *al.*, 2005b].

Annealing of the first very thin and quasiamorphous layer deposited at low temperature leads to the crystallization of the perovskite phase with substantial misfit dislocation formation, resulting in a completely relaxed template layer for the subsequent growth. Moreover, value of ε' is higher for ST films with thicker first layer film (10nm) than that of films with thinner (1.2nm or 5nm) or without first layer film (Fig.2.31) [Yamada et *al.*, 2005b]. Since the film was relaxed at the deposition temperature of the second layer (750°C), it shows higher ε' (Fig.2.31) and larger tuning (Fig.2.32) along the in-plane direction compared to the normally grown film which possessed compressive strain due to the weaker strain relaxation for the same annealing temperatures [Yamada et *al.*, 2005a; Yamada et *al.*, 2005b]. Yamada and co-authors concluded that ferroelectric transition temperature in ST films, obtained by a two-step growth technique, increases with strain relaxation during the growth [Yamada et *al.*, 2005a; Yamada et *al.*, 2005b].

Indeed the temperature of annealing or deposition plays an important role due to the difference between the thermal expansion coefficients of the substrate and films independently on the preparation method. The effect of deposition temperature on the dielectric response of ST films obtained by PLD method is further clarified by Wördenweber et *al.* [Wördenweber et *al.*, 2007]. As shown in Figure 2.33, the biaxial compressive strain on 400-nm-thick ST films deposited by PLD on CeO_2-coated Al_2O_3 substrates at different heater temperatures (770°C-850°C) leads to different ε' (Fig.2.33a) and to a considerable increase of the Curie temperature (Fig.2.33b) [Wördenweber et *al.*, 2007]. The temperature dependence of the in-plane ε' of all films shows a pronounced maximum around 80-120K and the position of the maximum depends on the annealing temperature (Fig.2.33a). In contrast to ST single crystals, these films show a Curie-Weiss like behaviour with $T_c \approx$ 50-75K only at high temperatures $T >$ 150K (Fig.2.33b) [Wördenweber et *al.*, 2007]. Moreover, according to measurements of the hysteretic behaviour, ferroelectricity persists even up to 180-220K in these compressively strained ST films [Wördenweber et *al.*, 2007]. However, increase of T_c was demonstrated by Haeni et *al*. for tensile in-plane strained ST films on $DyScO_3$ but not for compressively strained ST films on LSAT [Haeni et *al.*, 2004]. Thus, Wördenweber and co-authors concluded that not only biaxial tensile but also compressive strain can lead to a substantial increase of T_c and a considerable increase of the ε' and tunability of ST thin films in technically relevant temperature regimes [Wördenweber et *al.*, 2007].

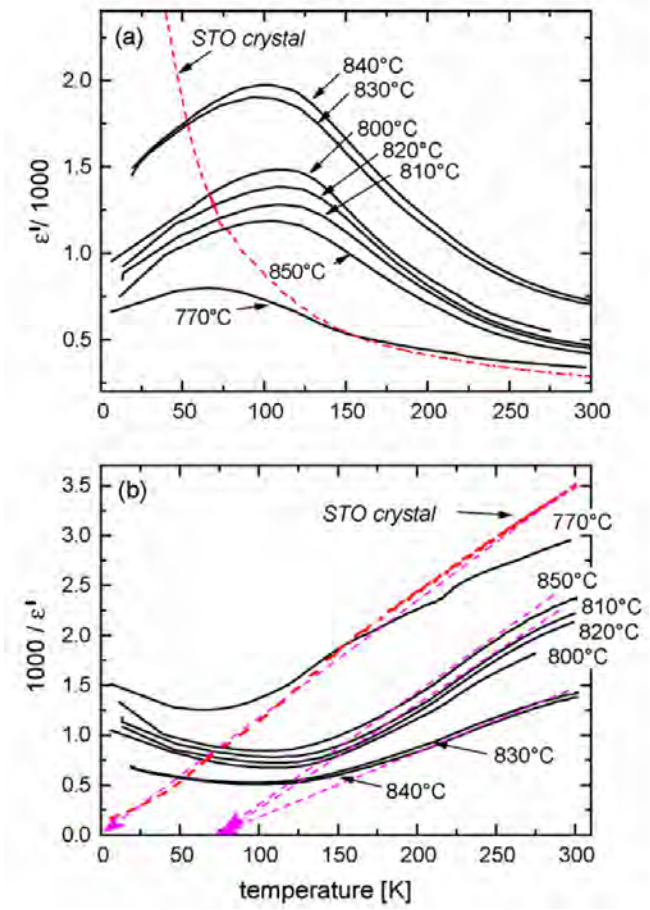

FIGURE 2.33. Temperature dependence of in-plane ε' (a) and inverse ε' (b) of 400-nm-thick $SrTiO_3$ films, deposited by PLD on CeO_2-coated Al_2O_3 substrates at different temperatures. Additionally the data obtained from measurements of a *planar* capacitor on a single crystalline $SrTiO_3$ substrate are presented. All data are recorded at 1MHz [Wördenweber et *al.*, 2007].

Besides the strain effect due to the lattice mismatch between substrate and film and temperature effect during preparation, the dielectric response of the films deposited by the same way can depend on bottom electrodes. ST films deposited by PLD on $SrTiO_3$ and $LaAlO_3$ substrates with $CaRuO_3$ or $SrRuO_3$ bottom electrodes, measured as parallel plate capacitors with Au top electrodes, presented four different *dc* electric field dependences of ε' (Fig.2.34) [Hyun and Char, 2001].

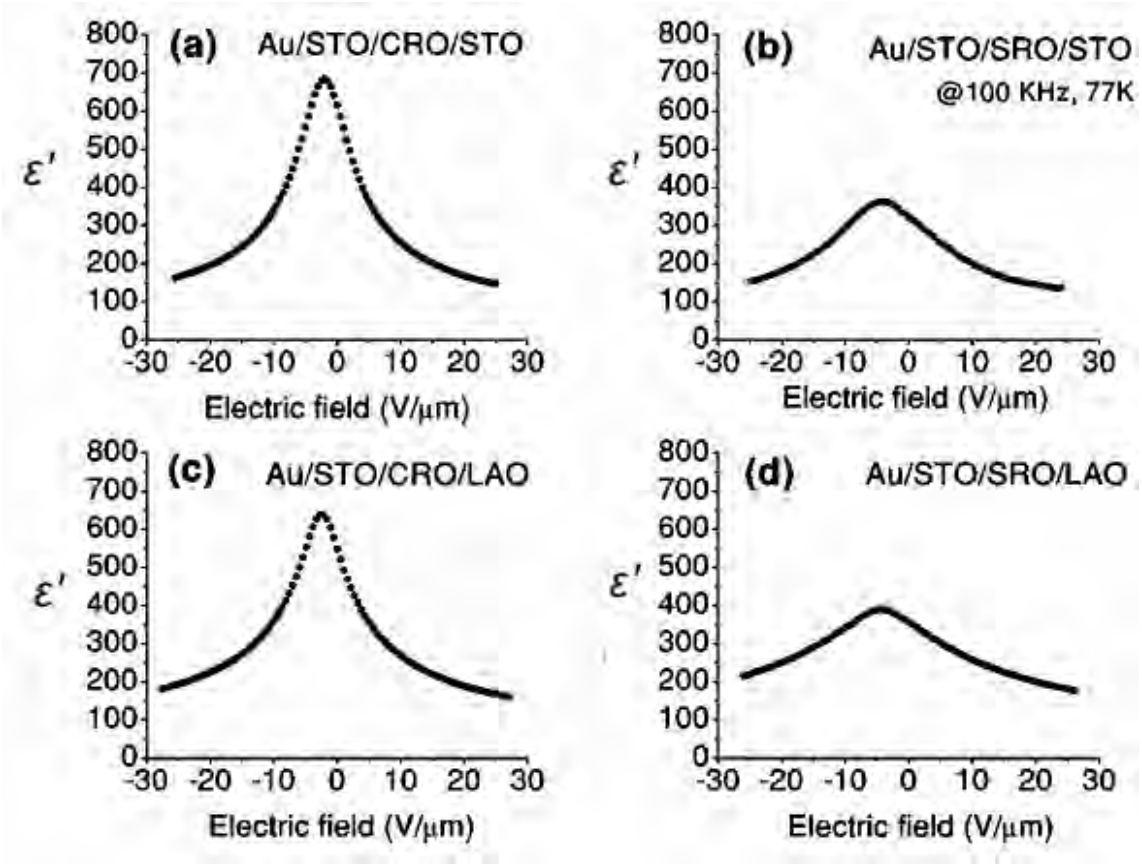

FIGURE 2.34. Out-of-plane *ε′ versus* electric field, measured at 77K and 100kHz on $Au/SrTiO_3/CaRuO_3/SrTiO_3$ (a), $Au/SrTiO_3/SrRuO_3/SrTiO_3$ (b), $Au/SrTiO_3/CaRuO_3/LaAlO_3$ (c) and $Au/SrTiO_3/SrRuO_3/LaAlO_3$ (d) parallel plate capacitors, prepared by PLD [Hyun and Char, 2001].

It is evident that ST films on $CaRuO_3$ electrodes (Fig.2.34a,c) present nearly two times larger tunability than that of films on $SrRuO_3$ electrodes (Fig.2.34b,d). Such behaviour was attributed to the different strain state of the ST films, induced by bottom electrodes and substrates [Hyun and Char, 2001]. From XRD measurements and calculation of the in-plane lattice parameters, it was detected that ST films on $CaRuO_3$ electrodes are under in-plane compressive strain that gives a tetragonal distortion elongated along the *c* axis and ST films on $SrRuO_3$ electrodes are under in-plane tensile strain that gives a tetragonal distortion shortened along the *c* axis [Hyun and Char, 2001]. Therefore the behaviour of tunability can be connected with the behaviour of soft mode [Hyun and Char, 2001]. As well known, the tunability in ST is closely related to the hardening of soft phonon mode, mainly related to the vibration of Ti and O ions in oxygen octahedra. Since the ionic displacement is affected by strain, the tunability should change largely. The decreasing of the lattice parameter leads to the decreasing of the ionic displacement, hardening the soft

phonon mode and lessening the tunability. On the other hand, the increasing of lattice parameter leads to the increasing of the ionic displacement, resulting in the enhanced tunability. Therefore Hyun and Char concluded that the in-plane compressive strain in ST films on $CaRuO_3$ electrodes that elongates the unit cell along electric field in the parallel plate capacitor structure enhances the tunability, whereas the in-plane tensile strain in ST films on $SrRuO_3$ electrodes that makes the out-of-plane lattice parameters shorter than the in-plane lattice parameters decreases the tunability in the parallel plate structure (Fig.2.35) [Hyun and Char, 2001].

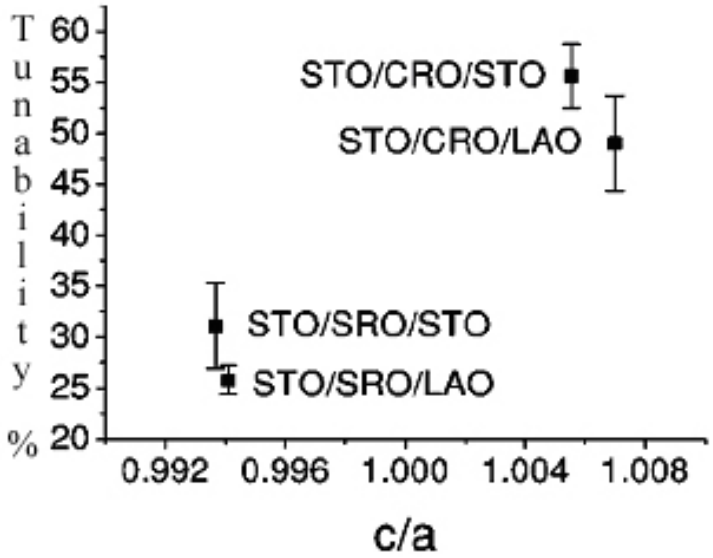

FIGURE 2.35. Tunability *versus* tetragonality (*c/a* ratio), measured at 10V/µm, 77K and 100kHz on Au/$SrTiO_3$/$CaRuO_3$/$SrTiO_3$ (STO/CRO/STO), Au/$SrTiO_3$/$SrRuO_3$/$SrTiO_3$ (STO/SRO/STO), Au/$SrTiO_3$/$CaRuO_3$/$LaAlO_3$ (STO/CRO/LAO) and Au/$SrTiO_3$/$SrRuO_3$/$LaAlO_3$ (STO/SRO/LAO) parallel plate capacitors, prepared by PLD [Hyun and Char, 2001].

It needs to be stressed here that the main part of the publications under review show results obtained for planar capacitors. Moreover, although almost all the results reported in these publications were explained as "the influence of strain" (by lattice distortion or tetragonality), the values of total stress that includes the thermal effect as well as lattice effect were not shown [Haeni et *al.*, 2004; Yamada et *al.*, 2005a; Astafiev et *al.*, 2003; Hyun and Char, 2001]. In this way, complete and detailed studies on the evaluation of strain/stress in polycrystalline ST films and parallel plate capacitors based on them need consequently to be done.

2.3. Dielectric behaviour in doped $SrTiO_3$

Improvement of the dielectric properties of material is possible by a doping with different chemical elements. The incorporation of a dopant ions into the $SrTiO_3$ lattice depends on the ionic size and electronic structure of both dopant and host ions. In the case of ST, the host ionic sizes are 1.44Å for Sr^{2+} and 0.605Å for Ti^{4+} [Shannon, 1976]. So in the perovskite structure of strontium titanate (Fig.2.1) with a general formula ABO_3, there are two kinds of possible substitution sites: *1)* Sr^{2+} site (or A-site) and *2)* Ti^{4+} site (or B-site). However, from the reported results, it appears that isovalent B-site dopants, such as Zr^{4+}, Sn^{4+}, Ge^{4+}, have much smaller effect on dielectric properties of $SrTiO_3$, compared to isovalent A-site dopants, namely with Ca^{2+}, Ba^{2+}, Pb^{2+}, Cd^{2+} [Lemanov et *al.*, 2004]. On the other hand, anomalies in the dielectric response with remarkable frequency dispersion were observed in $SrTiO_3$ doped with A-site heterovalent dopants, such as rare-earth ions (La^{3+}, Pr^{3+}, Nd^{3+}, Sm^{3+}, Gd^{3+}, Tb^{3+}, Dy^{3+}, Ho^{3+}, Er^{3+}, Tm^{3+}, Yb^{3+}, Lu^{3+}) [Johnson et *al.*, 1970; Iguchi and Lee, 1993] and Bi^{3+} [Ang et *al.*, 1998].

Whereas there is a number of reports on the doping effect in ST ceramics for such dopants as Ca [Zhang et *al.*, 2002; Ranjan et *al.*, 2000; Hirata et *al.*, 1996], La [Wang et *al.*, 2000; Ang and Yu, 1992], Sm, Li, Y [Wang et *al.*, 2000], Mg [Hirata et *al.*, 1996; Tkach et *al.*, 2004a; Tkach et *al.*, 2005b], Pb [Lemanov et *al.*, 1997], Cd [Guzhva et *al.*, 2001], Mn [Tkach et *al.*, 2004b; Lemanov et *al.*, 2004; Tkach et *al.*, 2005a; Tkach et *al.*, 2006; Tkach et *al.*, 2007a; Tkach et *al.*, 2007b] and Bi [Yu, 1997; Ang et *al.*, 1998], whose main results will be presented in the next subchapters, doped ST films have not been so deeply studied.

2.3.1. Ba doped $SrTiO_3$ bulk and films

Based on extrapolation of the Curie temperature of the $BaTiO_3$ - $SrTiO_3$ solid solution, Rushman and Strivens have proposed in 1946 that ST is a ferroelectric, whose Curie temperature is near 0K [Smolenskii, 1984]. Since that time, $BaTiO_3$ - $SrTiO_3$ solid solutions have been the subject of extensive studies, mostly for high $BaTiO_3$ concentration and at temperatures above 100K [Jaffe et *al.*, 1971; Lin and Wu, 1990].

Barium strontium titanate ($Ba_xSr_{1-x}TiO_3$, BST), as its end members ST and $BaTiO_3$, have a perovskite-type structure and a solid solution is formed in the whole composition range, as can be seen from the phase diagram shown in Figure 2.36 [Lemanov et *al.*, 1996].

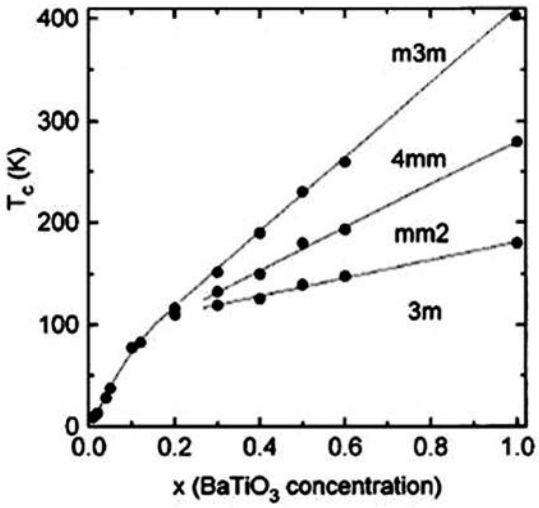

FIGURE 2.36. Phase diagram of $Ba_xSr_{1-x}TiO_3$ solid solution [Lemanov et *al.*, 1996].

It is well known that $BaTiO_3$ has a loosely packed oxygen octahedra due to the presence of large Ba^{2+} ions in the perovskite lattice and the spontaneous polarisation results from cooperative displacements of Ti ions in oxygen octahedra [Lin and Wu, 1990]. When Ba^{2+} ions with 12-coordination ionic radius 1.61Å are substituted with smaller Sr^{2+} ones with 12-coordination ionic radius 1.44Å [Shannon, 1976], the adjacent oxygen ions displace towards the doped ones forming a more closely packed structure.

In contrast to quantum paraelectric $SrTiO_3$, $BaTiO_3$ transforms from the cubic paraelectric phase (point group *Pm3m*) to a ferroelectric phase with three distinct crystal structures: below 393K to a *P4mm* tetragonal, then to a *Pmm2* orthorhombic at about 273-278K and finally to a *R3m* trigonal phase below 183K. The polar axis for the three ferroelectric phases is [001], [011] and [111] respectively and all the three phase transitions are displacive type ones of first order [Lines and Glass, 1977].

Decreasing $BaTiO_3$ content leads to a linear decrease of all the phase transition temperatures, but with different rates. Thus, a "multicritical point" around x=0.15 appears in the phase diagram, where the three phase transition lines converge, and four phases are in equilibrium. Near this point the structural phase transition characteristic of ST is also likely to converge with the ferroelectric transition [Lemanov et *al.*, 1996]. Further decrease of x, T_c obeys the relation, typical for doped incipient ferroelectrics [Vugmeister and Glinchuk, 1990]:

$$T_c = A(x - x_c)^{1/2} \tag{2.11}$$

where factor A equals 300K and the critical concentration x_c equals 0.035. And finally a very small addition of $BaTiO_3$ to $SrTiO_3$ ($x < x_c = 0.035$) induces a glasslike state, rather than a ferroelectric one. This was supported by: *1)* the absence of ferroelectric hysteresis loops; *2)* a frequency dispersion of the ε' and *3)* a time dependence of the dielectric permittivity after field cooling [Lemanov et *al.*, 1996]. Later, two relaxation processes were observed in BST ceramics with Ba content x=0.005-0.1 in the temperature ranges from 15K to 50K and from 55K to 100K.

The temperature dependence of the real part of dielectric permittivity of BST ceramics and crystals is illustrated in Figure 2.37. It is evident that the temperature of the paraelectric-ferroelectric phase transition in $Ba_xSr_{1-x}TiO_3$ increases linearly with x with the slope $dT_c/dx \approx 360$K [Lemanov et *al.*, 1999]. T_c versus x dependence was found to be close for BST ceramics and single crystals [Tagantsev et *al.*, 2003; Lemanov et *al.*, 1996]. In addition, a diffused phase transition is observed for $x < 0.5$ [Benguigui and Bethe, 1976].

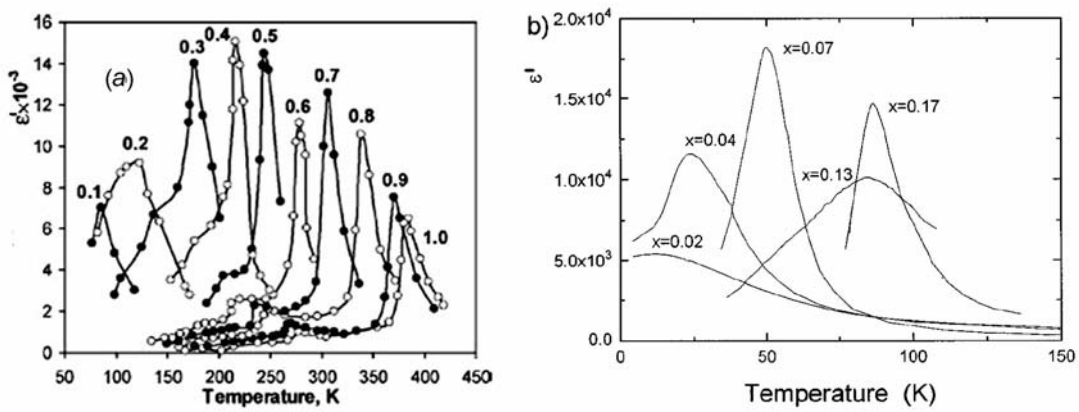

FIGURE 2.37. Temperature dependences of the ε' of $Ba_xSr_{1-x}TiO_3$ ceramics (a) [Tagantsev *et al.*, 2003] and $Ba_xSr_{1-x}TiO_3$ crystals (b) [Lemanov *et al.*, 1996] (numbers near the curves refer to $BaTiO_3$ concentration x).

BST solid solution is a very suitable material for tunable applications, being currently one of the most important materials for tunable devices operating at high frequencies [Varadan et *al.*, 1992; Babbit et *al.*, 1992]. As clearly seen from Figure 2.38, a high enough value of the ε' can be obtained by choosing a proper $BaTiO_3$ concentration. The variation of the ε' of $Ba_{0.1}Sr_{0.9}TiO_3$ ceramics as a function of temperature and applied electric *dc* bias field at 100kHz is displayed in Figure 2.38a, showing a relative dielectric tunability of about 83% under a *dc* bias field of 25kV/cm at the transition temperature of 86K [Wu et

al., 1994]. However, microwave loss increasing with $BaTiO_3$ concentration was observed, as one can see in Figure 2.38b [Vendik et *al*., 1999b]. Thus, higher insertion loss of BST has restricted its application in phased array antennas [Vendik et *al*., 1999; Tagantsev et *al*., 2003].

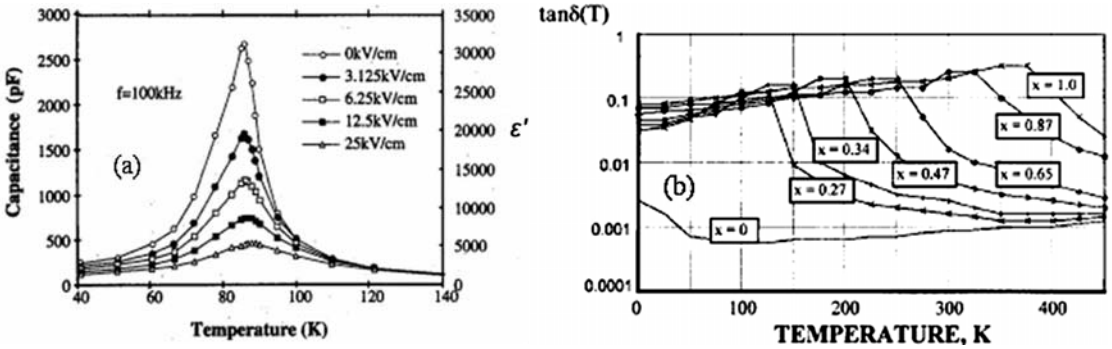

FIGURE 2.38. Temperature dependences of the capacitance (*left axis*) and ε' (*right axis*) of $Sr_{0.9}Ba_{0.1}TiO_3$ ceramics under bias field of 0, 3.125, 6.25, 12.5 and 25kV/cm at 100kHz (a) [Wu et *al*., 1994] and tanδ of $Ba_xSr_{1-x}TiO_3$ system scaled to 10GHz (b) [Vendik et *al*., 1999].

In general, the value of the real part of dielectric permittivity ε' of bulk BST is higher than that of BST films (similarly to ST system). In Figure 2.39 the temperature dependence of ε' of a bulk $Ba_{0.7}Sr_{0.3}TiO_3$ ceramic is compared to that of a thin film of the same composition [Shaw et *al*., 1999]. The bulk ceramic undergoes the paraelectric-to-ferroelectric phase transition near room temperature, whereas no sharp peak is clearly depicted for films but ε' is much lower (Fig.2.39) [Shaw et *al*., 1999]. As possible causes for the ε' reduction in the film include, it was proposed following [Shaw et *al*., 1999]:

- fine grains. There is no dependency of ε' on grain size in BST films in opposite to BST ceramics with high permittivity grains and low permittivity grain boundaries, leading to serious variation of ε' with grain size. However, the effect of fine grains on the ε' of the BST films remains unclear;
- interfacial capacitance. In a film, near film-electrode interface the ionic contribution to the dielectric response is suppressed, that is, a region a few lattice cell thick acts as a low permittivity or “dead” layer;
- residual stress due to substrate effect and preparation process.

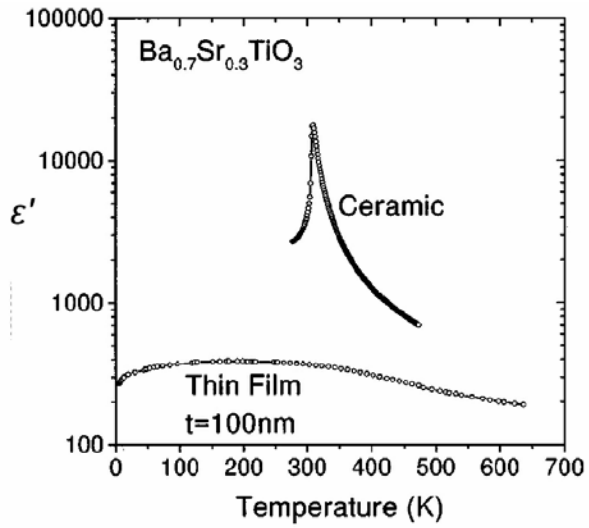

FIGURE 2.39. Variation of the ε' of $Ba_{0.7}Sr_{0.3}TiO_3$ bulk ceramic and 100-nm-thick $Ba_{0.7}Sr_{0.3}TiO_3$ film, prepared by chemical vapour deposition method between Pt electrodes on Si substrate, as a function of temperature [Shaw et *al*., 1999].

As previously observed for ST films, the dielectric properties of BST films can also be different and dependent on the type of substrate, deposition method and film thickness, among others factors. As an example, out-of-plane ε' of $Ba_{0.7}Sr_{0.3}TiO_3$ films, prepared by liquid-source metalorganic chemical vapour deposition between Pt electrodes on Si substrate, with thicknesses ranging from 15 to 580nm is depicted in Figure 2.40 as a function of temperature [Parker et *al.*, 2002]. Three important observations were indicated: *i)* the temperature of the maximum ε' shifts to lower values as the thickness is reduced; *ii)* the maximum ε' value increases towards ~700 with thickness increasing to 580 nm; *iii)* the dielectric anomaly becomes broader as the film becomes thinner [Parker et *al.*, 2002]. A broadened dielectric anomaly means that the phase transition occurs over a wider temperature range [Parker et *al.*, 2002]. For understanding of such a changing on dielectric response in analyzed films with decreasing of thickness Parker and co-workers used a model, which includes interior and surface components into the physical description [Parker et *al.*, 2002]. According to this model the physical picture following this approach would be a three layer structure. The centre layer would correspond to a bulk-like but thickness dependent slab, while the exterior layers would correspond to regions that remain ferroelectrically active, but with significantly reduced ε'. The surface component, having reduced average polarization vector, will have lowered ε' and transition temperature. The reduced ε' lowers the effective permittivity of the entire stack, while the lower transition

temperature results in anomaly broadening. Meanwhile, Parker et *al.* stressed that the polarization falls smoothly (as opposed to a discrete step) in the surface region [Parker et *al.*, 2002]. This region corresponds to a distribution of materials with progressively reduced value of maximum ε' and temperature of the maximum ε' as the surface is approached. Thus, the used model can describe the extreme diffuseness of the thinnest films and it could be useful for others films [Parker et *al.*, 2002].

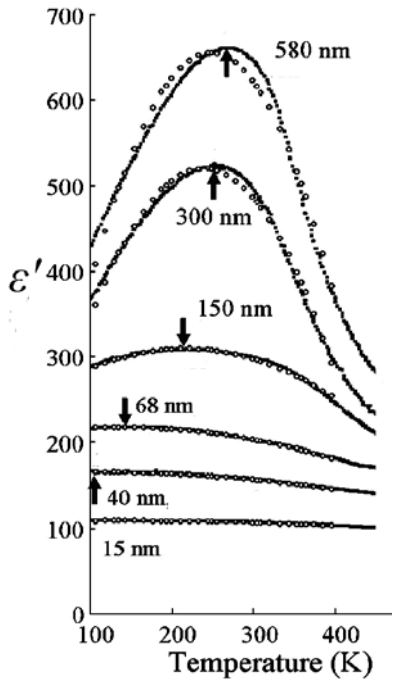

FIGURE 2.40. Temperature dependence of out-of-plane ε' of $Ba_{0.7}Sr_{0.3}TiO_3$ films, prepared by chemical vapour deposition method between Pt electrodes on Si substrate, with different thicknesses [Parker et *al.*, 2002].

BST films, grown by PLD method on $LaAlO_3$ substrates by Gim et *al.*, show that in-plane ε' has a maximum value ~1000 (Fig.2.41a, *right scale*). The peak temperatures, corresponding to the maximum ε', are about 70 degrees higher than that of bulk BST and room-temperature ε' and tunability are relatively high, when Sr content is ≤ 0.4. However, the peak temperatures are similar to that of bulk BST and room-temperature ε' and tunability start to decrease rapidly with increasing Sr content, when it is > 0.4 (Fig.2.41b) [Gim et *al.*, 2000].

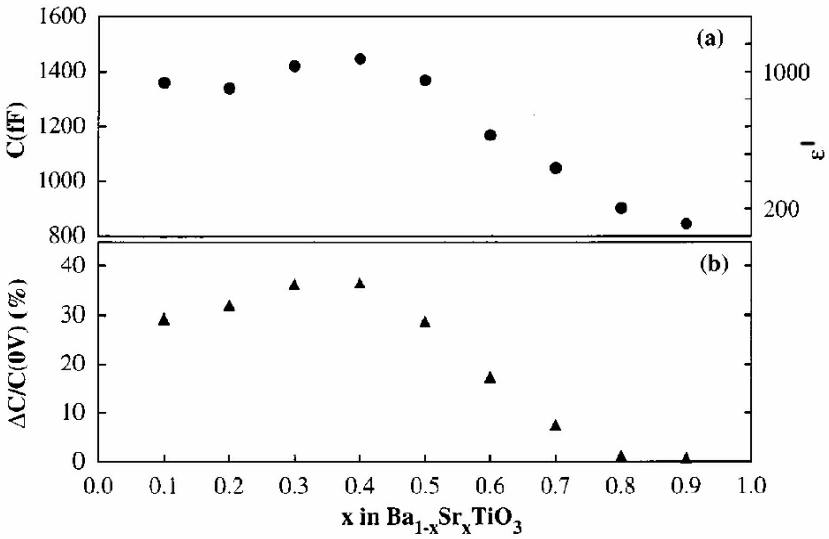

FIGURE 2.41. Room-temperature in-plane capacitance *C* (*left scale*), real part of dielectric permittivity *ε'* (*right scale*) (a) and tunability as *ΔC/C(0V)* (b) of 300-nm-thick $Ba_{1-x}Sr_xTiO_3$ films, prepared by PLD on $LaAlO_3$ substrates, as a function of Sr content *x* [Gim et *al.*, 2000].

Such difference between BST bulk and film was mainly related to the particular microstructural properties of the films, including the stress and grain size that strongly affect the dielectric response of BST films [Gim et *al.*, 2000].

2.3.2. Pb doped $SrTiO_3$ bulk and films

$PbTiO_3$ is a classic example of a displacive ferroelectric transition. It undergoes a first order transition at around 770K from cubic perovskite *Pm3m* to a tetragonal ferroelectric *P4mm* phase. $PbTiO_3$ is isomorphic with tetragonal $BaTiO_3$ at room temperature, however in contrast to $BaTiO_3$ no additional transitions were established for $PbTiO_3$ [Lines and Glass, 1977]. $Sr_{1-x}Pb_xTiO_3$ (SPT) forms a continuous solid solution over the entire range of concentration *x* [Lemanov et *al.*, 1997]. The structural phase transition temperature in SPT at small *x* behaves similarly to BST, strongly decreasing with *x* and finally converging to the ferroelectric transition at $x \approx 0.04$ [Smirnova et *al.*, 2005]. Because of the high ferroelectric transition temperature of $PbTiO_3$, SPT solid solution reveals a peak of the *ε'* near the room temperature already at *x*=0.3, as one can see from the phase diagram illustrated in Figure 2.42 [Lemanov et *al.*, 1997].

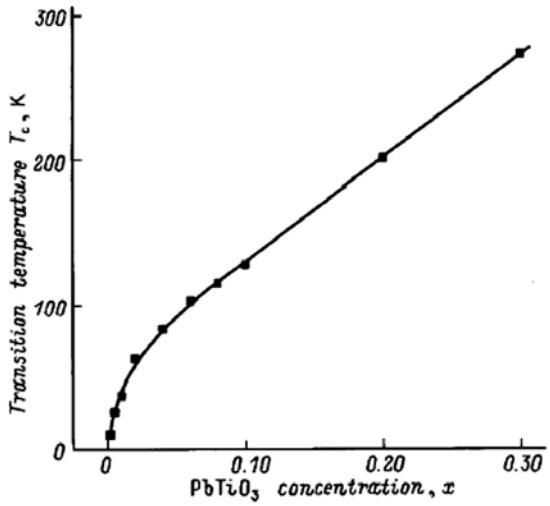

FIGURE 2.42. Phase diagram of $Sr_{1-x}Pb_xTiO_3$ solid solution [Lemanov et *al.*, 1997].

As follows from Figure 2.42, the transition temperature T_c depends linearly on x down to 0.04 as T_c=40+770x. On the other hand, for $x \leq 0.04$ the experimental points fit to the $T_c=A(x-x_c)^{1/2}$ line, where A=440 and x_c=0.002. Note that this relation is based on the assumption that there is no ferroelectric phase transition (T_c=0) at x=0.002, since no ferroelectric hysteresis loops at this concentration were observed [Lemanov et *al.*, 1997]. The usual explanation for higher transition temperature of $PbTiO_3$ comparing with $BaTiO_3$ and, consequently, for the faster T_c increasing with the concentration of the second member in $Sr_{1-x}Pb_xTiO_3$ than in $Ba_xSr_{1-x}TiO_3$ system is related to higher electronic polarisability of Pb^{2+} than Ba^{2+} and Sr^{2+}, apart from its smaller ionic radius of Pb^{2+} (1.49Å for coordination number N_c=12) when compared with the Ba^{2+} one (1.61Å) [Shannon, 1976]. This polarisability intensifies the interactions between the Ti ions and thus raises the T_C [Mitsui and Westphal, 1961]. However, the fact that the ionic size of Pb^{2+} is bigger than that of Sr^{2+} (1.44Å) [Shannon, 1976] also assists to the displacement of Ti ions and consequently to the increase of T_c of $Sr_{1-x}Pb_xTiO_3$ solid solutions with x. The temperature of the maximum of real part of dielectric permittivity T_m (as well as lattice parameter) was shown to be strongly dependent on the composition non-stoichiometry [Lemanov et *al.*, 1997].

SPT solid solutions do not have nowadays relevant commercial applications because of the well-known difficulty in obtaining the precise stoichiometry in lead-containing compounds, connected with a high volatility and toxicity of Pb, which do not fill the European requirements for lead free materials. However, some studies [Somiya et *al.*, 2001] suggest the potentiality of SPT system for field tunable devices. Suppression of the

ε' was observed under *dc* bias field, as shown in Figure 2.43 (*left axis*) and the dielectric loss held small values (*right axis*) for $Sr_{1-x}Pb_xTiO_3$ ceramics (x=0.2, 0.25, 0.3).

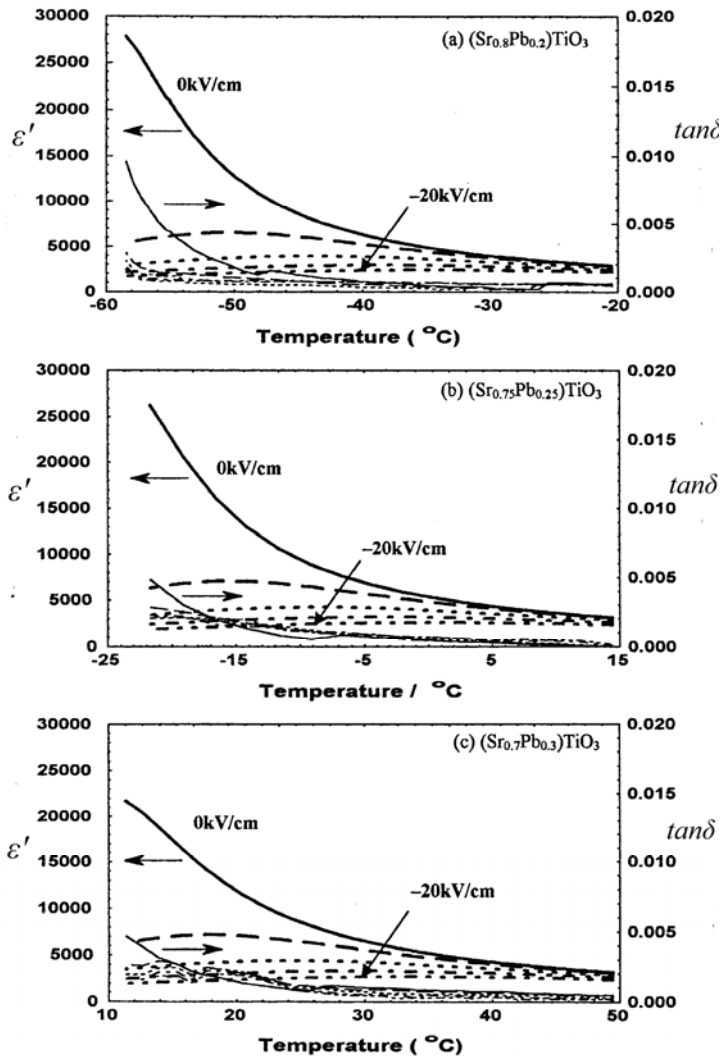

FIGURE 2.43. Dielectric responses of $Sr_{1-x}Pb_xTiO_3$ ceramics with x=0.20 (a), 0.25 (b) and 0.30 (c) at 10kHz as a function of temperature under -20, -15, -10, -5 and 0kV/cm [Somiya et *al.*, 2001].

Values of tanδ (less than 0.1%) and relative dielectric tunability (3, 15 and 70% under 20kV/cm bias field) were measured on $Sr_{1-x}Pb_xTiO_3$ ceramics with x=0.2, 0.25 and 0.3 at room temperature and at 10kHz (Fig.2.43, *right axis*) [Somiya et *al.*, 2001]. In addition, composites fabricated from SPT and Al_2O_3 that show ε' ~100, tanδ < 0.005 at 20kV/cm at 10kHz over the range ~313-423K were developed [Somiya et *al.*, 2004].

There is only one publication by Jain *et al.* reporting a dielectric study on Pb doped ST films: 380-nm-thick $Sr_{0.7}Pb_{0.3}TiO_3$ thin films, synthesized by chemical solution deposition

technique on Pt/Si and $LaAlO_3$ substrates [Jain et *al.*, 2004]. The low dielectric loss (<2%) of $Sr_{0.7}Pb_{0.3}TiO_3$ film on $LaAlO_3$ substrate (Fig.2.44) was claimed to be attractive for fabrication of tunable dielectric devices. The maximum figure of merit k of an eight-element coupled microstrip phase shifter (CMPS) (k=phase shift per dB loss), based on $Sr_{0.7}Pb_{0.3}TiO_3$ film on $LaAlO_3$ substrate, was found to be equal to ~56°/dB at 400V (or 533kV/cm), which was claimed to be better than 38°/dB, commonly observed value in barium strontium titanate films, deposited by sol-gel and tested in the similar device structure [Majumder et *al.*, 2001]

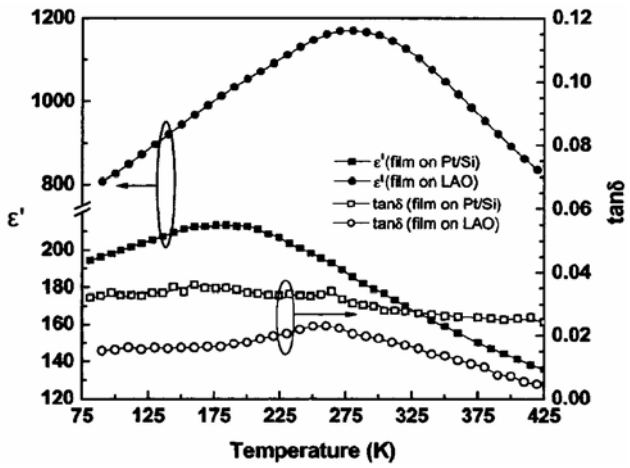

FIGURE 2.44. Temperature dependence of ε' and tanδ of 380-nm-thick $Sr_{0.7}Pb_{0.3}TiO_3$ films, synthesized by chemical solution deposition on Pt/Si and $LaAlO_3$ substrates [Jain et *al.*, 2004].

2.3.3. Ca doped $SrTiO_3$ bulk and films

$CaTiO_3$ has a cubic *Pm3m* structure at T > 1523-1580K and orthorhombic *Pcmn* structure at T < ~1380K [Redfern, 1996; Kennedy et *al.*, 1999], although the deviation from the cubic perovskite structure is small. The dielectric behaviour of $CaTiO_3$ is typical of incipient ferroelectrics: relatively high dielectric properties ($\varepsilon' \approx 170$ at room temperature), large and negative value of $d\varepsilon'/dT$, and saturation of the ε' at low temperatures ($\varepsilon' \approx 330$ at 4.2K). Orthorhombic $CaTiO_3$ does not undergo a ferroelectric phase transition down to T=0 and the paraelectric state would be stable even without the effect of quantum fluctuations, which suppress the ferroelectric phase transition in $SrTiO_3$. As a result, $CaTiO_3$ should be classified as an incipient ferroelectric but not as a quantum paraelectric [Mitsui and Westphal, 1961].

A complete solid solution can be formed in $Sr_{1-x}Ca_xTiO_3$ (SCT) system. The behaviour

of SCT phase transitions, connected with the dielectric anomalies is rather complicated. In 1961, Mitsui and Westphal reported a dielectric anomaly in $\varepsilon'(T)$ of SCT ceramic samples with Ca content up to x=0.20 [Mitsui and Westphal, 1961]. However, slim hysteresis loops were observed at 4.3K for only $Sr_{1-x}Ca_xTiO_3$ ceramics with $x \leq 0.10$. The field dependent remnant polarisation decreased with increasing of temperature, but the loop did not disappear at the temperature where ε' reached its maximum. The ferroelectric phase produced by the small Ca addition was ascribed to the enlarged atomic polarisability of Ca^{2+} in the SCT compound, due to the smaller ionic radius of Ca^{2+} (1.34Å) when compared with Sr^{2+} (1.44Å) [Shannon, 1976] in spite of its smaller electronic polarisability in comparison to Sr^{2+}, and to the occupancy of the off-centre positions at Sr^{2+} sites [Mitsui and Westphal, 1961].

More detailed studies of the dielectric properties of $Sr_{1-x}Ca_xTiO_3$ system have been done by Bednorz and Müller [Bednorz and Müller, 1984] on single crystals with $0 \leq x \leq 0.12$ in the temperature range 4.2-300K at ~1.6kHz (Fig.2.45a) and later completed by Ranjan et *al.* [Ranjan et *al.*, 2000] on ceramics with $0.18 \leq x \leq 0.40$ in the temperature range 100-400K at 10kHz (Fig.2.45b).

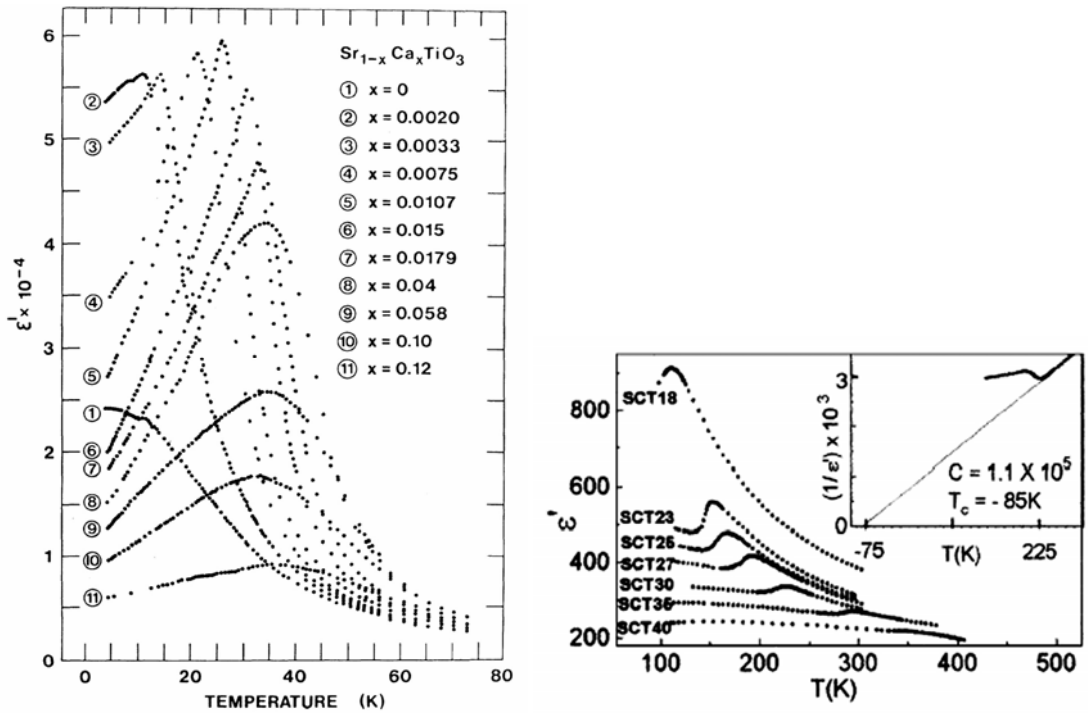

a b

FIGURE 2.45. Temperature dependence of ε' of $Sr_{1-x}Ca_xTiO_3$ crystals (x=0.00-0.12) at ~1.6kHz (a) [Bednorz and Müller, 1984] and of $Sr_{1-x}Ca_xTiO_3$ (SCT) ceramics (x=0.18-0.40) at 10kHz (b). Inset shows Curie-Weiss fit for x=0.30 [Ranjan et *al.*, 2000].

Structural and dielectric measurements of $Sr_{1-x}Ca_xTiO_3$ system revealed following: *1)* superlattice reflections in XRD patterns, connected to antiparallel displacement of cations/anions in the low temperature state; *2)* that $\varepsilon'(T)$ above the T_c strictly follows the Curie-Weiss law (inset to Figure 2.45b); *3)* that the peak in the $\varepsilon'(T)$ becomes less smeared and its temperature coincides with the dielectric loss peak temperature; *4)* no hysteresis loop, characteristic of either ferroelectric or relaxor, was observed below the T_c even after applying an electric field as high as 60kV/cm [Ranjan et *al.*, 2000; Ranjan and Pandey, 2001], supporting the assumption of the suggested antiferroelectric phase transition. In addition, a very broad dielectric anomaly of yet unknown nature was observed below antiferroelectric phase transition, as also shown in Figure 2.45b [Ranjan et *al.*, 2000].

A strong increase of the maximum of real part of dielectric permittivity (compared to undoped ST) for $Sr_{1-x}Ca_xTiO_3$ single crystals with Ca content as small as x=0.002 together with the peak occurring in the $\varepsilon'(T)$ was reported by Bednorz and Müller [Bednorz and Müller, 1984]. The transition temperature was found to rise with Ca concentration, following the relation $T_c=298(x - 0.0018)^{1/2}$ up to $x \approx 0.016$.

For compositions with x=0.002, 0.005 and 0.011, a small zero-field polarisation was detected by pyroelectric current measurements [Lacerda-Arôso et *al.*, 2001]. The relaxor-ferroelectric/dipole-glass behaviour in the quantum ferroelectric regime ($0.002 < x < 0.016$) has then been explained in terms of phonon associated dissipative quantum tunnelling of the Ca^{2+} dipoles between potential minima in the four-well potential [Bianchi et *al.*, 1995]. At further increase of Ca content $x > 0.016$ the round $\varepsilon'(T)$ peaks in $Sr_{1-x}Ca_xTiO_3$ attributed by Bednorz and Müller to the onset of a random-field induced domain state [Bednorz and Müller, 1984]. The smearing of the peak in the $\varepsilon'(T)$ has been attributed to the coupling of random strains (due to ionic size difference between Ca^{2+} and Sr^{2+} ions) to the polarisation. The random fields, generated by the Ca^{2+}-V_O centre dipoles (probably due to a partial Ca incorporation into the Ti sites) are claimed to be responsible for the ferroelectric domain state, induced by random fields in this regime and characterised by the rounded ε' peaks [Bednorz and Müller, 1984]. Moreover, the relaxor-ferroelectric or dipole-glass behaviour ($0.016 < x < 0.12$) has been attributed to ferroelectric cluster and domain wall dynamics [Kleemann and Schremmer, 1989]. Thus, the relaxor-like phenomena in Ca-doped ST are believed to result from polar nanodomains, which were evidenced to exist in the temperature range between high-temperature para- and low-

temperature ferroelectric regime by second harmonic generation of light, Brillouin and Raman scattering [Kleemann et *al.*, 2000].

Later, the dielectric behaviour of $Sr_{1-x}Ca_xTiO_3$ system for $x < 0.12$ was explained, considering that impurity-polarized clusters induce the second order phase transition, while quenched random fields give rise to a smeared peak in the $\varepsilon'(T)$ [Zhang et *al.*, 2002]. Frozen fields result in the appearance of a multidomain state and due to that SCT has no global ferroelectric polarisation. However, the reversal of domains under an *ac* field can induce a "remnant polarization". The deviation of T_c from $(x-x_c)^{1/2}$ law for $x > 0.016$ together with the decrease of maximum ε' is attributed to the decrease of the cell volume with increasing Ca content in SCT [Zhang et *al.*, 2002]. The local reduction of the unit cell, caused by the substitution of bigger Sr^{2+} ions by smaller Ca^{2+} ones, is obvious and has an effect on the ε', an analogous effect to that of hydrostatic pressure known to strongly reduce the polarisability.

Whereas SCT bulk was very deeply studied, there is only one short report about SCT films. Knauss et *al.* analyzed the substitution of 5% Ca on Sr site of SCT films, prepared by PLD on $LaAlO_3$ substrates, and found that it does not change the temperature dependence of the capacitance, compared to undoped ST, but leads to an increase of tanδ at 60K to ~0.05 (Fig.2.46) [Knauss et *al.*, 1997].

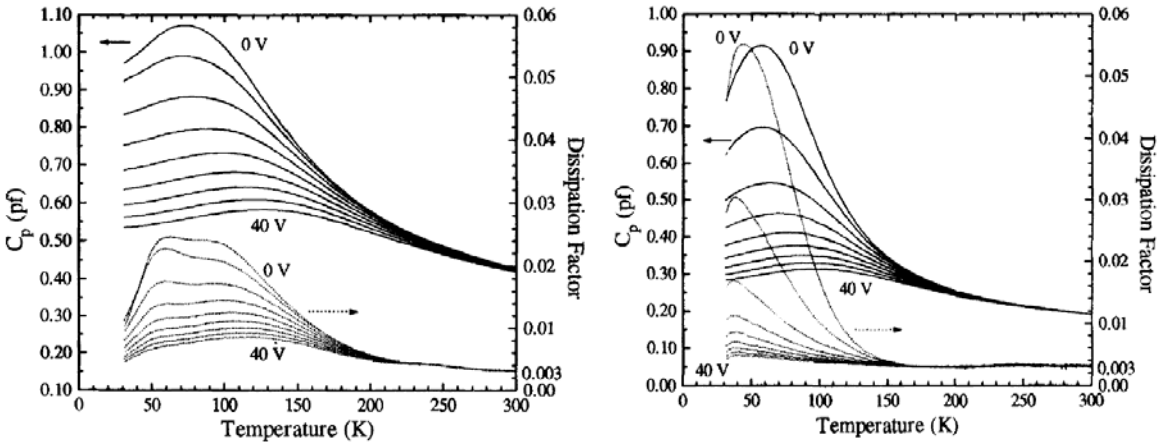

a b

FIGURE 2.46. Capacitance (*left axis*) and tanδ (*right axis*) of 500-nm-thick undoped $SrTiO_3$ film (a) and $SrTiO_3$ film with a 5% of Ca substitution (b), grown by PLD on $LaAlO_3$ substrate. The measurements were made at 1MHz under 0-40V *dc* bias with increment of 5V across a 5 μm gap (a) and 7.5 μm gap (b) [Knauss et *al.*, 1997].

In addition, the capacitance decreases more rapidly with low electric fields, giving higher tunability for partial Ca substitution (Fig.2.46) [Knauss et *al.*, 1997].

2.3.4. Mg doped $SrTiO_3$ bulk

Using a non-empirical Hartree-Fock-Roothaan formalism Kvyatkovskii has calculated the local potential for impurity ions on A site of ST [Kvyatkovskii, 2002]. According to these calculations, Ca, Ba, Pb and Cd, substituting Sr, move in a single-well potential and the corresponding solid solutions should be displacive-type ferroelectrics. On the other hand, Mg on Sr site occupying off-centre positions is suggested to move in a multi-well local potential, shown in Figure 2.47 for the [001] direction. The displacement from the central position and corresponding energy was estimated to be 0.32Å and 0.007eV respectively. Thus, a relaxation mechanism, which could lead to a relaxor-like behaviour similar to that observed in $K_{1-x}Li_xTaO_3$, was predicted for $Sr_{1-x}Mg_xTiO_3$ [Kvyatkovskii, 2002].

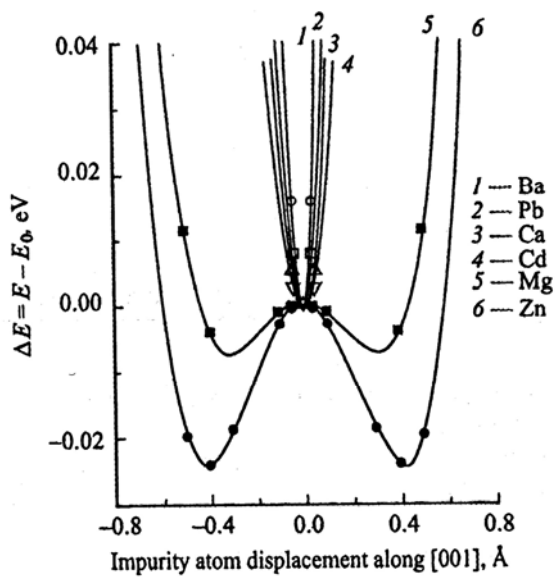

FIGURE 2.47. Local adiabatic potential for Ba (1), Pb (2), Ca (3), Cd (4), Mg (5) and Zn (6) doping atoms on Sr site of $SrTiO_3$ [Kvyatkovskii, 2002].

Thus, relatively small Mg^{2+} ions favourably occupy the off-centre positions on Sr sites, forming in such a way polar dipoles. Therefore, a ferroelectric or polar type anomaly may be induced in ST by Mg doping in spite of the fact that the ion dielectric polarisability

of Mg^{2+} is rather low (1.32Å), especially compared with that of Sr^{2+} (4.24Å) [Shannon, 1993].

The isovalent A-site substitution with Ca^{2+} [Bednorz and Müller, 1984], Ba^{2+} [Lemanov et *al.*, 1996], Pb^{2+} [Lemanov et *al.*, 1997] and Cd^{2+} [Guzhva et *al.*, 2001] have been reported to induce a low-temperature polar state. However, no ferroelectric-type anomaly was reported for A-site or B-site substituted ST ceramics with 1% of Mg^{2+} [Wang et *al.*, 2000a; Tkach et *al.,* 2004a], as shown in Figures 2.48 and 2.49.

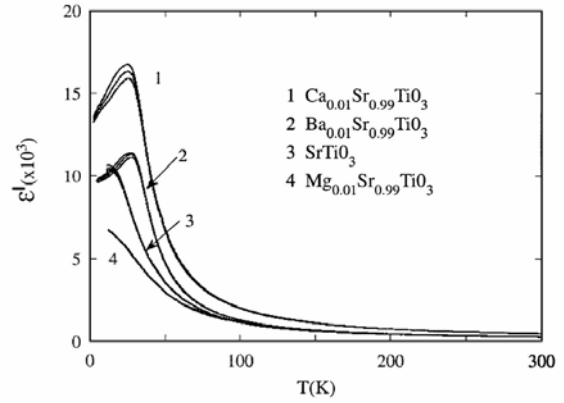

FIGURE 2.48. ε' of $Ca_{0.01}Sr_{0.99}TiO_3$ (1), $Ba_{0.01}Sr_{0.99}TiO_3$ (2), $SrTiO_3$ (3) and $Mg_{0.01}Sr_{0.99}TiO_3$ (4) ceramics at 10, 100 and 500kHz *versus* temperature [Wang et *al.*, 2000a].

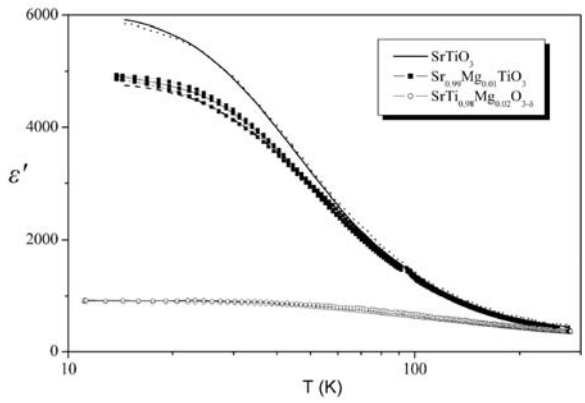

FIGURE 2.49. Temperature dependence of ε' of $SrTiO_3$, $Sr_{0.99}Mg_{0.01}TiO_3$ and $SrTi_{0.98}Mg_{0.02}O_{3-\delta}$ ceramics at 10^2, 10^4 and 10^6Hz [Tkach et *al.,* 2004a].

The ionic radius of Mg^{2+} ions is substantially smaller than that of Sr^{2+}: ionic radius of $Sr^{2+}_{(12)}$ is 1.44Å and $Mg^{2+}_{(12)}$ is 1.21Å (from the extrapolation using $Mg^{2+}_{(4)}$, $Mg^{2+}_{(5)}$, $Mg^{2+}_{(6)}$ and $Mg^{2+}_{(8)}$ ionic radius values) [Shannon, 1976]. More than 15 % difference between the ionic size of Mg^{2+} and Sr^{2+} cations, as well as the crystallization of $MgTiO_3$ with the ilmenite-type structure instead of the perovskite one, have been indicated as the restricting factors for the solid solubility of Mg^{2+} on Sr site of ST lattice [Kawada and Fujimoto, 1990; Hirata et *al.*, 1996; Tkach et *al.*, 2004a]. However, the data on solid solubility limit for Mg on Sr site of ST lattice is not consistent: whereas Hirata et *al*. [Hirata et *al.*, 1996] has found that formation of $Sr_{1-x}Mg_xTiO_3$ ceramics are restricted to $x \leq 0.2$ a solubility limit under 0.01 was reported by Kawada and Fujimoto [Kawada and Fujimoto, 1990] and in a systematic

study on Mg doped ST ceramics by Tkach et *al.* [Tkach et *al.*, 2004a].

On the other hand, Mg ions may occupy Ti sites of ST perovskite lattice as well, accompanied by the creation of compensating oxygen vacancies. However, Mg solubility on B site of the perovskite lattice should be restricted due to the bigger size of Mg^{2+} in comparison to the Ti^{4+} (ionic radius of $Ti^{4+}_{(6)}$ is 0.605Å and $Mg^{2+}_{(6)}$ is 0.72Å [Shannon, 1976]). In fact, a second phase was found by Inoue and co-workers [Inoue et *al.*, 1991] and by Tkach and co-authors [Tkach et *al.*, 2004a] for $SrTi_{0.90}Mg_{0.10}O_{3-\delta}$ composition (second phase was identified as MgO).

The low-temperature dielectric response of Mg-doped ST ceramics samples was analysed in details [Tkach et *al.*, 2004a], using Barrett's relation [Barrett, 1952] which is based on the mean-field theory taking quantum fluctuations into account:

$$\varepsilon' = C/[(T_1/2)\coth(T_1/2T) - T_0] \tag{2.12}$$

where C is the Curie–Weiss constant, T_1 represents the tunnelling integral and T_0 is the transition temperature at which the lattice instability would occur in the absence of quantum fluctuations. The obtained fitting parameters C and T_1 agreed well with those reported for undoped ST. Regarding the transition temperature T_0, A-site Mg doping did not tend to change it in contrast to B-site doping, which strongly reduced T_0, compared to undoped ST [Tkach et *al.*, 2004a].

Moreover, the dielectric loss of ST was reported to decrease in general with Mg doping [Tkach et *al.*, 2004a]. However, some additional peaks were detected in A- and B-site Mg-doped ST ceramics besides the dominant loss peak about 85K, similar to that in undoped ST and attributed to the ferroelastic domain-wall dynamics around the cubic-to-tetragonal phase transition (referred to as peak *C* in Fig.2.50) [Tkach et *al.*, 2004a]. As seen from Figure 2.50, A-site Mg doping induced a new broad peak, with a maximum around 23.5K (peak A) and a shoulder around 35K (peak *B*), whereas B-site Mg doping revealed a frequency-dependent smooth peak (peak *D*) in the range of 200-230K at 10kHz [Tkach et *al.,* 2004a]. Meanwhile, in both cases, the intensity of loss peak *C* decreased with Mg incorporation (Fig.2.50) [Tkach et *al.,* 2004a].

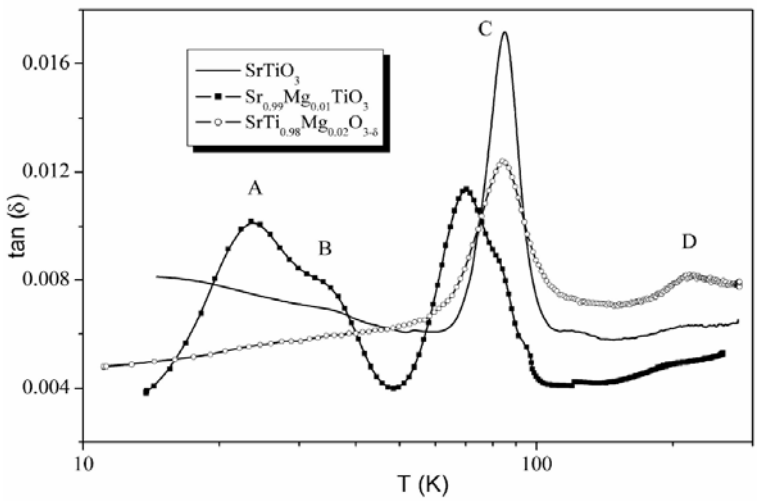

FIGURE 2.50. Temperature dependence of tanδ of $SrTiO_3$, $Sr_{0.99}Mg_{0.01}TiO_3$ and $SrTi_{0.98}Mg_{0.02}O_{3-\delta}$ ceramics at 10^2, 10^4 and 10^6Hz [Tkach et *al.,* 2004a].

Since the loss peak temperatures were frequency dependent, their relaxation dynamics in Mg doped ST ceramics was studied [Tkach et *al.*, 2004a], using a simple Arrhenius expression for the relaxation time τ:

$$\tau = \tau_0 \exp(U/k_B T) \tag{2.13}$$

where τ_0 stands for the pre-exponential term or inverse attempt frequency, U for the activation energy, k_B for the Boltzmann constant and T for the temperature. Particularly, dynamics of the loss peak *A*, observed for $Sr_{1-x}Mg_xTiO_3$ (Fig.2.50), was described by Arrhenius law with τ_0=(1.8-5.0)×10^{-12}s and U=28-34meV [Tkach et *al.*, 2004a].

The lattice vibration behaviour and dielectric responses in a wide range of frequency, temperature and *dc* bias field of ST and $Sr_{1-x}Mg_xTiO_3$ samples were found to be similar [Tkach et *al.*, 2005c]. As shown in Figure 2.51a, even dielectric tunability values are close for $SrTiO_3$ and $Sr_{0.99}Mg_{0.01}TiO_3$ ceramics. For $SrTi_{1-y}Mg_yO_{3-\delta}$ ceramics, along with the ε', the tunability in the *rf* range was progressively decreased with increasing dopant content (Fig.2.51b). Such behaviour was explained by the substitution of more polarisable Ti^{4+} ions by the less polarisable Mg^{2+} ions, respectively, which may break the Ti-Ti long-range interaction [Tkach et *al.,* 2005c]. In addition, $SrTi_{1-y}Mg_yO_{3-\delta}$ system was characterised by the reduction of the ε' and loss values in the microwave and terahertz ranges with very weak temperature dependence, accompanied with the stiffening of the soft mode in IR frequency range [Tkach et *al.,* 2005c].

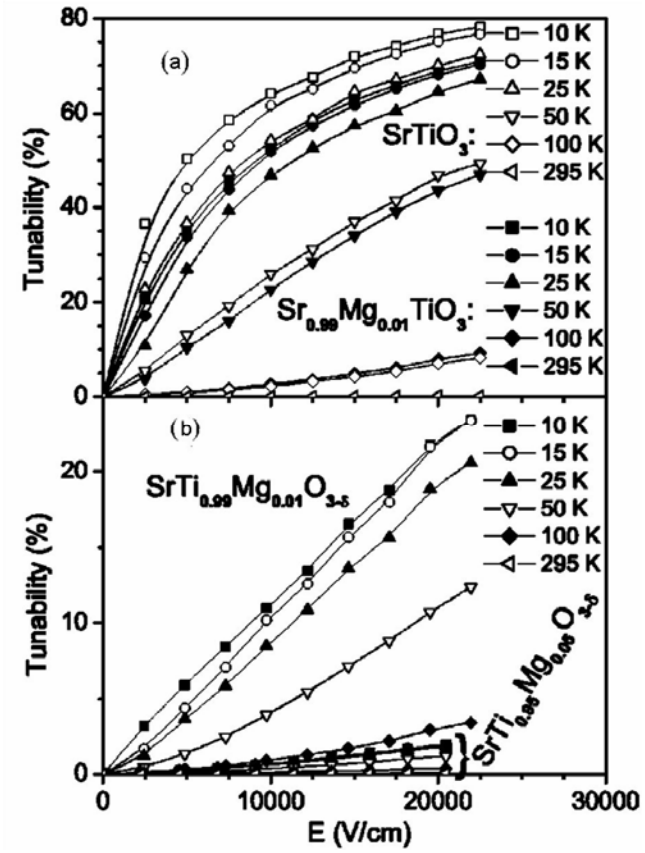

FIGURE 2.51. Field dependence of the tunability of $SrTiO_3$, $Sr_{0.99}Mg_{0.01}TiO_3$ (a), $SrTi_{0.99}Mg_{0.01}O_{3-\delta}$ and $SrTi_{0.95}Mg_{0.05}O_{3-\delta}$ (b) ceramics, measured at 10kHz and temperatures of 10, 15, 25, 50, 100 and 295K [Tkach et *al.,* 2005c].

Thus, according to results described above no ferroelectric or polar-type anomaly was induced by Mg incorporation neither on A-site nor on B-site of $SrTiO_3$ bulk material, although theoretically predicted.

Since no systematic study on the crystallographic structure, microstructure and dielectric behaviour of both $Sr_{1-x}Mg_xTiO_3$ and $SrTi_{1-y}Mg_yO_{3-\delta}$ films have been found in literature, such study on polycrystalline ST films doped with Mg was chosen as one of the tasks of current Thesis.

2.3.5. Bi doped $SrTiO_3$ bulk

Dielectric properties of $Sr_{1-1.5x}Bi_xTiO_3$ (SBiT) system were first investigated by Skanavi et *al*. in 1957 [Skanavi et *al*., 1957a]. In this study, a high ε' peak with frequency dispersion, induced by moderate Bi dopant concentrations in ST was reported. The authors suggested a polarisation mechanism by "hopping ions", rather than the occurrence of

ferroelectricity. However, based on the observation of the slim hysteresis loop in Bi-doped ST, Smolenskii et *al*. [Smolenskii, 1984] suggested a ferroelectric mechanism with the so called "diffuse phase transition" [Yu, 1997]. Later several researchers systematically studied Bi-doped ST system, establishing the relations between the structural and the dielectric response of Bi-doped ST ceramics [Yu, 1997; Ang et *al.*, 1998].

In contrast to Ba-, Pb- and Ca-doped ST systems ($Sr_{1-x}Ba_xTiO_3$, $Sr_{1-x}Pb_xTiO_3$ and $Sr_{1-x}Ca_xTiO_3$, respectively) $Sr_{1-1.5x}Bi_xTiO_3$ is a solid solution, in which the host Sr^{2+} ions are substituted by heterovalent Bi^{3+} ions. Thus to satisfy the charge neutrality, a strontium vacancy V_{Sr} has to be created upon the substitution of three divalent Sr^{2+} by two trivalent Bi^{3+}. Hence the appropriated chemical formula $[Sr_{1-1.5x}(V_{Sr})_{0.5x}Bi_x]TiO_3$ should be considered [Ang et *al.*, 2000b]. It is very probably that because of the formation of V_{Sr} solubility of Bi in the $SrTiO_3$ lattice is restricted to x=0.20 [Yu, 1997; Ang et *al*., 1998]. Below the solid solubility limit, room-temperature XRD profiles exhibit a cubic structure for Bi-doped ST.

Detailed studies of the dielectric properties of $Sr_{1-1.5x}Bi_xTiO_3$ ceramics in wide temperature [Ang et *al*., 1999] and frequency [Porokhonskyy et *al*., 2004] range revealed a complex structure of the dielectric response. Several relaxation processes were observed. Moreover, for some concentration of Bi, $Sr_{1-1.5x}Bi_xTiO_3$ ceramics was referred to as relaxor [Yu, 1997; Ang et *al*., 1998]. The main typical characteristics for relaxor behaviour are following:

1) rounded peaks in the temperature dependence of ε', in contrast to the sharp peak at the phase transition temperature observed for the classic ferroelectrics;
2) temperature of the ε' peak always higher than the temperature of the loss peak;
3) temperature dependence of the ε' obeying to relation: $1/\varepsilon'-1/\varepsilon'_m=(T-T_m)^\gamma/C$, with exponent γ close to 2 [Smolenskii, 1970], but not to 1 as for the classic ferroelectrics with the $\varepsilon'(T)$ following the Curie-Weiss law;
4) a frequency dispersion of ε' around the ε' peaks in the *rf* range and a long relaxation time, while the properties of classic ferroelectrics do not vary intensely with the frequency in the radio frequency range:
    a) maximum of the ε' decreases in value and its temperature shifts to higher temperatures with increasing measurement frequency;
    b) maximum of the tanδ increases in value and its temperature shifts to higher temperatures with increasing measurement frequency;

5) a square-to-slim transition of the hysteresis loops with the remnant polarisation decreasing with increasing temperature and tailing to zero in the diffuse range, in contrast to a sharp decrease to zero in classic ferroelectrics;
6) a compliance with a Vögel-Fulcher law, *etc.*

Considering the relaxation processes deduced from $\varepsilon'(T)$, the dielectric relaxation occurring at high temperatures in samples with Bi content of x=0.0133-0.133 were found to be closely related to the presence of oxygen vacancies [Yu, 1997; Ang et *al.*, 2000c] and some of them, as shown in Figure 2.52, can be completely suppressed by annealing in oxidizing atmosphere, whereas annealing in nitrogen enhances their dielectric values. By fitting to Arrhenius law rather high activation energy (U_{relaxA}=0.32-0.48eV; U_{relaxB}=0.74-0.89eV) and pre-exponential factor τ_0=(0.5-7)×10^{-12}s were obtained for these relaxation peaks *A* and *B* [Ang et *al.*, 2000c].

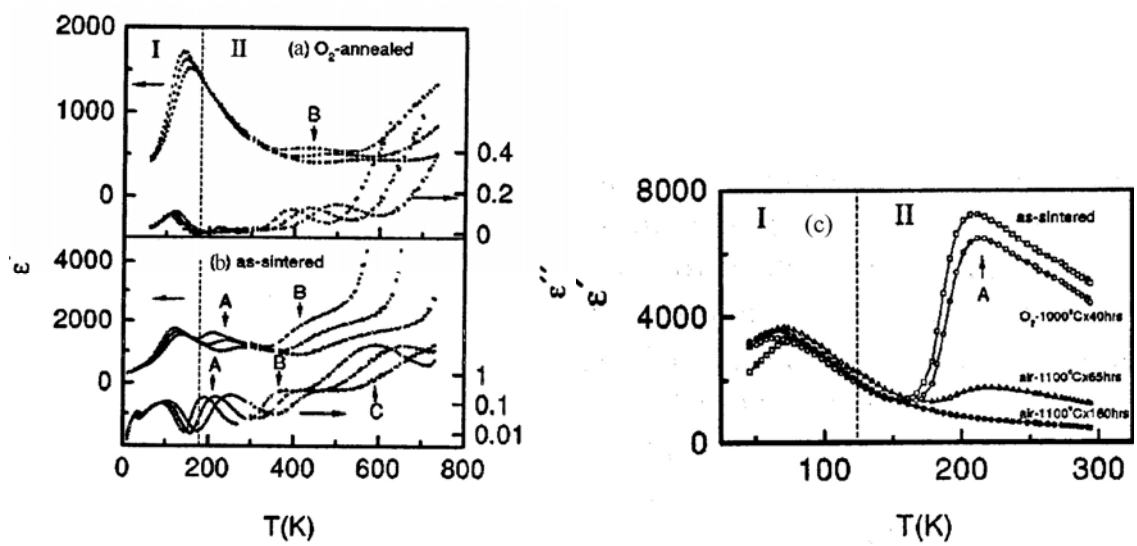

FIGURE 2.52. Temperature dependence of ε' (*left axis*) and ε'' (*right axis*) of $Sr_{0.92}Bi_{0.0533}TiO_3$ ceramics annealed in O_2 at 0.1, 1 and 10kHz (a), as-sintered $Sr_{0.92}Bi_{0.0533}TiO_3$ at 0.1, 1 and 10kHz (b) and of $Sr_{0.96}Bi_{0.0133}TiO_3$ annealed at different conditions at 1kHz (c) [Ang et *al.*, 2000c].

The anomaly in $\varepsilon'(T)$ with peak temperature T_m dependent on Bi content dominates below room temperature in $Sr_{1-1.5x}Bi_xTiO_3$ samples with x=0.0033-0.2 [Ang et *al.*, 1999], as presented in Figure 2.53 for both real ε' and imaginary ε'' parts of the complex dielectric permittivity (for x=0.0033-0.0133 marked as *C*). The quantum ferroelectric relationship $T_m \sim (x\text{-}0.0005)^{1/2}$ holds for $x \leq 0.0267$ [Ang et *al.*, 1998].

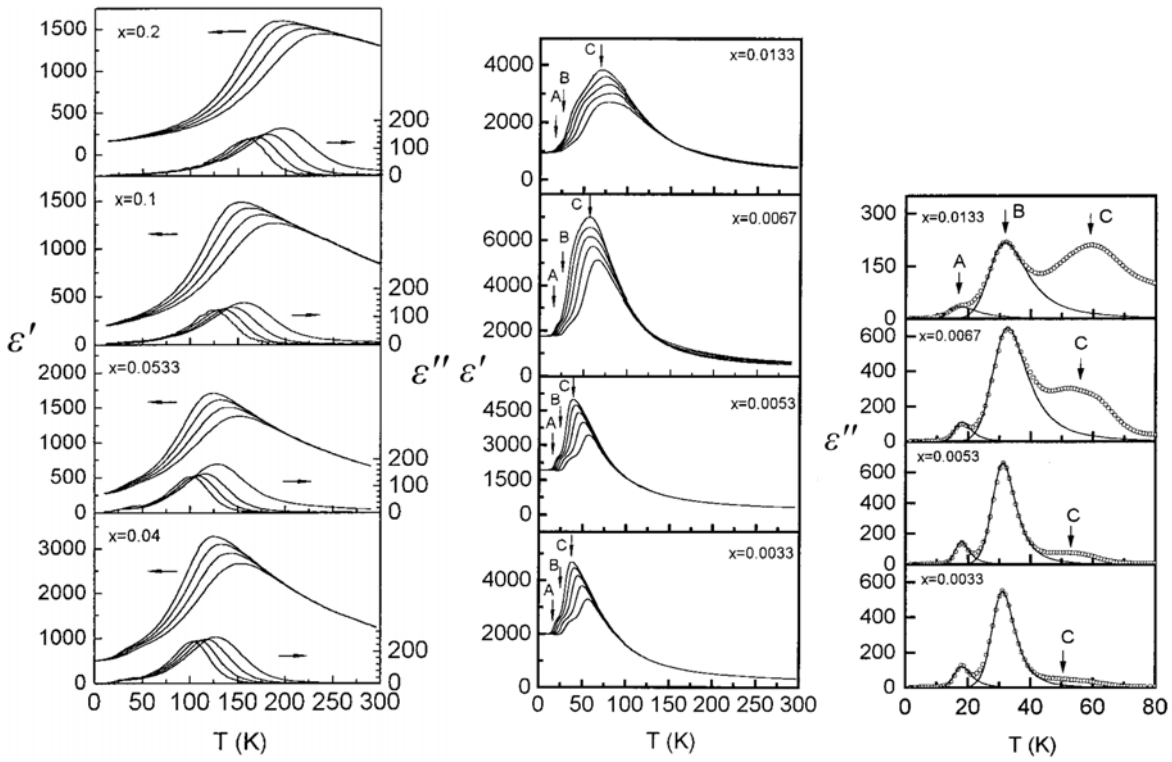

FIGURE 2.53. Temperature dependences: of ε' and ε'' of $Sr_{1-1.5x}Bi_xTiO_3$ ceramics with x=0.2, 0.1, 0.053 and 0.04 at 0.1, 1, 10 and 100kHz (a); of ε' of $Sr_{1-1.5x}Bi_xTiO_3$ ceramics with x=0.0133, 0.0067, 0.0053 and 0.0033 at 0.1, 1, 10, 100 and 1000kHz (b); and of ε'' of $Sr_{1-1.5x}Bi_xTiO_3$ ceramics with x=0.0133, 0.0067, 0.0053 and 0.0033 at 0.1kHz (c). Frequency increases from top to bottom for ε' and from left to right for ε'' [Ang and Yu, 2002].

In addition, the ε' peak value decreases and the temperature of the maximum of ε' increases with the frequency. It was found that the temperature dependence of the relaxation time for this anomaly can be well fitted to the Vögel-Fulcher law:

$$\tau = \tau_0 \exp[U/k_B(T_m - T_f)] \tag{2.14}$$

where k_B stands for the Boltzmann's constant, τ_0 for the pre-exponential factor, U for the activation energy, T_m for the temperature of the ε' maximum and T_f for the static freezing temperature at which the relaxation time τ tends to infinity [Viehland et *al.*, 1990], as depicted in Figure 2.54 for $Sr_{1-1.5x}Bi_xTiO_3$ ceramics with x=0.2, 0.1, 0.04, 0.0533, 0.0267 [Ang and Yu, 2002]. The fitting parameters U=0.024-0.047eV, τ_0=(0.10-5.26)$\times 10^{-9}$s and T_f increasing monotonously from 30.7K to 131.9K were obtained for $Sr_{1-1.5x}Bi_xTiO_3$ system with x=0.0133-0.2.

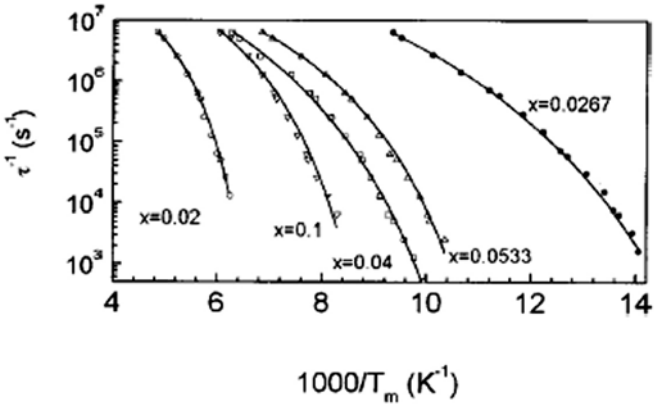

FIGURE 2.54. Arrhenius plots (inverse relaxation time τ^{-1} *versus* inverse temperature of maximum ε' $1000/T_m$) for $Sr_{1-1.5x}Bi_xTiO_3$ ceramics with x=0.2, 0.1, 0.04, 0.0533, 0.0267 [Ang and Yu, 2002].

Figure 2.55 show an example of slim but obvious *P(E)* (polarization *versus* field) hysteresis loops, observed for such concentration of Bi as x=0.0533, representing the concentration diapason of x=0.0133-0.2. When temperature is higher then 40K, the remnant polarisation P_r, obtained from the hysteresis loops, first increases with temperature increase until a maximum at about 80K and then decreases with further temperature increase. However, it does not go to zero at T_m, but inflects and tails to zero, like in typical relaxors. So, this relaxation process was assigned as relaxor-type behaviour, originated from off-centre Bi dipoles, forming dipole clusters due to local inhomogeneous distribution of Bi^{3+} ions [Ang and Yu, 2002].

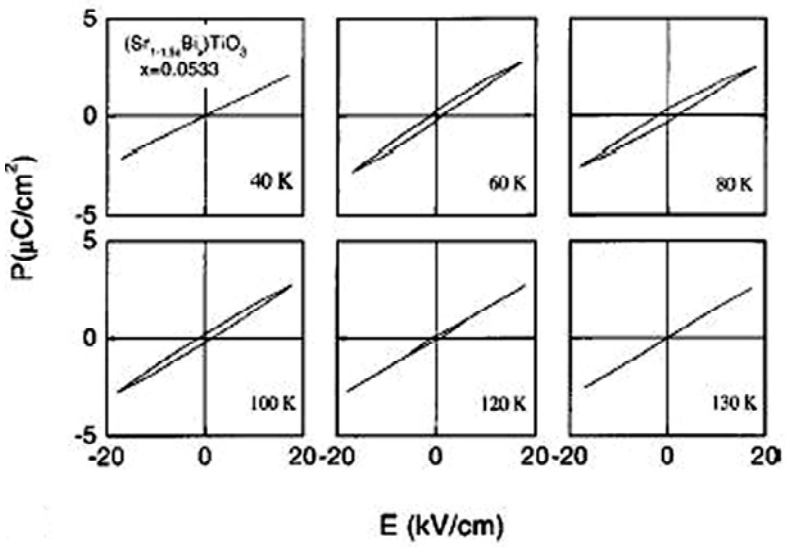

FIGURE 2.55. *P(E)* hysteresis loops of $Sr_{0.92}Bi_{0.0533}TiO_3$ ceramics at different temperatures [Ang et *al.*, 2000d].

With decreasing the Bi concentration, the interaction between the dipoles becomes much weaker, and less dipole clusters are formed. Thus, the polar relaxation mode *C* almost disappears at $x < 0.0033$. However, in this concentration range, low-temperature modes *A* and *B* are dominant, as one can see from Figure 2.56, especially from ε'' data shown in the insets of the figure. T_m's of the modes *A* and *B* are independent on doping content, but shift with the frequency. Dynamics of these peaks was described by Arrhenius law with U=33±1meV and τ_0=(0.4-2)×10^{-13}s for mode A and U=62±2meV and τ_0=(0.4-1)×10^{-13}s for mode *B* [Ang and Yu, 2002].

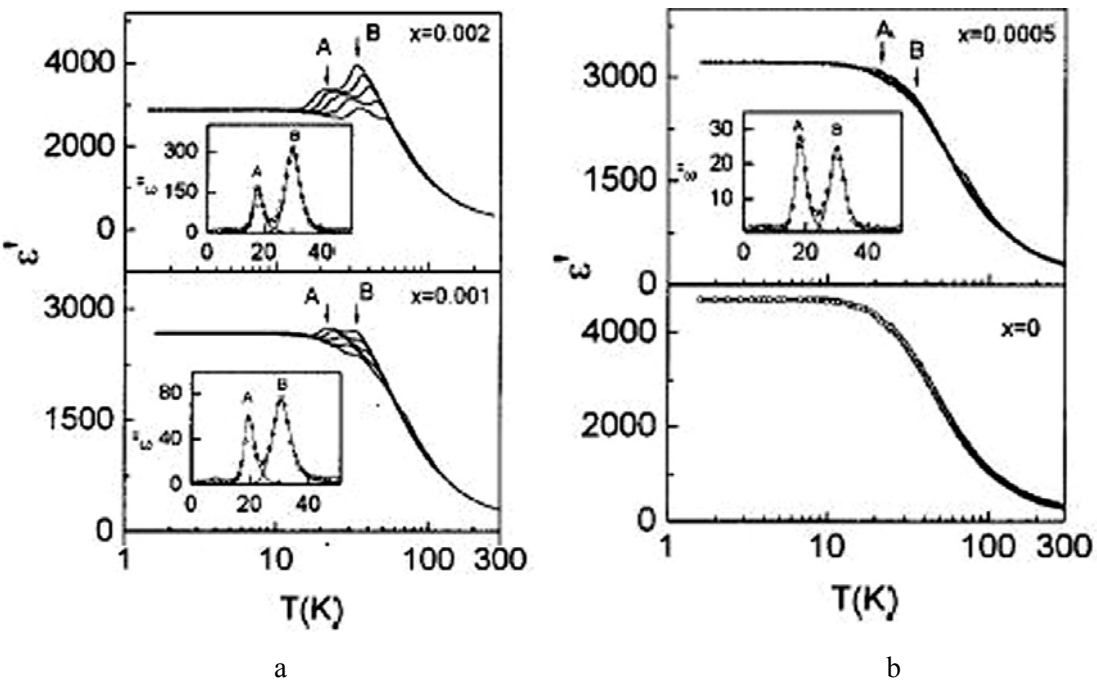

FIGURE 2.56. Temperature dependence of the ε' for $Sr_{1-1.5x}Bi_xTiO_3$ ceramics with x=0.002, 0.001 (a) and x=0.0005 and 0 (b) at 0.1, 1, 10, 100 and 1000kHz (*from top to bottom*). Insets show the temperature dependence of ε'' at 0.1kHz [Ang and Yu, 2002].

The temperature dependence of ε' under *dc* electric field up to 35kV/cm is depicted in Figure 2.57a for $Sr_{1-1.5x}Bi_xTiO_3$ with x=0.002 as a representative sample. With the application of *dc* bias, the amplitudes of *A* and *B* modes are gradually decreased, but their T_m's are not shifted that is more clearly seen from ε'' data, shown in the inset of Figure 2.57a. The latter fact provides evidence that modes A and B are different from the dipole glass mode or relaxor mode, whose T_m's are electric-field dependent [Ang and Yu, 2002]. At higher fields a broad ε' peak, similar to that observed in undoped ST under *dc* bias, is

induced, although the temperature range of the field dependent ε' is expanded from about 0-80K for undoped ST to about 0-150K for Bi-doped ST (Fig.2.57a).

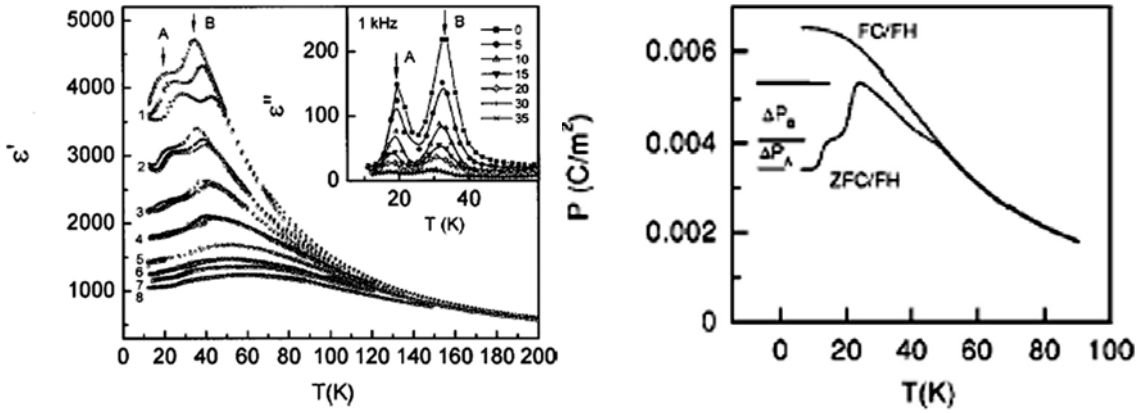

a b

FIGURE 2.57. Variation of ε' at 10, 50 and 100kHz (*from top to bottom*) (variation of ε'' at 1kHz is shown in inset) under 0 (1), 5 (2), 10 (3), 15 (4), 20 (5), 25 (6), 30 (7) and 35kV/cm (8) (a); and of the polarisation under zero field cooling/field heating (ZFC/FH) and field cooling/field heating (FC/FH) at 1kV/cm (b) of $Sr_{0.997}Bi_{0.002}TiO_3$ with temperature T [Ang and Yu, 2000d; Ang and Yu, 2002].

It is worthwhile also to refer to the polarisation data obtained from the measurements of the hysteresis loops for x=0.002, at 1Hz after zero field cooling/field heating (ZFC/FH) and field cooling/field heating (FC/FH) at 1kV/cm, with cooling and heating rates of 1K/min (Fig.2.57b) [Ang and Yu, 2000d]. From the temperature dependence of the polarisation P, illustrated for $Sr_{1-1.5x}Bi_xTiO_3$ with x=0.002 as an example in Figure 2.57b, two clear steps of the polarisation processes ΔP_A=0.08μC/cm^2 and ΔP_B=0.11μC/cm^2 are seen, which corresponds well to the modes A and B, respectively [Ang and Yu, 2000d].

As mentioned above, Sr-sites vacancies are induced in Bi-doped ST due to the charge balance, thus, two local environments in the ST lattice can be considered for Bi ions: *i)* Bi ions without any Sr vacancy nearby and *ii)* Bi ions with a Sr vacancy nearby, as shown in the schematic illustration of Figure 2.58. Meanwhile, Bi^{3+} ions on Sr sites are supposed to have off-centre displacement, which hence leads to the formation of dipoles [Ang and Yu, 2002]. So the occurrence of the two dielectric modes A and B was proposed to arise from the existence of two types of dipoles: off-centre Bi ions with and without Sr vacancy, with different allowed displacements [Ang and Yu, 2002].

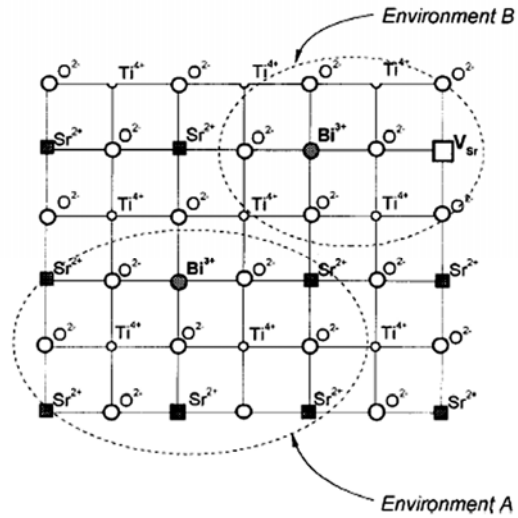

FIGURE 2.58. Schematic projection on the (100) plane for $Sr_{1-1.5x}Bi_xTiO_3$, showing two types of local environment of Bi ions [Ang and Yu, 2002].

Thus, dielectric behaviour of $Sr_{1-1.5x}Bi_xTiO_3$ is characterised by a broadened ε' peak with the temperature of the ε' maximum shifted to high temperatures as the frequency increases [Ang and Yu, 2002] and such behaviour is generally called relaxor behaviour. Moreover, two types of polar dielectric relaxation were introduced by Bi^{3+} ions in ST ceramics: 1) modes *A* and *B* occurring at low Bi concentrations described by Arrhenius law and related to individual off-centre Bi^{3+} ions on Sr sites and 2) mode *C* following the Vögel–Fulcher relation and attributed to polar clusters formed by interacting $Bi^{3+}{}_{Sr}$ dipoles for high Bi content [Yu, 1997 Ang et *al.*, 1998; Ang et *al.*, 1999a; Ang et *al.*, 1999b; Ang et *al.*, 1999c; Ang et *al.*, 2000b; Ang et *al.*, 2000d; Ang et *al.*, 2000e; Ang et *al.*, 2002; Yu and Ang, 2003; Porokhonskyy et *al.*, 2004; Ang and Yu, 2004].

At the same time, structural, microstructural and dielectric properties of the equivalent $Sr_{1-1.5x}Bi_xTiO_3$ thin films were not reported until recently. Moreover, the unique publication by Zhao et *al.* (besides those prepared by the author of current thesis) is related to the dielectric response at room temperature only [Zhao et *al.*, 2008]. In this way, the preparation and analysis of polycrystalline $Sr_{1-1.5x}Bi_xTiO_3$ thin films in a wide frequency and temperature diapason is necessary.

2.4. Methods for deposition of ferroelectric thin films

Film fabrication techniques can be divided into two general classes: Physical Vapour Deposition (PVD) techniques and chemical deposition techniques, which include Chemical Vapour Deposition (CVD) and Chemical Solution Deposition (CSD) [Vilarinho et *al.*, 2005].

PVD is a variety of vacuum deposition and in the former, atoms from a source are transferred in a continuous and controlled manner under a vacuum atmosphere ($<10^{-5}$Torr) to the substrate, in which the nucleation and growth of the film occur atomistically. Depending on how the particles (atoms or ions) are removed from the target, the following PVD techniques are considered: *rf*-sputtering, ion beam sputtering, electron beam evaporation and laser ablation, among others. The former allows for careful control of film thickness and orientation and compatibility with the semiconductor integrated circuit processing [Vilarinho et *al.*, 2005].

Chemical methods allow higher deposition rates, good stoichiometry control, and the production of large area defect-free films and have lower equipment-related costs. By using these methods, a fluid precursor undergoes a chemical change at a solid surface, leaving a solid layer.

Chemical vapour deposition (CVD) processes, where volatile compounds of the elements to be incorporated into the solids, the so-called precursors, are transported via the gas-phase to the region where deposition takes place, are well known [De Araujo et *al.*, 1996]. CVD is very attractive for industrial manufacturing of functional films to produce high-purity, high-performance solid materials. Microfabrication processes widely use CVD to deposit materials in various forms (monocrystalline, polycrystalline, amorphous, or epitaxial forms). However, the limited availability and toxicity of sources of precursors for functional materials restricts the use of this technology.

On the other hand, chemical solution deposition (CSD) methods have been increasingly used for the preparation of films of functional materials. The development of chemical solution deposition processes for perovskite thin films dates back to the mid-1980s. Publications on sol-gel processing of ferroelectric thin films were some of the first examples reported in the literature and demonstrated that it is possible to obtain the

desirable properties of bulk perovskite materials in a thin-film form using the chemical solution deposition technique [Budd and Payne, 1989; Dey et *al.*, 1988].

CSD uses a liquid precursor dissolved in an organic solvent. This relatively inexpensive and simple thin film process is able to produce stoichiometrically accurate crystalline phases. CSD describes a wet chemical method by which thin films are formed and encompasses a multitude of solution preparation and processing techniques. Wet processes comprise sol-gel, metalorganic decomposition (MOD), electrochemical reaction and hydrothermal routes [Vilarinho et *al.*, 2005]. Perhaps the most well-known and widely used solution process is the sol-gel. This technique does not require vacuum ambience, is cheaper and faster, allows for a good stoichiometry control and production of large area defect-free films and often produces films with better properties, although the texture degree of the film is inferior.

The preparation of films requires many different methodologies, as indicated below in Table 2.2 [adapted from Vilarinho et *al.*, 2005].

The main advantages and disadvantages between physical vapour deposition, chemical vapour deposition, and chemical solution deposition techniques are summarized in Table 2.3 [adapted from Vilarinho: European Master on Materials Science lectures "Advanced preparation methods"].

Among many different techniques presented above the more popular methods of deposition of undoped and doped $SrTiO_3$ films are: PLD [Hirano et *al.,* 1993; Li et *al.,* 1998a; Lippmaa et *al.,* 1999; Ang et *al.,* 2001a; Yu et *al.*, 2002; Takashima et *al.*, 2003; Astafiev et *al.,* 2003; Yamada et *al.,* 2005a; Wördenweber et *al.*, 2007], *rf*-spattering [Iwabuchi and Kobayashi, 1994; Hwang et *al.,* 1995; Kozyrev et *al.,* 1998; Morito et *al.,* 2001; Taylor et *al.,* 2003; Keane et *al.,* 2006], MBE [Haeni et *al.*, 2004; He et *al.*, 2005], MOCVD [He et *al.*, 2002; Tikhomirov et *al.*, 2002], sol-gel [Kamalasanan et *al.*, 1993; Thomas et *al.*, 1997; Tsuzuki et *al.*, 1997; Hofman et *al.*, 1997]. More detail about several methods for ST films preparation is described below as well as sol-gel method which is used in current Thesis.

TABLE 2.2. Thin and thick films deposition methods.

Thin Films Methods			**Thick Films Methods**
***Physical Vapour Deposition* (PVD)**	***Chemical Vapour Deposition* (CVD)**	***Chemical Solution Deposition* (CSD)**	
Film is formed by atoms directly transported from source to the substrate through gas phase	*Film is formed by chemical reaction on the surface of substrate*		
Evaporation: - molecular beam epitaxy (MBE) - electron-beam (EBE) - resistance	Classified by operating pressure: - atmospheric pressure CVD (APCVD) - low-pressure CVD (LPCVD) - ultrahigh vacuum CVD (UHVCVD)	Solution gelation (sol-gel)	Tape casting
Sputtering: - *rf* magnetron - *dc* - ion beam (IBS)	Classified by physical characteristics of vapour: - aerosol assisted CVD (AACVD) - direct liquid injection CVD (DLICVD)	Metallorganic deposition (MOD)	Screen printing
Laser Ablation (pusled laser deposition (PLD))	Plasma methods: - microwave plasma-assisted CVD (MPCVD) - plasma enhanced CVD (PECVD) - remote plasma-enhanced CVD (RPECVD)	Hybrid-chelate processes	Electrophoretic deposition
Reactive PVD	Atomic layer CVD (ALCVD)		
Cathodic Arc Deposition (Arc-PVD)	Metalorganic chemical vapour deposition (MOCVD)		

TABLE 2.3. The main advantages and disadvantages between physical vapour deposition, chemical vapour deposition, and chemical solution deposition techniques.

Advantages	***Disadvantages***
Physical vapour deposition	
-careful control of film thickness and orientation -compatibility with the semiconductor - integrated circuit processing	-difficult to control stoichiometry of multicomponent films -slow rates of deposition -need for high-temperature post-deposition crystallization annealing -high cost related with equipment acquisition and maintenance -need of vacuum operation
Chemical Vapour Deposition	
-high growth rates possible -can deposit materials which are hard to deposit -good reproducibility -good grow epitaxial films -used to produce high-purity, high-performance solid materials	-high temperatures -complex process -toxic and corrosive gases
Chemical Solution Deposition	
-usually no vacuum ambience -higher deposition rates -good stoichiometry control -production of large area defect-free films -lower equipment-related costs -easy preparation	-non epitaxial growth -toxicity of sources of precursors

2.4.1. Pulsed laser deposition

Pulsed laser deposition (PLD) technique works by an ablation process [Holland, 1956; Ohring, 1992], where the surface of the target material is converted to plasma (which usually reverts to a gas before reaching the substrate) by pulses of laser beam. A high power pulsed laser beam is focused inside a vacuum chamber to strike a target of the desired composition (Fig.2.59).

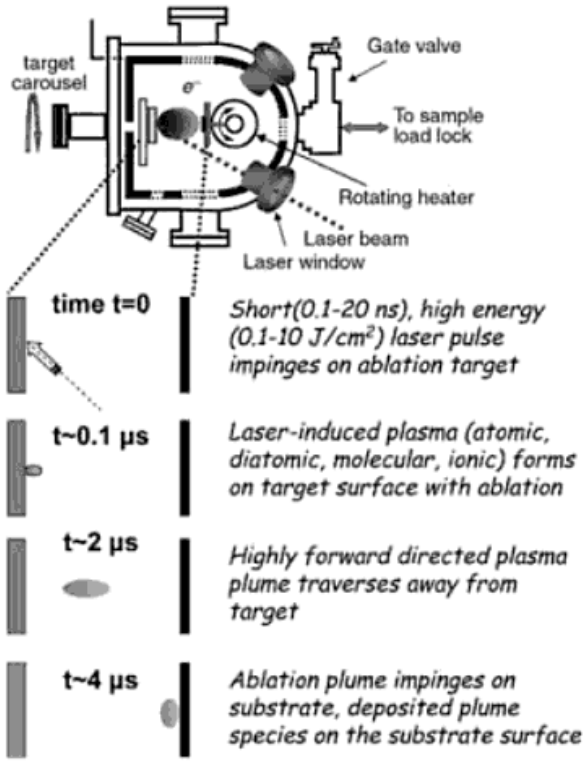

FIGURE 2.59. Schematic of pulsed laser deposition process: steps of deposition process (*text*) in different time (*t*) [Eason, 2006].

In general the process of PLD can generally be divided into four stages, that include: *i)* the laser ablation of the target material and creation of a plasma, *ii)* the dynamic of the plasma, *iii)* deposition of the ablation material on the substrate and *iv)* nucleation and growth of the film on the substrate surface. Each of these steps is crucial for the crystallinity, uniformity and stoichiometry of the resulting film.

The ablation of the target material upon laser irradiation and the creation of plasma are very complex processes. Deposition of the ablated material on the substrate is important to determine the quality of the deposited films. The removal of the atoms from the bulk material is done by vaporization of the bulk at the surface region in a state of non-equilibrium which is enhanced by microscopic cracks at the surface. The surface of the target is then heated up and the material is vaporized. The temperature of the generated plasma plume is typically 10000K.

The nucleation process and growth of a crystalline film on a substrate depend on several factors such as the density, energy, ionization degree of the ablated material and temperature, roughness and crystalline properties of the substrate. Although PLD has a much lower average deposition rate than other deposition techniques such as MBE and

sputtering it can be demonstrated that the fraction of stable nucleation sites is orders of magnitude higher for PLD than for sputtering and MBE. This has several implications on the growth mechanism in PLD. The critical nuclear radius is smaller and in the range of one or two atoms. Since the nucleation rate is proportional to the nucleation site density and the rate of impingement, it is much higher in the case of PLD. Furthermore, the high density of nucleation sites also increases the smoothness of the deposited film. This is the reason of high importance of PLD method for the growth of thin films [Holland, 1956; Ohring, 1992], although PLD is not very suitable for large-area deposition.

2.4.2. *rf*-sputtering deposition

Sputter deposition is a PVD method for thin films deposition by sputtering, i.e. ejecting, material from a target (source) which then deposits onto a substrate. The target can be kept at a relatively low temperature, since the process is not based on the evaporation, making this one of the most flexible deposition techniques [Bunshah, 1982; Schuegraf, 1988].

The sputtered ions can fly from the target in straight lines and impact energetically on the substrates or vacuum chamber (causing resputtering). The availability of many parameters that control sputter deposition make it a complex process, but also allow experts a large degree of control over the growth and microstructure of the film [Bunshah, 1982; Schuegraf, 1988].

Charge build-up on insulating targets can be avoided with the use of radio frequency (*rf)* sputtering (Fig.2.60) where the sign of the anode-cathode bias is varied at a high rate. *rf* sputtering works well to produce highly insulating oxide films but only with the added expense of *rf* power supplies and impedance matching networks.

The *rf* magnetron-sputtering technique is characterized by high reproducibility in the chemical composition, easy process control, and compositional change of the film can be achieved only by varying the composition of the target. *rf* sputtering can be used to sputter electrically insulating materials although the sputtering rate is low. A major disadvantage in *rf* sputtering of dielectric targets, is that most electrically insulating materials have poor thermal conductivity, high coefficients of thermal expansion, and are usually brittle materials. Since most of the bombarding energy produces heat; this means that large thermal gradients can be generated that result in fracturing the target if high power levels are used [Mattox, 1998; Wachtman and Haber, 1993].

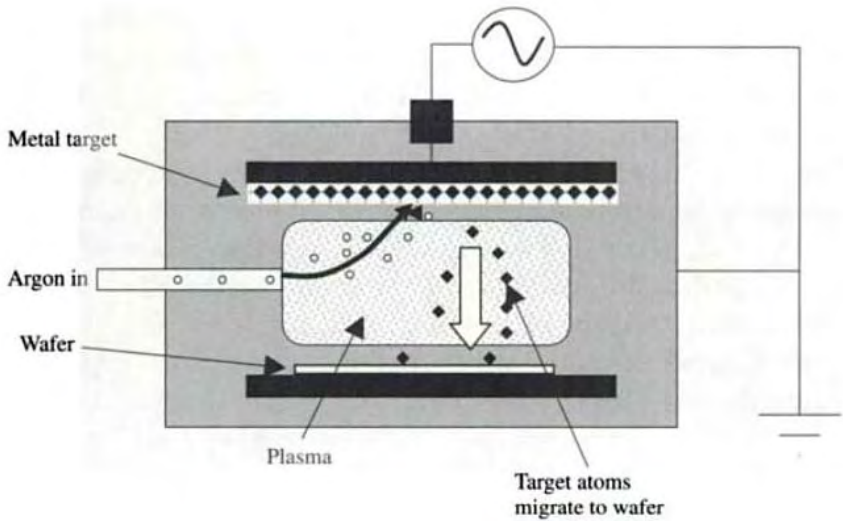

FIGURE 2.60. Schematic of an *rf*-sputtering system [Reed et *al*., 2004].

2.4.3. Molecular beam epitaxy

In molecular beam epitaxy (MBE) the slow streams of an element can be so directed at the substrate that one atomic layer of material is deposited at a time. MBE is a thin film growth technique relying on the evaporation of elements from individual sources in a high vacuum environment. It is a versatile technique for growing thin epitaxial structures with great precision and purity. A schematic and simplified view of a MBE system is shown in Figure 2.61 [Ledentsov, 1999].

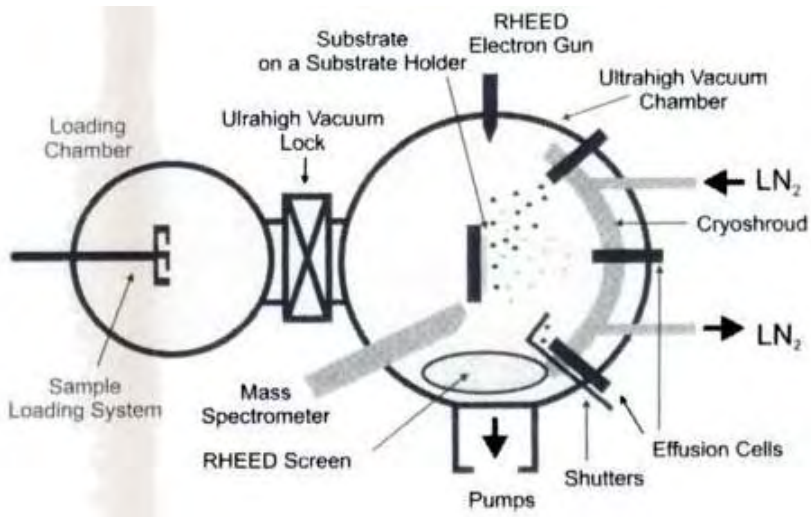

FIGURE 2.61. Schematic view of molecular beam epitaxy apparatus [Ledentsov, 1999].

Its unique capability to deposit monolayer doses of several different elements in rapid succession is difficult to reproduce with any other thin film deposition techniques such as sputtering, PLD, or CVD, and has determined the choice of this technique for the deposition of complex heterostructures in a variety of crystal systems [Gossard et *al.*, 1976; Sakamoto et *al.*, 1985]. In addition, unlike traditional single source sputtering and laser ablation, MBE does not require the fabrication of a target of the desired compound, instead relies on the evaporation from elemental source materials. This allows the growth of many metastable compounds and structures that cannot be realized by bulk synthesis techniques.

MBE method allows perfect layer by layer (LBL) growth control and fairly independent control of the different deposition components and is therefore very flexible. Due to ultra high vacuum (UHV) conditions very clean films can be obtained and the method therefore is ideally suited for basic investigation of growth processes. However, for application as a production tool there are major drawbacks due to rather slow LBL growth, the expensive UHV techniques and the large number of process parameters which have to be kept under control [Bunshah, 1982; Schuegraf, 1988].

2.4.4. Metallo-organic chemical vapour deposition

Metalorganic chemical vapour deposition (MOCVD) is a complicated process that includes surface- and gas- phase decomposition of source gases, transport phenomena of both source gases and decomposition products, and surface reactions of film precursors (metalorganic precursors) [Allendorf and Bernard, 1997]. The process is carried out using a commercial MOCVD reactor (Fig.2.62). The metalorganic precursors are transported into the reactor chamber using hydrogen carrier gas. High temperature in the chamber decomposes the precursors and the liberated atoms recombine forming a semiconducting compound. This takes place on substrates placed on a radiatively heated susceptor resulting in film growth [Bunshah, 1982; Schuegraf, 1988].

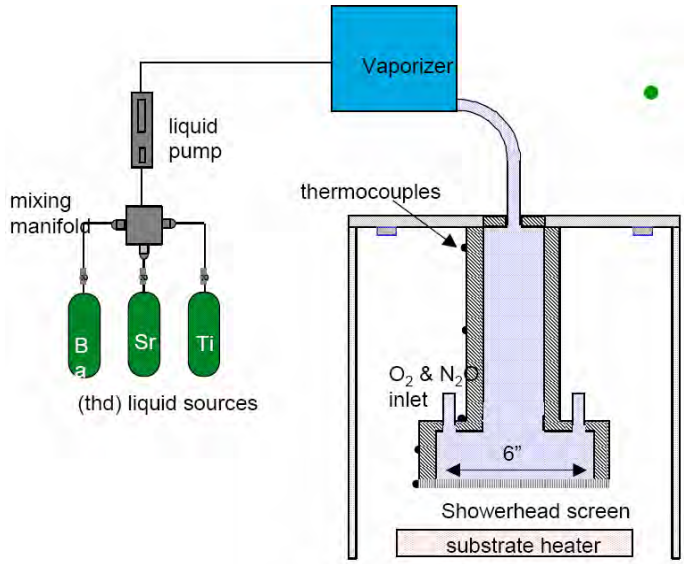

FIGURE 2.62. Typical metalorganic chemical vapour deposition equipment for (Ba,Sr)TiO_3 films deposition [York et *al.*, 2000].

The MOCVD method can be used for the fabrication of high quality, high temperature superconducting and ferroelectric materials in the form of thin films. Moreover, MOCVD is a technique allowing direct formation of thin films in the proper crystalline phase and even epitaxial films for lattice matched substrates. MOCVD can be easily scaled-up both in wafer throughput and in wafer diameter. This makes the technique particularly important for deposition on an industrial scale. However, the technique involves high investment and operating cost [Bunshah, 1982; Schuegraf, 1988].

2.4.5. Sol-gel fabrication of films

Sol-gel preparation of ceramic materials dates back to the 1840s [Ebelmen, 1846]. Since that time, sol-gel techniques have successfully been used to form a wide range of oxide materials, including complex oxides and in particular ferroelectric oxides. Solutions are prepared, dissolving metalorganics in solvents and mixing them on a molecular level that ensures a high level of chemical homogeneity in films. By adjusting the viscosity and concentration of the solutions, films of various thicknesses can be formed over large areas with limited necessity for complex and expensive capital equipment [Yi and Sayer, 1991; Tuttle and Schwartz, 1996].

As shown in Figure 2.63, sol-gel deposition of films is one of the wet chemical methods, entailing the preparation of the solution, the deposition of the solution onto the

substrate by dip- or spin-coating and the subsequent thermal treatment of the deposited layer to remove the organics and to achieve crystallization and densification of the coatings [Vilarinho et *al.*, 2005].

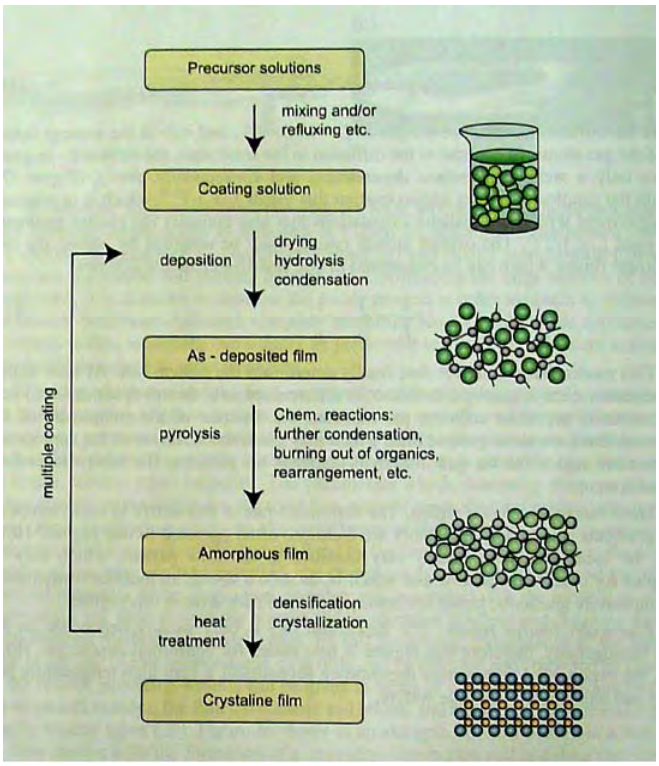

FIGURE 2.63. Flow diagram of the films preparation [Waser, 2003].

2.4.5.1. Preparation of chemical solutions

Sol-gel processes refer to chemistry that use alcohols as both solvents and reactants. Hybridchelate chemistry uses modifying ligands to react and stabilize a solution or component of the solution. In sol-gel processes an alcohol such as 2-methoxyethanol (2MOE) ($C_3H_8O_2$) is used as a solvent and reactant for alkoxide metalorganic precursors. Here alkoxide refers to a chemistry of a metal, M, bonded to oxygen, O, that is bonded to an alkyl group, R, ($M(OR)_n$) [Tuttle and Schwartz,1996].

For the formation of a gel from the solution, two common reactions occur. The first reaction is a hydrolysis, where water in the solution reacts with the metalorganic, and the second one is condensation, where the hydrated alkoxide precursor reacts to form water and a complex metalorganic oligomer with oxygen bridging two metal ions, as shown in Equations 2.15 and 2.16 [Tuttle and Schwartz, 1996].

$$M(OR)_n + H_2O \rightarrow M(OR)_{n-1}(OH) + ROH \text{ (hydrolysis)} \quad (2.15)$$

$$2M(OR)_{n-1}(OH) \rightarrow M_2O(OR)_{2n-2} + H_2O \text{ (condensation)} \quad (2.16)$$

Methoxyethanol can react with some alkoxide metal precursors to form methoxyethoxide molecules that are less reactive and thus more stable through the following reaction, where OR' is a methoxyethoxy group:

$$M(OR)_n + nR'OH \rightarrow M(OR')_n + nROH \text{ (alkoxy exchange)} \quad (2.17)$$

The simplicity of the reactions involved in true sol-gel systems makes it an ideal technique for studying the preparation of new compounds. By controlling temperature, water content, and reflux/distillation conditions the nature of the oligomeric species formed can be controlled.

While this particular solution chemistry has many advantages, it also has its drawbacks. One disadvantage is related to the fact that the solution preparation of sol-gel precursors requires extensive knowledge of chemistry and chemical preparation techniques. Additionally, 2-methoxyethanol is a known teratogen, which makes large-scale or industrial use unattractive [Yi and Sayer, 1991; Tuttle and Schwartz, 1996; Schwartz, 1997; Schwartz et *al.*, 2004].

2.4.5.2. Deposition process

Processing films by solution deposition occurs in general in three steps that are common to all of the solution systems above described. Films are wet deposited onto a substrate, followed by a drying step to remove the solvents and consolidate the film into an amorphous gel, and finally subject to a crystallization step to promote the formation of the desired crystalline phase and microstructure.

The chemical solution deposition process starts with the preparation of a suitable solution from a set of precursors chosen according to the designated film composition and the chemical route to be used. An important and initial step in the films deposition process is the cleaning of the substrate. Any contamination of the substrate surface is crucial to the deposition process, because any stain and/or debris present in the surface will provoke a coating flaw. Alcohol, acetone and aqueous detergent are standard products used in the cleaning substrate procedure [Klein, 1994; Matthes et *al.*, 1999; Lakeman and Payne,

1992]. After the solution preparation and cleaning process the coating solution is then deposited onto substrates by: *i)* dip-coating that is often used in the optics industry for large and non-planar substrate, or *ii)* spin-coating, where a photoresist spinner is employed and which is suitable for semiconductor wafers.

-Dip-coating deposition method

Film deposition by dip-coating is one of the most widely used methods due to the capability to prepare thin layers of precise thickness. The basic equipment consists of a movement control system, a tank, and a target (substrate). The substrate is immersed in a tank containing the coating solution by the movement control system and subsequently removed. The excess coating material is drained into a collection tank and the adherent layer is dried and heat treated. To obtain the best results the system should be isolated from the vibrations ensuring that the film´s surface remains completely undisturbed. The thickness of the film prepared by this deposition method is a function of the viscosity and liquid density of the precursor solution and withdrawal rate. The dip-coating method possess some advantages such as the possibility to prepare films with any size and shape, the possibility to cover conformal shaped substrates, the low preparation cost and the easy assembly and operation of the system. The main disadvantage is related with the large amount of solution required to prepare the films that can be overcame using the spin-coating method.

-Spin-coating deposition method

Spin coating is the preferred method for the deposition of thin and uniform films onto flat substrates. An excess of sol-gel solution is placed on the substrate (Fig.2.64). The substrate is then rotated at high speed in order to spread the fluid by centrifugal force. The rotation is continued for some time, with fluid being spun off the edges of the substrate, until the desired film thickness is achieved. The solvent is usually volatile, providing for its simultaneous evaporation.

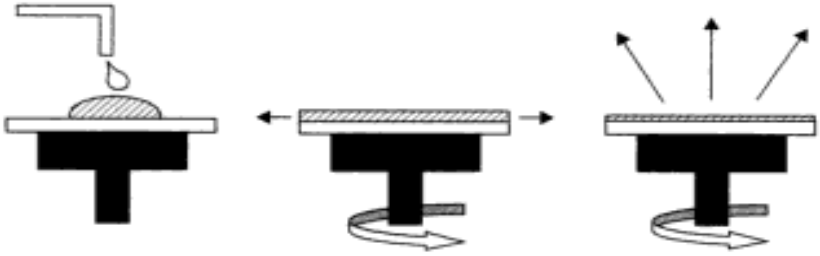

FIGURE 2.64. Schematic of the spin coating process: drop of solution (a), acceleration (b), final spinning (c) [Franssila, 2004].

The final film thickness using this method is a function of the viscosity, liquid density, spin frequency and spin time. Spin-coating method shows clear advantages including rapid processing, easy operation of the system, the need for small quantity of liquid for large substrate area preparation, etc., over other preparation methods. Due to these assets its use in the microelectronic industry and in the research field has expanded. However, dependence of the process on the substrate size and shape limits the applications of the spin coating method [Klein, 1994; Franssila, 2004; Carter and Norton, 2007].

2.4.5.3. Heat treatment process

The heat treatment is the last step of the film preparation. The objective of this stage is to form the desired crystalline phase and to produce crack-free and dense films as well [Tuttle and Schwartz, 1996; Sporn et *al.*, 1995; Budd and Payne, 1989].

Once a wet film is deposited onto a substrate, the process of gelation is started. The as-deposited film is typically amorphous and can contain a large volume fraction of organics. Schwartz has divided the nature of the as-deposited state into three subgroups [Schwartz, 1997; Schwartz et *al.*, 2004]. The first is a chemical gel; here a significant level of condensation reactions has occurred during and/or after deposition and the films cannot be re-dissolved in the parent solvent. The second group is that of a physical gel, where physical aggregation of the oligomers are present in the solution, and the condensation reactions, leading to extensive polymerization in chemical gels, has not occurred, hence the films can be re-dissolved in the parent solvent. The third group is that of non-gelling films, where a limited amount of condensation has taken place similarly to physical gels. These films tend to stay wet in appearance owing to the high boiling points and low volatility of the solvents and chemicals present in the precursor solution [Schwartz, 1997; Schwartz et *al.*, 2004].

Film consolidation may have happened during or right after the deposition, resulting in a chemical gel. In other cases, the films must be submitted to high temperatures (or permitted to stay at ambient conditions for some time to allow organic evaporation) to drive out remaining organics and to consolidate the gel. Pyrolysis (thermolysis) is the thermal processes that express the removal of organics by heat. The most common pyrolysis treatment of thin films is a hot-plate "drying", when films are taken directly from the spin coater and placed onto the surface of a hot-plate with a temperature ranging between 200 and 400°C. During this step, the films shrink significantly, as much as 30% of the original thickness.

The relatively high temperatures of the hot-plate pyrolysis are necessary to remove a large fraction of the organic constituents prior to the collapse of the amorphous structure upon later heat treatments that would trap remaining organics [Tuttle and Schwartz, 1996]. In general, the following hot-plate treatment is aimed to remove any remaining organic or hydroxyl species. Rapid thermal anneals, slow ramps, or hot-furnace insertions have all been used in this pyrolysis phase. At this stage the films are either crystallized at higher temperatures and recoated, or only recoated. This process can be carried out as many times as required to attain the desired film thickness [Tuttle and Schwartz, 1996; Schwartz et *al.*, 1997; Schwartz et *al.*, 2004].

The final processing step is the crystallization of the amorphous film. Crystallization and film morphology depend on several factors including, but not limited to: substrate, film composition, and prior pyrolysis steps. Films deposited on single-crystalline or textured substrates maintain a possibility to mimic the substrate crystallographic orientation and to grow in an epitaxial way. As the driving force for nucleation increases, the probability of a homogeneous nucleus formation increases. An increase in driving force for crystallization in an amorphous film would include an increase in the process temperature.

Thus, prior pyrolysis and heat treatment steps affect the film morphology. Annealing is used to crystallize the films with a desirable crystalline structure and to increase the density of the films [Tuttle and Schwartz, 1996; Schwartz, 1997].

2.5. Applications of $SrTiO_3$ films

Three main domains of applications of ferroelectric films are memory devices, microsystems (pyroelectric sensors and piezoelectric actuators) and high frequency electrical components (tunable microwave devices) [Setter et *al.*, 2006]. As already indicated in the precedent text, the main applications of $SrTiO_3$-based compositions are related to memory and tunable device application that will be presented below.

2.5.1. Memory device applications of $SrTiO_3$-based films

Currently semiconductor technology is the base for electronic memory devices and their simple classification is presented in Figure 2.65 (adapted from [FUJITSU, 2005]). Semiconductor memory devices are divided into two major types: *i)* volatile memories, which lose stored data unless it remains supplied with power from an external source and *ii)* non-volatile memories, which retain stored data even when its external power supply is disconnected.

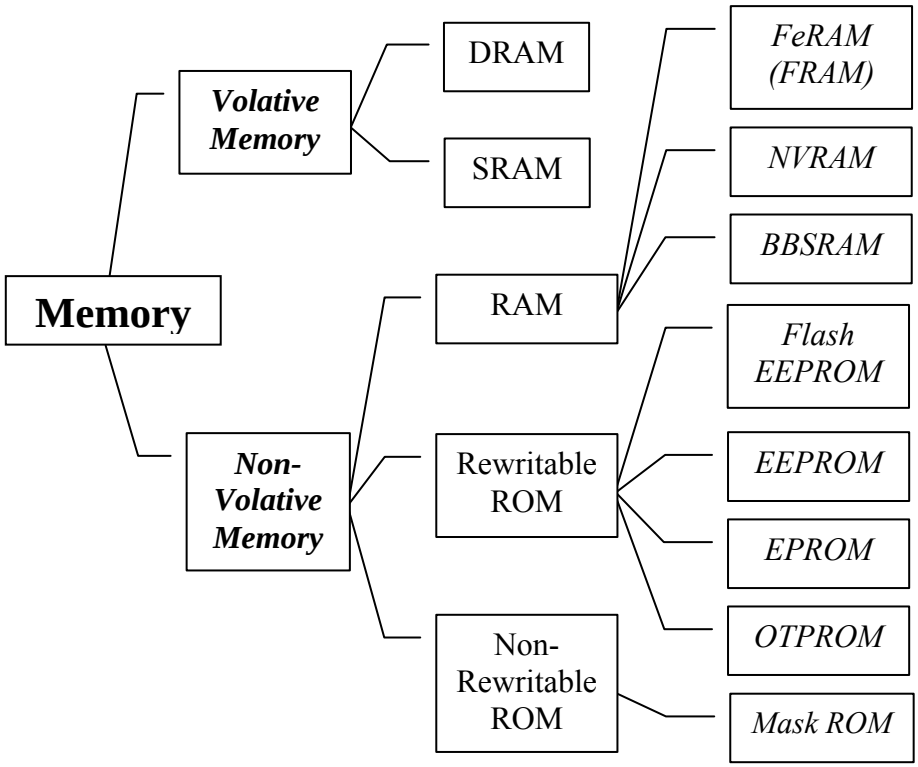

FIGURE 2.65. Classification of semiconductor memory (adapted from [FUJITSU 2005]).

Volatile memory is divided into two classes: Dynamic Random Access Memory (DRAM), which requires refreshing in order to retain data, and Static Random Access Memory (SRAM), which is capable of high-speed access and does not require refreshing. Because DRAMs are inexpensive and suited for high density application, they are used for temporary storage of large volumes of data in main memories for personal computers (PCs), and for graphics memories involving image processing [FUJITSU, 2005]. SRAM is faster in read/write access but it takes up a larger area than DRAM and has a smaller density than DRAMs. SRAMs are widely used as (internal) cache memory of processors for PCs and other equipment where small density and high-speed data processing is necessary, as well as for temporary storage in cellular phones [FUJITSU, 2005].

On the other hand, non-volative memory is divided into:

- Read-Only Memory (ROM), used to acquire programs, characters and other data. This type of memory is also divided into two classes, depending whether the user can write data to the memory or not:
  - Rewritable ROM: allows the user to write data. Examples are One Time Programmable ROM (OTPROM), Erasable Programmable ROM (EPROM), Electronically Erasable Programmable ROM (EEPROM) and Flash Memory (Flash EEPROM);
  - Non-rewritable ROM: does not allow the user to write data, it is written during manufacturing process. Example is Mask ROM, which is shipped after being programmed during manufacture in general.
- Random Access Memory (RAM) that does not lose data, when the power is turned off. This type of memory is divided into three classes:
  - Non-volatile RAM (NVRAM) that back up data in combination with another type of memory or use a battery to back up the power.
  - Battery Back-up SRAM (BBSRAM), which uses a battery to back up the power in case the power is turned off or the power supply causes a power failure.
  - Ferroelectric Random Access Memory (FeRAM or FRAM) is an ideal memory that can serve by itself either as RAM or as ROM. Ferroelectric films are a key component of FeRAMs. The ferroelectric film is polarized by the electric field applied from an external source and remains polarized even when the external electric field is removed, based on the remnant polarization property of the

ferroelectric film. In this way FeRAMs do not lose data when power is removed from it, and because of this characteristic they are called non-volatile. Changing the direction of the applied electric field inverts the direction of the polarization of the ferroelectric material, capable of updating data [FUJITSU, 2005].

Thus, the main interest to ferroelectric thin films is their application in FeRAM, which is based on the polarization reversal by an external electric field of metal-ferroelectric-metal capacitors. There are two main candidates for such application: Lead Zirconium Titanate and Strontium Bismuth Tantalate [Scott, 2000; Setter et *al.*, 2006].

At the same time, DRAM is the most widely used technology for temporary data storage, providing the "memory" for all PCs [Daglish and Kemmitt, 2000]. It comprises a transistor, connected to an integrated capacitor, and its binary state is stored by maintaining a potential on the capacitor. However, since the capacitor discharges with the time, the capacitor voltage has to be refreshed several times per second. In conventional DRAMs most of the space is occupied by the capacitor, therefore, in order to reduce the cell size the area of the capacitor must be decreased. One way to achieve this is to increase the ε' of the capacitor dielectric. For DRAM applications, ferroelectric properties such as polarization hysteresis are not essential, only a high ε' with good insulating properties is required [Parker and Tasch, 1990]. Also, a DRAM cell needs a film with high charge storage capacity and low current density. To date the most popular choice of ferroelectric materials is ST and ST-based compositions, namely $(Ba,Sr)TiO_3$ (BST).

Thus, 500-nm-thick $SrTiO_3$ film, deposited by MOCVD, was reported as one of the dielectric materials suitable for DRAM applications, possessing the unit area capacitance of 3.5fF/μm^2 and a charge storage density of 36.7fC/μm^2 under applied electric field of 200kV/cm [Joshi and Krupanidhi, 1993]. Similar values are applicable for a planar bit cell capacitor for 64Mbit DRAMS [Parker and Tasch, 1990]. Moreover, based on ST films obtained by similar MOCVD method, 1Gbit DRAM capacitor, which demonstrates a cell capacitance of 25fF and leakage current density of 8×10^{-7}A/cm^2 in a 0.125μm^2 capacitor area, was developed (Fig.2.66) [Lesaicherre et *al.*, 1994].

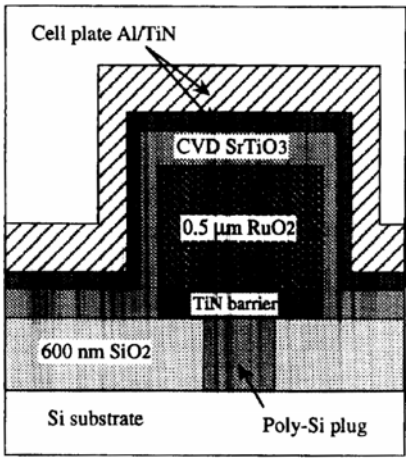

FIGURE 2.66. Cross-sectional schematic representation of the 1Gbit dynamic random access memory capacitor structure [Lesaicherre et *al.*, 1994].

There are also a number reports about DRAM based on BST films. Hwang and co-workers presented very thin BST thin films from 15 to 50nm prepared by a *rf* magnetron sputtering on $Pt/SiO_2/Si$ substrates with a leakage current density, less than $40\times10^{-9}A/cm^2$ at ±1.5V what is useful for ultra-large-scale integrated DRAM [Hwang, et *al.*, 1995].

Figure 2.67 shows a TEM image of a DRAM cell with $(Ba,Sr)TiO_3$ film [Kotecki et *al.*, 1999]. As the lithographic feature size decreases from 0.25 to 0.10µm, the area of the DRAM cell is expected to decrease by a factor of more than 10x [Kotecki et *al.*, 1999]. Therefore, due to small size of film in comparison to bulk, ferroelectric thin-film based DRAM is used in cellular telephones [Daglish and Kemmitt, 2000].

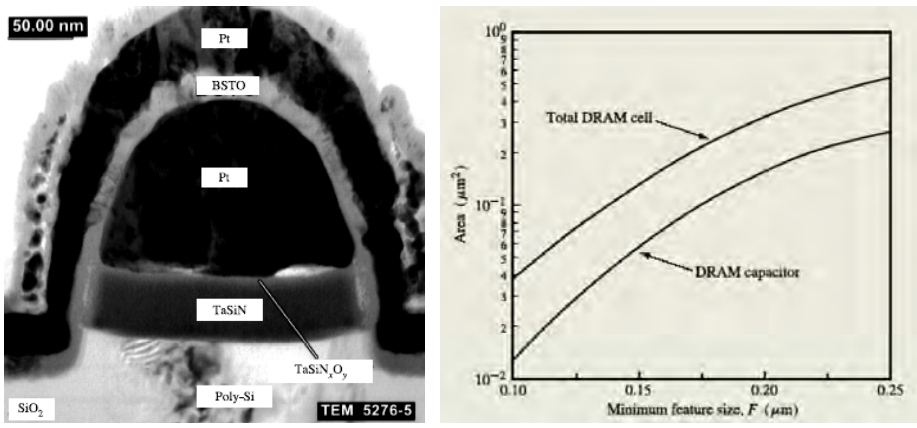

a b

FIGURE 2.67. TEM image of a stacked-capacitor structure with a $(Ba,Sr)TiO_3$, Pt electrodes, and a TaSiN barrier layer (a) and expected area of a dynamic random access memory cell and the area available for the capacitor as a function of the minimum feature size (b) [Kotecki et *al.*, 1999].

It is known that more than one type of memory is used in electronic devices, increasing the utilised energy and additional circuitry [Kingon, 2006]. However, the possibility for better memory devices was demonstrated within the oxide material $SrTiO_3$ studied by conductive-tip scanning probe microscopy, suggesting a configuration for the *"ultimate" Non-Volatile Memory for high-storage density applications* [Szot et *al.*, 2006]. It was shown that the electrical transport in a network of dislocations in ST can be moderated by the amount of charge passed through the dislocation. Application of a field and current above a critical threshold results in the dislocation becoming resistive. When a field and current of opposite sign are applied, the dislocation returns to a metallic state. [Szot et *al.*, 2006]. Thus, ST and ST-based systems are still popular and useful for different types of memory applications.

2.5.2. Tunable applications of $SrTiO_3$ films

One more electronic application of ST films is related to tunable microwave (MW) devices. The main driving force for resurgent attention to ferroelectric thin film materials is the potential for substantial miniaturization of MW components and systems accompanied also by a large cost reduction and the prospects for integration with microelectronic circuits. As an example of small size-element application, Figure 2.68 shows an integrated passive device for the power amplifier module of cellular phones at 2GHz, in which a high-capacitance ST capacitor is fabricated on the Si substrate [Ikeda et *al.*, 2003; Ota et *al.*, 2002].

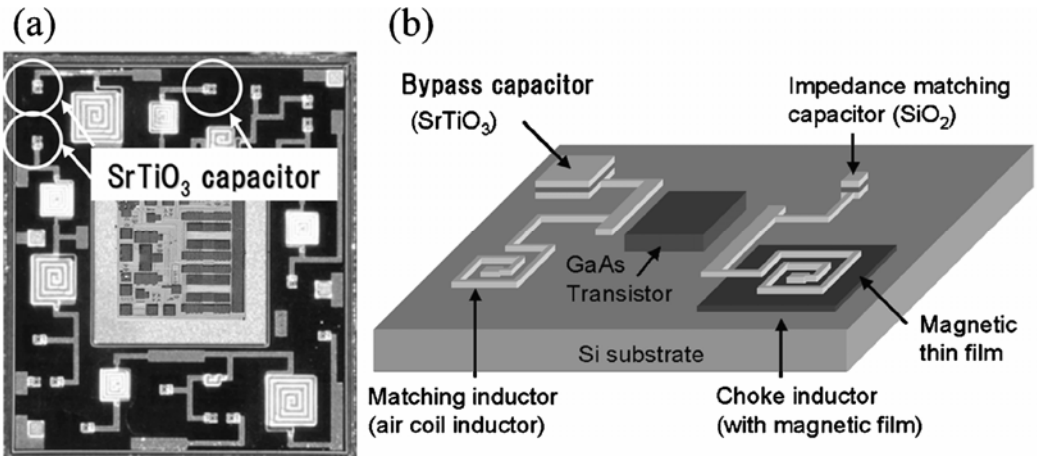

FIGURE 2.68. Layout (a) and schematic view (b) of the power amplifier module integrated on a silicon substrate with thin-film passives [Suzuki et *al.*, 2005].

Moreover, thin films are very attractive for MW tunable applications due to the low tuning voltages compared to the bulk materials. There is a number of review papers that cover the different aspects of tunable ferroelectric materials and their applications [Vendik et *al.*, 1999; Lancaster et *al.*, 1998; Xi et *al.*, 2000; Miranda et *al.*, 2001]. From the point of view of a microwave engineering, the main attraction for the use of ferroelectric materials is tunability. Also, loss is a crucial characteristic of the material for MW applications as well as the temperature dependence of ε' in the work-range temperature interval [Alford et *al.*, 1997; Penn et *al.*, 1997].

Electric-field-tunable ST thin films are attractive for a variety of advanced wireless applications [Jia et *al.*, 2000]. And examples of applications of ST-based materials in the field of microwave engineering include tunable capacitors, and based on them tunable resonators, tunable filters, phase shifters, *etc.* [Lancaster et *al.*, 1998]. Some examples of tunable devices based on $SrTiO_3$ films will be presented here.

- *Tunable capacitors*

The simplest tunable passive component based on thin ferroelectric films is voltage-variable capacitors which can be made as a planar structure, the so-called "planar capacitor" (Fig.2.69a), or as a tri-layer "sandwich" structure (Fig.2.69b) [Vendik et *al.*, 1999; Vendik et *al.*, 1993].

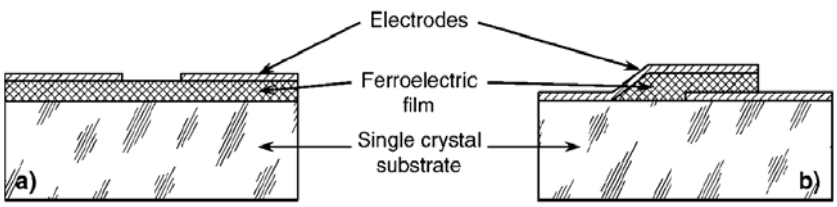

FIGURE 2.69. Planar (a) and trilayer (b) planar capacitors based on ferroelectric film [Vendik et *al.*, 1999; Vendik et *al.*, 1993].

Planar capacitor with $YBa_2Cu_3O_7$ (YBCO) electrodes, based on 100-nm-thick ST film, deposited by PLD on MgO substrate (Fig.2.70), and measured at 77K in a frequency range 25-50GHz reveals such typical parameters as: capacitance of 30-40fF, tunability C(0V)/C(40V) of 1.2, and leakage current less than 0.25nA, when a *dc* bias of 40V was applied [Petrov et *al.*, 2000]. These results show applicability of the fabricated ST-based tunable capacitor at *Ka* band (26.5 to 40GHz) and higher frequencies [Petrov et *al.*, 2000].

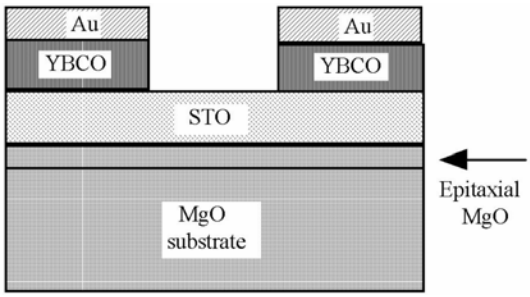

FIGURE 2.70. Cross section of the ST-based tunable capacitor [Petrov et *al.*, 2000].

Other tunable devices, such as tunable resonators, tunable filters, *etc,* based on tunable capacitors similar to those described above, were fabricated as to be present below.

- *Tunable resonators and filters*

A resonator is a component that exhibit resonance for a narrow range of frequencies. Tunable resonators are applicable for realization of tunable filters. Such resonators together with other tunable components can form, for example, tunable bandpass filter presented in Figure 2.71 [Moeckly et *al.*, 2003]. The six thin-film ST flip-chip capacitor dies are used as tuning elements; each capacitor tunes the centre frequency of the corresponding resonator without mechanical tuning. For such a filter, operating at 60K, a frequency slope of 83dB/MHz and a rejection of 60dB at 2MHz from the band edge was attained [Moeckly et *al.*, 2003].

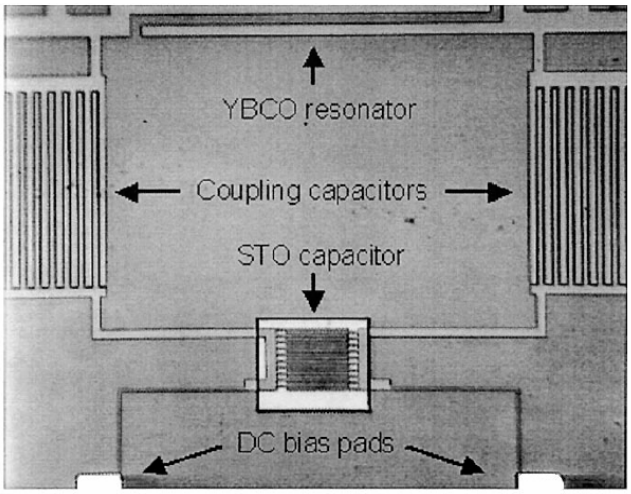

FIGURE. 1.71. Photograph of a portion of a monolithic tunable resonator, in which $SrTiO_3$ and $YBa_2Cu_3O_{7-x}$ are deposited on the same substrate [Moeckly et *al.*, 2003].

Schematic diagrams of the microstrip resonator with ST capacitors evaluated by Kozyrev and co-authors are shown in Figure 2.72 [Kozyrev et *al*., 1998]. The nonlinear behaviour of ST thin film tunable capacitor is used to tune the resonant frequency [Kozyrev et *al*., 1998]. Both conductance and capacitance were found to display nonlinear behaviour at 1.7-1.9GHz [Kozyrev et *al.*, 1998]. Microwave losses in ST films were reported to be over 10 times higher than the losses in single crystal bulk materials, decreases with increasing *dc* bias voltage. Moreover, no frequency dispersion in ε' was observed at 1MHz, 3GHz, and 10GHz at temperatures ranging from 78 to 300K [Kozyrev et *al.*, 1998]. So the obtained dielectric response of analyzed ST capacitors was proposed to provide a framework for evaluation of the nonlinear behaviour of ST films, and confirmed that ST films can be used in tuning applications with moderately high microwave levels [Kozyrev et *al.*, 1998].

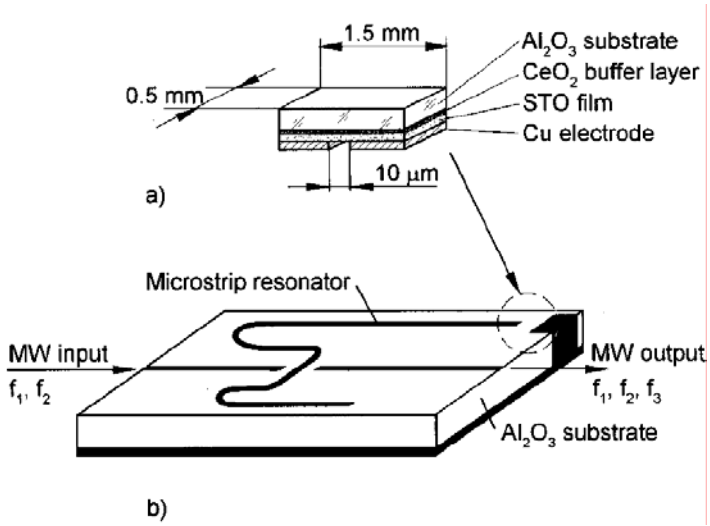

FIGURE 2.72. Ferroelectric planar capacitor (a) and the microstrip resonator (b) based on $SrTiO_3$ films for intermodulation distortion measurements [Kozyrev et *al*., 1998].

Another example of practical application of ST films for an electrically tunable MW device is an adaptive half-wave bandpass 3-pole coplanar waveguide (CPW) filter [Findikoglu et *al.*, 1996]. Such electrically tunable and adaptive filter incorporating 1.2-μm-thick ST bottom layer and 0.4-μm-thick superconducting $YBa_2Cu_3O_{7-x}$ top electrode layer was prepared on a $LaAlO_3$ substrate (Fig.2.73) [Findikoglu et *al.*, 1996].

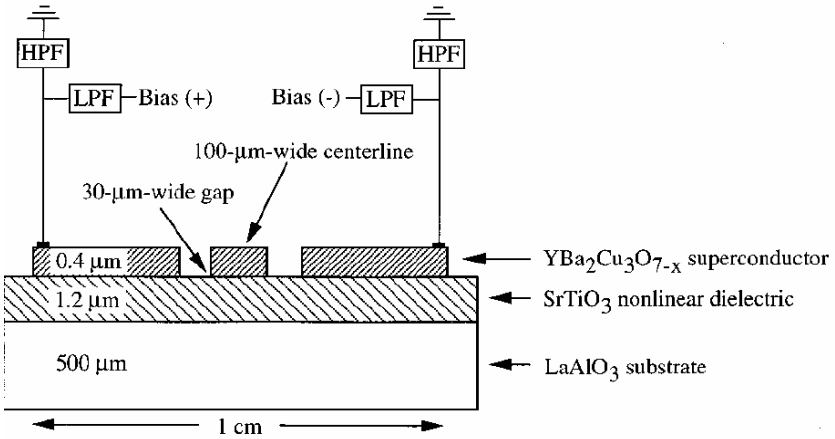

Figure 2.73. Cross-sectional schematic of tunable and adaptive bandpass coplanar waveguide (CPW) filter. LPF and HPF stand for Low-Pass Filter and High-Pass Filter, respectively [Findikoglu et *al.*, 1996].

The poles of the filter are half-wave resonators, which are capacitively coupled to each other and to the microwave feeds (Fig.2.74), giving a possibility for electrical tuning of ε' of ST film at different locations of the device [Findikoglu et *al.*, 1996].

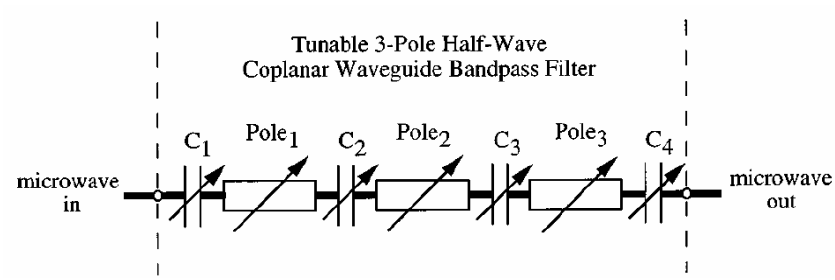

Figure 2.74. Simplified equivalent circuit diagram of tunable and adaptive bandpass CPW filter [Findikoglu et *al.*, 1996].

The device package including the 3-pole half-wave CPW bandpass filter shows about 3dB insertion loss and 27dB return loss at the centre frequency of the bandpass at liquid helium temperature and under 125V bias [Findikoglu et *al.*, 1996]. Moreover, applying a separate bias voltage on each pole and also on each coupling capacitance of the device at 4K and 76K, the filter response is not only fine tuned to achieve symmetric and optimized filter characteristics with less than 2% bandwidth, centred around 2.5GHz, but also broadband tuned to shift the bandpass by more than 15% [Findikoglu et *al.*, 1996].

One more example of a high pass filter using ST films as coupling capacitors connected to integrated circuit was described in paper of Defaÿ and co-authors [Defaÿ et

al., 2007]. Surface capacitance density of these ST capacitors achieved 10nF/mm^2 with capacitance value of 1.2nF. Such a functional high pass filter exhibited a cut-off frequency at 6.5kHz and a constant gain at higher frequencies of -1.3dB [Defaÿ et *al.*, 2007]. Wide usage of ferroelectric thin films in microwave tunable filters have also been demonstrated in others works [Keis et *al.*, 1998; Moeckly and Zhang, 2001].

- *Microwave ferroelectric phase shifters*

Microwave ferroelectric phase shifters are the most extensively fabricated and studied tunable ferroelectric components. Their importance arises from the role they could play in phased array antennas. A phased array antenna consists of thousands of radiating elements which should be served by thousands of phase shifters (Fig.2.75 as example).

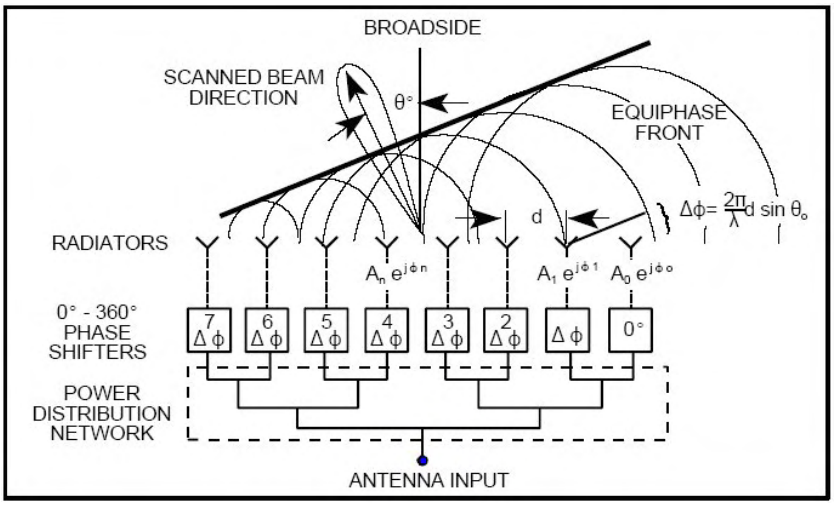

FIGURE 2.75. Corporate fed phased array [Microwave encyclopedia].

The phase shifters are used to modify and control the width and angle of the steered radar beam. Each phase shifter is inside in microwave semiconductor module. Instead the use of ferroelectric films enables the integration of the phase shifters with the microwave circuits on one substrate thus substantially reducing the size, mass, and cost of the antennas. $(Ba,Sr)TiO_3$ films can be used in phase shifters as demonstrated below.

It is possible to tune the phase velocity of the electromagnetic wave passed through the coplanar line by loading this line with tunable ferroelectric capacitors [Acikel et *al.*, 2002]. The phase shifters using parallel plate and interdigital $(Ba,Sr)TiO_3$ thin film capacitors on sapphire and glass substrates achieved 45°/dB at 30GHz [Acikel et *al.*, 2001].

A simple coplanar line structure patterned on a ferroelectric thin film coated substrate

can be used as a phase shifter (Fig.2.76a), in which the phase velocity of the electromagnetic wave that passes through the line is proportional to $\sqrt{\varepsilon'}$ of the film and hence controlled by the applied *dc* electric field, U_{dc} [Kozyrev et *al.*, 2000].

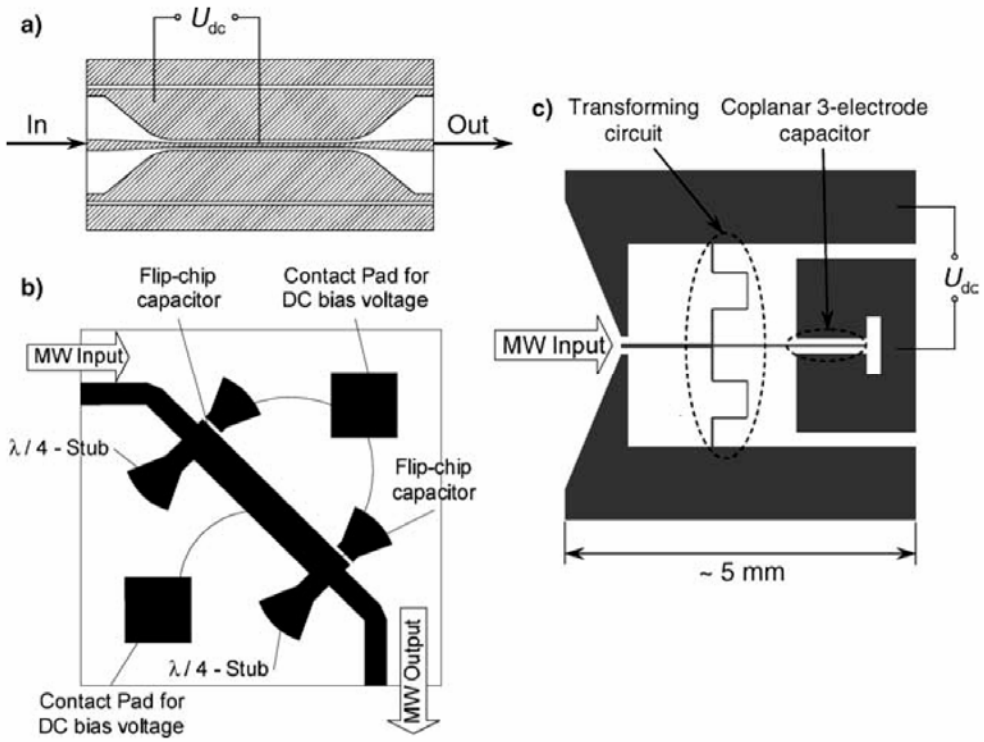

FIGURE 2.76. Ferroelectric microwave phase shifters: coplanar line analog phase shifter (a) [Kozyrev et *al*., 2000], periodically loaded line phase shifter (b) [Kozyrev et *al.*, 1999], reflection type digital phase shifter (c) [Sherman et *al*., 2001].

Another possibility is the so-called digital phase shifter which is used only at two values of the tuning voltage providing a fixed phase shift (e.g. 45° or 90°). Examples of this kind of phase shifters are presented in Figure 2.76b and c. Figure 2.76b shows a layout of a periodically loaded line digital phase shifter with two planar capacitors connected in parallel to the line as flip chip elements [Kozyrev et *al.*, 1999]. Another solution is presented in Figure 2.76c [Sherman et *al.*, 2001] showing a phase shifter that consists of a transforming circuit, terminated by a coplanar 3-electrode capacitor. Such reflection-type one-bit phase shifter using BST films results in 60°/dB at 5.4GHz with 350V [Sherman et *al.*, 2001]. The advantage of the digital phase shifters compared to those based on the simple coplanar line is that the former can be better optimized [Tagantsev et *al.*, 2003].

Summary

$SrTiO_3$ is a well know material that has been studied and used for many years. The first report on the dielectric characterization of ST dates from 1950's. However, its practical importance in terms of applications of ST films, in particular in the thin film form, to respond to the most recent requirements for miniaturization from the microelectronics industry, fully justify the renewed interests in this material, ranging from beginning of 1990's until now [Defaÿ et *al.*, 2007].

It is also evident from the above literature review that the majority of the works on ST films have been conducted on the fabrication and characterization of epitaxially grown films, trying to mimic the properties of single crystals, but seldom on the fabrication of films by chemical solution deposition methods. At the same time, the properties of the films, particularly prepared by chemical solution deposition, are inferior to those of their bulk counterparts (ceramics or single crystals). Within this scope the approaches to improve the quality and the dielectric properties of the polycrystalline undoped and doped ST films are proposed and analyzed in this Thesis.

Concomitantly, no systematic studies on doped ST films have been reported. In particular, the crystallographic structure, microstructure and dielectric behaviour of Mg doped $SrTiO_3$ films have not been deeply studied until now and there are no reports on the low-temperature dielectric study of Bi doped $SrTiO_3$ films. The lack of the reports and the absence of theoretical works on the dielectric properties of such systems are evident. Polycrystalline Mg and Bi doped ST films, prepared by sol-gel, are the subjects of a detail study, conducted in this work.

Chapter 3. Experimental procedure: preparation and characterization of thin films

In this chapter a detailed description of the experiments conducted in the present work, that include the solution preparation, film deposition, characterization of structure, microstructure and dielectric properties of undoped and doped $SrTiO_3$ films, are presented. A brief description of the instrumentation used for the characterization of the fabricated films is presented as well.

3.1. Sol-gel fabrication of thin films

As it was mentioned in the "Chapter 2", sol-gel has been widely used in the preparation of thin films due to its easiness of using and control of the material composition. In general, film fabrication involves the deposition of the precursor solutions onto a clean substrate. The resulting as-deposited film is generally amorphous. The most common method for the transformation of the amorphous films into crystalline ones begins with a pyrolysis step of the as-deposited film for short periods of time to promote the removal of the organic species. The transformation from the amorphous pyrolyzed film to the crystalline one occurs by nucleation and growth processes in which the increasing of temperature during film annealing provided the energy to overcome the barrier heights of homogeneous and heterogeneous nucleation. All these process are described below.

3.1.1. Preparation of solutions

General information about the preparation of solutions for the deposition of electroceramics films were given before in the "Chapter 2". In the current experiments several different solutions were prepared using the hybrid-chelate sol gel chemical route for the fabrication of the films listed in Table 3.1.

TABLE 3.1. List of the compositions of the fabricated films for which corresponding precursor solutions were prepared.

Composition	Concentration of doping element
$SrTiO_3$	
$Sr_{1-x}Mg_xTiO_3$ (SMT)	x = 0.01, 0.02, 0.05, 0.10, 0.20, 0.30, 0.40
$SrTi_{1-y}Mg_yO_{3-\delta}$ (STM)	y = 0.01, 0.05, 0.10, 0.20, 0.30, 0.40, 0.50
$Sr_{1-1.5x}Bi_xTiO_3$ (SBiT)	x = 0.002, 0.0053, 0.0067, 0.0133, 0.0267, 0.04, 0.1, 0.167, 0.267, 0.35, 0.4

For the preparation of the sols with a concentration of about 0.2M the following reagents were used: strontium acetate $C_4H_6O_4Sr$ (98%, ABCR Germany), tetra-n-butyl orthotitanate $C_{16}H_{36}O_4Ti$ (98%, MERCK Germany), magnesium acetate tetrahydrate $C_4H_6MgO_4 \times 4\ H_2O$ (99.5%, MERCK Germany) or bismuth acetate $C_6H_9BiO_6$ (99%, ABCR GmbH, Germany) depending on film's composition (Table 2.1), acetic acid $C_2H_4O_2$ (99.8%, MERCK Germany), 1,2-propanediol $C_3H_8O_2$ (99.5%, Riedel-de Haën Germany) and absolute ethanol C_2H_6O (99.8%, MERCK Germany).

For the case of *undoped ST films* strontium acetate was initially dissolved into heated acetic acid (T~60°C) in closed flask under constant stirring to form a transparent solution. After cooling to room temperature the former solution was diluted in 1,2-propanediol and kept under constant stirring to form a transparent solution (about 1h). After that tetra-n-butyl orthotitanate was dropped. The obtained solution was maintained under constant stirring for about 12h. As a final step, ethanol was added to this transparent solution. The resultant solution was maintained under constant stirring for about 1 to 2h and after that it was ready for deposition.

For the case of the preparation of the precursor solutions of *Mg* or *Bi doped ST films* one more step was added to the previously described: after the complete dissolution of strontium acetate into heated acetic acid, magnesium or bismuth acetate was added.

3.1.2. Deposition of films

In the "Chapter 2" the spin-coating process was generally described. The films under study in current Thesis were prepared by spin coating and some more details are described below.

Using the previously prepared precursor solutions, layers were deposited on the substrates by spin-coating at 4000rpm for 30sec. Before utilization, the substrates were cleaned in boiling ethanol and dried after that on hot plate. Subsequently the films (substrate with wet layer) were heated on a hot plate at 350ºC for ~1min. This step was repeated after each spinning to ensure complete removal of volatile species between each layer. After the deposition of the required number of layers (in this work it is equal to 10 layers for the films used for the dielectric measurements and 15 layers for the films used for Raman and Infrared analyses), films were annealed at defined temperatures for 60min in air. Depending on the film composition and use, small modifications were introduced in this procedure and are described in the next paragraphs.

1) For fabrication process study in particular, a set of samples was prepared according to the *"one-step"* procedure in which no intermediate heat treatment was done between the deposited layers and the samples were submitted only to one final annealing step at different temperatures: 750°C (these samples are hereafter designated as ST 750°C) and 900°C (these samples are hereafter designated ST 900°C) during 60min. in air. The other set of samples was prepared according to the "*two-steps*" procedure, i.e. after the deposition of the two first layers, a first heat treatment at 600°C during 30min. was conducted and, after cooling the films to room temperature 8 layers more were deposited and a final annealing step took place at 750°C (these samples are hereafter designated ST 2l 750°C) and at 900°C (these samples are hereafter designated ST 2l 900°C) for 60min. in air. List of the samples analysed in the current work presented in the Table 3.2. All samples were deposited on $Si/SiO_2/TiO_2/Pt$ substrates.

2) For the study of strain/stress effect, ST films were deposited on 5 different platinized substrates with dissimilar lattice constants and thermal expansion coefficients (TEC), namely: Al_2O_3/Pt, $Si/SiO_2/TiO_2/Pt$ (Si/…/Pt), $(LaAlO_3)_{0.3}$-$(Sr_2AlTaO_6)_{0.7}/Pt$ (LSAT/Pt), $SrTiO_3/Pt$ (ST/Pt) and MgO/Pt (Table 3.3) and annealed at $T_{ann.}$=900°C for 60min. in air for obtaining high stress values in the films to assess the stress influence on the

structure, microstructure and dielectric properties of ST films. The lattice parameters and thermal expansion coefficients (TEC) of the used substrates are presented in the Table 3.3.

TABLE 3.2. List of the samples analysed in the "Chapter 4. Polycrystalline $SrTiO_3$ thin films: influence of processing on the microstructure, structure and low temperature dielectric properties".

Samples	*Buffer layers*	*$T_{ann.}$ after buffer layers deposition*	*Main film*	*Final $T_{ann.}$*	*Denoted as*
ST films	-	-	10 layers	750°C	ST 750°C
ST films	-	-	10 layers	900°C	ST 900°C
ST films	2 layers	600°C	8 layers	750°C	ST 2l 750°C
ST films	2 layers	600°C	8layers	900°C	ST 2l 900°C

TABLE 3.3. The lattice parameters and thermal expansion coefficients (TEC) of the used substrates in the "Chapter 5. Polycrystalline $SrTiO_3$ thin films: influence of substrate on the microstructure, structure and low temperature dielectric properties".

	Al_2O_3	Si	LSAT	$SrTiO_3$	MgO
Lattice parameter (Å) (data from the supplier company)	3.730	3.841	3.868	3.903	4.203
TEC $\times 10^{-6}$/°C (data from the supplier company)	5.4||a 6.2|c	2.3	10.0	9.0	8.0

Due to technical requirements, films to be analysed by Raman and Infrared spectroscopies were deposited on Al_2O_3 and MgO substrates without Pt bottom electrodes.

3) Mg doped ST films were deposited from the corresponding solutions on $Si/SiO_2/TiO_2/Pt$ substrates by the above described method. To study the effect of the heat treatment on the solubility of Mg in the ST lattice, films were annealed at 750ºC, 800ºC, 850ºC and 900°C for 60min. in air. All samples were deposited on $Si/SiO_2/TiO_2/Pt$ substrates. Raman and IR measurements were performed on Mg doped ST films deposited on single crystal Al_2O_3 substrates without Pt and annealed at 750°C and 900°C for 60min

in air.

4) For the case of Bi doped ST films the corresponding solutions were used for deposition of films on $Si/SiO_2/TiO_2/Pt$ substrates and the obtained samples were annealed at 750°C for 60min. in air. All samples were deposited on $Si/SiO_2/TiO_2/Pt$ substrates. Raman and IR measurements were performed on Bi doped ST films deposited on single crystal Al_2O_3 substrates without Pt.

$Si/SiO_2/TiO_2/Pt$ substrates were bought from Inostek INC, Korea. Al_2O_3, $(LaAlO_3)_{0.3}$-$(Sr_2AlTaO_6)_{0.7}$, $SrTiO_3$ and MgO substrates were bought from Crystal GmbH, Germany with following platinization in Inostek INC, Korea.

3.2. Crystallographic and microstructure characterization

3.2.1. X-Ray diffraction analysis

Generally, the structural characterization of the materials begins with X-Ray diffraction because it is a versatile and non-destructive technique that reveals detailed information about the crystallographic structure of the manufactured materials. At present, a variety of X-Ray application techniques for various material classes is available [Jenkins and Snyder, 1996].

3.2.1.1. Standard X-Ray diffraction measurements

The development of a simple way to understand and predict the diffraction phenomena from a crystal was presented by Henry and Lawrence Bragg in 1913 [Jenkins and Snyder, 1996]. They introduced the idea that a crystal lattice is a regular three dimensional distribution of atoms. These are arranged so that they form a series of parallel planes separated from one another by a distance *d*, which varies according to the nature of the material. When a monochromatic X-Ray beam with a wavelength *lambda* (λ) is projected onto a crystalline material at an angle *theta* (θ), diffraction occurs only when the distance travelled by the rays reflected from successive planes differs by a complete number *n* of wavelengths, as described by the well known Bragg´s law [Bragg, 1913]:

$$\kappa\lambda = 2d_{hkl}\sin\theta \tag{3.1}$$

where d stands for the space between the planes and (hkl) for the Miller indices. By varying the angle *theta (θ)*, the Bragg's law conditions are satisfied by different d-spacings in polycrystalline materials, κ is the complete number of wavelengths. From this experiment out-of-plane lattice parameter c (equal to d_{hkl} in Eq.3.1 for corresponding hkl peak) can be calculated.

In this work, these measurements were performed by X-Ray diffraction (XRD) with a Rigaku (D/Max-C series) X-Ray diffractometer, using Cu-Kα radiation (λ=0.15064nm), equipped with MDI data scan 3.2 controller software. The XRD was typically operated at 40kV and 30mA. The configuration of XRD experiment is θ-2θ scan technique adopted to collect diffraction intensity data with Cu-Kα radiation at rate 1°/min. with step 0.02 between 4-80°.

3.2.1.2. Grazing incidence measurements

X-Rays penetrate to a certain depth into the sample, where they are diffracted. However, when the sample layer is too thin, the X-Rays could be completely transmitted by the sample or part of them could be diffracted by the substrate provoking no diffraction signal or an overlap between the substrate and the sample diffraction peaks. In these circumstances, in-plane diffraction is used. In-plane diffraction refers to a diffraction technique in which both the incident and diffracted beams are nearly parallel to the sample surface (Fig.3.1) [Guinier and Fournet, 1955].

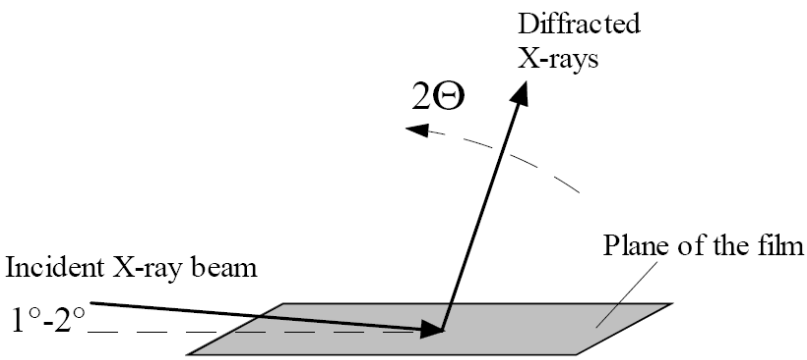

FIGURE 3.1. Scheme of grazing incidence XRD experiment.

With standard diffraction geometries (such as the Bragg-Brentano geometry), lattice planes that are parallel to the sample surface are then measured. In-plane diffraction has two major features:

- since the beam is incident at a grazing angle (small angle), the penetration depth of the beam is limited to within 100nm of the surface.

- the in-plane diffraction technique measures diffracted beams, which are scattered nearly parallel to the sample surface and hence measures lattice planes that are (nearly) perpendicular to the sample surface. These planes are inaccessible by other techniques.

In-plane diffraction is then an excellent technique to be used in the phase analysis and microstructural characterization of polycrystalline thin films.

In the current Thesis, the in-plane incidence measurements of the different thin films by grazing incidence XRD experiment to determine in-plane lattice parameters *a* were performed using a Philips X'Pert MPD X-Ray diffractometer, equipped with a mobile arm and X'Pert Data Collector controller software, with CuKα radiation. The X-Ray diffraction patterns were obtained between 20 and 80 degree in two theta with a step mode of $0.01^{o}/10s$ and using a grazing incidence angle of 3°.

3.2.1.3. Residual strain measurements and stress calculations

Residual stress can be defined as the stress which remains in a material in the absence of any external forces. There are many stress determination methods [Withers and Bhadeshia, 2001, and references there], such as hole drilling, curvature method, neutron diffraction, electron diffraction, compliance methods, magnetic and electrical techniques, ultrasonic methods, piezospectroscopic techniques, thermoelastic methods, photoelastic methods, *etc*, and X-Ray diffraction, among others. Short summary of the several popular methods for the characterisation of residual stress is presented in Table 3.4 (adopted from [Withers and Bhadeshia, 2001]).

Some of those methods are destructive and some are nondestructive. X-Ray diffraction together with the other diffraction techniques for residual stress measurement uses the distance between crystallographic planes as a strain gage. X-Ray residual stress measurement is considered as a nondestructive method. Indeed, X-Ray diffraction is a well established method for measuring elastic strain in polycrystalline materials at centimetre and millimetre length scales [Noyan and Cohen, 1987].

TABLE 3.4. Summary of various measurement techniques and their attributes: values of resolution, penetration and accuracy of technique (adopted from [Withers and Bhadeshia, 2001]).

Method	Penetration	Spatial resolution	Accuracy
Hole drilling (*distortion caused by stress relaxation*)	~1.2×hole diameter	50μm depth	±50MPa, limited by reduced sensitivity with increasing depth
Curvature (*distortion as stresses arise or relax*)	0.1–0.5 of thickness	0.05 of thickness; no lateral resolution	Limited by minimum measurable curvature
X-Ray diffraction (*atomic strain gauge*)	<50μm (Al); <5μm (Ti); <1mm (with layer removal)	1mm laterally; 20mm depth	±20MPa, limited by non-linearities in $\sin^2\Psi$ or surface condition
Hard X-Rays (*atomic strain gauge*)	150 – 50mm (Al)	20μm lateral to incident beam; 1mm parallel to beam	$\pm 10\times10^{-6}$ strain, limited by grain sampling statistics
Neutrons (*atomic strain gauge*)	200mm (Al); 25mm (Fe); 4 mm (Ti)	500μm	$\pm 50\times10^{-6}$ strain, limited by counting statistics and reliability of stress free references
Ultrasonics (*stress related changes in elastic wave velocity*)	>10cm	5mm	10%
Magnetic (*variations in magnetic domains with stress*)	10mm	1mm	10%
Raman	<1μm	<1μm approx.	$\Delta\lambda \approx 0.1\text{cm}^{-1}$=50MPa

X-Ray diffraction method requires that the sample under analyses be rotated with respect to the incident X-Ray beam in order to obtain diffraction from differently oriented sets of planes needed to determine the different components of the strain. The mechanical deformations of the crystalline sample cause changes in the spacing of the lattice planes from their stress free state to the new stressed state that corresponds to the magnitude of the residual stress. Because of Poisson's ratio effect, if a tensile stress is applied, the lattice spacing will increase for planes perpendicular to the stress direction, and decrease for planes parallel to the stress direction. This new spacing will be the same in any similarly oriented planes, with respect to the applied stress. Therefore the method can only be applied to crystalline, polycrystalline and semi-crystalline materials.

It is important to note that stress value is not directly measured by the X-ray diffraction; it is always the value of strain that is measured. Then the stress is calculated using appropriate equations of elasticity that relates strain with stress. For thin layers, a biaxial state of stress is assumed and, the lattice strain, $\varepsilon_{\phi,\psi}^{hkl}$, in a direction defined by Euler angles ϕ and ψ (Fig.3.2a) can be expressed as follow [Noyan and Cohen, 1987]:

$$\varepsilon_{\phi,\psi}^{hkl} = \frac{d_{\phi,\psi}^{hkl} - d_0^{hkl}}{d_0^{hkl}} = S_1^{hkl}(\sigma_{11} + \sigma_{22}) + \frac{1}{2} S_2^{hkl} \sigma_\phi \sin^2 \psi \tag{3.2}$$

with stress $\sigma_\phi = \sigma_{11}\cos^2\phi + \sigma_{12}\sin 2\phi + \sigma_{22}\sin^2\phi$, where ψ stands for the tilt angle between the normal of the planes (*hkl*) and the normal of the sample surface, ϕ for the rotational angle, d_0^{hkl} for the strain free lattice spacing, and S_1^{hkl} and S_2^{hkl} for the X-Ray elastic constants (XECs) for (*hkl*) planes. S_1 and S_2 are assessed by the ST elastic constants and they are different for each (*hkl*) diffraction plane.

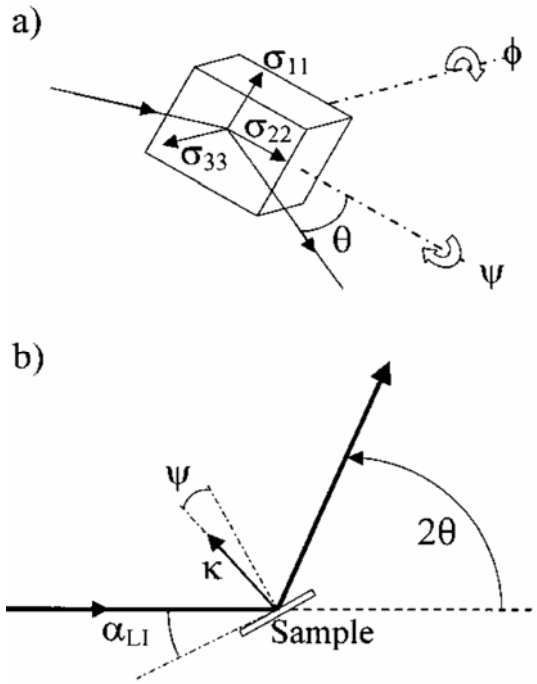

FIGURE 3.2. Schematic representation of the diffraction system configuration used in (a) texture and stress determination and (b) low incident beam angle (LIBAD) experiments. ψ is the angle between the surface normal and the diffraction vector *k*, ϕ is the rotation angle, σ_{11} and σ_{22} are the in-plane stress, σ_{33} is the perpendicular stress, α_{LI} is the angle between the incident beam and the film surface, and 2θ is the Bragg angle [Noyan and Cohen, 1987].

When no shear stress appears in plane stress, then σ_{11} and σ_{22} (the in-plane stress) is equal to σ_{33} (the perpendicular stress): $\sigma_{||}= \sigma_{11}= \sigma_{12}= \sigma_{22}$ and stress can be calculated as [Noyan and Cohen, 1987]:

$$\varepsilon_{\psi}^{hkl} = \frac{d_{\psi}^{hkl} - d_{0}^{hkl}}{d_{0}^{hkl}} = 2S_{1}^{hkl}\sigma_{||} + \frac{1}{2}S_{2}^{hkl}\sigma_{||}\sin^{2}\psi \tag{3.3}$$

The strain free lattice spacing, d_{0}^{hkl}, corresponds to $d_{\phi,\psi}^{hkl}$, if $\psi = \psi_{0}$, where ψ_{0} stands for the unique direction for which the strain experienced in the lattice-spacing determination equals zero. It called strain-free measurement direction [Hauk and Macherauch, 1987].

In this Thesis, the diffraction angles 2θ are measured experimentally and then the lattice spacing $d_{\phi,\psi}^{hkl}$ is calculated from the diffraction angle, and the known X-ray wavelength using Bragg's Law. Once the *d*-spacing values are known, they can be plotted versus $sin^2\psi$. The plot of *d vs* $sin^2\psi$ is a straight line which slope is proportional to the stress.

In the case that the surface layer is composed of elastically isotropic material, the X-Ray elastic constants can be replaced by:

$$S_{1} = -\gamma / E \tag{3.4}$$

$$\frac{1}{2}S_{2} = \frac{(1+\gamma)}{E} \tag{3.5}$$

where γ stands for the Poisson ratio and E for the Young´s modulus. XEC S_1 and S_2 can be obtained from the literature or experimentally. For the present case the values of γ and E of bulk ST are already known and published (for example [Bernard et *al*., 2004]).

In this Thesis, Young´s modulus E was calculated as:

$$E = \frac{1}{s_{11}} \tag{3.6}$$

And value Poisson ratio γ was obtained from:

$$\gamma = -\frac{s_{12}}{s_{11}} \tag{3.7}$$

where $s_{11}=S_1$ and $s_{12}=S_2$ stand for the elastic constants or compliance constants.

From the work of Poindexter and Giardini [Poindexter and Giardini, 1958] the following values of elastic constants were found $s_{1111} = s_{11} = 3.3*10^{-13}cm^2/dyn$ and $s_{1122} = s_{12} = -0.74*10^{-13}cm^2/dyn$.

The elastic constants s_{11} and s_{12} can also be calculated from the following formulas:

$$c_{11} = \frac{s_{11} + s_{12}}{(s_{11} - s_{12})(s_{11} + 2s_{12})} \tag{3.8}$$

$$c_{12} = \frac{-s_{12}}{(s_{11} - s_{12})(s_{11} + 2s_{12})} \tag{3.9}$$

where c_{11} and c_{12} are the stiffness constants. The value of these stiffness constants have been also published by different research groups and their values vary slightly: *i)* $c_{11}=3.4817*10^{11}N/m^2$ (or $10^{12}dyn/cm^2$) and $c_{12}=1.0064*10^{11}N/m^2$ (or $10^{12}dyn/cm^2$) [Lide, 2000]; or *ii)* $c_{11}=3.18*10^{11}N/m^2$ (or $10^{12}dyn/cm^2$) and $c_{12}=1.02*10^{11}N/m^2$ (or $10^{12}dyn/cm^2$) [Kityk et *al.*, 2000]; or *iii)* $c_{11}=3.176*10^{11}N/m^2$ (or $10^{12}dyn/cm^2$) and $c_{12}=1.025*10^{11}N/m^2$ (or $10^{12}dyn/cm^2$) [Bell and Rupprecht, 1963].

In the current experiments next values E and γ were calculated: E=303GPa and γ=+0.2242. These values are closed to the published already data of E=238GPa [Paufler et *al.*, 2006] and γ=+0.232 [Tse et *al.*, 2006].

Using previous Equations, Eq.3.4 and Eq.3.5, relative change in *d*-value due to stressed situation is calculated by the following formula [Noyan and Cohen, 1987]:

$$\varepsilon_{\psi}^{hkl} = \frac{d_{\psi}^{hkl} - d_0^{hkl}}{d_0^{hkl}} = \frac{1+\gamma}{E} \times \sigma \times \sin^2 \Psi \tag{3.10}$$

Thus, the stress value can be calculated like:

$$\sigma = \frac{d_{\psi}^{hkl} - d_0^{hkl}}{d_0^{hkl}} \times \frac{E}{1+\gamma} \times \frac{1}{\sin^2 \psi} \tag{3.11}$$

In this Thesis, stress measurements of the samples, that exhibit a linear behaviour of strain *vs* $\sin^2 \psi$ plots as in the case of a homogenous isotropic sample in a biaxial stress state, is presented. This method is known as $sin^2\ \psi$, because it utilizes multiple ψ values [Noyan and Cohen, 1987].

Due to the overlapping of diffraction peaks from ST films and peaks from substrates

observed in preliminary Bragg–Brentano geometry analysis, the stresses were analyzed in the (211) plane because it gives the most isolated ST peak. The tests consisted of sequentially θ/2θ measurements with a 0.02° step width and 5s of counting time per step in 43°-45°, for ψ values ranging from -62° to 62°. The Philips X'Pert MRD was used in the same configuration as in the texture experiments, except that the receiving slit was 0.2mm. For each θ/2θ scan subsequent analysis of the diffraction peaks was made to determine precisely the correspondent Bragg angle and therefore the d_{ψ}^{211} value for a certain sample tilt. The peaks were fitted by pseudo-Voigt functions using the PROFIT program taking into account subtraction of the necessary background and $K\alpha_2$ contribution. d_{ψ}^{211} values correspond to the maximum of the pseudo-Voigt functions and were used to calculate ε_{ψ}^{211} and the relative interplanar distance variation to the d_0^{211} value.

3.2.2. Microstructure analysis

Electron microscopes consist of an electron source, an accelerating high voltage structure, electromagnetic lenses, a specimen and detectors enclosed in a column that is evacuated in order to stop the electrons being scattered by gas molecules. Originally designed for imaging only, they can now carry out chemical analysis by the use of X-Rays (energy dispersive spectrometer (EDS)) or electrons (electron energy loss spectroscopy (EELS)), which are by products of the electron-specimen interaction.

There are three general types of electron microscopes: scanning electron microscope (SEM), transmission electron microscope (TEM), and scanning transmission electron microscope (STEM), of which the first two microscopes were used in this thesis.

3.2.2.1. Scanning electron microscopy

In general, scanning electron microscope (SEM) is routinely used to generate high-resolution images of shapes of objects and to show spatial variations in chemical compositions. This instrument is also widely used to identify phases based on qualitative chemical analysis and/or crystalline structure. SEM is a type of electron microscope that images the sample surface by scanning it with a high-energy beam of electrons in a raster scan pattern (schematic view presented in Fig.3.3).

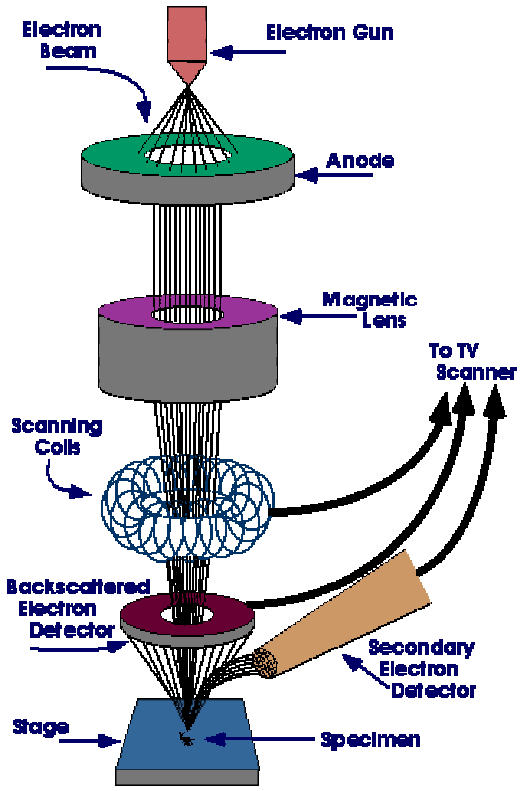

FIGURE 3.3. Schematic drawing of SEM [Iowa State University SEM Homepage].

The electrons interact with the atoms that make up the sample producing signals that contain information about the sample's surface topography, composition and other properties. In SEM, an electron beam source emits electrons, which are then collected and focused by lenses to form few nanometres sized probes. Deflection coils are used to operate electron beam and scan sample surface. Simultaneously, another electron beam runs over a TV monitor screen in a synchronized mode. The image magnification is the ratio of the scanned monitor range to the scanned sample range, and it is easily controllable by beam deviation elements. Primary electron beam interacts with the specimen surface in a complicated manner resulting in different emitted signals (secondary and back scattered electrons, X-Ray radiation, *etc.*), which could be registered with the appropriate detector [Goldstein, 1992; Goldstein et *al.*, 2003].

In the current Thesis SEM was used to characterize the surface and interface between substrate and film of the films (density, defects, *etc.*) and to determine the thickness of the films. For interface study, cross-sections of the films were prepared. For this, film's samples were cut and pasted in a special sample holder using a conductive carbon paste for SEM analysis. The samples were oriented with the surface up and lateral up in order to

analyze the surface (plan view) and the interface (cross section) of the films, respectively. Glued samples and dried for 24 hours at room temperature were covered with a thin layer of carbon in order to create a conductive surface layer, avoid charge effects and improve the image quality. The carbon layer was deposited by thermal evaporation using a SEM carbon coater (model K950).

SEM experiments were performed using a field emission scanning electron microscope (Hitachi S4100), working under the electron acceleration field of 25kV and filament emission current of 11μA. To increase the contrast between the grains and the boundary the samples were tilted 40 degree to the incident beam. This effect was compensated by the microscope tilt compensation controller.

3.2.2.2. Transmission electron microscopy

The Transmission Electron Microscope (TEM) was the first type of Electron Microscope to be developed and widely described in a number of references [Williams and Carter, 1996; Reimer, 1997; Buseck, 1992; Thomas, 1979].

The local microstructure and chemical analysis of undoped and of some doped-ST films were carried out in this work by means of transmission electron microscopy (TEM) / energy dispersive spectroscopy (EDS) (Fig.3.4).

In a TEM setup, a thin specimen is illuminated with electrons (the primary electrons). Whatever part is transmitted is projected onto a phosphor screen for the user to see. The darker areas of the image represent those areas of the sample, where fewer electrons were transmitted through (they are thicker or denser). The lighter areas of the image represent those areas of the sample that more electrons were transmitted through (they are thinner or less dense). An image in TEM can be formed by using the central spot of unscattered electrons, or by some or all of the scattered electrons.

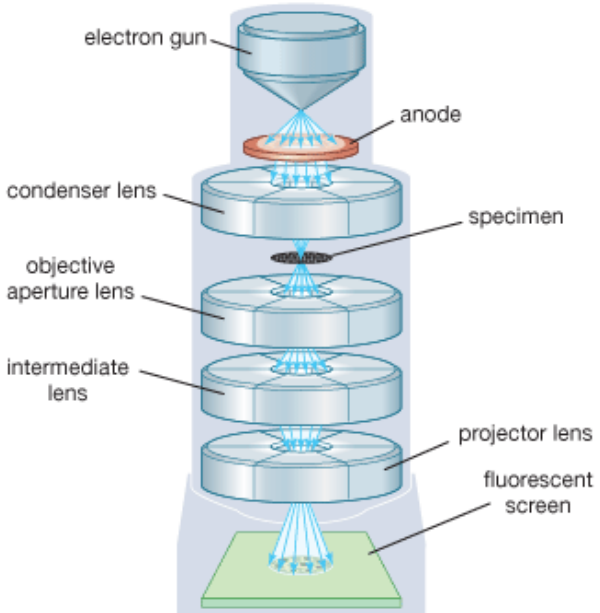

FIGURE 3.4. Schematic drawing of TEM [Encyclopaedia Britannica, Inc.].

The kind of the electrons (primary or scattered electrons) is chosen by an insertion of aperture into the back focal plane of the objective lens, thus blocking out most of the diffraction pattern except the one that is visible through the aperture. If the direct beam is selected, the resultant image is called a bright-field image, and if scattered electrons of any form are selected, one calls it a dark-field image. If no aperture is inserted, electron diffraction pattern is observed [Williams and Carter, 1996].

In this work, cross section and plan view samples were prepared for TEM observation. For TEM cross section measurements the samples were cut and two small parts were glued face to face as a "sandwich" using an epoxy resin (M-band 610glue). After that the stack was polished; one substrate side at a time and after that the sample was rotated and glued again to polish the other side. Polishing was done with a Disc Grinder (Model 623, Gatan, Inc.) using fine-grade silicon carbide paper in order to reduce their thickness to approximately 30μm.

In the case of plan view preparation, samples were carefully polished with grinding paper in order to reduce their thickness to approximately 30μm from the substrate side.

The samples were then glued to copper rings and ion beam milled using a BAL-TEC Ion Mill (RES 100). The angle between the ion beam and the sample plane of 20º, the voltage of 6kV and the current of 23mA were used until the appearance of the hole in the centre of the sample. Then the milling was conducted during 10min. with the angle

decreased to 8º in order to improve (decrease the thickness) the area near the hole, later used for TEM / EDS analysis.

The EDS system offers a rapid mean of evaluation (qualitative and semi – quantitative analysis) of the elemental composition of the sample. The EDS measurements were carried out using a Rontec UHV Dewar Detector coupled to TEM and equipped with Winshell acquisition software. For the surface analysis EDS was carried out less than 45 degree in order to avoid the bulk contribution of the films.

TEM microstructural analysis of the undoped and doped ST thin films was performed using a Hitachi (Model H-9000) transmission electron microscope with a thermoionic gun emission. The images were obtained in dark and bright field using an acceleration field of 300kV. Finally, the images were digitalized and some of them were later processed using Carine crystallography 3.1 software.

3.2.2.3. Atomic force microscopy

The atomic force microscope (AFM) (or scanning force microscope (SFM)) is a very high-resolution type of scanning probe microscope, with demonstrated resolution of fractions of a nanometer (schematic view in Fig.3.5).

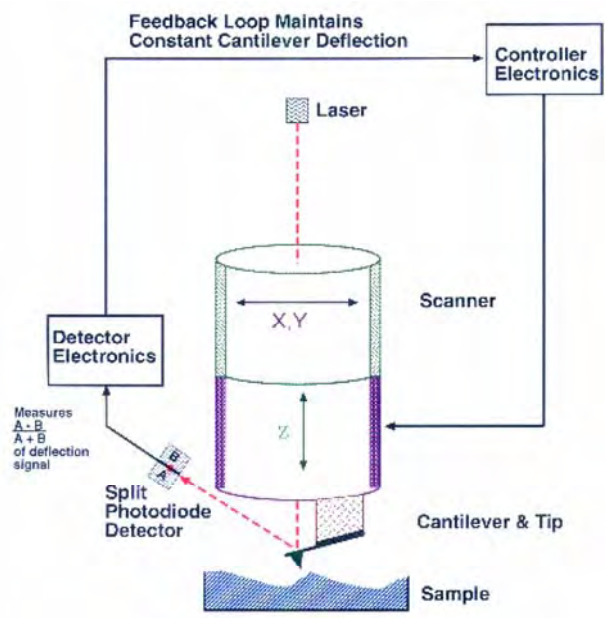

FIGURE 3.5. Schematic diagram showing the operating principles of the atomic force microscope in the contact mode [Blanchard, 1996].

The AFM consists of a microscale cantilever with a sharp tip (probe) at its end that is used to scan the specimen surface [West, 2007]. The cantilever is typically silicon or silicon nitride with a tip radius of curvature on the order of nanometers. When the tip is brought into proximity of a sample surface, forces between the tip and the sample lead to a deflection of the cantilever according to Hooke's law. Depending on the situation, forces that are measured in AFM include mechanical contact force, Van der Waals forces, capillary forces, chemical bonding, electrostatic forces, magnetic forces, Casimir forces, solvation forces, *etc*. [Blanchard, 1996]. As well as force, additional quantities may simultaneously be measured through the use of specialised types of probe. Typically, the deflection is measured using a laser spot reflected from the top surface of the cantilever into an array of photodiodes [West and Starostina, 2004].

For soft or fragile samples, AFM can perform non-contact scans by scanning a tip attached to the end of an oscillating cantilever across the sample surface. The tip does not contact the sample surface, but oscillates above the adsorbed fluid layer on the surface during scanning. The cantilever's resonant frequency is decreased by the van der Waals forces and the decrease in resonant frequency causes the amplitude of oscillation to decrease. The feedback loop maintains a constant oscillation amplitude or frequency by vertically moving the scanner at each (x,y) data point until a “setpoint” amplitude or frequency is reached. The distance the scanner moves vertically at each (x,y) data point is stored by the computer to form the topographic image of the sample surface [Digital Instruments, 2000].

In this work, the surface microstructure of undoped and doped ST films was analyzed by atomic force microscope (AFM) in contact mode.

In contact mode, AFM works by bringing a cantilever tip in contact with the surface to be imaged. An ionic repulsive force from the surface applied to the tip bends the cantilever upwards. The amount of bending, measured by a laser spot reflected on to a split photo detector, can be used to calculate the force. By keeping the force constant while scanning the tip across the surface, the vertical movement of the tip follows the surface profile and is recorded as the surface topography by the AFM [Digital Instruments, 2000].

In the current Thesis, a commercial AFM system (*Multimode* Digital Instrument, *Nanoscope IIIa)* equipped with a hard silicon conducting tip was used to examine the surface structure of the studied films. The AFM tip which used for analyzed sample is: tip

type: PPP-NCHR-20, from Nanosensorstm, made of n^+-silicon with resistivity of 0.01-0.02ohm/cm, force constant 42N/m and resonance frequency 331kHz. Finally, the topography images were processed using WSxMbeta6_0 software.

3.2.3. Raman spectroscopy

Raman spectroscopy is a spectroscopic technique used in condensed matter physics and chemistry to study vibrational, rotational, and other low-frequency modes in a system [Gardiner, 1989; Ferraro and Nakamoto, 1994]. Raman is used to obtain information about the structure and properties of molecules from their vibration transitions [Ferraro and Nakamoto, 1994]. It relies on inelastic scattering, or Raman scattering, of monochromatic light, usually from a laser in the visible, near infrared, or near ultraviolet range. The laser light interacts with phonons or other excitations in the system, resulting in the energy of the laser photons being shifted up or down. The shift in energy gives information about the phonon modes in the system [Lewis and Edwards, 2001; Ferraro and Nakamoto, 1994].

Raman scattering involves a two-phonon process, simultaneously annihilating the incident phonon ($\hbar\omega_{in}$) and creating the scattering phonon ($\hbar\omega_{sc}$). Scattering from time-dependent vibration of atoms is accompanied with conservation of energy:

$$\hbar\omega_{in}=\hbar\omega_{sc} \pm \hbar\Omega \tag{3.12}$$

where $\hbar$ stands for the reduced Plank's constant, $\hbar\Omega$ for the energy associated with the phonon created (Stokes) or annihilated (anti-Stokes) in the scattering process. The positive frequency difference $\Delta\omega=\omega_{in} -\omega_{sc}$ is most commonly measured in Raman experiments and is called the Raman shift. Only those vibrations, which modulate polarisability, appear in the Raman spectra. Usually a Raman spectrum consists of a set of frequencies or bands and each band corresponds to a specific elementary excitation of the lattice [Ibach and Lüth, 1993].

In a Raman spectroscopy experiment, the sample surface is irradiated with a monochromatic polarized light (usually from Ar- or HeNe-laser). The scattered light is then registered with an appropriate detector. Since the intensity of inelastically scattered light is several orders of magnitude weaker than that of elastically scattered (Rayleigh scattering), up-to-date Raman experiment involves a number of sophisticated techniques

for signal registration and processing. Apart from the investigations of lattice dynamic processes in solid matter, Raman spectroscopy is actively used in materials science to analyse the structural properties and quality of surfaces and thin films.

In this Thesis, Raman spectroscopy was used for the detailed structural characterisation of samples of selected compositions. Raman spectra were acquired in the back scattering geometry using a Renishaw Raman microscope after the samples being excited by an argon laser beam with the wavelength of 514.5nm and the spot size of 1-2μm in diameter. The measurements were performed at room temperature and at several fixed temperatures from 300K to 10K.

These measurements were carried out at the Department of Dielectrics, Institute of Physics, Academy of Sciences of the Czech Republic.

3.2.4. Rutherford backscattering spectrometry

For the deep studies of doped ST films, analysis of the distribution of doped elements through the thickness of the samples was done by Rutherford Backscattering Spectrometry (RBS).

RBS is an analytical technique used in materials science [Chu et *al.*, 1978; Chu and Liu, 1996]. RBS is utilised to determine the structure and composition of materials by measuring the backscattering of a beam of high energy ions impinging on a sample. The elements contained in a sample can be determined from the positions of peaks in the energy spectrum. Depth can be determined from the width and shifted position of these peaks, and relative concentration from the peak heights. This is especially useful for the analysis of a multilayer sample, for example, or for a sample with a composition which varies more continuously with depth.

RBS is based on collisions between atomic nuclei and well described in a number of references [Oura et *al.*, 2003; Feldman et *al.*, 1982; Feldman and Mayer, 1986]. It involves measuring the number and energy of ions in a beam which backscatter after colliding with atoms in the near-surface region of a sample at which the beam has been targeted. With this information, it is possible to determine atomic mass and elemental concentrations versus depth below the surface. RBS is ideally suited for determining the concentration of trace elements heavier than the major constituents of the substrate. When a sample is bombarded with a beam of high energy particles, the vast majority of particles are

implanted into the material and do not escape. The energy loss of a backscattered ion is dependent on the energy lost in scattering events with sample nuclei, and the energy lost to small-angle scattering from the sample electrons. The numbers of backscattering events that occur from a given element in a sample depend upon two factors: the concentration of the element and the effective size of its nucleus.

For the films analyzed in this Thesis, RBS using ion beams with energies in the MeV range were used for accurate determination of stoichiometry, elemental density, and impurity distribution. Measurements of the number and energy distribution of the ions backscattered from atoms in the near-surface region of solid materials allows the identification of the atomic masses and determination of the distribution of the elements as a function of depth below the surface. Simulation results are presented as layer distributions in the form of ORIGIN graphs.

RBS spectra were obtained with 2 Schottky barrier detectors placed in IBM geometry at 140º and 180º scattering angles, with resolutions of 15 and 25keV respectively. Samples deposited on $Si/SiO_2/TiO_2/Pt$ were also analysed using a 2.4MeV He^+ beam. Analyses were performed with samples tilted at 0º, 15º and 30º (angle between beam direction and sample normal). All spectra obtained for the same sample were simultaneously analysed with WINDF and a unique solution was found.

RBS spectra measurements were carried out at the Institute of Nuclear Technology, Sacavém, Portugal.

3.3. Dielectric measurements

Dielectric properties were assessed on metal/film/metal capacitors, where Pt was the bottom electrode and Au was used as the top electrode material. Top Au electrodes were sputtered onto the films using an SEM coating unit (E5000, Polaron Equipment Limit) with an argon partial pressure of 2mtorr, an acceleration voltage of 12kV and an emission current of 12mA. After the deposition the electrodes were annealed in a conventional furnace at 300°C during 1min., to release the stresses in the film caused by the deposition of the electrodes and improved the film-electrode quality.

3.3.1. Dielectric response measurements in *rf* range

The complex permittivity was measured as a function of temperature and frequency in the capacitive cell illustrated in Figure 3.6a.

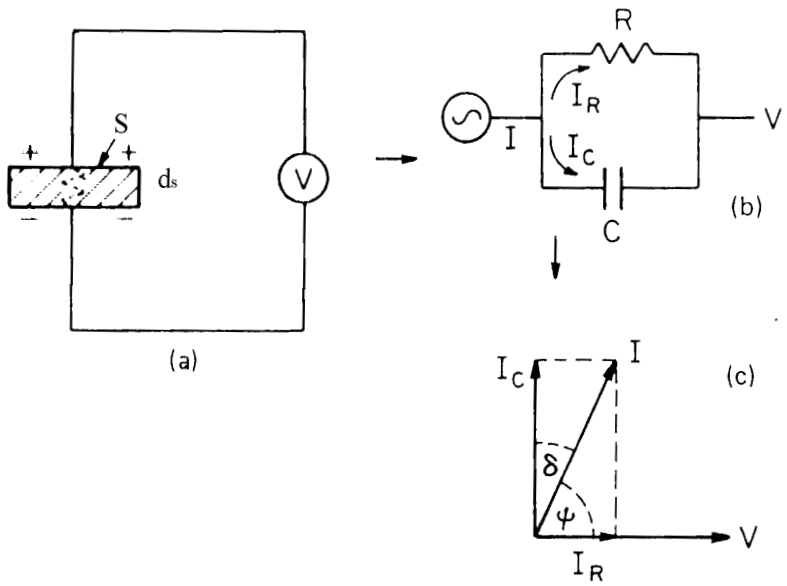

FIGURE 3.6. Equivalent circuit diagrams of capacitive cell (a) of charging and loss current (b) and of loss tangent for a typical dielectric (c) [Buchanan, 1991].

For the case of sinusoidal applied voltage V, the current discharge flow I of the capacitive cell may be written as:

$$I = i\omega\varepsilon^* V\varepsilon_0 S/d_s = i\omega(\varepsilon'-i\varepsilon'')V\varepsilon_0 S/d_s = I_C + I_R \qquad (3.13)$$

where i stands for the imaginary operator, $\omega=2\pi f$ for the angular frequency, ε_0 for the dielectric constant of the vacuum with the value 8.85×10^{-12}F/m, S for the area of the electrodes for a sample capacitor, d_s for the distance between electrodes or sample thickness, ε^* for the complex permittivity, ε' for the real part of the permittivity, and ε'' for the imaginary part of the permittivity, related to dielectric loss. Therefore, because the dielectric loss exists in dielectric materials, it can be represented by the circuit analogue of a resistance in parallel with a capacitor, and the current I has vector components I_C and I_R, as illustrated in Figure 3.6b,c.

The current I_C represents a capacitive current proportional to charge stored in the capacitor. It is frequency dependent. The current I_R is an *ac* conduction current in phase

with the voltage V, which represents the energy loss or power dissipated in the dielectric. From the ratio of the magnitude of I_R to magnitude of I_C, therefore, one can define a dissipation factor $\tan\delta = \varepsilon''/\varepsilon'$ [Buchanan, 1991].

In this work, dual impedance parameter Z-ψ were measured by Precision LCR Meter (HP 4284A) under an applied alternative electric field $E_0 = V/d_s$ of about 0.1V/cm at 21 frequencies in the frequency range of 100Hz - 1MHz with further recalculation to

$$\varepsilon' = d_s \sin\psi / \omega Z \varepsilon_0 S \qquad \text{and} \qquad \tan\delta = \tan(90° - \psi) \tag{3.14}$$

Measurements were performed in the temperature range of 10-300K during the cooling step at a rate of 0.75K/min. in a He closed cycle cryogenic system (Displex ADP-Cryostat HC-2) till the lowest attainable temperature (~10K), stabilized for 1hour and further heated at the same rate. The temperature of the sample was controlled by a Scientific Instrument Model 9650 Digital temperature controller with silicon diode thermometers.

3.3.2. Dielectric measurements at applied field in *rf* range

3.3.2.1. Permittivity under bias field

Electrical fields inside dielectrics polarize the material. For a ferroelectric materials the polarization is a nonlinear *S*-shaped function of field. And in the case of a large area parallel plate device, a capacitance C is a nonlinear function of the voltage V causing the field [De Araujo et *al*., 2001*;* Musikant, 1991]. Thus, the real part of dielectric permittivity ε' changes as a function of the applied *dc*-electrical field as well as capacitance C.

Thus, in this work capacitance C versus *dc* voltage measurements, referred to as C-V (also tunability), were used to study the ferroelectric properties of the undoped and doped ST films under the *dc* applied voltages. C-V (tunability) measurement was performed using a *Hewlett-Packard* precision LCR meter (HP 4284A) controlled by a design Labview program. For the dielectric tunability measurements at low temperatures in the range of 10-300K, samples were cooled/heated in a He closed cycle cryogenic system (Displex ADP-Cryostat HC-2) controlled by a digital temperature controller (Scientific Instrument Model 9650) with silicon diode thermometers till the required temperature and stabilised. For these measurements, top gold electrodes were sputtered on the films. The measurements

were done at selected temperatures and a frequency of 10kHz, as a function of *dc* electric field in range from 0 to ~5V.

3.3.2.2. Polarization versus electric field

Polarization reversal (switching) is a characteristic of the ferroelectricity. It is a thermodynamic process of nucleation, growth, and coalescence of domains. It can be observed by measuring the polarization *vs* electric field curve (*P*(*E)* hysteresis loop). A typical *P*(*E)* hysteresis loop of ferroelectrics is shown in Figure 3.7 [Xu, 1991].

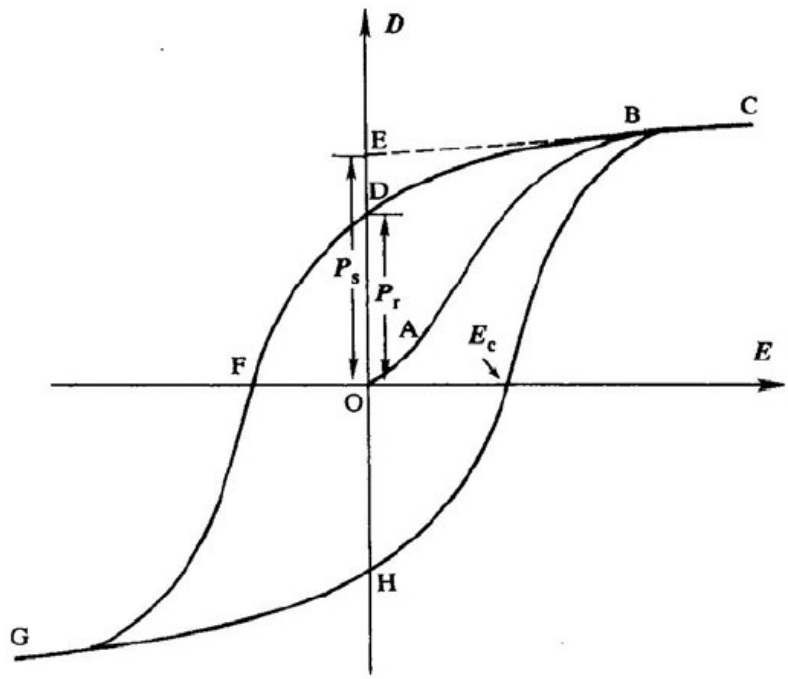

FIGURE 3.7. A typical *P*(*E)* hysteresis loop of ferroelectric materials [Xu, 1991].

As shown in Figure 3.7, initially the unpoled ferroelectric materials have zero polarization (origin point *O*). As the electric field increases, the spontaneous polarization directions of domains will be forced to switch towards the field direction, resulting in a rapid increase in polarization (segment *OAB*). A saturation state is reached (*BC*) when all the domains are aligned as close as possible to the field direction. The linear extrapolation of the segment *BC* back to the polarization axis (*CBE*) represents a linear dielectric and piezoelectric response. Appropriately oriented single crystals may provide such a stable polarization state. The polarization value at point *E* is the saturated polarization (P_s). Note

this is the volume averaging of the spontaneous polarization of all domains. As the field strength decreases, the polarization will actually decrease to point *D* (*BD*). This value is called the remnant polarization (P_r). This value is smaller than P_s but nonzero because for piezoceramics some of the domains will remain aligned and some will be reoriented due to grain and domain interaction. The remnant polarization (poling state) holds until the applied field in the opposite direction reaches a certain value (at the point *F* in the figure). The strength of the field required to reduce the polarization back to zero is called the coercive field (E_c). Further increase of the field will cause an alignment of the dipoles in this direction. Reversing the field direction once again leads to a cycle and the relation of *P* and *E* is represented by a hysteresis loop (*CDFGHC*) as shown in the Figure 3.7 [Xu, 1991].

In the current work, the hysteresis loop measurement was performed using the ferroelectric analyzer *TF Analyzer* 1000 AIXACT. The commonly accepted criterion of ferroelectricity is a *P(E)* hysteresis loop is usually run at low frequencies. The input parameters were selected in order to control the hysteresis measurement including frequency (100Hz), variable amplitude of the driving voltage, signal waveform and number of point recorded to plot the loop. The current applied to the films was auto-controlled by the acquisition software. For the measurements in the temperature range of 10-300K, samples were cooled under zero field in a He closed cycle cryogenic system (Displex ADP-Cryostat HC-2) controlled by a digital temperature controller (Scientific Instrument Model 9650) with silicon diode thermometers till the lowest temperature and stabilised. Then the samples were successively heated till the required temperature and stabilized at each temperature before measuring. The remnant polarisation was, thus, obtained as a function of temperature.

3.3.3. Infrared spectroscopy

Infrared (IR) spectroscopy is the subset of spectroscopy that deals with the infrared region of the electromagnetic spectrum. It covers a range of techniques, the most common being a form of absorption spectroscopy and it widely used in both research and industry as a simple and reliable technique for measurement, quality control and dynamic measurement for applications in organic, inorganic chemistry and in the field of semiconductor microelectronics [Lau, 1999].

IR involves the absorption of infrared light causing vibrational excitation of covalently bonded atoms and groups. The motion of positive ions relative to the negative ones gives rise to an instantaneous dipole moment, which couples with the electromagnetic field of IR radiation and, therefore, forms polar variation modes. In other words, infrared radiation is not only selectively absorbed, but also reflected. Both effects are complementary, allowing the reflection spectroscopy to give information on vibrational modes in IR region [Brame and Edward, 1977; Ibach and Lüth, 1993; Stuart, 2004].

In this Thesis IR spectroscopy was used to study the lattice dynamic of undoped and doped ST films. Analyzed films were deposited on the 2 sides of polished transparent Al_2O_3 single crystal substrates and IR reflectivity spectra were obtained using a Fourier transform spectrometer (Bruker IFS 113v) with pyroelectric deuterated triglycine sulfate detectors in the frequency range of 20-3300cm^{-1} with the resolution of 0.5cm^{-1}.

Transmittance spectra of the studied films were fitted to determine the TO mode parameters and to obtain the complex dielectric response function. The dielectric response function of each layer was evaluated using classical damped oscillator dispersion model [Ostapchuk et *al*., 2002, and references therein] by:

$$\hat{\varepsilon}(\omega) = \varepsilon^{'}(\omega) - i\varepsilon^{''}(\omega) = \varepsilon(\infty) + \sum_{j=1}^{n} \Delta\varepsilon_j \frac{\omega_{TO_j}^2}{\omega_{TO_j}^2 - \omega^2 + i\omega\gamma_{TO_j}} \qquad (3.15)$$

where $\varepsilon_\infty = n^2$ stands for the high frequency optical permittivity, $\omega_{TO_j}, \gamma_{TO_j}$ and $\Delta\varepsilon_j$ denote the eigenfrequency, damping, and dielectric strength of the jth transverse phonon mode, respectively. In order to reduce the ambiguity of the fit, the parameters of the substrate were obtained from an independent fit of transmittance spectra of a bare sapphire substrate and then fixed during the subsequent fits of film layers.

The measurements were carried out at the Department of Dielectrics, Institute of Physics, Academy of Sciences of the Czech Republic.

3.3.4. Terahertz time-domain spectroscopy

To normalize results, obtained by IR spectroscopy, some doped ST films were measured by Terahertz time-domain spectroscopy (THz-TDS) to obtain value of real part of dielectric permittivity.

THz-TDS is a spectroscopic technique where a special generation and detection scheme is used to probe material properties with short pulses of terahertz radiation [Grüuner, 1998]. The generation and detection scheme is sensitive to the sample material's effect on both the amplitude and the phase of the terahertz radiation.

THz-TDS technique is based on the measurement of the temporal profile of the electric field of a picosecond terahertz (THz) pulse transmitted through an investigated sample. The complex spectrum of this pulse is normalized by a reference spectrum, obtained without the sample. Finally, the complex transmittance and, consequently, the complex dielectric function of the sample in the whole frequency range studied are obtained through numerical solution of a system of two real non-linear equations for the transmittance [Kužel and Petzelt, 2000].

In the present work, a custom-made THz-TD spectrometer was used to obtain the complex dielectric response of samples, in the range from 3 to 50cm^{-1} (90-1500GHz). This spectrometer uses a femtosecond Ti:Sapphire laser and (011)-oriented ZnTe crystal as a THz emitter, generating pulses owing to optical rectification effect. The detection of THz waveforms is performed by an electro-optic sampling technique using another ZnTe crystal. Terahertz data for some samples were used to normalize IR data and a joint generalised multi-oscillator fit was used to calculate the real and imaginary parts of the dielectric permittivity.

The measurements were carried out at the Department of Dielectrics, Institute of Physics, Academy of Sciences of the Czech Republic.

Chapter 4. Polycrystalline $SrTiO_3$ thin films: influence of processing on the microstructure, structure and low temperature dielectric properties

In this chapter the relation between the processing – microstructure – dielectric properties of undoped $SrTiO_3$ films deposited by sol-gel on $Si/SiO_2/TiO_2/Pt$ substrates is established. The changing of the annealing temperature and inserting of the buffer layers on properties of $SrTiO_3$ films is analysed. Results of dielectric measurements of these films as a function of frequency f and temperature T are also presented. ε' versus *dc* electric field E_{dc} and polarization P versus *ac* electric field E of $SrTiO_3$ films prepared under different conditions are analyzed as well. The obtained data indicates methods to improve the dielectric response of polycrystalline $SrTiO_3$ films**.**

Introduction

As mentioned before ("Chapter 2") the application of ferroelectric thin films for tunable microwave devices has been intensely studied because of their excellent dielectric properties such as high permittivity, low dielectric loss, and high tunability [Vendik et *al.*,1999a; Tagantsev et *al.*, 2003]. However, it is well known that the electrical properties of thin films are very dependent on the preparation conditions: method of fabrication, conditions of fabrication (temperature, atmosphere, heating cycles) and substrate or underneath layers. As described in "Chapter 2" the dielectric properties of the ferroelectric films can be engineered by the mechanical misfit strain between the film and the substrate [Tagantsev et *al.*, 2003; Pertsev et *al.*, 2000b; Ban and Alpay, 2002; Canedy et *al.*, 2000; Li et *al.*, 2001; Astafiev et *al.*, 2003]. In addition, the dielectric properties are also markedly affected by the chemical composition, degree of stoichiometry and oxygen vacancies and defects content, which depend on the experimental conditions such as oxygen pressure, growth temperature, and annealing process and on the processing method (sputtering, pulsed laser deposition (PLD), chemical vapour deposition, or sol-gel process).

In order to optimise the properties of ST thin films several attempts have been tried. It was reported that increasing of the thickness of ST films from 1.2μm to 2.5μm leads to

decreasing of tanδ from 6×10^{-3} to 6×10^{-4} due to stress, either due to the lattice mismatch or due to nanoscale defects such as oxygen vacancies [Li et *al*., 1998a; Li et *al*., 2001]. Significant increasing of ε' from ~2000 to ~5000 was observed for ST films with changing of the oxygen partial pressure from 300mTorr to 600mTorr during deposition [Dalberth et *al*., 1998]. Moreover, inserting a thin layer between film and substrate (can be also bottom electrode or buffer layer) leads to different dielectric response of ST films. For example, ST films on Si substrate with $CoSi_2$ buffer layer shown higher ε' (~90) than that with CeO_2 buffer layer (~60) [Nakagawara et *al.*, 1995]. ST film on ST substrate with $SrRuO_3$ (SRO) bottom electrode and ST film on $LaAlO_3$ (LAO) substrate with $La_{0.5}Sr_{0.5}CoO_3$ bottom electrode shown broad peaks (crossovers) occur with increasing temperature related to the field induced ferroelectric to paraelectric phase transition [Park et *al.*, 2001]. At the same time, for ST film deposited on the same LAO substrate but with SRO bottom electrode the applied electric field reduces the dielectric response without showing any crossover resulting from the field induced ferroelectric phase transition [Park et *al.*, 2001]. Thickness of the bottom electrode is also important for dielectric properties. And systematic study of the influence of thickness of SRO bottom electrode (from 50nm to 500nm) on dielectric properties of ST films deposited on LAO substrate shown that the lowest tanδ and highest ε' can be obtained for 150nm thickness of SRO [James and Xi, 2002].

Other approaches to optimise the electric response of thin films contemplate the so-called "two-steps" growth technique. This technique was used for a experimental investigation of the mechanical strain of epitaxial ST films on $LaAlO_3$ substrates prepared by PLD [Yamada et. *al.*, 2005a; Yamada et. *al.*, 2005b]. In this method, very thin film below ten-odd nanometers is first grown on the substrate at a low temperature. After the deposition of this first thin layer, the substrates are heated up to the temperature suitable for epitaxial growth and are kept in this temperature for a while. After this annealing the film growth proceeds until the desired film thickness is obtained. Thus, the film thickness, deposition conditions and substrate are the same and no additional layers of different compositions are used, changing only the deposition temperature in the very initial growth stage of the film during the deposition [Yamada et. *al.*, 2005a; Yamada et. *al.*, 2005b]. Using this method ε' of *epitaxial* ST films obtained by PLD was reported to increased from 440 to 720 at room temperature [Yamada et. *al.*, 2005b] and tanδ reported to decrease from 7.4% to 6.9% at 78K and 8GHz [Yamada et. *al.*, 2005a].

At the same time, the sol-gel process used in the current work for the preparation of ST films, as other chemical solution deposition techniques, is attractive because it provides a very good control of the stoichiometry, a large area deposition, and a uniformity of the thickness of the deposited films, as previously presented. However, due to their polycrystalline nature the microstructure of these films is more complicated when compared to the one of *epitaxial* films, including randomly oriented grains, a higher number of grain boundaries and no preferential crystallographic orientation. As a consequence the influence of the deposition parameters on the properties of polycrystalline films prepared by sol-gel method is more complicated to be analyzed. And ST sol-gel derived thin films in particular are much less studied than epitaxial ST films. However, the modification of the technological process, such as the inserting of buffer layers and intermediate heat treatments could lead to changing the final properties ST films and it is possible to expect improved dielectric properties.

The analysis of the impact of modifications in the deposition process on the dielectric properties of polycrystalline ST films is necessary and was conducted in this work. The next chapters present the results on the study of the effect of the processing temperature and on the use of buffer layers on the dielectric response of polycryctalline ST films, conducted in this Thesis.

4.1. Preparation and characterisation

In order to study the effects of the processing conditions on the structure, microstructure and dielectric response, ST films were prepared on $Si/SiO_2/TiO_2/Pt$ substrates by sol-gel under four different conditions.

The preparation process was described in "Chapter 3". For this study in particular, a set of samples was prepared according to the *"one-step"* procedure in which no intermediate heat treatment was done between the deposited layers and the samples were submitted only to one final annealing step at different temperatures: 750°C (these samples are hereafter designated as ST 750°C) and 900°C (these samples are hereafter designated ST 900°C) during 60min. in air. The other set of samples was prepared according to the "*two-steps*" procedure, i.e. after the deposition of the first two layers, a first heat treatment at 600°C during 30min. was conducted and, after cooling the films to room temperature 8 layers more were deposited and a final annealing step took place at 750°C (these samples

are hereafter designated ST 2l 750°C) and at 900°C (these samples are hereafter designated ST 2l 900°C) for 60min. in air. List of the samples analysed in the current work presented in Table 4.1.

TABLE 4.1. List of the samples analysed in the current Chapter.

Samples	Buffer layers	Annealing temperature after buffer layers deposition	Main film	Final annealing temperature	Denoted as
ST films	-	-	10 layers	750°C	ST 750°C
ST films	-	-	10 layers	900°C	ST 900°C
ST films	2 layers	600°C	8 layers	750°C	ST 2l 750°C
ST films	2 layers	600°C	8layers	900°C	ST 2l 900°C

Structural and microstructure properties of ST 750°C, ST 900°C, ST 2l 750°C and ST 2l 900°C thin films were analysed by XRD, SEM and AFM. Measurements of ε', tanδ, hysteresis response, *dc*-field effect were conducted in the temperature range from 10K to 300K and frequency range from 100Hz to 1MHz.

4.2. Microstructural properties

4.2.1. SEM analysis

ST films prepared under different conditions: ST 750°C, ST 900°C, ST 2l 750°C and ST 2l 900°C were analysed by SEM. Top views and cross sections micrographs of ST 750°C and ST 900°C films are presented in Figures 4.1 and 4.2, respectively.

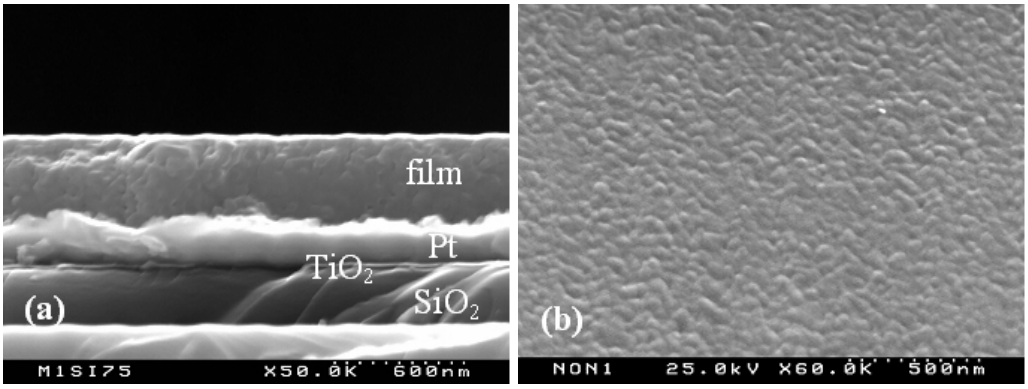

FIGURE 4.1. SEM cross-section (a) and plan view (b) micrographs of $STiO_3$ thin films prepared by "one-step" procedure and annealed at 750°C (ST 750°C).

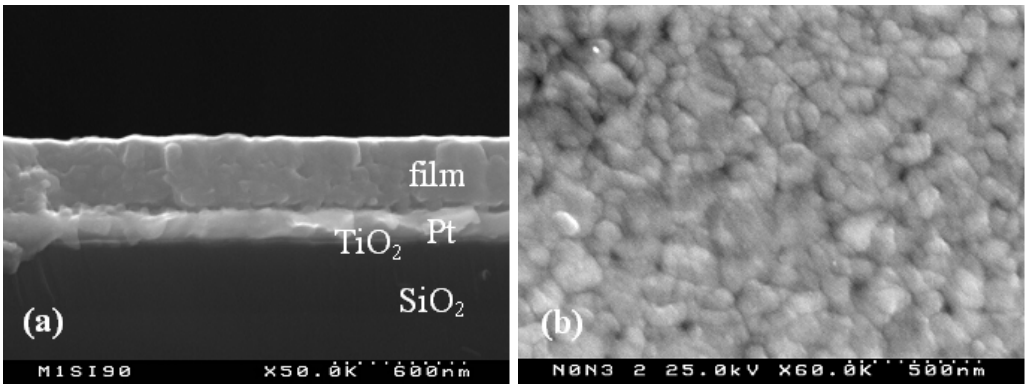

FIGURE 4.2. SEM cross-section (a) and plan view (b) micrographs of $STiO_3$ thin films prepared by "one-step" procedure and annealed at 900°C (ST 900°C).

Both samples ST 750°C and ST 900°C reveal quite dense and crack free microstructures. The calculation of the grain size from the obtained plan-view micrographs was quite difficult due to the small grains. The grain size was assessed from the AFM analysis at a later stage. However, grains of ST films annealed at 900°C without buffer layers (Fig.4.2b) are bigger when compared to the grains of films obtained at lower annealing temperatures, ST 750°C (Fig.4.1b). From cross-section images of the two sets of ST films prepared by "one-step" process no preferential grain or columnar growth occurred (Figs. 4.1a and 4.2a).

Figure 4.3 presents the SEM cross-section micrographs of ST thin films prepared by "two-steps" procedure. As previously, both films ST 2l 750°C and ST 2l 900°C reveal the quite dense and crack free microstructures.

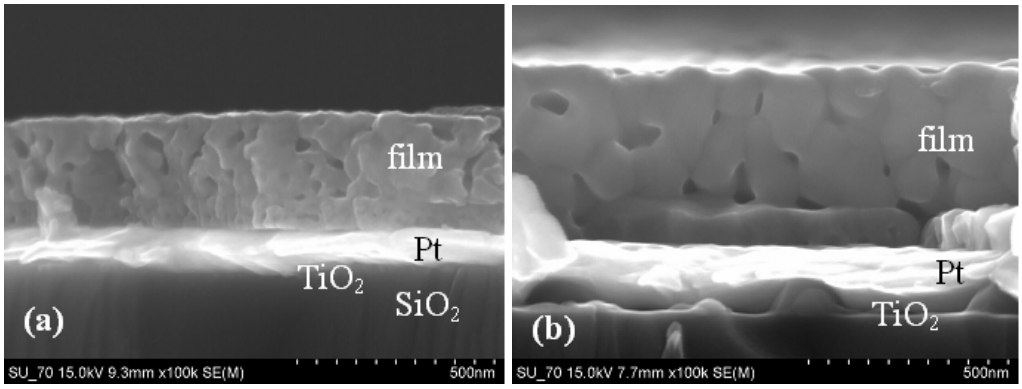

FIGURE 4.3. SEM cross-section micrographs of $STiO_3$ thin films prepared by "two-steps" procedure and annealed at 750°C (ST 2l 750°C) (a) and 900°C (ST 2l 900°C) (b).

Independently on the processing, films annealed at 900°C (ST 900°C and ST 2l 900°C) (Figs.4.2b and 4.3b) show bigger grain size compared to those annealed at 750°C (ST 750°C and ST 2l 750°C) (Figs.4.1b and 4.3a). The grain growth that occurs with the increase of the annealing temperature is very obvious in the cross section of ST 2l 900°C (Fig.4.3b). The cross section images of the samples prepared by the "two-steps" procedure, ST 2l 750°C (Fig.4.3a) and ST 2l 900°C (Fig.4.3b) clearly depict a thin layer of ~50nm just on the top of Pt, that corresponds to the 2 initial layers deposited as buffers.

4.2.2. AFM analysis

The surface morphology and 3D view of ST films prepared under different conditions, ST 750°C, ST 900°C, ST 2l 750°C and ST 2l 900°C was analyzed by AFM and is depicted in Figures 4.4 and 4.5, respectively.

ST 750°C and ST 900°C films show relatively smooth surface. The average grain size of these ST films varies between ~85nm for ST 750°C and ~145nm for ST 900°C ones, confirming the previous observation by SEM.

For the films prepared by "two-steps" procedure the average grain size varies between ~80nm for ST 2l 750°C and ~125nm for ST 2l 900°C indicating a smaller average grain size for these films when compared with the ones prepared by the "one-step" procedure.

The average roughness for these films was computed from the AFM images to vary between ~1nm for ST 750°C, ~3.54nm for ST 900°C, ~3.45nm for ST 2l 750°C and ~3.84nm for ST 2l 900°C, and is represented in Figure 4.6 together with the average grain size values the analyzed ST films.

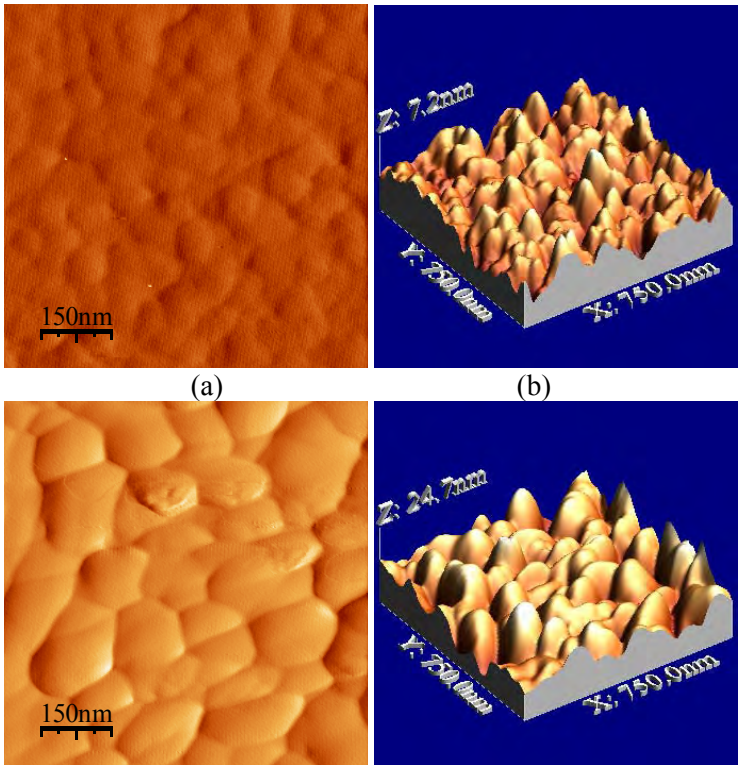

(a) (b)

(c) (d)

FIGURE 4.4. Surface morphology and 3D view of $STiO_3$ thin films prepared by "one-step" procedure and annealed at 750°C (ST 750°C) (a,b) and 900°C (ST 900°C) (c,d).

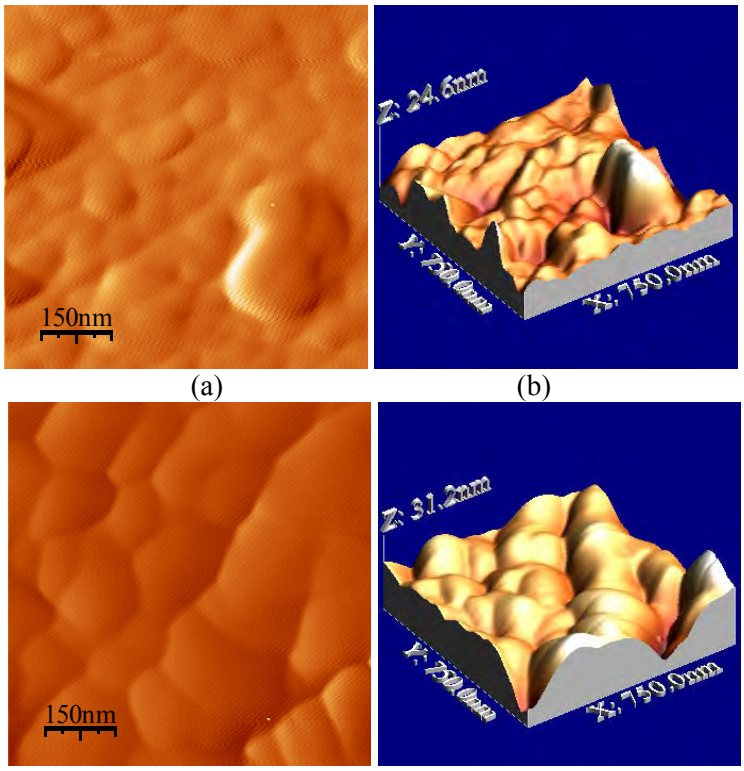

(a) (b)

(c) (d)

FIGURE 4.5. Surface morphology and 3D view of $STiO_3$ thin films prepared by "two-steps" procedure and annealed at 750°C (ST 2l 750°C) (a,b) and 900°C (ST 2l 900°C) (c,d).

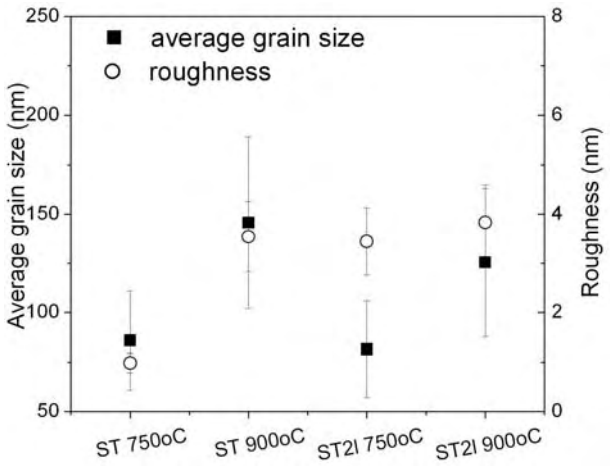

FIGURE 4.6. Average grain size (*left axis*) and roughness (*right axis*) of $SrTiO_3$ films prepared under different processing conditions: by "one-step" procedure and annealed at 750°C (ST 750°C) and at 900°C (ST 900°C), and by "two-steps" procedure and annealed at 750°C (ST 2l 750°C) and 900°C (ST 2l 900°C).

Figure 4.6 clearly illustrates that the average grain size of the films increases with the increase of the annealing temperature and decreases with the introduction of the buffer layers. Concomitantly the film roughness increases with the annealing temperature as well. The buffer layers as in the "two-steps" process, due to its reduced thickness, will play a role of seed layers facilitating the nucleation of the crystallites over their growth and the film deposited over these initial layers will mimic this microstructure; at a later stage these films will exhibit a lower grain growth than the films prepared by the "one-step" procedure. As was expected, films with bigger average grain size (ST 900°C and ST 2l 900°C) will show higher roughness when compared with the films with smaller grains (ST 750°C and ST 2l 750°C).

4.3. Crystal structure and stress calculation

The XRD spectra of the ST films prepared under different conditions ST 750°C, ST 900°C, ST 2l 750°C and ST 2l 900°C are depicted in Figure 4.7.

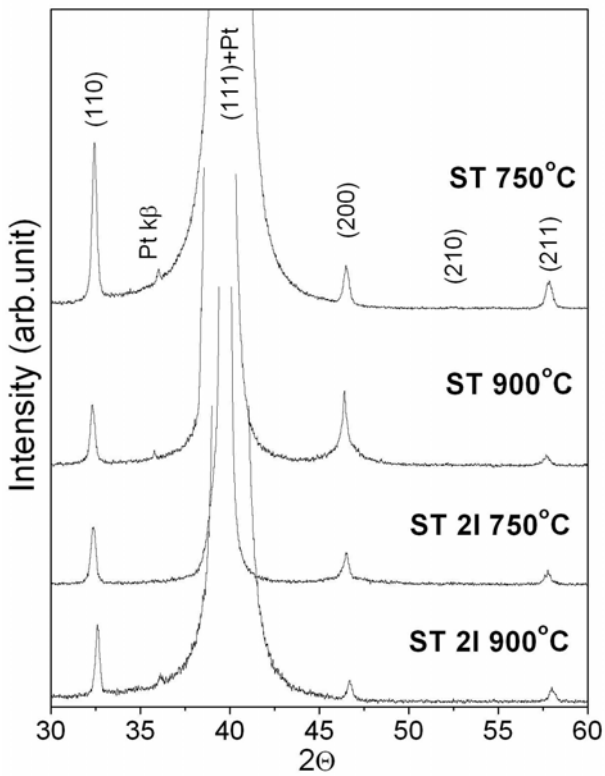

FIGURE 4.7. XRD spectra of $SrTiO_3$ films prepared under different conditions: by "one-step" procedure and annealed at 750°C (ST 750°C) and 900°C (ST 900°C), and by "two-steps" procedure and annealed at 750°C (ST 2l 750°C) and 900°C (ST 2l 900°C).

All films are monophasic and only the diffraction peaks of ST and substrates are detected. ST films prepared under different conditions show no marked difference in their structure. In particular no preferable orientation due to the intermediate heat treatment or due to the increase of the annealing temperature was detected.

The effect of the deposition conditions on the lattice cell was further studied by XRD analysis and the values of out-of-plane lattice parameter *c* and in-plane lattice parameter *a* were assessed, as described in "Chapter 3". The calculated lattice parameters of the different undoped ST films are depicted in Figure 4.8.

Some differences between in-plane *a* and out-of plane *c* lattice parameters of ST films prepared under different conditions can be observed (Fig.4.8):

1. ST films prepared under the "one-step" methodology, ST 750°C and ST 900ºC, exhibit lattice parameters more close to the lattice parameter of ST single crystal, that has a cubic structure with a lattice parameter a=3.905Å [Mitsui and Westphal, 1961]: a and c≈3.905Å for ST 750°C; a≈3.9107Å and c≈3.908Å for ST 900°C.

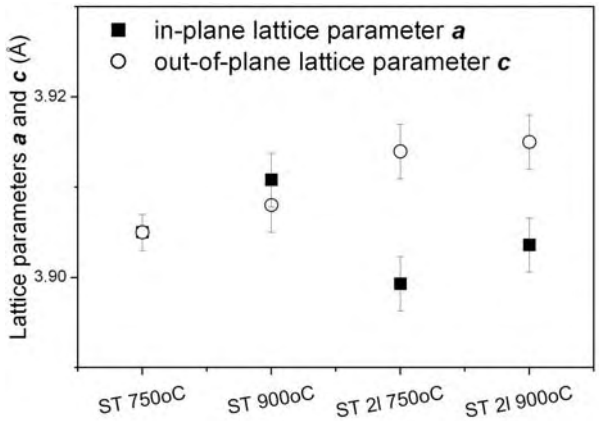

FIGURE 4.8. In-plane lattice parameters *a* and out-of-plane lattice parameters *c* of $SrTiO_3$ films prepared under different conditions: by "one-step" procedure and annealed at 750°C (ST 750°C) and 900°C (ST 900°C), and by "two-steps" procedure and annealed at 750°C (ST 2l 750°C) and 900°C (ST 2l 900°C).

2. On the other hand the films prepared by "two-steps" methodology exhibit a much higher out-of-plane lattice parameter *c* than in-plane lattice parameter *a: a*≈3.899Å and *c*≈3.914Å for ST 2l 750°C, *a*≈3.904Å and *c*≈3.915Å for ST 2l 900°C. This is an indication that as the processing temperature increases the distortion of the lattice increases for both processes, when compared with the lattice dimensions of ST crystals. Moreover, the "one-step" prepared films are less distorted than the films prepared with buffer layers.

As explanation of the difference between the lattice parameters of samples prepared by "one-step" and "two-steps", it could be supposed here, that ST 2l 750°C and ST 2l 900°C films grown up in out-of-plane direction better than in in-plane direction. It means, that buffer layer after intermediate annealing at 600°C during 30min. begins to crystallization and their lattice cell is lock in. And the lattice cells of following deposited main film (8 layers) are clamped from already crystalline lattice cells of buffer layer in in-plane direction, but free for growing in out-of-plane direction. At the same time, ST 750°C and ST 900°C do not have such buffer layer and could grown up in both in-plane and out-of-plane directions.

Meanwhile, lower values of the lattice parameters of the films with buffer layer compare to that of films without buffer layer was reported before for $(Ba,Sr)TiO_3$ thin films [Peng and Meng, 2003].

It was already presented in "Chapter 2" that, effect of lattice mismatch between the

film and the substrate and thermal stress, induced during heat treatment process, contribute to the value of total stress, as well. However, as it was mentioned before, all analyzed samples were deposited on $Si/SiO_2/TiO_2/Pt$ substrates. And theoretical lattice mismatch between ST and Pt layer was calculated according to following mathematical expression:

$$Lattice\ Mismatch = \frac{a_{sub} - a_{film}}{a_{sub}} \tag{4.1}$$

where a_{sub} and a_{film} are in-plane lattice parameters of substrate and ST film, respectively. However, because the *theoretical* in-plane lattice mismatch was calculated before deposition of ST film, in this calculation, the lattice parameter of bulk ST a_{STbulk} (3.905Å) was used as in-plane lattice parameter of ST film a_{film} and the lattice parameter of Pt a_{Pt} (~3.912Å) as $a_{substrate}$. In this case the theoretical mismatch between ST and Pt is calculated equal to 0.18% and should be the same for all studied ST samples deposited at different conditions. However, after deposition ST films under different conditions and measurements by XRD, the in-plane parameters *a* were found different as presented in Figure 4.8. And lattice mismatch was calculated by Eq.4.1 and it was differ from the *theoretical* lattice mismatch (0.18%) as shown in Figure 4.9.

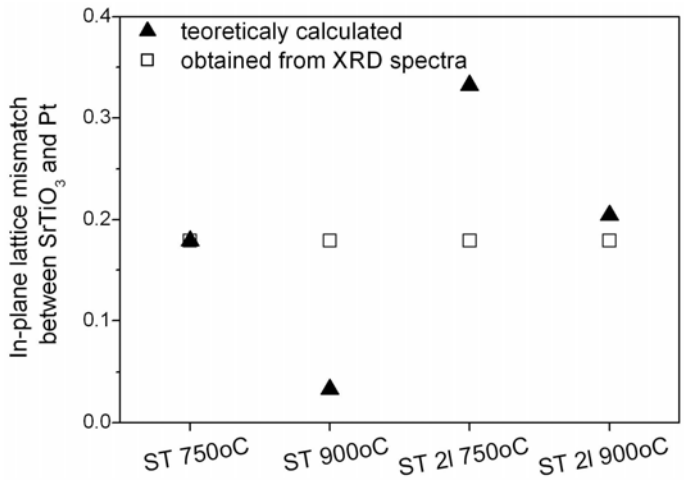

FIGURE 4.9.Theoreticaly calculated (*closed triangle*) and obtained after XRD measurements (*open square*) in-plane lattice mismatch for $SrTiO_3$ films prepared under different conditions: by "one-step" procedure and annealed at 750°C (ST 750°C) and 900°C (ST 900°C), and by "two-steps" procedure and annealed at 750°C (ST 2l 750°C) and 900°C (ST 2l 900°C).

It is visible from the Figure 4.9 that with increasing of annealing temperature from 750°C to 900°C the in-plane lattice mismatch decrease significantly: from 0.18% to 0.033% for ST films prepared by "one-step" procedure and from 0.33% to 0.20% for ST films prepared by "two-steps". However, it is also can be found that ST films with buffer layer have higher the in-plane lattice mismatch than ST films without buffer layer.

For a detail study, the films prepared under the different conditions were conducted and the total stress of the films assessed by $sin^2\psi$ method (described in "Chapter 3"). Total stress of the undoped ST films was calculated by following formula and presented in Figure 4.10:

$$\sigma = \frac{d_{\psi}^{hkl} - d_0^{hkl}}{d_0^{hkl}} \times \frac{E}{1+\gamma} \times \frac{1}{\sin^2\psi} \tag{4.2}$$

where d_{ψ}^{hkl} stands for the lattice spacing, ψ for the tilt angle between the normal of the planes (*hkl*) and the normal of the sample surface, the strain free lattice spacing, d_0^{hkl}, corresponds to d_{ψ}^{hkl}, if $\psi = \psi_0$, where ψ_0 is the unique direction for which the strain in lattice-spacing determination is equal zero, γ stands for the Poisson ratio and E for the Young's modulus; In the current work the values for E and γ were calculated as E=303GPa and γ=+0.2242.

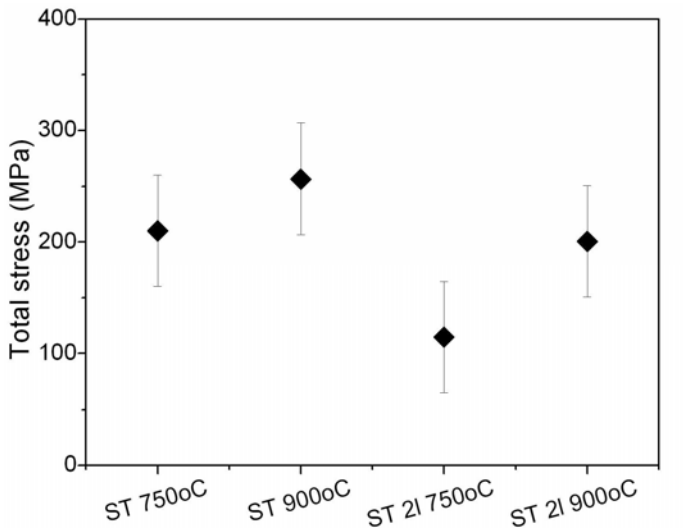

FIGURE 4.10. Average values for the total stress of $SrTiO_3$ films prepared under different conditions: by "one-step" procedure and annealed at 750°C (ST 750°C) and 900°C (ST 900°C), and by "two-steps" procedure and annealed at 750°C (ST 2l 750°C) and 900°C (ST 2l 900°C).

Three clear observations that come out from this plot (Fig.4.10):

i) For all samples the total stress has the positive sign means that all films are under tensile total stress.

ii) The total stress state of the films increases with the increasing of the annealing treatment from 750°C to 900°C: from 210MPa to 256MPa for ST film deposited by "one-step" procedure and from 115MPa to 201MPa for ST film deposited by "two-steps" procedure.

iii) The use of the buffer layers decreases the total stress state in the films annealed at similar temperature: from ~210MPa (ST 750°C) to ~115MPa (ST 2l 750°C) and from ~256MPa (ST 900°C) to ~201MPa (ST 2l 900°C).

Moreover, it is possible to see that ST films deposited by "one-step" procedure and less distorted ($a \approx c$) represent higher values of the total stress than that of ST film deposited by "two-steps" procedure with high distortion ($a<c$).

One more stress, the thermal stress σ_{th}, that appears during the cooling after the heat treatment can be calculated by the following equation:

$$\sigma_{th} = \int_{RT}^{T_{ann.}} \frac{E_f}{1-\gamma_f} \times (\alpha_{film}(T) - \alpha_{substrate}(T))dT \qquad (4.3)$$

where α_{film} and $\alpha_{substrate}$ stand for the thermal expansion coefficients (TEC's) of the film and substrate, respectively, E_f and γ_f for the Young's modulus and Poisson's ratio of the film, respectively, $T_{ann.}$ for the temperature of annealing of the films and RT for room temperature.

For the calculation of the theoretical thermal stress the value of TEC of Si (~2.9 $\times 10^{-6}$/°C) was used for the $\alpha_{substrate}$ and the value of TEC of ST_{bulk} (~9×10^{-6}/°C) was used α_{film}. It is understandable, that the difference between TECs of ST_{bulk} and Si in Eq.4.3 is positive (such as difference between values of the annealing and room temperature), what means that σ_{th} has positive sign and is tensile for all studied ST films. It was calculated, that σ_{th} is different for samples annealed at different temperatures: for films annealed at 750°C (ST 750°C and ST 2l 750°C) $\sigma_{th} \approx$2380MPa, and for ST films annealed at 900°C (ST 900°C and ST 2l 900°C) $\sigma_{th} \approx$2936MPa.

Thus, from such big difference between the values of theoretical thermal stress

(~2380-2936MPa) and total stress (~115-256MPa) next conclusion could be presented: *in analyzed polycrystalline ST films deposited on the same substrates the thermal stress play more important role than the lattice mismatch strain*.

4.4. Low temperature dielectric properties

4.4.1. Dielectric response as function of temperature and frequency

Real part of the dielectric permittivity ε' of ST films prepared under the "one-step" procedure (ST 750°C and ST 900°C) and "two-steps" procedure (ST 2l 750°C and ST 2l 900°C) measured from 100Hz to 1MHz from 300K to 10K are illustrated in Figure 4.11 at selected frequencies.

All the films show an increase of ε' with decreasing of the measured temperature as is typical for an incipient ferroelectric and observed for ST single crystal and ceramics, as well [Müller and Burkard, 1979; Tkach et *al.*, 2004a]. Besides, the appearance of a small broad peak at low temperature is noticeable in all of the films. Such small peak in $\varepsilon'(T)$ was also observed in ST films prepared by other methods and attributed to the appearance of the ferroelectricity [Astafiev et *al.*, 2003; Yu et *al.*, 2002; Hirano et *al.*, 1993]. Finally almost no frequency dispersion of ε' was detected for the studied ST films (Fig.4.11).

Figure 4.11 illustrates the effect of the processing on the dielectric response of ST sol-gel derived films. As expected and because of the high degree of crystallinity, the films annealed at 900ºC present higher ε' than the that of films annealed at 750ºC, well noticed for the low temperature part of the curves.

In the meantime, due to the observed effects of the buffer layers on the structural and microstructural features of ST films it is then expected an improvement of the dielectric properties of these films. Indeed films prepared with buffer layers present, for each annealing temperature, the highest values of ε': ~662 for ST 2l 900°C compared to ~415 for ST 900°C and ~376 for ST 2l 750°C compared to ~267 for ST 750°C. Similar improving of dielectric properties by inserting of buffer layer was reported for $(Ba,Sr)TiO_3$ thin films: capacitance increases from ~1.5pF to ~3.7pF [Peng and Meng, 2003].

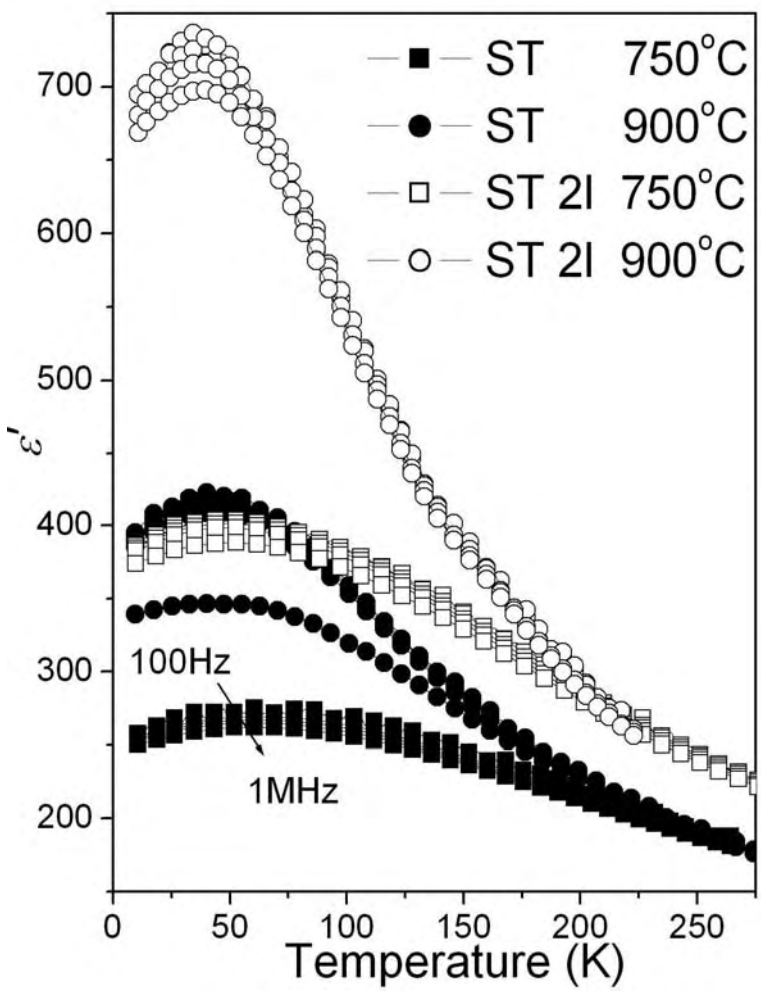

FIGURE 4.11. Temperature dependence of the real part of the dielectric permittivity ε' of $SrTiO_3$ films prepared under different conditions: "one-step" procedure and annealed at 750°C (ST 750°C) and 900°C (ST 900°C), and "two-steps" procedure and annealed at 750°C (ST 2l 750°C) and 900°C (ST 2l 900°C) at 100Hz, 1kHz, 10kHz, 100kHz and 1MHz.

At the same time the position of the temperature maximum $T_{\varepsilon'max}$ of the broad peak $\varepsilon'(T)$ depends on the process of preparation and shifts to low temperature with increasing of the annealing temperature, from 750°C to 900°C and with the insertion of buffer layers (Fig.4.11). The highest temperature for $\varepsilon'_{max}(T)$ $T_{\varepsilon'max}$=~60K was measured for ST 750°C and it shifts to ~44K with increasing of annealing temperature (ST 900°C). Similar tendency was observed for the films prepared by the "two-steps" procedure: $T_{\varepsilon'max}$=~48K for ST 2l 750°C shifts to $T_{\varepsilon'max}$=~38K for ST 2l 900°C.

The temperature dependence of tanδ of ST films prepared by the different processing conditions was measured together with $\varepsilon'(T)$ and is presented in Figure 4.12 at 10kHz.

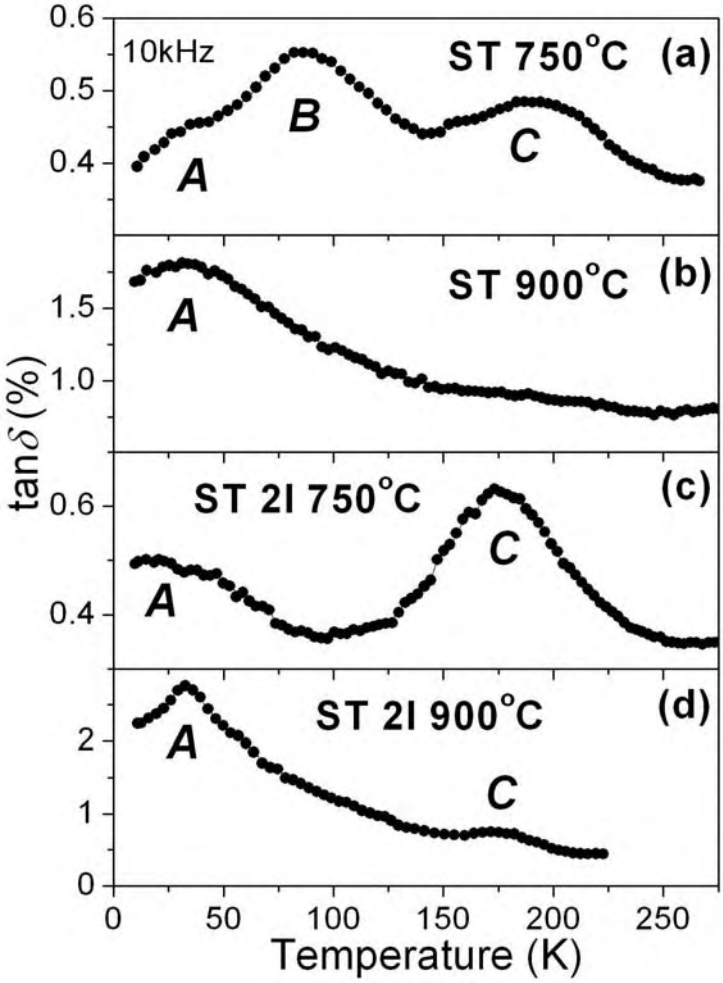

FIGURE 4.12. Temperature dependence of tanδ of $SrTiO_3$ films prepared under different conditions: by "one-step" procedure and annealed at 750°C (ST 750°C) (a) and 900°C (ST 900°C) (b), and by "two-steps" procedure and annealed at 750°C (ST 2l 750°C) (c) and 900°C (ST 2l 900°C) (d) at 10kHz.

The following main observations of the Figure 4.12 and discussion can be done.

1. 3 main "peaks" can be observed in tanδ of ST films and are marked as peak *A* at ~30-35K, peak *B* at ~90K and peak *C* at ~175-185K (Table 4.2).
2. The peak position is almost independent on the process of fabrication and temperature of the thermal heat treatment. However, the magnitude and presence or absence of some of the peaks is dependent on the fabrication history of the films.
3. For films heat treated at high temperatures, ST 900ºC and ST 2l 900ºC only peak *A* is observed for the first set of samples and together with peak *A* a small peak *C* is observed for ST 21 900ºC samples. Peak *C* is more obvious for the samples heat treated at low temperatures, being undetectable for ST 900ºC films. Both ST films

annealed at 750°C show similar maximal loss values of tanδ (~0.6%). As the annealing temperature increases the dielectric loss increase approximately 3 times for "one-step" derived ST films (~1.75% for ST 900°C) and more than 4 times for "two-steps" derived ST films (~2.8% for ST 2l 900°C), being the highest dielectric loss observed for this last set of films at around 50K; this observation is in agreement with the highest value of ε' and with the highest degree of crystalinity observed for this sample.

4. It is worthwhile to state that the dielectric loss spectra of ST materials is quite sensitive to the nature of the material, crystalline state (ceramics or single crystals), purity (impurities and dopants) and fabrication process (heat treatment atmospheres).
5. That in ST single crystals and ceramics several peaks in tanδ (similar to presented in this analyse) were also observed [Viana et *al.*, 1994; Bidault et *al.*, 1995; Mizaras and Loidl, 1997; Ang et *al.*, 2000c; Yu et *al.*, 2002; Tkach et *al.*, 2004].
6. The peaks in the loss spectra of ST have been mainly attributed: *i)* peak *A* at low temperatures (5K<*T*<15K) could be considered as a stress/strain induced ferroelectric phase transition [Astafiev et *al.*, 2003], *ii)* peak *B* in the temperature interval 60K<*T*<130K has been attributed for single crystals, to the antiferrodistortive phase transition that occurs at 105K, namely to the ferroelastic domain-wall dynamics around the cubic-to-tetragonal phase transition [Viana et *al.*, 1994; Mizaras and Loid, 1997], and *iii)* peak *C*, observed in ceramics to unavoidable defects (oxygen vacancies) [Mizaras and Loidl, 1997; Yu et *al.*, 1999; Lemanov et *al.*, 2002].
7. Hence in the present case the appearance of a peak *A* at around 30K corroborating the peak observed in the dielectric loss are an indication of some polar instability of the lattice, similar to the ferroelectric type one. This peak was observed for all the prepared films, but is more obvious for the films annealed at 900ºC in which the final strain level is the highest one. Due to the well defined peak *A*, peak *B* associated with ferroelastic domain-wall dynamics around the cubic-to-tetragonal phase transition is not clearly observed, except for films in which peak *A* is less intense, namely ST 750ºC. Concerning peak *C*, as the annealing temperature increases and the degree of crystalinity increases the concentration of defects of these sol-gel based films tends to diminish and as consequence peak *C* decreases for the films heat treated at higher temperatures.

In order to discuss the origin of these peaks and their dependence on the processing conditions, the dynamics of the relaxations was further analysed by Arrhenius law:

$$\tau = \tau_0 \exp(U/k_B T) \tag{4.4}$$

where, τ_0 stands for the pre-exponential term or inverse attempt frequency, U for the activation energy, k_B for the Boltzmann constant and T for the temperature.

The relaxation dynamics parameters of the loss peaks A, as well as peak B and peak C were then deducted from the temperature and frequency value of ε'' peaks ($\varepsilon''=\varepsilon' \times \tan\delta$) and Figure 4.13 represents the Arrhenius plots of $\ln(\tau)=\ln(w^{-1})$ versus $1000/T_{\varepsilon''max}$ (w is the angular frequency, $w = 2\pi f$; $\tau = w^{-1}$). As one can see, the logarithm of the relaxation time τ of these peaks depends linearly on the inverse of the temperature, i.e., relaxation peaks A, B and C exhibit a thermally activated behaviour, described by the Arrhenius relation.

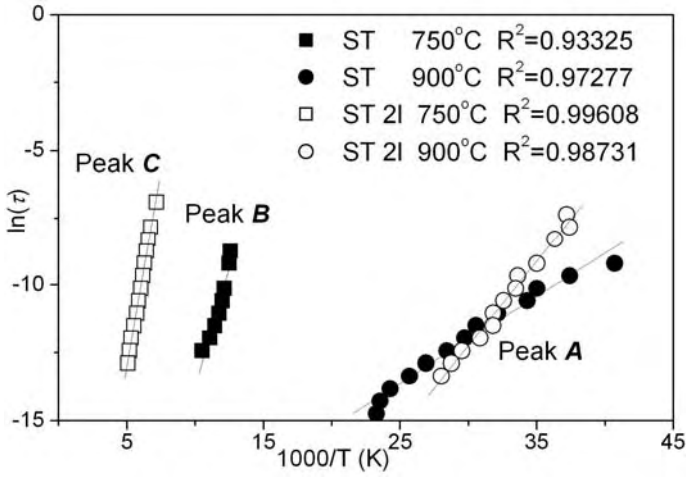

FIGURE 4.13. Arrhenius plots of $\ln(\tau)$ versus $1000/T_{\varepsilon''\max}$ ($T_{\varepsilon''\max}$ is the temperature at which maximum of ε'' occurs at the angular frequency $w = 2\pi f$; $\tau = w^{-1}$) for the loss peaks A, B and C of $SrTiO_3$ films prepared under different conditions: by "one-steps" procedure and annealed at 750°C (ST 750°C) and 900°C (ST 900°C), and by "two-steps" procedure and annealed at 750°C (ST 2l 750°C) and 900°C (ST 2l 900°C). The correlation coefficients R^2 for the obtained fits are presented inside in Figure.

The τ_0 and U values were calculated for the samples for which the peaks are well detectable, and shown in Table 4.2. At the same time, relaxation mechanisms observed for undoped ST crystals, ceramics and films and their Arrhenius-law parameters represented in Table 4.3 for comparison and discussion.

TABLE 4.2. Temperature of position of the loss peaks *A*, *B*, *C* and parameters of the Arrhenius law describing the dynamics of the relaxation of loss peaks of $SrTiO_3$ thin films prepared under different conditions: by "one-step" procedure and annealed at 750°C (ST 750°C) and 900°C (ST 900°C), and by "two-steps" procedure and annealed at 750°C (ST 2l 750°C) at 750°C (ST 2l 750°C) and 900°C (ST 2l 900°C).

Composition	Temperature of the peak, K	*ARRHENIUS LAW*	
		U, meV	τ_0, s
ST 750°C	Peak *B* at ~87	151	26×10^{-15}
ST 900°C	Peak *A* at ~31	27	4×10^{-10}
ST 2l 750°C	Peak *C* at ~180	250	1.2×10^{-12}
ST 2l 900°C	Peak *A* at ~33	53	35×10^{-15}

TABLE 4.3. Relaxation mechanisms observed for undoped $SrTiO_3$ crystals, ceramics and films and their Arrhenius-law parameters.

System	Temperature of reported peak	*U*, meV	τ_0, s	Proposed mechanism	Ref	Corresponding peak in studied films
ST crystal	20K	13.6	2.5×10^{-12}	Arising from the domain dynamics.	Viana et *al.*, 1994	Peak *A*
	10-40K	5.7	2×10^{-8}	Polaronic relaxation.	Bidault et *al.*, 1995	
	140K	120	8×10^{-13}	Associated with structural phase transition at 105K	Viana et *al.*, 1994	Peak *B*
	80-140K	105	3.2×10^{-12}	Domain wall dynamics. Slow dynamic is the creation and decay of clusters of ordered regions and the motion of domain walls below the structural phase-transition temperature.	Mizaras and Loidl, 1997	
	50-100K	105	1.6×10^{-12}	Explained in terms of dynamics of domain walls.	Ang et *al.*, 2000c	
ST ceramics	85K	142	3.6×10^{-13}	Attributed to ferroelastic domain-wall dynamics around cubic-to-tetragonal phase transition.	Tkach et *al.*, 2004	Peak *B*
ST film	75K	110	2×10^{-13}	Attributed to dynamic response of domain walls that occur at cubic-to-tetragonal phase transition.	Yu et *al.*, 2002	Peak *B*
	165K	250	3.2×10^{-12}	Related to oxygen vacancies.	Yu et *al.*, 2002	Peak *C*

In the current study, the loss peak *A* is characteristic of ST films prepared without and with buffer layers and annealed at 900°C (ST 900°C and ST 2l 900°C, respectively). The values calculated for peak *A* varied between U=27meV and $\tau_0=4\times10^{-10}$s for ST 900°C and $U=53$meV and $\tau_0=35\times10^{-15}$s for ST 2l 900°C (Table 4.2) are very different to compare to relaxation dynamics of low-temperature peak detected in ST single crystals, for which U=5.7-13.6meV and $\tau_0=2\times10^{-8}$ - 2.5×10^{-12}s [Viana et *al.*, 1994; Bidault et *al.*, 1995] (Table 4.3). One of the proposed mechanisms for this low-temperature loss peak in ST crystal attributed to polaronic relaxation [Bidault et *al.*, 1995]. It is possible to suppose in the case of polaronic relaxation in the analyzed films, that increasing of annealing temperature leads to acceleration of the hopping of the polarons between lattice sites that leads to observation of high intensity and well detected peak *A* in the samples annealed at high temperature (ST 900°C and ST 2l 900°C). Although the variations between all samples are not clear at the moment and further studies are required.

The dielectric loss of ST 750°C is characterised by a peak *B* at ~87K, that by analogy with the reported literature can be attributed to the dynamics of the elastic domain walls that occur at the cubic-to-tetragonal phase transition around 105K in ST single crystals [Mizaras and Loidl, 1997; Viana et *al.*, 1994; Ang et *al.*, 2000c]. The calculated parameters for peak *B* U=151meV and $\tau_0=26.0\times10^{-15}$s (Table 4.2) are close to the values U=120meV and $\tau_0=8.0\times10^{-13}$s obtained for ST single crystals [Viana et *al.*, 1994] and to the values U=140meV and $\tau_0=6.4\times10^{-14}$s obtained for ST ceramics [Tkach et *al.*, 2004] and to the values U=110meV and $\tau_0=2\times10^{-13}$s obtained for ST films [Yu et *al.*, 2002]. Because peak *B* is only visible for ST 750°C films it is suggested that with the increase of the stress value (Fig.4.10), due to the increase of the annealing temperature, a change of the dynamics of the elastic domain walls occurs and peak *B* is not visible in ST 900°C films. However, ST 2l 750ºC and ST 21 900ºC samples presented low value of stress but did not show such peak B and it is not clear at the moment and further studies are required.

Finally, one more peak, peak *C* with a temperature maximum around ~172K-188K at 10kHz was detected. Similar peak at ~165K-175K was observed in some thin films [Li et *al.*, 1998a; Xi et *al.*, 1999] though in several ST films and crystals such peak is absent as well [Ang et *al.*, 2001a; Ang et *al.*, 2001b; Mizaras et *al.*, 1997; Viana et *al.*, 1994]. Because it is well known that oxygen vacancies are a common defect in ST thin films as well as in single crystals and ceramics, and by analogy with the literature, it was assumed

that this loss peak *C* is related to the reorientation of oxygen-vacancy dipoles [Lemanov et *al.*, 2002]. Arrhenius law parameters of the loss peak *C*, related to the thermally activated jumps of the oxygen vacancies around the impurity ions and well observed in ST 2l 750°C, were calculated to be U=250meV and $\tau_0=1.2\times10^{-12}$s (Table 4.2). Very similar values of U=250meV and $\tau_0=3.2\times10^{-12}$s for ST films deposited on ST substrates by PLD were also reported (Table 4.3) [Yu et *al.*, 2002].

4.4.2. *dc* field effect and dielectric tunability

In the current work the real part of the dielectric permittivity ε' of ST thin films deposited under different processing conditions: ST 750°C, ST 900°C, ST 2l 750°C and ST 2l 900°C was measured as a function of temperature at selected *dc* applied fields and plotted in Figure 4.14. Description of this measurement was done in "Chapter 3".

For all presented in Figure 4.14 samples as the applied *dc* electric field increases the ε' decreases. As it was mention before in the "Chapter 2", the behaviour of ε' in ST films is similar to that of ST single crystals and ceramics: the ε' decreases with increasing of the applied field and the broad peak that appears with increasing of the voltage shifts to high temperature [Saifi and Cross, 1970].

It is possible to observe from Figure 4.14, that behaviour of $\varepsilon'(E_{dc})$ is similar for studied ST films but *dc*-field effect on ε' is different for analyzed films. And the smallest influence of applied field is found for ST 750°C films (Fig.4.14a). With increasing of annealing temperature, the effect of field on ε' increases for sample ST 900°C (Fig.4.14b). Meanwhile, incorporation of 2 buffer layers and heat treatment after that also leads to changing of effect field on ε' for sample ST 2l 750°C (Fig.4.14c). Such way, in comparison, the highest dependence of bias on ε' was found for ST 2l 900°C prepared by "two-steps" procedure (Fig.4.14d). Moreover, all studied ST films show ε' decreases with increasing of the applied field but no clear visible broad peak in $\varepsilon'(T)$ that appears with increasing of the voltage as it was found in bulk ST [Saifi and Cross, 1970].

For the characterisation of the dependence of ε' on the applied *dc* bias electric field parameter of tunability was introduced and described in the "Chapter 2". So, for ST thin films prepared under different conditions and analyzed here, relative tunability was calculated by the formula:

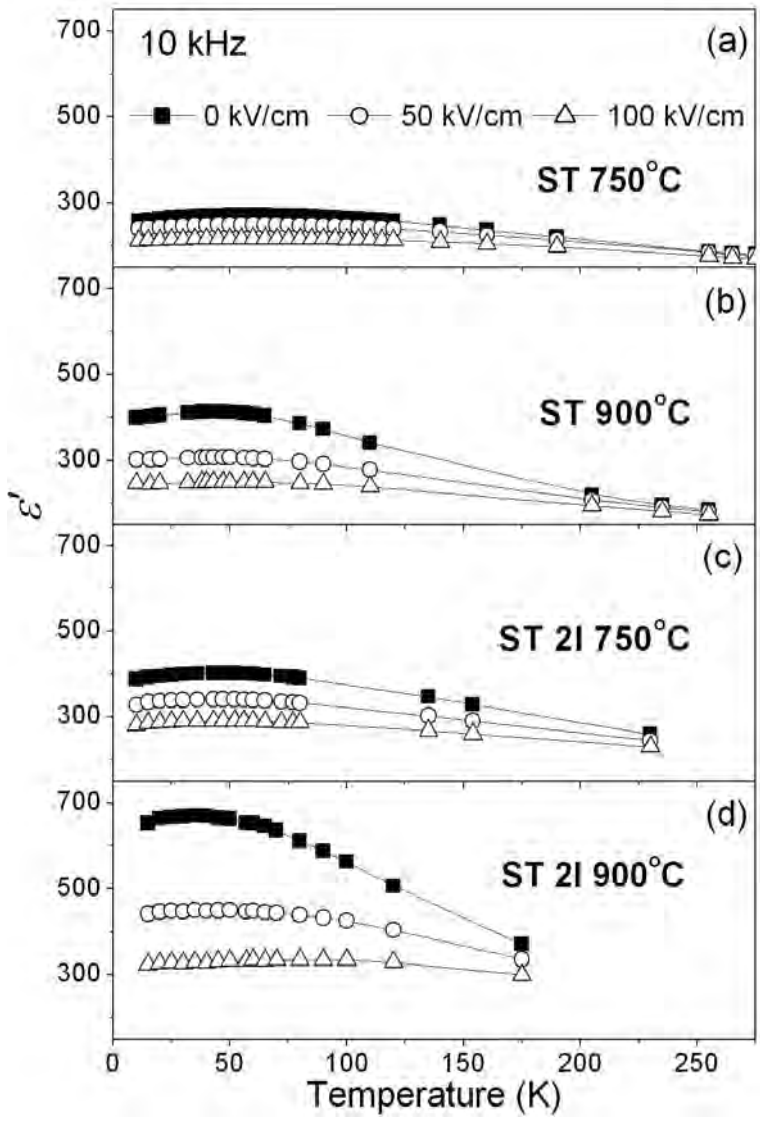

FIGURE 4.14. Temperature dependence of real part of the dielectric permittivity ε' of $SrTiO_3$ thin films prepared under different conditions: "one-step" procedure and annealed at 750°C (ST 750°C) (a) and 900°C (ST 900°C) (b), and "two-steps" procedure and annealed at 750°C (ST 2l 750°C) (c) and 900°C (ST 2l 900°C) (d) under different bias fields at 10kHz.

$$n_r = [\varepsilon'(E=0) - \varepsilon'(E)] / \varepsilon'(E=0) \times 100\% \quad (4.5)$$

where $\varepsilon'(E=0)$ stands for the real part of dielectric permittivity at zero bias and $\varepsilon'(E)$ for the real part of dielectric permittivity at the applied *dc* electric field.

For better understanding how ε', tanδ and relative tunability n_r of ST 750°C, ST 900°C, ST 2l 750°C and ST 2l 900°C depend on applied *dc* electric field, these sample were measured at 10kHz and are presented in Figure 4.15 at selected temperatures.

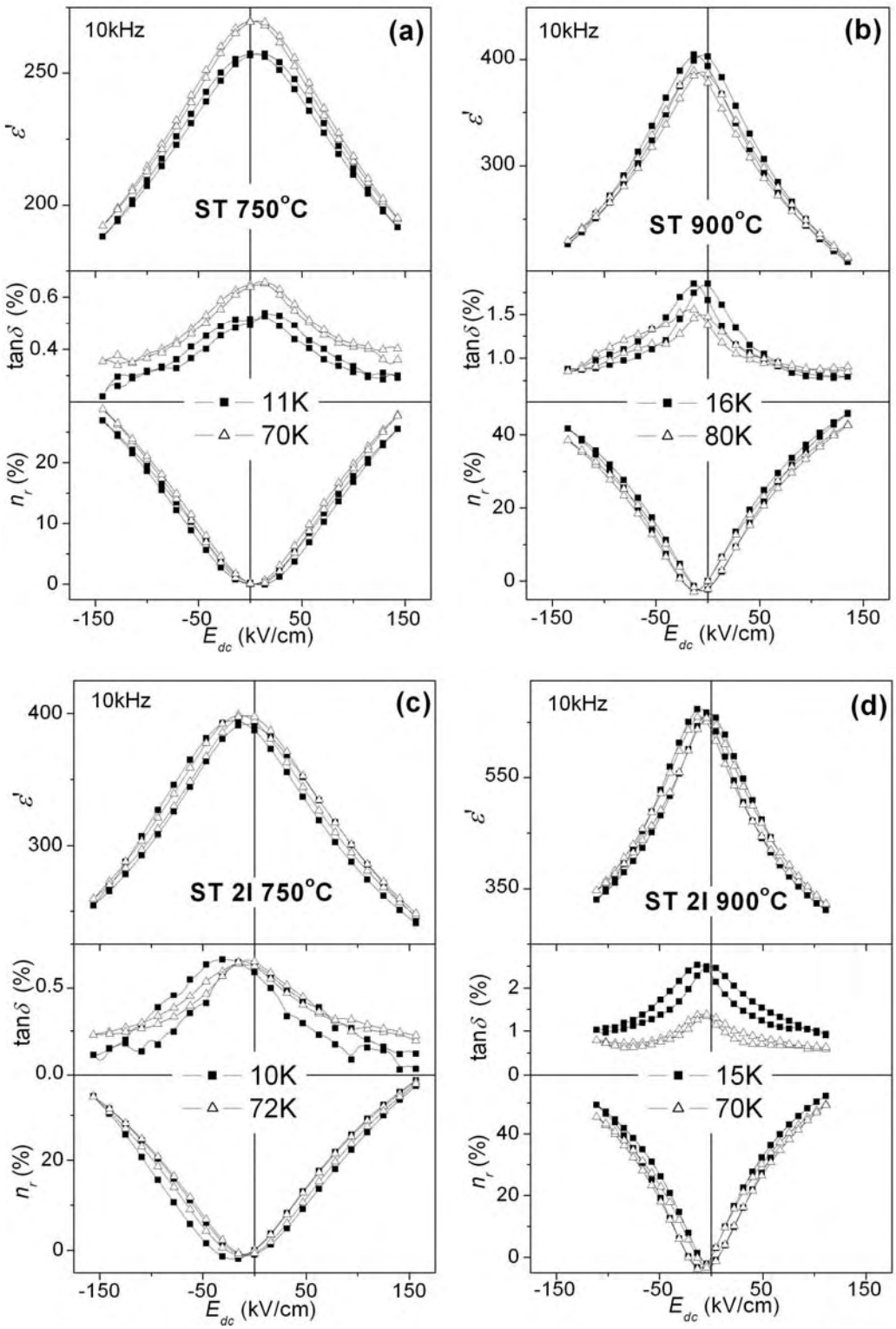

FIGURE 4.15. Field dependence at selected temperatures of real part of dielectric permittivity ε' (*top panel*), tanδ (*middle panel*) and relative tunability n_r (*bottom panel*) of $STiO_3$ films prepared under different conditions: "one-step" procedure and annealed at 750°C (ST 750°C) (a) and 900°C (ST 900°C) (b), and "two-steps" procedure and annealed at 750°C (ST 2l 750°C) (c) and 900°C (ST 2l 900°C) (d) at 10kHz.

It is possible to conclude from the Figure 4.15, that:

1. ε', tanδ and n_r are dependent on applied field, but almost do not changed for presented temperatures.
2. ε', tanδ and n_r show very thin hysteresis loops at both presented temperatures.
3. ST films annealed at 900°C (ST 900°C and ST 2l 900°C) represent more narrow form of $\varepsilon'(E_{dc})$, tan$\delta(E_{dc})$ and $n_r(E_{dc})$, what means stronger dependency on applied field compare to that of films annealed at low temperature (ST 750°C and ST 2l 750°C).
4. Used high annealing temperature and following intermediate heat treatment after buffer layers lead to increasing of field influence on values of $\varepsilon'(E_{dc})$ and $n_r(E_{dc})$ in films deposited by "two-steps" procedure (ST 2l 750°C and ST 2l 900°C) compare to samples prepared by "one-step" procedure (ST 750°C and ST 900°C).
5. Increasing of annealing temperature as well as incorporation of buffer layers do not show serious increasing of field influence on value of tanδ (E_{dc}) of the samples deposited in "one-step" (ST 750°C and ST 900°C) and samples obtained in "two-steps" (ST 2l 750°C and ST 2l 900°C).

Due to the relative dielectric tunability n_r is the useful and quantitative characteristic of field effect on ε', the temperature dependence of n_r of all analyzed ST films prepared under different processing conditions presented in Figure 4.16 at 100kV/cm at 10kHz.

n_r of all studied ST films increases with decreasing of measured temperature what is typical for ST films. n_r shows the lowest value for ST 750°C films (~21% in the maximum at ~55K) and increases for ST 2l 750°C film, when intermediate heat treatment was done, (~28% in the maximum at ~40K) or with increasing of annealing temperature ST 900°C films (~41% in the maximum at ~30K). The highest value of n_r was observed for ST 2l 900°C films (~54% in the maximum at ~55K). Such increasing of n_r with increasing of annealing temperatures could be explained by higher value of measured ε' at E_{dc}=0 for ST 900°C and ST 2l 900°C compare to ε' at E_{dc}=0 for ST 750°C and ST 2l 750°C.

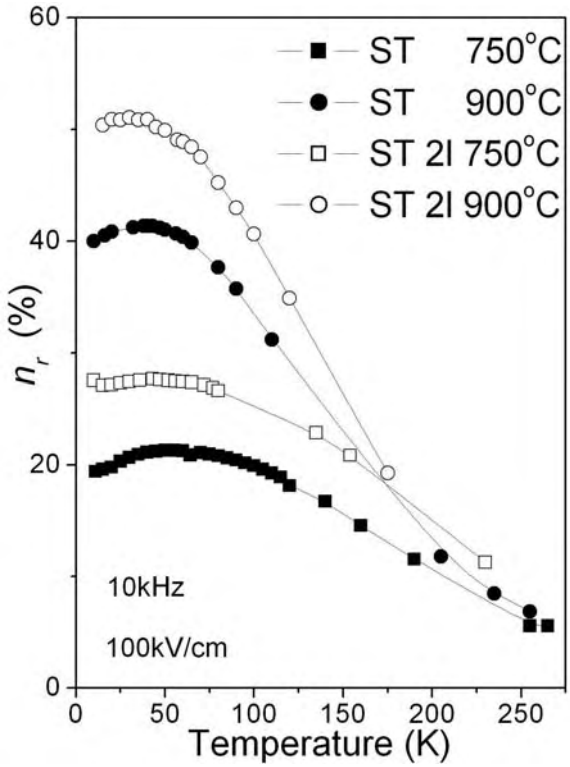

FIGURE 4.16. Temperature dependence of the relative dielectric tunability n_r of $SrTiO_3$ films prepared under different conditions: "one-step" procedure and annealed at 750°C (ST 750°C) and 900°C (ST 900°C), and "two-steps" procedure and annealed at 750°C (ST 2l 750°C) and 900°C (ST 2l 900°C) at 10kHz and 100kV/cm.

However, it is difficult to compare the values of n_r of analyzed ST films to those from others group due to experimental factors such as the range of the applied electric field, the different temperature taken, different measurement frequencies and calculated formula, for example, Hodak and Rogers reported about n_r ≈67% at 4V/μm 2GHz 4K for 400nm ST film deposited by PLD directly on $NdGaO_3$ substrate [Hodak and Rogers, 2008]; Li and co-authors presented n_r ≈70% up 100K at 40-50V/μm 1kHz for 2.5μm ST film obtained by PLD on $SrRuO_3/LaAlO_3$ substrate [Li et *al*., 1998a]; Yamada and co-workers calculated tunability as $n=\varepsilon'(0)/\varepsilon'(E)$ equal to 1.3 at 100kV/cm 8GHz 78K for 250nm ST film fabricated by PLD on $LaAlO_3$ substrate [Yamada et *al*, 2005b].

Thus, the influence of *dc* field on dielectric properties of ST films is strongly dependent on conditions of the preparation of the samples. And in the current work deposition of the buffer layers and increasing of the annealing temperature from 750°C to 900°C leads to increasing of tunability in 2 times and obtained values of tunability (n_r~54% for ST 2l 900°C films) look significant for tunable device application.

4.4.3. *P(E)* hysteresis response

To test the ferroelectric properties of $SrTiO_3$ films prepared under the different conditions the polarization *P* versus applied *ac* field *E* (*P(E)*) hysteresis loops was measured at 100Hz under applied *ac* fields up to ~5V at different temperatures for ST 750°C, ST 900°C, ST 2l 750°C ST 2l 900°C, as described in the "Chapter 3" and are displayed in Figures 4.17-4.20 at 15K and 100K.

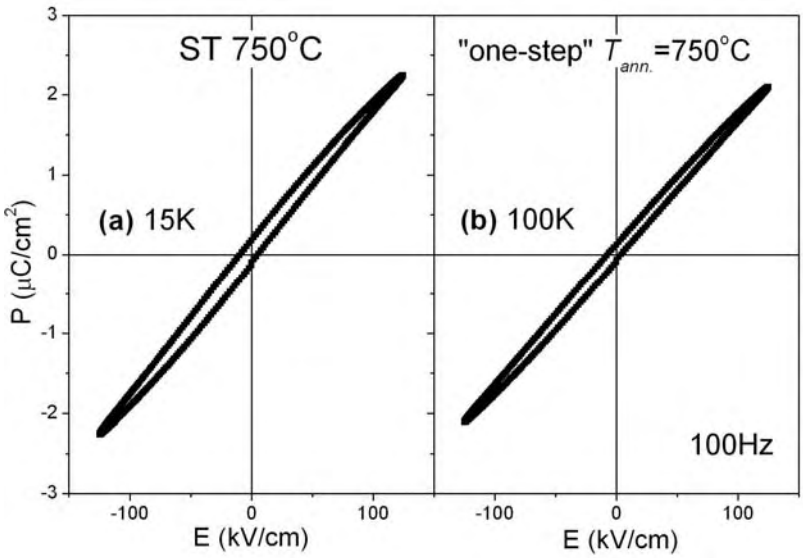

FIGURE 4.17. Hysteresis loops *P(E)* of $SrTiO_3$ films prepared by "one-step" procedure and annealed at 750°C (ST 750°C) at 15K (a) and 100K (b) at 100Hz.

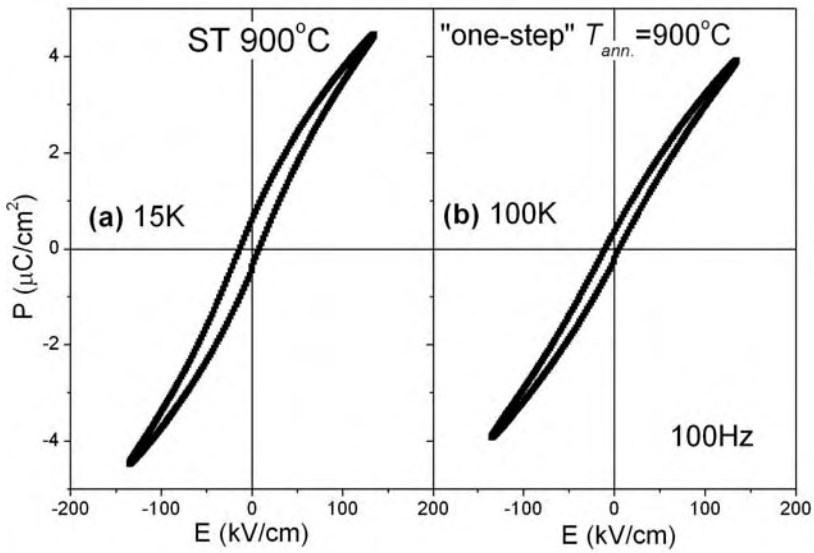

FIGURE 4.18. Hysteresis loops *P(E)* of $SrTiO_3$ films prepared by "one-step" procedure and annealed at 900°C (ST 900°C) at 15K (a) and 100K (b) at 100Hz.

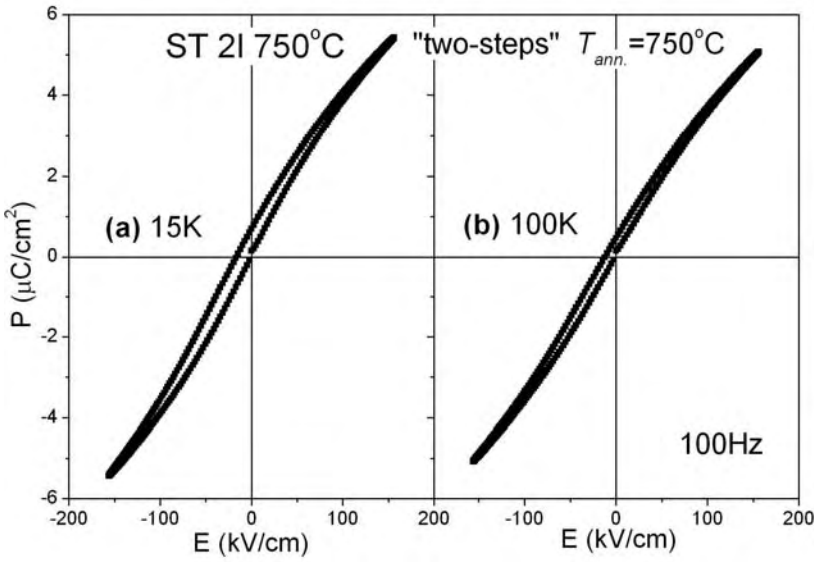

FIGURE 4.19. Hysteresis loops *P(E)* of $SrTiO_3$ films prepared by "two-steps" procedure and annealed at 750°C (ST 2l 750°C) at 15K (a) and 100K (b) at 100Hz.

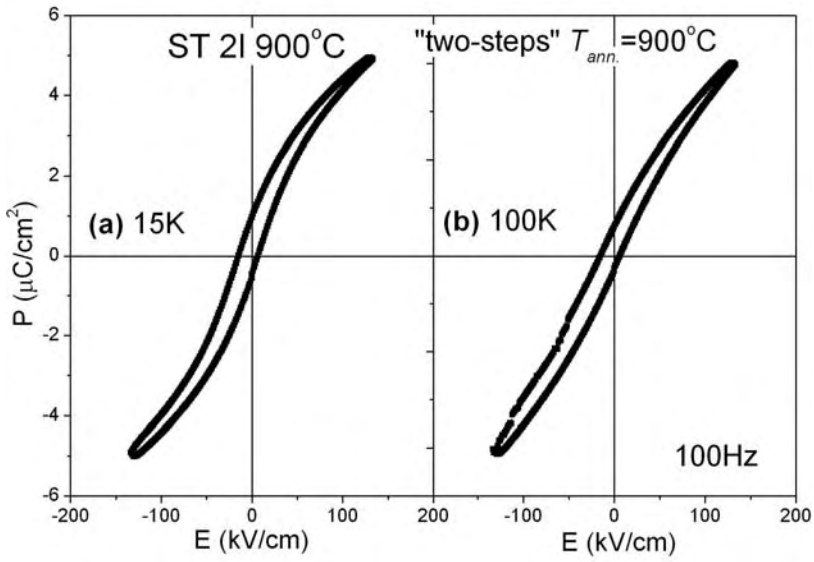

FIGURE 4.20. Hysteresis loops *P(E)* of $SrTiO_3$ films prepared by "two-steps" procedure and annealed at 900°C (ST 2l 900°C) at 15K (a) and 100K (b) at 100Hz.

The obtained loops have different shapes as well as different remnant polarization P_r and coercive field E_c values. An almost linear behaviour of *P(E)* was observed for ST 750°C sample for both selected temperatures (Fig.4.17) and the loop becomes more closed with increasing of measured temperature.

In contrast to ST 750°C (Fig.4.17) the *P(E)* of ST 900°C samples reveals a non linear behaviour with small *s*-shape curve (Fig.4.18). E_c decreases with increasing of measured temperature and the hysteretic curve becomes more linear.

Similar to hysteresis response of ST 900°C sample (Fig.4.18) ST 2l 750°C thin films shown slim *s*-shaped loops at both selected temperatures but with different E_c (Fig.4.19). The obtained loops for ST 2l 750°C are also very thin (Fig.4.19). However, loops of analyzed ST 2l 750°C films show higher magnitude of P and E_c compare to it of ST film annealed at the same 750°C but deposited in "one-step" (ST 750°C) (Fig.4.17).

Nice *s*-shaped loops and high magnitude of *P(E)* is observed for ST 2l 900°C films for selected 15K and 100K (Fig.4.20). The changing from almost linear behaviour of *P(E)* for ST 750°C (Fig.4.17) to *s*-shaped loops for ST 2l 900°C (Fig.4.20), observed at both presented temperatures, suggests the appearance of a polar state with non-zero remnant polarization P_r.

For better visual comparison, hysteresis loops measured at 15K of all studied films presented together in Figure 4.21 and values of P_r and E_c were calculated and presented in Table 4.4.

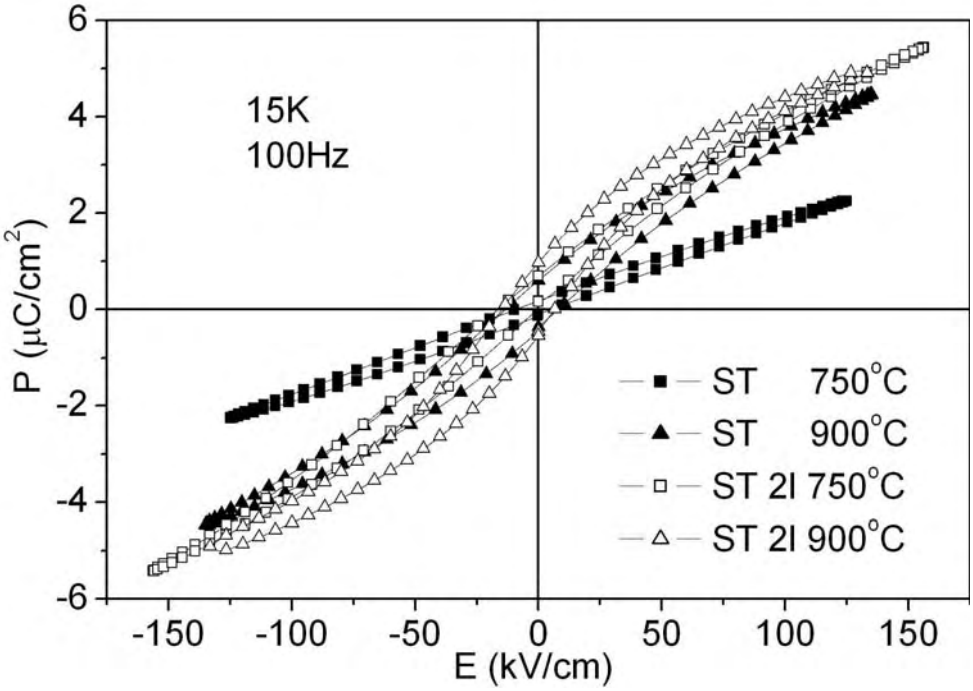

FIGURE 4.21. Hysteresis loops *P(E)* of $SrTiO_3$ thin films prepared $SrTiO_3$ films prepared under different conditions: by "one-step" procedure and annealed at 750°C (ST 750°C) and 900°C (ST 900°C), and by "two-steps" procedure and annealed at 750°C (ST 2l 750°C) at 750°C (ST 2l 750°C) and 900°C (ST 2l 900°C) at 15K at 100Hz.

TABLE 4.4. Remnant polarization P_r and coercive field E_c obtained from hysteresis loop measurements at 15K and 100K for $SrTiO_3$ thin films prepared under different conditions: by "one-step" procedure and annealed at 750°C (ST 750°C) and 900°C (ST 900°C), and by "two-steps" procedure and annealed at 750°C (ST 2l 750°C) at 750°C (ST 2l 750°C) and 900°C (ST 2l 900°C).

Compositions	P_r, μC/cm^2		E_c, kV/cm	
	at 15K	at 100K	at 15K	at 100K
ST 750°C	0.14	0.09	7.8	5.9
ST 900°C	0.48	0.27	10.5	8.4
ST 2l 750°C	0.43	0.35	9.5	7.3
ST 2l 900°C	0.72	0.43	10.6	10

From the Figure 4.21 and Table 4.4 it can be concluded:

1) For all samples P_r and E_c increase with increasing of annealing temperature.
2) Deposition of buffer layers lead to better *s*-shape hysteresis loops and higher value of P_r and E_c for ST films annealed at similar temperature: ST 2l 750°C compare to ST 750°C and ST 2l 900°C compare to ST 900°C.

So, it seems that hysteresis response (appearance of hysteresis loops) is related with the degree of crystallinity of the analyzed sample. Thus, the changing behaviour of *P(E)* from almost linear for ST 750°C (Fig.4.17) to nice *s*-shaped loops for ST 2l 900°C (Fig.4.20), is clear indication of a relaxor like state with non-zero P_r as result of increasing of annealing temperature and intermediate heat treatment after buffer layers deposition.

Summary

$SrTiO_3$ thin films were deposited by sol-gel method on $Si/SiO_2/TiO_2/Pt$ substrates under different processing conditions: by "one-step" procedure and annealed at 750°C (ST 750°C) and 900°C (ST 900°C), and "two-steps" procedure and annealed at 750°C (ST 2l 750°C) and 900°C (ST 2l 900°C). The main results of microstructure, structure and dielectric properties study of these samples are:

1. Modification of the deposition procedure by the inserting of buffer layers and increasing of annealing temperature makes strong effect on value of stress of films

what leads to changing of microstructure, structure and dielectric properties.

2. According to XRD data all analyzed samples have no preferable orientation and their spectra are typical for $SrTiO_3$. However, samples with buffer layer have more distorted lattice ($a<c$) what is differ from that of the samples without buffer layer ($a \approx c$). It explained as in-plane clamping effect between the already annealed buffer layer and the lattice cells of next deposited layers in the samples prepared by "two-steps" procedure. Meanwhile, a and c increase with increasing of the final annealing temperature, what means that all analyzed films are under thermal stress during heat treatment.
3. In accordance to SEM and AFM in-plane observations the grain size increases with annealing temperature but decreases for ST films with buffer layers, similarly to the roughness behaviour. And it could be due to clamping effect which occurs in the samples prepared by "two-steps" procedure between annealed already buffer layers and deposited on them the main film.
4. Incorporation of buffer layers, that decreases mismatch strain, and intermediate heat treatment, that leads to improving of crystallinity, result on decreasing of the total stress in full deposited films prepared by "two-steps" procedure. As result, dielectric properties of ST films prepared by "two-steps" procedure shown higher values of ε' and stronger dependency on *dc* electric field and consequently tunability than samples without buffer layer.
5. More obvious *s*-shape hysteresis loops in *P(E)* measurements was found for ST films prepared by "two-steps" procedure. Average values of P_r and E_c for these samples were also calculated higher than that for samples without buffer layers. Meanwhile, well observed hysteresis loops of ST films deposited by "one-step" procedure and annealed at 900°C were found more similar to that of sample deposited by "two-steps" procedure and annealed at 750°C than to linear-type of loop of films deposited also by "one-step" procedure and annealed at low 750°C. Thus, increasing of annealing temperature leads to increasing of *s*-form of hysteresis loop in *P(E)* analyse.

Chapter 5. Polycrystalline $SrTiO_3$ thin films: influence of substrate on the microstructure, structure and low temperature dielectric properties

In this chapter the study of the influence of the substrate (through strain/stress) on the microstructural and structural properties of undoped polycrystalline $SrTiO_3$ films is presented. For that thin $SrTiO_3$ films were deposited by sol-gel on Al_2O_3/Pt, Si/SiO_2/TiO_2/Pt, $(LaAlO_3)_{0.3}$-$(Sr_2AlTaO_6)_{0.7}$/Pt, $SrTiO_3$/Pt and MgO/Pt substrates. Results of dielectric measurements of these films as a function of frequency f and temperature T are also presented. ε' versus *dc* electric field E_{dc} and polarization P versus *ac* electric field E of $SrTiO_3$ films prepared on different substrates are analyzed as well The resulting data show that $SrTiO_3$ films deposited on Al_2O_3/Pt substrates are under the highest tensile total stress and represent the lowest value of ε', and the lowest influence of *dc* and *ac*-field. At the same time, $SrTiO_3$ films deposited on MgO/Pt substrates are under the highest compressive total stress and have the highest value of ε', tunability and hysteresis response.

Introduction

It is well known and mentioned before, that thin-film form $SrTiO_3$ (ST) exhibits lower dielectric permittivity and higher dielectric loss than its single-crystal counterpart and the reasons behind this are not yet very clear. Some of the reasons indicated for this lowering of permittivity in ST films have been strains [Chang et *al.*, 1999], the effect of a "dead layer" at the interface between the substrate and the film [Zhou and Newns, 1997], local polar regions near the charged defects like oxygen vacancies [Sirenko et *al.*, 1999], inter alia.

Thin films on substrates are generally not in a stress free state. During the film processing, owing to lattice mismatch, differences in thermal expansion coefficient (TEC) and phase transformations, stresses arise [Pertsev et *al.*, 1999]. These stresses may either be tensile or compressive. Due to the mechanical interaction with a much thicker substrate, the film is clamped in two dimensions and strained to a certain extent.

Stresses may: *i)* induce anisotropy of dielectric properties (out-of-plane and in-plane),

ii) induce the rotation of spontaneous polarization relatively to film plane (out-of-plane into in-plane polarization) [Emelyanov et *al.,* 2002], *iii)* shift the Curie temperature T_c [Rossetti et *al.* 1991] and hence dramatically change the dielectric (and piezoelectric) constant [Streiffer et *al.*, 1999; Taylor et *al.*, 2002]; *iv)* determine the type of dielectric anomaly (sharp or diffuse) [Tagantsev et *al.*, 2001], and critically affect the dielectric loss of both intrinsic (caused by optical-phonon interaction with the applied electric field) and extrinsic (caused by lattice defects/films processing/substrate) nature [Tagantsev et *al.*, 2003]. It was shown that crystalline $SrRuO_3$, $YBa_2Cu_3O_7$ and amorphous buffer layers as well as annealing treatments decrease residual stresses of the thin films deposited on their top, reducing loss [Li et *al.*, 1998a; Knauss et *al.*, 1996]. Thus, the evolution of strain during *in situ* growth and subsequent cooling is a complex process, and a clear understanding of the nature of strain in ferroelectric and incipient ferroelectric thin films is of both scientific and technological importance.

As mentioned before in epitaxial film systems it was predicted that the mismatch strain between the film and the substrate can suppress the stable ferroelectric phase [Pertsev et *al.,* 1998; Pertsev et *al.,* 1999]. Corroborating this theoretical prediction [Pertsev et *al.,* 2000b], it was observed a ferroelectric anomaly at room temperature in in-plane strained epitaxial ST films on $DyScO_3$ substrates [Haeni et *al.,* 2004].

However, the stress effect in *polycrystalline* films is more complicated when compared to epitaxial ones and has been less studied. In this way, the influence of stress, including lattice strain and thermal stress during heat treatment, on the properties of ST thin films deposited on different substrates by sol-gel was studied in current work. A series of substrates, that include Al_2O_3/Pt, $(LaAlO_3)_{0.3}$-$(Sr_2AlTaO_6)_{0.7}$/Pt, Si/SiO_2/TiO_2/Pt, $SrTiO_3$/Pt and MgO/Pt, were used in this study due to their different values of lattice parameters and TEC's what lead to different values of total stress and different influence on the properties of films. The variation of electrical properties and tunabilities on a wide temperature range of ST films deposited on different substrates is presented.

5.1. Preparation and characterisation

ST films were deposited by sol-gel on 5 different substrates: Al_2O_3/Pt, $(LaAlO_3)_{0.3}$-$(Sr_2AlTaO_6)_{0.7}$/Pt (designated as LSAT/Pt), Si/SiO_2/TiO_2/Pt (designated as Si/…/Pt), $SrTiO_3$/Pt (designated as ST/Pt) and MgO/Pt. Some characteristics of the substrates are

recalled in Table 5.1.

Using the prepared transparent solutions of ST, layers of sol were deposited on Al_2O_3/Pt, Si/…/Pt, LSAT/Pt, ST/Pt and MgO/Pt substrates by spin-coating and after drying all the obtained films were annealed at 900°C for 60min. in air, as described in the "Chapter 3". Lattice parameters and strain measurements were performed by XRD. The microstructure of films was studied by SEM, AFM and TEM. The dielectric response capacitance-voltage, *dc*-field and hysteresis loops of ST films were assessed in a wide range of temperature and frequency. IR transmittance and Raman scattering measurements were performed from 300K to 10K for ST films deposited on Al_2O_3 and MgO substrates, as well.

TABLE 5.1. The lattice parameters and Thermal Expansion Coefficients (TEC's) of the substrates used in the current Chapter.

	Al_2O_3	Si	LSAT	$SrTiO_3$	MgO
Lattice parameter (Å) (data from the supplier company)	3.730	3.841	3.868	3.903	4.203
TEC, $\times 10^{-6}/^oC$ (data from the supplier company)	5.4||a, 6.2|c	2.3	10.0	9.0	8.0
TEC, $\times 10^{-6}/^oC$ (measured for $T_{ann.}$=900°C)	7.7	2.1	11.3	10.7	14.3

5.2. Structural characterization

5.2.1. Crystal structure and lattice parameter

The XRD spectra of ST films deposited on the different substrates: Al_2O_3/Pt, Si/SiO_2/TiO_2/Pt (Si/…/Pt), $SrTiO_3$/Pt (ST/Pt), $(LaAlO_3)_{0.3}$-$(Sr_2AlTaO_6)_{0.7}$/Pt (LSAT/Pt) and MgO/Pt are presented in Figure 5.1. These XRD patterns were obtained from a low incident beam angle (LIBAD) experiments ("Chapter 3") with the purpose to subtract the substrate response from the spectra of the studied films. Independently on the substrate all the ST films are monophasic and no preferable orientations or textured structure were observed for any of the films.

To check the presence of any lattice distortion, in-plane *a* and out-of-plane *c* lattice parameters of ST films deposited on the different platinized substrates were calculated from the XRD spectra, plotted in Figure 5.2a and together with the lattice parameters of the

bare substrates (Fig.5.2b, left scale) and presented in Table 5.2.

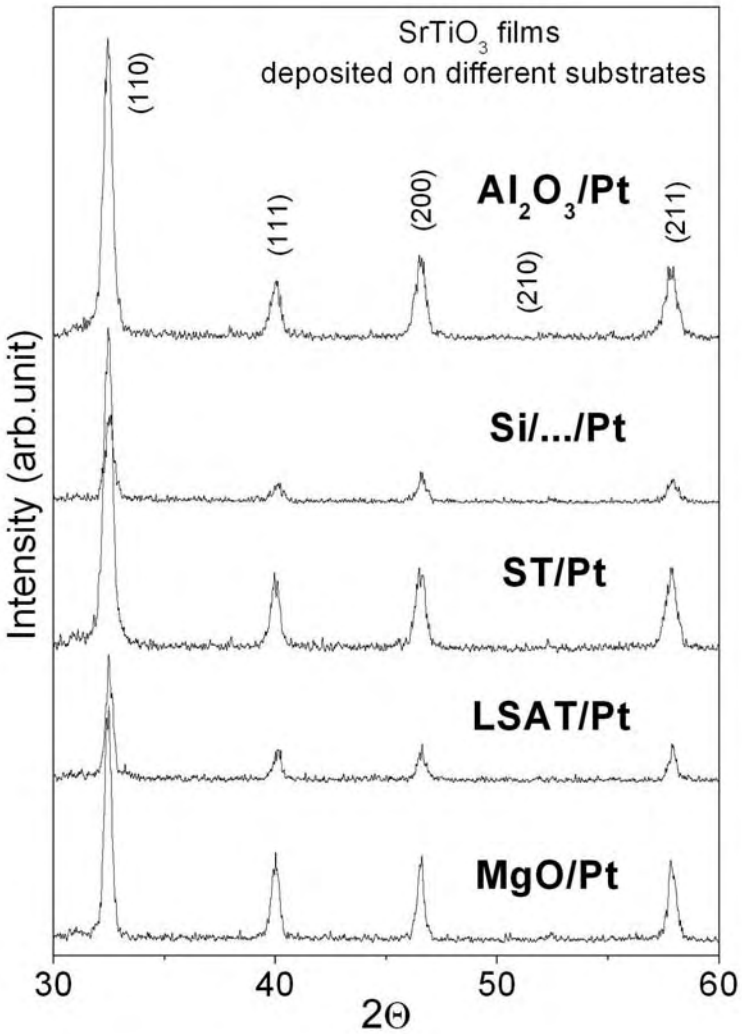

FIGURE 5.1. XRD spectra of $SrTiO_3$ films prepared on different substrates: Al_2O_3/Pt, Si/SiO_2/TiO_2/Pt (Si/…/Pt), $SrTiO_3$/Pt (ST/Pt), $(LaAlO_3)_{0.3}$-$(Sr_2AlTaO_6)_{0.7}$/Pt (LSAT/Pt) and MgO/Pt obtained from low incident beam angle experiments.

The calculated lattice parameters of the prepared films vary for *a* between ~3.9026Å (on MgO/Pt) to the highest value ~3.9107Å (on Si/…/Pt), and for *c* between ~3.9046Å (on LSAT/Pt), to ~3.908Å (on Si/.../Pt) (Table 5.2). All of the analyzed ST films have very similar *a* and *c* lattice parameters (Fig.5.2a), but different from that of single ST crystals that have a cubic structure with a lattice parameter *a*=3.905Å [Mitsui and Westphal, 1961].

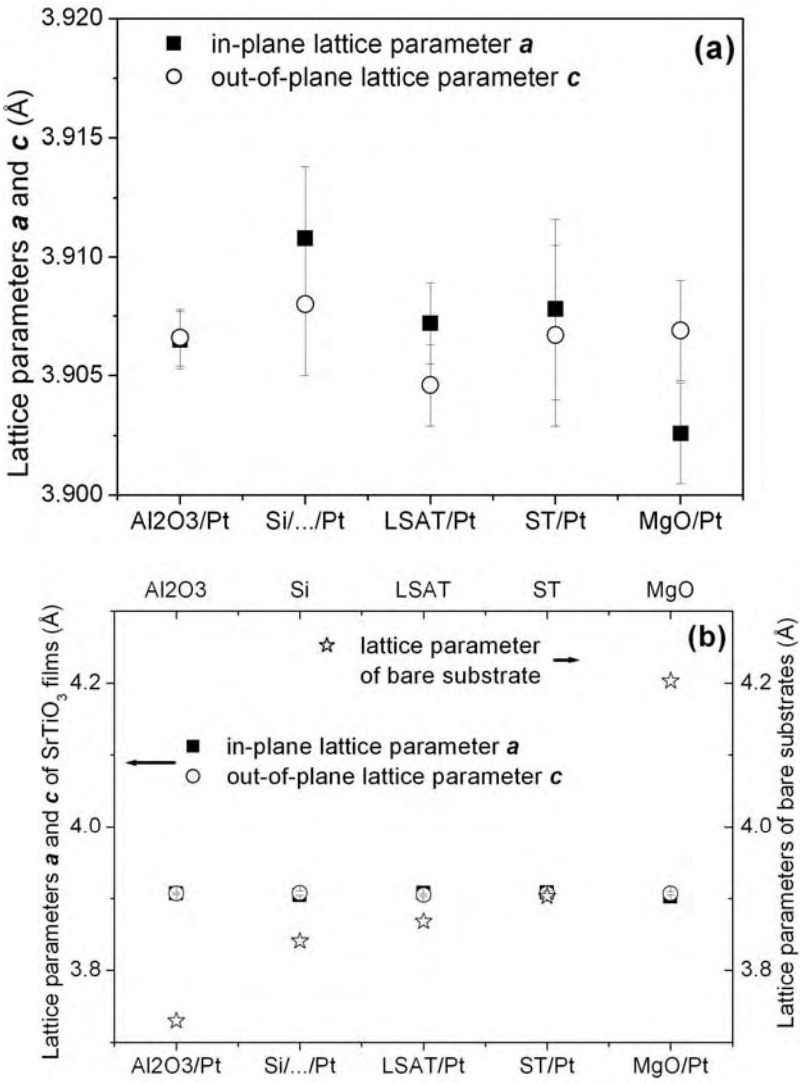

FIGURE 5.2. Lattice parameters *a* and *c* of $SrTiO_3$ films *vs* different substrates: Al_2O_3/Pt, Si/SiO_2/TiO_2/Pt (Si/…/Pt), $(LaAlO_3)_{0.3}$-$(Sr_2AlTaO_6)_{0.7}$/Pt (LSAT/Pt), $SrTiO_3$/Pt (ST/Pt), MgO/Pt (a) and lattice parameters *a* and *c* of $SrTiO_3$ films (*left axis*) *vs* different platinized substrates (*bottom axis*) together with the lattice parameters of bare substrate (*right axis*) Al_2O_3, Si, $SrTiO_3$ (ST), $(LaAlO_3)_{0.3}$-$(Sr_2AlTaO_6)_{0.7}$ (LSAT) and MgO (*top axis*) (b).

However the difference between *a* and *c* of the analyzed ST films and *a* of ST crystals is only about ~0.25%. Thus, from the Figure 5.2a it is possible to state that all of the analyzed ST films possess a very close structure to the ideal cubic of single crystals. At the same time the lattice parameters of the films does not directly reflect the lattice mismatch between the film and the substrate. Moreover, from Figure 5.2b and Table 5.2 the biggest difference is expected for ST films deposited on Al_2O_3 and on MgO substrates (Fig.5.2b).

TABLE 5.2. The in-plane *a* and out-of-plane *c* lattice parameters of $SrTiO_3$ films prepared on different substrates.

Lattice parameters of ST films	Values of lattice parameters of ST films deposited on:				
	Al_2O_3/Pt	Si/…/Pt	LSAT/Pt	ST/Pt	MgO/Pt
a	~3.9065 ±0.0012Å	~3.9107 ±0.003Å	~3.9072 ±0.0017Å	~3.9078 ±0.0038Å	~3.9026 ±0.0021Å
c	~3.9066 ±0.0012Å	~3.908 ±0.003Å	~3.9046 ±0.0017Å	~3.9067 ±0.0038Å	~3.9069 ±0.0021Å

Before choosing the type of substrates for the current study, the *theoretical* in-plane lattice mismatch for ST films deposited directly on bare substrates without Pt was calculated according to the following formula:

$$Lattice\ Mismatch = \frac{a_{sub} - a_{film}}{a_{sub}} \tag{5.1}$$

where a_{sub} and a_{film} are in-plane lattice parameters of substrate and ST film, respectively. However, because the *theoretical* in-plane lattice mismatch was calculated before deposition of ST film, in this calculation, the lattice parameter of bulk ST a_{STbulk} (3.905Å) was used as in-plane lattice parameter of ST film a_{film}. Obtained results are presented in Figure 5.3.

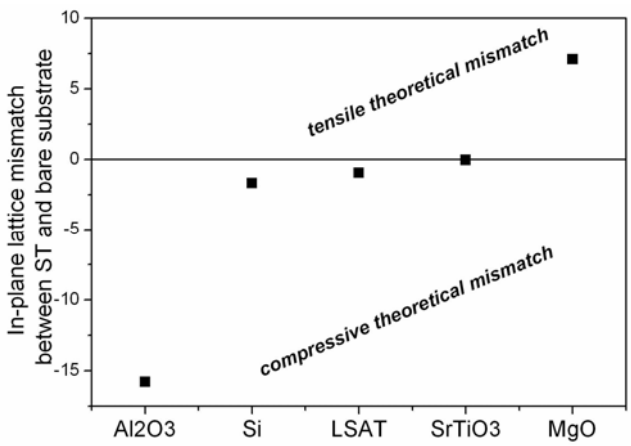

FIGURE 5.3.Theoretical in-plane lattice mismatch for $SrTiO_3$ films deposited on bare Al_2O_3, Si, $(LaAlO_3)_{0.3}$-$(Sr_2AlTaO_6)_{0.7}$ (LSAT), $SrTiO_3$ and MgO substrates without Pt.

The highest value of the *theoretical* in-plane lattice mismatch for analyzed samples was predicted for ST films on Al_2O_3, with a compressive in-plane lattice mismatch of ~15% and on MgO with a tensile in-plane lattice mismatch of ~7%. The other substrates provide small compressive in-plane lattice mismatch: ~1.7% on Si, ~0.9% on LSAT and ~0.1% on ST substrates.

However, for further dielectric measurements of ST films analyzed in current Thesis, Pt layer was deposited on all the substrates and the *theoretical* in-plane lattice mismatch for ST films deposited on substrates with Pt was recalculated again by Eq.5.1 with a_{STbulk} as a_{film}, and a_{Pt} (~3.912Å) as $a_{substrate}$. In this case the theoretical in-plane mismatch between ST and Pt is ~0.18% and it is equal for all the analyzed samples deposited on platinized substrates (Fig.5.4 *open circle*).

However, after deposition of ST films on different substrates with Pt following in-plane lattice parameters *a* values were obtained from XRD spectra: ~3.906Å on Al_2O_3/Pt, ~3.9108Å on Si/…/Pt, ~3.907Å on LSAT, ~3.9078Å on ST and ~3.9026Å on MgO/Pt substrates. Thus; the *measured* in-plane lattice mismatch between deposited ST films and platinized substrates was also calculated by Eq.5.1 and presented in Figure 5.4 (solid square) is different for all samples and is not equal to calculated before the *theoretical* in-plane lattice mismatch:

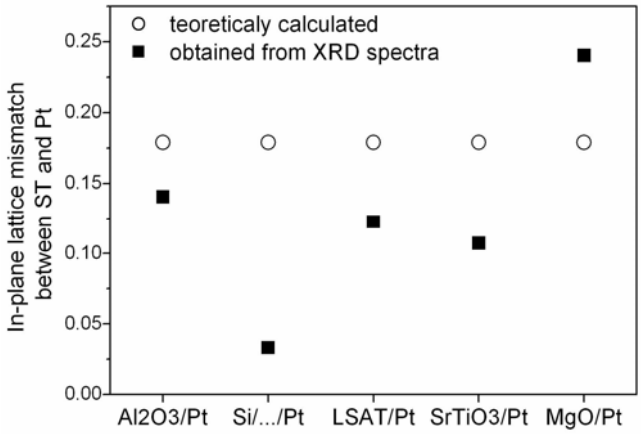

FIGURE 5.4. Theoretical in-plane lattice mismatch (*open circle*) and in-plane lattice mismatch obtained from XRD spectra (*solid square*) of $SrTiO_3$ films deposited on Al_2O_3/Pt, Si/SiO_2/TiO_2/Pt (Si/…/Pt), $SrTiO_3$/Pt (ST/Pt), $(LaAlO_3)_{0.3}$-$(Sr_2AlTaO_6)_{0.7}$/Pt (LSAT/Pt) and MgO/Pt substrates.

The values of theoretical and obtained from XRD in-plane lattice mismatch are not the same for all analyzed ST films. Moreover, values in-plane lattice mismatch obtained from

XRD are very different from ~0.18% (the theoretically calculated in-plane lattice mismatch between ST and Pt), and are dissimilar from the data presented in Figure 5.3, calculated for the case of ST films on bare substrates, as well. All studied ST films shown that the lattice is tensile stressed in in-plane direction: the smallest measured value is ~0.03% for films on Si/…/Pt, intermediate values ~0.10% on ST/Pt, ~0.12% on LSAT/Pt, ~0.14% on Al_2O_3/Pt, and the highest value ~0.24% for the films on MgO/Pt.

Thus, there is a significant difference between the theoretical and real values of in-plane lattice mismatch of ST films deposited on the different substrates. These results clearly show that besides the in-plane lattice mismatch other aspects are playing a determinant role on the final stress state of the films, namely related with the difference between the thermal expansion coefficient of ST and the several substrates. Indeed, it is well known that the total stress state of a film comprises two contributions: the input coming from the lattice mismatch and the input coming from the TEC's difference between films and substrates.

5.2.2. Strain measurements and stress calculations

Strain measurements were conducted as previously described in "Chapter 3" by the XRD $sin^2\ \psi$ method. For that lattice spacings d of a specific (hkl) plane were measured at different tilt angles ψ (inclined exposure). And from the shift of (211) peak of ST as a function of tilt angle ψ, strains were measured. By fitting the (211) peak with a Gaussian function, the central peak position belonging to the $K\alpha$ line were obtained for all ψ values. The lattice spacings d_ψ of ST films deposited on different substrates were then calculated as well as strain $(d_\psi - d_0)/d_0$ and plotted as a function of $sin^2\psi$ in Figure 5.5.

The linear behaviour of the obtained strains of the analyzed samples (Figure 5.3) indicates a homogeneous stress level in all ST films. This fact reinforces the applicability of the $sin^2\ \psi$ method to the calculation of the total stresses in these ST films. The positive slope in these plots indicates that strain in ST film on Si/…/Pt, Al_2O_3/Pt and LSAT/Pt substrates are tensile. And the negative slope of the plots for ST films prepared on ST/Pt and MgO/Pt substrates indicates a compressive strain level for these films.

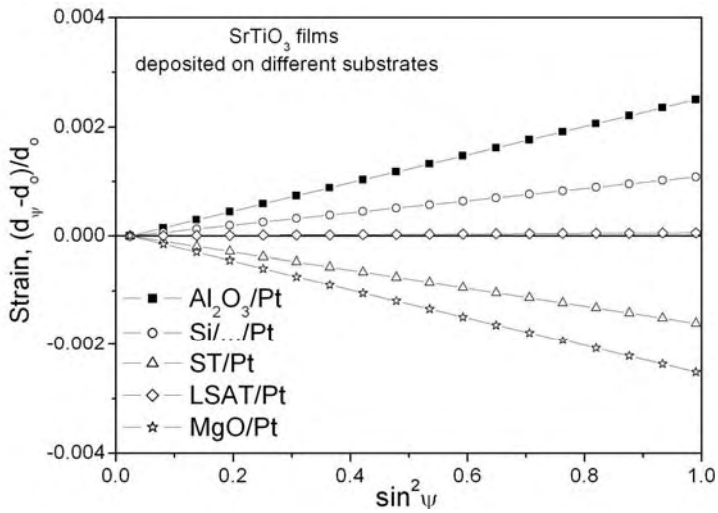

FIGURE 5.5. Strain $(d_\psi - d_0)/d_0$ of $SrTiO_3$ films deposited on different substrates: Al_2O_3/Pt, Si/SiO_2/TiO_2/Pt (Si/…/Pt), $SrTiO_3$/Pt (ST/Pt), $(LaAlO_3)_{0.3}$-$(Sr_2AlTaO_6)_{0.7}$/Pt (LSAT/Pt) and MgO/Pt.

Using the average values of the obtained strain, the stress values can be calculated through the following formula:

$$\sigma = \frac{d_\psi^{hkl} - d_0^{hkl}}{d_0^{hkl}} \times \frac{E}{1+\gamma} \times \frac{1}{\sin^2\psi} \tag{5.2}$$

where E and γ stand for the Young's modulus and Poisson's ratio of the film, respectively, d_ψ for the lattice spacing at each ψ and d_0 for the d value for ψ =0° (perpendicular exposure). As mentioned in the "Chapter 3", E and γ were calculated as E=303GPa and γ=+0.2242.

The resulting values of the average total stress for ST films deposited on different substrates were calculated and plotted in Figure 5.6.

The dependence between the stress values and the type of substrate used grow ST films is very obvious. The highest tensile stress (~611MPa) was calculated for ST films deposited on Al_2O_3/Pt substrates and the highest compressive stress (~-612MPa) was obtained for ST films deposited on MgO/Pt substrates. Apparently the tensile stress of ST on Al_2O_3/Pt will allow the development of a ST lattice with almost no distortion form the cubic structure ($a \approx c$, as it shown in Fig.5.2a), being the opposite valid for the films on MgO characterised by a mechanical compressive state ($a < c$, as it shown in Fig.5.2a). ST films on Si/../Pt and LSAT/Pt substrates show tensile stresses (~256MPa and ~15MPa

respectively) and for samples deposited on ST/Pt substrates compressive stress was calculated (~-114MPa).

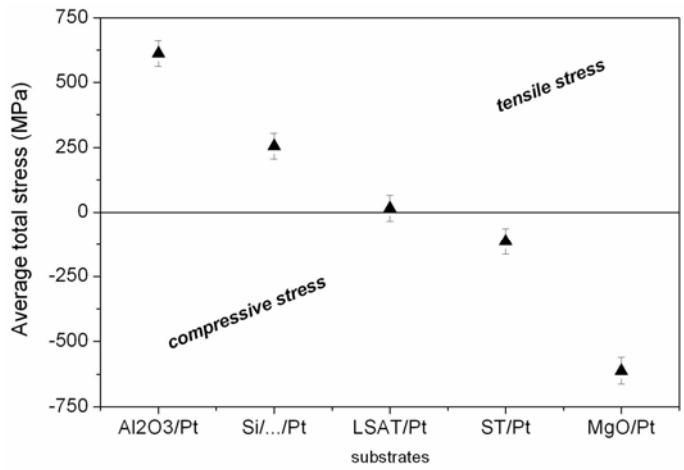

FIGURE 5.6. Values of the average total stress of $SrTiO_3$ films deposited on different substrates: Al_2O_3/Pt, Si/SiO_2/TiO_2/Pt (Si/…/Pt), $SrTiO_3$/Pt (ST/Pt), $(LaAlO_3)_{0.3}$-$(Sr_2AlTaO_6)_{0.7}$/Pt (LSAT/Pt) and MgO/Pt.

It was expected, that ST films deposited on ST substrate, with the same lattice parameters and TEC's, would present zero stress, but, as it is shown in Figure 5.6, ST film on ST substrate has compressive stress. As the possible reasons can be the presence of 150nm-Pt layer on the substrate ST/Pt or influence of thermal stress (described below).

The thermal stress originated during the films cooling process was calculated using the following formula:

$$\sigma_{th} = \int_{RT}^{T_{ann.}} \frac{E}{1-\gamma} \times (\alpha_f(T) - \alpha_{sub}(T))dT \qquad (5.3)$$

where $\alpha_f(T)$ and $\alpha_{sub}(T)$ stand for the temperature dependence of the TEC of ST films and corresponding substrate (Table 5.1), E for the Young's modulus and γ for Poisson's ratio of the film.

From these calculations ST films deposited on Al_2O_3 bare substrates have tensile thermal stress ~1011MPa on Si substrates ~2936MPa (the highest tensile thermal stress, as expected), ~-199MPa for films on LSAT, zero thermal stress for ST films on ST substrates (as expected), and the highest compressive thermal stress ~-1232MPa was found for ST samples on MgO substrates (as was expected) (Fig.5.7 *left axis*).

The calculated theoretical thermal stress of ST films deposited on different bare substrates without Pt layer is presented in Figure 5.7 *left axis* together with TEC's of bare substrates (Fig.5.7 *right axis*) for comparison.

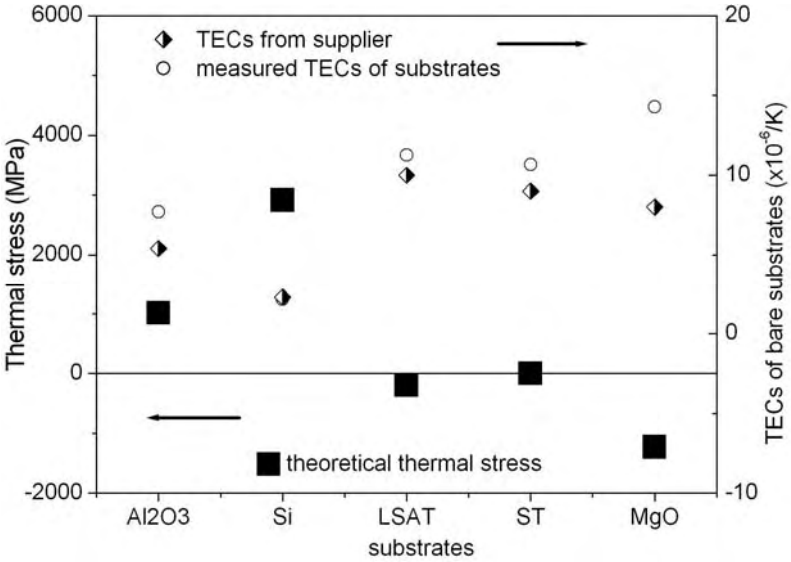

FIGURE 5.7. Calculated values of the theoretical thermal stress (*closed symbol*) for $SrTiO_3$ films deposited on: Al_2O_3, Si, $(LaAlO_3)_{0.3}$-$(Sr_2AlTaO_6)_{0.7}$ (LSAT), $SrTiO_3$ (ST), and MgO substrates without Pt layer. (*left axis*) And TEC's of substrates according to supplier data (*half-closed symbol*) and measured under the current work (*open symbol*) for $T_{ann.}$=900°C (*right axis*).

Values of the obtained from XRD in-plane lattice mismatch (Fig.5.4), the average total stress (Fig.5.6) and the calculated theoretical thermal stress (Fig.5.7) are summarized in Table 5.3 for comparison and discussion.

TABLE 5.3. In-plane lattice mismatch from XRD, average total stress and theoretical thermal stress obtained for $SrTiO_3$ films on different substrates Al_2O_3/Pt, Si/SiO_2/TiO_2/Pt (Si/…/Pt), $SrTiO_3$/Pt (ST/Pt), $(LaAlO_3)_{0.3}$-$(Sr_2AlTaO_6)_{0.7}$/Pt (LSAT/Pt) and MgO/Pt.

Substrate	In-plane lattice mismatch, %	Average total stress, MPa	Theoretical thermal stress, MPa
Al_2O_3/Pt	~0.14	~611	~1011
Si/…/Pt	~0.03	~256	~2963
LSAT/Pt	~0.12	~15	~-199
ST/Pt	~0.10	~-114	0
MgO/Pt	~0.24	~-612	~-1232

Based on Figures 5.4, 5.6, 5.7 and Table 5.3 it is possible to conclude, that:

- for ST films on Al_2O_3/Pt and on MgO/Pt substrates, the theoretical thermal stress is major part of the average total stress;
- for ST films on Si/…/Pt substrates, the average total stress (~256MPa) is much lower than the theoretical tensile thermal stress (~2936MPa). In this case, very high tensile thermal stress is compensated by very high compressive lattice stress for these samples. However, the average *in-plane* lattice mismatch obtained for analyzed films was found small and also tensile (0.03%). Thus, the average *out-of-plane* lattice mismatch should be compressive for analyzed films.
- due to ST films on LSAT/Pt substrates represent the low value of tensile average total stress (~15MPa) their high compressive theoretical thermal stress (~-199MPa) need to be compensated by high tensile lattice stress. Moreover, the *in-plane* lattice mismatch was already calculated as tensile (~0.12%).
- for ST films deposited on ST/Pt substrates the theoretical thermal stress is zero, but total stress is compressive (~-114MPa). It means that lattice stress is the main contributor for the value of the average total stress of ST films deposited on ST/Pt substrates. However, measured *in-plane* lattice mismatch is tensile (~0.10%). Thus, as in case ST film on Si/…/Pt, it could be supposed that lattice stress in *out-of-plane* direction should be compressive.
- for ST films deposited on MgO/Pt substrates, the highest compressive theoretical thermal stress (~-1232MPa) leads to the highest compressive total stress (~-612MPa) for analyzed films. And due to *in-plane* lattice mismatch is tensile (~0.24%), it could be supposed that lattice stress in *out-of-plane* direction in these samples should be compressive.

So, for polycrystalline ST films, prepared on substrates with different TEC's and lattice parameters (but with Pt layer), thermal stress plays the determinant role in the case of Al_2O_3/Pt (shown the highest tensile total stress) and MgO/Pt substrate (shown the highest compressive total stress). For Si/…/Pt and LSAT/Pt substrates both thermal and lattice stress have comparable influence on the film.

5.2.3. Raman analysis

For a better understanding of these films lattice structure, Raman spectroscopy was conducted and Figure 5.8 presents the Raman spectra of ST films deposited on different

platinized substrates: Al_2O_3/Pt, Si/SiO_2/TiO_2/Pt (Si/…/Pt), $SrTiO_3$/Pt (ST/Pt), $(LaAlO_3)_{0.3}$-$(Sr_2AlTaO_6)_{0.7}$/Pt (LSAT/Pt) and MgO/Pt.

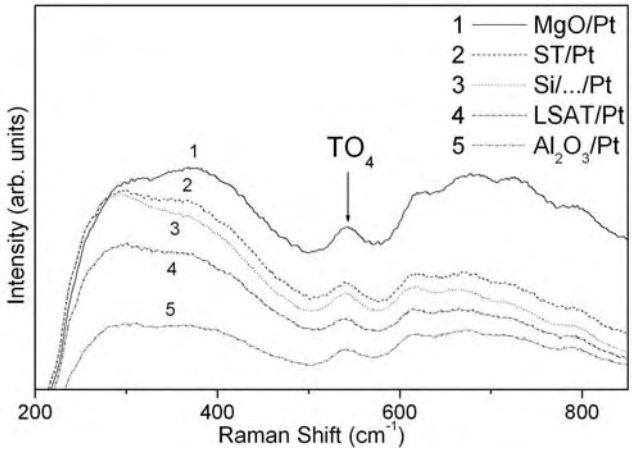

FIGURE 5.8. Raman spectra of $SrTiO_3$ films prepared on different substrates: Al_2O_3/Pt, Si/SiO_2/TiO_2/Pt (Si/…/Pt), $SrTiO_3$/Pt (ST/Pt), $(LaAlO_3)_{0.3}$-$(Sr_2AlTaO_6)_{0.7}$/Pt (LSAT/Pt) and MgO/Pt.

These Raman spectra at room temperature look similar for all the samples in which TO4 mode against the background of second-order features are well observed. The appearance of this TO4 mode at ~547cm^{-1} is similar to the one observed in pure ST bulk [Petzelt et *al.*, 2001] and ST films [Ostapchuk et *al.*, 2002]. No additional information was obtained from these spectra. Such vagueness can be explained by the presence of Pt layer on the used substrates and for a more detailed analysis, ST films were deposited on bare Al_2O_3 and MgO substrates and measured at different temperatures from 300K to 10K (Fig.5.9). These substrates were choosing due to the highest values of tensile (Al_2O_3) and compressive (MgO) total stresses previously calculated.

Except of the modes of the sapphire substrates for the sample on Al_2O_3 (Fig.5.9 *left picture*), modes at ~540cm^{-1} and ~800cm^{-1} are observed for both samples, but their presence in ST film on MgO substrates is not so obvious (Fig.5.9 *right picture*). These modes are identified as TO4 and LO4 modes, respectively, similarly to ST bulk [Petzelt et *al.*, 2001] and films [Ostapchuk et *al.*, 2002].

Symmetry forbidden TO4 and LO4 modes appeared at room temperature in ST films deposited on Al_2O_3 and TO4 mode on MgO substrates and they are slightly strengthen with further cooling (Fig.5.9). At the same time for ST films deposited on MgO the very small and very weak LO4 mode at ~800cm^{-1} was almost undetectable (Fig.5.9 *right picture*).

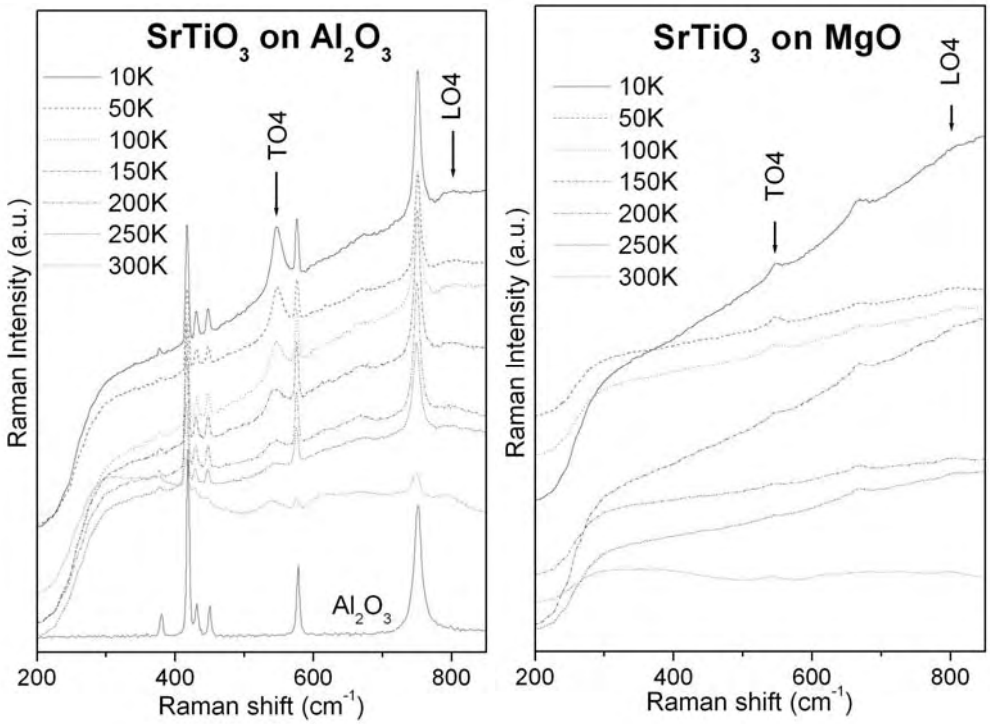

FIGURE 5.9. Raman spectra of $SrTiO_3$ films deposited on Al_2O_3substrate (*left picture*) and on MgO substrate (*right picture*) measured from 300K to 10K.

Meanwhile, Petzelt et *al.* reported for ST ceramics that the positions of these TO4 and LO4 modes were almost independent of the decrease of the measuring temperature: TO4 was detected at 546cm^{-1} at 15K and 300K and at 545cm^{-1} at 50K and 100K, LO4 mode was founded at 795cm^{-1} at 15K and 50K and at 797cm^{-1} at 100K and 300K [Petzelt et *al.*, 2001]. In this way, it could be concluded, that position of detected TO4 and LO4 modes in ST films does not reveal appreciable temperature dependence, what is similar to bulk ST, as it observed from Figure 5.9.

5.3. Microstructure analysis

5.3.1. SEM analysis

The microstructure of ST films deposited on different platinized substrates: Al_2O_3/Pt, Si/SiO_2/TiO_2/Pt, $SrTiO_3$/Pt (ST/Pt), $(LaAlO_3)_{0.3}$-$(Sr_2AlTaO_6)_{0.7}$/Pt (LSAT/Pt) and MgO/Pt, was analysed by SEM (Fig.5.10).

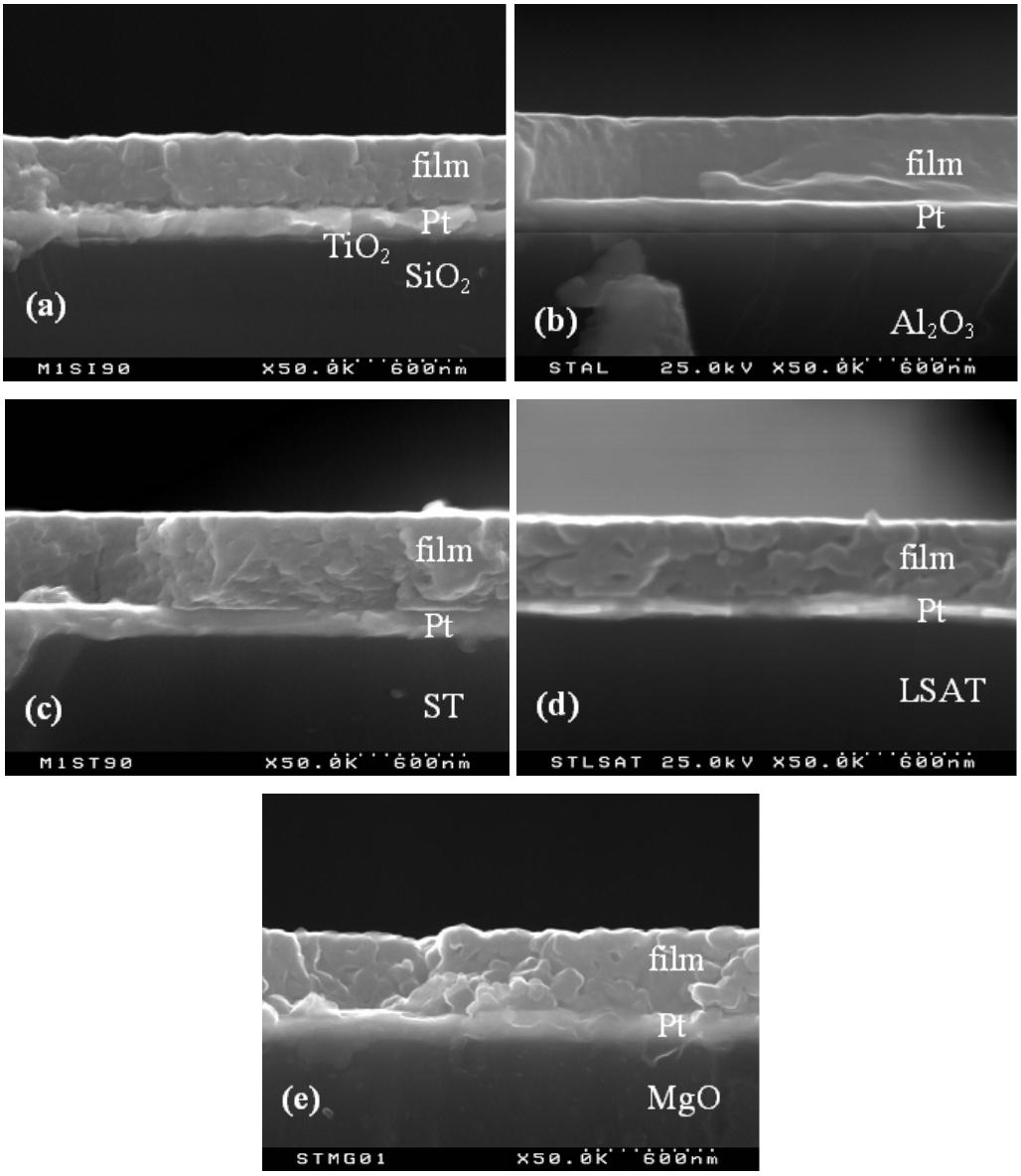

FIGURE 5.10. SEM cross-section micrographs of $STiO_3$ thin films deposited on different substrates: $Si/SiO_2/TiO_2/Pt$ (a), Al_2O_3/Pt (b), $SrTiO_3/Pt$ (ST/Pt) (c), $(LaAlO_3)_{0.3}$-$(Sr_2AlTaO_6)_{0.7}/Pt$ (LSAT/Pt) (d) and MgO/Pt (e).

The films on all the used substrates reveal a quite dense and crack free microstructure with a smooth surface. The cross-section micrographs evidence the polycrystalline nature of these sol-gel films with the absence of any orientation or textured features (Fig.5.10), corroborating the XRD analysis. The measured film thickness is about ~350-370nm. The calculation of the grain size from the obtained micrographs was quite difficult due to the small grains that characterise these films and the grain size was calculated from AFM analyses.

5.3.2. AFM analysis

The in-plane surface morphology (Fig.5.11 *left pictures*) and the corresponding 3D views (Fig.5.11 *right pictures*) of ST films deposited on different substrates: Al_2O_3/Pt, Si/SiO_2/TiO_2/Pt (Si/…/Pt), $SrTiO_3$/Pt (ST/Pt), $(LaAlO_3)_{0.3}$-$(Sr_2AlTaO_6)_{0.7}$/Pt (LSAT/Pt) and MgO/Pt were analyzed by AFM.

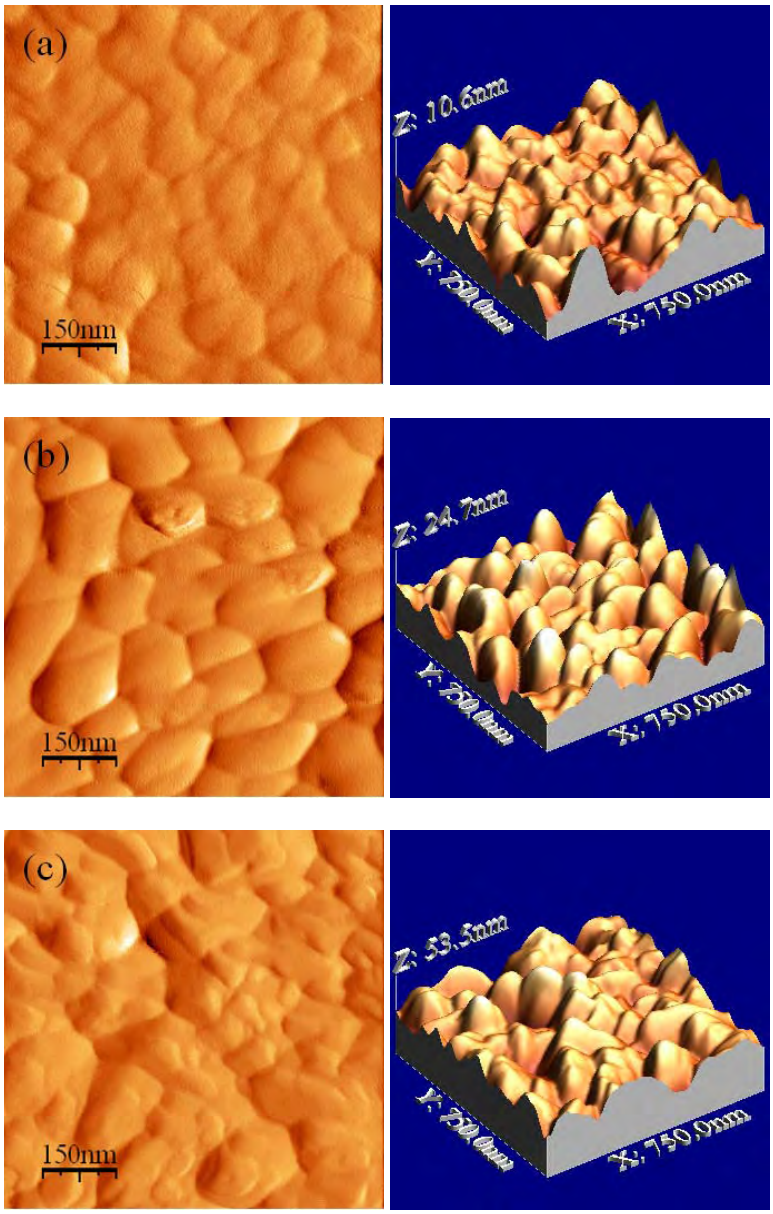

FIGURE 5.11. **a, b, c** - Atomic force micrographs of $SrTiO_3$ thin films deposited on different substrates: Al_2O_3/Pt (a), Si/SiO_2/TiO_2/Pt (b), $(LaAlO_3)_{0.3}$-$(Sr_2AlTaO_6)_{0.7}$/Pt (c), $SrTiO_3$/Pt (d), and MgO/Pt (e) substrates.

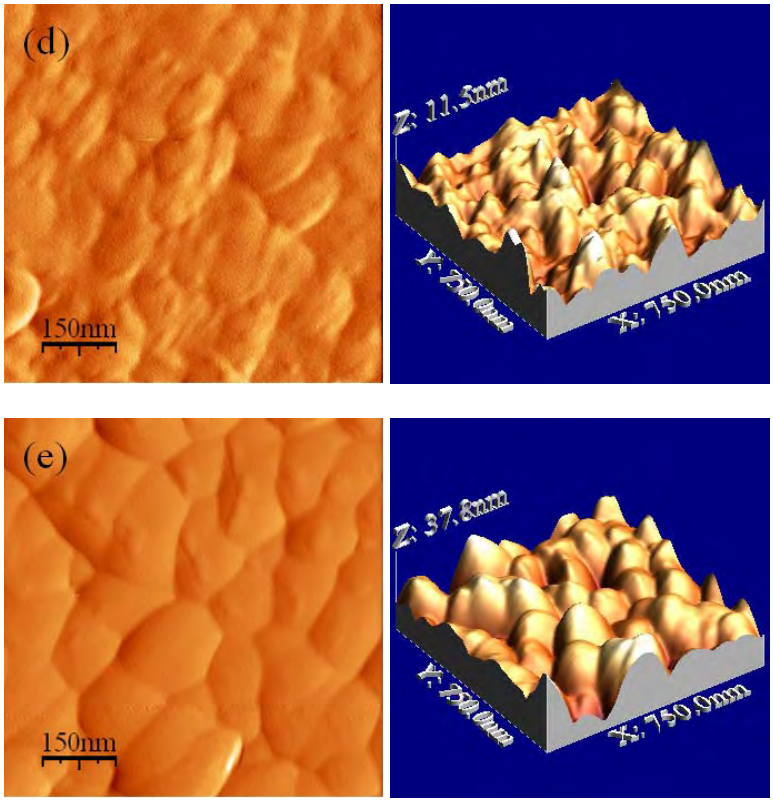

FIGURE 5.11. **d, e** - Atomic force micrographs of $SrTiO_3$ thin films deposited on different substrates: Al_2O_3/Pt (a), Si/SiO_2/TiO_2/Pt (b), $(LaAlO_3)_{0.3}$-$(Sr_2AlTaO_6)_{0.7}$/Pt (c), $SrTiO_3$/Pt (d), and MgO/Pt (e) substrates.

The analyzed ST films deposited on the different substrates exhibit almost spherical grains in all *x,y,z*-directions (Fig.5.11 *right pictures*). The in-plane grain size of the films was calculated from these AFM micrographs and is presented in Figure 5.12 *left axis*.

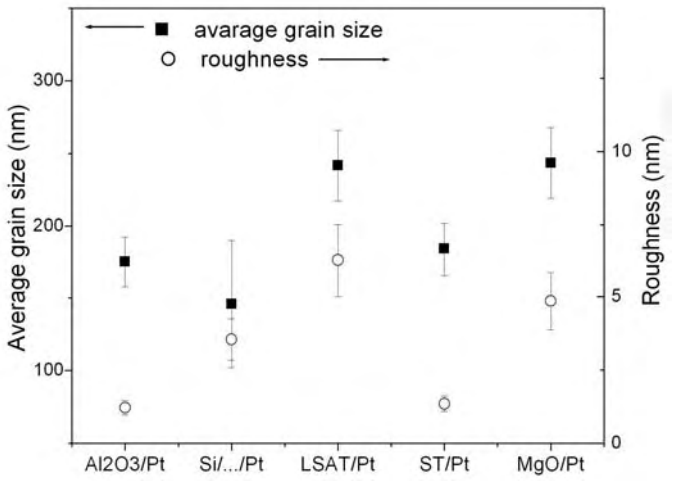

FIGURE 5.12. In-plane average grain size (*left axis*) and roughness (*right axis*) of $SrTiO_3$ films deposited on different substrates: Al_2O_3/Pt, Si/SiO_2/TiO_2/Pt (Si/…/Pt), $(LaAlO_3)_{0.3}$-$(Sr_2AlTaO_6)_{0.7}$/Pt (LSAT/Pt), $SrTiO_3$/Pt (ST/Pt) and MgO/Pt.

The biggest in-plane average grain size was found for ST films deposited on LSAT/Pt (~240nm) as well as on MgO/Pt substrates (~245nm). ST films on Al_2O_3/Pt substrate show the smallest average grain size (~175nm) similar to that on ST/Pt substrate (~183nm). Grains of ST films deposited on Si/.../Pt substrates present an average size ~145nm (Fig.5.12 *left axis*) and a little sharper in *z*-direction grains than that for the others ST films.

The roughness of the films is depicted in Figure 5.12 as well. All the films possess a smooth surface (Fig.5.12 *right axis*). As expected, the highest roughness was observed for ST films with big grain size: on LSAT/Pt (~6.26nm) and MgO/Pt (~4.86nm) substrates. In opposition, the smallest roughness was calculated for ST films on Al_2O_3/Pt (~1.21nm) and ST/Pt (~1.35nm) substrates with smaller grains than that on LSAT/Pt and MgO/Pt. Roughness of ST films deposited on Si/…/Pt substrates was ~3.54nm (Fig.5.12 *right axis*).

It is possible to summarize, that the biggest grain size and the highest roughness were calculated for ST films deposited on the substrates with the highest TEC's (LSAT and MgO) and, consequently, with highest compressive thermal stress (Fig.5.12).

5.3.3. TEM analysis

The microstructure of the interfaces between ST films and the different substrates was further analysed by TEM. TEM micrographs of cross-sections microstructures of ST films on Si/…/Pt, LSAT/Pt and MgO/Pt substrates are represented in Figures 5.13-5.16.

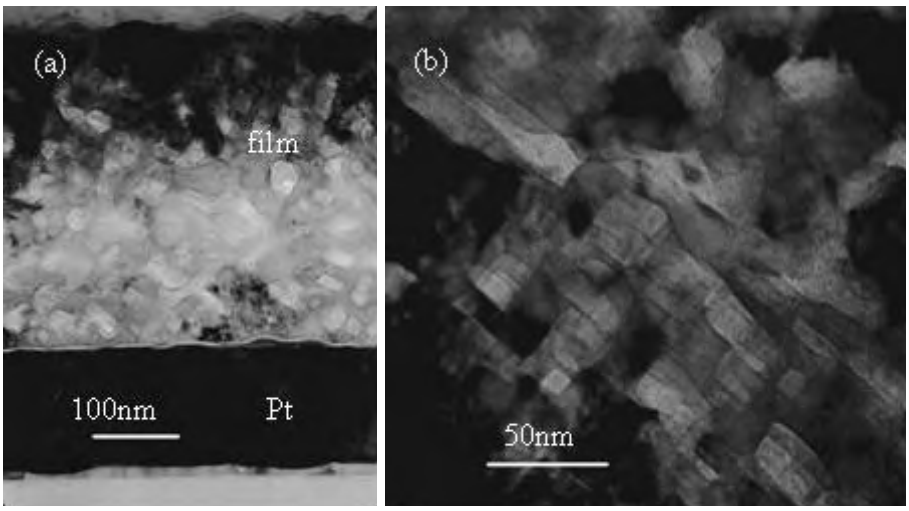

FIGURE 5.13. Cross-section TEM micrographs of film/substrate (a) and area of film near film/Pt interface (b) of $SrTiO_3$ film deposited on Si/SiO_2/TiO_2/Pt substrate.

Very clear film/substrate interface was observed for ST films deposited on Si/…/Pt (Fig.5.13a) and the films show very dense structure without any particular orientation (Fig.5.13b). These films exhibit very small grain size in out-of-plane direction (~30-40nm) (Fig.5.13) when compared to the much bigger in-plane grain size (~145nm) (Fig.5.11b).

Similar microstructure characterizes the cross-sections of ST films on LSAT/Pt (Fig.5.14a,b). Out-of-plane direction grain size of ST film on LSAT/Pt is bigger (~50-70nm) (Fig.5.14a,b) than previous films but smaller in comparison to the in-plane grain size of ST on LSAT/Pt films (~240nm) (Fig.5.11c).

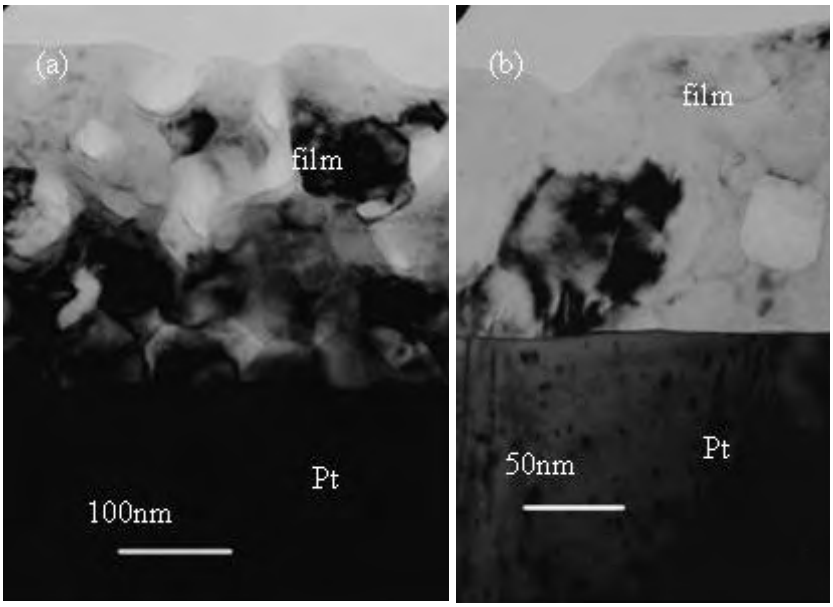

FIGURE 5.14. Cross-section TEM micrographs of film/Pt interface (a) and film/Pt interface more detail (b) of $SrTiO_3$ films deposited on $(LaAlO_3)_{0.3}$-$(Sr_2AlTaO_6)_{0.7}$/Pt substrate.

The cross-sections of ST films on Al_2O_3/Pt (Fig.5.15a) and ST/Pt (Fig.5.15b) substrates present ~350nm thick according to the scale bars on TEM images similar to SEM observation. The films appear uniform, indicating a well-controlled deposition process. There is evidence of features parallel to the substrate surface which is believed to arise from the multi-step spin-coating and crystallisation process. ST on Al_2O_3/Pt (Fig.5.15a) shows better contrast as compared with the ST on ST/Pt substrate (Fig.5.15b), which is either due to the TEM specimen being thinner or a better crystallisation condition employed in this case.

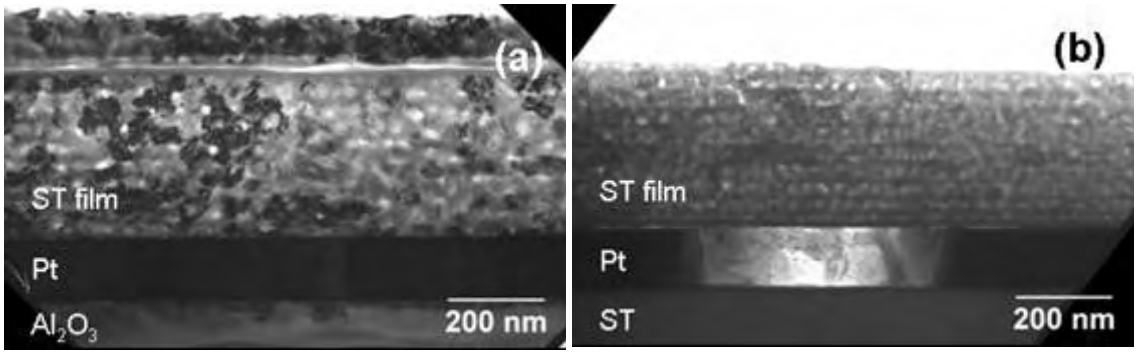

FIGURE 5.15. Cross-section TEM micrographs of $SrTiO_3$ (ST) films on Al_2O_3/Pt (a) and on $SrTiO_3$/Pt (b) substrates.

The most striking differences were observed in the mcrostructure of the interface of ST films on MgO/Pt substrates (Fig.5.16).

"Slip band type dislocations" ("lines") in ST grains are easily observed, as depicted in Figure 5.16b,c. These "lines" start at the MgO substrate and continue through the 150nm layer of Pt and cross the ST grains (Fig.5.16b,c). This is in total agreement with the compressive effect of MgO substrate on ST films.

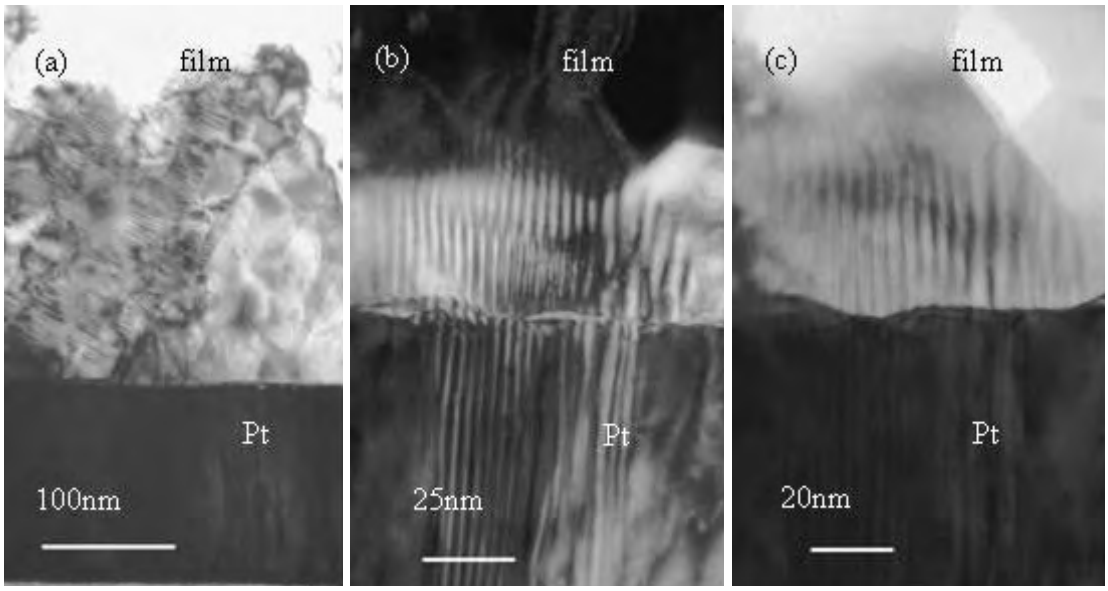

FIGURE 5.16. Cross-section TEM micrographs of full cross-section (a) and smaller areas (b,c) of $SrTiO_3$ films deposited on MgO/Pt substrates. Slip band type dislocations are clearly seen in some $SrTiO_3$ grains (b,c).

Once more the out-of-plane direction grain size of the analyzed ST films on MgO/Pt (~50-70nm) (Fig.5.16a,b) was smaller than the in-plane grain size (~245nm) (Fig.5.11d). It could be explained as influence of very high tensile in-plane lattice mismatch, what leads to compressive out-of-plane lattice mismatch, and this is in agreement to calculation of in-plane lattice mismatch (Fig.5.4).

From the analysis of TEM cross-sections, ST films under tensile stress on Si/…/Pt and LSAT/Pt substrates do not represent any specific features in the microstructure, however in contrast, ST films on MgO with high compressive total stress obvious "slip band type dislocations" were displayed through the Pt layer and ST film (Fig.5.16b,c).

5.4. Low temperature dielectric properties

5.4.1. Dielectric response as function of temperature

The real part of the dielectric permittivity ε′ of ST films deposited on different substrates: Al_2O_3/Pt, Si/SiO_2/TiO_2/Pt (Si/…/Pt), $SrTiO_3$/Pt (ST/Pt), $(LaAlO_3)_{0.3}$-$(Sr_2AlTaO_6)_{0.7}$/Pt (LSAT/Pt) and MgO/Pt was measured from 100Hz to 1MHz from 300K to 10K and is presented in Figure 5.17. In terms of curve features, the dielectric response of all the films is similar and similar to the results previously presented in the "Chapter 4", no additional peaks are observed.

All the films exhibit a wide ε′ peak at low temperatures (~35-55K) and ε′ increases with decreasing of the measured temperature for all the samples, until ~50K (Fig.5.17). In addition the dependence on the measuring frequency is not very obvious, being higher at lower temperatures and higher frequencies (Fig.5.17). As discussed before ("Chapter 4"), the appearance of the small broad peak in $\varepsilon'(T)$ at low temperatures for all the studied films, signals the existence of a ferroelectric type order in these films. Such peak was also observed in ST films prepared by other methods and similarly attributed to the appearance of the ferroelectricity [Astafiev et *al.*, 2003; Yu et *al.*, 2002; Hirano et *al.*, 1993].

For a better comparison the dielectric response of the films deposited on different substrates $\varepsilon'(T)$ is presented in Figure 5.18 for 10kHz. The highest value of ε' (ε'_{max}) was observed for films on MgO/Pt (~620 at 25K), corresponding to the samples under the highest compressive stress state and the smallest ε' observed for films on Al_2O_3/Pt (~360 at ~53K), those under the highest tensile strained state. ε' of films on Si/…/Pt, ST/Pt and

LSAT/Pt have intermediate values of ε' (summarised in Table 5.2).

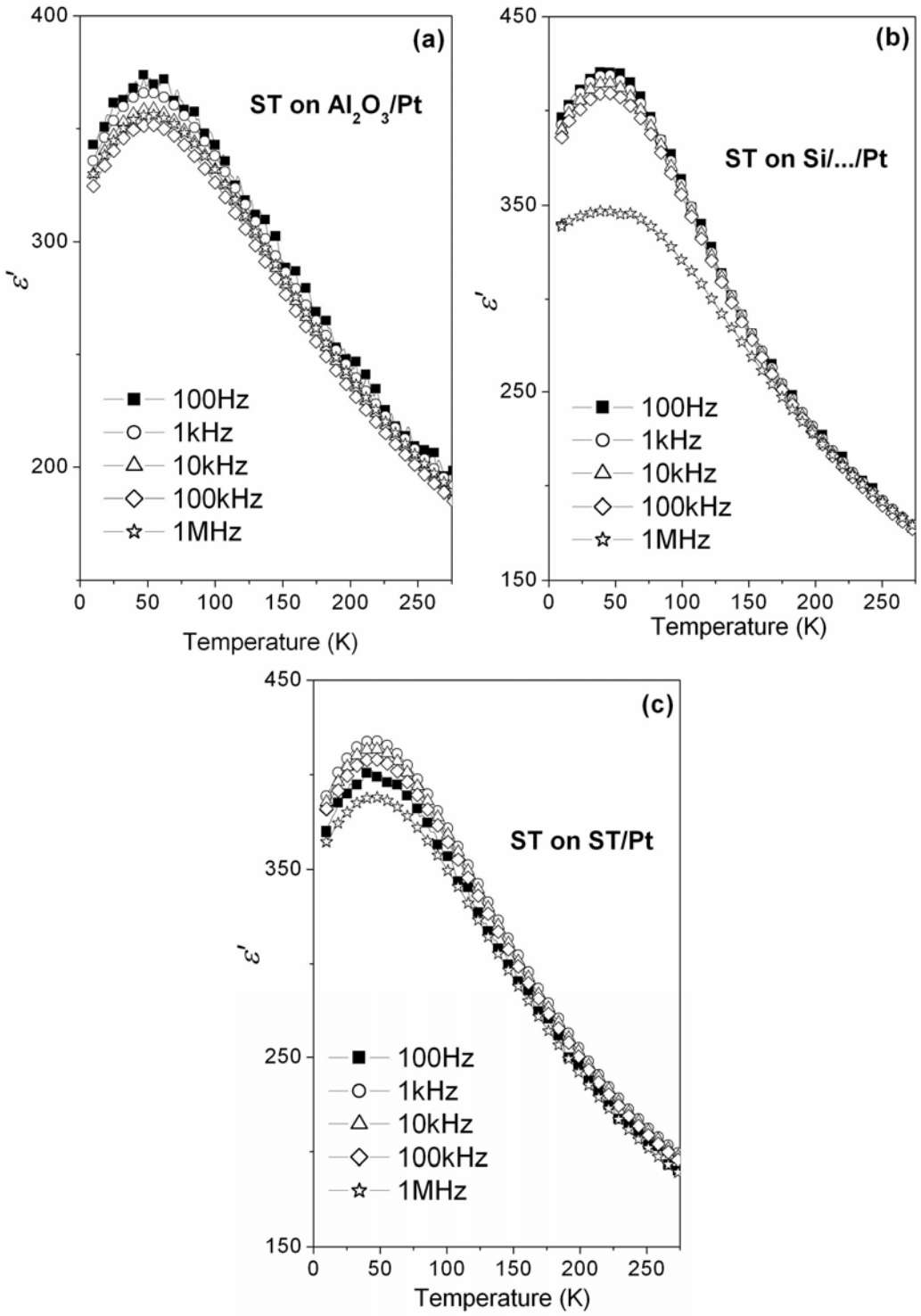

FIGURE 5.17. **a, b, c -** Temperature dependence of real part of the dielectric permittivity of ε' of $SrTiO_3$ (ST) thin films deposited on Al_2O_3/Pt (a), Si/SiO_2/TiO_2/Pt (Si/…/Pt) (b), $SrTiO_3$/Pt (ST/Pt) (c), $(LaAlO_3)_{0.3}$-$(Sr_2AlTaO_6)_{0.7}$/Pt (LSAT/Pt) (d) and MgO/Pt (e) substrates at 100Hz, 1kHz, 10kHz and 100kHz.

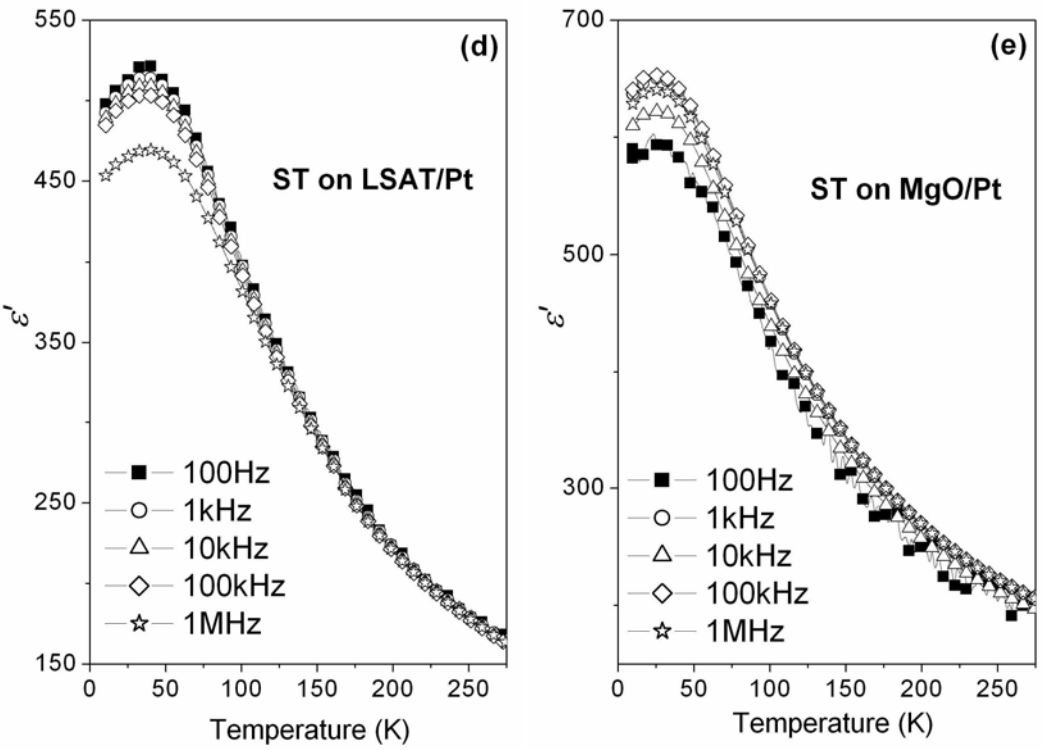

FIGURE 5.17. **d, e** - Temperature dependence of real part of the dielectric permittivity of ε' of $SrTiO_3$ (ST) thin films deposited on Al_2O_3/Pt (a), Si/SiO_2/TiO_2/Pt (Si/…/Pt) (b), $SrTiO_3$/Pt (ST/Pt) (c), $(LaAlO_3)_{0.3}$-$(Sr_2AlTaO_6)_{0.7}$/Pt (LSAT/Pt) (d) and MgO/Pt (e) substrates at 100Hz, 1kHz, 10kHz and 100kHz.

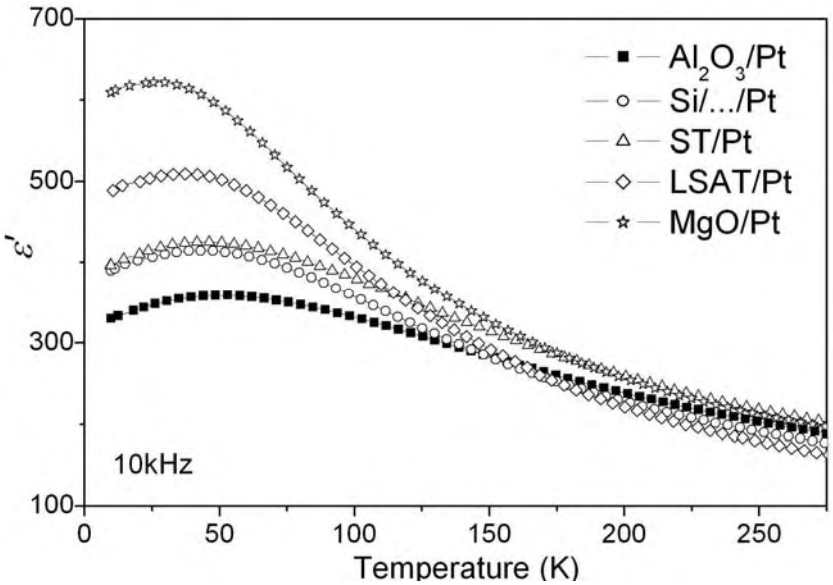

FIGURE 5.18. Temperature dependence of the real part of the dielectric permittivity ε' of $SrTiO_3$ thin films deposited on different substrates: Al_2O_3/Pt, Si/SiO_2/TiO_2/Pt (Si/…/Pt), $SrTiO_3$/Pt (ST/Pt), $(LaAlO_3)_{0.3}$-$(Sr_2AlTaO_6)_{0.7}$/Pt (LSAT/Pt) and MgO/Pt at 10kHz.

Figure 5.19 depicts the temperature dependence of tanδ of $SrTiO_3$ thin films deposited on different substrates deposited on different substrates: Al_2O_3/Pt, Si/…/Pt, ST/Pt, LSAT/Pt and MgO/Pt at 10kHz.

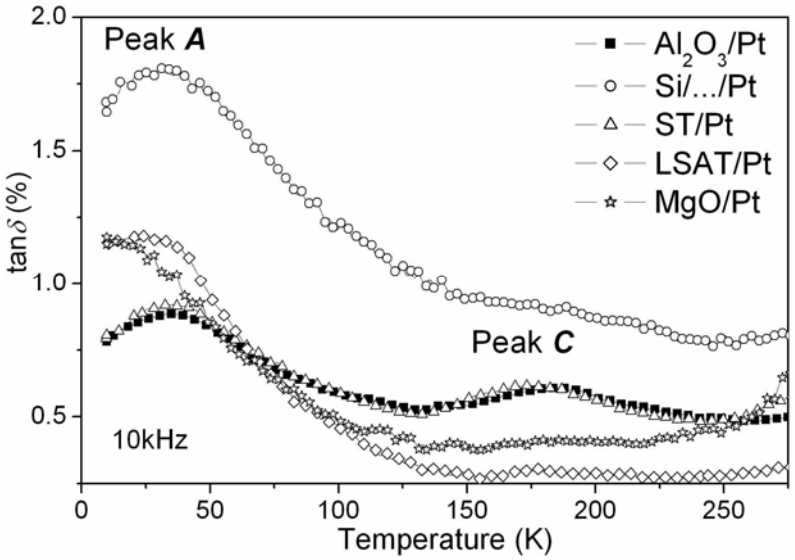

FIGURE 5.19. Temperature dependence of the tanδ of $SrTiO_3$ thin films deposited on different substrates: Al_2O_3/Pt, Si/SiO_2/TiO_2/Pt (Si/…/Pt), $SrTiO_3$/Pt (ST/Pt), $(LaAlO_3)_{0.3}$-$(Sr_2AlTaO_6)_{0.7}$/Pt (LSAT/Pt) and MgO/Pt at 10kHz.

Similar to the films prepared under different processing conditions and analysed in "Chapter 4" a well defined peak *A* and a small broad peak *C* can be observed in the variation of tanδ as a function of the temperature for all the ST films. In accordance with the dielectric permittivity, no additional peaks induced by substrate stress appear in tanδ response of these films.

Well defined *A* peaks were detected in ST films on Al_2O_3/Pt at ~33K, Si/…/Pt at ~31K and on ST/Pt at ~35K substrates and it was almost not visible on LSAT/Pt (the highest tanδ at ~29K) and MgO/Pt substrates (the highest tanδ at ~10K) (Fig.5.19).

A small broad peak *C* can be observed in ST films on Al_2O_3/Pt at ~180K and on ST/Pt at ~175K. On LSAT/Pt substrate a small increasing on tanδ at ~177K was observed but it was not possible to calculate precisely its position. Moreover, it was completely impossible to find peak *C* in ST films on Si/…/Pt and MgO/Pt substrates (Fig.5.19).

The obtained dielectric response for all the ST films deposited on different substrates is summarized in Table 5.4.

TABLE 5.4. Total stress values, maximum of ε', $T_{\varepsilon'max}$ and positions of peaks *A* and *C* in tanδ *(T)* of $SrTiO_3$ films deposited on different platinized substrates.

Substrate	Total stress, MPa	ε'_{max}	$T_{\varepsilon'max}$, K	Positions of peaks in tanδ, K	
				Peak *A*	Peak *C*
Al_2O_3/Pt	~611	~360	~53	~33	~180
Si/…/Pt	~256	~415	~44	~31	-
LSAT/Pt	~15	~510	~35	~29	-
ST/Pt	~-114	~425	~44	~35	~175
MgO/Pt	~-612	~620	~25	~10	-

From the presented data it is possible to conclude that:

1. ST films deposited on Al_2O_3/Pt substrates, which present the highest total tensile stress (~611MPa), have the lowest value of ε'_{max} (~360) at the highest temperature $T_{\varepsilon'max}$ (~53K).
2. ST films deposited on MgO/Pt substrates, which present the highest compressive stress (~612MPa), have the highest value of ε'_{max} (~620) at the lowest temperature $T_{\varepsilon'max}$ (~25K).
3. Dielectric loss peak *A* (could be considered as a stress/strain induced ferroelectric phase transition [Astafiev et *al.*, 2003]) is presented in all ST films deposited on the different substrates. In comparison with ST films on Si/…/Pt substrates annealed at low temperature 750°C ("Chapter 4"), this peak is more obvious in the films annealed at 900°C suggesting that the appearance of peak *A* in tanδ is somehow related with the high thermal stress level developed during heat treatment of ST films at the high annealing temperatures, besides the higher degree of crystallinity of these films.
4. Positions of peaks *A* and *C* in tanδ of ST films deposited on different substrates are not constant, and no visible correlation between peaks positions and total stress or with the behaviour of ε'_{max} and $T_{\varepsilon'max}$ was found.

In order to discuss the origin of these peaks and their dependence on the stress level in ST films deposited on different substrates, the dynamics of the relaxations was further analysed by Arrhenius law:

$$\tau = \tau_0 \exp(U/k_B T) \tag{5.4}$$

where, τ_0 stands for the pre-exponential term or inverse attempt frequency, U for the activation energy, k_B for the Boltzmann constant and T for the temperature.

The relaxation dynamics parameters of the peaks *A* and *C* of ST films deposited on different substrates were deducted from the temperature and frequency value of ε'' peaks ($\varepsilon''=\varepsilon' \times \tan\delta$). Figure 5.20 represents the corresponding Arrhenius plots $\ln(\tau)=\ln(w^{-1})$ versus $1000/T_{\varepsilon''\max}$.

Fitted pre-exponential term τ_0 and activation energy U values were obtained for the ST films deposited on Al_2O_3/Pt, Si/SiO_2/TiO_2/Pt (Si/…/Pt), $SrTiO_3$/Pt (ST/Pt), $(LaAlO_3)_{0.3}$-$(Sr_2AlTaO_6)_{0.7}$/Pt (LSAT)/Pt and MgO/Pt, and are presented in Table 5.5.

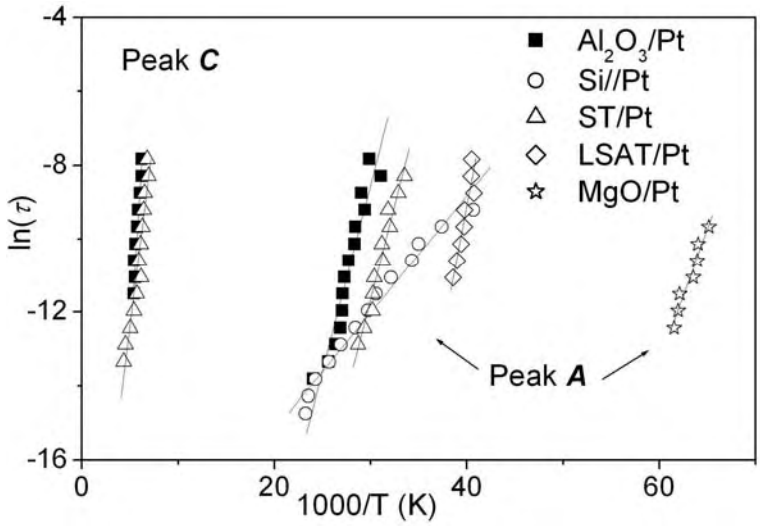

FIGURE 5.20. Arrhenius plots of $\ln(\tau)$ versus $1000/T_{\varepsilon''\max}$ ($T_{\varepsilon''\max}$ is the temperature at which maximum of ε'' occurs at the angular frequency $w = 2\pi f$; $\tau = w^{-1}$) for the loss peaks *A* and *C* of $SrTiO_3$ films deposited on different substrates: Al_2O_3/Pt, Si/SiO_2/TiO_2/Pt (Si/…/Pt), $SrTiO_3$/Pt (ST/Pt), $(LaAlO_3)_{0.3}$-$(Sr_2AlTaO_6)_{0.7}$/Pt (LSAT/Pt) and MgO/Pt. Correlation coefficients for the obtained fits are the following: for peak *A:* R^2=0.9353 on Al_2O_3/Pt, R^2=0.97277 on Si/.../Pt, R^2=0.91936 on ST/Pt, R^2=0.89549 on LSAT/Pt and R^2=0.94794 on MgO/Pt, for peak *C*: R^2=0.91361 on Al_2O_3/Pt and R^2=0.9615 on ST/Pt substrate.

TABLE 5.5. Arrhenius law parameters used to describe the relaxational dynamics of the loss peaks *A* and *C* in $SrTiO_3$ thin films deposited on Al_2O_3/Pt, Si/SiO_2/TiO_2/Pt (Si/…/Pt), $SrTiO_3$/Pt (ST/Pt), $(LaAlO_3)_{0.3}$-$(Sr_2AlTaO_6)_{0.7}$/Pt (LSAT/Pt) and MgO/Pt.

Composition	ARRHENIUS LAW			
	Peak *A*		Peak *C*	
	U, meV	τ_0, s	*U*, meV	τ_0, s
Al_2O_3/Pt	~87	~1.2×10^{-17}	~335	~10×10^{-10}
Si/…/Pt	~27	~4×10^{-10}		
ST/Pt	~88	~3.9×10^{-19}	~180	~1.2×10^{-10}
LSAT/Pt	~65	~7.2×10^{-18}		
MgO/Pt	~63	~1.6×10^{-25}		

In the current study, the loss peak *A* was obtained for all ST films deposited on different substrates (Fig.5.19). The values calculated for peak *A* varied between *U*=27meV and τ_0=~4×10^{-10}s for ST on Si/…/Pt and *U*=88meV and τ_0=~3.9×10^{-19}s for ST on ST/Pt. *U* and τ_0 of films on Al_2O_3/Pt, LSAT/Pt and MgO/Pt have intermediate values (Table 5.5). In comparison with the equivalent data reported for ST single crystals (*U*=~13.6meV and τ_0=~2.5×10^{-12}s [Viana *et al.*, 1994]) the values for the activation energy *U* of the peak *A* for all the studied ST films on the different substrates are higher: varying from 27meV to 88meV depending on the substrate. At the same time, the value of the pre-exponential term τ_0 of peak *A* for ST films on Si/…/Pt substrates (τ_0=~4×10^{-10}s) is quite close to that of ST crystals [Viana *et al.*, 1994]. For all the other films on Al_2O_3/Pt, ST/Pt, LSAT/Pt and MgO/Pt calculated τ_0 was significantly smaller (10^{-17}-10^{-25}s). However, such small value of τ_0 (<10^{-13}s) have no physical meaning. It was also found that films deposited on Si/…/Pt substrates with the highest tensile thermal stress (~2936MPa) exhibit the highest pre-exponential term τ_0 (4×10^{-10}s) for peak *A*. However the behaviour of *U* for these films can not to be directly related to the changing of thermal stress (or total stress).

Concerning peak *C*, detected in current work with a maximum around ~175K on ST/Pt substrates and at ~180K on Al_2O_3/Pt substrates at 10kHz, it was mention before that similar peak at ~165K-175K was observed in some thin films [Li et *al.*, 1998; Xi et *al.*, 1999] and ceramics [Ang et *al.*, 1999a; Ang et *al.*, 1999b; Iguchi et *al.*; 1993, Lemanov et

al., 2000]. Because it is well known that oxygen vacancies are a common defect in ST thin films, single crystals, and ceramics it was assumed that this loss peak *C* may be originated from the reorientation of oxygen-vacancy dipoles [Lemanov et *al.*, 2002]. Arrhenius law parameters of the loss peak *C*, related to the thermally activated jumps of the oxygen vacancies around the impurity ions, and well observed for ST films on Al_2O_3/Pt and ST/Pt substrates, were calculated to: U=~335meV and τ_0=~10×10^{-10}s and U=~180meV and τ_0=~1.2×10^{-10}s, respectively (Table 5.5.). Values of U=~250meV for peak *C* of ST films deposited on ST substrate by PLD were reported before [Yu et *al.*, 2002] and it is close to the values obtained in this work for ST on Al_2O_3/Pt and on ST/Pt substrates.

5.4.2. IR measurements

ST films deposited on Al_2O_3 and MgO substrates without Pt layer were analysed in the IR-frequency-range from 300K to 10K (Fig.5.21).

ST films deposited on Al_2O_3 and MgO substrates shown broad temperature-dependent minimum (indicated as mode TO1) with small shifting to low frequency with decreasing of the measured temperature. In both films TO1 mode was started to be detected at room temperature at ~90-100cm^{-1} similarly to ST ceramics (~93cm^{-1}) [Petzelt et *al.*, 2001] and to ST films (~83cm^{-1}) [Ostapchuk et. *al.*, 2002]. The weak second minimum at ~170cm^{-1}, indicated as the TO2 phonon response, was observed in both analyzed samples from the room temperature. Identical behaviour was reported before for ST films on Al_2O_3 substrates (at ~176cm^{-1}) [Ostapchuk et. *al.*, 2002] and for ST ceramics (at the same ~176cm^{-1}) [Petzelt et *al.*, 2001]. The asymmetric spectral form of TO2 suggests its coupling to the neighbouring modes, and therefore the fit with independent oscillators is not optimal in this range [Ostapchuk et. *al.*, 2002].

The transmittance spectra of ST films on different substrates (Fig.5.21) were fitted to determine the TO mode parameters and to obtain the complex dielectric response function as described in "Chapter 3". The resulting spectra of real ε' and imaginary ε'' parts of the dielectric permittivity in the IR range are presented in Figure 5.22.

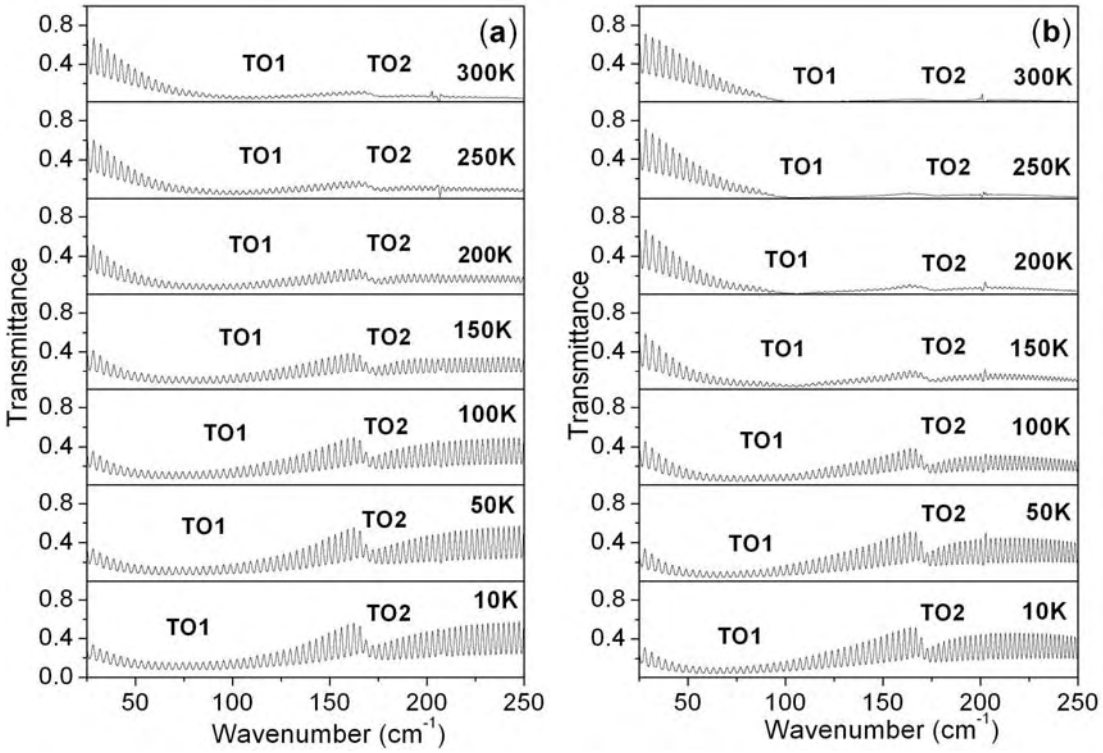

FIGURE 5.21. IR transmittance spectra of $SrTiO_3$ films deposited on Al_2O_3 (a) and on MgO (b) substrates at different temperatures.

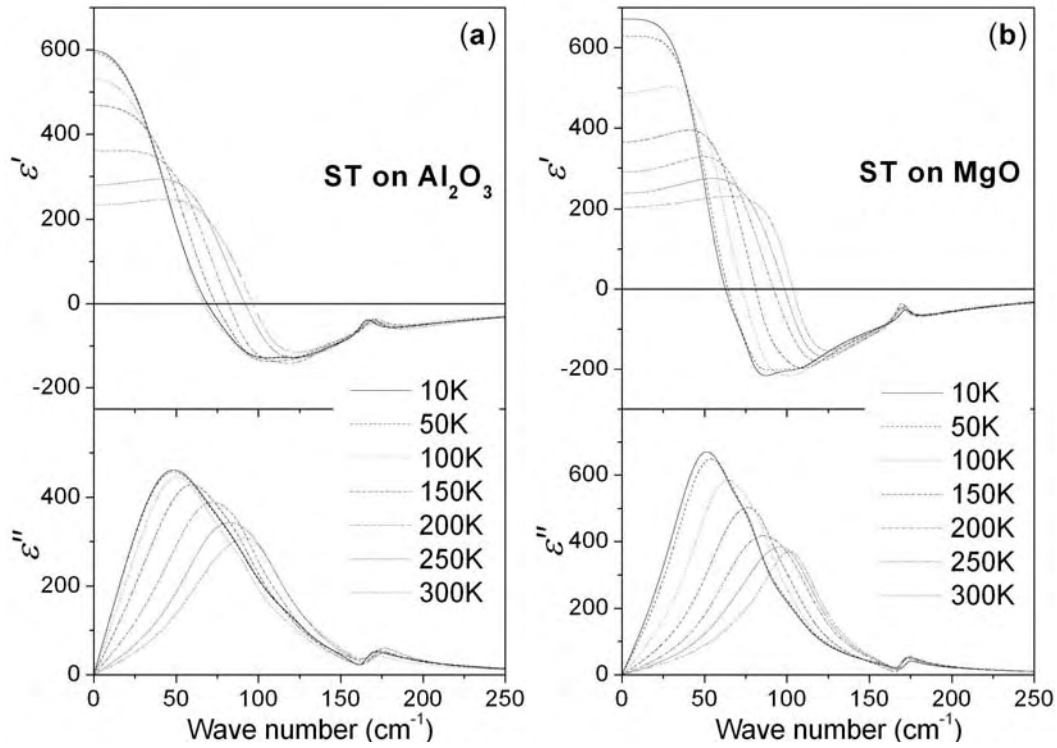

FIGURE 5.22. Spectra of the real ε' and imaginary ε'' part of the dielectric permittivity in the IR range, of $SrTiO_3$ thin films deposited on Al_2O_3 (a) and on MgO (b) substrates, obtained from the transmittance fits at different temperatures.

The eigenfrequency of TO1 modes (position of the maximum in the spectra of ε'' in IR range, obtained from the temperature dependent transmittance fits, shifts considerably to low frequency range with cooling: from ~91cm^{-1} at 300K to ~48cm^{-1} at 10K for ST film on Al_2O_3 (Fig.5.22a, *bottom panel*) and from ~101cm^{-1} at 300K to ~51cm^{-1} at 10K for ST film on MgO (Fig.5.22b, *bottom panel*). Similar decreasing of eigenfrequency TO1 mode was reported for ST single crystals (~91 cm^{-1} at 300K and ~48 cm^{-1} at 10K) [Fedorov et. *al.*, 1998] and ST ceramics (~93 cm^{-1} at 300K and ~15 cm^{-1} at 15K) [Petzelt et. *al.*, 2001]. The shift of TO2 mode in both analyzed films was not so strong (~171-177cm^{-1}) what is also typical for ST ceramics (172-176cm^{-1}) [Petzelt et. *al.*, 2001]. Detail calculation of the eigenfrequency of TO1 and TO2 modes was done and presented in Figure 5.23.

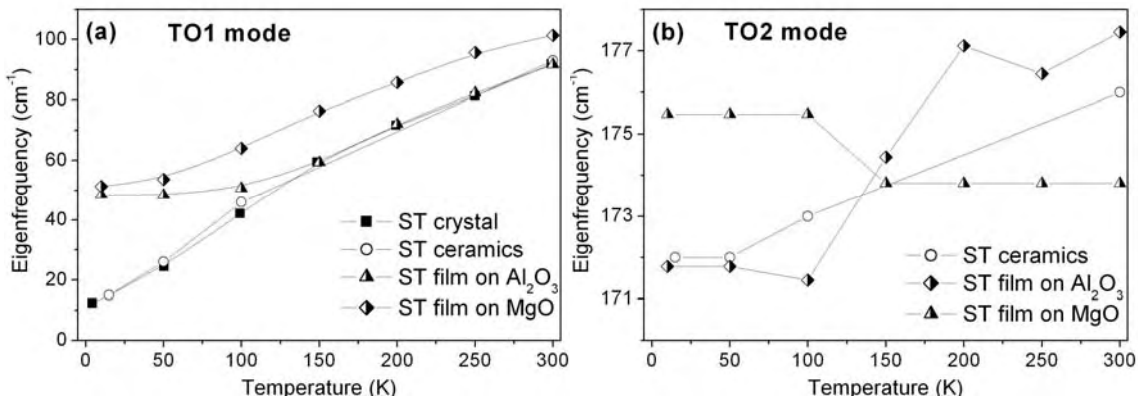

FIGURE 5.23. Temperature dependence of the fitted parameters of the TO1 (a) and TO2 (b) modes in $SrTiO_3$ (ST) films deposited on Al_2O_3 and MgO substrates and comparison with a single crystal [Ostapchuk et *al.*, 2002] and ceramics [Petzelt et. *al.*, 2004].

TO1 has very close eigenfrequency between ST films on Al_2O_3 and on MgO substrates only at very low measured temperature: at 10K ~48.5cm^{-1} (on Al_2O_3) and ~51cm^{-1} (on MgO). Compared to single crystals [Fedorov et. *al.*, 1998] and ST ceramics [Petzelt et. *al.*, 2001], the eigenfrequency of TO1 mode are markedly enhanced for films deposited on MgO substrates (with the highest compressive stress state) in all temperature range (Fig.5.23a). In the case of ST films deposited on Al_2O_3 substrate (with the highest tensile stress state) the eigenfrequency of the TO1 mode was detected at the same frequency as in ST single crystal [Fedorov et. *al.*, 1998] or in ST ceramics [Petzelt et. *al.*, 2001] with cooling from 300K to 150K and is higher from that of ST bulk only at low temperature (< 150K). The decreasing of eigenfrequency of TO1 mode from high to low frequency with decreasing of measured temperature was observed already for ST films on

Al_2O_3 [Ostapchuk et. *al.*, 2002], but the value of the eigenfrequency of TO1 mode of the analyzed films is much closer to that of ST crystals compared to previously reported [Ostapchuk et. *al.*, 2002]. The difference between the position of TO1 mode in ST films deposited on Al_2O_3 and MgO substrates should then be related to the stress effect. Compressive stress causes an increase of the eigenfrequency of TO1 mode.

The eigenfrequency of the TO2 mode of ST films deposited on Al_2O_3 and MgO substrates was changed between 171cm^{-1} and 178cm^{-1} (Fig.5.23b) what is typical for ST system [Petzelt et. *al.*, 2001; Ostapchuk et. *al.*, 2002]. But such inconsequent behaviour of this TO2 mode (increasing at low temperature for ST film on MgO or "jumps" for ST on Al_2O_3) could be explained as not perfect fit of TO2 spectra with independent oscillators in this range [Ostapchuk et. *al.*, 2002].

However, the values of ε' obtained from this technique can not to be compared to the previously obtained dielectric results because in IR measurements the *in-plane* dielectric response of ST films directly deposited on Al_2O_3 and MgO substrates is acquired while previously the measurements were done in a MIM capacitor configuration.

5.4.4. *dc*-field effect and dielectric tunability

The real part of the dielectric permittivity ε' of ST thin films deposited on different substrates: Al_2O_3/Pt, Si/…/Pt, ST/Pt, LSAT/Pt and MgO/Pt as a function of measured temperature at selected applied fields is illustrated in Figure 5.24. Details on these measurements can be found in the "Chapter 3".

For all the curves as the applied electric field increases the dielectric permittivity ε' decreases. In addition a small broad peak at low temperature is presented at E=0kV/cm for all the samples and it smoothed with increasing voltage and shifts to high temperature, what is typical for ST materials (as described in "Chapter 2"). However, no new *dc*-field induced peak was observed. Supporting the previous results, the highest *dc*-field effect was observed for ST films with the highest compressive stress on MgO/Pt substrates and the lowest *dc*-field influence was detected for ST films on Al_2O_3/Pt substrates with the highest tensile stress.

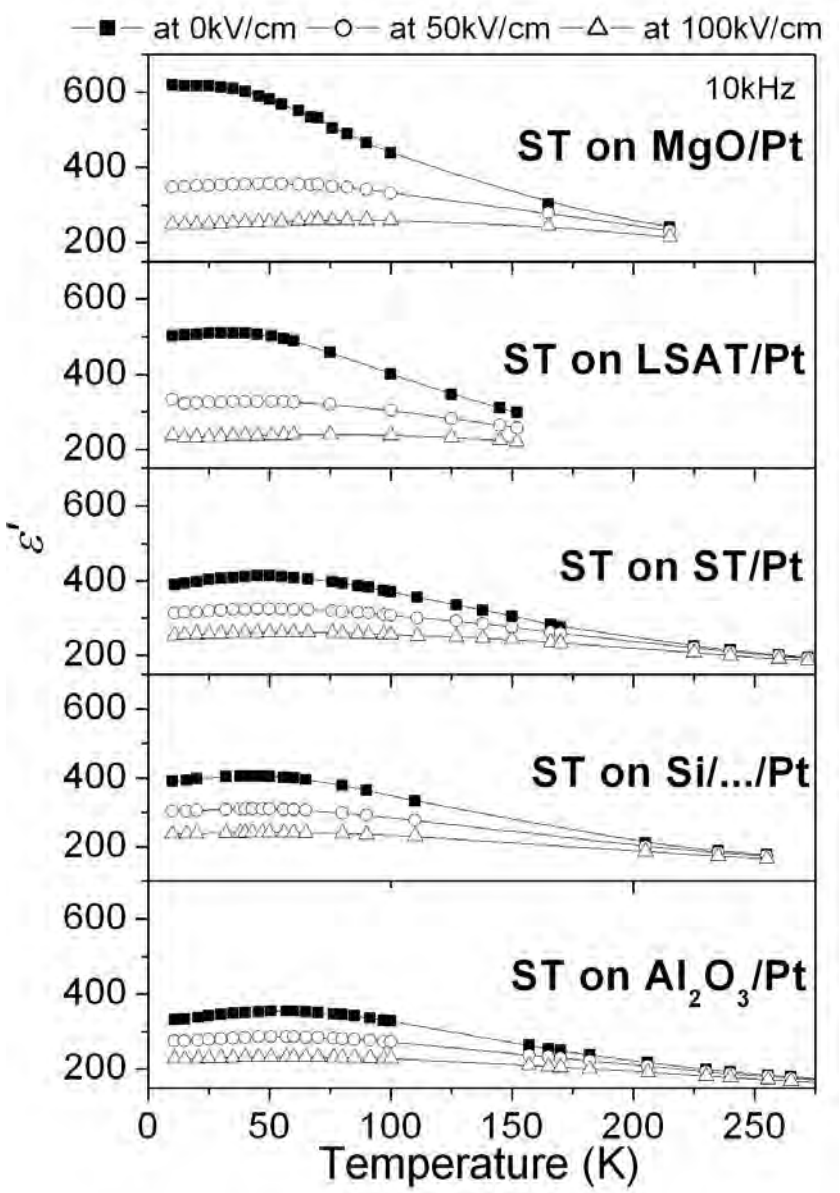

FIGURE 5.24. Temperature dependence of the real part of the dielectric permittivity ε' of $SrTiO_3$ (ST) films deposited on different substrates: Al_2O_3/Pt, Si/SiO_2/TiO_2/Pt (Si/…/Pt), $SrTiO_3$/Pt (ST/Pt), $(LaAlO_3)_{0.3}$-$(Sr_2AlTaO_6)_{0.7}$/Pt (LSAT/Pt) and MgO/Pt under different bias fields at 10kHz.

For the characterisation of the dependence of the ε' on the applied *dc* bias electric field, the parameter of tunability was calculated for ST films on the different substrates by the following relation:

$$n_r = [\varepsilon'(E=0) - \varepsilon'(E)] / \varepsilon'(E=0) \times 100\% \qquad (5.5)$$

where $\varepsilon'(E=0)$ stands for the real part of dielectric permittivity at zero bias and $\varepsilon'(E)$ for the

real part of dielectric permittivity at the applied *dc* electric field.

The relative tunability n_r of the studied films is shown in Figure 5.25 (*bottom panels)* at selected temperatures together with the *dc*-field dependence of ε' (*top panels*), tanδ (*middle panels*) measured at 10kHz.

From these results the following information can be withdrawn:

1. Small hysteresis loops are present in $\varepsilon'(E_{dc})$ and tan$\delta(E_{dc})$ for all ST films independent on the substrate nature.
2. ST films on MgO/Pt with the highest compressive total stress present the strongest response under *dc* fields ($\varepsilon'(E_{dc})$, tan$\delta(E_{dc})$ and $n_r(E_{dc})$) with the "narrow bell" with high magnitude: ε' changes from ~240 to ~640 at 10K.
3. ST films on Al_2O_3/Pt substrates with the highest tensile total stress present the lowest response of *dc* field $\varepsilon'(E_{dc})$, tan$\delta(E_{dc})$ and $n_r(E_{dc})$ with a "wide bell" with not so high magnitude: ε' changes from ~220 to ~340 at 10K.

For a better comparison, $\varepsilon'(E_{dc})$ at 10kHz and at 10K of ST films on all the used substrates is presented in Figure 5.26.

Similarly to the other properties reported in the previous subsections the stress state of the film markedly affects the electric field effect, namely tunability, of the films. Once more the highest effect of *dc*-bias on ε' took place in the films on MgO/Pt substrates, with high compressive stress and the smallest effect of *dc*-bias on ε' was found for films on Al_2O_3/Pt substrates, with high tensile total stress.

Temperature dependence of the relative dielectric tunability n_r of ST films deposited on Al_2O_3/Pt, Si/…/Pt, ST/Pt, LSAT/Pt and MgO/Pt is depicted in Figure 5.27 at 10kHz and 100kV/cm. n_r increases with the decrease of measured temperature for all studied films. At room temperature n_r is similar for all the samples (~4-5%), but at low temperatures ST films on MgO/Pt present the highest tunability (~60% at ~15K). The value of n_r and the temperature of the tunability maximum decreases and shifts to higher temperature for ST films on the other substrates, being the smallest for ST films on Al_2O_3/Pt (~35% at ~50K).

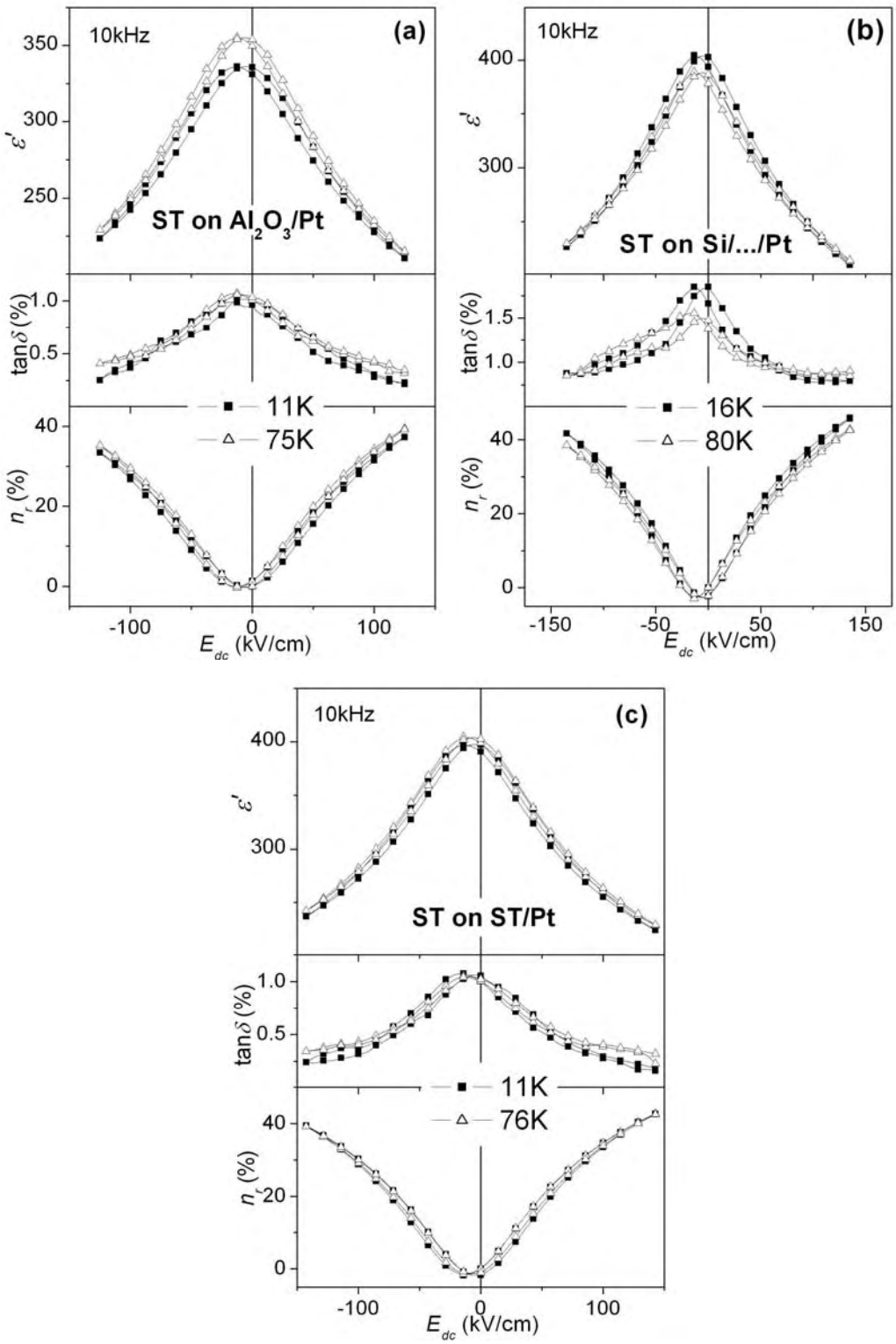

FIGURE 5.25. **a, b, c -** Field dependence of the real part of the dielectric permittivity ε' (*top panel*), tanδ (*middle panel*) and relative tunability n_r (*bottom* panel) of $SrTiO_3$ (ST) films on Al_2O_3/Pt (a), Si/SiO_2/TiO_2/Pt (Si/…/Pt) (b), $SrTiO_3$/Pt (ST/Pt) (c), $(LaAlO_3)_{0.3}$-$(Sr_2AlTaO_6)_{0.7}$/Pt (LSAT/Pt) (d) and MgO/Pt (e) substrates at 10kHz and at selected temperatures.

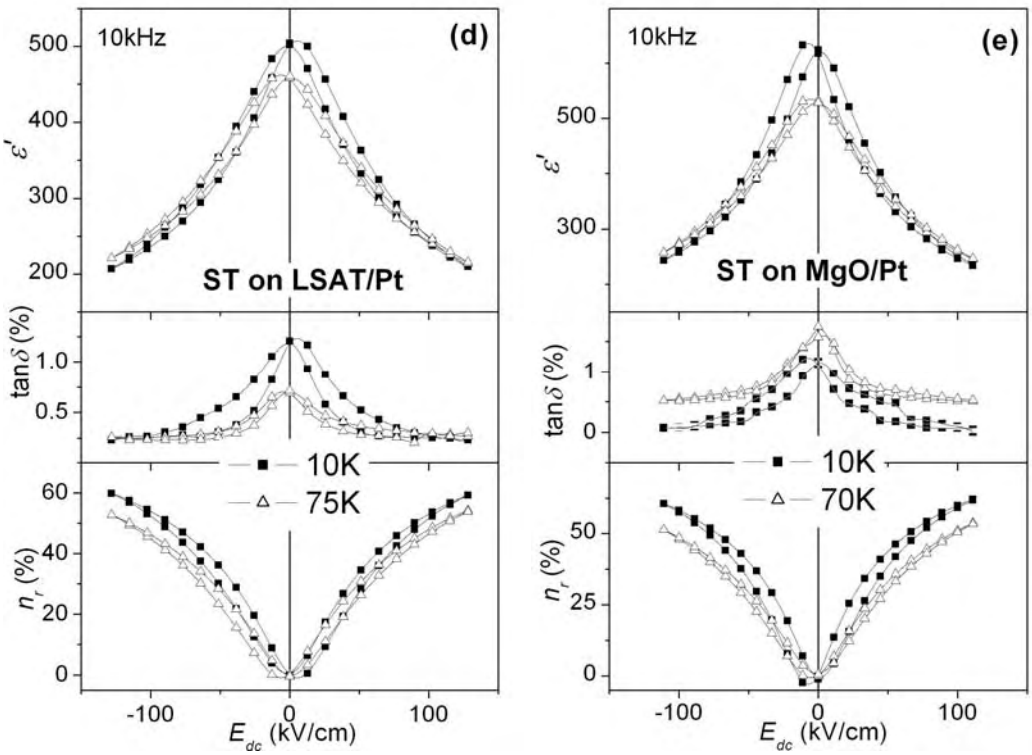

FIGURE 5.25. **d, e -** Field dependence of the real part of the dielectric permittivity ε' (*top panel*), tanδ (*middle panel*) and relative tunability n_r (*bottom* panel) of $SrTiO_3$ (ST) films on Al_2O_3/Pt (a), Si/SiO_2/TiO_2/Pt (Si/…/Pt) (b), $SrTiO_3$/Pt (ST/Pt) (c), $(LaAlO_3)_{0.3}$-$(Sr_2AlTaO_6)_{0.7}$/Pt (LSAT/Pt) (d) and MgO/Pt (e) substrates at 10kHz and at selected temperatures.

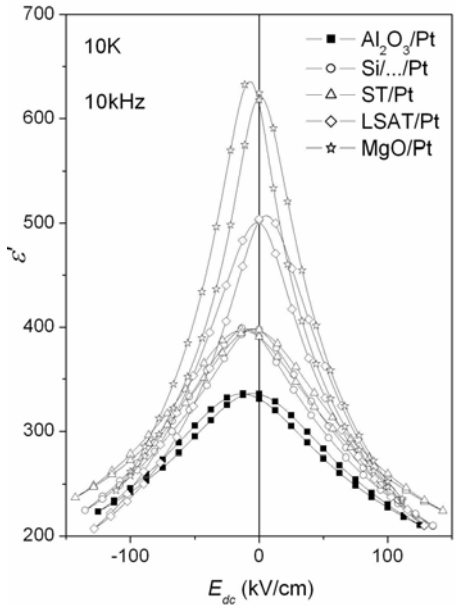

FIGURE 5.26. Field dependence of the real part of the dielectric permittivity ε' of $SrTiO_3$ films deposited on different substrates: Al_2O_3/Pt, Si/SiO_2/TiO_2/Pt (Si/…/Pt), $SrTiO_3$/Pt (ST/Pt), $(LaAlO_3)_{0.3}$-$(Sr_2AlTaO_6)_{0.7}$/Pt (LSAT/Pt) and MgO/Pt at 10kHz and at 10K.

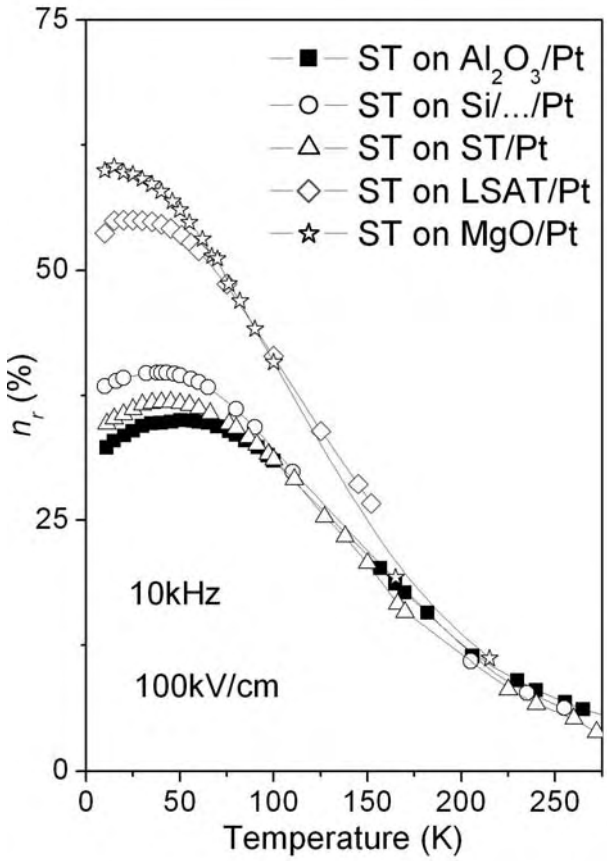

FIGURE 5.27. Temperature dependence of the relative dielectric tunability n_r of $SrTiO_3$ (ST) films deposited on different substrates: Al_2O_3/Pt, Si/SiO_2/TiO_2/Pt (Si/…/Pt), $SrTiO_3$/Pt (ST/Pt), $(LaAlO_3)_{0.3}$-$(Sr_2AlTaO_6)_{0.7}$/Pt (LSAT/Pt) and MgO/Pt at 10kHz and 100kV/cm.

The obtained tunability of ~60% at ~15K of ST films on MgO/Pt is an important result, that clearly indicates that by controlling the stresses induced by the substrate the properties of polycrystalline films can be optimised.

As already mentioned in the "Chapter 4", it is difficult to compare the values of n_r of the current ST films with reported ones due to different used experimental conditions that include the range of the applied electric field temperature and frequency. However in comparison with the values of ST films prepared under different conditions on Si/…/Pt substrates ("Chapter 4"), for which the highest tunability (~54% in the maximum at ~55K) was obtained for the samples with buffer layers and heat treated at high temperature (ST 2l 900°C), a higher tunability can be obtained by controlling the total stress level in the films by choice of appropriate substrates, in this case on MgO/Pt substrates (~65% at ~15K).

5.4.3. *P(E)* hysteresis response

Since the hysteretic response of the change of polarisation *P* under an applied *ac* field *E* (*P(E)*) is a demonstration of the ferroelectric properties of a material, *P(E)* of ST films deposited on the different substrates: Al_2O_3/Pt, Si/SiO_2/TiO_2/Pt, $SrTiO_3$/Pt, $(LaAlO_3)_{0.3}$-$(Sr_2AlTaO_6)_{0.7}$/Pt and MgO/Pt was measured at 100Hz under *ac* fields at different temperatures. The description of these measurements was done in the "Chapter 3".

Figures 5.28-5.32 present the hysteresis loops at selected temperatures of these ST thin films. All the studied films prepared on the different substrates show a *s*-type dependence of *P(E)* that is expanded with the increase of the temperature of the measurements.

Hysteresis loops *P(E)* of ST films deposited on Al_2O_3/Pt substrates (Fig.5.28) present a slim *s*-shape loop with P_r=~0.355μC/cm^2 and E_c=~14.05kV/cm at 10K and P_r=~0.185 μC/cm^2 and E_c=~8.27kV/cm at 100K.

The hysteresis loops *P(E)* of ST films deposited on Si/…/Pt substrates presented in Figure 5.29 are slighter slimmer than the previous one. P_r=~0.48μC/cm^2 and E_c=~10.535kV/cm at 10K and P_r=~0.27μC/cm^2 and E_c=~8.45kV/cm at 100K were calculated.

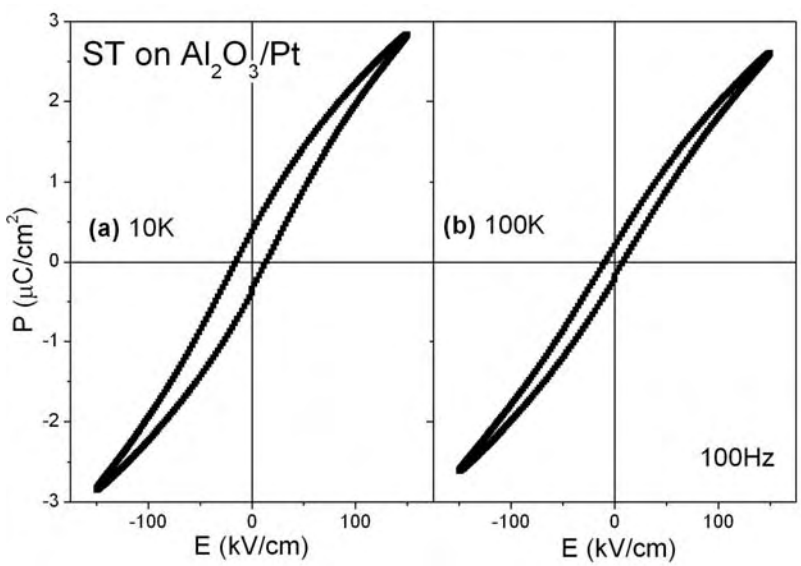

FIGURE 5.28. Hysteresis loops *P(E)* of $SrTiO_3$ (ST) thin films on Al_2O_3/Pt substrate at 10K (a) and 100K (b) at 100Hz.

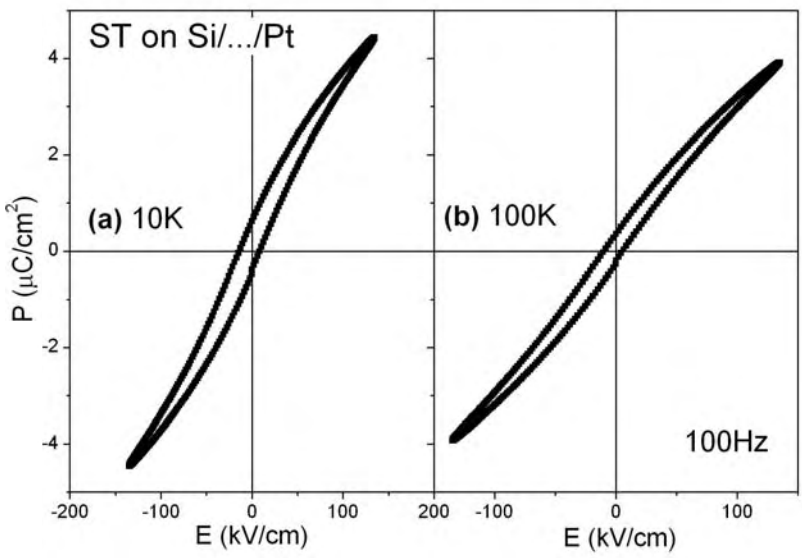

FIGURE 5.29. Hysteresis loops *P(E)* at 100Hz of $SrTiO_3$ (ST) thin films on $Si/SiO_2/TiO_2/Pt$ (Si/…/Pt) substrate at 10K (a) and 100K (b).

Figure 5.30 presents the hysteresis loops *P(E)* obtained for ST films deposited on ST/Pt substrates. These films show slim *s*-shape loops very similar to the hysteresis loops of the samples on Al_2O_3/Pt substrates (Fig.5.28). For these films P_r=~0.395μC/cm^2 and E_c=~13.38kV/cm at 10K and P_r=~0.195μC/cm^2 and E_c=~7.845kV/cm at 100K were obtained.

For ST films deposited on LSAT/Pt substrates the hysteresis loops *P(E)* are depicted in Figure 5.31 and are similar to the curves of the films on Si/…/Pt (Fig.5.29). P_r=~0.395μC/cm^2 and E_c=~8.035kV/cm at 10K and P_r=~0.3μC/cm^2 and E_c=~7.015kV/cm at 100K were calculated for these films.

Finally, Figure 5.32 represents the hysteresis loops *P(E)* of ST films on MgO/Pt substrates. Well defined *s*-shape hysteresis loops were detected for these samples at both measured temperatures: P_r=~0.525μC/cm^2 and E_c=~11.49kV/cm at 10K and P_r=~0.29μC/cm^2 and E_c=~9.385kV/cm at 100K.

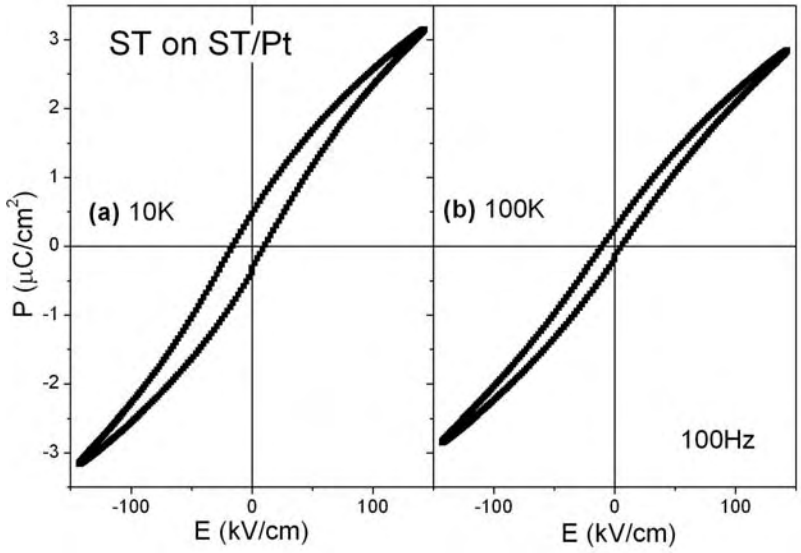

FIGURE 5.30. Hysteresis loops *P(E)* of $SrTiO_3$ (ST) thin films on $SrTiO_3$/Pt (ST/Pt) substrate at 10K (a) and 100K (b) at 100Hz.

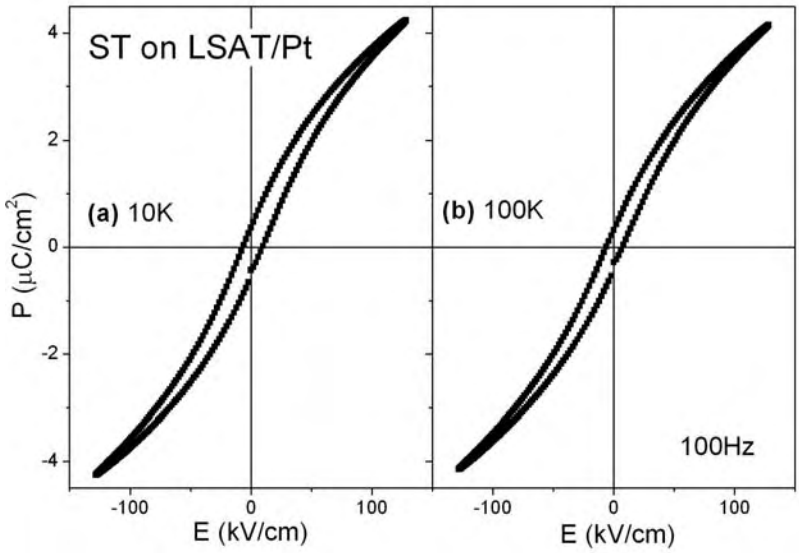

FIGURE 5.31. Hysteresis loops *P(E)* of $SrTiO_3$ (ST) thin films on $(LaAlO_3)_{0.3}$-$(Sr_2AlTaO_6)_{0.7}$/Pt (LSAT/Pt) substrate at 10K (a) and 100K (b) at 100Hz.

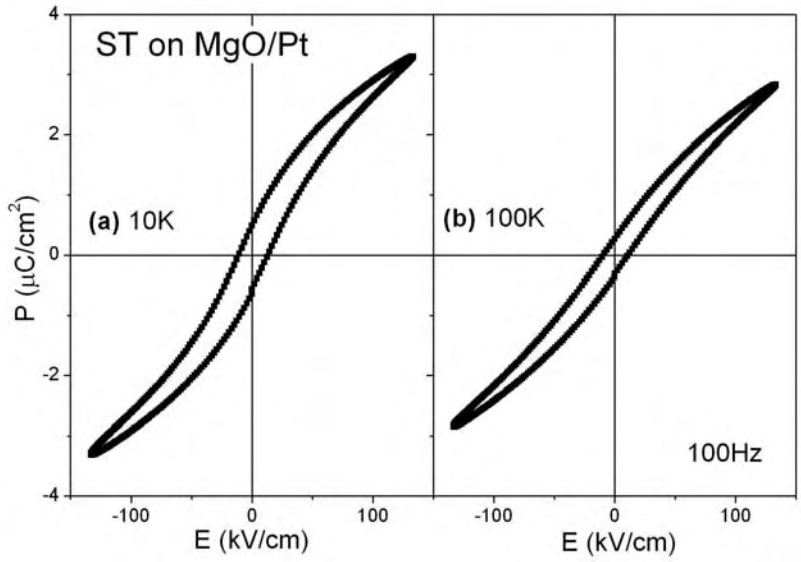

FIGURE 5.32. Hysteresis loops *P(E)* of $SrTiO_3$ (ST) thin films on MgO/Pt substrate at 10K (a) and 100K (b) at 100Hz.

For comparison the hysteresis loops *P(E)* of all these films measured at 10K at 100Hz are depicted in Figure 5.33 and the values of P_r and E_c summarized in Table 5.6.

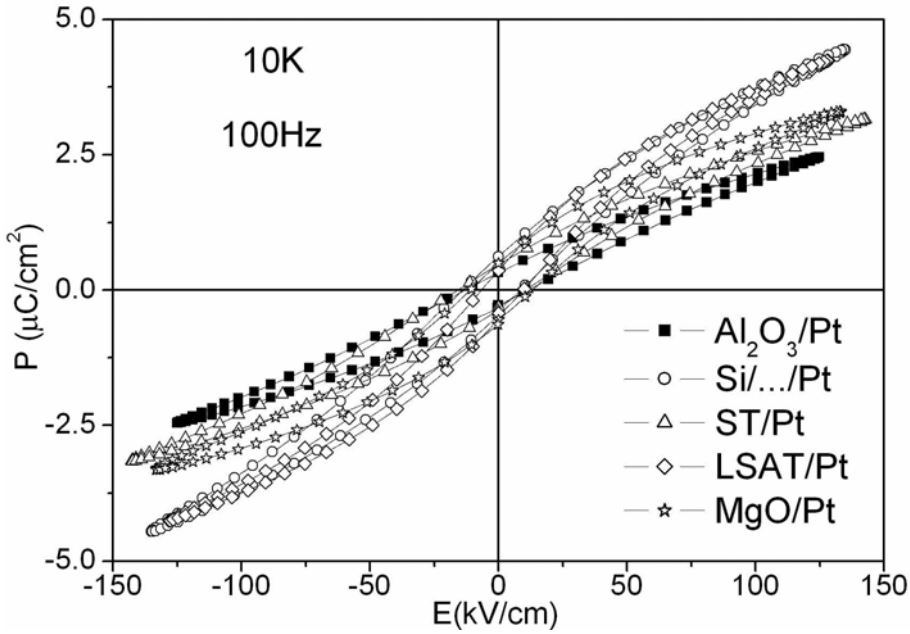

FIGURE 5.33. Hysteresis loops *P(E)* of $SrTiO_3$ thin films deposited on different platinized substrates Al_2O_3/Pt, Si/SiO_2/TiO_2/Pt (Si/…/Pt), $SrTiO_3$/Pt (ST/Pt), $(LaAlO_3)_{0.3}$-$(Sr_2AlTaO_6)_{0.7}$/Pt (LSAT/Pt) and MgO/Pt at 10K and 100Hz.

TABLE 5.6. The average value of the remnant polarization P_r and coercive field E_c of $SrTiO_3$ films deposited on different platinized substrates.

Substrate	P_r, μC/cm^2		E_c, kV/cm^2	
	at 10K	*at 100K*	*at 10K*	*at 100K*
Al_2O_3/PT	~0.36	~0.19	~14.05	~8.27
Si/…/Pt	~0.48	~0.27	~10.535	~8.45
ST/Pt	~0.39	~0.19	~13.38	~7.85
LSAT/Pt	~0.39	~0.30	~8.04	~7.02
MgO/Pt	~0.53	~0.29	~11.49	~9.36

It is visible from Figure 5.33 and Table 5.6 that P_r and E_c decrease with increasing of the measurement temperature for all the studied films. Films on MgO with the highest compressive total stress have the best defined hysteresis curve with the highest remnant polarization. As the stress level in the film decreases the hysteretic response is weakened and the lowest values of P_r were found for ST films on Al_2O_3/Pt substrates with the highest tensile total stresses. These observations are in good agreement with the dielectric response of these films, in which the higher ε' was measured for ST films on MgO/Pt was and the lowest one for ST films on Al_2O_3/Pt, indicating that the compressive stress majors the out-of-plane polarization response and as a result, under the current MIM configuration the dielectric response and the hysteretic response are enhanced.

Summary

$SrTiO_3$ thin films were deposited under the same processing conditions by sol-gel method and annealed at 900°C on 5 different platinized substrates: Al_2O_3/Pt, Si/SiO_2/TiO_2/Pt (Si/…/Pt), $(LaAlO_3)_{0.3}$-$(Sr_2AlTaO_6)_{0.7}$/Pt (LSAT/Pt), $SrTiO_3$/Pt (ST/Pt) and MgO/Pt substrates. The microstructure, structure and dielectric properties of the samples were studied and the following conclusions obtained:

1. ST films are polycrystalline independently on the type of the substrate used.
2. Lattice parameters *a* and *c* have shown an insignificant difference between all the films and all of them very close to cubic structure of the single crystals.
3. The total stress of the films was dependent on the type of the substrate and was found

to be tensile for ST films deposited on Al_2O_3/Pt, Si/…/Pt and LSAT/Pt substrates and compressive for ST/Pt and MgO/Pt substrates. It was observed that in the case of polycrystalline multilayer films, as the studied in the current work, the lattice mismatch between substrate and film plays less significant role in value of total stress compare to the thermal stress.

4. Microstructure properties were similar between all ST films deposited on different substrates, except for the case of films on MgO/Pt substrate, in which some "slip band dislocations" from the MgO substrate through Pt metal electrode in ST grains of film (due to high compressive stress) were detected.
5. IR analysis highlighted the difference in the TO1 mode behaviour of ST film deposited on Al_2O_3 (TO1 detected at equal frequency to ST single crystals and ceramics in the range from 300K to 150K) and on MgO (TO1 mode was detected at much higher frequency than that on Al_2O_3 or in bulk ST) related with the different nature and level of stress in the films.
6. ST films, deposited on MgO/Pt substrate with the highest compressive stress, have shown the highest value of ε', the highest dependency on *dc*-field, the best *s*-type hysteresis loop (with the highest value of P_r), and the highest value of n_r. In opposite, ST films, deposited on the Al_2O_3/Pt substrate, with the highest tensile stress, shown the lowest value of ε', the lowest dependency on *dc*-films, almost linear behaviour *P(E)* (with the lowest value of P_r), and the lowest value of n_r.

Chapter 6. Mg-doped $SrTiO_3$ thin films: microstructure, structure and low temperature dielectric properties

In the current chapter the study of Mg incorporation on Sr or Ti sites in $SrTiO_3$ films deposited by sol-gel on $Si/SiO_2/TiO_2/Pt$ substrates and its influence on microstructural, structural and dielectric properties of the films are presented. The effect of increasing of annealing temperature from 750°C to 900°C on the solid solubility limit in $(Sr,Mg)TiO_3$ films are studied also.

Introduction

Isovalent *A*-site substitutions in $SrTiO_3$ (ST) lattice with Ca [Bednorz and Müller, 1984], Ba [Carlson et *al.*, 2000] and Pb [Karaki et *al.,* 2002] were reported to induce a low temperature ferroelectric-type anomaly, but no polar state was reported for Mg doping in ST ceramics as well known [Kawada and Fujomoto, 1990; Tkach et *al.*, 2004].

Recent studies [Tkach et *al.*, 2004; Tkach et *al.*, 2005c] showed that the solid solubility of Mg in ST ceramics is limited, in opposition to the complete solid solution formation with the above mentioned isovalent cations, Ba^{2+} and Pb^{2+}, and is dependent on the substitution lattice site. No dielectric anomaly was observed in $Sr_{1-x}Mg_xTiO_3$ ceramics, in spite that a dielectric relaxation, similar to the one observed in $K_{1-x}Li_xTaO_3$ [Vugmeister and Glinchuk, 1990] was predicted by Kvyatkovskii [Kvyatkovskii, 2005]. Moreover, Mg *B*-site doping in ST ceramics drives the system away from the ferroelectric instability [Tkach et *al.*, 2004].

Considering that:

(i) the absence of polar anomaly in Mg doped ST ceramics, predicted by Kvyatkovskii, can be related to the absence of incorporation of Mg in the *A* site of bulk material;

(ii) chemical solution deposition processes allowing a higher degree of precursors homogeneity might favour a higher solid solubility in the lattice;

(iii) for thin films the substrate effect can not be neglected and might affect the solid solubility limit of the dopant and properties of films;

(iv) the doping effect on ST materials has been mainly studied on single crystals and ceramics, not systematically on thin films and no data on low temperature dielectric properties Mg doped ST films were reported until now;

(v) moreover it is well known that dielectric loss of thin films is considerably higher than those of single crystals due to point defects, local polar regions, stresses, *etc*. [Tagantsev et *al.*, 2003] and increases with decrease of the film thickness [Li et *al.*, 1998a], restricting the application of films for example in tunable microwave devices. Hence, if the loss of ST thin films can be reduced to the single crystal level, while a large tunability is maintained, devices utilizing these films would have a much more attractive performance;

(vi) in addition dielectric loss can be reduced by acceptor doping on Ti site (Mg doped $Ba_{0.6}Sr_{0.4}TiO_3$ thin films [Joshi and Cole, 2000] or La, Fe, Mn dopants in ST films [Hofman et *al.*, 1997]) although no low-temperature dielectric characterisation was reported yet on ST films with Mg incorporation on Ti position.

Concerning the equivalent Mg doped ST films, only the work of Suzuki et *al.* was reported [Suzuki et *al.*, 2000]. However, this work describes only the structural study of $Sr_{1-x}Mg_xTiO_3$ thin films deposited by PLD on ST substrates and annealed at 600°C [Suzuki et *al.*, 2000]. In ST films with high concentrations of Mg (30% and 50%) amorphous regions were detected by HRTEM on the top surface of the films and the solid solubility limit of Mg on the *A*-site substitution for samples with x=0.15, 0.30 and 0.50 is $x \leq 0.30$. However, no others analyses or dielectric measurements were presented.

In this way, the influence of Mg incorporation in ST lattice of thin films prepared by sol-gel on $Si/SiO_2/TiO_2/Pt$ substrates needs to be studied. And the obtained results of the dopant effect on the microstructural, structural and dielectric properties of thin $(Sr,Mg)TiO_3$ films are reported in this chapter as well as effect of annealing temperature on the dopant solid solubility limit.

6.1. Preparation and characterisation

To obtain $Sr_{1-x}Mg_xTiO_3$ (SMT) (x=0.01, 0.02, 0.05, 0.10, 0.20, 0.30, 0.40) and $SrTi_{1-y}Mg_yO_{3-\delta}$ (STM) (y=0.01, 0.05, 0.10, 0.20, 0.30, 0.40, 0.50) thin films, corresponding SMT and STM solutions were prepared by the method described in detail in the "Chapter

3". Using these transparent solutions, 10 layers of SMT and STM solutions were deposited on $Si/SiO_2/TiO_2/Pt$ substrates by spin-coating with drying between layers and obtained films annealed at 750°C for 60min. in air. To study of the effect of the annealing treatment on the solubility of Mg in the ST lattice, $Sr_{1-x}Mg_xTiO_3$ films were annealed at 750ºC, 800ºC, 850ºC and 900°C for 60min. in air. The film's crystalline structure was evaluated by XRD and Raman analysis. The film's microstructure was examined by SEM, AFM and TEM. RBS analysis was used to evaluate the in depth chemical composition of the films. Raman analyses and IR measurements (together with THz-TDS fitting) were performed on SMT and STM films deposited on single crystal Al_2O_3 substrates. The dielectric response, capacitance-voltage curves and hysteresis response were measured from 300K to 10K.

6.2. Microstructure properties

6.2.1. SEM analysis

Microstructure of $Sr_{1-x}Mg_xTiO_3$ films annealed at 750°C and 900°C and $SrTi_{1-y}Mg_yO_{3-\delta}$ annealed at 750°C were analysed by SEM and cross-section and plan view micrographs of the studied films are presented in Figures 6.1-6.3. Calculation of grain size from obtained plan-view micrographs was quite difficult due to the small grains of SMT and STM samples and because of it, more precise calculation of grain sizes was done from AFM analyses.

The SEM cross-sections and plan view micrographs of $Sr_{1-x}Mg_xTiO_3$ annealed at 750°C thin films with x=0.01, 0.05, 0.10 and 0.30 are presented in Figure 6.1. All SMT films annealed at 750°C are quite dense and, as expected, no visible orientation or textured structure was detected. Very small increasing of the grain size with Mg content was observed.

The SEM cross-sections and plan views of $SrTi_{1-y}Mg_yO_{3-\delta}$ thin films with y=0.01, 0.05, 0.10 and 0.15 annealed at 750°C are shown in Figure 6.2. Similar to the previous results STM films annealed at 750°C present dense microstructures and the absence of orientation or textured structure and a slightly smaller grain size than that of SMT films.

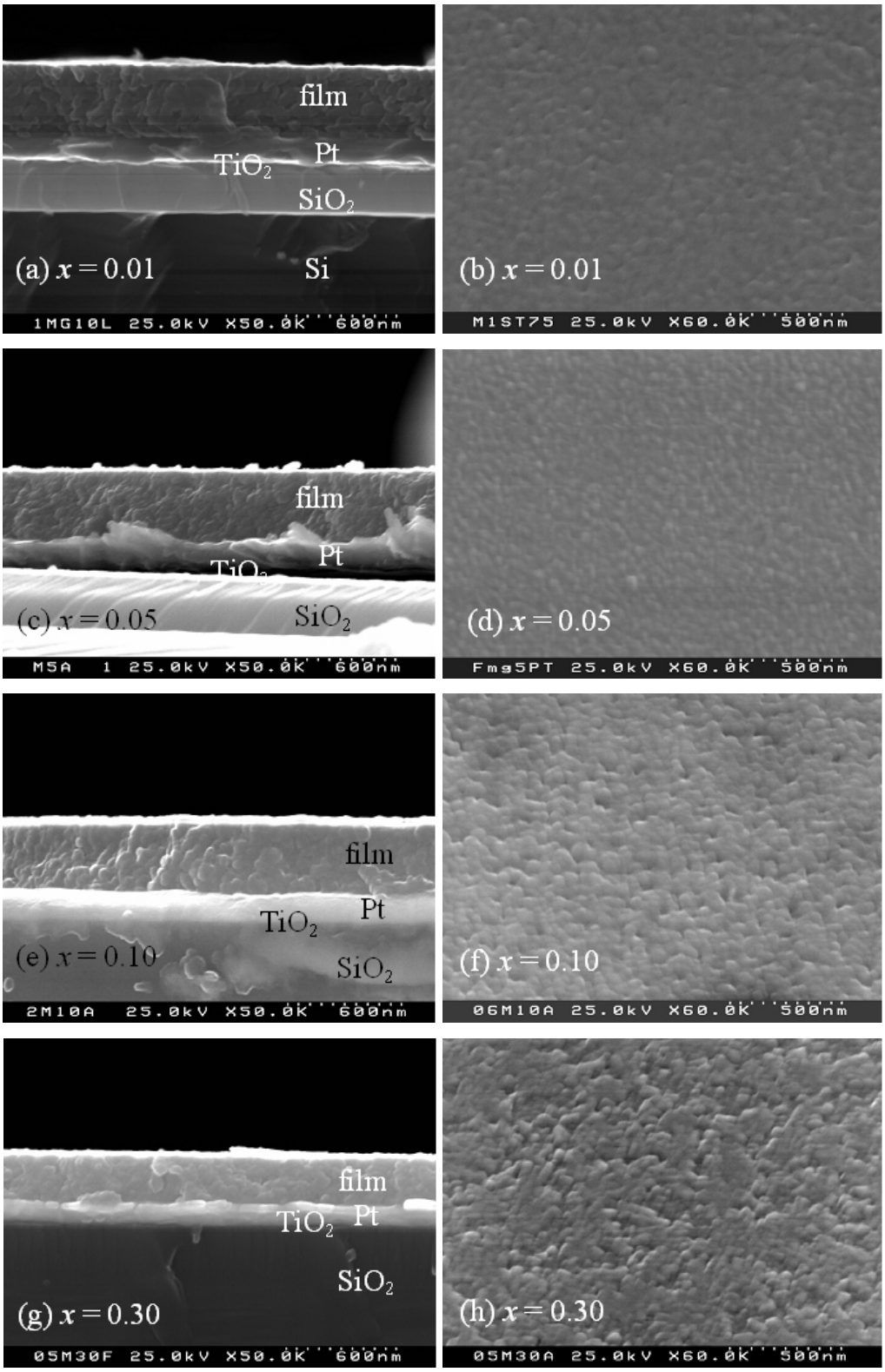

FIGURE 6.1. SEM cross-section and plan view micrographs of $Sr_{1-x}Mg_xTiO_3$ thin films with x=0.01 (a, b), x=0.05 (c,d), x=0.10 (e,f), x=0.30 (g,h) annealed at 750°C.

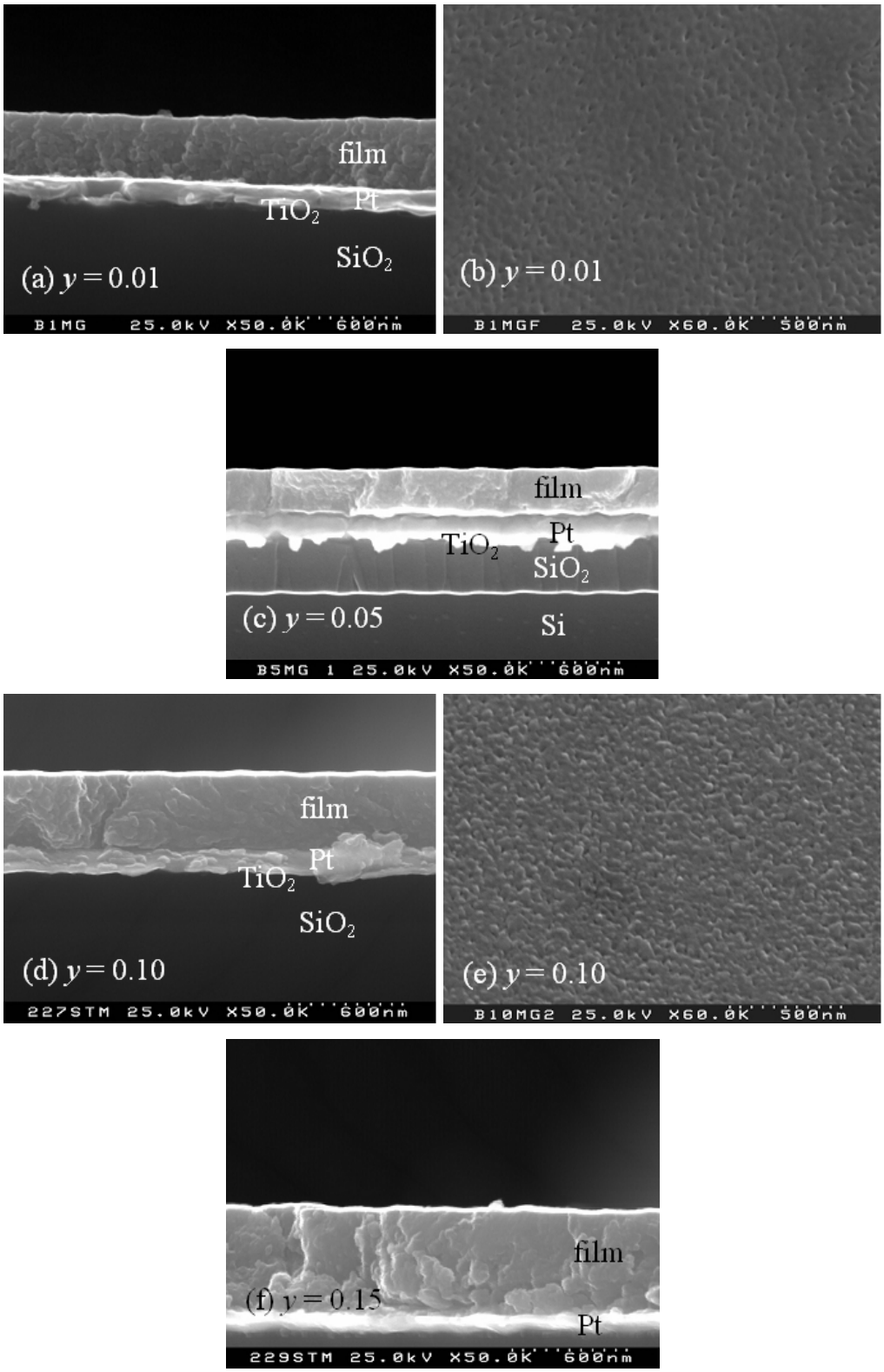

FIGURE 6.2. SEM cross-section and plan view micrographs of $SrTi_{1-y}Mg_yO_{3-\delta}$ thin films with y=0.01 (a, b), y=0.05 (c), y=0.10 (d,e), y=0.15 (f) annealed at 750°C.

SEM micrographs of $Sr_{1-x}Mg_xTiO_3$ thin films (x=0.01, 0.10 and 0.30) annealed at 900°C are depicted in Figure 6.3. All samples present dense microstructures and no textured structure as well, but the grain size of SMT films annealed at 900°C is considerably higher when compared to that of SMT or STM films annealed at 750°C (Figs.6.1 and 6.2). All Mg-doped ST thin films have smooth surface and the film thickness is similar to all the samples (~350nm) and is independent on Mg content.

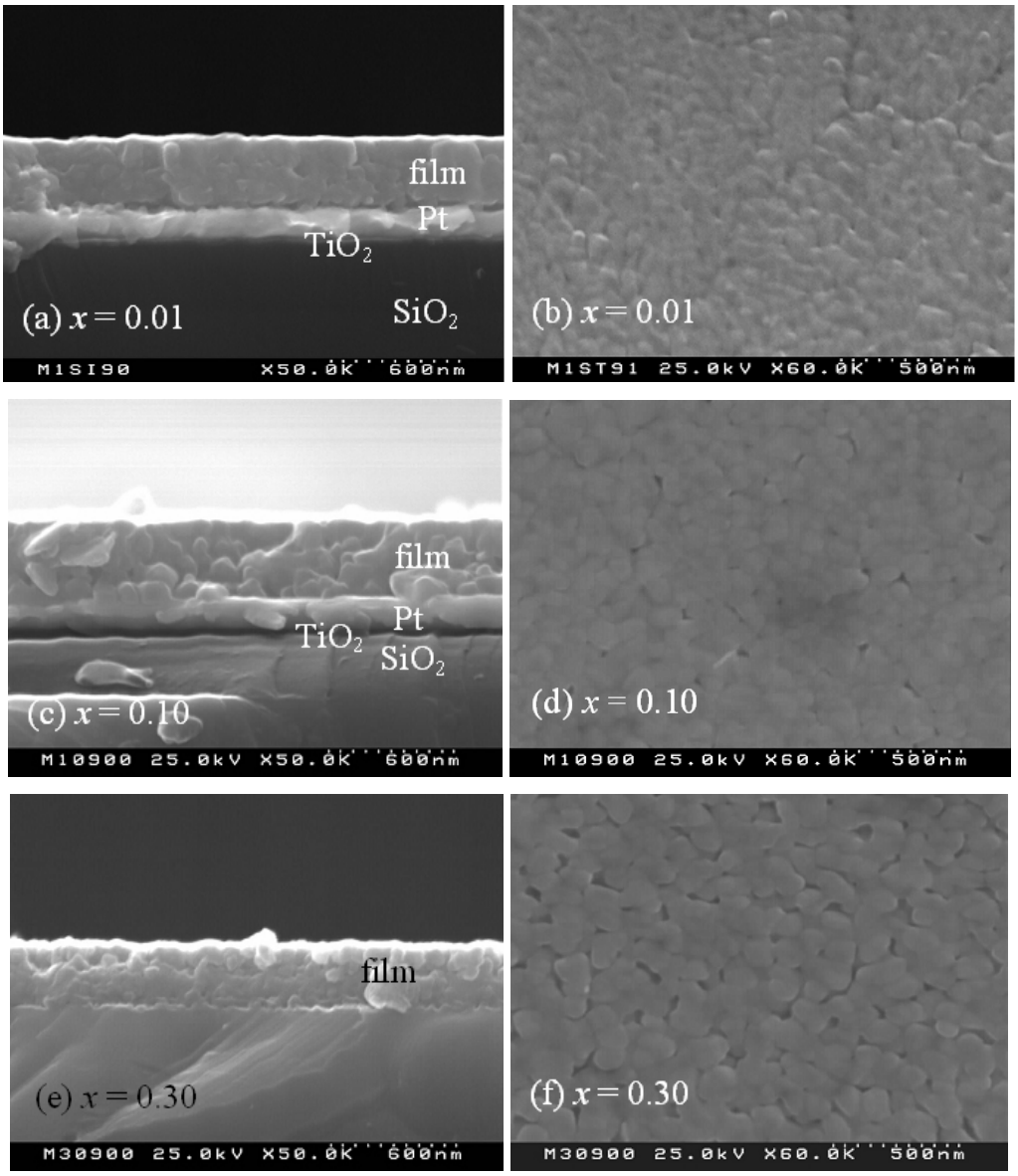

FIGURE 6.3. SEM cross-section and plan view micrographs of $Sr_{1-x}Mg_xTiO_3$ thin films with x=0.01 (a, b), x=0.10 (c,d), x=0.30 (e,f) annealed at 900°C.

6.2.2. AFM analysis

The in-plane surface morphology of $Sr_{1-x}Mg_xTiO_3$ and $SrTi_{1-y}Mg_yO_{3-\delta}$ films annealed at 750°C and $Sr_{1-x}Mg_xTiO_3$ films annealed at 900°C were analyzed by AFM.

AFM micrographs of in-plane surface (*left pictures*) and 3D view (*right pictures*) of SMT films with x=0.01, 0.10 and 0.20 annealed at 750°C are depicted in Figure 6.4. Confirming the results obtained from SEM, all these films show a smooth surface (roughness less 3nm) and small in-plane grain size (~90-110nm) which was found almost independent on Mg concentration (Fig.6.4).

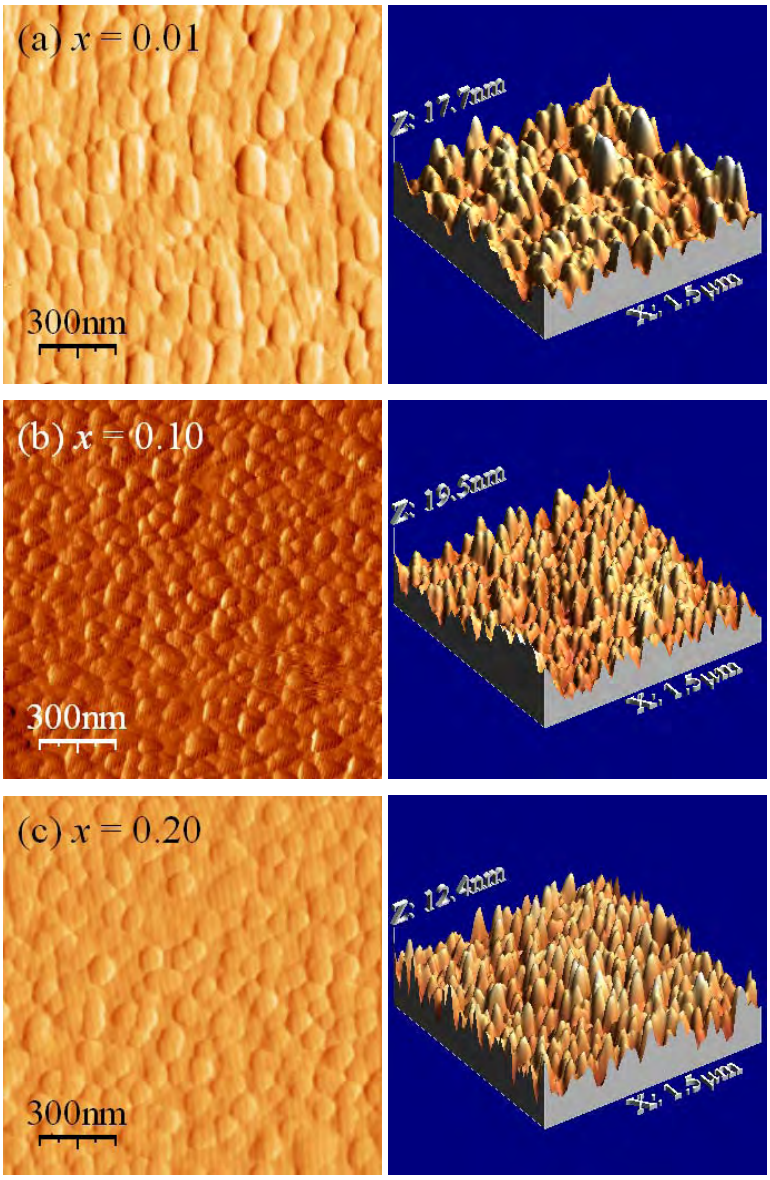

FIGURE 6.4. Atomic force micrographs of in-plane surface (*left pictures*) and 3D view (*right pictures*) of $Sr_{1-x}Mg_xTiO_3$ thin films with x=0.01 (a), x=0.10 (b) and x=0.20 (c) annealed at 750°C.

Figure 6.5 presents the micrographs of in-plane surface (*left pictures*) and 3D view (*right pictures*) of STM thin films with y=0.01, y=0.05 and y=0.10 annealed at 750°C. All these films show a smooth surface (roughness lower than 2nm), and small in-plane grain size (~80-90nm) almost independent on Mg concentration (Fig.6.5). STM films with y=0.01 have more flat surface that the others STM films or SMT films.

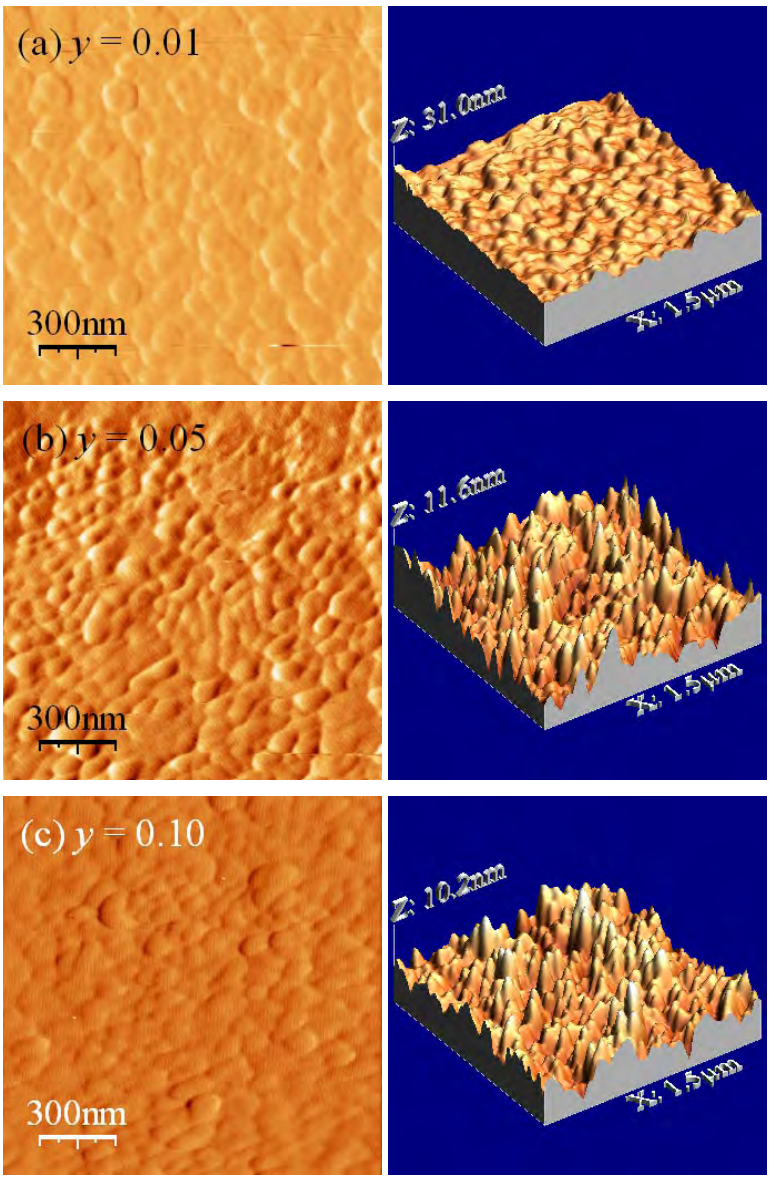

FIGURE 6.5. Atomic force micrographs of in-plane surface (*left pictures*) and 3D view (*right pictures*) of $SrTi_{1-y}Mg_yO_{3-\delta}$ thin films with y=0.01 (a), y=0.05 (b) and y=0.10 (c) annealed at 750°C.

AFM micrographs of in-plane surface (*left pictures*) and 3D view (*right pictures*) of SMT thin films with x=0.10, 0.20 and 0.30 annealed at 900°C depicted in Figure 6.6. AFM

analysis clearly shows the increase grain size for the films heat treated at 900ºC, in relation to SMT and STM films annealed at lower temperatures, though the surface of the films remains smooth (roughness ~3nm) (Fig.6.6).

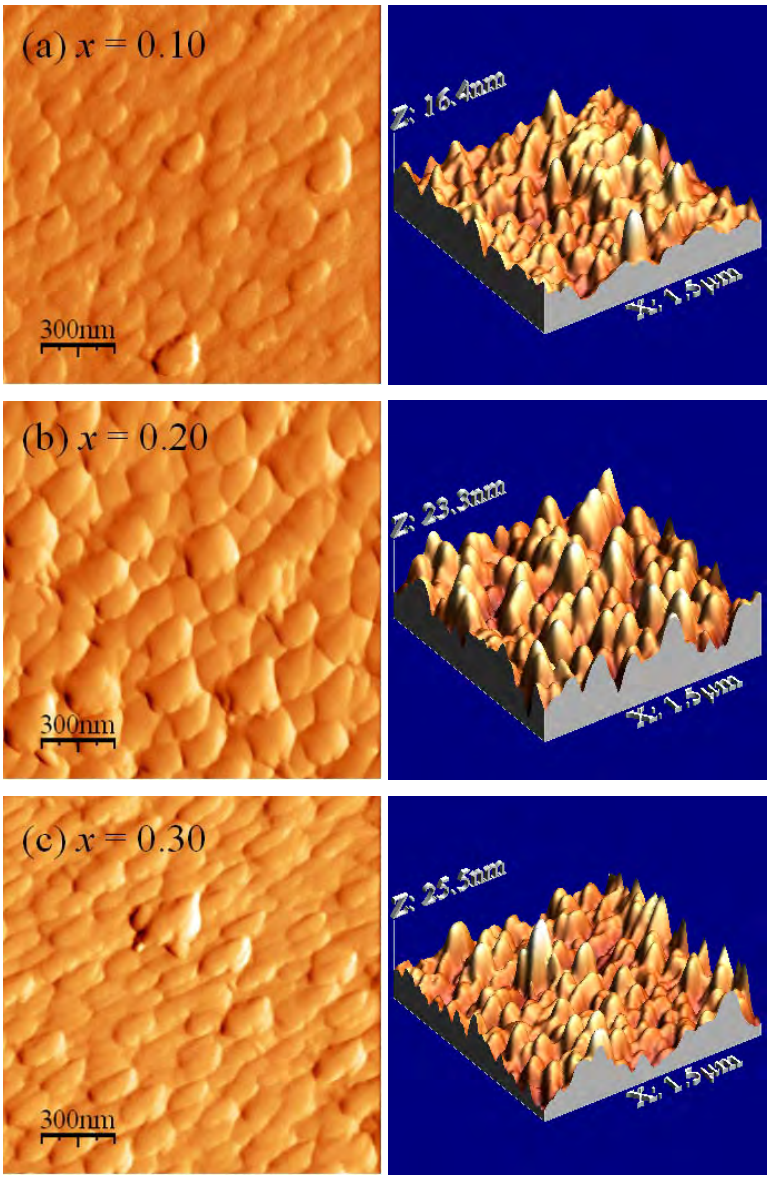

FIGURE 6.6. Atomic force micrographs of in-plane surface (*left pictures*) and 3D view (*right pictures*) of $Sr_{1-x}Mg_xTiO_3$ thin films with x=0.10 (a), x=0.20 (b) and x=0.30 (c) annealed at 900ºC.

Average in-plane grain size and roughness of the studied films were calculated from AFM micrographs and the results are summarised in Figure 6.7.

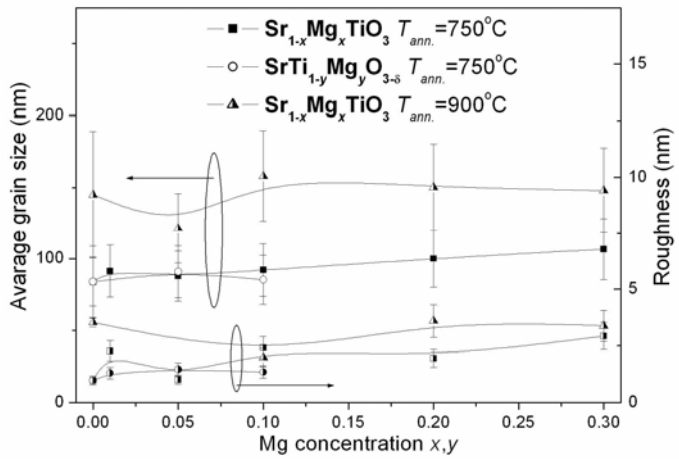

FIGURE 6.7. Average grain size (*left axis*) and roughness (*right axis*) *vs* Mg concentration of $Sr_{1-x}Mg_xTiO_3$ films annealed at 750°C and 900°C and $SrTi_{1-y}Mg_yO_{3-\delta}$ films annealed at 750°C. Values of grain size and roughness for undoped $SrTiO_3$ films are from Chapter 4.

6.2.3. TEM analysis

The microstructures of $Sr_{1-x}Mg_xTiO_3$ and $SrTi_{1-y}Mg_yO_{3-\delta}$ thin films annealed at 750°C as well as $Sr_{1-x}Mg_xTiO_3$ films annealed at 900°C were analyzed by TEM.

The plan view TEM micrographs of $Sr_{0.99}Mg_{0.01}TiO_3$ and $SrTi_{0.99}Mg_{0.01}O_{3-\delta}$ films annealed at 750°C are depicted in Figure 6.8a and Figure 6.8b, respectively.

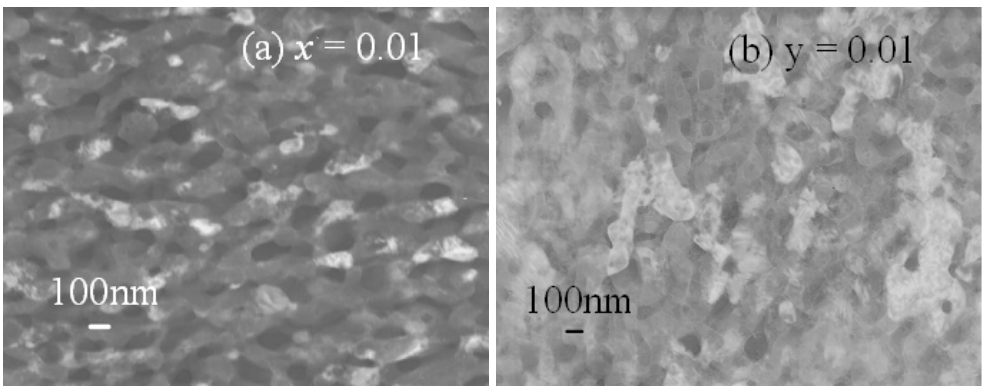

FIGURE 6.8. TEM plan view micrographs of $Sr_{1-x}Mg_xTiO_3$ (a) and $SrTi_{1-y}Mg_yO_{3-\delta}$ (b) thin films with *x,y*=0.01annealed at 750°C.

SMT and STM films annealed at 750°C presented quite dense microstructures and no obvious defects or non homogeneity and have small grain size (~100nm) confirming the AFM results (~85nm for *x,y*=0.01).

Figure 6.9 depicted the cross-section TEM micrographs (Fig.6.9a) and EDS spectra (Fig.6.9b) of $Sr_{0.90}Mg_{0.10}TiO_3$ films annealed at 750°C and cross-section image of $Sr_{0.80}Mg_{0.20}TiO_3$ films annealed at 900°C (Fig.6.9c).

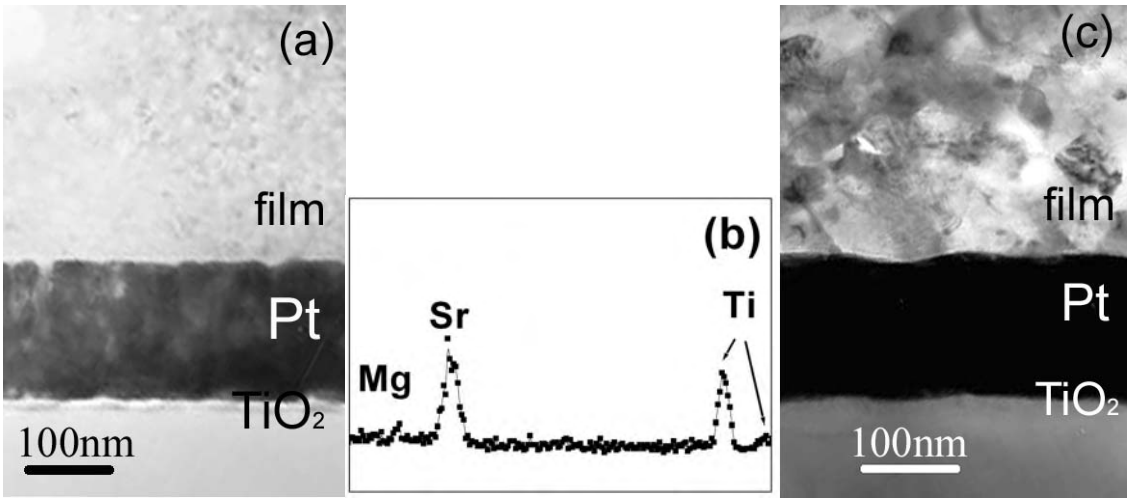

FIGURE 6.9. Cross-section TEM micrographs (a) and EDS spectra (b) of $Sr_{0.90}Mg_{0.10}TiO_3$ films annealed at 750°C (a) and cross- section TEM micrographs of $Sr_{0.80}Mg_{0.20}TiO_3$ films annealed at 900°C (c).

No significant thickness variation was observed for Mg-doped ST films with different Mg contents or annealed at different temperatures, confirming the SEM observations. The TEM cross-section micrographs revealed dense microstructure of studied SMT films at both annealing temperatures 750°C and 900°C (Fig.6.9a and 6.9c). Moreover, SMT films with x,y=0.01 annealed at 750°C and 900°C exhibit a small out-of-plane grain size (~20–50nm), what is much smaller compare to the in-plane grain size obtained from AFM analyse (~90nm for SMT film with x=0.10 at $T_{ann.}$=750°C and ~150nm for SMT film with x=0.20 annealed at 900°C (Fig.6.9c)). Meanwhile, SMT films annealed at 900°C presented a bit bigger grain size (> 40nm) (Fig.6.9c) in contrast to SMT films heat treated at 750°C (Fig.6.9a). No evidences of second phases were observed for films annealed at 750°C according to the presented EDS spectra of SMT films with x=0.10 and annealed at 750°C (Fig.6.9b) confirming of XRD results.

TEM plan-view micrographs, EDS spectra and electron diffraction (ED) pattern of $Sr_{0.30}Mg_{0.30}TiO_3$ films annealed at 750°C and 900°C are depicted in Figure 6.10.

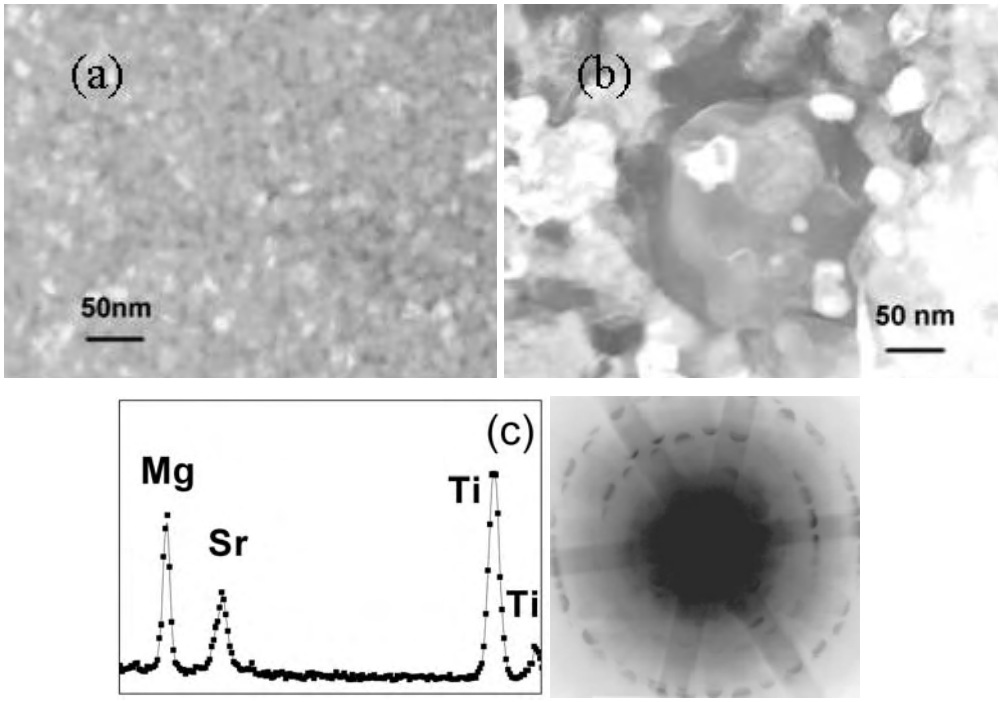

FIGURE 6.10. Plan section images of $Sr_{0.30}Mg_{0.30}TiO_3$ films annealed at 750°C (a) and at 900°C (b). EDS spectra (c) and ED pattern (d) from ilmenite grain in $SrTiO_3$ matrix annealed at 900°C.

SMT with x=0.30 and annealed at 750°C (Fig.6.10a) shown homogeneous films with small grains in contrast to SMT with x=0.30 annealed at 900°C (Fig.6.10b) in which large second phase grains were observed (~150nm) (Fig.6.10b). According to EDS (Fig.6.10c) these large second phase grains are Mg rich being the surrounding grains essentially ST. ED pattern of these grains in $Sr_{0.70}Mg_{0.30}TiO_3$ film annealed at 900°C (Fig.6.10d) confirms the ilmenite structure, which was not observed for equivalent $Sr_{0.70}Mg_{0.30}TiO_3$ films annealed at 750°C (Fig.6.10a). The number and size of the Mg-rich grains increased with increasing Mg content.

As the temperature increases, there is start of crystallisation which occurs homogeneously throughout the layer and is complete by 750°C. During this process, "nucleation dominates crystallisation" and there is only limited diffusion. All Mg^{2+} ions therefore become incorporated into the rapidly nucleating perovskite lattice on the A-site in order to maintain the local A/B stoichiometry. The enhanced solid solubility limit of Mg^{2+} on the A-site can therefore be attributed to a rapid nucleation and limited growth.

On the other hand at higher temperatures, 900°C, there is sufficient activation energy for diffusion to occur. Mg^{2+} ions diffuse to form Mg rich ilmenite grains ($MgTiO_3$) in an essentially pure $SrTiO_3$ matrix. Effectively, at 900°C the microstructure is dominated by

the phase equilibria of the ilmenite and perovskite structures, as illustrated by the peaks in the XRD and Raman traces and the presence of second phases in TEM images.

For all SMT films annealed at different temperatures analyzed in current work by TEM no residual amorphous phase was detected in cross sectional images. These results are in contradiction with those reported by Suzuki *et al.* [Suzuki et *al.*, 2000] in which high concentrations of amorphous regions were detected by HRTEM on the top surface of $Sr_{1-x}Mg_xTiO_3$ (x=0.50) thin films annealed at 600°C and deposited by PLD on ST substrates. In that work [Suzuki et *al.*, 2000] no ilmenite-type second phase was observed.

6.3. Rutherford backscattering spectrometry analysis

In the current work the distribution of elements in Mg-doped ST films was analysed by Rutherford backscattering spectrometry (RBS) which was described in detail in the "Chapter 3". The elemental distribution of Sr, Ti, Mg, O, Pt, Si in SMT films with x=0.10, 0.15, 0.30 annealed at 750°C and 900°C by RBS is depicted in the Figures 6.11 and 6.12.

Figure 6.11 presents the RBS data and simulation (fit) obtained for $Sr_{0.70}Mg_{0.30}TiO_3$ thin films annealed at 750°C. In this Figure the partial elemental contributions (Sr, Ti, O, Mg, Pt and Si response) are shown. Thus, the simulation (fit) is the sum of all contributions.

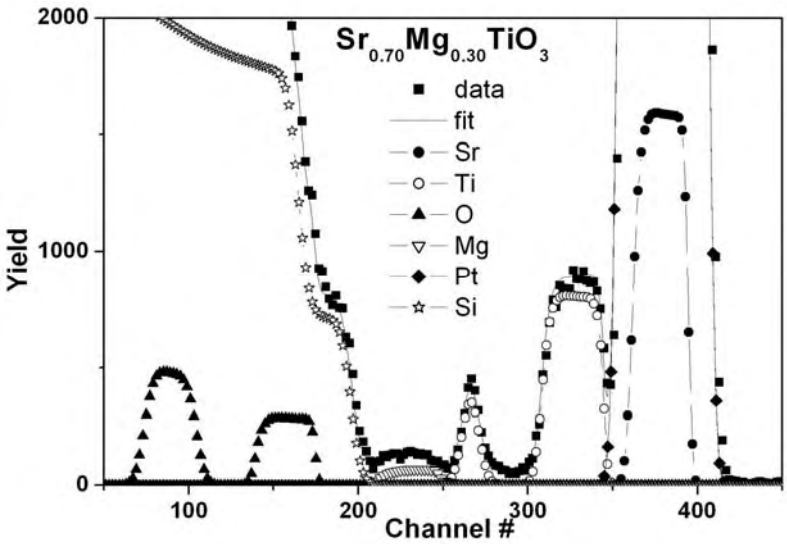

FIGURE 6.11. RBS analysis of $Sr_{0.70}Mg_{0.30}TiO_3$ thin films annealed at 750°C: RBS data (■) and simulation (-).

The signal from Mg element was observed very well only in RBS spectra of 2 samples: SMT films with x=0.30 annealed at 750°C and SMT films with x=0.30 annealed at 900°C due to high Mg content. In all others samples (SMT films with x=0.10 and 0.15 at 750°C and 900°C) Mg signal was almost unvisible due to low concentration of Mg.

Figure 6.12a and Figure 6.12b correspond to the simulated elemental contributions in terms of elemental atomic percentage as a function of thickness of SMT films with x=0.10, 0.15 and 0.30 annealed at 750°C and 900°C, respectively.

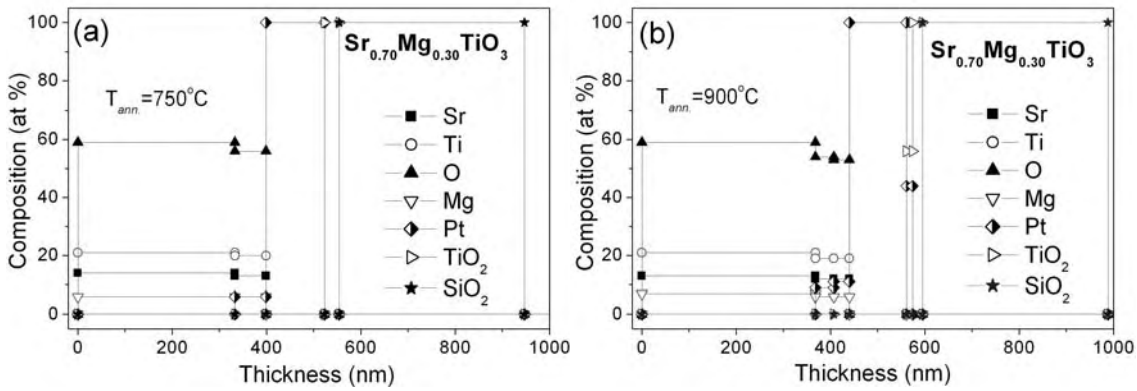

FIGURE 6.12. Distribution of the elements of $Sr_{0.70}Mg_{0.30}TiO_3$ thin films annealed at 750°C (a) and 900°C (b).

RBS spectra and fits calculation showed that all films have mostly uniform Sr, Ti and Mg (where this element could be assessed by RBS) distributions all over the films, with compositions similar to the nominal $Sr_{1-x}Mg_xTiO_3$ with x=0.10, 0.15, 0.30.

The above data is consistent with TEM observations for films annealed at 750°C but inconsistent with those annealed at 900°C, in which discrete $MgTiO_3$ rich grains were observed. It could be due to the homogeneous distribution of constituent ions obtained by RBS in all films attributed to the relatively large probe size (~1mm) compared to the size of the ilmenite $MgTiO_3$ regions (~150nm), utilised in this technique, which limits the spatial resolution parallel with film surface and averages the composition. In the $Si/SiO_2/TiO_2/Pt$ substrates some Pt/film interface mixing is observed in all samples, with more pronounced mixing in the 900ºC annealed samples (Fig.6.12b) that was not observed by SEM or TEM results. In these samples, the simulations also indicate some Pt/TiO_2 interface mixing, which is not observed in the 750ºC annealed samples (Fig.6.12a). The thickness of the interface Pt/film of $Sr_{0.70}Mg_{0.30}TiO_3$ films at 750°C was less than for equivalent films annealed at 900°C (66nm and 72nm, respectively).

6.4. Crystal structure and lattice parameters

XRD patterns of $Sr_{1-x}Mg_xTiO_3$ (SMT) (x=0.01, 0.02, 0.05, 0.10, 0.20, 0.30, 0.40) and $SrTi_{1-y}Mg_yO_{3-\delta}$ thin films (STM) (y=0.01, 0.05, 0.10, 0.20, 0.30, 0.40, 0.50) thin films deposited by sol-gel on $Si/SiO_2/TiO_2/Pt$ substrate and annealed at 750°C are depicted in Figure 6.13 together with spectra of undoped ST films.

It can be seen that all $Sr_{1-x}Mg_xTiO_3$ films with x=0.01-0.40 have a spectra similar to undoped ST and are monophasic (Fig.6.13a). However, for dopant concentrations x>0.30 the solutions were not transparent, becoming opaque just immediately after last step of the preparation and some powder precipitation appears in the solution after several hours. It is then considered that the highest concentration for monophasic SMT solutions/films annealed at 750°C is x=0.30, under the present experimental conditions.

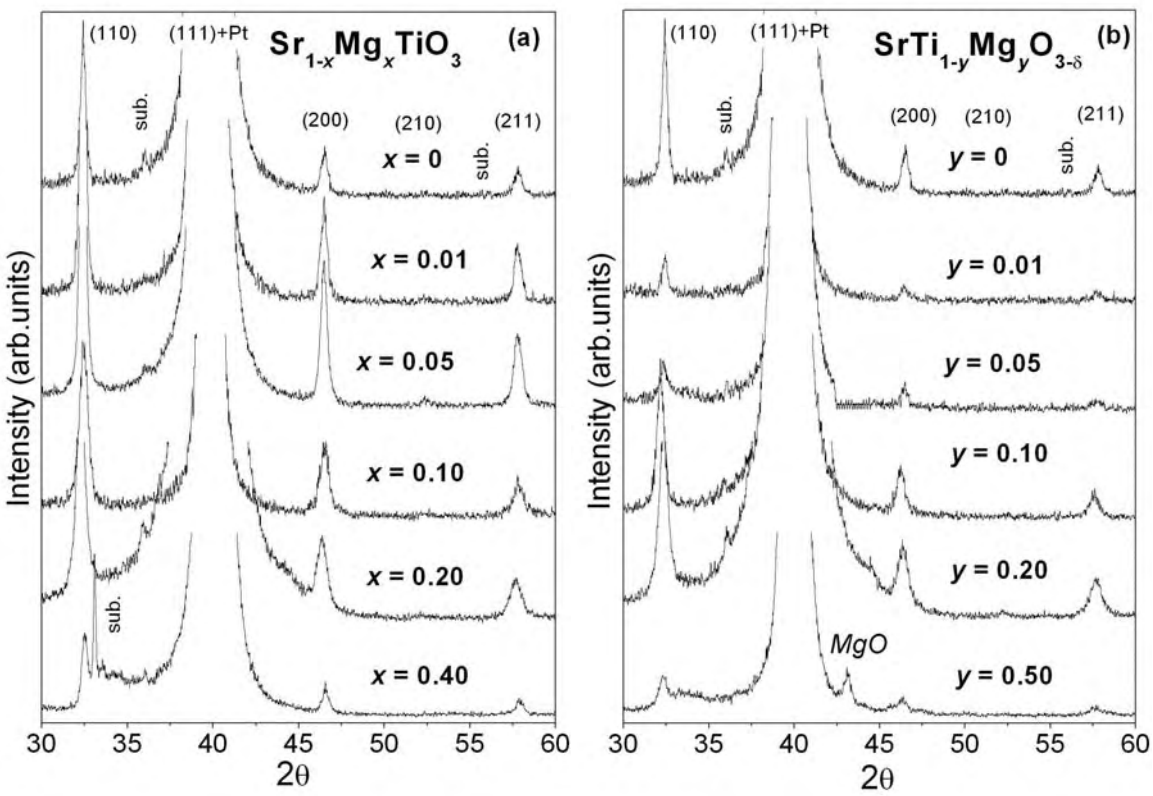

FIGURE 6.13. XRD patterns of $Sr_{1-x}Mg_xTiO_3$ (a) and $SrTi_{1-y}Mg_yO_{3-\delta}$ (b) films.

At the same time $SrTi_{1-y}Mg_yO_{3-\delta}$ films exhibit a single perovskite phase with the exception of y=0.50 (Fig.6.13b). For STM films with y=0.50 the MgO phase is clearly observed. Thus, the solid solubility of Mg in ST films prepared by sol-gel and annealed at 750°C is around 30% for *A* and 40% for *B* site of ST lattice, respectively. In the earlier work of Suzuki et *al.* [Suzuki et *al.,* 2000] the solid solubility limit of Mg for $Sr_{1-x}Mg_xTiO_3$ films was also reported to be 30%, though determined for samples annealed at lower temperatures (600°C) and deposited by PLD on ST substrates. Much lower solid solubility limits was reported for Mg doped ST ceramics (< 1% for SMT and < 15% for STM) [Tkach et *al.*, 2004].

To study the annealing effect on the solubility of Mg on Sr position, $Sr_{1-x}Mg_xTiO_3$ films with x=0.10, 0.15 and 0.30 were annealed at 800°C, 850°C and 900°C and the obtained XRD spectra are presented in Figure 6.14.

No visible second phases were detected by XRD for SMT films annealed at 800°C and 850°C (Fig.6.14a, b). Only for SMT films with x=0.30 and annealed at 900°C small peaks associated with an ilmenite-type $MgTiO_3$ second-phase appeared (Fig.6.14c).

According to the values of in-plane lattice parameters *a* and out-of-plane lattice parameters *c* obtained from XRD measurements in previous "Chapter 4" and from the "Chapter 5" it is possible to suppose that $a \approx c$ in this study also. Thus, in the current analysis only out-of-plane lattice parameters *c* were calculated from the XRD data of $Sr_{1-x}Mg_xTiO_3$ and $SrTi_{1-y}Mg_yO_{3-\delta}$ films annealed at 750°C (Fig.6.15) and for $Sr_{1-x}Mg_xTiO_3$ films annealed at different temperatures (Fig.6.16).

The out-of-plane lattice parameters *c* of undoped ST at $T_{ann.}$=750°C was calculated already in the previous "Chapter 4" and presented c=~3.905±0.0029Å, what is in close agreement with the literature data for single crystals of ST, that has a cubic structure with a lattice parameter a=3.905Å [Mitsui and Westphal, 1961].

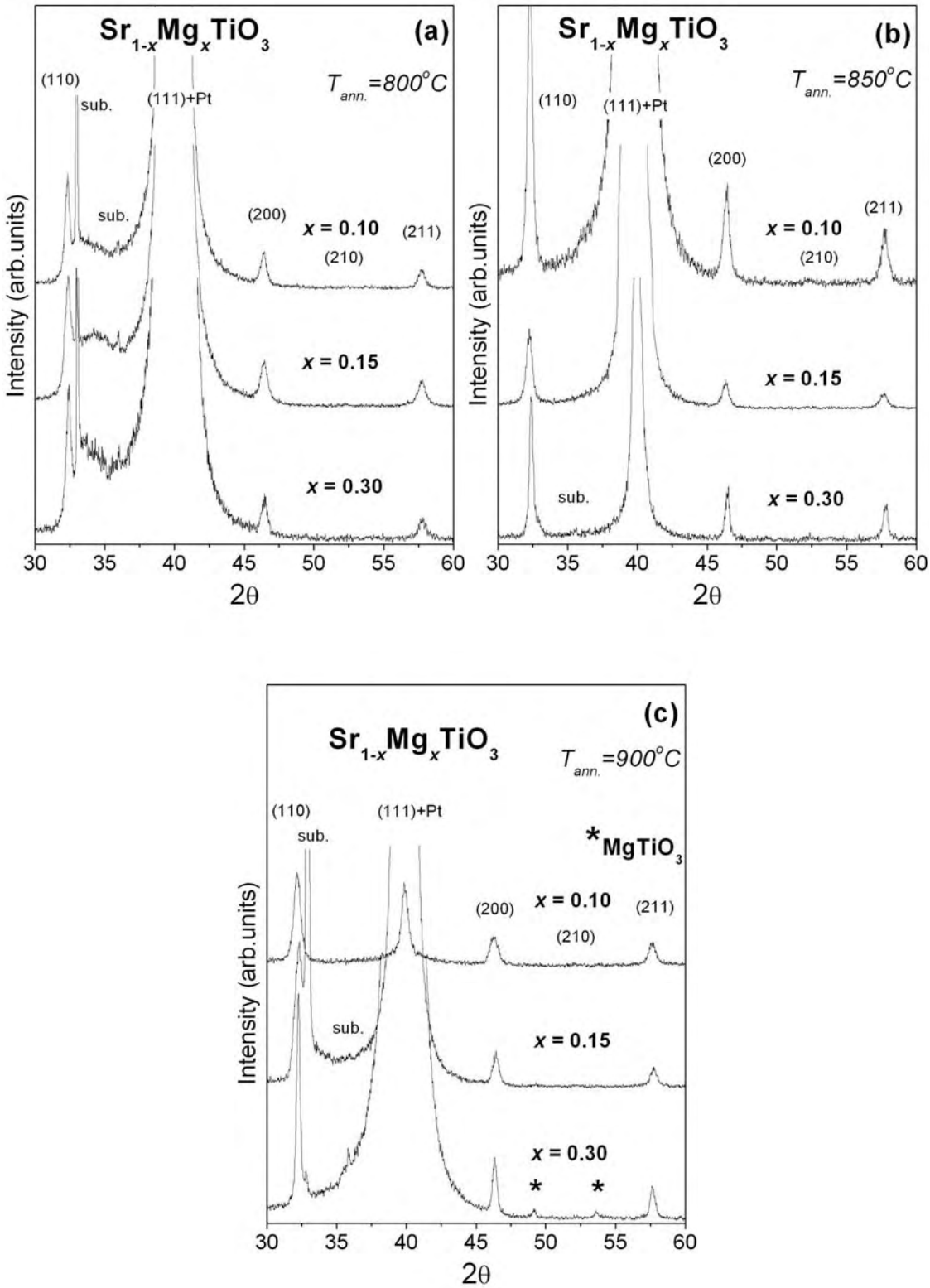

FIGURE 6.14. XRD patterns of $Sr_{1-x}Mg_xTiO_3$ thin film annealed at 800°C (a), 850°C (b) and 900°C (c) (* denotes $MgTiO_3$ phase).

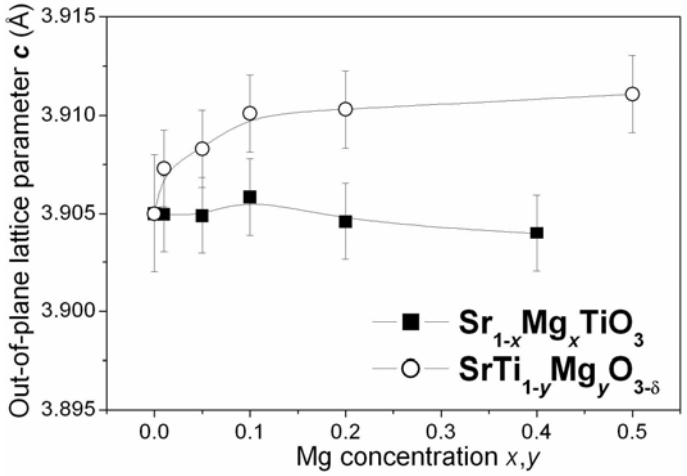

FIGURE 6.15. Out-of-plane lattice parameter *c* of $Sr_{1-x}Mg_xTiO_3$ and $SrTi_{1-y}Mg_yO_{3-\delta}$ thin films annealed at 750°C as a function of Mg concentration in analyzed films.

It was observed that the lattice parameter *c* is almost constant with increasing of the Mg concentration for $Sr_{1-x}Mg_xTiO_3$ thin films annealed at 750°C, varying from ~3.90497Å (*x*=0.01) to ~3.9049Å (*x*=0.05) to ~3.9059Å (*x*=0.10) to ~3.9046Å (*x*=0.20) and to ~3.904Å (*x*=0.40). *c* variation in SMT ceramics was also reported to be very small what indicated a very weak Mg solubility in Sr sites of ST grains [Tkach et *al.*, 2004]. Concerning the $(Sr,Mg)TiO_3$ films obtained by PLD on ST substrates at 600°C, Suzuki *et al.* reported that the out-of-plane lattice parameters of these films (with 15%, 30% and 50% of Mg) were slightly elongated in comparison with that of ST (*a*=3.905Å) and increase with the magnesium/strontium ratios [Suzuki et *al.*, 2000].

On the other hand the lattice parameter of STM films increases with the increasing of Mg content, until *y*=0.10 (Fig.6.3). For $SrTi_{1-y}Mg_yO_{3-\delta}$ thin films annealed at 750°C (Fig.6.3), *c* varies from ~3.9073Å (*y*=0.01) to ~3.9083Å (*y*=0.05) to ~3.91Å (*y*=0.10) to ~3.9103Å (*y*=0.20) and to ~3.911Å (*y*=0.50) with increasing of Mg concentration. Similar increase of the lattice parameter, was observed for STM ceramics and confirmed the introduction of Mg in the BO_6 sub-lattice of ST [Tkach et *al.*, 2004].

At the same time, according to results obtained for undoped ST films annealed at different temperatures, the out-of-plane lattice parameters *c* of $Sr_{1-x}Mg_xTiO_3$ films annealed at 750°C and 900°C are expected to be different at different temperatures, due to the variation of the thermal stress level in the films. In this way, *c* of SMT films with *x*=0, 0.10, 0.15, 0.20 and 0.30 at $T_{ann.}$=800°C, 850°C and 900°C were calculated from the XRD spectra and presented in Figure 6.16 as function of Mg concentration.

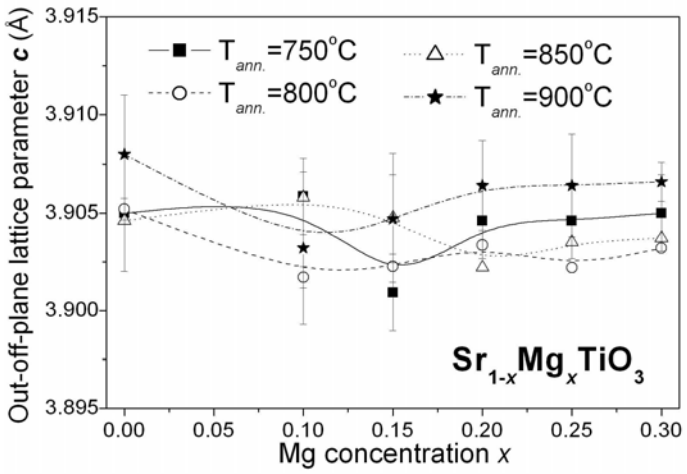

FIGURE 6.16. Out-of-plane lattice parameter c of $Sr_{1-x}Mg_xTiO_3$ films annealed at different temperatures (750°C, 800°C, 850°C and 900°C) as a function of Mg concentration.

It can be seen in Figure 6.16 that in SMT samples annealed at 900°C, c slightly changed with x, but the mean values remained at ~3.905Å and lie within the error bar for that of ST. Therefore, these data do not demonstrate a statistically significant variation in c. However, for samples annealed at 750°C, c decreased before $x \leq 0.15$, but increased after $x > 0.15$. The lattice parameter c of SMT films annealed at 800°C decreases similarly to that of samples annealed at 750°C but only until x=0.10 and after that show a small increase and it is almost constant for $x \geq 0.15$. SMT films annealed at higher temperatures 850°C show an increase of c for x=0.10, after that it decreases for $x \geq 0.20$ it increases again for $x > 0.20$. This non monotonous and unexpected variation can be somehow related to the existence at low annealing temperatures of some amorphous Mg-rich regions that crystallize in the second phase at high enough annealing temperatures.

Expected decreasing of the lattice parameter in $Sr_{1-x}Mg_xTiO_3$ and observed increasing of the lattice parameter in $SrTi_{1-y}Mg_yO_{3-\delta}$ system with increasing of Mg content is reasonable taking into consideration the smaller ionic radius of Mg^{2+} when substituting Sr^{2+} ions (ionic radius of $Sr^{2+}_{(12)}$ is 1.44Å and $Mg^{2+}_{(12)}$ is 1.21Å (from the extrapolation using $Mg^{2+}_{(4)}$, $Mg^{2+}_{(5)}$, $Mg^{2+}_{(6)}$ and $Mg^{2+}_{(8)}$ ionic radius values) [Shannon, 1976]) and bigger Ti^{2+} ions (ionic radius of $Ti^{4+}_{(6)}$ is 0.605Å and $Mg^{2+}_{(6)}$ is 0.72Å [Shannon, 1976]) (Fig.6.17).

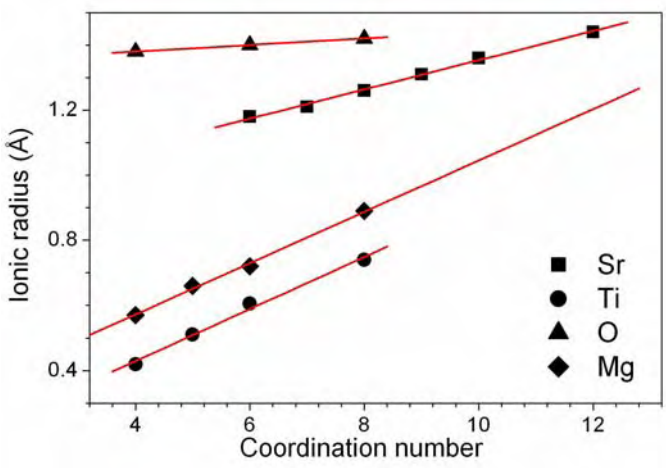

FIGURE 6.17. Ionic radii of several ions *versus* coordination number following Shannon [Shannon, 1976].

6.5. Lattice dynamics study

6.5.1. Raman spectroscopy analysis

For better understanding of the lattice structure obtained after incorporation of Mg in Sr site of ST lattice and to analyze the influence of annealing temperature on the samples structure, SMT thin films annealed at 750°C and 900°C and STM thin films annealed at 750°C were studied by Raman spectroscopy.

Figure 6.18 depicts the obtained room temperature Raman spectra of $Sr_{1-x}Mg_xTiO_3$ films (x=0.10, 0.15, 0.30) at $T_{ann.}$=750°C and 900°C and $SrTi_{1-y}Mg_yO_{3-\delta}$ films (y=0.10, 0.15) at $T_{ann.}$=750°C together with the spectra of undoped ST films annealed at 750°C. The spectrum of the sapphire substrate, used for all analyzed here samples (with peaks located at about 379, 418, 430, 449, 578 and 750 cm^{-1}) is also represented for comparison.

As well described in the literature, and mention in previous "Chapter 5" the spectra of undoped ST ceramics are characterized by TO2, TO4 and LO4 room-temperature (at ~172, 546 and 792cm^{-1}, respectively) in the presented range of wave lengths from 150cm^{-1} to 850cm^{-1} [Petzelt et *al.*, 2001].

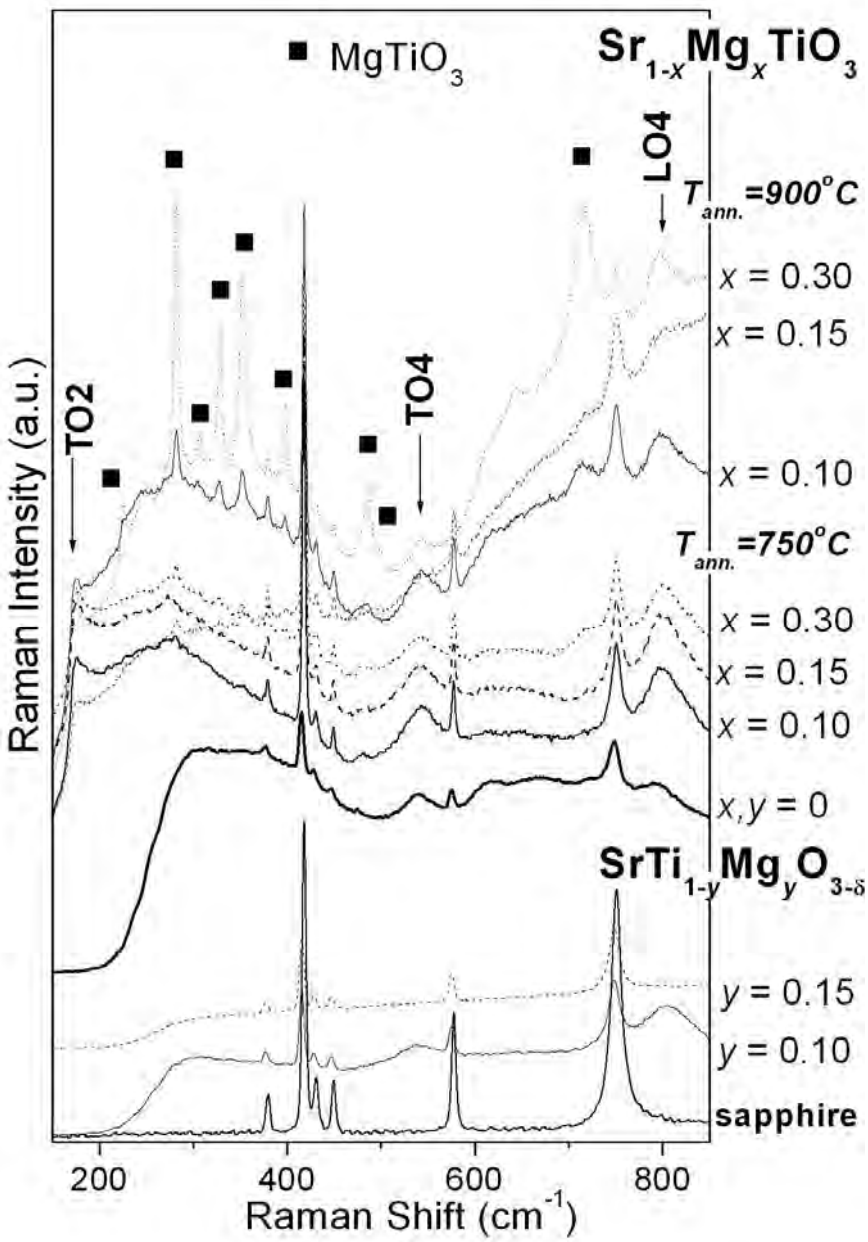

FIGURE 6.18. Room temperature Raman spectra of $Sr_{1-x}Mg_xTiO_3$ films annealed at 750°C and 900°C (▪ denotes $MgTiO_3$ phase) and $SrTi_{1-y}Mg_yO_{3-\delta}$ films annealed at 750°C.

TO4 (at ~546cm^{-1}) and LO4 (at ~800cm^{-1}) modes were observed in studied undoped ST and STM samples annealed at 750°C. These LO4 mode and polar TO4 mode are also clearly seen in room temperature Raman spectra of SMT films annealed at both 750°C and 900°C, as well as TO2 mode (~178cm^{-1}) (Fig.6.18). As was described in the literature for undoped ST ceramics [Petzelt et *al.*, 2001] and previously mentioned for undoped ST films

("Chapter 5"), the Raman spectra of ST system in the used wavelengths range are characterized by TO4 and LO4 modes (at ~546cm^{-1} and ~792cm^{-1}, respectively), observed due to local loss of symmetry at the grain boundaries [Petzelt et *al.*, 2001].

Obtained Raman spectra of STM films annealed at 750°C are very similar to undoped ST films annealed at 750°C. In the meantime the spectra of SMT films with small Mg content (x=0.10 and 0.15) annealed at 750ºC look very close to that of undoped ST films annealed at 750°C, as well in which the second-order features dominate, as in ST ceramics [Petzelt et *al.*, 2001]. However, in SMT films with x=0.30 annealed at 750°C several additional peaks at ~306, 328, 352, 398 and 484cm^{-1} were detected. And one small peak at 484cm^{-1} was observed in SMT films with x=0.15 annealed at 750°C, what could indicate the appearance of a second phase contradicting the 30% of solid solubility limit of Mg for *A* site of ST films annealed at 750°C determined by XRD.

These same peaks at ~306, 328, 352, 398 and 484cm^{-1} were found in the Raman spectra of all SMT films annealed at 900°C, as well, together with others peaks at ~501, 642, 714, 796cm^{-1}. Some of these Raman modes appeared only at high annealing temperature 900°C and increased in intensity with the increase of Mg content. Particularly, the 712cm^{-1} mode, characteristic of $MgTiO_3$ and assigned to the Ti-O stretching vibration of TiO_6 units, appears for SMT films with x=0.10 and becomes sharp with increasing of x.

It is possible to conclude from this structural analysis that the solid solubility limit of Mg in ST films is restricted to $x < 0.15$ for SMT films annealed at 750°C and to $x < 0.10$ for SMT films annealed at 900°C, and confirmed the XRD results concerning the solid solubility limit of STM films annealed at 750°C (40% for *B* site of ST lattice).

6.5.2. IR and THz-TDS analysis

SMT and STM films deposited on Al_2O_3 substrates without Pt layer were investigated in IR-frequency-range for better understanding of incorporation Mg ions on ST lattice and influence of annealing temperature increasing on structural properties of Mg doped ST films. Dielectric response of these films was obtained from IR spectra (using THz-TD spectroscopy) for comparison with the behaviour of the early presented dielectric properties of these films.

SMT films with x=0.10, 0.15, 0.30 annealed at 750°C and 900°C were analysed at room temperature and the obtained IR-spectra are presented in Figures 6.19 and 6.20.

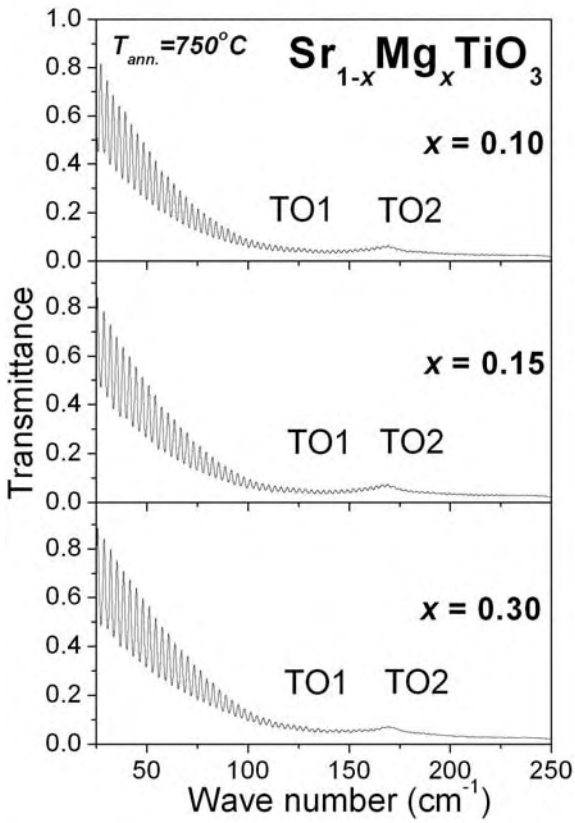

FIGURE 6.19. IR transmittance spectra of $Sr_{1-x}Mg_xTiO_3$ films annealed at 750°C.

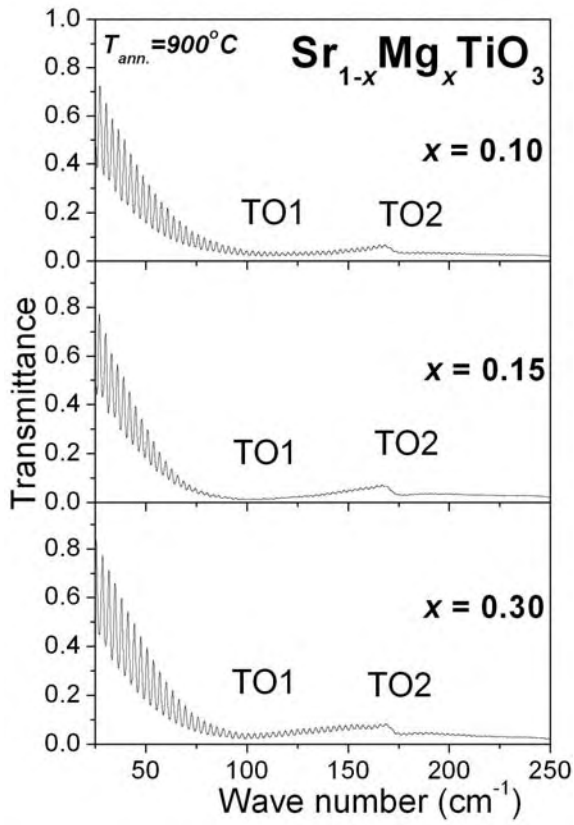

FIGURE 6.20. IR transmittance spectra of $Sr_{1-x}Mg_xTiO_3$ films annealed at 900°C.

As presented in the "Chapter 5", ST films deposited on Al_2O_3 substrates and annealed at 900°C show a broad minimum (indicated as mode TO1) detected at ~91cm^{-1} what is similar to ST ceramics (~93cm^{-1}) [Petzelt et *al.*, 2001] and to ST films (~83cm^{-1}) [Ostapchuk et. *al.*, 2002]. The weak second minimum at ~170cm^{-1}, indicated as weaker TO2 phonon response is similar to the reported before at ~176cm^{-1} for ST films deposited on Al_2O_3 substrates [Ostapchuk et. *al.*, 2002] and at the same ~176cm^{-1} for ST ceramics [Petzelt et *al.*, 2001].

Similar to undoped ST films, TO1 and TO2 modes were detected for all analyzed SMT films annealed at 750°C and 900°C. For SMT films annealed at 750°C the frequency of TO1 shifts to the high values (hardening) with increasing of Mg content (Fig.6.19). In contrast, TO1 modes of SMT films annealed at 900°C show negligible shift to low frequency with the increasing of the Mg content (Fig.6.20).

Transmittance spectra of SMT films at 750°C and 900°C films were fitted to determine the TO mode parameters and to obtain the complex dielectric response function. These

results for SMT films with x=0.10, 0.15, 0.30 annealed at 750°C and at 900°C are presented in Figures 6.21 and 6.22.

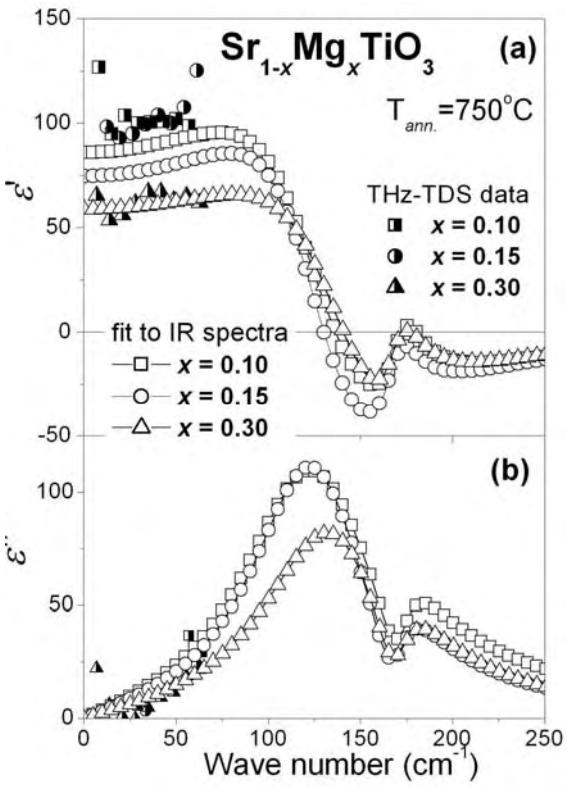

FIGURE 6.21. Spectra of real ε' and imaginary ε'' parts of the dielectric permittivity in the IR range, obtained from the room temperature transmittance spectra of $Sr_{1-x}Mg_xTiO_3$ thin films with x=0.10, 0.15 and 0.30 annealed at 750°C (open symbols – fit to IR spectra, fill symbol – THz-TDS data).

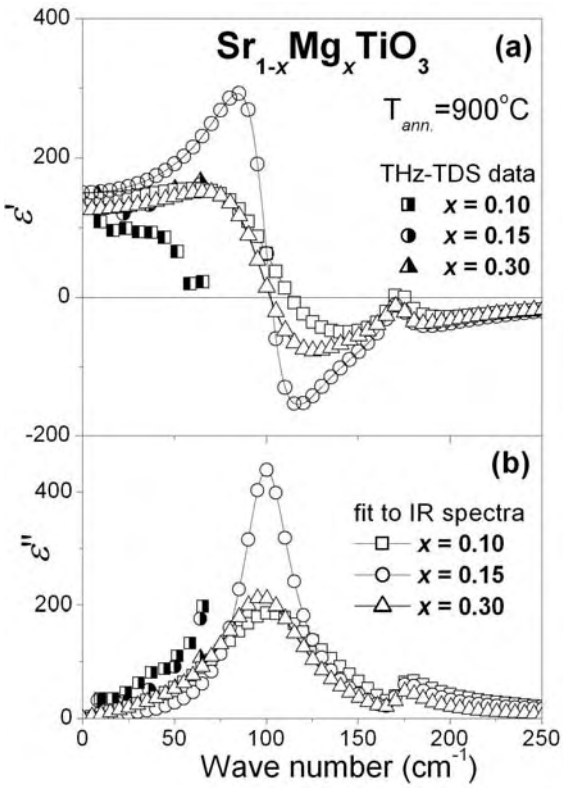

FIGURE 6.22. Spectra of real ε' and imaginary ε'' parts of the dielectric permittivity in the IR range, obtained from the room temperature transmittance spectra of $Sr_{1-x}Mg_xTiO_3$ thin films with x=0.10, 0.15 and 0.30 annealed at 900°C (open symbols – fit to IR spectra, fill symbol – THz-TDS data).

ε' of SMT films annealed at 750°C decreased with increasing of Mg doping concentration. From the spectra of the imaginary part of the dielectric permittivity ε'' of SMT thin films annealed at 750°C (Fig.6.21b) the position of TO1 mode hardening shifted from ~122cm^{-1} for x=0.10 and 0.15 to ~131cm^{-1} for x=0.30.

ε' of SMT films annealed at 900°C (Fig.6.22a) is higher (~155 for x=0.10, ~290 for x=0.15, ~150 for x=0.30) than ε' for films annealed at 750°C with equivalent contents of Mg (~95 for x=0.10, ~85 for x=0.15, ~65 for x=0.30) (Fig.6.21a). However, according to

Raman study (Fig.6.18), SMT films with x=0.10, 0.15, 0.30 annealed at 900°C show additional modes characteristic of $MgTiO_3$. Meanwhile, ε' of SMT films with x=0.15 annealed at 900°C is higher than that of SMT films with x=0.10 and 0.30 (Fig.6.22), what is not clear at the moment. Moreover, fitting THz-TDS data and IR spectra for SMT films with $T_{ann.}$=900°C are differ as it shown in Figure 6.22b. As explanation of such difference could be presented following: fitting of IR spectra and THz-TDS data only by fitting parameters for monophasic sample (as for films annealed at 750°C) was not enough due to second phase in SMT films annealed at 900°C (according to Raman results). So, because of that, unclear tendency in behaviour of TO1 mode in these samples annealed at 900°C (softening with changing of Mg content: ~101cm^{-1} for x=0.10, ~100cm^{-1} for x=0.15, ~97cm^{-1} for x=0.30) was observed (Fig.6.22b).

It is possible to say, that TO1 soft mode in SMT films annealed at 750°C does not stiffen in the IR spectra with strong up-shift of frequency (Fig. 6.21). It indicates that SMT films annealed at 750°C go far from the ferroelectric instability with increasing of Mg concentration in ST lattice.

IR transmittance spectra and spectra of real ε' and imaginary ε'' parts of the dielectric permittivity in IR range obtained from the room temperature transmittance spectra of STM films with y=0.10 and y=0.15 annealed at 750°C are represented in Figures 6.23 and 6.24, respectively.

IR spectra of STM films with y=0.10 and y=0.15 are in general similar: only the response from TO1 and TO2 modes were detected in the analyzed samples, what is similar to the previously presented undoped ST or SMT films annealed at 750°C. The broad minimum of the soft TO1 mode shifts with increasing of Mg content (Fig.6.23) from ~135cm^{-1} for y=0.10 to ~148cm^{-1} for y=0.15 (Fig.6.23) indicating the hardening of TO1 mode for these STM films. ε' of STM films with y=0.10 presents higher value (~78) than that for y=0.15 (~60) (Fig.6.24).

In the comparison of the values of ε' obtained in this chapter with the obtained dielectric response presented in the next subchapter, care should be taken, since in this analysis the *in-plane* dielectric response of the films deposited directly on Al_2O_3 substrates was measured in opposition to the dielectric response acquisition in a MIM capacitor structure analyzed in current work. However, in this measurement a decreasing tendency of ε' with increasing Mg concentration was detected for the studied STM films annealed at

750°C. With increasing of Mg concentration in ST lattice STM films annealed at 750°C move away from the ferroelectric instability, similarly to SMT films annealed under the same conditions.

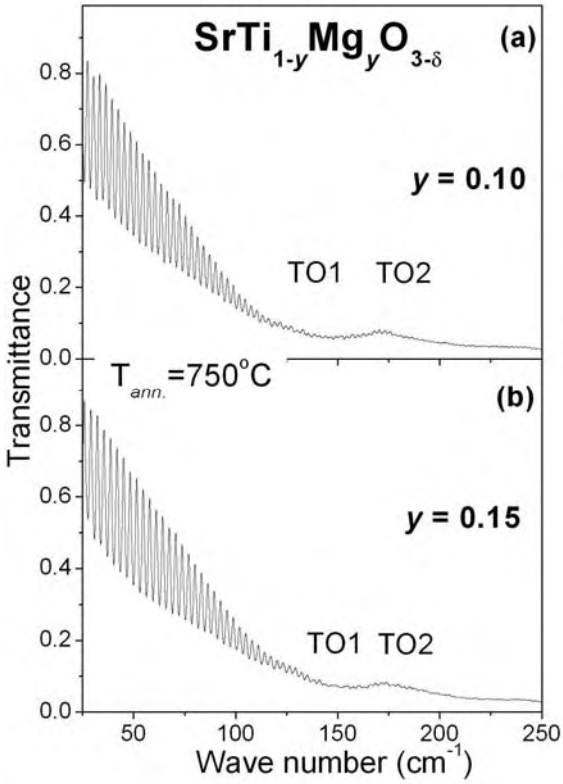

FIGURE 6.23. IR transmittance spectra of $SrTi_{1-y}Mg_yO_{3-\delta}$ films annealed at 750°C.

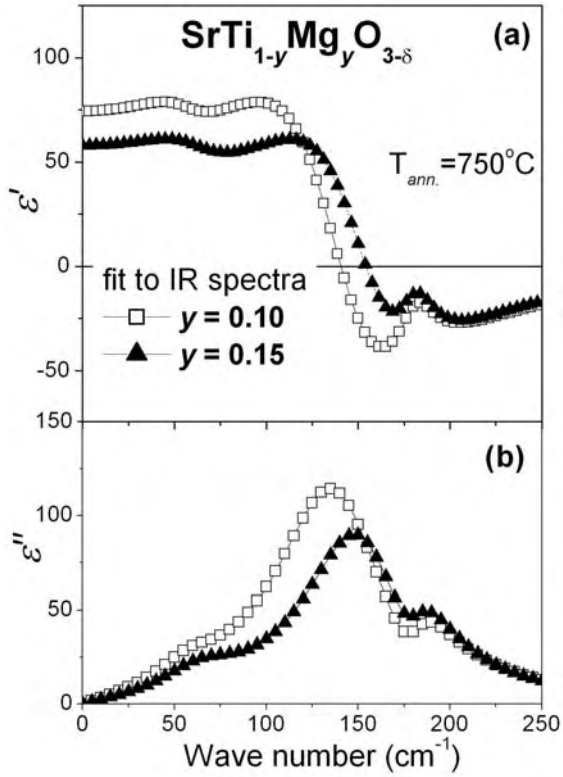

FIGURE 6.24. Spectra of real ε' and imaginary ε'' part of the dielectric permittivity in IR range, obtained from the room temperature transmittance spectra of $SrTi_{1-y}Mg_yO_{3-\delta}$ films annealed at 750°C.

6.6. Low temperature dielectric properties

6.6.1. Dielectric response as function of temperature

Temperature dependence of the real part of the dielectric permittivity ε' and tanδ of $Sr_{1-x}Mg_xTiO_3$ and $SrTi_{1-y}Mg_yO_{3-\delta}$ thin films annealed at 750°C and $Sr_{1-x}Mg_xTiO_3$ thin films annealed at 900°C was measured from 300K to 10K and from 100Hz to 1MHz.

The obtained results for SMT thin films with x=0.01, 0.02, 0.05, 0.10 annealed at

750°C are depicted in Figure 6.25 and for STM films with y=0.01, 0.05 in Figure 6.26 at 1kHz, 10kHz and 1MHz together with data of undoped ST films also annealed at 750°C (from the "Chapter 4") for comparison.

Undoped ST films present higher value of ε' than that of Mg-doped ST films. And, similar to the behaviour of undoped ST films there is a steep increase of the ε' and levelling-off at high values, as the temperature approaches 0K with no dielectric anomaly, for SMT (Fig.6.25) and STM (Fig.6.26) films. No significant frequency dispersion was observed for ε' of Mg doped ST films in all the temperature range. $\varepsilon'(T)$ decreased with increasing of Mg content: slightly in the case of Sr site doping (from ~188 for x=0.01 at ~58K to ~162 for x=0.02 at ~58K to ~155 for x=0.05 at ~55K to ~130 for x=0.10 at ~58K) and dramatically in the case of Ti site doping (from ~198 for y=0.01 at ~60K to ~113 for y=0.05 at ~60K). A similar behaviour was observed for SMT and STM ceramics [Tkach et *al.*, 2004]. All SMT and STM compositions reveal monotonous curves, differing only in maximum and minimum ε' values.

In Figure 6.25 for SMT films and in Figure 6.26 for STM films small broad peak in $\varepsilon'(T)$ at low temperature ~55K was detected similar to that of undoped ST film. Such small peak in $\varepsilon'(T)$ was observed in undoped ST films prepared by other methods as well [Astafiev et *al.*, 2003; Yu et *al.*, 2002; Hirano et *al.*, 1993] and in the current Thesis ("Chapter 4") and attributed to the appearance of ferroelectricity ("Chapter 2").

Thus, according to data from Figures 6.25 and 6.26, Mg doping itself does not induce dielectric relaxation in ST films, either introduced in the Sr or Ti site of the ST lattice, in spite of theoretical prediction [Kvyatkovskii, 2002]. All the compositions, SMT and STM, exhibit a gradual increase of ε' on cooling and low-temperature levelling-off similarly to ST. The absence of any dielectric anomaly and decreasing ε' were also reported in the literature for Mg doped ST ceramics [Wang et *al.*, 2000; Tkach et *al.*, 2004].

The temperature dependence of the tanδ of $Sr_{1-x}Mg_xTiO_3$ (x=0.01, 0.02, 0.05, 0.10) and $SrTi_{1-y}Mg_yO_{3-\delta}$ (y=0.01, 0.05) thin films together with undoped ST films is presented in Figure 6.27 at 10kHz.

Dielectric properties of undoped ST films deposited on $Si/SiO_2/TiO_2/Pt$ substrates annealed at 750°C were previously measured in "Chapter 4" and several well defined peaks were detected in tanδ: peak *A* (< 35K), peak *B* (~87K), and peak *C* (~188K). As already mentioned peak *A* could be considered as a stress/strain induced ferroelectric phase

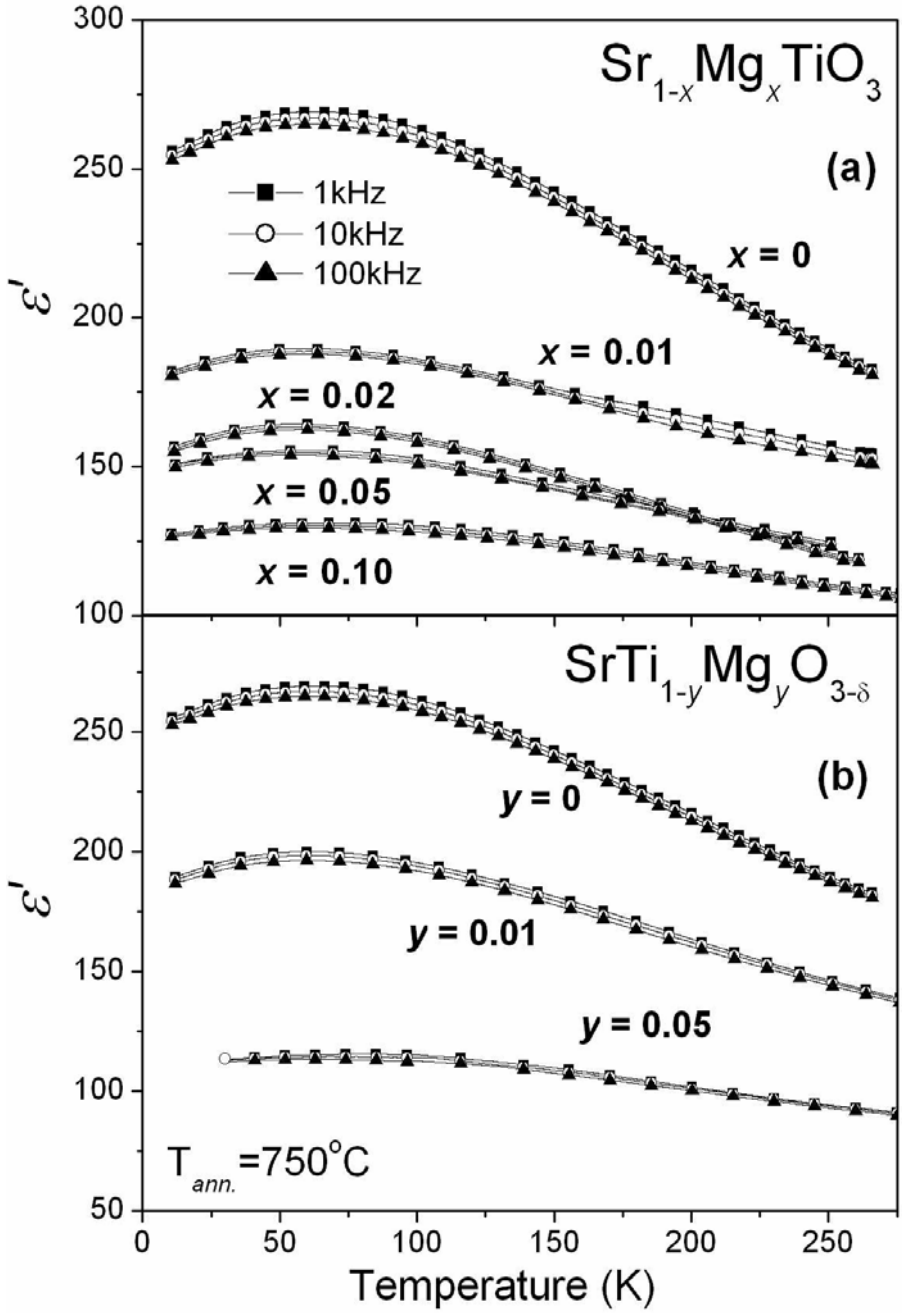

FIGURE 6.25. Temperature dependence of real part of dielectric permittivity of ε' of $Sr_{1-x}Mg_xTiO_3$ (a) and $SrTi_{1-y}Mg_yO_{3-\delta}$ (b) thin films annealed at 750°C at 1kHz, 10kHz and 100kHz.

transition [Astafiev et *al.*, 2003], peak *B* attributed to the dynamics of the elastic domain walls that occur at the cubic-to-tetragonal phase transition around 105K [Mizaras and Loidl, 1997], and peak *C* could be associated with the effect of defect/impurity like oxygen vacancy [Lemanov et *al.*, 2002].

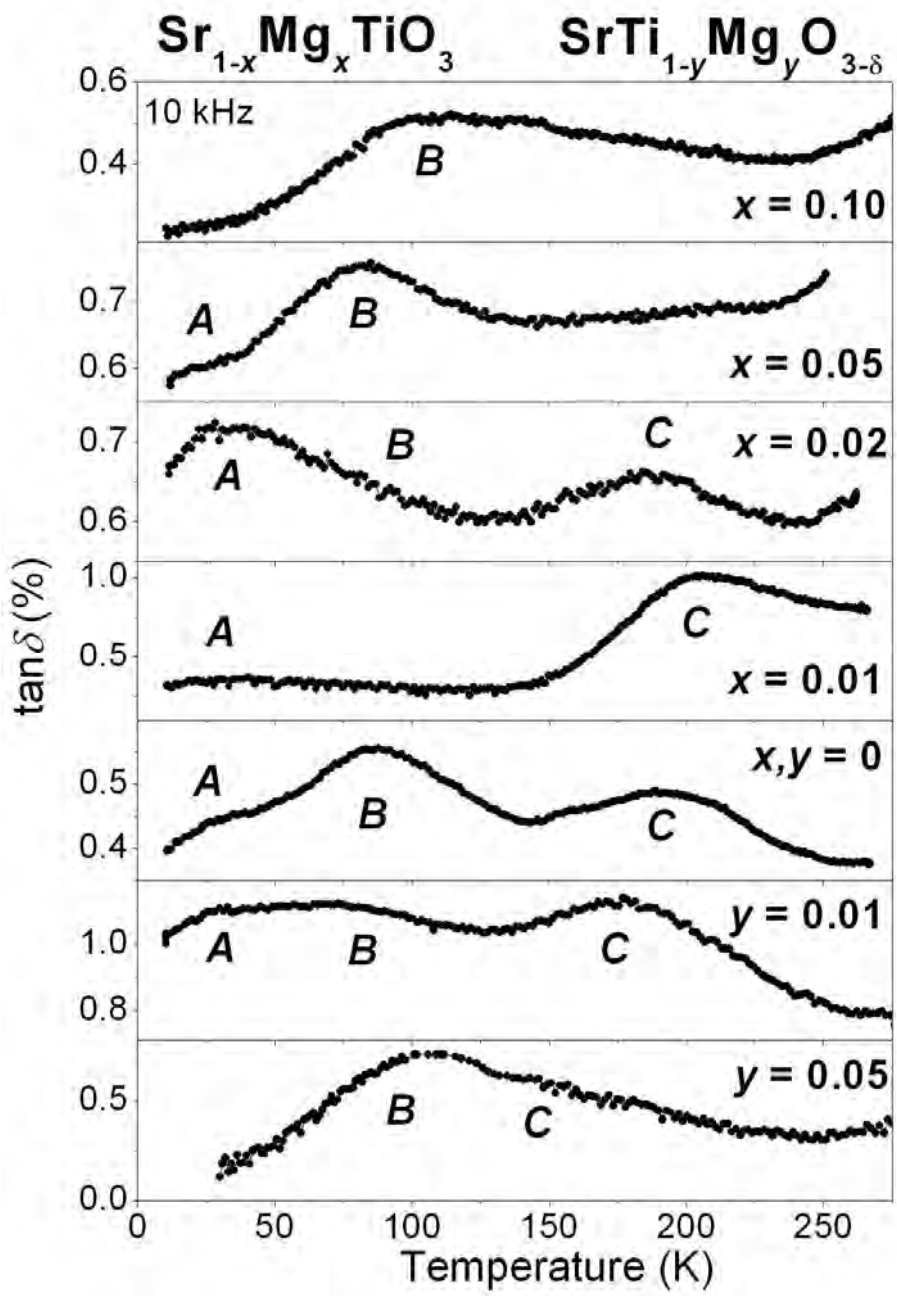

FIGURE 6.26. Temperature dependence of tanδ of $Sr_{1-x}Mg_xTiO_3$ and $SrTi_{1-y}Mg_yO_{3-\delta}$ thin films annealed at 750°C at 10kHz.

The value of tanδ for all analyzed SMT and STM samples are less that 1.2% in the maximum. SMT films exhibit ~1% for x=0.01 (peak *C*), ~0.7% for x=0.02 (peak *A*), ~0.8% for x=0.05 (peak *B*), ~0.5% for x=0.10 (peak *B*). For STM films values of tanδ were found to be ~1.2% for y=0.01 (peak *C*), ~0.7% for y=0.05 (peak *B*). In general the tanδ values of SMT and STM films were a bit higher than that of undoped ST films (< 0.6% in peak *B*).

Meanwhile, the above described *A*, *B* and *C* peaks were not all observed in all of the SMT films (Fig.6.26). Peak *A* and peak *C* were detected in SMT films with *x*=0.01 and 0.02, peaks *B* and *C* were found in SMT films with *x*=0.05 and only peak *B* was observed in SMT films with *x*=0.10. Moreover, peak *A* was not stable and shifted with increasing of Mg content from ~33K (*x*=0.01) to ~38K (*x*=0.02). As well peak *B* moved from ~81K (*x*=0.05) to ~97K (*x*=0.10) but not far from that in undoped ST films (~87K). At the same time, peak *C* was detected in SMT films at temperatures ranging from ~205K (*x*=0.01) to ~185K (*x*=0.02) to ~223K (*x*=0.05), similar to that in undoped ST.

In contrast to SMT films and similar to undoped ST films, all peaks *A*, *B* and *C* were found in the loss spectra of STM films with *y*=0.01 (although peak *A* and peak *B* were joined). STM films with *y*=0.05 presented only two peaks: peak *B* at ~105K and peak *C* at ~164K.

Positions of the peaks *A*, *B* and *C*, as well as values in the maximum of real part dielectric permittivity ε' (ε'_{max}) and positions of ε'_{max} ($T_{\varepsilon'max}$) detected in undoped ST, SMT and STM films annealed at $T_{ann.}$=750°C are presented in Table 6.1.

TABLE 6.1. Values of ε' in the maximum and positions of $T_{\varepsilon'max}$ and of the peaks *A*, *B* and *C* in tanδ*(T)* spectra of $Sr_{1-x}Mg_xTiO_3$ and $SrTi_{1-y}Mg_yO_{3-\delta}$ films annealed at 750°C at 10kHz.

$Sr_{1-x}Mg_xTiO_3$ and $SrTi_{1-y}Mg_yO_{3-\delta}$ compositions	ε'	$T_{\varepsilon'max}$	Peak *A*	Peak *B*	Peak *C*
x=0.10	~130	~58K		~97K	
x=0.05	~155	~55K		~81K	~223K
x=0.02	~162	~58K	~38K		~185K
x=0.01	~188	~58K	~33K		~205K
x,y=0	~267	~60K	~27K	~87K	~188K
y=0.01	~198	~60K	~18K	~71K	~184K
y=0.05	~113	~60K		~105K	~164K

It is well observed from the Figures 6.25, 6.26 and Table 6.1 that none of the peaks in tanδ (*A*, *B* or *C*) corresponds to an almost constant position of $T_{\varepsilon'max}$.

The broad *A* peak observed in undoped ST thin films with $T_{ann.}$=750°C shifts to higher temperature with the incorporation of Mg in Sr position. Peak *A* was also detected in SMT

ceramics and a similar behaviour, although more obvious, was observed with increasing Mg content (from ~23.5K for x=0.01 to ~26K for x=0.10) [Tkach et *al.*, 2004]. In undoped ST and STM ceramics peak *A* was not detected [Tkach et *al.*, 2004].

Meanwhile, in undoped ST films presented in the current work peak *A* was detected and detected almost at the same temperature ~30-35K for films annealed at 750 and 900ºC, being more clear and sharper for the annealed at higher temperature. Moreover, all undoped ST films deposited on 5 different substrates and annealed at high 900°C present peak *A* in the same temperature region ("Chapter 5").

Peak *B* detected in undoped ST films annealed at 750°C was not found in SMT films with small Mg content, but it was detected in SMT with x=0.05 and x=0.10. However, in SMT films with x=0.10 very broad response from this peak *B* was detected similar to that of STM films with y=0.10. Peak *B* was detected also in both undoped ST ceramics, and Mg doped ST ceramics (around ~74-88K) [Tkach et *al.*, 2004], and it was reported that the background value of the loss decreases monotonically with the increase of Mg content as well as the intensity of the peak *B*, and this peak becomes undetectable for Mg content high as y=0.10 [Tkach et *al.*, 2004]. In current work, the position of peak *B* in SMT and STM films varied in the range from ~71K to 105K what is in good agreement with the claim that peak *B* is attributed to the dynamics of the elastic domain walls that occur at the cubic-to-tetragonal phase transition around 105K [Mizaras and Loidl, 1997].

On the other hand peak *C*, is presented in all SMT (except x=0.10) and STM films as well as in undoped ST films annealed at 750°C (Figure 6.26 and Table 6.1). In the case of SMT films peak *C* moves in the range of 185K-223K without a marked dependency on the content of Mg. It was mention already, that thermally activated oxygen vacancies jumping around the impurity ions in perovskites are suggested as the origin of such peak *C* [Lemanov et *al.*, 2002 and references therein]. At the same time, decreasing of the temperature of peak *C* position was noticed in the case of STM films, when the oxygen vacancy concentration increases due to the heterovalent substitution of Mg^{2+} for Ti^{4+} in the ST lattice and hereby, theoretically, the activation energy for the reorientation of oxygen-vacancy dipoles decreases, what leads to shift of peak *C* to lower temperature. Similar peaks *C* were observed in $Sr_{1-1.5x}Bi_xTiO_3$ ceramics for $x \leq 0.08$ [Yu et *al.*, 1999] and attributed to oxygen vacancy. Moreover, studied in $Sr_{1-x}Mg_xTiO_3$ samples shift of peak *C* to low temperatures was not detected (increasing to~223K for SMT x=0.05 compare to

decreasing to ~164K for STM y=0.05 and ~188K for undoped ST) seems to indicate that Mg ions are not on Ti position in SMT films. The obtained results highlight the different interactions of Mg with the ST lattice depending on the lattice site occupancy.

The effect of the increasing of annealing temperature from 750°C to 900°C on the dielectric response of SMT films was studied also. The temperature dependence of ε' and tanδ of $Sr_{1-x}Mg_xTiO_3$ thin films (x=0.01, 0.05) annealed at 900°C is depicted in Figure 6.27 in the frequency range of 10^3-10^5Hz together with data of undoped ST films also annealed at 900°C for comparison.

ε' of SMT films annealed at 900°C is lower (~358 at ~30K for x=0.05 and ~173 at ~40K for x=0.10) when compared to that of undoped ST films (~415 at ~43K). However, values of ε' for SMT films annealed at 900°C are higher than those of SMT or STM films annealed at 750°C (Figs.6.25 and 6.26). Thus, increasing the annealing temperature from 750°C to 900°C does not lead to the observation of any dielectric anomaly in SMT samples.

As was mentioned already, the lower polarisability of the Mg ions might account for ε' decreases together with the suppression of the ferroelectric instability. The absence of any dielectric anomaly and decreasing ε' in SMT and STM ceramics were also reported [Wang et *al.*, 2000; Tkach et *al.*, 2004].

The temperature dependence of tanδ at 10kHz of $Sr_{1-x}Mg_xTiO_3$ thin films annealed at 900°C (Fig.6.27b) indicates a decreasing of the loss values with increasing of Mg concentration what was not observed for identical films annealed at 750°C. However, SMT films annealed at 900°C present slightly higher values of tanδ (~1% peak *B* at ~90K for x=0.05 and ~0.94% peak *B* for 0.10) in comparison to equivalent SMT films annealed at 750°C (~0.8% for x=0.05 and ~0.5% for x=0.10). Meanwhile, undoped ST films annealed at 900°C show only a peak *A* at ~30K and this peak is also present for SMT films with x=0.05 (~35K) but disappears for x=0.10. Peak *B*, detected in SMT with x=0.05, 0.10 with $T_{ann.}$=900°C, was not observed in undoped ST films prepared under different conditions ("Chapter 4") or in undoped ST films deposited on different substrates ("Chapter 5"), or even in SMT films with equivalent Mg concentration but annealed at 750°C, however this peak *B* was found in STM films annealed at 750°C.

One more very small/broad response about ~150K-180K, probably from peak *C*, could be expected in SMT films annealed at 900°C, but due to its very small intensity it is not

possible to obtain the precisely position of this peak.

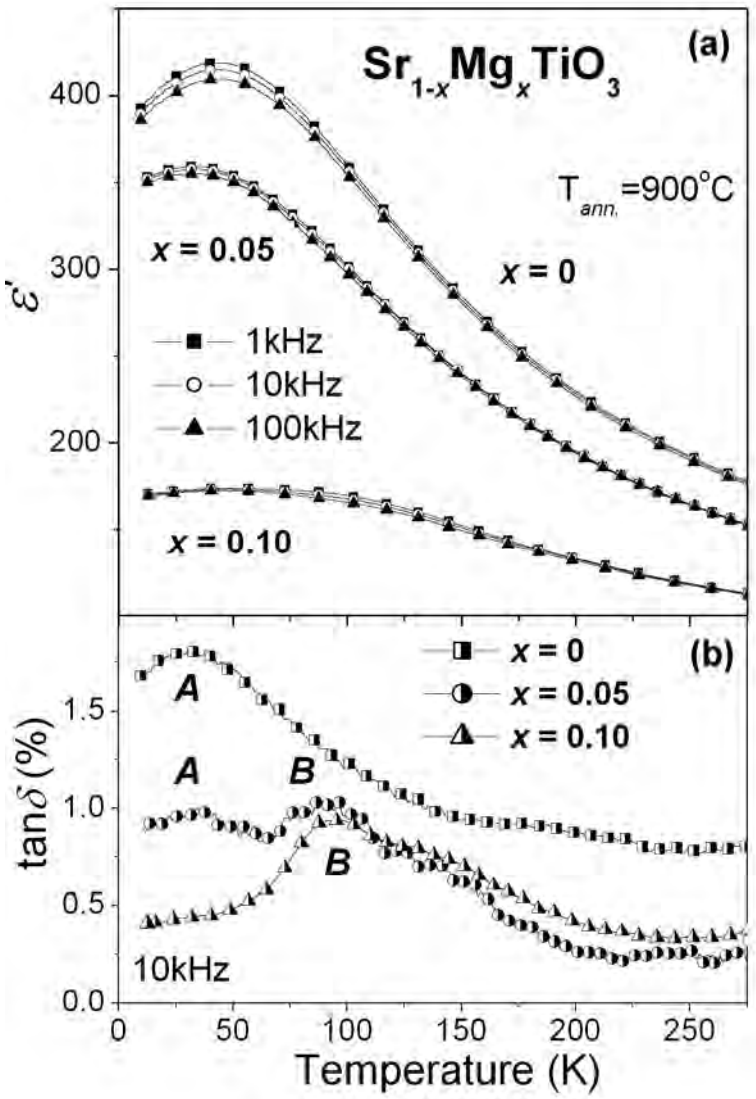

FIGURE 6.27. Temperature dependence of real part of the dielectric permittivity of ε' at 1kHz, 10kHz and 100kHz (a) and tanδ at 10kHz (b) of $Sr_{1-x}Mg_xTiO_3$ thin films with x=0, 0.01 and 0.05 annealed at 900°C.

Meanwhile, it was reported that loss in $(Ba,Sr)TiO_3$ films decreases from 0.013 to 0.007 due to incorporation of 5% Mg on Ti position [Joshi and Cole, 2000]. In this work, tanδ at 10kHz of $Sr_{0.90}Mg_{0.01}TiO_3$ (at low measured temperature <150K) and $SrTi_{0.95}Mg_{0.05}O_{3-\delta}$ (at high measured temperature >150K) films with $T_{ann.}$=750°C is lower when compared to that of undoped ST and, moreover, tanδ decreases with increasing of Mg content also in SMT films with $T_{ann.}$=900°C (Fig.6.27b), however it is still high.

6.6.2. *dc* field effect and dielectric tunability

The influence of *dc* applied field on the real part of the dielectric permittivity ε' of undoped and Mg-doped ST thin films annealed at 750°C and 900ºC was studied in current subchapter, and the obtained results are plotted in Figures 6.28 and 6.29. The description of these measurements was done in "Chapter 3".

In Figure 6.28 the temperature dependence of ε' of undoped and Mg-doped ST films (SMT with x=0.01, 0.10 and STM with y=0.01, 0.05) annealed at 750°C and measured at 10kHz is presented, under zero and 50, 100, 125kV/cm. The data for undoped ST films annealed at 750°C was obtained in "Chapter 4".

In all the curves of Mg doped ST films annealed at 750°C as the applied electric field increases the real part dielectric permittivity ε' decreases similarly to undoped ST films. In all the studied films a small broad peak at low temperature is presented at E=0kV/cm and it smoothes with increasing of the voltage, shifts to high temperature, what is typical for ST materials (as it was mentioned before, "Chapter 2"). However, no new *dc*-field induced peak was observed. The highest *dc*-field effect for Mg doped ST films annealed at 750°C, was observed for STM films with y=0.01 and for SMT films with x=0.01, but with increasing of Mg concentration in SMT and STM samples, the detected influence of *dc*-field on ε' decreased.

In Figure 6.29 the temperature dependence of ε' of undoped ST and SMT films with x=0.05 and 0.10 annealed at 900°C and measured at 10kHz is presented, under zero and 50, 100, 125kV/cm. Data of undoped ST films at 900°C was obtained in "Chapter 4".

Similar to SMT films annealed at 750°C and undoped ST films annealed at 900°C, ε' of Mg doped ST films annealed at 900°C decreases as the applied electric field increases. And, in all studied films heat treated at 900°C a small broad peak at low temperature is observed at E=0kV/cm and it become smoothed with increasing of the voltage, shifts to high temperature, what is typical of ST materials as mentioned. In these films no new *dc*-field induced peak was also observed. With the increase of Mg concentration in SMT samples annealed at 900°C the influence of *dc*-field on ε' decreases (Figure 6.29).

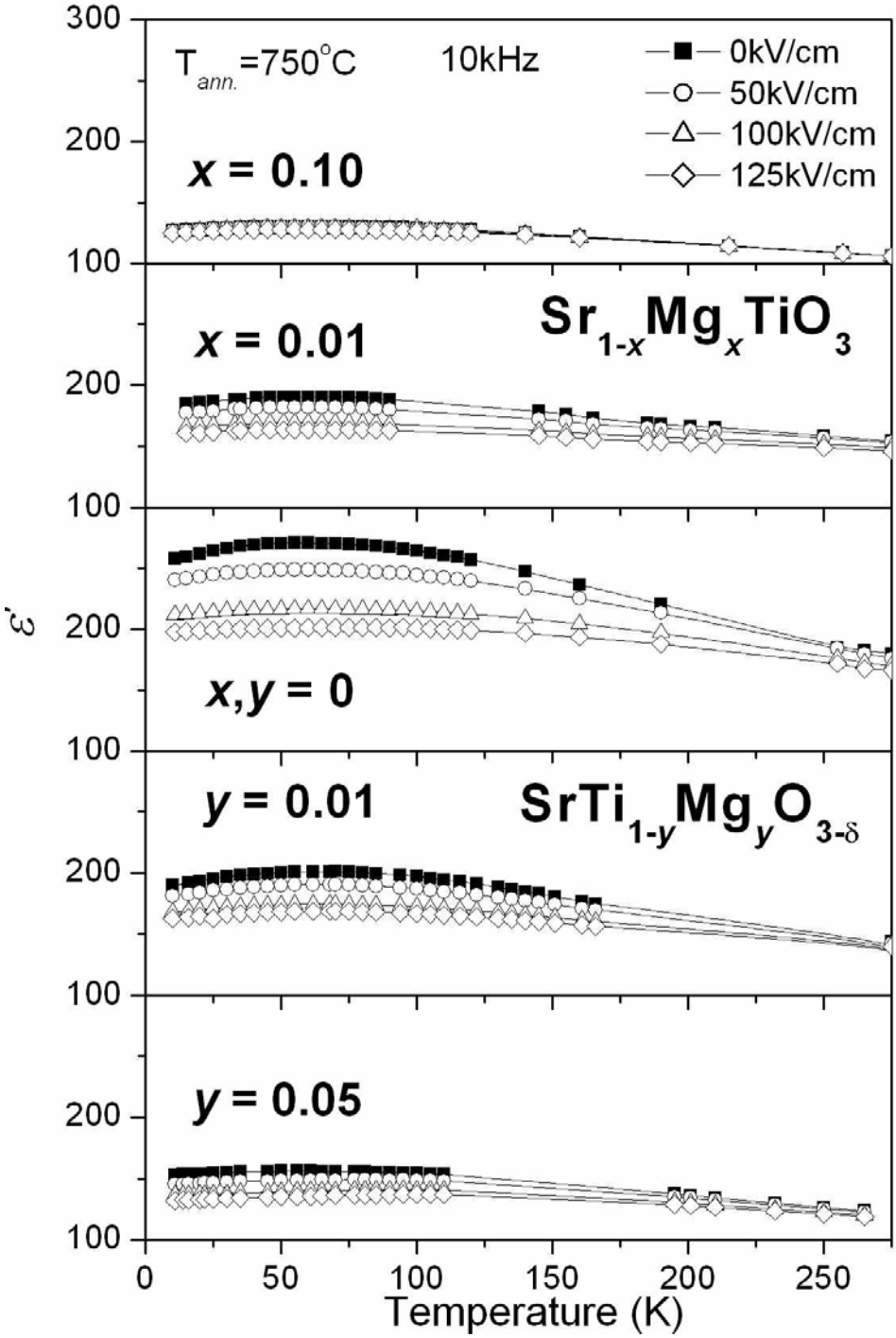

FIGURE 6.28. Temperature dependence of real part of the dielectric permittivity ε' of undoped and Mg-doped $SrTiO_3$ films annealed at 750°C under different *dc* bias fields at 10kHz.

The highest dependence of ε' on the bias was observed for undoped ST films at both annealing temperatures and it becomes weaker with the incorporation of Mg for both *A* and

B site.

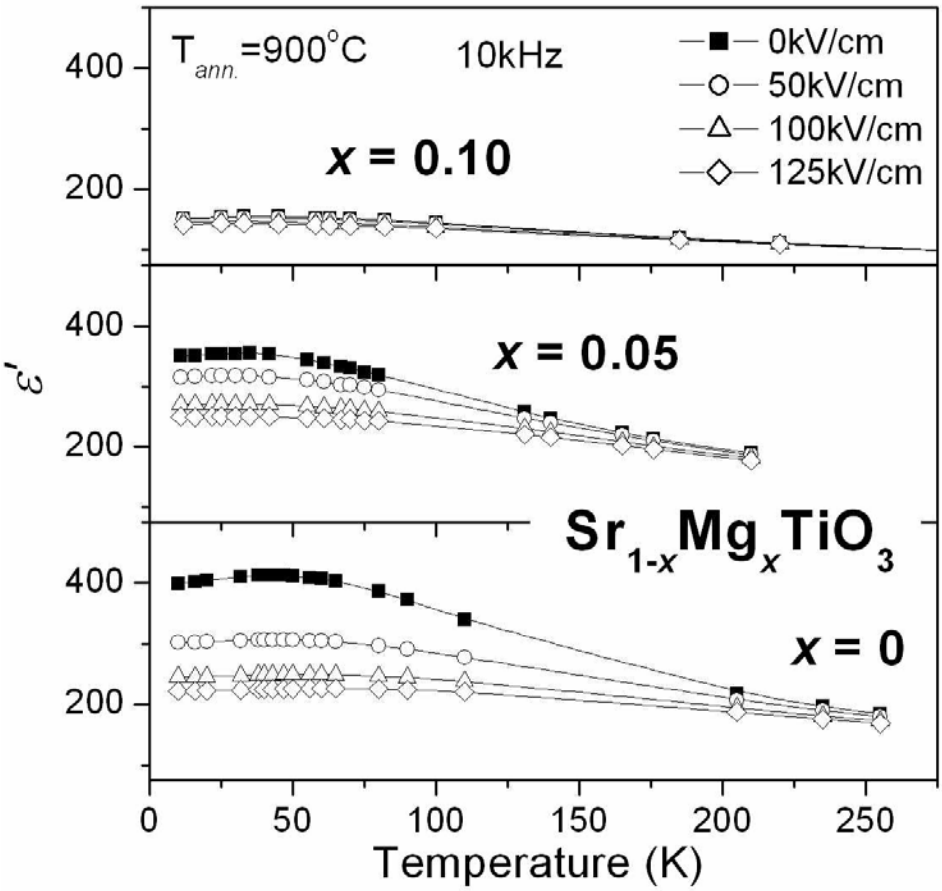

FIGURE 6.29. Temperature dependence of real part of dielectric permittivity ε' of undoped and Mg-doped $SrTiO_3$ films at $T_{ann.}$=900°C under different *dc* bias fields at 10kHz.

For the characterisation of the dependence of ε' on the applied *dc* bias electric field, the parameter of tunability was introduced and in the current work, the relative tunability of Mg doped ST thin films was calculated by the formula:

$$n_r = [\varepsilon'(E=0) - \varepsilon'(E)] / \varepsilon'(E=0) \times 100\% \quad (6.1)$$

where $\varepsilon'(E=0)$ stands for the real part of dielectric permittivity at zero bias and $\varepsilon'(E)$ for the real part of dielectric permittivity at the applied *dc* electric field.

Relative tunability n_r together with the electric-field dependence of ε' and tanδ of $Sr_{1-x}Mg_xTiO_3$ (x=0.01, 0.10) and $SrTi_{1-y}Mg_yO_{3-\delta}$ (y=0.01, 0.05) films annealed at 750°C measured at 10kHz is presented in Figure 6.30 at selected temperatures.

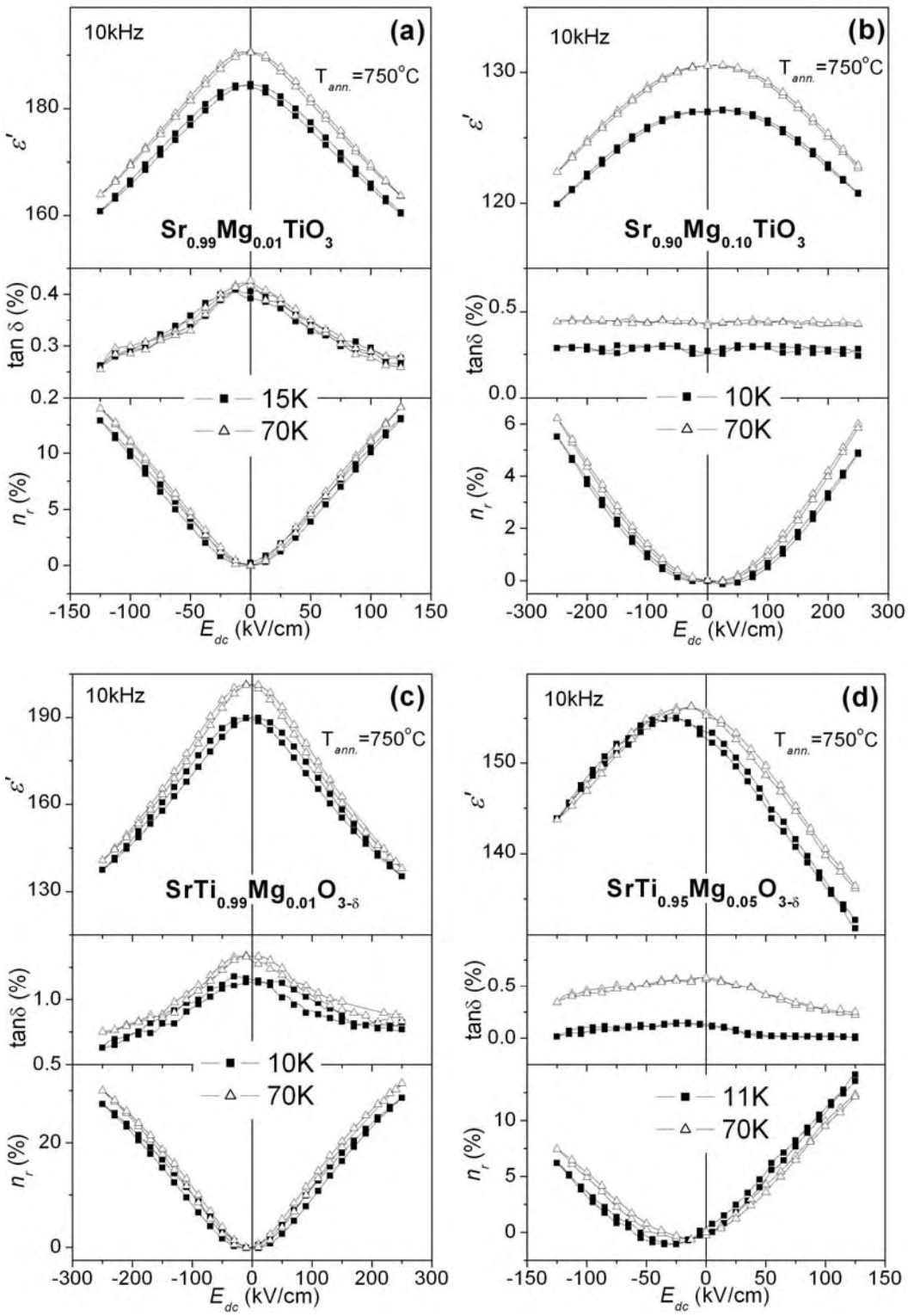

FIGURE 6.30. Field dependence of the real part of the dielectric permittivity ε' (*top panel*), tanδ (*middle panel*) and relative tunability n_r (*bottom panel*) of $Sr_{1-x}Mg_xTiO_3$ films with x=0.01 (a), x=0.10 (b) and $SrTi_{1-y}Mg_yO_{3-\delta}$ films with y=0.01 (c), y=0.05 (d) annealed at 750°C at 10kHz at selected temperatures.

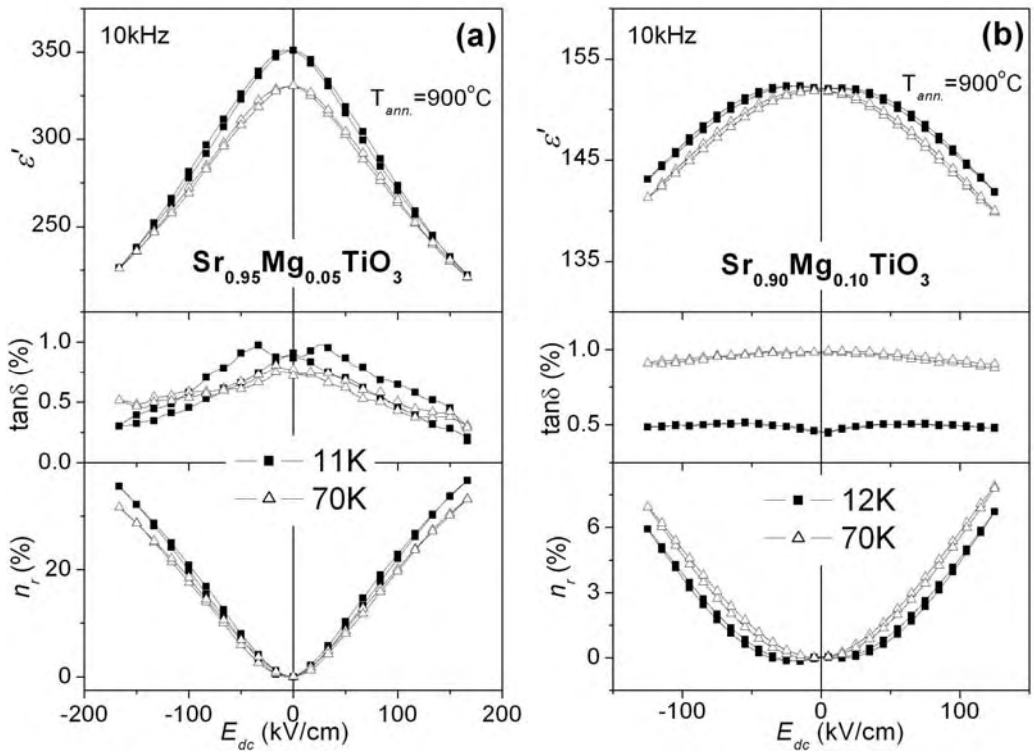

FIGURE 6.31. Field dependence of real part of dielectric permittivity ε' (*top panel*), tanδ (*middle panel*) and relative tunability n_r (*bottom panel*) of $Sr_{1-x}Mg_xTiO_3$ films with x=0.05 (a), x=0.10 (b) films annealed at 900°C at 10kHz at selected temperatures.

And the following information for samples annealed at 750°C can be implied from the Figure 6.30:

1. *dc*-field effect on $\varepsilon'(E_{dc})$, tan$\delta(E_{dc})$ and $n_r(E_{dc})$ of SMT and STM films depends on Mg concentration, and it decreases with increasing of Mg for both sites substitution.
2. $\varepsilon'(E_{dc})$ and $n_r(E_{dc})$ of SMT and STM films with x,y=0.01 represent higher response from applied *dc*-field (Fig.6.30a,c *top* and *bottom panels*) than in others studied samples.
3. No hysteresis was detected in $\varepsilon'(E_{dc})$ and tan$\delta(E_{dc})$ of SMT and STM films independent on Mg content (Fig.6.30 *middle* and *bottom panels*).
4. n_r of Mg doped ST films decreases with increasing of Mg content (Fig.6.30 *bottom panel*).

For $Sr_{1-x}Mg_xTiO_3$ films (x=0.05, 0.10) annealed at 900°C the relative tunability n_r was also calculated and together with the *dc*-field dependence of ε' and tanδ measured at 10kHz presented in Figures 6.31 at selected temperatures.

From Figure 6.31 the following results obtained for SMT films with $T_{ann.}$=900°C:

1. *dc*-field effect on $\varepsilon'(E_{dc})$, $\tan\delta(E_{dc})$ and $n_r(E_{dc})$ of SMT films strongly depends on Mg concentration, and it decreases with increasing of Mg (Fig.6.31).
2. $\varepsilon'(E_{dc})$ and $n_r(E_{dc})$ of SMT films with x=0.05 show higher response from applied *dc*-field than SMT films with x=0.10 (Fig.6.31 *top* and *bottom panel*).
3. No hysteresis was detected for analyzed films independent on Mg content.

For better comparison, *dc*-field dependence of SMT and STM films annealed at 750°C and with SMT films annealed at 900°C, $\varepsilon'(E_{dc})$ of all these films was plotted in Figure 6.32 at 20K and 110K at 10kHz.

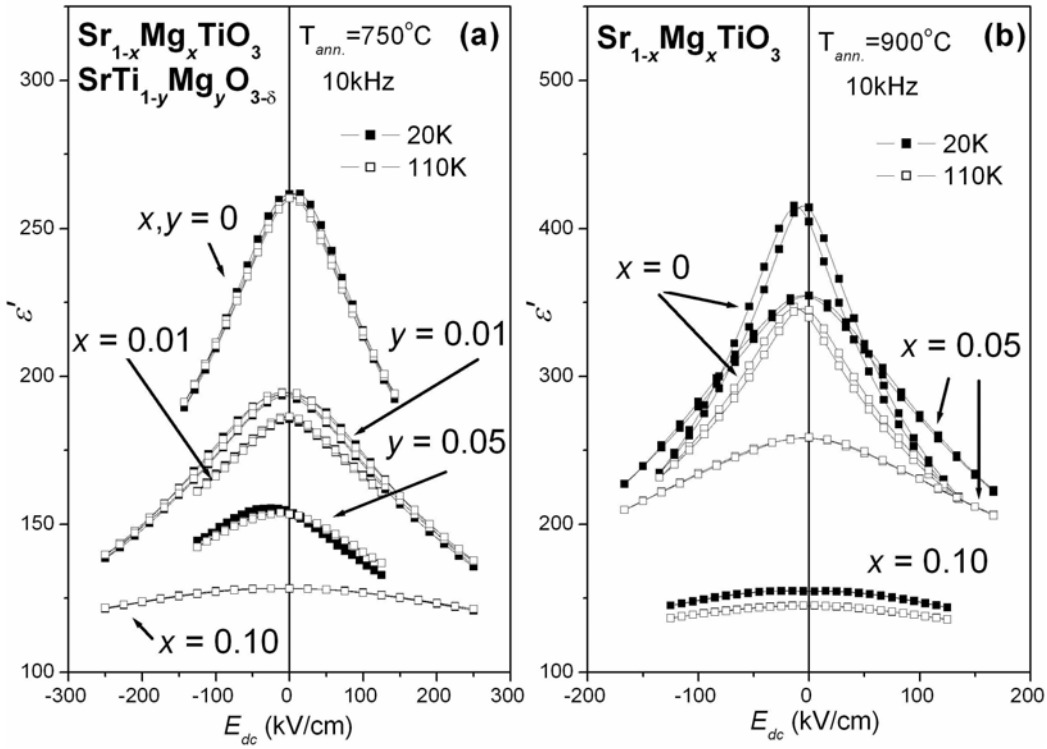

FIGURE 6.32. *dc*-field dependence of the real part of the dielectric permittivity ε' of undoped and Mg-doped $SrTiO_3$ films annealed at 750°C (a) and 900°C (b) at 10kHz at 20K and 110K.

The biggest influence of the bias field on ε' is observed for undoped ST films annealed at both temperatures (Fig.6.32a and Fig.6.32b) compared to that of SMT or STM films. Films annealed at 900°C show different values of $\varepsilon'(E_{dc})$ for selected temperatures in contrast to the samples with $T_{ann.}$=750°C which present the same data for 20K and 110K independent on the site incorporation. Moreover, the small hysteresis, observed in undoped ST films annealed at 900°C under applied *dc*-field, disappears with Mg incorporation.

Temperature dependence of the relative dielectric tunability n_r of undoped and Mg-

doped ST films is presented in Figure 6.33 together with values for undoped ST films annealed at 750°C and 900°C at 10kHz and 100kV/cm.

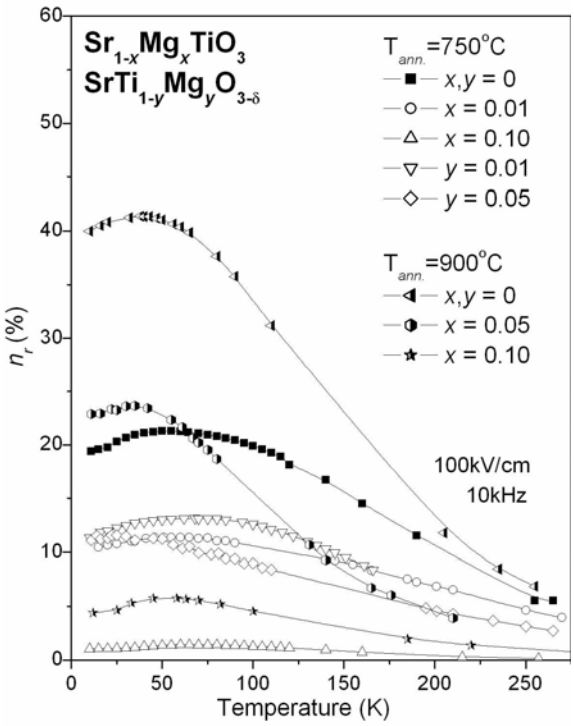

FIGURE 6.33. Temperature dependence of the relative dielectric tunability n_r of undoped and Mg-doped $SrTiO_3$ films annealed at different temperatures at 10kHz and 100kV/cm.

n_r of undoped ST and SMT films with x=0.01 and 0.10 annealed at 750°C has maximum values at ~55-65K, being ~21% (~55K x=0), ~11% (~60K x=0.01) and ~1.4% (~60K x=0.10), respectively. For STM films annealed at 750°C, the maximum value of n_r changes from 13% for y=0.01 to 11% for y=0.05 with the shift of the maximum position from 68K to 25K, respectively. For STM ceramics, low tunability values were reported even at low temperatures [Joshi and Cole, 2000] thus confirming that the temperature region of ferroelectric instability is likely to be suppressed.

For SMT films annealed at 900°C n_r decreases also with increasing of Mg content. n_r of undoped ST annealed also at 900°C (equal to ~42% at ~30K) decreases to ~24% at ~35K for $Sr_{0.95}Mg_{0.05}TiO_3$ films and ~6% at ~58K for $Sr_{0.90}Mg_{0.10}TiO_3$ films.

6.6.3. *P(E)* hysteresis response

Since the hysteric behaviour of the polarisation *P* under an applied *ac* field is one of the demonstrations of ferroelectric properties of a material, the *P(E)* response of Mg doped ST films deposited on $Si/SiO_2/TiO_2/Pt$ substrates and annealed at 750°C (SMT with x=0.01, 0.05 and STM films with y=0.01, 0.05) and at 900°C (SMT films with x=0.05) was measured at 100Hz under applied *ac* fields up to ~200kV/cm at different temperatures. The description of these measurements was done in "Chapter 3". Based on these results the remnant polarization P_r and coercive field E_c were also calculated.

The *P(E)* response of $Sr_{0.99}Mg_{0.01}TiO_3$ films annealed at 750°C is presented in Figure 6.34. The analyzed films are characterised by an almost linear dependence of the polarization *vs* the electric field at 10K (Fig.6.34a) and 100K (Fig.6.34b), what is very similar to the *P(E)* response of undoped ST films prepared without buffer layers annealed at 750°C (ST 750°C) ("Chapter 4"). P_r of SMT films with x=0.01 annealed at 750°C is ~0.1μC/cm^2 at 10K and ~0.087μC/cm^2 at 100K, lower when compared to that of undoped ST: ~0.14μC/cm^2 at 15K and ~0.09μC/cm^2 at 100K. E_c of these SMT films with x=0.01 at 750°C also presented lower values (~5.24kV/cm at 10K and ~4.14kV/cm at 100K) when compared to undoped ST ones (~7.8kV/cm at 15K and ~5.9kV/cm at 100K).

The hysteresis loops *P(E)* of $Sr_{0.95}Mg_{0.05}TiO_3$ thin films annealed at 750°C and measured at 100Hz are presented in Figure 6.35 at 10K and 100K. Slim but a bit *s*-shape hysteresis loops of SMT films with x=0.05 annealed at 750°C were observed for both selected temperatures in contrast to the linear behaviour of *P(E)* in $Sr_{0.99}Mg_{0.01}TiO_3$ samples (Fig.6.34). These films are characterised by P_r~0.24μC/cm^2 at 10K, what is higher than that of undoped ST and SMT with x=0.01, and P_r~0.023 at 100K, what is lower than that was detected for undoped ST and SMT with x=0.01. E_c is ~9.15kV/cm for 10K and 100K what is higher than E_c of undoped ST and SMT with x=0.01 annealed at 750°C.

The influence of high annealing temperature on the hysteresis response was studied in $Sr_{0.95}Mg_{0.05}TiO_3$ films annealed at 900°C at 100Hz and presented in Figure 6.36 at 10K and 100K. Very slim *s*-shape hysteresis loops were detected for SMT films with x=0.05 annealed at 900°C. These hysteresis loops are much slimmer than the loops of $Sr_{0.95}Mg_{0.05}TiO_3$ annealed at low 750°C (Fig.6.34). Similar *s*-shape of loops were also detected in the *P(E)* response of undoped ST films prepared without buffer layers annealed at 900°C (ST 900°C) ("Chapter 4"). P_r of SMT films with x=0.05 annealed at 900°C is ~0.13μC/cm^2 at 10K and ~0.08μC/cm^2 at 100K, what is lower when compared to that of ST 900°C (~0.48μC/cm^2 at 15K and ~0.27μC/cm^2 at 100K).

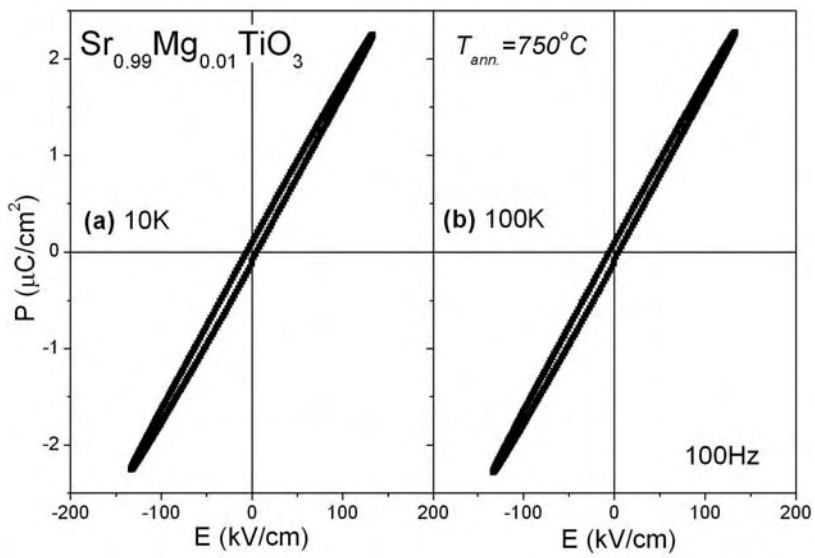

FIGURE 6.34. Hysteresis loops *P(E)* of $Sr_{0.99}Mg_{0.01}TiO_3$ thin film annealed at 750°C at 10K (a) and 100K (b) at 100Hz.

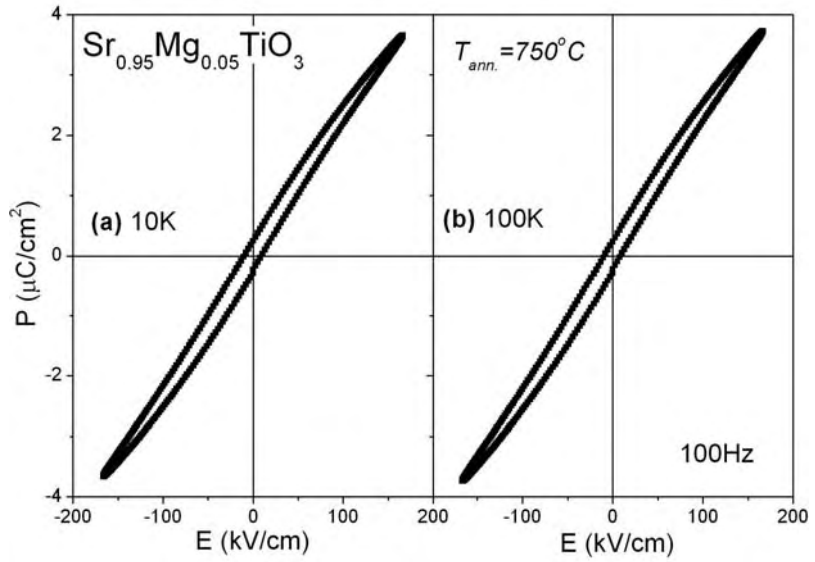

FIGURE 6.35. Hysteresis loops *P(E)* of $Sr_{0.95}Mg_{0.05}TiO_3$ thin film annealed at 750°C at 10K (a) and 100K (b) at 100Hz.

E_c of SMT films with x=0.05 annealed at 900°C is also lower (~3.36kV/cm at 10K and ~2.24kV/cm at 100K) than that of ST 900°C (~10.5kV/cm at 15K and ~8.4kV/cm at 100K). Meanwhile, studied samples presents *s*-shape loops typical for undoped ST films deposited on different substrates and annealed at 900°C ("Chapter 5").

Hysteresis loops *P(E)* of $SrTi_{1-y}Mg_yO_{3-\delta}$ films with y=0.01 annealed at 750°C measured at 100Hz are presented in Figure 6.37. Identically to $Sr_{0.99}Mg_{0.01}TiO_3$ films, $SrTi_{0.99}Mg_{0.01}O_{3-\delta}$ films present thin and almost linear *P(E)* response. P_r is 0.12μC/cm^2 at 10K and ~0.07 at 100K, what is very close to values of P_r obtained for $Sr_{0.99}Mg_{0.01}TiO_3$

films (Fig.6.34), but lower than those measured for undoped ST and SMT with x=0.05. E_c was ~8.97kV/cm for 10K and ~5.98kV/cm 100K, higher than E_c of undoped ST and for SMT with x=0.01 annealed at 750°C but lower than that for SMT films with x=0.05.

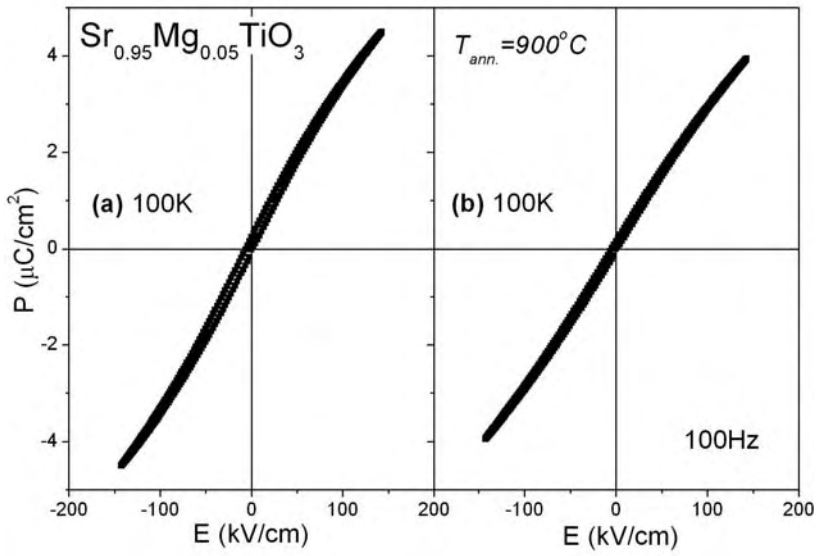

FIGURE 6.36. Hysteresis loops *P(E)* of $Sr_{0.95}Mg_{0.05}TiO_3$ thin film annealed at 900°C at 10K (a) and 100K (b) at 100Hz.

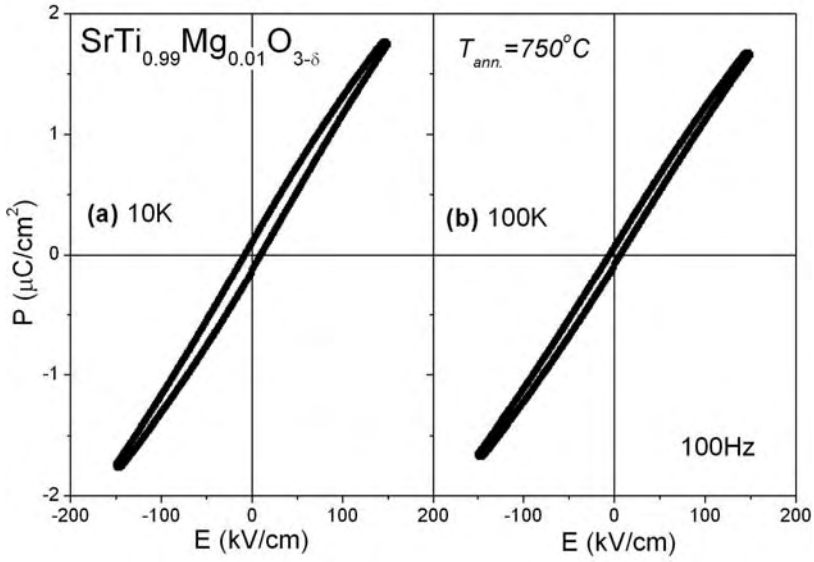

FIGURE 6.37. Hysteresis loops *P(E)* of $SrTi_{0.99}Mg_{0.01}O_{3-\delta}$ thin film annealed at 750°C measured at 10K (a) and 100K (b) at 100Hz.

Hysteresis loops *P(E)* of STM films with y=0.05 annealed at 750°C measured at 100Hz are presented in Figure 6.38 at 10K and 100K. These films present thin and almost linear *P(E)* response similarly to the response obtained for $Sr_{0.99}Mg_{0.01}TiO_3$ (Fig.6.34) and $SrTi_{0.99}Mg_{0.01}O_{3-\delta}$ (Fig.6.37). P_r is ~0.82μC/cm^2 at 10K, what is much higher compare to that at 10K of all previously analyzed samples, and P_r~0.082μC/cm^2 at 100K, what is

lower than that of undoped ST and SMT with x=0.01, but higher than that of SMT with x=0.05 and STM with y=0.01 annealed at 750°C.

For comparison, the hysteresis loops of SMT and STM films measured at 10K at 100Hz are depicted in Figure 6.39 together with undoped ST films annealed at 750°C and 900°C. All values of P_r and E_c analyzed films at 10K and 100K at 100Hz are summarized in Table 6.2.

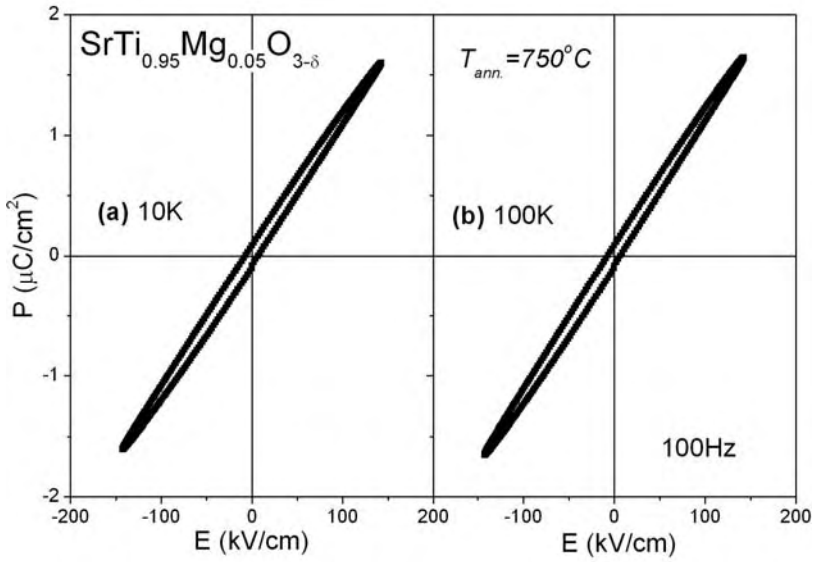

FIGURE 6.38. Hysteresis loops *P(E)* of $SrTi_{0.95}Mg_{0.05}O_{3-\delta}$ thin film annealed at 750°C at 10K (a) and 100K (b) at 100Hz.

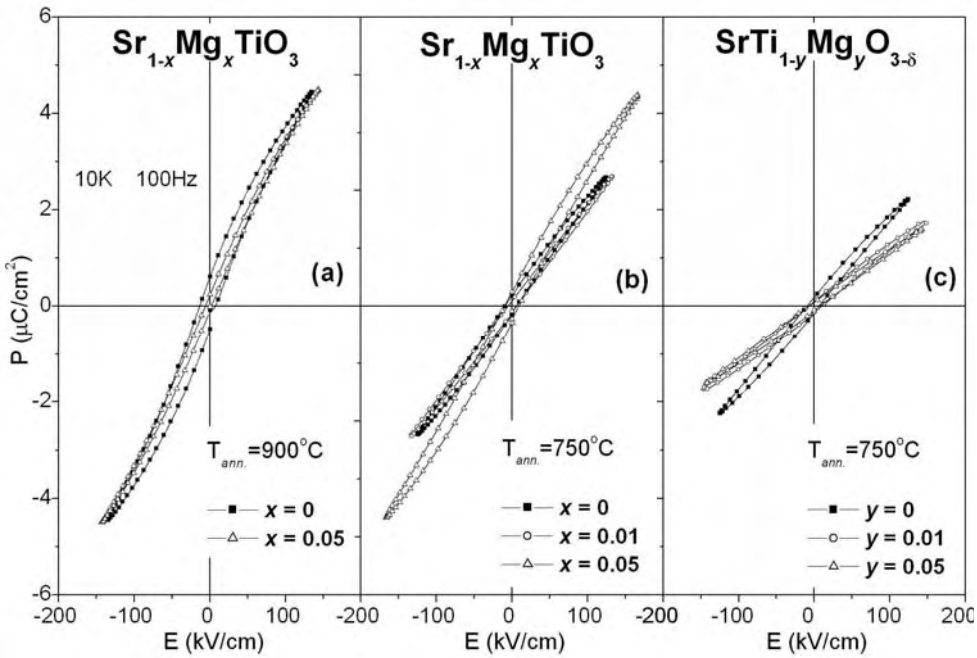

FIGURE 6.39. Hysteresis loops *P(E)* of undoped and Mg-doped $SrTiO_3$ thin films annealed at different temperatures at 10K at 100Hz.

TABLE 6.2. The average value of remnant polarization P_r and coercive field E_c of undoped ST films, $Sr_{1-x}Mg_xTiO_3$ and $SrTi_{1-y}Mg_yO_{3-\delta}$ films annealed at $T_{ann.}$=750°C and 900°C at selected 10K and 100K.

$Sr_{1-x}Mg_xTiO_3$ and $SrTi_{1-y}Mg_yO_{3-\delta}$ compositions	P_r, $\mu C/cm^2$		E_c, kV/cm	
	at 10K	at 100K	at 10K	at 100K
$x,y=0$ $T_{ann.}$=750°C	0.14 (at 15K)	0.09	7.8 (at 15K)	5.90
x=0.01 $T_{ann.}$=750°C	0.10	0.08	5.24	4.14
x=0.05 $T_{ann.}$=750°C	0.24	0.03	9.15	9.15
$x,y=0$ $T_{ann.}$=900°C	0.48 (at 15K)	0.27	10.5 (at 15K)	8.40
x=0.05 $T_{ann.}$=900°C	0.13	0.08	3.36	2.24
y=0.01 $T_{ann.}$=750°C	0.12	0.07	8.97	5.98
y=0.05 $T_{ann.}$=750°C	0.82	0.08	6.74	6.74

Accordingly it can be concluded that:

- SMT and STM films annealed at 750°C (Fig.6.33b,c) present similar almost linear *P(E)* dependency and it is still linear for STM films with increasing of Mg content;
- no strong dependence of P_r and E_c was noted with the Mg content in SMT and STM films annealed at 750°C;
- increasing of the annealing temperature leads to the formation of *s*-shape loops for SMT films with x=0.05 annealed at 900°C ;
- increasing of the annealing temperature from 750°C to 900°C in SMT films with x=0.05 (Fig.6.33a) leads to a decreasing of E_c, in opposition to the increasing of E_c observed in undoped ST ("Chapter 4");
- SMT films with x=0.05 (Fig.6.30) and STM films with the same y=0.05 (Fig.6.32) present completely different hysteresis response *P(E)* what corroborates the hypothesis that Mg is in different positions in the ST lattice in these films and supports the previous results.

Summary

1. The solid solubility of Mg in ST thin films is limited and depends on the lattice site occupancy as observed for identical ceramic compositions. However the solid solubility limit of Mg in ST films (*A* and *B* site) prepared by sol-gel is higher, than in

ST ceramics and is dependent on the annealing temperature.

2. According to XRD and TEM results all SMT films ($x \leq 0.30$) and STM ($y \leq 0.40$) annealed at 750°C crystallised with the perovskite phase and are monophasic. However, room temperature Raman study showed some second-order features for SMT films with x=0.30 annealed at 750°C.
3. For SMT and STM films annealed at 750°C, no dielectric relaxation in the range from room temperature to 10K was induced in contradiction to the theoretical prediction.
4. The low-temperature ε' and n_r of SMT films at $T_{ann.}$=750°C were not enhanced. Moreover, ε' and n_r were suppressed and more strongly than in the case of $SrTiO_3$-$MgTiO_3$ ceramics, implying the incorporation of Mg into ST lattice.
5. For STM films annealed at 750°C the shift of the maximum of n_r to low temperatures, from 68K to 25K in opposition to the others studied films, and shift to low temperature of the loss peak *C* from 184K to 164K with increasing Mg content confirms the substitution of small and highly-polarisable Ti^{4+} ions by big Mg^{2+} ions with the formation of oxygen vacancies as a charge compensation mechanism. In addition, despite that due to such substitution the low-temperature ε' and n_r were continuously decreased, similarity to equivalent ceramics, the low-temperature dielectric loss could also be considerably decreased by doping with Mg what is important for microwave applications.
6. SMT films annealed at 900°C with Mg concentrations higher than x=0.10 exhibited a Mg second phase, visible by TEM and Raman spectroscopy, and identified as the ilmenite type $MgTiO_3$, and that was not detected by XRD.
7. Similar to results obtained for SMT and STM films annealed at 750°C, in SMT films annealed at 900°C Mg doping itself does not induce ferroelectricity or a relaxor-like behaviour in strontium titanate, either introduced in the Sr or Ti site of the ST lattice, in spite of theoretical predictions.
8. The ε' of SMT films annealed at 900°C is higher than ε' of the films annealed at 750°C, but lower than that of undoped ST prepared under the same conditions, and it decreased with increasing of Mg concentration.
9. *dc*-field does not induce any additional peak in $\varepsilon'(E_{dc})$ of SMT and STM films independent on annealing temperature, and all of the analyzed samples presented lower dependency of ε' and n_r on applied E_{dc} compared to that of undoped ST films.

Chapter 7. Bi doped $SrTiO_3$ thin films: microstructure, structure and low temperature dielectric properties

In the current chapter, structure and microstructure of $Sr_{1-1.5x}Bi_xTiO_3$ films, prepared by sol-gel and deposited on $Si/SiO_2/TiO_2/Pt$ substrates, are studied. Dielectric response of these films is also measured as a function of frequency f and temperature T. Real part of dielectric permittivity ε' versus *dc* electric field E_{dc} and polarization P versus *ac* electric field E hysteresis response of $Sr_{1-1.5x}Bi_xTiO_3$ films are analyzed as well. The relaxations, detected both in real ε' and in imaginary ε'' parts of the dielectric permittivity, are analysed using Arrhenius and Vögel-Fulcher equations. Results are compared with the behaviour of equivalent ceramics.

Introduction

Dielectric properties of Mg doped $SrTiO_3$ (ST) films, reported in the "Chapter 6", revealed no dopant induced dielectric anomaly. Hence the experimental confirmation of Kvyatkovskii's theoretical prediction of dielectric relaxation was not obtained [Kvyatkovskii, 2005] both in films and in ceramics of Mg doped ST. On the contrary, the introduction of Mg^{2+} ions in ST lattice gives rise to a remarkable decrease of the ε', driving the system away from the ferroelectric instability.

Strong low-temperature dielectric relaxation was observed in the case of heterovalent doping as Bi^{3+} substituting for Sr^{2+} in $SrTiO_3$ ceramics, $Sr_{1-1.5x}Bi_xTiO_3$ (SBiT) [Yu, 1997; Ang et *al.*, 1998]. It was assumed that dopant Bi^{3+} ions, having ionic radius smaller than that of the host Sr^{2+}, occupy off-centre positions and undergo thermally activated hopping in multiminima potentials [Yu, 1997; Ang et *al.*, 1998]. On the other hand, due to the heterovalent substitution of Bi^{3+} for Sr^{2+}, the strontium vacancies V_{Sr} are created as a charge compensation mechanism, according to formula $[Sr_{1-1.5x}Bi_x(V_{Sr})_{0.5x}]TiO_3$, and the distortion of the crystal lattice occurs. The appearance of strontium vacancies V_{Sr} was claimed to lead to the formation of associated defects of Bi^{3+}-V_{Sr}. Such off-centre Bi ions and Bi^{3+}-V_{Sr} centres form the dipoles and thus set up local electric fields and/or strain

fields. So SBiT was considered as a random-site electric dipole system, where off-centre Bi and/or Bi^{3+}-V_{Sr} dipoles randomly distributed in the highly polarisable host lattice of ST [Ang et *al.*, 1998] and local electric fields brake their long range interaction, suppressing the ferroelectricity [Yu, 1997]. Thus, the introduction of Bi ions in ST ceramics produced two effects: a ferroelectric-like behaviour for low Bi concentrations ($x \leq 0.0267$), and a relaxor-like behaviour for high Bi content [Yu, 1997; Ang et *al.*, 1998]. Although the contribution/competition of these two different effects in Bi doped $SrTiO_3$ ceramics was reported in several publications [Yu, 1997; Ang et *al.*, 1998; Ang et *al.*, 1999a; Ang et *al.*, 1999b; Ang et *al.*, 1999c; Ang et *al.*, 2000b; Ang et *al.*, 2000d; Ang et *al.*, 2000e; Ang et *al.*, 2002; Yu and Ang, 2003; Porokhonskyy et *al.*, 2004; Ang and Yu, 2004] the properties of the equivalent $Sr_{1-1.5x}Bi_xTiO_3$ thin films have not been yet systematically studied.

In this chapter, the influence of the incorporation Bi ions into the Sr sites of $SrTiO_3$ films on the structure, microstructure and lattice dynamics is studied, using XRD, SEM, TEM, AFM, IR and Raman spectroscopy techniques. Dielectric response of Bi doped ST films is also measured in the frequency range of 10^2-10^6Hz, temperature range of 10-300K and *dc* electric field range of 0-125kV/cm and completed by the hysteresis measurements of the polarization response. For the samples revealing the dielectric relaxation, the relaxation parameters are determined using Arrhenius and Vögel-Fulcher equations. The dielectric behaviour of the films is compared with that of equivalent ceramics and the origin of the relaxation is discussed.

7.1. Preparation and characterisation

$Sr_{1-1.5x}Bi_xTiO_3$ (SBiT) thin films with x=0.002, 0.0053, 0.0067, 0.0133, 0.0267, 0.04, 0.1, 0.167 and 0.267 were prepared using similar process of film preparation described in the "Chapter 3". Films were deposited from the corresponding transparent solutions onto $Si/SiO_2/TiO_2/Pt$ substrates and annealed at 750ºC for 1h in air. Only for Raman and IR spectroscopy measurements, SBiT films were deposited on single crystal Al_2O_3 substrates. For TEM study, samples were carefully polished to reduce their thickness to approximately 30μm, glued to copper rings and ion beam milled. Dielectric properties, hysteresis response, *dc*-field effect (capacitance-voltage data) in a wide frequency and temperature range were measured on the films with sputtered Au top electrodes.

7.2. Microstructural properties

7.2.1. SEM analysis

The microstructure of $Sr_{1-1.5x}Bi_xTiO_3$ films deposited on $Si/SiO_2/TiO_2/Pt$ substrates was analysed by SEM at room temperature. SEM cross-section micrographs of $Sr_{1-1.5x}Bi_xTiO_3$ films with x=0.002, 0.0053, 0.0067, 0.04 and 0.167 are shown in Figure 7.1.

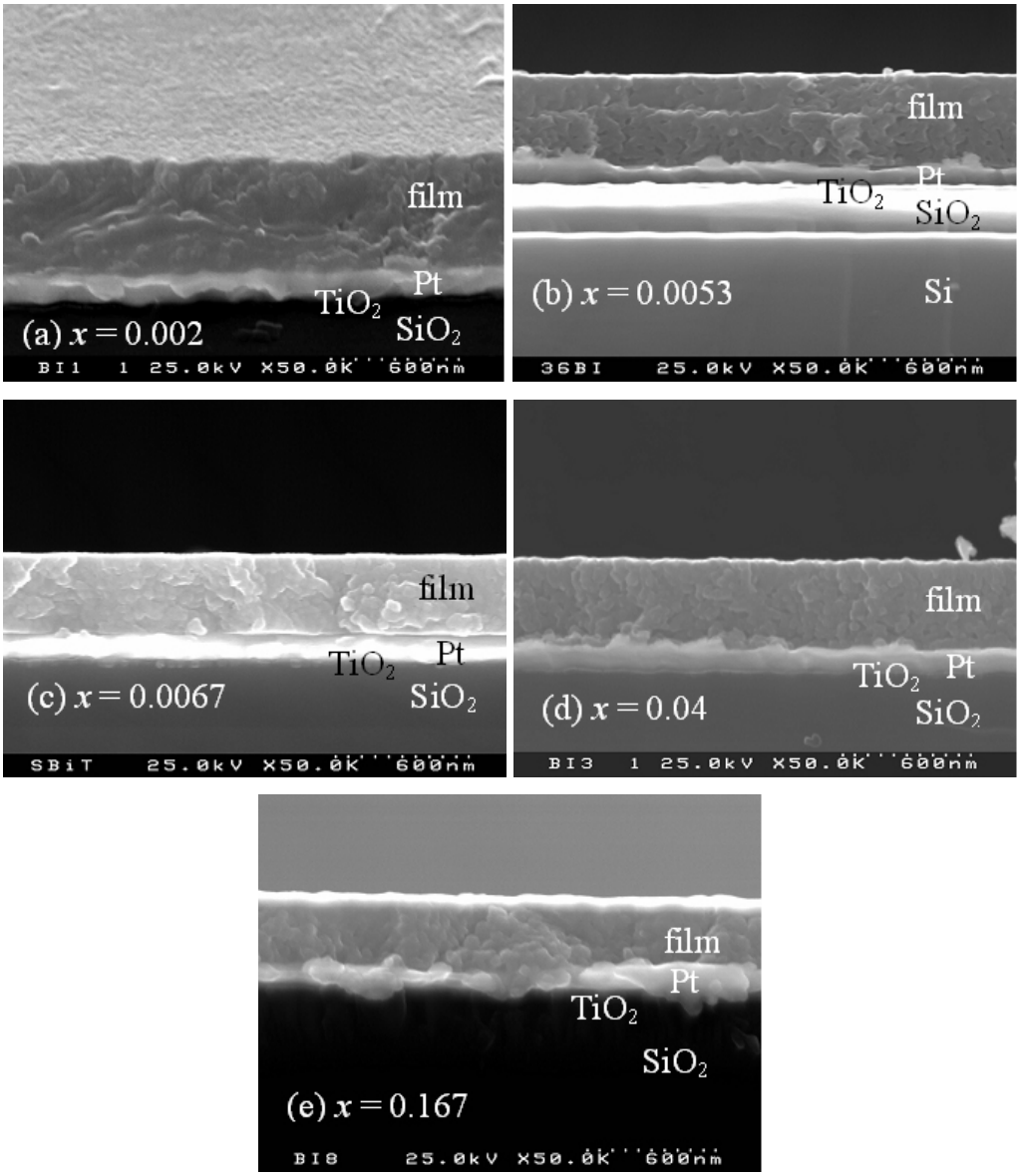

FIGURE 7.1. SEM cross-section micrographs of $Sr_{1-1.5x}Bi_xTiO_3$ thin films with x=0.002 (a), 0.0053 (b), 0.0067 (c), 0.04 (d) and 0.167 (e).

SBiT films exhibit a crack-free, continuous and fine-grained microstructure with no particulates (Fig.7.1). The thickness of studied films was estimated to be ~450nm and independent on Bi concentration. Since SEM magnification is not enough for precise calculation of the grain size of SBiT thin films, AFM is used for analysis of the film grains, as presented in the next subchapter.

7.2.2. AFM analysis

In addition to SEM cross sectional view, the surface morphology of $Sr_{1-1.5x}Bi_xTiO_3$ films was analyzed by AFM at room temperature and the in-plane surface (*left pictures*) and 3D view (*right pictures*) micrographs of SBiT thin films with x=0.053, 0.04 and 0.167 are depicted in Figure 7.2.

Confirming the results obtained from SEM study, all SBiT films show a smooth surface (roughness less than 2nm) and with average grain size varying from ~120nm for x=0.0053, ~112nm for x=0.04 to ~80nm for x=0.167 (Fig.7.2 *left pictures*). 3D images of SBiT films revealed that the grains were grown in all three *x,y,z*-directions (Fig.7.2 *right pictures*).

The AFM derived average in-plane grain size and roughness of undoped and Bi doped ST films are plotted in Figure 7.3 as a function of the Bi content.

Compared to undoped ST films, small content Bi doping increases the grain size. However, the variation of the grain size with the Bi content is not monotonous; after a first increase the grain size decreases with further increase of the dopant (Fig.7.3 *left axis*). The roughness of all the studied samples varies between 1nm and 2nm, slightly increasing with the dopant content (Fig.7.3 *right axis*). As was reported in the literature no systematic variation of the grain size with change in the Bi content was observed in $Sr_{1-1.5x}Bi_xTiO_3$ ceramics [Yu, 1997].

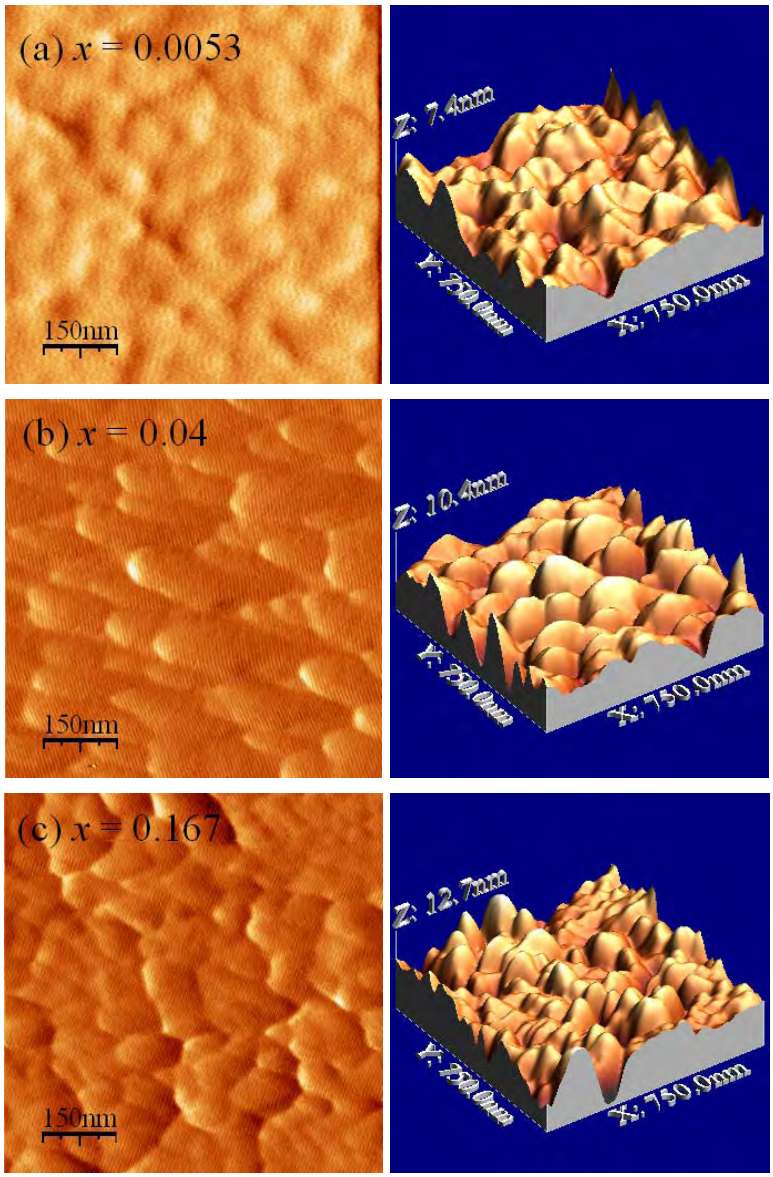

FIGURE 7.2. AFM micrographs of $Sr_{1-1.5x}Bi_xTiO_3$ films with x=0.0053 (a), 0.04 (b) and 0.167 (c).

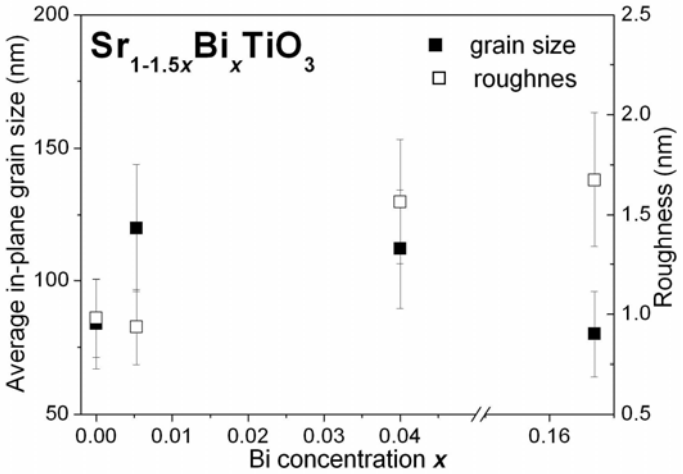

FIGURE 7.3. Average grain size distribution (*left axis*) and roughness (*right axis*) *versus* Bi concentration of $Sr_{1-1.5x}Bi_xTiO_3$ films.

7.2.3. TEM analysis

Microstructural and elemental analysis of some SBiT films was done by TEM/EDS also. TEM plane-view micrographs and EDS spectra of $Sr_{1-1.5x}Bi_xTiO_3$ films with x=0.0267 and x=0.10 are depicted in Figure 7.4a,b and c,d, respectively.

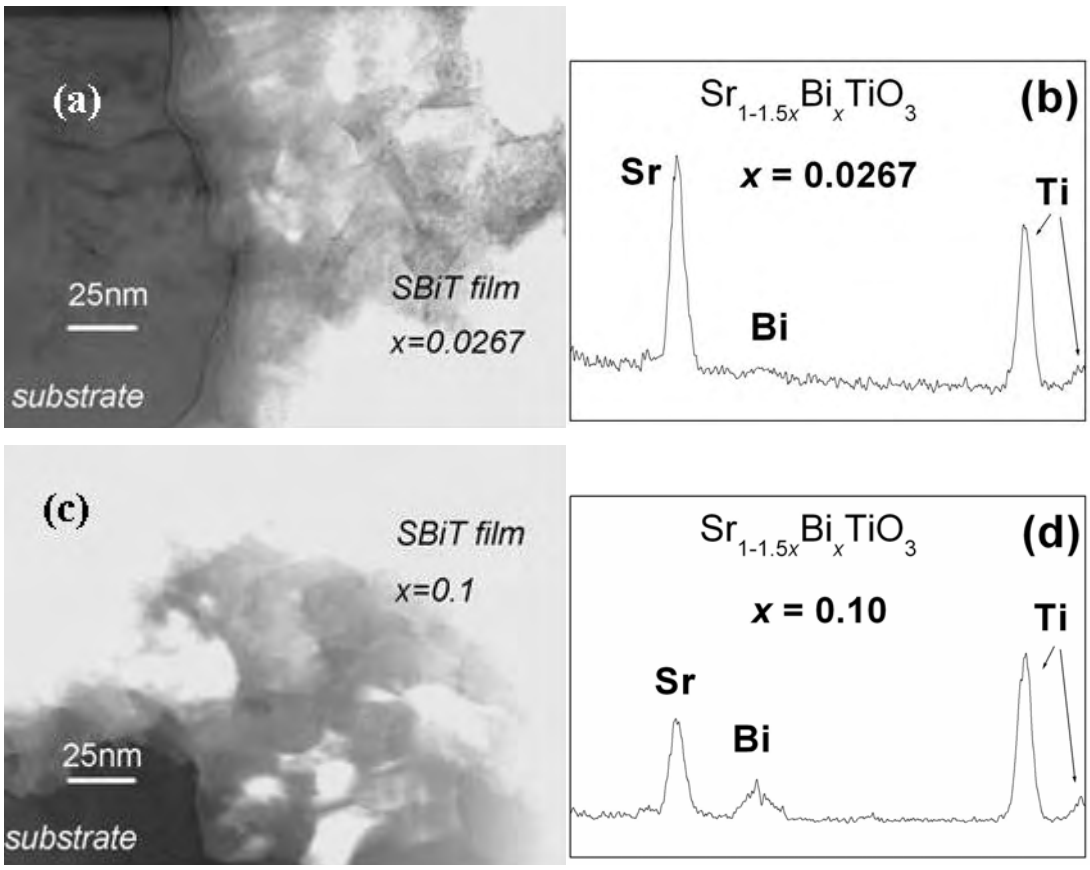

FIGURE 7.4. Plan view TEM micrographs (a,c) and EDS spectra (b,d) of $Sr_{1-1.5x}Bi_xTiO_3$ (SBiT) films with x=0.0267 (a,b) and 0.10 (c,d).

Supporting the SEM and AFM results, homogeneous monophasic microstructure of SBiT thin films with x=0.0267 and 0.10 was observed by TEM (Fig.7.4a,c). The grain size of SBiT films with x=0.0267 is higher than that of sample with x=0.10, although the absolute values are very difficult to determine. In spite of the small size of the grains, no second phases were detected. In agreement with the initial stoichiometry the EDS analysis of these films indicates an increase of the Bi peak intensity with the increasing of the Bi concentration in the films (Fig.7.4b,d).

7.3. Crystal structure and lattice parameter

The XRD patterns of $Sr_{1-1.5x}Bi_xTiO_3$ (SBiT) thin films with x=0, 0.002, 0.0053, 0.0067, 0.0267, 0.04, 0.167 and 0.267 prepared on $Si/SiO_2/TiO_2/Pt$ substrates annealed at 750°C are depicted in Figure 7.5.

The XRD patterns of analyzed SBiT films present only the diffraction reflections of cubic ST system for all the samples with concentrations of Bi $x \leq 0.167$, whereas the second phase $Bi_4Ti_3O_{12}$ is detected for the doping concentration x=0.267 (Fig.7.5). These results are in accordance with $Sr_{1-1.5x}Bi_xTiO_3$ ceramics, in which the monophasic compositions were obtained for $x \leq 0.20$ and $Sr_2Bi_4Ti5O_{18}$, $Bi_4(TiO_4)_3$ and $Bi_2Ti_4O_{11}$ second phases were identified for ceramics samples with $0.227 \leq x \leq 0.267$ [Yu, 1997].

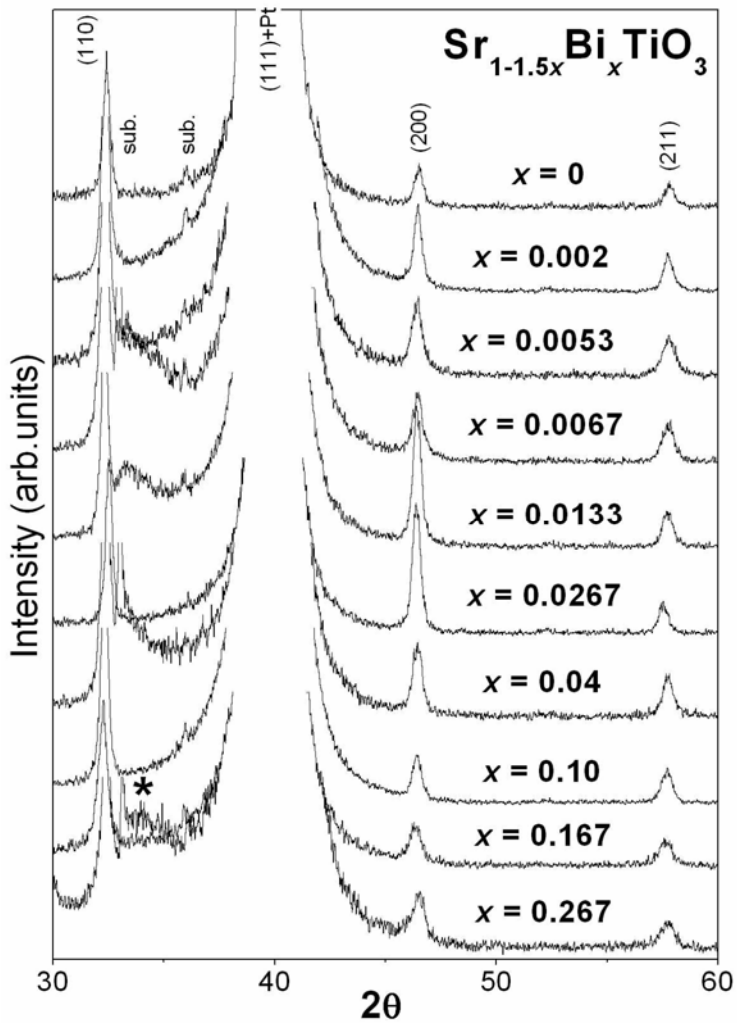

FIGURE 7.5. X-ray diffraction patterns of $Sr_{1-1.5x}Bi_xTiO_3$ thin films (* denotes $Bi_4Ti_3O_{12}$ as a second phase).

The variation of the lattice parameter *c* as a function of the Bi content is shown in Figure 7.6. Since the values of in-plane *a* and out-of-plane *c* lattice parameters, obtained from XRD measurements of undoped ST films annealed at 750°C in the "Chapter 4", were equal, only out-of-plane lattice parameter *c* of $Sr_{1-1.5x}Bi_xTiO_3$ thin films is analyzed.

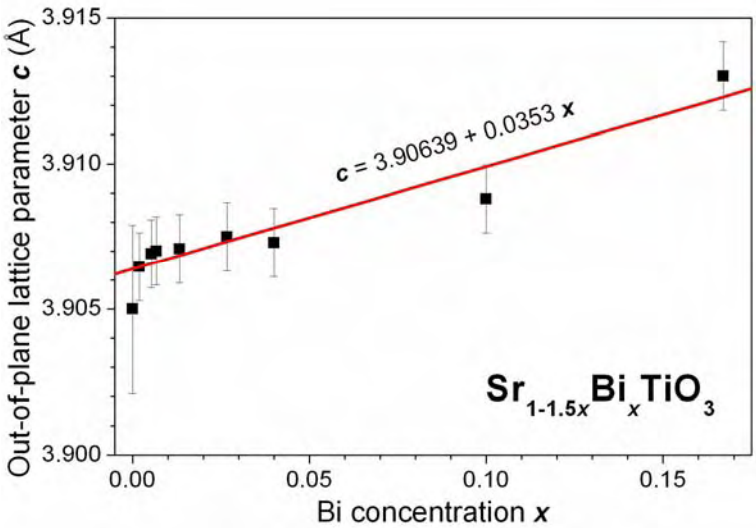

FIGURE 7.6. Lattice parameter *c* of $Sr_{1-1.5x}Bi_xTiO_3$ thin films as a function of Bi concentration.

The lattice parameter *c* of SBiT films increases with increasing of Bi content from ~3.905Å for undoped ST to ~3.913Å for *x*=0.167 with the slope about 0.035Å (Fig.7.6). A similar increase of the lattice parameter was reported for SBiT ceramics as well [Yu, 1997; Yu et *al.*, 1998; Ang et *al.*, 1998], but it was not explained, probably because Bi^{3+} ions with coordination number of 6 and 8 are much smaller than that of Sr^{2+} and there is no data for the coordination number of 12 [Shannon, 1976]. However, linear extrapolation of the ionic radius values of $Bi^{3+}_{(5)}$, $Bi^{3+}_{(6)}$ and $Bi^{3+}_{(8)}$ to the coordination number of 12 reveals that ionic radius of $Bi^{3+}_{(12)}$ is 1.45Å (Fig.7.7), i.e. it is slightly larger than the substituted Sr^{2+} ions (ionic radius of $Sr^{2+}_{(12)}$=1.44Å) [Shannon, 1976].

Such a way, increase of the lattice parameter in $Sr_{1-1.5x}Bi_xTiO_3$ films and ceramics with Bi content can be expected. Moreover, assumption that expansion of the unit cell is also due to the formation of V_{Sr} and corresponding electrostatic repulsion of adjacent oxygen anions can be reasonable as well.

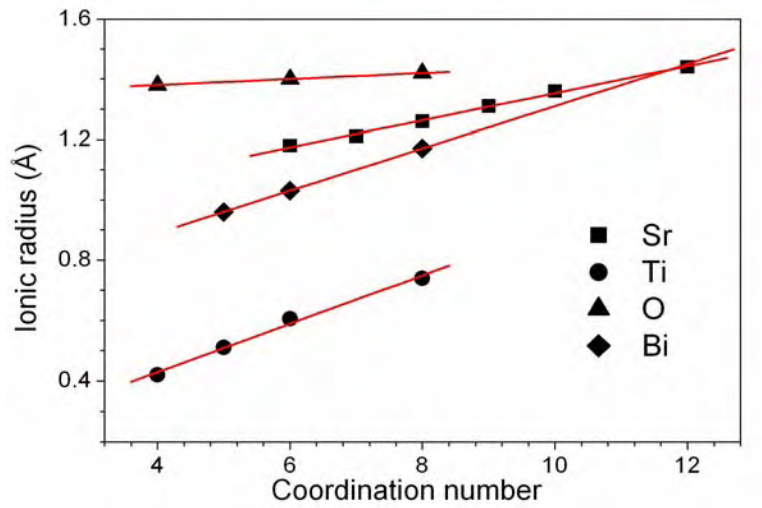

FIGURE 7.7. Ionic radii of several ions *versus* coordination number following Shannon [Shannon, 1976].

7.4. Lattice dynamics study

7.4.1. Raman spectroscopy analysis

The effect of Bi incorporation into the lattice of ST films was further analysed by Raman spectroscopy studies of $Sr_{1-1.5x}Bi_xTiO_3$ thin films with x=0.0053 and 0.167, conducted from 300K to 10K. The acquired Raman spectra are presented in Figure 7.8.

As was described in the literature for undoped ST ceramics [Petzelt et *al.*, 2001] and previously mentioned for undoped ST films ("Chapter 5"), the Raman spectra of ST system in the used wavelengths range are characterized by TO4 and LO4 modes (at ~546cm^{-1} and ~792cm^{-1}, respectively), observed due to local loss of symmetry at the grain boundaries [Petzelt et *al.*, 2001]. As shown in Figure 7.8, these two modes are also observed in the Raman spectra of both Bi doped ST films with x=0.0053 (Fig.7.8a) and x=0.167 (Fig.7.8b) together with the vibration modes from the sapphire substrates.

For x=0.0053, TO4 mode is well defined below 150K, but it is weak above this temperature, whereas LO4 mode is week in all temperature range of 10-300K. For x=0.167, both TO4 and LO4 modes are well seen from 10 to 300K, although TO4 mode is more diffuse than that of the film with x=0.0053. Moreover, frequency of TO4 mode of both SBiT films slightly increases with decreasing temperature: from ~538cm^{-1} at 300K to ~545cm^{-1} at 10K for x=0.0053 and from ~541cm^{-1} at 300K to ~555cm^{-1} at 10K for x=0.167.

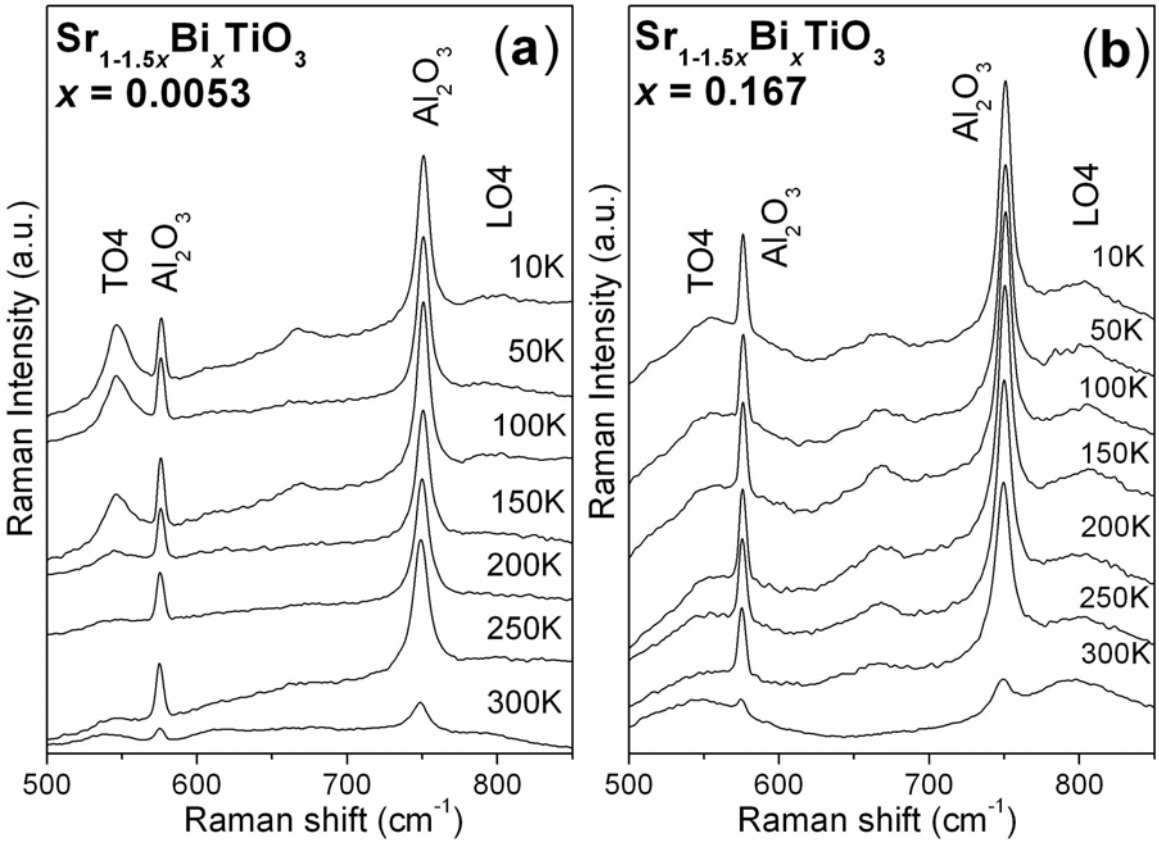

FIGURE 7.8. Raman spectra of $Sr_{1-1.5x}Bi_xTiO_3$ thin films with x=0.0053 (a) and 0.167 (b) at selected temperatures.

A mode at frequency of ~550cm^{-1} was also observed in the Raman spectra of $Sr_{1-1.5x}Bi_xTiO_3$ ceramics [Ang and Yu, 2000e; Porokhonskyy et *al.*, 2004]. Intensity of the mode was found to increase with Bi content and attributed to the lattice distortion, induced by Bi doping and increasing with Bi concentration [Ang and Yu, 2000e; Porokhonskyy et *al.*, 2004]. Thus, Bi incorporation into the lattice of ST film, accompanied by the lattice distortion similar to that of the bulk, can be confirmed by observed behaviour of Raman spectra of SBiT films (Fig.7.8).

7.4.2. IR spectroscopy analysis

For additional study of the lattice dynamics, behaviour of TO modes of $Sr_{1-1.5x}Bi_xTiO_3$ films with x=0.0053 and x=0.167 deposited on Al_2O_3 substrates without Pt layer were analysed in IR frequency range from 300K to 10K, as depicted in Figure 7.9.

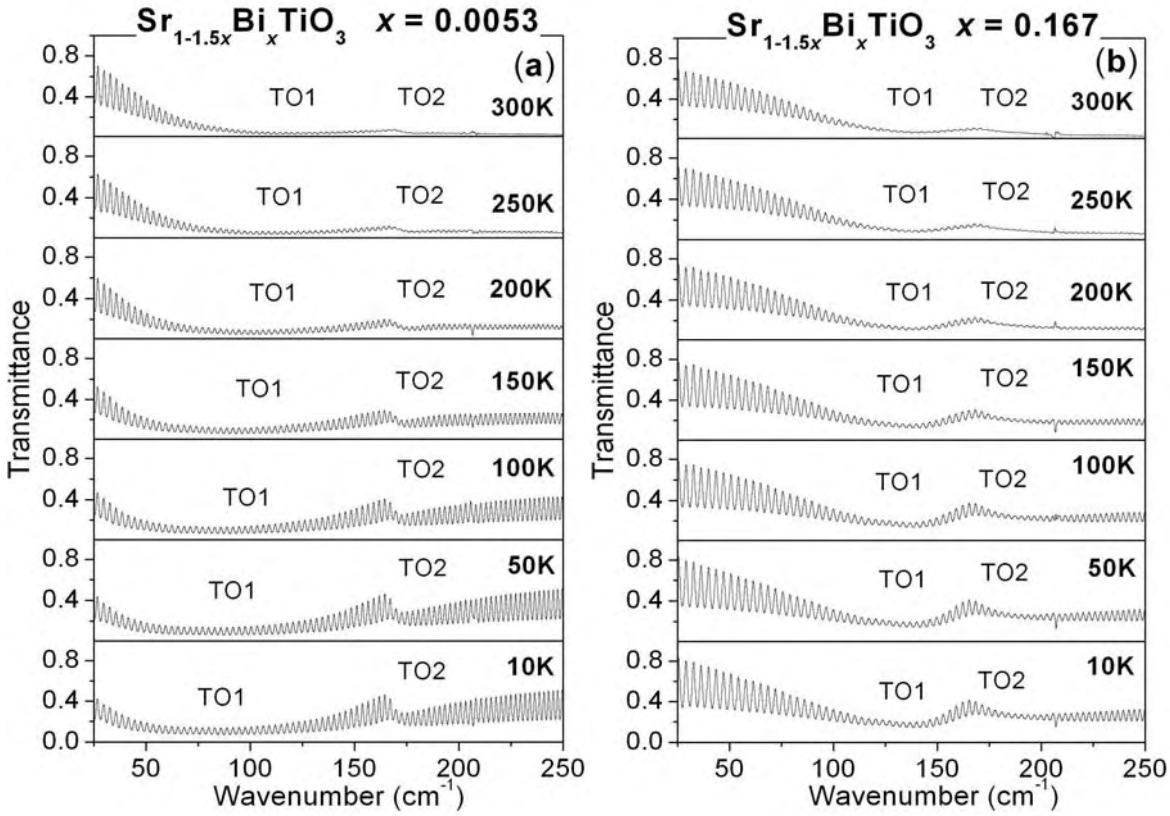

FIGURE 7.9. IR transmittance spectra of $Sr_{1-1.5x}Bi_xTiO_3$ thin films with x=0.0053 (a) and 0.167 (b) at selected temperatures.

Similarly to undoped ST films deposited on Al_2O_3 substrates ("Chapter 5"), TO1 mode (at ~100cm^{-1}) and TO2 mode (at ~176cm^{-1}) are detected in both $Sr_{1-1.5x}Bi_xTiO_3$ thin films with x=0.0053 (Fig.7.9a) and x=0.167 (Fig.7.9b). For the film with small Bi content x=0.0053 TO1 mode is shifted to the low frequency with the temperature decrease (Fig.7.9a) similarly to that of undoped ST. In contrast, no softening of TO1 mode was observed in SBiT film with high doping concentration x=0.167 (Fig.7.9b).

The transmittance spectra of $Sr_{1-1.5x}Bi_xTiO_3$ films (Fig.7.9) were fitted to determine the TO mode parameters and to obtain the complex dielectric response function as described in the "Chapter 3". The resulting fitted spectra of real ε' and imaginary ε'' part of dielectric permittivity of analyzed SBiT films in IR range are presented in Figure 7.10. However, the values of the dielectric permittivity derived from the IR analysis can not be directly compared to the results of dielectric measurements due to the fact that in this analysis the *in-plane* dielectric response of SBiT films deposited directly on Al_2O_3 substrates was

obtained in opposition to the *out-of-plane* dielectric permittivity measured on SBiT films based MIM capacitors.

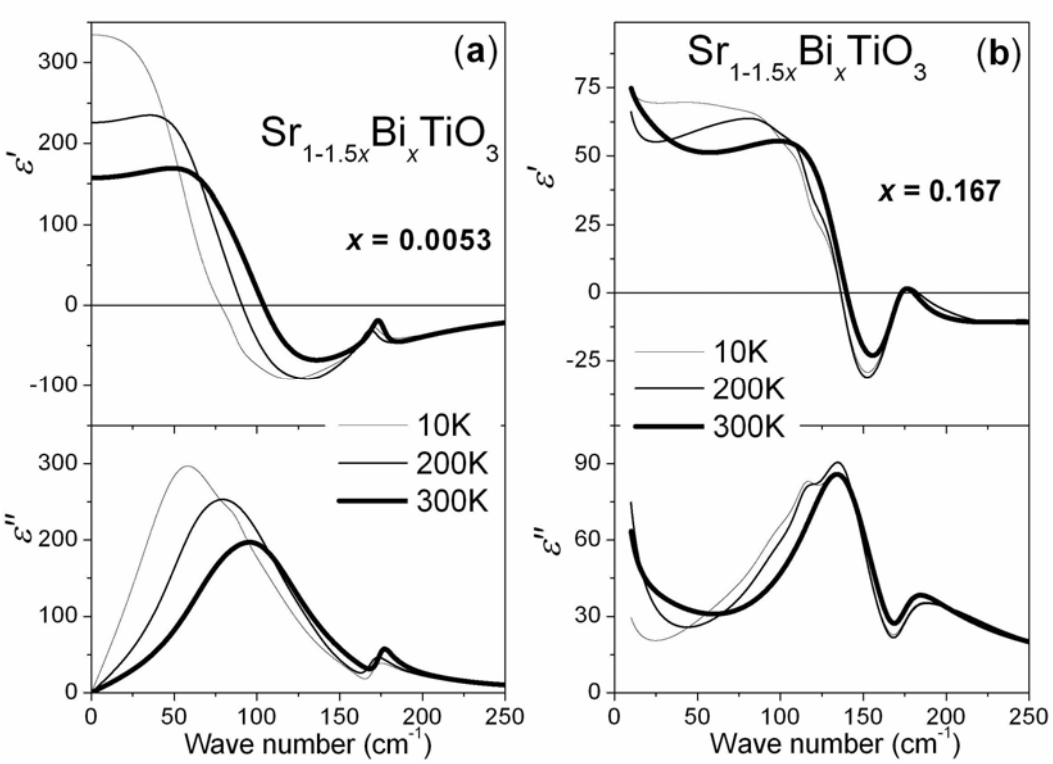

FIGURE 7.10. Spectra of real ε' and imaginary ε'' part of dielectric permittivity in IR range, obtained from the transmittance fits of $Sr_{1-1.5x}Bi_xTiO_3$ thin films with x=0.0053 (a) and 0.167 (b) at selected temperatures.

As seen from Figure 7.10a, with the temperature decrease the frequency of TO1 mode of SBiT film with x=0.0053 shifts from ~95cm^{-1} (at 300K) through ~79cm^{-1} (at 200K) to ~58cm^{-1} (at 10K). These values of eigenfrequency of TO1 mode in SBiT film with x=0.0053 are very close to the values presented before for undoped ST film (~91cm^{-1} at 300K and ~48cm^{-1} at 10K from the "Chapter 5"). In $Sr_{1-1.5x}Bi_xTiO_3$ ceramics position of TO1 mode also showed shifts for small Bi content x=0.0067: from 103cm^{-1} at 300K to 44cm^{-1} at 20K and TO1 mode was almost constant for high concentration x=0.133: from 126cm^{-1} at 300K to 107cm^{-1} at 20K [Porokhonskyy et *al.*, 2004]. At the same time, the frequency of TO1 mode of SBiT film with x=0.167 is equal to ~134cm^{-1} in all the temperature range from 300K to 10K as shown in Figure 7.10b. Thus, TO1 mode represented similar behaviour in SBiT films and ceramics.

In addition, one new mode of unknown nature appears at ~117cm^{-1} at 200K and 10K

for SBiT film with x=0.167 (Fig.7.10b), although it was not reported for SBiT ceramics [Porokhonskyy et *al.*, 2004]. Moreover, an additional relaxation was observed on the low-frequency soft mode wing (below 30cm^{-1} or ~1THz) of SBiT films with x=0.167 (Fig.7.10b), but was not detected for SBiT films with x=0.0053 (Fig.7.10a) as well as for other films studied in current thesis (in undoped ST or in Mg doped ST films). It was reported that wide-frequency spectra of SBiT ceramics with high Bi content (x=0.08) reveal several relaxation regions and two of them revealed very wide frequency distribution up to THz range [Porokhonskyy et *al.*, 2004]. These relaxations were related: *i)* to reorientation of dipoles created by the off-centered Bi ions (individual hopping of the Bi ions), and *ii)* to dynamics of the polar nanoclasters surrounding the Bi ions which interact with each other via the highly polarisable host crystal lattice (cooperative hopping of the off-centred Bi ions). Presented in current thesis SBiT films were not analyzed in THz diapason. However, it can be supposed, that additional relaxation observed in SBiT films with x=0.167 at ~10-50cm^{-1} (Fig.7.10b) have the same origin as in $Sr_{1-1.5x}Bi_xTiO_3$ ceramics.

7.5. Low temperature dielectric properties

7.5.1. Dielectric response as function of temperature and Bi content

Temperature dependence of the real ε' and imaginary ε'' parts of the dielectric permittivity of $Sr_{1-1.5x}Bi_xTiO_3$ films with x=0, 0.002, 0.0053, 0.0067, 0.0133, 0.04, 0.10, 0.133, 0.167 at 10kHz is depicted in Figures 7.11 and 7.12, respectively. Variation of the $\tan\delta=\varepsilon''/\varepsilon'$ as a function of the temperature is shown as well in Figure 7.13.

It is seen from the Figure 7.11 and 7.12, that ε' and ε'' of Bi doped ST films is higher than that of undoped ST films. Obtained values of the $\tan\delta$ of SBiT films are higher than that of undoped ST films as well and increase with increasing Bi content: from ~0.5% for undoped ST films to ~5% for SBiT samples with x=0.167 (Fig.7.13). Moreover, in contrast to the broad peak at ~55K detected in $\varepsilon'(T)$ of undoped ST films, a strong peak in $\varepsilon'(T)$ of SBiT films (Fig. 7.11), accompanied by strong peaks induced in loss (Figs.7.12 and 7.13), can be easily observed.

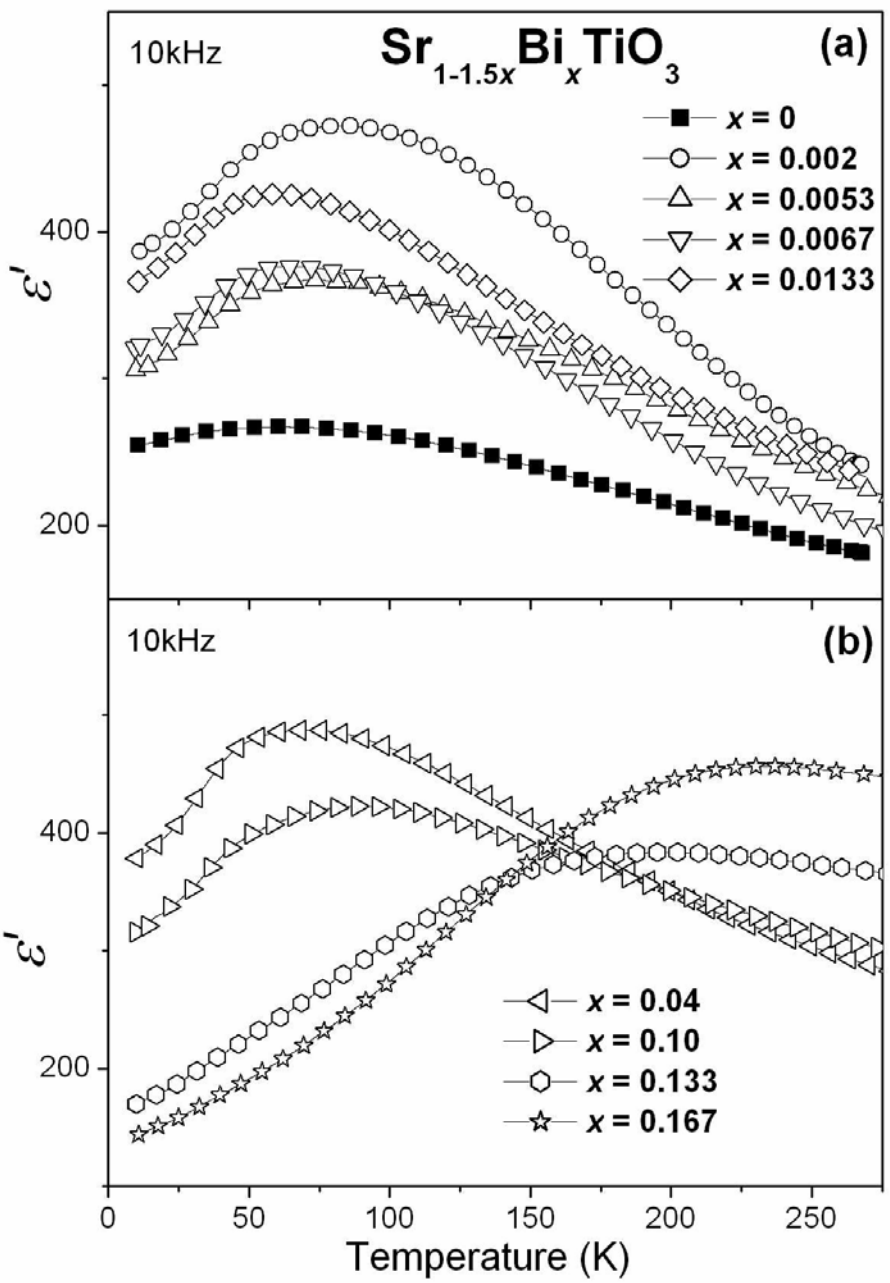

FIGURE 7.11. Temperature dependence of the real part of dielectric permittivity ε' of $Sr_{1-1.5x}Bi_xTiO_3$ films with x=0, 0.002, 0.0053, 0.0067, 0.0133 (a) and x=0.04, 0.10, 0.133, 0.167 (b) at 10kHz.

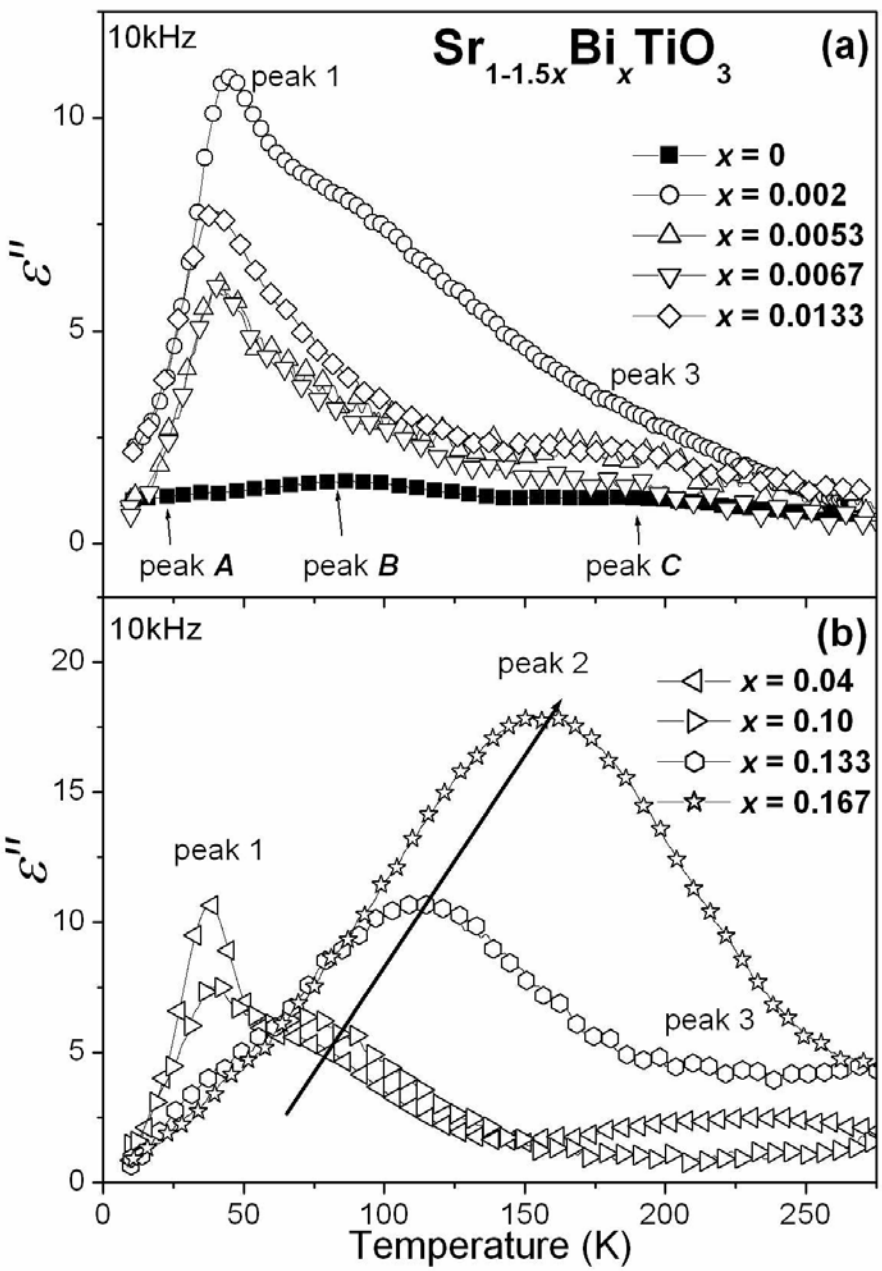

FIGURE 7.12. Temperature dependence of the imaginary part of dielectric permittivity ε'' of $Sr_{1-1.5x}Bi_xTiO_3$ films with x=0, 0.002, 0.0053, 0.0067, 0.0133 (a) and x=0.04, 0.10, 0.133, 0.167 (b) at 10kHz.

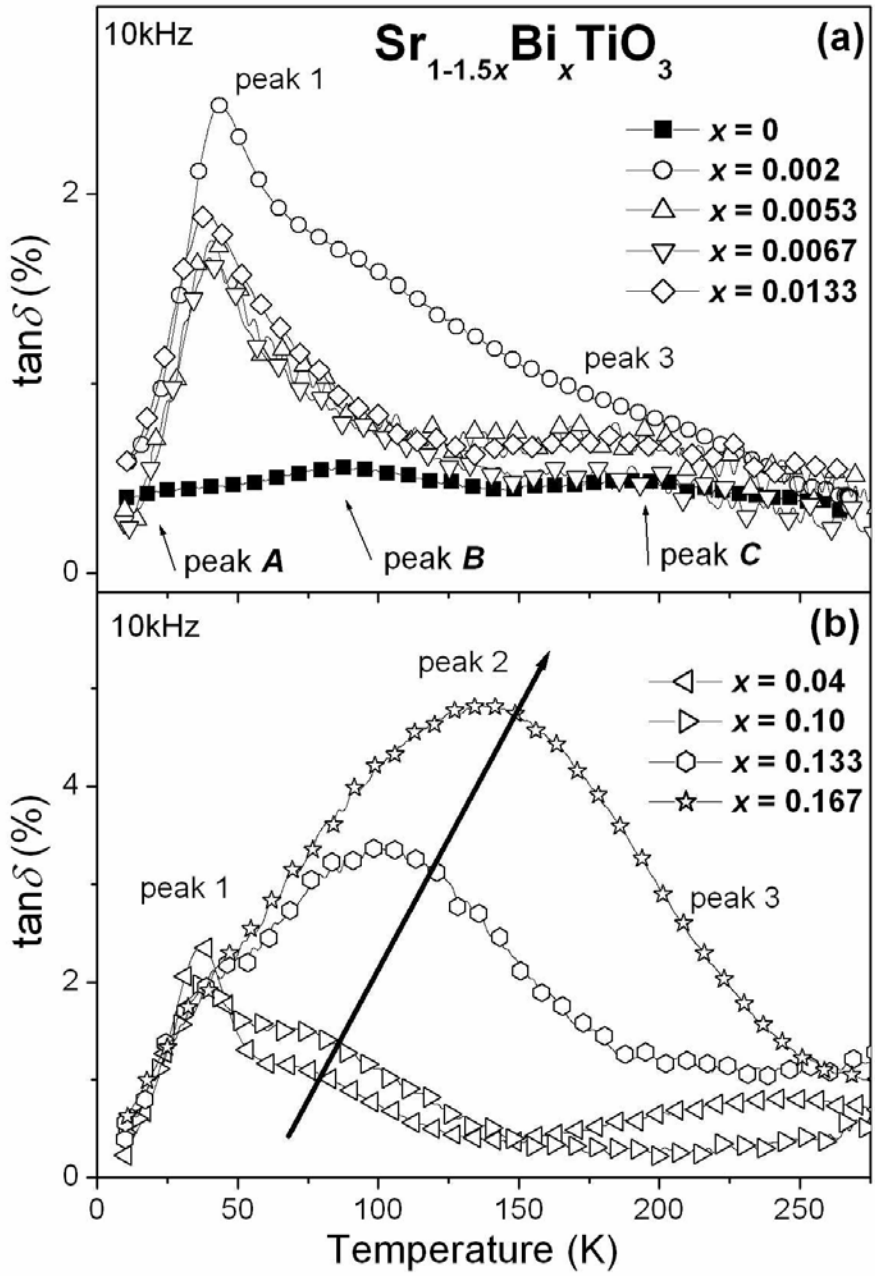

FIGURE 7.13. Temperature dependence of the tanδ of $Sr_{1-1.5x}Bi_xTiO_3$ films with x=0, 0.002, 0.0053, 0.0067, 0.0133 (a) and x=0.04, 0.10, 0.133, 0.167 (b) at 10kHz.

The magnitude of the peak ε'_{max} depends on Bi content and the temperature of ε'_{max} ($T_{\varepsilon'max}$) increases with Bi concentration, as plotted in Figure 7.14. A marked increase is observed in ε'_{max} for low dopant concentrations, being followed by a non monotonous variation for higher Bi content. The highest ε'_{max} is observed for x=0.04.

The increase of ε'_{max} for small x and a later decrease for high x was also observed in SBiT ceramics, where the augment in Bi concentration leads to a variation of ε'_{max} and a shift of $T_{\varepsilon'max}$ to higher temperatures [Yu, 1997; Ang et *al*.,1998]. However, the highest value of ε'_{max} in $Sr_{1-1.5x}Bi_xTiO_3$ ceramics was observed at x=0.0067 (ε'_{max} ~6000 at $T_{\varepsilon'max}$ ~66K) [Yu, 1997; Ang et *al*., 1998]. Moreover, in opposite to analyzed SBiT films, two induced anomalies occurred in $\varepsilon'(T)$: at ~18K and at ~30K (with $T_{\varepsilon'max}$ independent on Bi content), whereas one more dielectric anomaly (whose $T_{\varepsilon'max}$ increases with increasing of Bi) was observed for $Sr_{1-1.5x}Bi_xTiO_3$ ceramics with $x \geq 0.0133$ [Yu, 1997; Ang and Yu, 2000e; Ang and Yu, 2002].

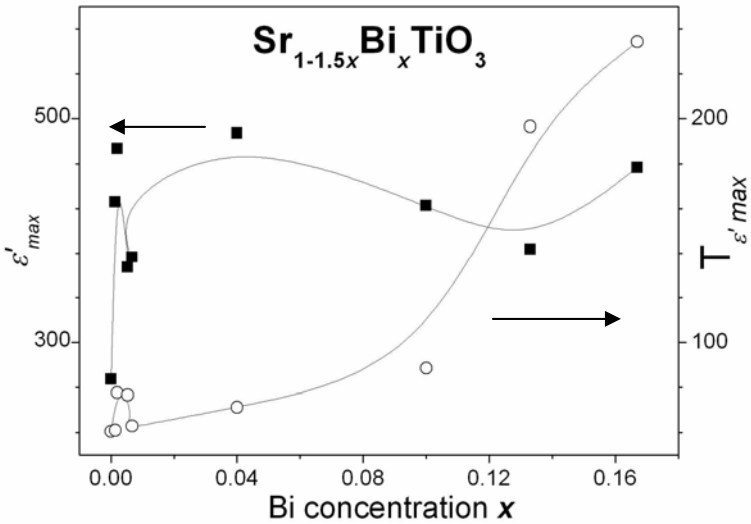

FIGURE 7.14. Variation of the maximum of the real part of the dielectric permittivity ε'_{max} (*left scale*) and of the temperature of the maximum of the real part of the dielectric permittivity $T_{\varepsilon'max}$ (*right scale*) of $Sr_{1-1.5x}Bi_xTiO_3$ thin films with Bi content at 10kHz.

Both $\varepsilon''(T)$ and $\tan\delta(T)$ of SBiT films reveal three peaks, marked as peak 1, peak 2 and peak 3 in Figures 7.12 and 7.13, respectively. The dielectric loss of undoped ST films were also characterised by three peaks, described in the "Chapter 4" as following: *1)* peak *A* could be considered as a stress/strain induced ferroelectric phase transition [Astafiev et *al.*, 2003]; *2)* peak *B* was attributed to the dynamics of the elastic domain walls that occur at the cubic-to-tetragonal phase transition around 105K [Mizaras and Loidl, 1997]; *3)* peak *C*

was associated with the effect of defect/impurity like oxygen vacancies [Lemanov et *al.*, 2002; Yu et *al.*, 1999]).

For better understanding the difference or similarity of nature of the peaks 1, 2 and 3 detected in $Sr_{1-1.5x}Bi_xTiO_3$ thin films and peaks *A, B* and *C* of undoped ST (from the "Chapter 4"), the diagram of the temperatures of these peaks, obtained from $\varepsilon''(T)$ at 10kHz, is presented in the Figure 7.15. It is seen that peak 1 (almost independent on Bi content) is detectable in $\varepsilon''(T)$ of SBiT films with $x \leq 0.10$ at temperatures between 38K and 44K that is twice higher than the temperature of peak *A* in undoped ST films (~22K), implying a difference in the origin of these peaks. Meanwhile, the peak about 30K was observed in $\varepsilon''(T)$ of $Sr_{1-1.5x}Bi_xTiO_3$ ceramics with small Bi concentration ($x \leq 0.04$) [Ang et *al.*, 1999a; Ang et *al.*, 1999b; Ang et *al.*, 1999c]. The temperature of this peak in SBiT ceramics was almost independent on the Bi content [Ang et *al.*, 1999a] similarly to peak 1, observed in analyzed SBiT films.

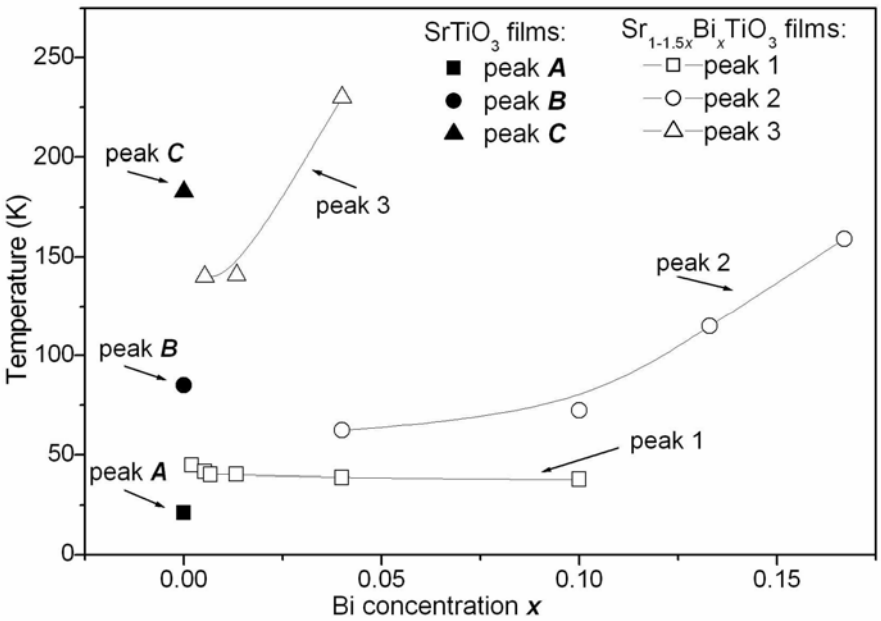

FIGURE 7.15. Diagram of temperature positions of peaks 1, 2 and 3 detected in $Sr_{1-1.5x}Bi_xTiO_3$ thin films in comparison to peaks *A, B* and *C* of undoped $SrTiO_3$ obtained from $\varepsilon''(T)$ at 10kHz.

At the same time, the peak 2 was detected in SBiT films with $x \geq 0.04$ at different temperatures: from ~62K to ~160K due to strong dependency on Bi content, in contrast to almost stable peak 1 in analyzed SBiT films and in contrast to ~85K at which peak *B* was detected in undoped ST films (Fig.7.15). Thus, origin of the peak 2 in SBiT films is

different from that of the peak 1 of the same films or from that of the peak *B* of undoped ST films. Similarly to the peak 2, observed in SBiT films, the relaxor peak appeared in SBiT ceramics, becoming dominant for x>0.0267 [Yu, 1997; Ang et *al.*, 1999c]. The coexistence of peak 2 with peak 1 in SBiT films with intermediate Bi content ($0.04 \leq x \leq 0.10$) indicates that several kinds of dipoles or polar clusters, which are responsible for different dielectric relaxation in different temperature ranges, coexist in Bi doped ST system.

Concerning the very broad and almost undetectable peak 3 (not clearly observed at ~140K- ~230K), its position is not far from the peak *C* in undoped ST films (~183K) ("Chapter 4"). Moreover, as it was reported in the literature, similar broad peak can be observed in undoped ST films in wide temperature diapason: from ~160K [Yu et *al.*, 2002] to >230K [James and Xi, 2002]. Thus, based on this information, a similar nature, associated with the oxygen vacancies, of peak 3 in SBiT films and peak *C* in undoped ST films can be supposed.

Comparing Figures 7.13 and 7.14, it is worthwhile to note that $T_{\varepsilon'max}$ in SBiT films is higher than the temperatures of both independent on Bi content loss peak 1 and dependent on Bi content loss peak 2.

Considering the Bi concentration effect, three main concentration ranges, which reveal different dielectric loss behaviour of SBiT films, are determined (Figs.7.12 and 7.13):

- $0.002 \leq x \leq 0.0133$. For these films only peak 1 is well presented. $T_{\varepsilon''max}$ of peak 1 is almost independent on x in this concentration range and only slightly decreases with increasing of Bi concentration for samples with $0.002 \leq x \leq 0.0133$ (~44.78K for x=0.002, ~41.68K for x=0.0053, ~40.1K for x=0.0067, ~40.23K for x=0.0133). For some concentration of Bi (x=0.0053 and 0.0133), a very broad and almost undetectable peak 3 can be found in SBiT films at ~140K;
- $0.04 \leq x \leq 0.10$. There is the coexistence of peak 1 and peak 2. $T_{\varepsilon''max}$ of peak 1 still slightly decreases (~38.6K for x=0.04 and ~37.76K for x=0.10) and $T_{\varepsilon''max}$ of peak 2 moves to high temperature (~62.3K for x=0.04 and ~72.27K for x=0.10). For x=0.04 broad peak 3 at ~230K is detected;
- $0.133 \leq x \leq 0.167$. For these films only peak 2 is observed. The magnitude and $T_{\varepsilon''max}$ of peak 2 increase with the increase of Bi content and maximum of peak 2 moves to high temperature (~114.83K for x=0.133 and ~159.05K for x=0.167).

Also three concentration regions in $\varepsilon''(T)$ were reported for Bi doped ST ceramics:

- $0.0005 \leq x < 0.0033$. "Defect phase", revealing peaks independent on the Bi content.
- $0.0033 \leq x < 0.04$. "Mixed phase", where except peaks independent on the Bi content, one additional relaxation, moving to high temperature with increasing of Bi concentration was found around 50K.
- $0.04 \leq x \leq 0.167$. "Relaxor phase" with strong relaxation dependent on Bi content, observed at T>100K [Ang et *al.*, 1999b].

Thus, despite that SBiT ceramics as well as the analyzed SBiT films show 3 concentration regions, revealing different dielectric loss behaviour, their diapasons do not completely coincide but are shifted to higher concentration range in SBiT films, compared to ceramics.

As mentioned already in the "Chapter 2", the temperature dependence of $\varepsilon'(T)$ of normal ferroelectrics follows the Curie-Weiss law:

$$1/\varepsilon' = (T - T_c) / C \tag{7.1}$$

where C stands for the Curie constant and T_c for the Curie temperature.

However, fitting of the present $\varepsilon'(T)$ experimental results to Curie-Weiss law gave negative values of Curie temperature T_0 without a systematic variation/dependence on Bi content. It indicates a limited applicability of Curie-Weiss law, used to describe the dielectric behaviour of classical ferroelectrics, to the $Sr_{1-1.5x}Bi_xTiO_3$ films. In the meantime, a quadratic equation for the $\varepsilon'(T)$ of ferroelectrics with diffused phase transition (such as the relaxor systems) was proposed by Smolenskii [Smolenskii, 1970]:

$$1/\varepsilon' - 1/\varepsilon'_{max} = (T - T_{\varepsilon'max})^2 / C_1 \tag{7.2}$$

where C_1 stands for a constant. However, this description is only valid for a narrow temperature range. In order to improve this description for relaxors with the frequency dispersion and diffuseness of the phase transition, the following empirical expression is usually used to describe the dielectric behaviour on the high temperature side of $T_{\varepsilon'max}$ [Bednorz and Müller, 1984; Wang and Itoh, 2001]:

$$1/\varepsilon' - 1/\varepsilon'_{max} = (T - T_{\varepsilon'max})^{\gamma} / C_1 \tag{7.3}$$

with an effective exponent γ that reflects the diffuseness of the permittivity peak, ranging from $1 < \gamma < 2$. The limit values $\gamma=1$ and $\gamma=2$ reduce the expression to the Curie-Weiss law type, which is valid for the case of classic ferroelectrics, and to the quadratic dependence, which is indicative of a typical relaxor, respectively.

Thus, $\varepsilon'(T)$ data on the high temperature side of $T_{\varepsilon'max}$ at 10kHz were recalculated to $1/\varepsilon'-1/\varepsilon'_{max}$, plotted in a log-log scale *vs* $T-T_{\varepsilon'max}$ and fitted with Eq.7.3, as demonstrated in Figure 7.16 to get the values of an effective exponent γ (the slope of the straight line), presented in Table 7.1. For these fittings, ε'_{max} and $T_{\varepsilon'max}$ values, shown in Figure 7.14 and in Table 7.1 as well, were used.

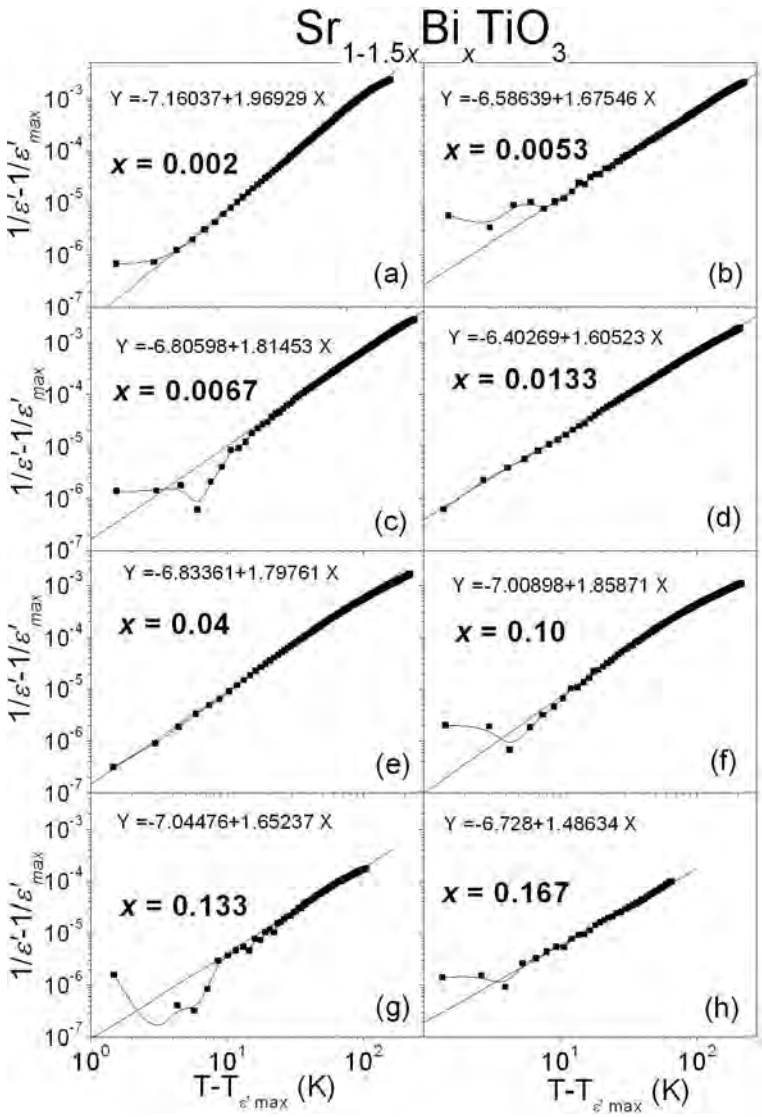

FIGURE 7.16. Plots of $1/\varepsilon'-1/\varepsilon'_{max}$ at 10kHz *vs* $T-T_{\varepsilon'max}$ in logarithmic scale (*solid squares*) and fits to the Eq.7.3 (*solid lines*) for $Sr_{1-1.5x}Bi_xTiO_3$ films with x=0.002 (a), 0.0053 (b), 0.0067 (c), 0.0133 (d), 0.04 (e), 0.10 (f), 0.133 (g) and 0.167 (h).

TABLE 7.1. Effective exponent γ, maximum real part of the dielectric permittivity ε'_{max}, its temperature $T_{\varepsilon'max}$ deduced from $\varepsilon'(T)$ of $Sr_{1-1.5x}Bi_xTiO_3$ films at 10kHz.

x	0.002	0.0053	0.067	0.0133	0.04	0.10	0.133	0.167
γ	1.96	1.68	1.81	1.60	1.79	1.85	1.65	1.48
ε'_{max}	~473	~371	~376	~426	~487	~423	~384	~456
$T_{\varepsilon'max}$, K	~77	~73	~63	~68	~73	~93	~199	~245

The best fitting was obtained for $Sr_{1-1.5x}Bi_xTiO_3$ films with the smallest Bi concentration of x=0.002 and the highest calculated effective exponent $\gamma \approx 1.96$. For $0.0053 \leq x \leq 0.133$, the effective exponent γ lie in the range 1.6-1.85. Finally, the highest Bi concentration x=0.167 reveals the lowest $\gamma \approx 1.48$. Due to the observed approximation of γ to the value of 2, $Sr_{1-1.5x}Bi_xTiO_3$ films with $x \leq 0.133$ can be regarded as system with relaxor like behaviour, similarly to equivalent $Sr_{1-1.5x}Bi_xTiO_3$ ceramics with γ varied from 1.39 to 1.94 [Yu, 1997].

7.5.2. Frequency dependence and relaxation dynamics

The analysis of the frequency influence on the real part $\varepsilon'(T)$ and imaginary part $\varepsilon''(T)$ of the dielectric permittivity and the examination of the temperature dependence of relaxation times is helpful in understanding the relaxation mechanism of $Sr_{1-1.5x}Bi_xTiO_3$ films. The frequency dispersion of the dielectric response of SBiT films with x=0.002, 0.0053, 0.0067, 0.0133, 0.04, 0.10, 0.133 and 0.167 is shown in Figure 7.17, which present $\varepsilon'(T)$ at 100Hz, 1kHz, 10kHz, 100kHz and 1MHz (*left picture*) and $\varepsilon''(T)$ at 1kHz, 10kHz and 100kHz (*right picture*).

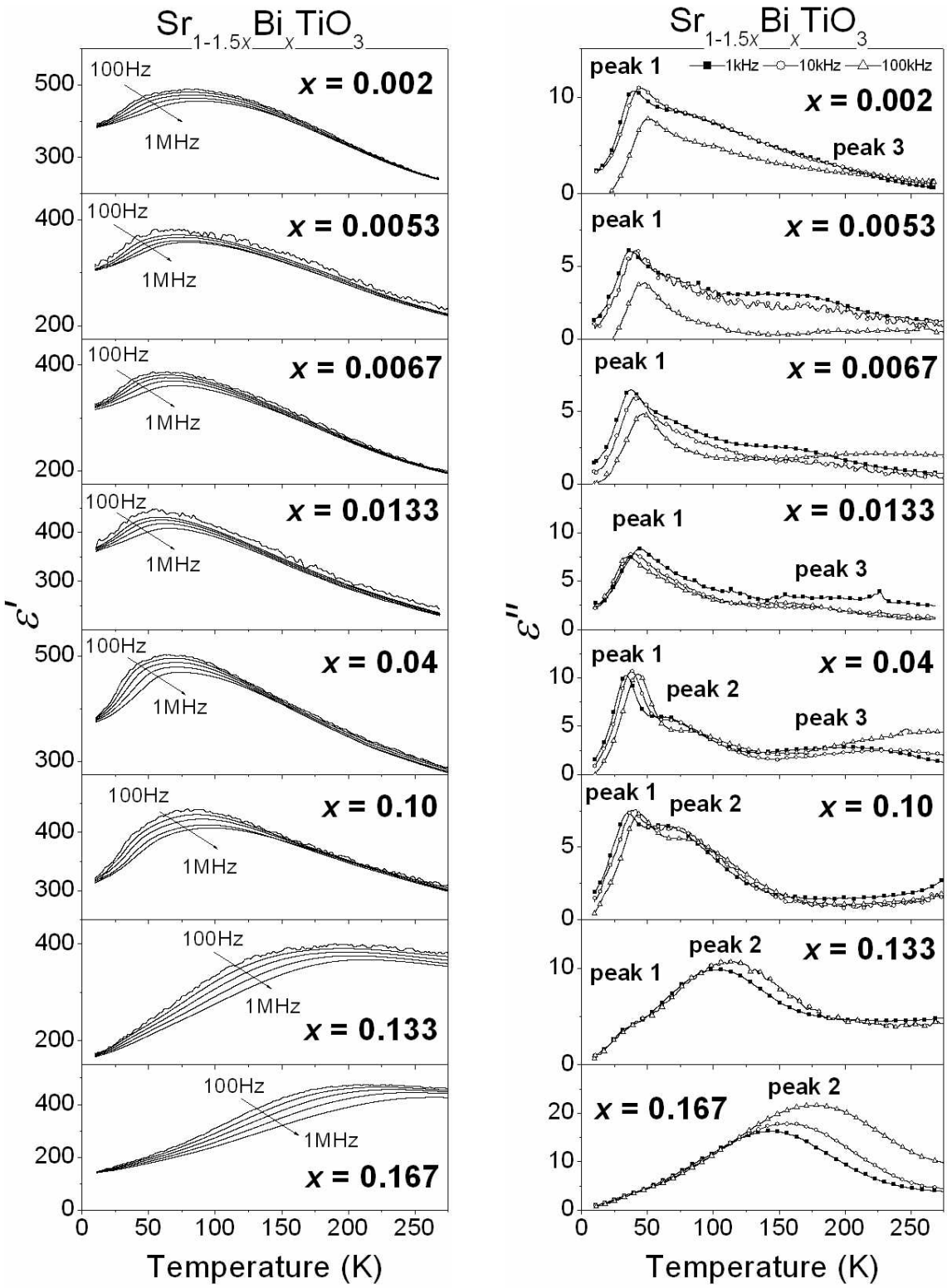

FIGURE 7.17. Temperature dependence of real part of dielectric permittivity ε' at 100Hz, 1kHz, 10kHz, 100kHz, 1MHz (*left picture*) and imaginary part of dielectric permittivity ε'' at 1kHz, 10kHz, 100kHz (*right picture*) of $Sr_{1-1.5x}Bi_xTiO_3$ films with x=0.002, 0.0053, 0.0067, 0.0133, 0.04, 0.10, 0.133 and 0.167.

A peak is present in all the $\varepsilon'(T)$ curves of analyzed SBiT samples at all frequencies (Fig.7.17 *left picture*). As the frequency increases the peak becomes broader, the ε'_{max} decreases and the temperature of the maximum $T_{\varepsilon'max}$ increases. Shift of $T_{\varepsilon'max}$ to higher temperatures suppression of ε'_{max} with frequency increase become more obvious with increaseng Bi concentration (Fig.7.17 *left picture*). Such diffusing and frequency dependency of $\varepsilon'(T)$, that becomes more and more visible with increasing Bi content, was also observed in $Sr_{1-1.5x}Bi_xTiO_3$ ceramics [Yu, 1997; Ang et *al.*, 1998]. Meanwhile, $T_{\varepsilon'max}$ is always higher than the temperature of the loss peak at equivalent frequency. $\varepsilon''(T)$ of SBiT films was also found as frequency dependent (Fig.7.17 *right picture*) and the increasing of the temperature position of the peaks in the $\varepsilon''(T)$ with measured frequency indicates that the microscopic process of the dielectric anomaly is a thermally activated polar motion.

In a dielectric material, if the dielectric relaxation process is governed by a thermally activated motion, the temperature dependence of the relaxation time follows the Arrhenius law:

$$\tau = \tau_0 \exp(U/k_B T) \tag{7.4}$$

where τ_0 stands for the pre-exponential term, U for activation energy, T for temperature and k_B for the Boltzmann constant.

So, Arrhenius law was used for analysis of the Bi induced relaxation processes of all SBiT thin films. However, only data points related to peak 1 in $\varepsilon''(T)$ of SBiT thin films with $0.002 \leq x \leq 0.10$ are well fitted by the straight lines on the Arrhenius plots ($\ln(\tau)$ versus $1000/T_{\varepsilon''max}$), as shown in Figure 7.18. In the case of peak 2, well detectable in $\varepsilon''(T)$ of SBiT films with $x \geq 0.04$, the pre-exponential term τ_0 appears to be extremely low: for example $\tau_0=3.3\times10^{-18}$s for x=0.133 that is close to the electronic reciprocal collision time and seem to be physically unreasonable. Therefore, the data for such compositions were fitted using an alternative empirical description of relaxation, that is, the Vögel-Fulcher relation:

$$\tau = \tau_0 \exp[U/(T_{\varepsilon''max}-T_f)] \tag{7.5}$$

where T_f stands for the freezing temperature at which the relaxation time τ tends to infinity and $T_{\varepsilon''max}$ for the temperature at which maximum of ε'' occurs at the angular frequency $\omega=2\pi f$; $\tau=\omega^{-1}$ [Viehland et *al.*, 1990]. Compared to Arrhenius law, the empirical Vögel-

Fulcher relation (Eq.7.5) includes one additional fitting parameter T_f, interpreted as a static freezing temperature, at which motion of all dipole moments slows down, and is often used to describe the behaviour of relaxor polar clusters or strongly correlated dipoles in the frequency window of 10^2-10^6Hz. Thus, plots of the logarithm of τ *vs* $1000/T_{\varepsilon''max}$ for the loss peak 2 of $Sr_{1-1.5x}Bi_xTiO_3$ with $x \geq 0.04$ are presented in Figure 7.19 together with fittings to Vögel-Fulcher relation.

The fitting parameters of the Arrhenius law for peak 1 and of the Vögel-Fulcher relation for peak 2, obtained for the SBiT samples, are presented in Table 7.2.

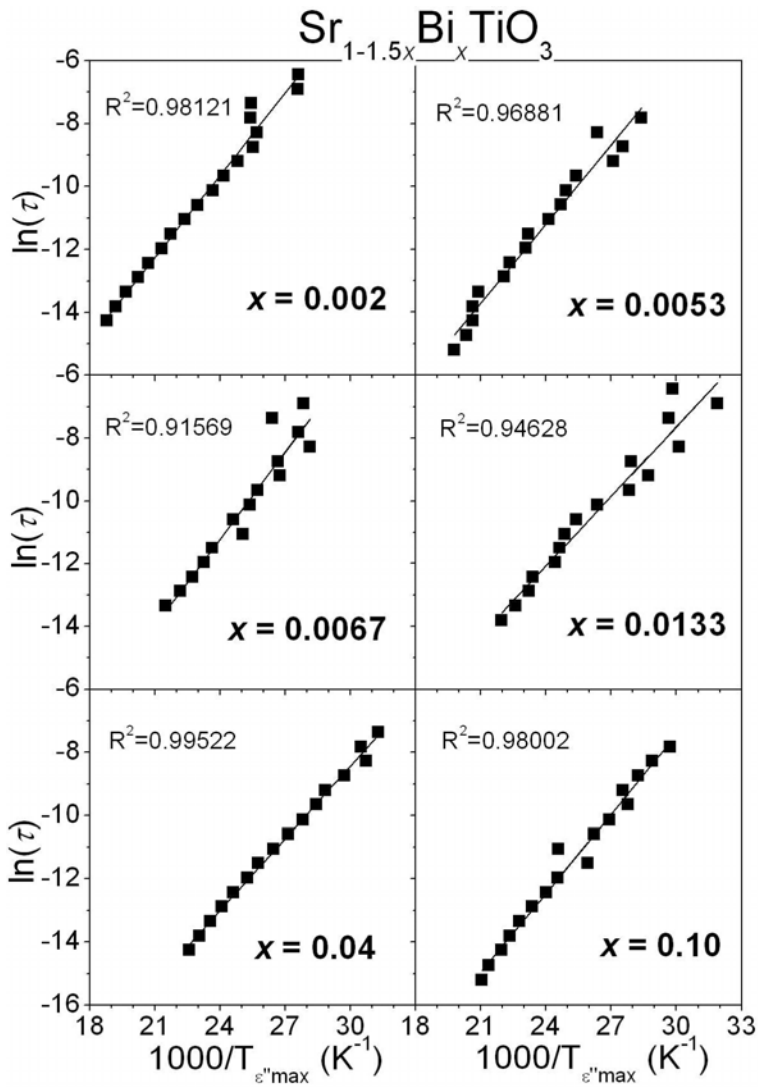

FIGURE 7.18. $\ln(\tau)$ versus $1000/T_{\varepsilon''max}$ ($T_{\varepsilon''max}$ is the temperature at which maximum of ε'' occurs at the angular frequency $\omega=2\pi f$; $\tau=\omega^{-1}$) for the peak 1 in $\varepsilon''(T)$ of $Sr_{1-1.5x}Bi_xTiO_3$ films with $x \leq 0.10$ (symbols correspond to the experimental data, the solid line to the fitting to the Arrhenius law). Correlation coefficients R^2 for obtained fits of $Sr_{1-1.5x}Bi_xTiO_3$ films presented inside the Figure.

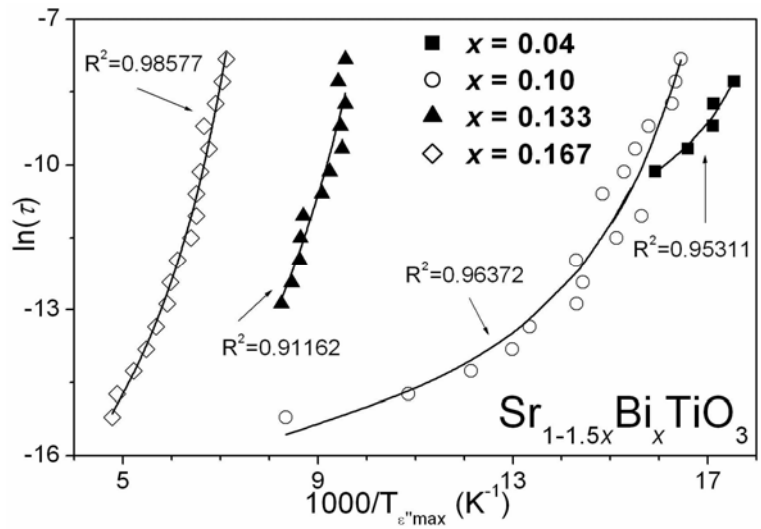

FIGURE 7.19. Plots ln(τ) versus 1000/$T_{\varepsilon''max}$ ($T_{\varepsilon''max}$ is the temperature at which maximum of ε'' occurs at the angular frequency $\omega=2\pi f$; $\tau=\omega^{-1}$) for the peak 2 in $\varepsilon''(T)$ of $Sr_{1-1.5x}Bi_xTiO_3$ films with $x \geq 0.04$ (symbols: the experimental data, the solid line: the fitting to the Vögel-Fulcher relation). Correlation coefficients R^2 for obtained fits of $Sr_{1-1.5x}Bi_xTiO_3$ films presented inside the Figure.

TABLE 7.2. Positions of peak 1 and peak 2 detected in the $\varepsilon''(T)$ of $Sr_{1-1.5x}Bi_xTiO_3$ films at 10kHz and their relaxation dynamics parameters, obtained for peak 1 from the fitting to Arrhenius law and for peak 2 from the fitting to Vögel-Fulcher relation.

x	Peak 1			Peak 2			
	$T_{\varepsilon''max}$ at 10kHz, K	***Arrhenius Law***		$T_{\varepsilon''max}$ at 10kHz, K	***Vogel-Fulcher Relation***		
		U, meV	τ_0, *s*		***U, meV***	τ_0, *s*	T_f, *K*
0.002	44.8	75	5.6×10^{-14}				
0.0053	41.7	74	1.3×10^{-14}				
0.0067	40.1	80	0.3×10^{-14}				
0.0133	40.2	64	10.8×10^{-14}				
0.04	38.6	65	2.5×10^{-14}	62.3	2	5×10^{-6}	50
0.10	37.8	74	0.4×10^{-14}	72.3	7	5×10^{-8}	51
0.133				114.8	36	5×10^{-10}	71
0.167				159.0	38	4×10^{-9}	102

As seen from Table 7.2 for $Sr_{1-1.5x}Bi_xTiO_3$ films with small Bi content $0.002 \leq x \leq 0.10$, Arrhenius law parameters U=64-80meV and τ_0=(0.3-10.8)$\times10^{-14}$s are obtained for peak 1 detected in $\varepsilon''(T)$ at such low temperatures as 38K-44K. Arrhenius law parameters U=60–64meV and τ_0=(4−10)$\times10^{-14}$s were obtained in SBiT ceramics as well, for peak,

observed about 30 K in $\varepsilon''(T)$ independently on Bi content [Ang and Yu, 2002]. By analogy and due to the similarities in the behaviour, it is possible to assume that peak 1 in SBiT films has a similar nature to that of the relaxation peak at ~30K observed in SBiT ceramics. Thus, individual polar dipoles formed by off-centre dopant ions, proposed as a relaxation mechanism in SBiT ceramics, can be attributed for peak 1 detected in $\varepsilon''(T)$ of SBiT films with $0.002 \leq x \leq 0.10$.

As seen from Figures 7.18 and 7.19, the relaxation dynamics of the loss peaks in SBiT films with x=0.04 and x=0.10 follows both Arrhenius law for peak 1 and Vögel-Fulcher relation for peak 2 with U, τ_0, T_f shown in Table 7.2. For SBiT films with higher Bi concentration (x>0.10), only peak 2 is well detected in $\varepsilon''(T)$ and only Vögel-Fulcher relation that describes a polar cluster relaxation can be applied. The switching of relaxation dynamics from Arrhenius law to Vögel-Fulcher relation implies a crossover from hopping of individual off-centre Bi^{3+} ions to polar clusters reversal dominant mechanism in SBiT films with increasing Bi content.

As Bi concentration increases, the average distance between Bi dipoles decreases and the interaction between the dipoles appears. Therefore, some dipoles form dipole clusters due to the local inhomogeneous distribution of Bi ions, and this leads to the occurrence of the peak 2 and it shift to higher temperatures with increasing Bi content. The coexistence of the individual dipoles that contribute to the peak 1 and the dipole clusters that contribute to the peak 2 is a singular characteristic of Bi doped ST. With further increasing Bi concentration (SBiT films with x>0.10), the interaction between the dipoles becomes much stronger, and more dipole clusters are formed. It results in an increase in the intensity of peak 2 and a decrease in the intensities of peak 1 (Fig.7.12). Finally, at a high Bi doping level, all dipoles form dipole clusters, and only a relaxation peak 2 remains. Simultaneously the freezing temperature T_f increases with Bi content from T_f=50K for x=0.04 to T_f=102K for x=0.167.

For SBiT ceramics with x=0.04, T_f was reported to be about 70K-74K [Yu, 1997; Ang and Yu, 2000d] that is close to T_f obtained for equivalent films. Moreover, the increase of T_f with Bi content is observed both in ceramics (T_f=91K, 104K, and 112K for x=0.10, 0.133, 0.167, respectively) [Yu, 1997], and films (T_f =51K, 74K, 102K obtained in current work for SBiT films with x=0.10, 0.133, 0.167, respectively), as shown in Table 7.2.

Other parameters of Vögel-Fulcher relation are found to be similar as well: U=2-38meV and τ_0=5×10^{-10}-5×10^{-6}s for SBiT films with x=0.04-0.167 are comparable to U=31-39meV and τ_0=(2.21-5.26)×10^{-9}s for corresponding SBiT ceramics with x=0.04-0.167 [Yu, 1997].

Thus, after low-frequency analysis of dielectric response of SBiT films, according to the proximity between the relaxation parameters obtained by Arrhenius law and by Vögel-Fulcher relation for films and ceramics samples, it is possible to summarize that incorporation of Bi in ST films leads to similar effect as that observed for SBiT ceramics:

- in SBiT films with small Bi doping (x<0.04), dynamics of the induced relaxation (peak 1 detected in $\varepsilon''(T)$) was described by Arrhenius law, similarly to SBiT ceramics, and assigned to individual hopping of the Bi ions;
- with increasing Bi concentration ($0.04 \leq x \leq 0.167$), the interactions between the dipoles or dipole clusters become stronger. It can be considered as a cooperative hopping of the off-centred Bi ions followed by the highly polarisable host crystal lattice and corresponds to relaxation peak 2 detected in $\varepsilon''(T)$ of analyzed SBiT films with dynamics described by Vögel-Fulcher relation.

Thus, the main typical features, characterizing SBiT ceramics as system with relaxor like behaviour, were also observed in $Sr_{1-1.5x}Bi_xTiO_3$ films:

1) a rounded peaks in the temperature dependence of ε' (Fig.7.11), in contrast to the sharp peak at the phase transition temperature observed for the classic ferroelectrics;
2) temperature of the ε' peak always higher than the temperature of the loss peak (Figs.7.11, 7.12 and 7.13);
3) temperature dependence of the dielectric constant obeying to relation: $1/\varepsilon'-1/\varepsilon'_m=(T-T_m)^{\gamma}/C$, with exponent γ close to 2 [Smolenskii, 1970], but not to 1 as for the classic ferroelectrics with the $\varepsilon'(T)$ following the Curie-Weiss law (Fig.7.16);
4) a frequency dispersion of ε' around the ε' peaks in the *rf* range and a long relaxation time, while the properties of classic ferroelectrics do not vary intensely with the frequency in the radio frequency range:
   a) maximum of the ε' (ε'_{max}) decreases in value and its temperature shifts to higher temperatures with increasing measurement frequency (Fig.7.17a);
   b) maximum of the tanδ (as well as ε'') increases in value and its temperature shifts to higher temperatures with increasing measurement frequency (Fig.7.17b);
5) a compliance with a Vögel-Fulcher relation (Fig.7.18), *etc*.

7.5.3. *dc* field effect and dielectric tunability

The influence of applied *dc* electric field on the dielectric response of $Sr_{1-1.5x}Bi_xTiO_3$ films was studied, according to the measurements description, done in the "Chapter 3". Figure 7.20 depicts the temperature dependence of the real part of dielectric permittivity ε' of $Sr_{1-1.5x}Bi_xTiO_3$ films (with x=0, 0.002, 0.0053, 0.0133, 0.04, 0.10, 0.133, 0.167) measured under 0, 50 and 100kV/cm *dc* bias fields at 10kHz.

As the applied *dc* electric field increases, ε' of Bi doped ST samples decreases similarly to undoped ST films. Maximum decrease of ε' is observed around the peak temperature. The highest influence of *dc* bias field on ε' is observed for SBiT films with $0.002 \leq x \leq 0.04$.

Meanwhile, *dc* electric field was reported to suppress significantly the peak in $\varepsilon'(T)$ of SBiT ceramics with x=0.002, 0.0033 and 0.0067, induced by Bi incorporation [Ang and Yu, 2002; Yu, 1997].

The relative tunability of Bi doped ST thin films was calculated by the formula:

$$n_r = [\varepsilon'(E_{dc}=0) - \varepsilon'(E_{dc})] / \varepsilon'(E_{dc}=0) \times 100\% \qquad (7.6)$$

where $\varepsilon'(E_{dc}=0)$ stands for the real part of dielectric permittivity at zero bias and $\varepsilon'(E_{dc})$ for the real part of dielectric permittivity at the applied *dc* electric field.

The electric-field dependences of ε', $\tan\delta$ and n_r of $Sr_{1-1.5x}Bi_xTiO_3$ films (x=0.002, 0.0133, 0.04, 0.167) in *dc* field range ±150kV/cm measured at 10kHz are presented in Figure 7.21 for selected temperatures.

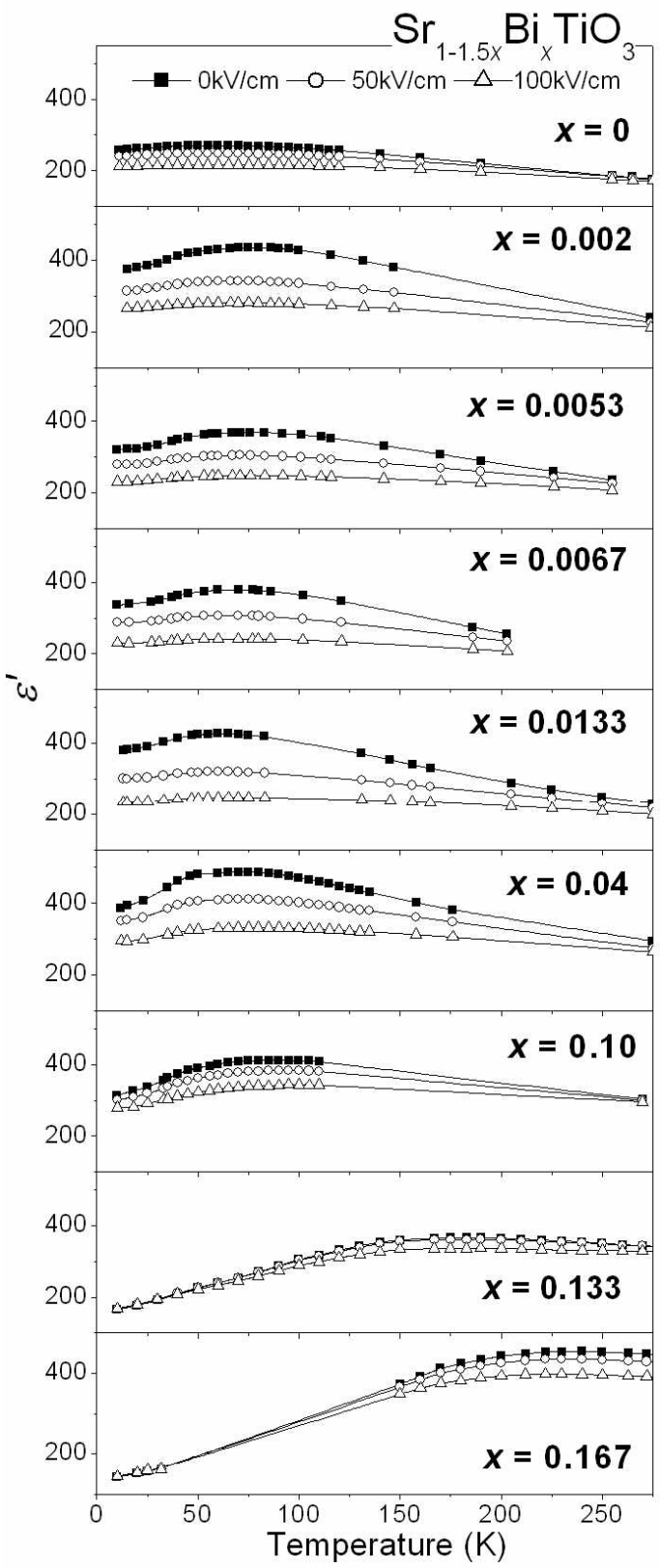

FIGURE 7.20. Variation of real part of the dielectric permittivity ε' of $Sr_{1-1.5x}Bi_xTiO_3$ thin films as a function of temperature under selected *dc* bias fields at 10kHz.

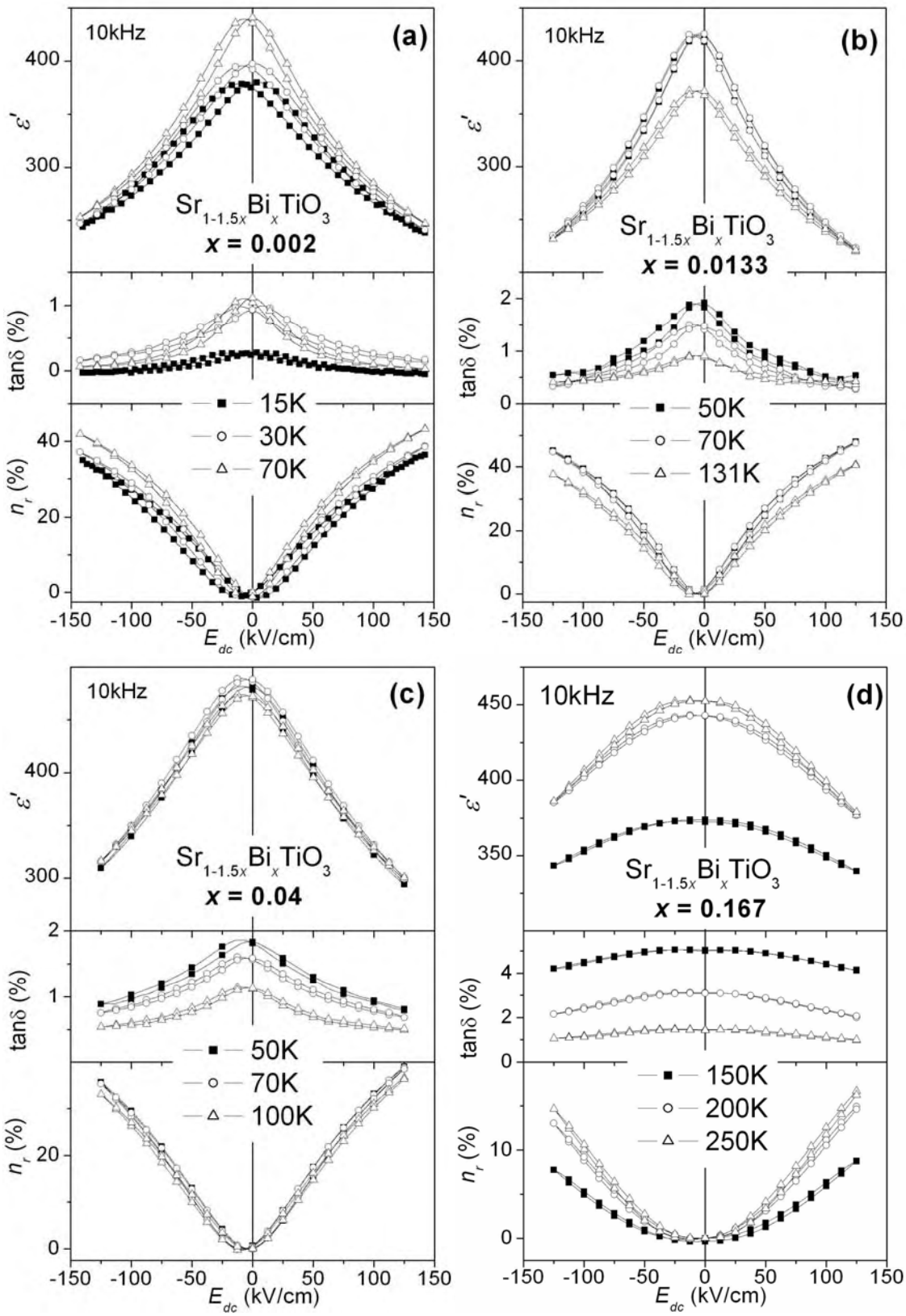

FIGURE 7.21. Variation of real part of the dielectric permittivity ε' (*top panel*), tanδ (*middle panel*) and relative tunability n_r (*bottom panel*) of $Sr_{1-1.5x}Bi_xTiO_3$ thin films with x=0.002 (a), 0.0133 (b), 0.04 (c) and 0.167 (d) as a function of *dc* electric field at 10kHz .

It is seen from Figure 7.21, that with increasing Bi concentration $\varepsilon'(E_{dc})$, $\tan\delta(E_{dc})$ and $n_r(E_{dc})$ dependences are strongly decreased and their bell-like shape changes from *narrow* for SBiT films with x=0.002 (Fig.7.21a) to a *round* shape for x=0.167 (Fig.7.21d).

The well developed loop in $\varepsilon'(E_{dc})$, $\tan\delta(E_{dc})$ and $n_r(E_{dc})$, found for SBiT films with x=0.002 (Fig.7.21a), suggests the presence of a polar phase. However, the loops in $\varepsilon'(E_{dc})$, $\tan\delta(E_{dc})$ and $n_r(E_{dc})$ become thinner for x=0.0133 (Fig.7.21b) and x=0.04 (Fig.7.21c) and disappear completely for x= 0.167 (Fig.7.21d).

Temperature dependence of the relative dielectric tunability n_r at 10kHz and 100kV/cm of Bi-doped ST films is presented in Figure 7.22 together with the values of undoped ST films annealed at 750°C from the "Chapter 4".

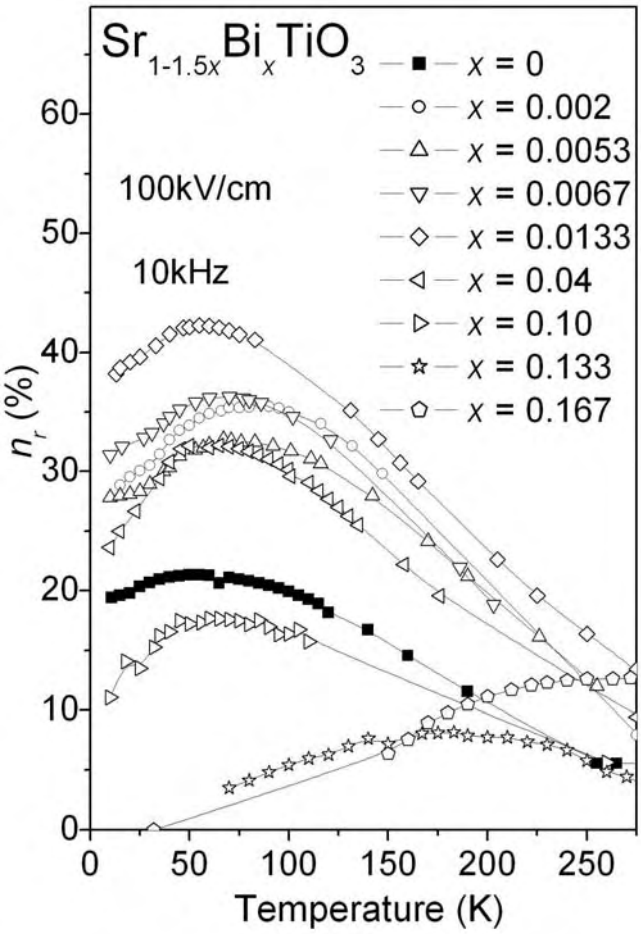

FIGURE 7.22. Temperature variation of the relative tunability n_r of $Sr_{1-1.5x}Bi_xTiO_3$ thin films.

All SBiT films present broad peak in $n_r(T)$ similar to that in $n_r(T)$ of undoped ST. This peak shifts with increasing Bi content similarly to that in $\varepsilon'(T)$. Tunability of SBiT films

with x<0.10 is higher than that for undoped ST films (~21% in the maximum at ~55K) in all temperature range and shows a maximum value ~42% at ~55K for SBiT films with x=0.0133. Other samples with $0.002 \leq x \leq 0.04$ present following values of n_r in the maximum: ~36% at ~86K for x=0.002, ~36% at ~70K for x=0.0067, ~33% at ~67K for x=0.0053, ~33% at ~65K for x=0.04. With further increase of Bi concentration (x>0.04), n_r is smaller than those of undoped ST and SBiT films with small Bi content and the maximum of these n_r strongly shifts to high temperature: ~18% at ~60K for x=0.10, ~8% at ~183K for x=0.133 and ~13% at ~272K for x=0.167.

To characterise these films in terms of possible practical tunable applications the communication quality factor was calculates, based on the following equation [Vendik, 1999b]:

$$K = \frac{(n-1)^2}{n \times \tan\delta(0) \times \tan\delta(E_{max})} \tag{7.7}$$

where n stands for the tunability and can be calculated as $n=\varepsilon'(0)/\varepsilon'(E_{max})$.

K values of $Sr_{1-1.5x}Bi_xTiO_3$ thin films were calculated by Eq.7.7 using data of $\varepsilon'(E)$ and $\tan\delta(E)$ at applied *dc*-field 100kV/cm and 10kHz and are presented in Figure 7.23 as a function of the temperature.

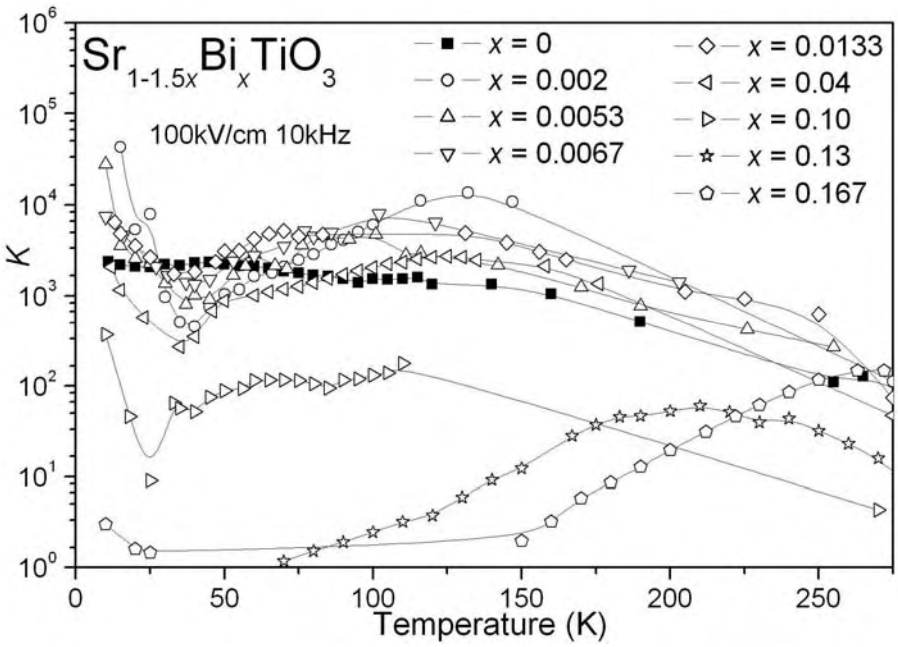

FIGURE 7.23. Temperature variation of communication quality factor K of $Sr_{1-1.5x}Bi_xTiO_3$ films.

It is obvious, that SBiT films with low Bi content $0.002 \leq x \leq 0.04$ show higher K than that of undoped ST from 50-100K to room temperature. At the same time SBiT films with high Bi content x>0.04 present K values lower than that of undoped ST in all temperature range due to decrease of tunability and increase of tanδ.

As claimed by Vendik et *al*., the tunable component with K>2000 is suitable for practical application [Vendik et *al*., 1999b]. Thus, the analyzed polycrystalline $Sr_{1-1.5x}Bi_xTiO_3$ films with $x \leq 0.0133$ are appropriate candidates for tunable application.

7.5.4. *P(E)* hysteresis response

The polar nature of the dielectric anomaly observed in $Sr_{1-1.5x}Bi_xTiO_3$ films with x=0.002, 0.04 and 0.10 was further studied by the measurement of the $P(E)$ curves, shown in Figures 7.24-7.26. Hysteresis response of SBiT films was measured at 100Hz under applied *ac* voltage up to ~5V at different temperatures according to the description of the "Chapter 3". From these curves the remnant polarisation P_r and coercive field E_c were derived and compared in Figure 7.27.

Figure 7.24 displays $P(E)$ curves of SBiT films with x=0.002 at selected temperatures from 15 to 295K. Well developed *s*-shaped loops with non-zero remnant polarization P_r suggest the appearance of a polar state in agreement with the $\varepsilon'(E_{dc})$ hysteresis loops observed for this sample (Fig.7.24a). The loop area as well as P_r and E_c decrease with increasing temperature (Fig.7.24). The highest hysteretic response with P_r=~0.73μC/cm^2 and E_c=~15.7kV/cm is detected in SBiT film with x=0.002.

Similarly to SBiT films with x=0.002, *s*-shaped loops were observed in the films with x=0.04 (Fig.7.25). However, for this concentration (x=0.04) the curves are much slimmer than for x=0.002. The highest remnant polarisation and coercive field are P_r=~0.40μC/cm^2 and E_c=~12.7kV/cm at 15K (Fig.7.25a), decreasing with increasing temperature as well (Fig.7.25b-f).

Figure 7.26 depicts the *P(E)* hysteresis loops of SBiT films with x=0.10. In contrast to the previous SBiT films the loops are very slim without visible *s*-shape. P_r and E_c values decrease from P_r=~0.20μC/cm^2 and E_c=~6.1kV/cm at 15K toward zero at room temperature as well (Fig.7.26).

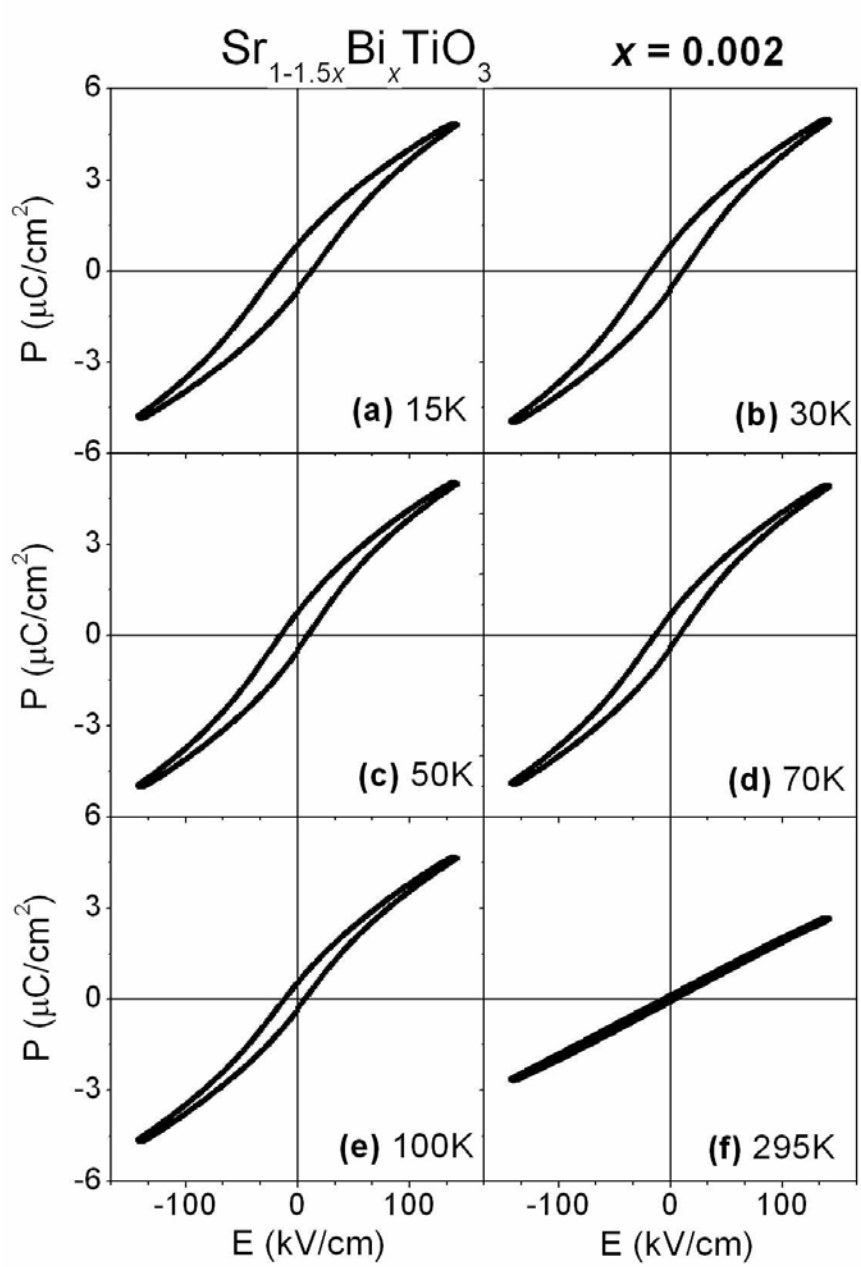

FIGURE 7.24. Hysteresis loops *P(E)* of $Sr_{1-1.5x}Bi_xTiO_3$ thin films with x=0.002 at 15K (a), 30K (b), 50K (c), 70K (d), 100K (e) and 295K (f) at 100Hz.

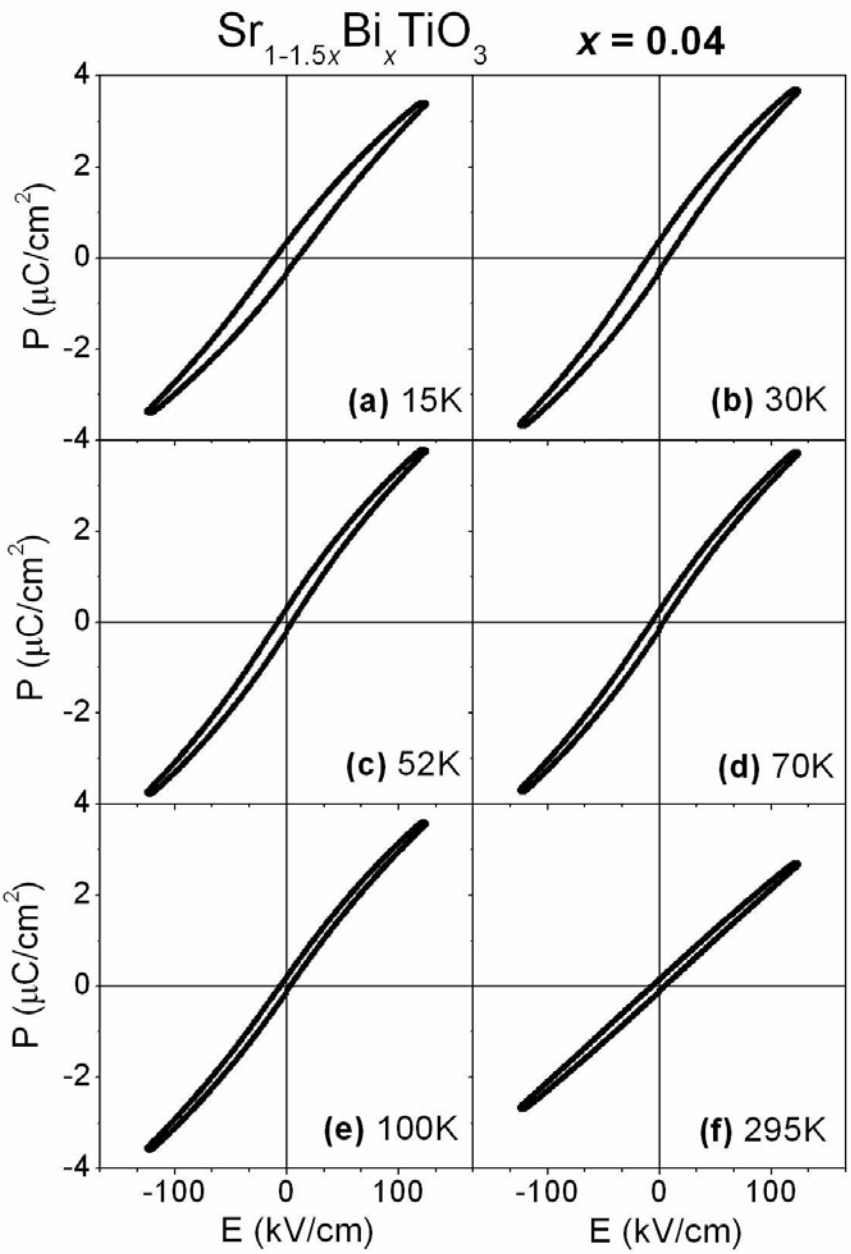

FIGURE 7.25. Hysteresis loops *P(E)* of $Sr_{1-1.5x}Bi_xTiO_3$ thin films with x=0.04 at 15K (a), 30K (b), 52K (c), 70K (d), 100K (e) and 295K (f) at 100Hz.

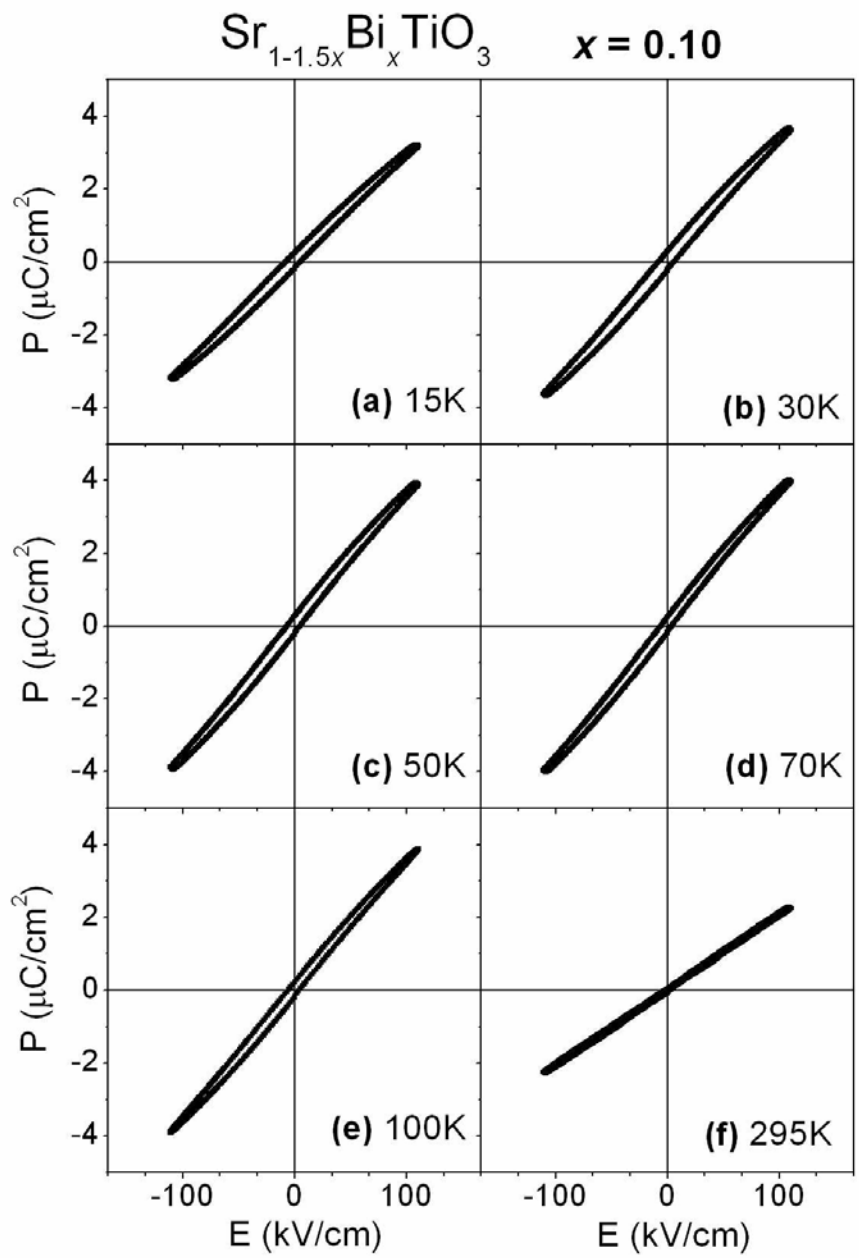

FIGURE 7.26. Hysteresis loops *P(E)* of $Sr_{1-1.5x}Bi_xTiO_3$ thin films with x=0.10 at 15K (a), 30K (b), 50K (c), 70K (d), 100K (e) and 295K (f) at 100Hz.

Figure 7.27a and b presents the detailed evolution of P_r as well as E_c of the studied Bi doped ST films together with undoped ST (data for the film ST 750°C from the "Chapter 4") for comparison. P_r of all studied Bi doped ST films is higher than that of undoped ST. P_r and E_c have the highest values for the lowest Bi content x=0.002 and monotonously decrease for higher dopant contents x=0.04 and x=0.10. At room temperature the polarization *vs* electric field response is linear for all presented films (Figs.7.24f, 7.25f, 7.26f). Smooth decrease of P_r and E_c with increasing temperature, observed for all studied Bi doped ST films is typical for ferroelectric relaxors [Smolenski, 1970].

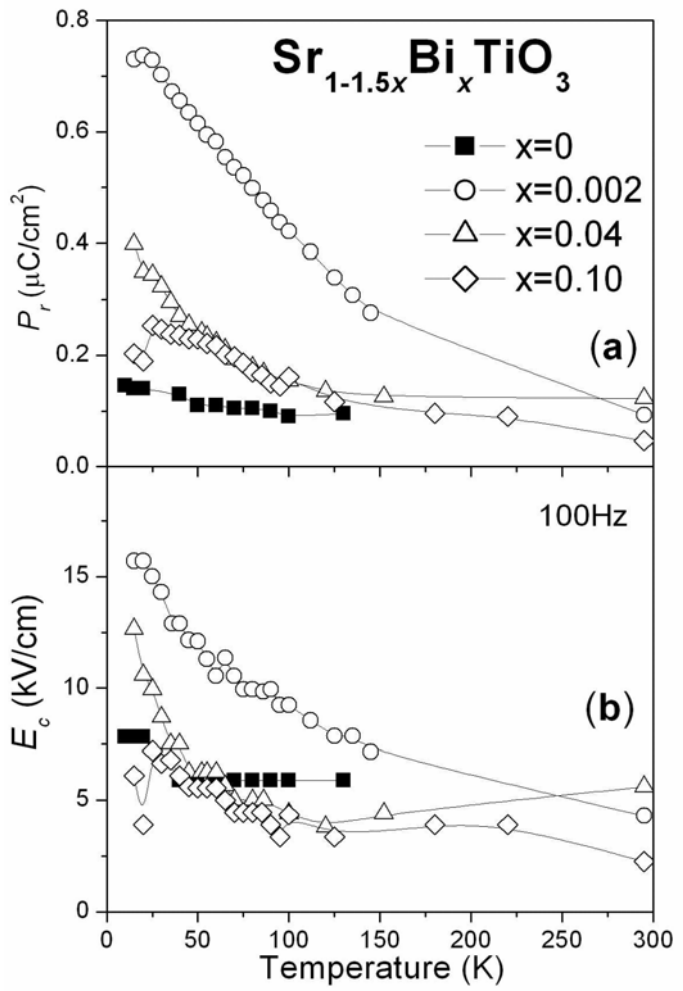

FIGURE 7.27. Remnant polarisation P_r (a) and coercive field E_c (b) of $Sr_{1-1.5x}Bi_xTiO_3$ films with x=0, 0.002, 0.04 and 0.10 as a function of temperature.

For SBiT ceramics, *S*-shape hysteresis loops with remnant polarisation ~0.31μC/cm^2 for x=0.0033, ~0.83μC/cm^2 for x=0.0067 and ~0.47μC/cm^2 for x=0.0133 at 11K and 50Hz were reported [Yu, 1997; Ang et *al.*, 1998]. Similarly to the films of this study, as the Bi

content increases in SBiT ceramics (x=0.0533), a slimmer hysteresis loop with low polarization and without *S*-shape were observed disappearing with the increase of temperature [Yu, 1997; Ang et *al.*, 1998].

Summary

Polycrystalline $Sr_{1-1.5x}Bi_xTiO_3$ films with thickness of ~450nm, roughness less than 2nm and average grain size from ~80nm to ~120nm were prepared by sol-gel on $Si/SiO_2/TiO_2/Pt$ substrates. The solid solubility limit of Bi in ST thin films is x=0.167, as determined by XRD. For higher Bi content $x \geq 0.267$, $Bi_4Ti_3O_{12}$ appears as an extra-phase. Similarly to $Sr_{1-1.5x}Bi_xTiO_3$ ceramics, the lattice parameter of SBiT films was found to increase with increasing Bi content. Expansion of the unit cell is explained by slightly larger ionic size of $Bi^{3+}_{(12)}$ than that of the substituted $Sr^{2+}_{(12)}$ as well as by the formation of V_{Sr} and corresponding electrostatic repulsion of adjacent oxygen anions. Although XRD indicates only a cubic perovskite structure, two forbidden modes TO4 and LO4 were detected in the Raman spectra of SBiT films with small (x=0.0053) and high (x=0.167) Bi content, indicating a lattice distortion. However, similar detection of these modes was reported in undoped ST ceramics and films before. In addition, TO1 and TO2 modes were observed in the analyzed SBiT films by IR spectroscopy. In contrast to softening of TO1 mode observed for SBiT film with x=0.0053, position of TO1 mode in SBiT film with x=0.167 was constant and 2 additional relaxations were detected.

$\varepsilon'(T)$ of all $Sr_{1-1.5x}Bi_xTiO_3$ films revealed a strong rounded peak in the low frequency range. Moreover, strong frequency dispersion occurs and ε'_{max} significantly decreases and shifts to the high temperature region with increasing frequency. Two peaks were induced in $\varepsilon''(T)$ below the temperature of the peak in $\varepsilon'(T)$ by Bi doping of ST films. Peak 1 was well observed at ~38K-44K in $Sr_{1-1.5x}Bi_xTiO_3$ films with $0.002 \leq x \leq 0.10$ independently on Bi content, whereas peak 2 was well seen from ~60K for films with x=0.04 to ~160K for x=0.167. All loss peaks of $Sr_{1-1.5x}Bi_xTiO_3$ films are frequency dependent. The relaxation peak 1 follows Arrhenius law with activation energy U=64-80meV and pre-exponential term τ_0=(0.3-10.8)×10^{-14}s and is ascribed to reorientation of dipoles created by the off-centre Bi ions (individual hopping of the Bi ions). The relaxation peak 2 described by Vögel-Fulcher relation with U=2-38meV, τ_0=5×10^{-10}-5×10^{-6}s and freezing temperature

T_f =50-102K and attributed to the clusters of Bi ions, which interact with each other via the highly polarisable host crystal lattice. Additionally, the oxygen-vacancy related relaxation peak 3 was found to contribute to the dielectric loss of SBiT films around 200K. Furthermore, slim hysteresis loops of relaxor type were observed in SBiT films at low temperatures, implying the appearance of a polar state. Thus, it is possible to conclude that effect of Bi incorporation in ST films is qualitatively the same to the relaxor-like behaviour observed for Bi doped ST ceramics, differing only in details like:

- observation of only peak 1 independent on Bi content in $\varepsilon''(T)$ of SBiT films compared to several peaks, detected at low temperatures in $\varepsilon''(T)$ of SBiT ceramics;
- detection of the relaxation peak 2 with temperature increasing with Bi content in $\varepsilon''(T)$ SBiT films only for $x \geq 0.04$, whereas in SBiT ceramics such peak was found for $x \geq 0.0067$.

Such differences can be first of all related to the presence of high substrate influence on the film, for example, it induces strain/stress states that are not present in bulk ceramics. Moreover, high homogeneity of studied films (higher than that in conventionally prepared ceramics) can prevent the segregation of Bi ions, suppressing the interaction between the dipoles created by the off-centre Bi ions for SBiT films with low Bi concentration. These factors could result in the "delay" in the appearance/detection of the relaxation peak 2 in studied films compared to equivalent ceramics. Though, according to the results presented above, $Sr_{1-1.5x}Bi_xTiO_3$ films prepared by sol-gel can be considered as promising material for tunable device application due to the high values of relative tunability and communication quality factor.

Chapter 8. Conclusions

As was shown in the previous Chapters, $SrTiO_3$-based materials attracted a great interest not only from the fundamental but also from the application point of view, particularly for tunable electronic components. Moreover, due to the current trend of miniaturization of the electronic devices and need to increase the packing of the different circuit elements, tunable microwave devices based on ST films are under consideration for industrial applications due to the expected substantial cost reduction when comparing with single crystals. For this particular application, the challenge is the shift of the temperature range of high tunability towards room temperature what can be somehow solved by inducing a dielectric anomaly in ST. Among the possible ways to engineer this response in ST films one may consider the manipulation of the stress level in the film or chemical doping.

This work was a systematic study of undoped and doped strontium titanate based polycrystalline thin films fabricated by sol gel under different processing conditions, and the following conclusions were attained.

8.1. Polycrystalline thin films of undoped $SrTiO_3$: influence of the fabrication procedure and substrate

The main results of the study of the effects of processing parameters (deposition of buffer layers and temperature of the annealing process) on the properties of ST thin films prepared under different conditions: by “one-step” and by “two-steps” on $Si/SiO_2/TiO_2/Pt$ substrates and annealed at 750°C and 900°C can be summarised as following.

The set of samples was prepared according to the “one-step” procedure in which no intermediate heat treatment was done between the deposited layers and the samples were submitted only to one final annealing step at different temperatures: 750°C (these samples are designated as ST 750°C) and 900°C (these samples are designated ST 900°C) during 60min. in air. The other set of samples was prepared according to the “two-steps” procedure, i.e. after the deposition of the two first layers, a first heat treatment at 600°C during 30min. was conducted and, after cooling the films to room temperature 8 layers more were deposited and a final annealing step took place at 750°C (these samples are

designated ST 2l 750°C) and at 900°C (these samples are designated ST 2l 900°C) for 60min. in air.

All analyzed ST films show dense microstructures and relatively smooth surface. According to AFM analysis the grain size increases with annealing temperature (from 80-85nm for $T_{ann.}$=750°C to 125-145nm for $T_{ann.}$=900°C) but decreases for ST films with buffer layers, confirming the observation by SEM. The lowest average roughness equal to ~1nm was found for ST 750°C and ~3.45-3.84nm for all others samples.

According to XRD data all the analyzed samples possess a single ST phase and have no preferable orientation and their spectra are typical for $SrTiO_3$. However, the insertion of buffer layers leads to a high distortion of the ST lattice ($a<c$). It is explained as a in-plane clamping effect between the already annealed buffer layer and the lattice cells of next deposited layers in the samples prepared by the "two-steps" procedure.

The total stress state of the films increases with increasing the annealing treatment temperature from 750°C to 900°C (from ~210MPa to ~256MPa for ST films deposited by "one-step" procedure and from ~1150MPa to ~201MPa for ST films deposited by "two-steps" procedure). The use of the buffer layers decreases the total stress state in the films annealed under identical temperature treatment: from ~210MPa (ST 750°C) to ~115MPa (ST 2l 750°C) and from ~256MPa (ST 900°C) to ~201MPa (ST 2l 900°C). Thermal stress, as one part of the total stress, was calculated for samples annealed at different temperatures and found equal ~2380MPa for films annealed at 750°C (ST 750°C and ST 2l 750°C) and ~2936MPa for ST films annealed at 900°C (ST 900°C and ST 2l 900°C). Thus, in analyzed polycrystalline ST films deposited on the same substrates the thermal stress play a major role than the lattice mismatch strain.

Dielectric properties of ST films prepared with buffer layers and with improved crystallinity exhibit higher values of ε' than samples without buffer layers: ~662 for ST 2l 900°C compare to ~415 for ST 900°C, and ~376 for ST 2l 750°C compared to ~267 for ST 750°C. Moreover, samples with buffer layers present a stronger dependence on the *dc* electric field and, consequently a enhanced tunability when compared to that of the samples prepared without buffer layers: ~54% in the maximum at ~55K for ST 2l 900°C; ~28% in the maximum at ~40K for ST 2l 750°C; ~41% in the maximum at ~30K for ST 900°C and ~21% in the maximum at ~55K for ST 750°C films.

More obvious *s*-shape hysteresis loops in *P(E)* measurements were found for ST films prepared with buffer layers, in accordance with the ameliorated microstructure. And higher annealing temperature leads to an increase of the *s*-form of the hysteresis loop in *P(E)* response.

The buffer layers as in the "two-steps" process, due to its reduced thickness, play a role of seed layers facilitating the nucleation of the crystallites over their growth and the films deposited over these initial layers will mimic this structure and microstructure; at a later stage these films will exhibit a lower grain growth than the films prepared by the "one step" procedure and the final electrical response will be a direct consequence of these features. Thus, inserting buffer layers and annealing at high temperature strongly improves the dielectric response of undoped sol gel based ST thin films.

Figure 8.1 clear represents the difference between ε' of reported before ST films obtained by sol-gel (*stars*) and polycrystalline ST films analyzed in current work (ST 2l 900°C). Improving of dielectric properties of polycrystalline ST films is obvious in all temperature range.

Concerning the role of the substrate (Al_2O_3/Pt, Si/SiO_2/TiO_2/Pt, $(LaAlO_3)_{0.3}$-$(Sr_2AlTaO_6)_{0.7}$/Pt, $SrTiO_3$/Pt and MgO/Pt substrates) all the ST films were polycrystalline independently on the type of the substrate used and present a very close to cubic structure similar to the single crystals one.

As expected, the total stress of the films was markedly dependent on the type of the substrate and it was possible to tailor the film stress from tensile to compressive. ST films deposited on Al_2O_3/Pt, Si/…/Pt and LSAT/Pt substrates were under tensile stresses and under compression when on ST/Pt and MgO/Pt substrates. It was observed that in the case of polycrystalline multilayer films, such as the one studied in the current work, the lattice mismatch between the substrate and the film plays less significant role in the value of total stress when compared to the thermal stress.

The microstructure was similar between all ST films deposited on the different substrates, except for the case of films on MgO/Pt substrate, in which some "slip band dislocations" formed from the MgO substrate through the Pt metal electrode were visualised in the grains of these films.

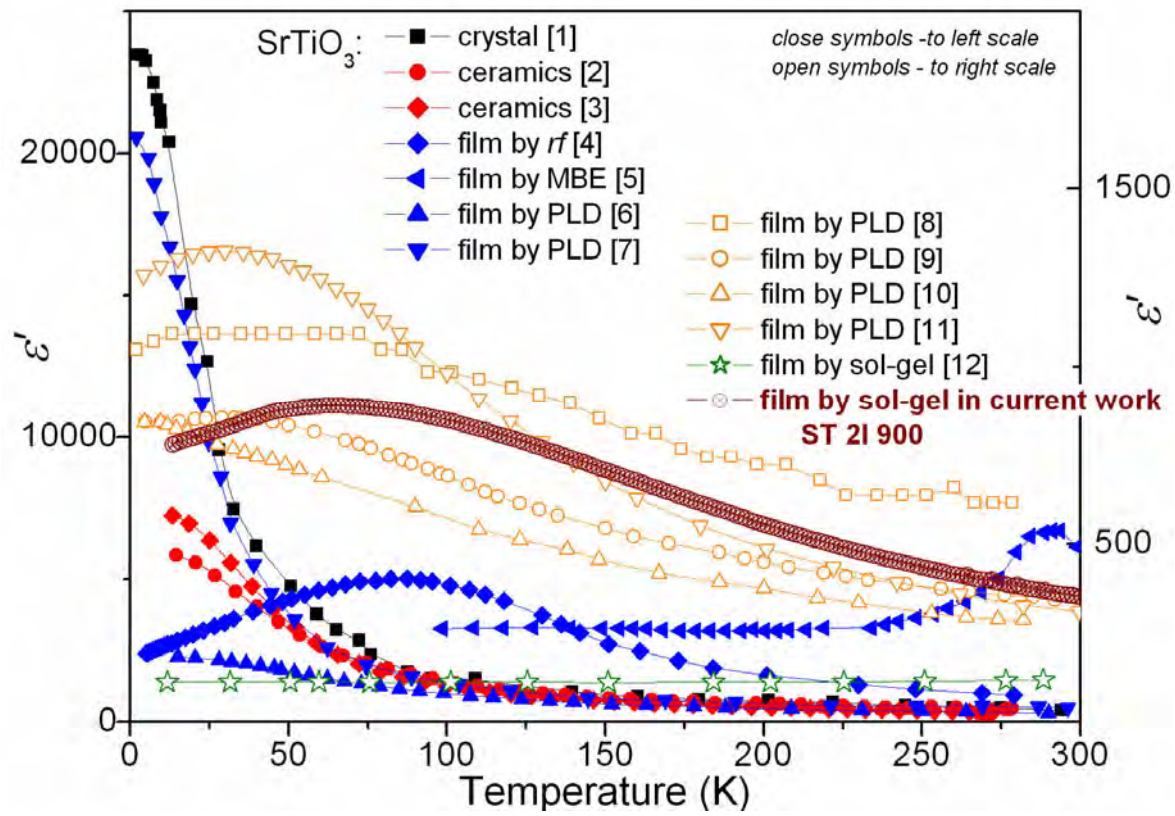

FIGURE 8.1. Temperature dependence of the real part of dielectric permittivity ε' of: [1] $SrTiO_3$ crystal, *parallel-plate capacitor* [Müller and Burkard, 1979]; [2] $SrTiO_3$ ceramics obtained by conventional mixed oxide method, *parallel-plate capacitor* [Tkach et *al.*, 2004a]; [3] $SrTiO_3$ ceramics obtained from solutions prepared by sol-gel, *parallel-plate capacitor* [Tkach et *al.*, 2008] [4] $SrTiO_3$ film deposited by *rf*-sputtering, thickness 300nm, *parallel-plate capacitor* $YBa_2Cu_3O_7/SrTiO_3/YBa_2Cu_3O_7/SrTiO_3$, [Fuchs et *al.*, 1999]; [5] $SrTiO_3$ film deposited by MBE, thickness 500Å, *planar capacitor* $Ag/SrTiO_3/DyScO_3$ [Haeni et. *al.*, 2004]; [6] $SrTiO_3$ film deposited by PLD, thickness 1μm, *parallel-plate capacitor* $Au/SrTiO_3/SrRuO_3/SrTiO_3$ [Ang et *al.*, 2001a]; [7] $SrTiO_3$ film deposited by PLD, thickness 1μm, *parallel-plate capacitor* $YBa_2Cu_3O_7/SrTiO_3/YBa_2Cu_3O_7/SrTiO_3$ [Takashima et *al.*, 2003]; [8] $SrTiO_3$ film deposited by PLD, thickness 320nm, *parallel-plate capacitor* $Pt/SrTiO_3/Ni/Cr/Au/ST+Nb$ [Lippmaa et *al.*, 1999]; [9] $SrTiO_3$ film deposited by PLD, thickness 1.2μm, *parallel-plate capacitor* $Au/SrTiO_3/SrRuO_3/LaAlO_3$ [Li et *al.*, 1998a]; [10] $SrTiO_3$ film deposited by PLD, thickness 350nm, *parallel-plate capacitor* $Au/SrTiO_3/SrRuO_3/LaAlO_3$ [James et *al.*, 2002]; [11] $SrTiO_3$ film deposited by PLD, thickness 800nm, *parallel-plate capacitor* $YBa_2Cu_3O_7/SrTiO_3/YBa_2Cu_3O_7/LaAlO_3$ [Findikoglu et *al.*, 1993]; [12] $SrTiO_3$ film deposited by sol-gel, thickness 1.1μm, *parallel-plate capacitor* $Al/SrTiO_3/Pt/Si$ [Thomas et *al.,* 1997], and $SrTiO_3$ thin films prepared by "two-steps" procedure annealed at 900°C (ST 2l 900°C), deposited by sol-gel, thickness 350nm, *parallel-plate capacitor* $Au/SrTiO_3/Pt/TiO_2/SiO_2/Si$ [analyzed in current Thesis].

Moreover, IR analysis highlighted the differences in the TO1 mode behaviour of ST film deposited on Al_2O_3 (TO1 detected at equal frequency to ST single crystals and ceramics in the range from 300K to 150K) and on MgO (TO1 mode was detected at much higher frequency than that on Al_2O_3 or in bulk ST) related with the different nature and level of stresses in these films.

ST films, deposited on MgO/Pt substrate with the highest compressive stress, have shown the highest value of ε', the highest dependency on *dc*-field and the best *s*-type hysteresis loop (with the highest value of P_r), and the highest value of n_r. In opposite, ST films, deposited on the Al_2O_3/Pt substrate, with the highest tensile stress, shown the lowest value of ε', the lowest dependency on *dc*-films, almost linear behaviour *P(E)* (with the lowest value of P_r), and the lowest value of n_r.

8.2. Effect of Mg incorporation in $SrTiO_3$ thin films

Two series of samples with the nominal compositions $Sr_{1-x}Mg_xTiO_3$ (SMT) (x=0.01, 0.02, 0.05, 0.10, 0.20, 0.30, 0.40) and $SrTi_{1-y}Mg_yO_{3-\delta}$ (STM) (y=0.01, 0.05, 0.10, 0.20, 0.30, 0.40, 0.50) thin films were obtained by sol-gel method and annealed at $T_{ann.}$=750°C-900°C.

The solid solubility of Mg in ST thin films is limited and depends on the lattice site occupancy as observed for identical ceramic compositions. However the solid solubility limit of Mg in ST films (*A* and *B* site) prepared by sol-gel is higher, than in ST ceramics and is dependent on the annealing temperature. According to XRD and TEM results all SMT films ($x \leq 0.30$) and STM ($y \leq 0.40$) annealed at 750°C crystallised with the perovskite phase and are monophasic. However, room temperature Raman study showed some second-order features for SMT films with x=0.30 annealed at 750°C. SMT films annealed at 900°C with Mg concentrations higher than x=0.10 exhibited a Mg second phase, visible by TEM and Raman spectroscopy, and identified as the ilmenite type $MgTiO_3$, and that was not detected by XRD.

The low-temperature ε' and n_r of the analyzed films were not enhanced. Moreover, ε' and n_r were suppressed and more strongly than in the case of $SrTiO_3$-$MgTiO_3$ ceramics, implying the incorporation of Mg into ST lattice.

For STM films annealed at 750°C the shift of the maximum of n_r to low temperatures, from 68K to 25K in opposition to the other studied films, and the shift to low temperatures of the loss peak *C* from 184K to 164K with increasing Mg content, confirms the

substitution of small and highly-polarisable Ti^{4+} ions by big Mg^{2+} ions with the formation of oxygen vacancies as a charge compensation mechanism. Additionally, despite that due to such substitution the low-temperature ε' and n_r were continuously decreased, similarly to the behaviour of equivalent ceramics, the low-temperature dielectric loss could also be considerably decreased by doping with Mg what is of crucial importance for microwave applications.

In analogy to the results obtained for SMT and STM films annealed at 750°C, in SMT films annealed at 900°C Mg doping itself does not induce ferroelectricity or a relaxor-like behaviour in strontium titanate, either introduced in the Sr or Ti site of the ST lattice, in spite of theoretical predictions.

The ε' of SMT films annealed at 900°C is higher than ε' of the films annealed at 750°C, but lower than that of undoped ST prepared under the same conditions, and it decreased with increasing of Mg concentration.

dc-field does not induce any additional peak in $\varepsilon'(E_{dc})$ of SMT and STM films independent on the annealing temperature, and all of the analyzed samples presented lower dependency of ε' and n_r on applied E_{dc} compared to that of undoped ST films.

8.3. Effect of Bi incorporation in $SrTiO_3$ thin films

$Sr_{1-1.5x}Bi_xTiO_3$ (SBiT) thin films with x=0.002, 0.0053, 0.0067, 0.0133, 0.0267, 0.04, 0.1, 0.167 and 0.267 were deposited onto $Si/SiO_2/TiO_2/Pt$ substrates and annealed at 750ºC.

The solid solubility limit of Bi in ST thin films is x=0.167, as determined by XRD. For higher Bi content $x \geq 0.267$, $Bi_4Ti_3O_{12}$ appears as an extra-phase. Similarly to $Sr_{1-1.5x}Bi_xTiO_3$ ceramics, the lattice parameter of SBiT films was found to increase with increasing Bi content. Expansion of the unit cell is explained by the slightly larger ionic size of $Bi^{3+}_{(12)}$ than that of the substituted $Sr^{2+}_{(12)}$ as well as by the formation of strontium vacancies (V_{Sr}) and corresponding electrostatic repulsion of adjacent oxygen anions. Although XRD indicates only a cubic perovskite structure, two forbidden modes TO4 and LO4 were detected in the Raman spectra of SBiT films with small (x=0.0053) and high (x=0.167) Bi content, indicating a lattice distortion. However, similar detection of these modes was reported in undoped ST ceramics and films before. In addition, TO1 and TO2 modes were observed in the analyzed SBiT films by IR spectroscopy. In contrast to

softening of TO1 mode observed for SBiT films with x=0.0053, the position of TO1 mode in SBiT films with x=0.167 was constant and two additional relaxations were detected.

$\varepsilon'(T)$ of all $Sr_{1-1.5x}Bi_xTiO_3$ films revealed a strong rounded peak in the low frequency range. Moreover, a strong frequency dispersion occurs and ε'_{max} significantly decreases and shifts to the high temperature region with increasing frequency. By doping with Bi, two peaks were induced in the $\varepsilon''(T)$ response of ST films that appear below the temperature of the peak in $\varepsilon'(T)$. Peak 1 was well observed at ~38K-44K in $Sr_{1-1.5x}Bi_xTiO_3$ films with $0.002 \leq x \leq 0.10$ independently on Bi content, whereas peak 2 was well seen from ~60K for films with x=0.04 to ~160K for x=0.167. All loss peaks of $Sr_{1-1.5x}Bi_xTiO_3$ films are frequency dependent. The relaxation peak 1 follows the Arrhenius law with an activation energy of U=64-80meV and a pre-exponential term of τ_0=(0.3-10.8)×10^{-14}s and is ascribed to the reorientation of dipoles created by the off-centre Bi ions (individual hopping of the Bi ions). The relaxation peak 2 is described by the Vögel-Fulcher relation with U=2-38meV, τ_0=5×10^{-10}-5×10^{-6}s and a freezing temperature of T_f =50-102K and is attributed to the clusters of Bi ions, which interact with each other via the highly polarisable host ST crystal lattice. Additionally, the oxygen-vacancy related relaxation peak 3 was found to contribute to the dielectric loss of SBiT films around 200K. Furthermore, slim hysteresis loops of the relaxor type were observed in SBiT films at low temperatures, implying the appearance of a polar state. Thus, it is possible to conclude that the effect of Bi incorporation in ST films is generally the same relaxor-like behaviour observed for Bi doped ST ceramics, differing only in the following details:

- observation of only peak 1 independently on the Bi content in $\varepsilon''(T)$ of SBiT films, compared to the several peaks, detected at low temperatures in $\varepsilon''(T)$ of SBiT ceramics;
- detection of the relaxation peak 2 in $\varepsilon''(T)$ SBiT films only for $x \geq 0.04$, whereas in SBiT ceramics such peak was found for $x \geq 0.0067$ (being x the Bi content);

Such differences can be related first of all to the presence the substrate that markedly influences the stress / strain state of films that are not present in the bulk ceramics. In addition, the high chemical homogeneity of the studied films (higher than in the ceramics prepared by the conventional solid state reaction) can prevent the segregation of Bi ions, suppressing the interaction between the dipoles created by the off-centre Bi ions for SBiT films with low Bi concentration. These factors can indeed result in the “delay” in the

appearance/detection of the relaxation peak 2 of the dielectric losses of the films when compared to equivalent ceramics. Though, according to the results presented above, $Sr_{1-1.5x}Bi_xTiO_3$ films prepared by sol-gel can be considered as promising material for tunable device application due to the high values of relative tunability and communication quality factor.

8.4. Suggestions for further work

This Thesis is a systematic but not complete study of the structure, microstructure and dielectric properties in $SrTiO_3$, Mg:$SrTiO_3$ and Bi:$SrTiO_3$ thin films. Interesting physical phenomena were found, and possible physical mechanisms were discussed in these systems.

However, for further practical applications the preparation of ST capacitors of planar geometry and the study of the influence of in-plane lattice strain on their dielectric properties is necessary.

In addition, for a better understanding of the polarisation mechanism in the case of $Sr_{1-1.5x}Bi_xTiO_3$ films, that will allow a further exploitation of practical applications of these materials, the following work should be carried out:

- Experimental evidence of off-centre Bi ions (and Ti ions).
- A detailed inspection of the possible variation of the crystal symmetry in the low temperature range.
- A detailed analysis of the low-frequency dynamics.
- Measurement of the dielectric tunability at microwave frequencies.
- Measurement of the hysteretic response at different frequencies.

Bibliography

1. Abe K., and Komatsu S. (1993) *Jpn. J. Appl. Phys*. **32**, L1157
2. Acikel B., Liu Y., Nagra A.S., Taylor T.R., Hansen P.J., Speck J.S., and York R.A. (2001) *IEEE MTT-S Int. Microwave Symp. Dig.*, **3**, 1191
3. Acikel B., Taylor T.R., Hansen P.F., Speck J.S., and York R.A. (2002) *IEEE Microw. and Wireless Compon. Lett.*, **12**, 237
4. Akimov I. A., Sirenko A. A., Clark A. M., Hao J.-H., and Xi X.X. (2000) *Phys. Rev. Lett.* **84**, 4625
5. Alford N.M., Penn S.J., Templeton A., Wang X., Gallop J.C., Klein N., Zuccaro C., and Filhol P. (1997) *IEE Colloquium on Electro-Technical Ceramics - Processing, Properties and Applications*, 9/1
6. Allendorf M.D., and Bernard C.(1997) *Electrochemical Society High Temperature in Chemical Vapour Deposition: Proceedings of the Fourteenth International Conference and EUROCVD-11* The Electrochemical Society, Paris, France
7. Ang C., and Yu Z. (1992) *J. Appl. Phys.* **71**, 6025
8. Ang C., Yu Z., Vilarinho P.M., and Baptista J.L. (1998) *Phys. Rev. B* **57**, 7403
9. Ang C., Scott J.F., Yu Z., Ledbetter H., and Baptista J.L. (1999a) *Phys. Rev. B* **59**, 6661
10. Ang C., Yu Z., Hemberger J., Lunkhemer P., and Loid A. (1999b) *Phys. Rev. B* ***59***, 6665
11. Ang C., Yu Z., Hemberger J., Lunkhemer P., and Loid A. (1999c) *Phys. Rev. B* **59**, 6670
12. Ang C., Bhalla A.S., Guo R., and Cross L.E. (2000a) *Appl. Phys. Lett.* **76**, 1929
13. Ang C., Yu Z., and Cross L.E. (2000b) *Phys. Rev. B* **62**, 228
14. Ang C., Guo R., Bhalla A.S., and Cross L.E. (2000c) *J. Appl. Phys.* **87**, 3937
15. Ang C., Yu Z., and Zhi J. (2000d) *Phys. Rev. B* **61**, 957
16. Ang C., and Yu Z. (2000e) *Phys. Rev. B* **61**, 11363
17. Ang C, Cross L.E., Yu Z., Guo R., Bhalla A.S., and Hao J.H. (2001a) *Appl. Phys. Lett.* **78,** 2754
18. Ang C., Yu Z., Cross L.E., Guo R., and Bhalla A.S. (2001b) *Appl. Phys. Lett.* **79**, 818
19. Ang C., and Yu Z. (2002) *J. Appl. Phys.* **91**, 1487
20. Ang C., and Yu Z. (2004) *Phys. Rev. B* **69**, 1741109
21. Astafiev K., Sherman V., Tagantsev A., Setter N., Petrov P., Kaydanova T., Ginley D., Hoffmann-Eifert S., Böttger U., and Waser R. (2003) *Integr. Ferroelectr.* **59**, 1371
22. Axe J.D., Harada J., and Shirane G. (1970) *Phys. Rev. B* **1**, 1227
23. Babbit R.W., Koscica T.E., and Drach W.C. (1992) *Microwave J.* **35**, 63
24. Ban Z.G., and Alpay S.P.(2002) *J. Appl. Phys.* **91**, 9288

25. Barrett J.H. (1952) *Phys. Rev.* **86**, 118
26. Bascieri C., Strieffer S.K., Kingon A.I., and Waser R. (1997) *J. Appl. Phys.* **82**, 2497
27. Bednorz J.G., and Müller K.A. (1984) *Phys. Rev. Lett.* **52**, 2289
28. Bell R.O., and Rupprecht G. (1963) *Phys. Rev.*, 129, 90
29. Benguigui L., and Bethe K. (1976) *J. Appl. Phys.***47**, 2787
30. Bernard O., Andrieux M., Poissonnet S., and Huntz A.-M. (2004) *J. Eur. Ceram. Soc.* **24**, 763
31. Bianchi U., Dec J., Kleemann W. and Bednorz J.G. (1995) *Phys. Rev. B* **51**, 8737
32. Bidault O., Maglione M., Actis M., Kchikech M., and Salce B. (1995) *Phys. Rev. B* **52**, 4191
33. Blanchard C.R. (1996) *The Chemical Educator: Atomic Force Microscopy*, Springer-Verlag New York, Inc.
34. Bragg W.L. (1913) *The diffraction of short electromagnetic waves by a crystal*, Proceedings of the Cambridge philosophical society, **17**, 43
35. Brame E.G. (1977) *Infrared and Raman spectroscopy*. New York: Marcel Dekker
36. Buchanan R.C. (1991) *Ceramic Materials for Electronics - Processing, Properties and Applications*, Marcel Dekker, New York
37. Budd K.D., and Payne D.A. (1989) *Inst. Phys. Conf. Ser.* **1**, 13
38. Bunshah R. F. (1982) *Deposition Technologies for Films and Coatings*, Noyes Pub. Park Ridge, New. Jersey, USA
39. Burke W.J., and Pressley R.J. (1971) *Solid State Commun.* **9**, 191
40. Burns G. (1985) *Solid State Physics* Academic Press, Inc., New York
41. Buseck R. (1992) *High-resolution transmission electron microscopy and associated techniques*. New York: Oxford University Press

42. Cady W.G. (1946) *Piezoelectricity* McGraw-Hill, New York
43. Canedy C.L., Li H., Alpay S.P., Salamanca-Riba L., Roytburd A.L., and Ramesh R. (2000) *Appl. Phys. Lett.* **77**, 1695
44. Carlson C.M., Rivkin T.V., Parilla P.A., Perkins J.D., Ginley D.S., Kozyrev A.B., Oshadchy V.N., and Pavlov A.S. (2000) *Appl. Phys. Lett.* **76**, 1920
45. Carter C.B., and Norton M.G. (2007) *Ceramic Materials: Science and Engineering*, Springer
46. Chang W., Horwitz J.S., Carter A.C., Pond J. M., Kirchoefer S.W., Gilmore C.M., and Chrisey D.B. (1999) *Appl. Phys. Lett.* **74**, 1033
47. Chu W.K., Mayer J.W., and Nicolet M.-A. (1978) *Backscattering Spectrometry*. Academic Press, New York
48. Chu W.K., and Liu J.R. (1996) *Mat. Chem. and Phys.* **46**, 183
49. Cochran W. (1960) *Adv. Phys.* **9**, 387

50. Cross L.E. (1994) *Ferroelectrics* **151**, 305

51. Daglish M., and Kemmitt T. (2000) *IPENZ Transactions* **27**, 21
52. Dalberth M.J., Stauber R.E., Price J.C., Rogers C.T., and Galt D. (1998) *Appl. Phys. Lett.* **72**, 507.
53. Defaÿ E., Wolozan D., Blanc J.-P., Serret E., Garrec P., Verrun S., Pellissier D., Delpech P., Guillan J., André B., Ulmer L., Aïd M., and Ancey P. (2007) *Solid State Electronics* **51** 1624
54. De Flaviis F., Alexopoulos N.G., and Stafsudd O.M. (1997) *IEEE T. Microw. Theory* **45**, 963
55. Dey S.K., Budd K.D., and Payne D.A. (1988) *IEEE Trans. UFFC* **35**, 80
56. Dietz G.W., Antpöhler W., Klee M., and Waser R.J. (1995) *Appl. Phys*. **78**, 6113
57. Dietz G.W., and Waser R. (1997) *Thin Solid Films* **229**, 53
58. Digital Instruments (2000) Veeco Metrology Group *Scanning Probe Microscopy* Training notebook, Version 3.0
59. De Araujo C.P., and Taylor G.W. (1991) *Integr. Ferroelectr.* **116**, 215
60. De Araujo C.P., Scott J.F., and Taylor G.W. (1996) *Ferroelectric Thin Films: Synthesis and Basic Properties*, Gordon and Breach, Amsterdam
61. Dec J., Kleemann W., and Westwanski B. (1999) *J. Phys.: Condens. Matter.* **11**, L379

62. Eason R. (2006) *Pulsed laser deposition of thin films: applications-led growth of functional materials*, Wiley-Interscience
63. Ebelmen J.J. (1846) *Untersuchungen über die Verbindungen der Borsäure und Kieselsäure mit Aether*, Annalen der Chemie und Pharmacie **57**, 319
64. Emelyanov A.Y., Pertsev N.A., and Kholkin A.L. (2002) *Phys.Rev.B* **66**, 214108
65. Eriksson A., Deleniv A., and Gevorgian S. (2003) *J. Appl. Phys.* **93**, 2848

66. Fedorov I., Železný V., Petzelt J., Trepakov V., Jelínek M., Trtík V., Černanský M., and Studnička V. (1998) *Ferroelectrics* **208-209**, 413
67. Feldman L.C., Mayer J.W., and Picraux S.T. (1982) *Materials Analysis by Ion Channeling*, Academic Press
68. Feldman L.C., and Mayer J.W. (1986) *Fundamentals of Surface and Thin Film Analysis*, Prentice Hall
69. Ferraro J.R., and Nakamoto K. (1994) *Introductory Raman spectroscopy*. Boston: Academic Press
70. Findikoglu A.T., Doughty C., Anlage S.M., Li Qi, Xi X.X., and Venkatesana T. (1993) *Appl. Phys. Lett.* **63**, 3215
71. Findikoglu A.T., Jia Q.X., Wu X.D., Chen G.J., Venkatesan T., and Reagor D. (1996) *Appl.*

Phys. Lett. **68**, 1651

72. Fleury P.A., and Worlock J.M. (1968a) *Phys. Rev*. **174**, 613
73. Fleury P. A., Scott J. F., and Worlock J. M. (1968b) *Phys. Rev. Lett.* **21**, 16
74. Forsbergh P.W. (1953) *Phys. Rev*. **93**, 686
75. Franssila S. (2004) *Introduction to microfabrication*, John Wiley and Sons
76. Frenzel C., and Hegenbarth E. (1974) *Phys. Status Solidi A* **23**, 517
77. Frölich H. (1949) *Theory of Dielectrics* Oxford: Clarendon Press
78. Fuchs D., Schneider C.W., Schneider R., and Rietscel H. (1999) *J. Appl. Phys.* **85**, 7362
79. FUJITSU (2005) FRAM Guide Book

80. Gardiner, D.J. (1989). *Practical Raman spectroscopy*. Springer-Verlag
81. Gaucher P., Hector J., and Kurfiss J.C. (1995) *Organically modified sol-gel precursors for ferroelectric deposition by spin coating, Science and Technology of Electroceramic Thin Films*, Kluwer Academic Publishers
82. Gim Y., Hudson T., Kwon C., Findikoglu A.T., Gibbons B.J., Park B.H., and Jia Q.X. (2000) *Appl. Phys. Lett.* **77**, 1200
83. Gevorgian S., Carlsson E., Linnér P., Kollberg E., Vendik O., and Wikborg E. (1996) *IEEET Transactions on microwave theory and techniques* **44**, 1738
84. Gevorgian S. Eriksson A.; Deleniv A., and Pandey D. (2002) *J. Appl. Phys.* **92**, 6165
85. Goldstein J.I. (1992) *Scanning electron microscopy and X-ray microanalysis*, Plenum, New York
86. Goldstein J., Newbury D.E., Echlin P., Lyman C.E., Joy D.C., Lifshin E., Sawyer L., and Michael J.R. (2003) *Scanning Electron Microscopy and X-Ray Microanalysis,* Springer
87. Gossard A.C., Petroff P.M., Weigmann W., Dingle R., and Savage A. (1976) *Appl. Phys. Lett.* **29**, 323
88. Grüuner G., ed. *Millimeter and Submillimeter Wave Spectroscopy of Solids*. Springer-Verlag, Berlin, Heidelberg (1998)
89. Guinier A., and Fournet G. (1955) *Small-angle Scattering of X-rays,* John Wiley and Sons, New York
90. Gupta S., and Katiyar R.S. (2001) *J. Raman Spectrosc*. **32**, 885
91. Guzhva M.E., Lemanov V.V., and Markovin P.A. (2001) *Fiz. Tverd. Tela* **43**, 2058 (in Russian). English translation: *Phys. Solid State* **43**, 2146

92. Haeni J.H., Irvin P., Chang W., Uecker R., Reiche P., Li Y.L., Choudhury S., Tian W., Hawley M.E., Craigo B., Tagantsev A.K., Pan X.Q., Streiffer S.K., Chen L.Q., Kirchoefer S.W., Levy J., and Schlom D.G. (2004) *Nature* **370**, 758
93. Hauk V., and Macherauch E. (1987) *Residual Stresses in Science and Technology*,

Proceedings of the First International Conference on Residual Stresses, DGM Informationsgesellschaft mbH, Oberursel

94. He J.Q., Regnery S., Jia C.L., Qin Y.L., Fitsilis F., Ehrhart P., Waser R., Urban K., and Wang R.H. (2002) *J. Appl. Phys.* **92**, 7200
95. He J.Q., Jia C.L., Vaithyanathan V., Schlom D.G., Schubert J., Gerber A., Kohlstedt H.H., and Wang R.H. (2005) *J. Appl. Phys.* **97**, 104921
96. Hemberger J., Lunkhemer P., Viana R., Bohmer R., and Loidl A. (1995) *Phys. Rev. B* **52**, 13159
97. Hemberger J., Nicklas M., Viana R., Lunkenheimer P., Loidl A., and Böhmer R. (1996) *J. Phys.: Condens. Matter.* **8**, 4673
98. Hirata T., Ishioka K., and Kitajima M. (1996) *J. Solid State Chem.* **124**, 353
99. Hirano T., Taga M., and Kobayashi T. (1993) *Jpn. J. Appl. Phys.* **32**, L1760
100. Hodak S.K., and Rogers C.T. (2008) *Microelectronic Eng.* **85**, 444
101. Hofman W, Hoffmann S., and Waser R. (1997) *Thin Solid Films* **305**, 66
102. Holland L. (1956) *Vacuum deposition of thin films*. Wiley, New York
103. Hwang C.S., Park S.O., Cho H.J., Kang C.S., Kang H.K., Lee S., and Lee M.Y. (1995) *Appl. Phys. Lett.* **67**, 2819
104. Hyun S., and Char K. (2001) *Appl. Phys. Lett.* **79**, 254
105. Hünnefield H., Rütt U., Schneider J.R., and Kapphan S. (1998) *J. Phys.: Condens. Mat.* **10**, 6453

106. Ibach H., and Lüth H. (1993) *Solid-State Physics*, Springer, Berlin
107. Iguchi E., and Lee K.J. (1993) J. Mater. Science 28, 5809
108. Ikeda K., Kobayashi K., Ohta K., Kondo R., Suzuki T., and Fujimoto M. (2003) *IEEE Trans. Magnetics* **39**, 3057
109. Inoue T., Noriaki S., Kamimae J., Eguchi K. and Arai H. (1991) *Solid State Ionics* **48**, 283
110. Ishidate T., Abe S., Takahashi T., and Mori N. (1997) *Phys. Rev. Lett.* **78**, 2397
111. Itoh T., Lee C., Chu J., and Suga T. (1997) *IEEE 10th Annu. Int. Workshop MEMS'97* IEEE, New Jersey
112. Itoh M., Wang R., Inaguma Y., Yamaguchi T., Shan Y.-J., and Nakamura T.(1999) *Phys. Rev. Lett.* **82**, 3540
113. Iwabuchi M., and Kobayashi T. (2004) *J. Appl. Phys.* **75**, 5295

114. Jaffe B., Cook W.R.(Jr.), Jaffe H. (1971) *Piezoelectric Ceramics*, Academic Press, London
115. Jain M., Karan N.K., Katiyara R.S., Bhalla A.S., Miranda F.A., and Van Keuls F.W. (2004) *Appl. Phys. Lett* **85**, 275
116. James A.R., and Xi X.X. (2002) *J. Appl. Phys.* **92**, 6149

117. Jenkins R., and Snyder R. L. (1996) *Introduction to X-ray Powder Diffractometry*, John Wiley and Sons, New York
118. Jia Q., Miranda F.A., Oates D.E., and Xi X.X. (2000) *Materials for Tunable RF and Microwave Devices*. Materials Research Society
119. Johnson D.W., Cross L.E., and Hummel F.A. (1970) *J. Appl. Phys.* **41**, 2828
120. Joshi P.C., and Krupanidhi S.B. (1993) *J. Appl. Phys.* 73, 7627

121. Kaene S.P, Schmidt S., Jiwei Lu, Romanov A.E., and Stemmer S. (2006) *J. Appl. Phys*. **99**, 033521
122. Kamalasanan M.N, Kumar D.N., and Chandra S. (1993) *J. Appl. Phys.* **74**, 679
123. Karaki T., Du J., Fujii T., and Adachi M. (2002) *Jap. J. Appl. Phys.* **41**, 6761
124. Kawada Y., and Fujimoto M. (1990) *Jap. J.Appl. Phys*. **29**, L126
125. Keane S.P., Schmidt S., Lu J., Romanov A.E., and Stemmer S. (2006) *J. Appl. Phys.* **99**, 033521
126. Keis V., Kozyrev A., Khazov M., Sok J., and Lee J. (1998) *Electron. Lett.* **34**, 1107
127. Kennedy B.J., Howard C.J., and Chakoumakos B.C. (1999) *J. Phys.: Condens. Matter.* **11**, 1479
128. Kiat J.M., and Roisnel T. (1996) *J. Physics: Condens. Matter.* **8**, 3471
129. Kingon A. (2006) *Nature Materials* **5**, 250
130. Kityk A.V., Schranz W., Sondergeld P., Havlik D., Salje E.K.H., and Scott J.F. (2000) *Phys. Rev. B* **61**, 946
131. Klein L.C. (1994) *Sol-Gel Optics Processing and Application* Kluwer Academic Publishers, London
132. Kleemann W., and Schremmer H. (1989) *Phys. Rev. B* **40**, 7428
133. Kleemann W., Dec J., Wang Y.G., Lehnen P., and Prosandeev S.A. (2000) *J. Phys. Chem. Solids* **61**, 167
134. Knauss L.A., Pond J.M., Horwitz J.S., Chrisey D.B., Mueller C.H., and Treece R. (1996) *Appl. Phys. Lett.* **69**, 25
135. Knauss L.A., Horwitz J.S., Pond J.M., Kirchoefer S.W., Chrisey D.B., Mueller C.H., and Treece R. (1997) *Integr. Ferroelectr.* 15, 173
136. Kotecki D.E., Baniecki J.D., Shen H., Laibowitz R.B., Saenger K.L., Lian J.J., Shaw T.M., Athavale S.D., Cabral C.(Jr), Duncombe P.R., Gutsche M., Kunkel G., Park Y.-J., Wang Y.-Y., and Wise R. (1999) *IBM J. Res. and Dev.* **43**, 367
137. Kozyrev A.B., Samoilova T.B., Golovkov A.A., Hollmann E.K., Kalinikos D.A., Loginov V.E., Prudan A.M., Soldatenkov O.I., Galt D., Mueller C.H., Rivkin T.V., and Koepf G.A. (1998) *J. Appl. Phys.* **84**, 3326
138. Kozyrev A., Ivanov A., Prudan A., Soldatenkov O., Hollmann E., Loginov V., Ginley D.S.,

and Rivkin T. (1999) *Integr. Ferroelectr.* **24**, 287

139. Kozyrev A., Osadchy V., Pavlov A., and Sengupta L. (2000) *IEEE MTT-S Digest*, 1355
140. Kvyatkovskii O.E. (2002) *Fiz. Tverd. Tela* **44**, 1087 (in Russian). English translation: *Solid State Phys.* **44**, 1135
141. Kvyatkovskii O.E. (2005) *Ferroelectrics* **314**, 143
142. Kužel P., and Petzelt J. (2000) *Ferroelectrics* **239**, 949
143. Lacerda-Arôso M.T., Ribeiro J.L., Chaves M.R., Almeida B.G., and Almeida A. (2001) *J. Phys.: Condens. Matter.* **13**, 2615
144. Lakeman C.D.E., and Payne D.A. (1992) *J. Am. Ceram. Soc.* **75**, 3091
145. Lancaster M.J., Powell J., and Porch A. (1998) *Supercund. Sci. Technol.*, **11**, 1323
146. Landolt-Börnstein in *Numerical data and functional relationships in science and technology*, New series group III, Crystal and solid state physics (1981) Springer-Verlag, Berlin
147. Last J.T. (1957) *Phys. Rev.* **105**, 1740
148. Lau W.S. (1999) *Infrared characterization for microelectronics*. World Scientific
149. Ledentsov N.N. (1999) *Growth Processes and Surface Phase Equilibria in Molecular Beam Epitaxy*, Springer
150. Lemanov V.V., Smirnova E.R., Syrikov P.P., and Tarakanov E.A. (1996) *Phys. Rev. B* **54**, 3151
151. Lemanov V.V., Smirnova E.R., and Tarakanov E.A. (1997) *Fiz. Tverd. Tela* **39**, 714
152. Lemanov V.V., Sotnikov A.V., Smirnova E.P., Weihnacht M., and Kunze R. (1999) *Solid State Commun.* **110**, 611
153. Lemanov V.V., Sotnikov A.V., Smirnova E.P., and Weihnacht M. (2002) *Solid State Phys.* **44**, 1948
154. Lemanov V.V. (2004) *Ferroelectrics* **302**, 169
155. Lesaicherre P-Y., Yamamichi S., Yamaguchi H., Takemura K., Watanabe H., Tokashiki K., Satoh K., Sakuma T., Yoshida M., Ohnishi S., Nakajima K., Shibahara K., Miyasaka Y., and Ono H. (1994) *IEEE*
156. Lewis I.R., and Edwards H.G.M. (2001) *Handbook of Raman Spectroscopy: from the research laboratory to the process line*, Marcel Deccer, Inc.
157. Li H.-C., Si W., West A.D., and Xi X.X. (1998a) *Appl. Phys. Lett.* **73**, 190
158. Li H.-C., Si W., West A.D., and Xi X.X. (1998b) *Appl. Phys. Lett.* **73**, 464
159. Li H., Roytburd A.L., Alpay S.P., Tran T.D., Salamanca-Riba L., and Ramesh R. (2001) *Appl. Phys. Lett.* **78**, 2354
160. Lide D. (2000) *Handbook of chemistry and physics* CRC Press LLC
161. Lin J.N., and Wu T.B. (1990) *J. Appl. Phys.* **68**, 0985

162. Lines M.E., and Glass A.M. (1977) *Principles and Applications of Ferroelectric and Related Materials* Clarendon Press, Oxford
163. Lippmaa M., Nakagawa N., Kawasaki M., Ohashi S., Inaguma Y., Itoh M., and Koinuma H. (1999) *Appl. Phys. Lett*., **74**, 3543
164. Linz A. (1953) *Phys. Rev.* **91**, 753
165. Lyddane R.H., Sachs R.G., and Teller E. (1941) *Phys. Rev.* **59**, 673
166. Lyons B., and Fleury P.A. (1977) *Solid State Commun.* **23**, 477
167. Lytle F.W. (1964) *J. Appl. Phys.* **35**, 2212

168. Majumder S.B., Jain M., Martinez A., Van Keuls F.W., Miranda F.A., and Katiyar R.S. (2001) *J. Appl. Phys.* **90**, 896
169. Matthes B., Tomandl G., and Werner G. (1999) *J. Europ. Ceram. Soc.* **19**, 1387
170. Mattox D.M. (1998) *Handbook of Physical Vapor Deposition (PVD)* Processing: Film Formation, Adhesion, Surface Preparation and Contamination Control, Pub. William Andrew Inc.
171. Miranda F.A., VanKeuls F.W., Romanofsky R.R., Mueller C.H., Alterovitz S., and Subramanyam G. (2001) *Integr. Ferroelectr.* **42**, 131
172. Mitsui T., and Westphal W.B. (1961) *Phys. Rev.* **124**, 1354
173. Mizaras R., and Loidl A. (1997) *Phys. Rev. B* **56**, 10726
174. Moeckly B.H., and Zhang Y. (2001) *IEEE T. Appl. Supercond.*, **11**, 450
175. Moeckly B.H., Peng L.S.-J., and Fischer G.M. (2003) *IEEE T Appl. Supercond.* p.13712
176. Morita T. (2003) *Sens. Actuators* **103**, 291
177. Morito K., Suzuki T., and Fujimoto M. (*2001*) *Jpn. J. Appl. Phys* **40**, *1310*
178. Murarka S.P. (1997) *Microelectronic Eng.* **37**/**38**, 29
179. Müller K.A. (1959) *Phys. Rev. Lett.* **2**, 341
180. Müller K.A., and Berlinger W. (1971) *Phys. Rev. Lett.* **26**, 13
181. Müller K.A., and Burkard H. (1979) *Phys. Rev. B* **19**, 3595

182. Nagarajan V., Jenkins I.G., Alpay S.P., Li H., Aggarwal S., Salamanca-Riba L., Roytburd A.L., and Ramesh R. (1999) *J. Appl. Phys*. **86**, 595
183. Nakagawara O., Kobayashi M., Yoshino Y., Katayama Y., Tabata H., and Kawai T. (1995) *J. Appl. Phys*. **78**, 7226
184. Nes O.M., Müller K.A., Suzuki T., and Fossheim F. (1992) *Europhys. Lett.* **19**, 397
185. Neville R.C., Hoenstein B., and Mead C.A. (1972) *J. Appl. Phys*. **43**, 2124
186. Noyan C., and Cohen J.B. (1987) *Residual stress determination by Diffraction-Measurement and Interpretation*, Springer-Verlag, New York

187. Nuzhnyy D., Petzelt J., Kamba S., Yamada T., Tyunina M., Tagantsev A.K., Levoska J., and Setter N. (2009) *J. Electrocer.* **22**, 297

188. Ohring M. (1992) *The materials science of the thin films*, Academic Press., Inc.
189. Okai B., and Yoshimoto J. (1975) *J. Phys. Soc. Japan.* **39**, 162
190. Ostapchuk T., Petzelt J., Železný V., Pashkin A., Pokorný J., Drbohlav I., Kužel R., Rafaja D., Gorshunov B. P., Dressel M., Ohly C., Hoffmann-Eifert S., and Waser R. (2002) *Phys. Rev. B* **66**, 235406-1
191. Ota K., Iiauka F., Satomi M., Yasuda M., Nakajima K., Ogino T., and Fujimoto M. (2002) *J. Ceram. Soc. Japan* **110**, 436
192. Oura K., Lifshits V.G., Saranin A.A., Zotov A.V., and Katayama M. (2003) *Surface Science: An Introduction*. Berlin: Springer-Verlag

193. Park B.H., Peterson E.J., Jia Q.X., Lee J., Zeng X., Si W., and Xi X.X. (2001) *Appl. Phys. Lett.* **78**, 533
194. Parker L.H., and Tasch A.F. (1990) *IEEE Cir. Dev. Mag.* **6**, 17
195. Parker C.B., Maria J.-P., and Kingon A.I. (2002) *Appl. Phys. Lett.* **81**, 340
196. Paufler P., Bergk B., Reibold M., Belger A., Pätzke N., and Meyer D.C. (2006) *Solid State Sciences* **8**, 782
197. Penn S.J., McAlford N., Templeton A., Klein N., Gallop J.C., Filhol P., and Wang X. (1997) *IEE Colloquium on Advances in Passive Microwave Components*, 6/1
198. Peng D., and Meng Z.(2003) *Microelectronic Engineering* **66**, 631
199. Pertsev N.A., Zembilgotov A.G., and Tagantsev A.K. (1998) *Phys. Rev. Lett.* **80**, 1988
200. Pertsev N., Zembilgotov A.G., Hoffman S., Waser R., and Tagantsev A. (1999) *J. Appl. Phys*. **85**, 1698
201. Pertsev N.A., Kaoukhar V.G., Wasser R., and Hoffman S. (2000a) *Appl. Phys. Lett.* **77**, 2596
202. Pertsev N.A., Tagantsev A.K., and Setter N. (2000b) *Phys. Rev. B* **61**, R825
203. Pertsev N.A., Tagantsev A.K., and Setter N. (2002) *Phys. Rev. B* **65**, 19901(E)
204. Petrov P. Kr., Ivanov Z., and Gevorgian S. (2000) *IEEE European Microwave Conference*, **1**
205. Petzelt J., Ostapchuk T., Gregora I., Rychetsky I., Hoffmann-Eifert S., Pronin A.V., Yuzyuk Y., Gorshunov B.P., Kamba S., Bovtun V., Pokorny J., Savinov M., Porokhonskyy V., Rafaja D., Vanek P., Almeida A., Chaves M.R., Volkov A.A., Dressel M., and Waser R. (2001) *Phys. Rev. B* **64**, 184111-1
206. Poindexter E., and Giardini A.A. (1958) *Phys. Rev.* **110**, 1069
207. Porokhonskyy V., Pashkin A., Bovtun V, Petzelt J., Savinov M., Samoukhina P., Ostapchuk T., Pokorný J., Avdeev M., Kholkin A., and Vilarinho P. (2004) *Phys. Rev. B* **69**, 144104

208. Ranjan R., Pandey D., and Lalla N.P. (2000) *Phys. Rev. Lett.* **84**, 3726
209. Ranjan R., and Pandey D. (2001) *J. Phys. Cond. Matt.* **13**, 4239
210. Redfern S.A.T. (1996) *J. Phys.: Condens. Matter.* **8**, 8267
211. Reed G.T., and Knights A.P. (2004) *Silicon Photonics: An Introduction*, John Wiley and Sons
212. Reimer L. (1997) *Transmission electron microscopy: physics of image formation and microanalysis*. Berlin: Springer
213. Rimai L., and deMars G.A. (1962) *Phys. Rev.* **127**, 0702
214. Riste T., Samuelsen E.J., Onnes K., and Feder J. (1971) *Solid State Communications* **9**, 1455
215. Rohrer H. (1996) *Microelectronic Eng.* **32**, 5
216. Rossetti G.A., Cross L.E., and Kushida K. (1991) *Appl. Phys. Lett.* **59**, 2524
217. Rupprecht G., Bell R.O., and Silverman B.D. (1961) *Phys. Rev.* **123**, 97

218. Sakka J. (2006) *Sol-Gel Sci. Techn.* **37**, 135
219. Saifi M.A., and Cross L.E. (1970) *Phys. Rev. B* **2**, 677
220. Sakamoto T., Funabashi H., Ohta K., Nakagawa T., Kawai N.J., Kojima T., and Bando Y. (1985) *Superlattices Microstruct.* **1**, 347
221. Samara G.A. (1966) *Phys. Rev.* **151**, 378
222. Samara G.A., Sakudo T., and Yoshimitu K. (1975) *Phys. Rev. Lett.* **35**, 1767
223. Scanavi G.I., Ksendzov I.J., Trigubenko V.A., and Prokhvatilov V.G. (1957) *Zh. Eksp. Teor. Fiz.* **33**, 320 [*Sov. Phys. JETP* (1958) **6**, 250]
224. Scott A.W. (1993) *Understanding Microwaves*, Wiley, New York
225. Scott J.F. (2000) *Ferroelectric Memories* Springer, Berlin
226. Schimizu T. (1997) *Sol. State Commun.* **102**, 523
227. Schuegraf K.K. (1988) *Handbook of thin-film deposition processes and techniques* Noyes, Park Ridge
228. Schwartz R. W. (1997) *Chem. Mater.* **9**, 2325
229. Schwartz R.W., Schneller T., and Waser R. (2004) *Comptes Rendus Chimie* **7**, 433
230. Servoin J.L., Luspin Y., and Gervis F. (1980) *Phys. Rev. B* **22**, 5501
231. Setter N., Damjanovic D., Eng L., Fox G., Gevorgian S., Hong S., Kingon A., Kohlstedt H., Park N.Y., Stephenson G.B., Stolitchnov I., Taganstev A.K., Taylor D.V., Yamada T., and Streiffer S. (2006) *J. Appl. Phys.* **100**, 051606
232. Shannon R.D. (1976) *Acta Crystallog. A* **32**, 751
233. Shannon R.D. (1993) *J. Appl. Phys.* **73**, 348
234. Shaw T.M., Suo Z., Huang M., Liniger E., Laibowitz R.B., and Baniecki J.D. (1999) *Appl. Phys. Lett.* **75**, 2129

235. Sherman V., Astafiev K., Setter N., Tagantsev A., Vendik O., Vendik I., Hoffmann-Eifert S., Bottger U., and Waser R. (2001) *IEEE Microw. and Wireless Compon. Lett.* **11**, 407
236. Shirane G., and Yamada Y. (1969) *Phys. Rev.* **177**, 858
237. Sirenko A.A., Akimov I.A., Fox J.R., Clark A.M., Li H.C., Si W., and Xi X.X. (1999) *Phys. Rev. Lett.* **82**, 4500
238. Sirenko A.A., Akimov I.A., Bernhard C., Clark A.M., Hao J.-H., Weidong S., and Xi. X.X. (2000a) *AIP Conf. Proceed.* **535**, 201
239. Sirenko A.A., Bernhard C., Golnik A., Clark A.M., Hao J., Si W., and Xi X.X. (2000b) *Nature* **404**, 373
240. Slater J.C. (1950) *Phys. Rev.* **78**, 748
241. Smirnova E.P., Sotnikov A.V., Kunze R., Weihnacht M., Kvyatkovskii O.E. and Lemanov V.V. (2005) *Solid State Commun.* **133**, 421
242. Smolenskii G.A. (1970) *J. Phys. Soc. Japan* **28**, Suppl., 26
243. Smolenskii G.A., Isupov V.A., Agranovskaya A.A., and Popov S.N. (1961) *Fiz. Tv. Tela* **2**, 2906 [(1961) *Sov. Phys. Solid State* **2**, 2584]
244. Smolenskii G.A. (1984) editor, *Ferroelectrics and Related Materials.* Gordon and Breach Science Publishers, New York
245. Somiya Y., Bhalla A.S., and Cross L.E. (2001) *Int. J. Inorg. Mater.* **3**, 709
246. Speck J.S., and Pompe W. (1994) *J. Appl. Phys.* **76**, 466
247. Speck J.S., Daykin A.C., Seifert A., Romanov A.E., and Pompe W. (1995) *J. Appl. Phys*. **78**, 1696
248. Sporn D., Merklein S., Grond W., Seifert S., Wahl S., and Berger A. (1995) *Microelectronic Eng.* **29**, 161
249. Streiffer S.K., Basceri C., Parker C.B., Lash S.E., and Kingon A.I. (1999) *J. Appl. Phys.* **86**, 4564
250. Stuart B.H. (2004) *Infrared spectroscopy: fundamentals and applications*. Chichester: John Wiley and Sons
251. Suzuki T., Nishi Y., and Fugimoto M. (2000) *Jpn. J. Appl. Phys.* **39**, 192
252. Suzuki T., Morito K., and Iwazaki Y. (2005) *Integr. Ferroelectr.* **76**, 47
253. Szot K., Speier W., Bihlmayer G., and Waser R. (2006) *Nature Materials* **5,** 312

254. Tagantsev A.K. (1993) *In Ferroelectric Ceramics,* eds. Setter N., and Colla E.L. Basel: Birkhäuser
255. Tagantsev A.K., Pertsev N.A., Muralt P., and Setter N. (2001) *Phys. Rev. B* **65**, 012104
256. Tagantsev A.K., Sherman V.O., Astafiev K.F., Venkatesh J., and Setter N.J. (2003) *Electroceramics*, **11**, 5
257. Takashima H., Kasai N., and Shoji A. (2002) *Jpn. J. Appl. Phys.*, Part 2 **41**, L1062

258. Takashima H., Wang R., Kasa N.I., Shoji A, and Itoh M. (2003) *Appl. Phys. Lett.* **83**, 2883
259. Taylor T.R., Hansen P.J., Acikel B., Pervez N., York R.A., Streiffer S.K., and Speck J.S. (2002) *Appl. Phys. Lett.* **80**, 1978
260. Taylor T.R., Hansen P.J., Pervez N., Acikel B., York R.A., and Speck J.S. (2003) *J. Appl. Phys*. 94, 3390
261. Thomas G. (1979) *Transmission electron microscopy of materials*. New York. John Wiley
262. Thomas R., Dube D.C., Kamalasannan M.N., Chandra S., and Bhalla A.S. (1997) *J. Appl. Phys.* **82**, 4484
263. Tikhomirov O., Jiang H., and Levy J. (2002) *Phys. Rev. Lett.* **89**, 147601
264. Tkach A., Vilarinho P.M., and Kholkin A. (2004a) *Appl. Phys. A* **79**, 2013
265. Tkach A., Vilarinho P.M., and Kholkin A. (2004b) *Ferroelectrics* **304**, 917
266. Tkach A., Vilarinho P.M., and Kholkin A. (2005a) *Appl. Phys. Lett.* **86**, 172902
267. Tkach A., Vilarinho P.M., Kholkin A.L., Pashkin A., Samoukhina P., Pokorny J., Veljko S., and Petzelt J. (2005b) *J. Appl. Phys.* **97**, 044104
268. Tkach A., Vilarinho P.M., Senos A.M.R., and Kholkin A.L. (2005c) *J. Eur. Ceram. Soc.* **25**, 2769
269. Tkach A., Vilarinho P.M., and Kholkin A. (2006) *Acta Mater.* **54**, 5385
270. Tkach A., Vilarinho P.M., and Kholkin A. (2007a) *J. Appl. Phys.* **101**, 084110
271. Tkach A., Vilarinho P., Kholkin A., Reaney I., Pokorny J., and Petzelt J. (2007b) *Chem. Mater.* **19**, 6471
272. Tkach A., Okhay O., Vilarinho P., and Kholkin A. (2008) *J. Phys.: Condens. Matter.* **20**, 415224
273. Tosatti E., and Martoňák R. (1994) *Solid State Commun*. **92**, 167
274. Tse Y.Y., Koutsonas Y., Jackson T.J., Passerieux G., and Jones I.P. (2006) *Thin Solid Films* **515,** 1788
275. Tsuzuki K., and Torhi K. (1997) *J. Matter. Science Lett.* **16**, 1652
276. Tuttle B.A., and Schwartz R.W. (1996) *Mater. Res. Soc. Bull.* **6**, 49

277. Unoki H., and Sakudo T. (1967) *J. Phys. Soc. Japan* **23**, 546
278. Uwe H., Unoki H., Fujii Y., and Sakudo T. (1973) *Solid State Commun.* **13**, 737
279. Uwe H., and Sakudo T. (1976) *Phys. Rev. B* **13**, 271

280. Vacher R., Pelous J., Heanion B., Coddens G., Courtens E., and Müller K.A. (1992) *Europhys. Lett.* **17**, 45
281. Valasek J. (1920) *Phys. Rev.* **15**, 537
282. Valasek J. (1921) *Phys. Rev.* **17**, 475

283. Van Der Merwe J., Woltersdorf J., and Jesser W. (1986) *Mat. Science and Eng.* **81**, 33
284. Varadan V.K., Ghodgaonkar D.K., Varadan V.V., Kelly J.F., and Gilkerdas P. (1992) *Microwave J.* **35**, 116
285. Vendik O.G., Ter-Martirosyan L.T., Dedyk A.I., Karmanenko S.F., and Chakalov R.A. (1993) *Ferroelectrics*, **144**, 33
286. Vendik O.G., and Zubko S.P. (1997) *J. Appl. Phys*. **82**, 4475
287. Vendik O.G., Hollmann E.K., Kozyrev A.B., and Prudan A.M. (1999) *J. Supercond.* **12**, 325
288. Vendik O.G., and Zubko S.P. (2000) *J. Appl. Phys.* **88**, 5343
289. Venturini E.L., Samara G.A., Itoh M. and Wang R. (2004) *Phys. Rev. B* **69**, 184105
290. Viana R., Lunkenheimer P., Hemberger J., Böhmer R., and Loidl A. (1994) *Phys. Rev. B* **52**, 601
291. Viehland, D., Lang, S.J., Cross, L.E., and Wuttig, M. (1990) *J. Appl. Phys.* **68**, 2916
292. Vilarinho P. M., Rosenwaks Y., and Kingon A. (2005) *Scanning Probe Microscopy: Characterization, Nanofabrication and Device Application of Functional Materials*, Kluwer Academic Publishers, Netherlands
293. Vogt H. (1995) *Phys. Rev. B* **51**, 8046
294. Vugmeister B.E., and Glinchuk M.D. (1990) *Rev. Modern Phys*. **62**, 993
295. Wachtman J.B., and Haber R.A. (1993) *Ceramics films and coatings* Noyes Pub, New. Jersey, USA
296. Wang R., Inaguma Y., and Itoh M. (2000) *Phys. B* **284-288**, 1141
297. Waser R. (2003) *Nanoelectronics and Information Technology: Advanced Electronic Materials and Novel Devices*, Wiley-VHC CmbH and Co. KGaA, Weinheim
298. West P.E., and Starostina N. (2004) *Adv. Mat. and Proc.*, Feb., 35
299. West P.E. (2007) *Introduction to Atomic Force Microscopy,* Pacific Nanotechnology, Inc.
300. Williams D.B., and Carter C.B. (1996) *Transition Electron Microscopy: A Textbook for Material Science,* Plenum Press, New York
301. Withers P.J., and Bhadeshia H.K.D.H. (2001) *Mat. Science and Techn.* **17**, 355
302. Wooldridge I., Turner C.W., Warburton P.A. and Romans E.J. (1999) *IEEE T. Appl. Supercond.* **9**, 3220
303. Worlock J.M., and Fleury P.A. (1967) *Phys. Rev. Lett*. **19**, 1176
304. Wördenweber R., Hollmann E., Ali M., Schubert J., Pickartz G., and Lee T.K. (2007) *J. Eur. Ceram. Soc.* **27**, 2899
305. Wu H.-D., Zhang Z., Barnes F., Jackson C.M., A. Kain and Cuchiaro J.D. (1994) *IEEE T. Appl. Supercond.* **4**, 156
306. Wu J.S., Jia C.L., Urban K., Hao J.H., and Xi X.X. (2001) *J. Appl. Phys*. **89**, 5653

307. Xi X.X., Clark A.M., Hao J.H., and Si W. (1999) *Integr. Ferroelectr.* **24**, 239
308. Xi X.X., Li H.C., Si W.D., Sirenko A.A., Akimov I.A., Fox J.R., Clark A.M., and Hao J.H. (2000) *J. Electroceram.* **4**, 393
309. Xu Y. (1991) *Ferroelectric Materials and Their Application*, Elsevier Science Publisher, Amsterdam
310. Yamada T., Astafiev K., Sherman V., Tagantsev A., Muralt P., and Setter N. (2005a) *Appl. Phys. Lett.* **86**, 142904
311. Yamada T., Astafiev K., Sherman V., Tagantsev A., Su D., Muralt P., and Setter N. (2005b) *J. Appl. Phys.* **98**, 054105
312. Yi G.H., and Sayer M. (1991) *Amer. Cer. Soc. Bull.* **70**, 1173
313. York B., Nagra A., Speck J., Auciello O., and Streiffer S., *Thin Film Ferroelectrics: Deposition Methods and Applications*, Power Point Presentation from Argonne National Laboratories [available at http://my.ece.ucsb.edu/yorklab/Projects/ Ferroelectrics/IMS2000Workshop/Bob-oral.pdf]
314. Yu Z. (1997) *PhD Thesis*, University of Aveiro, Portugal
315. Yu Z., Ang C., Vilarinho P. M., Mantas P. Q., and Baptistat J. L. (1998) *J. Eur. Ceram. Soc.* **18**, 1613
316. Yu Z., Ang C., and Cross L.E. (1999) *Appl. Phys. Lett.* **74**, 3044
317. Yu Z., Ang C., Guo R., Bhalla A.S., and Cross L.E. (2002) *Appl. Phys. Lett.* **80**, 1034
318. Yu Z., and Ang C. (2003) *J. Matter. Sci.* **38**, 113
319. Zhang L., Kleemann W., and Zhong W.-L. (2002) *Phys. Rev. B* **66**, 104105
320. Zhao M., Yao X., Shi P., Wei X., Wu X., Ren W., and Lin P. (2008) *Ceram. Internation.* **34**, 997
321. Zhou C., and Newns D.M. (1997) *J. Appl. Phys.* **82**, 3081

List of Publications

1. **O. Okhay**, A. Wu, P.M. Vilarinho
   The influence of Mg on the properties of $SrTiO_3$ thin films
   Journal of the European Ceramic Society, Vol.25, 2005, p.3079.

2. **O. Okhay**, V.M.X. Bergano, A. Wu and P.M. Vilarinho
   Bi effect on the microstructure and dielectric properties of $SrTiO_3$ thin films
   Advanced Materials Forum III, Vol.514, 2006, p.245.

3. **O. Okhay**, A. Wu, P.M. Vilarinho, I.M. Reaney, A.R.L. Ramos, E. Alves, J. Petzelt, and J. Pokorny
   Microstructural studies and electrical properties of Mg-doped $SrTiO_3$ thin films
   Acta Materialia, Vol.55, 2007, p.4947.

4. V.A. Trepakov, M.E. Savinov, **O. Okhay**, A. Tkach, P.M. Vilarinho, A.L. Kholkin, I. Gregora, and L. Jastrabik
   Dielectric permittivity and Cr^{3+} impurity ion probe luminescence in $SrTiO_3$ sol–gel ceramics
   Journal of the European Ceramic Society, Vol.27, 2007, p.3705.

5. A. Tkach, **O. Okhay**, P.M. Vilarinho, and A.L. Kholkin
   High dielectric constant and tunability of strontium titanate ceramics modified by chromium doping
   Journal of Physics: Condensed Matter, Vol.20, 2008, p.415224.